A medieval cemetery sheds light on Jewish history p. 940

The reasons why Siberia is catching fire pp. 944 & 1005

Harmonize copyright to facilitate research p. 951

Science

$15
2 DECEMBER 2022
science.org

AAAS



DEEP HEAT

Imaging the magma under the Yellowstone supervolcano

pp. 945 & 1001

TRILLIONS OF MICROBES ONE ESSAY

The NOSTER *Science* Microbiome Prize is an international prize that rewards innovative research by investigators who have completed their terminal degree in the last 10 years and are working on the functional attributes of microbiota. The research can include any organism with the potential to contribute to our understanding of human or veterinary health and disease, or to guide therapeutic interventions. The winner and finalists will be chosen by a committee of independent "scientists" chaired by a senior editor of *Science*. The top prize includes a complimentary membership to AAAS, an online subscription to *Science*, and USD 25,000. Submit your research essay today.



Jennifer Hill, Ph.D.
2022 Winner

NOSTER | Science
MICROBIOME
PRIZE

Apply by 24 January 2023 at www.science.org/noster

Sponsored by Noster Inc

AP-ISI: A measure of sustainability promising prosperity and better opportunities in the Asia-Pacific region

The human race faces unprecedented challenges to address the rapid deterioration of the world's environmental quality and the depletion of its natural resources. At stake are the lives and health of many people as well as the potential for global economic growth.

The Asia-Pacific Region is going through rapid urbanization along with thriving industrial development. Sustainable growth is, therefore, a common concern for the survival of its cities, as only developmental plans embracing the sustainability of the region's industries will ensure a bright future balancing economic, social, and ecological development.

"Industrial sustainability is more important than ever, and cities not considering this first will put their future at peril," says Xue Lan, a distinguished professor at Tsinghua University.

To evaluate the current and future impact of regional industries on the ecological environment, the Center for Industrial Development and Environmental Governance (CIDEG) of Tsinghua University and the Asia-Pacific Economic Cooperation (APEC) China Business Council jointly launched the Asia-Pacific Industrial Sustainability Index (AP-ISI). The final goal of the AP-ISI is to help economies in the Asia-Pacific region balance sustainability and economic development.



Xue Lan and his collaborators launched the Asia-Pacific Industrial Sustainability Index, a yearly measurement of sustainability in the region.

Sustainability in the Asia-Pacific region

The Asia-Pacific region is vast and includes different levels of development. However, there is a broad consensus on the critical elements of sustainable development, such as green economic growth, social justice, environmental protection, and reduction of greenhouse gas emissions. Based on these general agreements, the AP-ISI evaluates industrial sustainability in five dimensions: driving forces, pressures, states, impacts, and responses. As economies in the same category tend to have similar experiences and challenges, the index divides economies into three types: major economy, emerging economy, and island economy. Nevertheless, for cities from emerging economies, the index also weighs in the extra challenges of trading off between economic growth and environmental impacts and implications due to political stability. Generally, the AP-ISI reflects a comprehensive and in-depth analysis of industrial sustainability and suggests areas of concern that need attention in order to support development opportunities for different regions and consequently to promote global development and improved quality of life in this region and worldwide.

The Asia- Pacific Industrial Sustainability Index 2022

The AP-ISI 2022 evaluates the industrial sustainability performance of 35 cities (regions) in the Asia-Pacific region from 2017 to 2020. The index highlights the top 10 cities (regions) for each first-level indicator and the top 10 cities (regions) for comprehensive ranking. Based on the different parameters analyzed, the cities from major economies maintain a leading position in driving forces, with a strong presence in the top-ranking levels for most indicators. However, cities from emerging and island economies also find their way to the top in terms of carrying capacity to tackle environmental stress. "It is still hard to undo the damage and waste done from all these social, economic, and political factors. Therefore, some emerging and island economies may perform much better than their developed counterparts. We can also see that capital is flowing into emerging markets that have not yet been exhaustively exploited for their resources and environment. This, of course, is both an opportunity and a challenge for these latecomers," says Lan, also a professor and cochair of the CIDEG academic committee and the lead specialist for the Sustainable China Industry Development Initiative 2022.

Recommendations for a brighter future

The AP-ISI and its global report aim to inform the public, businesses, and local governments about the progress of industrial sustainability in the Asia-Pacific region. Its ultimate goal is to raise public awareness of the need to balance industrial development and sustainability and empower residents' involvement in policy processes. The index will also help local governments evaluate their successes and challenges in promoting and achieving sustainable development. Finally, it can help identify regional and global industrial and sustainable development trends and guide the investment behaviors of businesses operating in the Asia-Pacific region and beyond.

Visit: www.science.org/content/resource/asia-pacific-industrial-sustainability-index-cities

Sponsored by

清华大学产业发展与环境治理研究中心
Center for Industrial Development and Environmental Governance
Tsinghua University

APEC China Business Council

IMAGE: © SAIMONSAILENT/SHUTTERSTOCK.COM; PHOTO: PROVIDED BY CIDEG

CONTENTS

2 DECEMBER 2022
VOLUME 378
ISSUE 6623



940

NEWS

IN BRIEF

932 News at a glance

IN DEPTH

934 Indictment of monkey importers could disrupt U.S. research
Alleged Cambodian smuggling ring poses dangers to wild macaques and the drug studies they're used in *By D. Grimm*

935 CRISPR is so popular even viruses may use it
Thousands of phages appear to have stolen the gene-cutting mechanism *By M. Leslie*

936 Pandemic accelerates 'GRExit'
Nearly all U.S. Ph.D. programs have dropped the standardized GRE exam as an admissions requirement *By K. Langin*

937 Europe pledges to launch Mars rover delayed by war
Replacing Russian launcher and lander means probe won't reach Mars until 2030
By D. Clery

938 Vaccines are in short supply amid global cholera surge
Climate change and pandemic may be fueling outbreaks *By K. Kupferschmidt*

939 New look at jaw fossil rewrites centuries-old bird history
Specimen flips evolutionary order of two key groups *By G. Vogel*

FEATURES

940 Meeting the ancestors
DNA from a medieval German cemetery opens a window on the history of today's largest Jewish population
By A. Curry
PODCAST

INSIGHTS

PERSPECTIVES

944 What set Siberia ablaze?
Shifting air currents and early snowmelt drove extreme Arctic fires from 2019 to 2021 *By G. Schaepman-Strub and J.-S. Kim*
REPORT p. 1005

945 What lies beneath Yellowstone?
There is more magma than previously recognized, but it may not be eruptible
By K. M. Cooper
REPORT p. 1001

947 Getting tougher in the ultracold
Certain alloys show exceptional toughness in a liquid helium environment
By P. Zhang and Z.-F. Zhang
RESEARCH ARTICLE p. 978

948 Active DNA demethylaiton damages DNA
Active DNA demethylation maintains enhancer activity in nonproliferating cells but can damage DNA
By I. F. López-Moyado and A. Rao
REPORT p. 983

949 Triggering rare HIV antibodies by vaccination
Clinical trial shows that an HIV vaccine can elicit rare antibodies, but there is more to do *By P. L. Moore*
RESEARCH ARTICLE p. 964

POLICY FORUM

951 Legal reform to enhance global text and data mining research
Outdated copyright laws around the world hinder research
By S. M. Fiil-Flynn et al.

BOOKS *ET AL.*

954 Religion in space
A sense of divine entitlement pervades private space colonization efforts
By R. D. Launius

955 Meet the Huxleys
A historian traces the scientific family's complicated lives and influential legacies
By P. J. Hale

LETTERS

956 Guizhou snub-nosed monkey in peril
By T. Ju and X. Dong

956 Combatting national research restrictions
By R. Buckley and A. Keto

957 Biological invasions in China's coastal zone
By X. Wang et al.

PHOTO: STEFANIE LOOS

RESEARCH

IN BRIEF

959 From *Science* and other journals

REVIEW

Biodiversity

962 Madagascar's extraordinary biodiversity: Evolution, distribution, and use *A. Antonelli* et al.
REVIEW SUMMARY; FOR FULL TEXT: DOI.ORG/10.1126/SCIENCE.ADF0869

963 Madagascar's extraordinary biodiversity: Threats and opportunities *H. Ralimanana* et al.
REVIEW SUMMARY; FOR FULL TEXT: DOI.ORG/10.1126/SCIENCE.ADF1466

RESEARCH ARTICLES

964 HIV clinical trials
Vaccination induces HIV broadly neutralizing antibody precursors in humans *D. J. Leggat* et al.
RESEARCH ARTICLE SUMMARY; FOR FULL TEXT: DOI.ORG/10.1126/SCIENCE.ADD6502
PERSPECTIVE p. 949

965 Synthetic biology
Monitoring of cell-cell communication and contact history in mammals *S. Zhang* et al.
RESEARCH ARTICLE SUMMARY; FOR FULL TEXT: DOI.ORG/10.1126/SCIENCE.ABO5503

966 Quantum simulation
Observing the quantum topology of light *J. Deng* et al.

971 Plant science
Phosphoenolpyruvate reallocation links nitrogen fixation rates to root nodule energy state *X. Ke* et al.

978 Metallurgy
Exceptional fracture toughness of CrCoNi-based medium- and high-entropy alloys at 20 kelvin *D. Liu* et al.
PERSPECTIVE p. 947

983 Molecular biology
Active DNA demethylation promotes cell fate specification and the DNA damage response *D. Wang* et al.
PERSPECTIVE p. 948

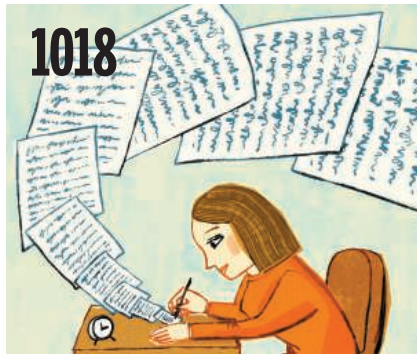
990 Machine learning
Mastering the game of Stratego with model-free multiagent reinforcement learning *J. Perolat* et al.

REPORTS

996 Quality control
The human signal peptidase complex acts as a quality control enzyme for membrane proteins *A. Zanotti* et al.



Tracing a history of cell interactions in the embryonic mouse



1001 Volcanology
Magma accumulation at depths of prior rhyolite storage beneath Yellowstone Caldera *R. Maguire* et al.
PERSPECTIVE p. 945; PODCAST

1005 Wildfires
Early snowmelt and polar jet dynamics co-influence recent extreme Siberian fire seasons *R. C. Scholten* et al.
PERSPECTIVE p. 944

1009 Ultracold chemistry
Creation of an ultracold gas of triatomic molecules from an atom–diatomic molecule mixture *H. Yang* et al.

DEPARTMENTS

931 Editorial
Science urgencies for Brazil
By H. B. Nader

1018 Working Life
Writing for the moment
By A. Ridgway

ON THE COVER

A long-exposure photograph shows the Clepsydra Geyser erupting on a moonlit night in Yellowstone National Park's Lower Geyser Basin. Geysers and other hydrothermal features in Yellowstone National Park are fueled by heat from a magma reservoir in Earth's upper crust. New seismic imaging of Yellowstone has provided further insight into the volume and distribution of magma in the subsurface. See pages 945 and 1001. *Photo: Paul D. Stewart/NPL/Minden Pictures*



Science Staff 930
Science Careers 1015

SCIENCE (ISSN 0036-8075) is published weekly on Friday, except last week in December, by the American Association for the Advancement of Science, 1200 New York Avenue, NW, Washington, DC 20005. Periodicals mail postage (publication No. 484460) paid at Washington, DC, and additional mailing offices.

Copyright © 2022 by the American Association for the Advancement of Science. The title SCIENCE is a registered trademark of the AAAS.

Domestic individual membership, including subscription (12 months): $165 ($74 allocated to subscription). Domestic institutional subscription (51 issues): $2212; Foreign postage extra: Air assist delivery: $98. First class, airmail, student, and emeritus rates on request. Canadian rates with GST available upon request, GST #125488122. Publications Mail Agreement Number 1069624. **Printed in the U.S.A.**
Change of address: Allow 4 weeks, giving old and new addresses and 8-digit account number. **Postmaster:** Send change of address to AAAS, P.O. Box 96178, Washington, DC 20090–6178. **Single-copy sales:** $15 each plus shipping and handling available from backissues.science.org; bulk rate on request. **Authorization to reproduce** material for internal or personal use under circumstances not falling within the fair use provisions of the Copyright Act can be obtained through the Copyright Clearance Center (CCC), www.copyright.com. The identification code for *Science* is 0036-8075. *Science* is indexed in the *Reader's Guide to Periodical Literature* and in several specialized indexes.

CREDSITS: (PHOTO) S. ZHANG *ET AL.*; (ILLUSTRATION) ROBERT NEUBECKER

Science AAAS

Editor-in-Chief Holden Thorp, hthorp@aaas.org

Executive Editor Valda Vinson

Editor, Research Jake S. Yeston **Editor, Insights** Lisa D. Chong **Managing Editor** Lauren Kmec

DEPUTY EDITORS Gemma Alderton (UK),Stella M. Hurtley (UK), Phillip D. Szuromi, Sacha Vignieri **SR. EDITORS** Caroline Ash (UK), Michael A. Funk, Brent Grocholski, Pamela J. Hines, Di Jiang, Priscilla N. Kelly, Marc S. Lavine (Canada), Mattia Maroso, Yevgeniya Nusinovich, Ian S. Osborne (UK), L. Bryan Ray, Seth Thomas Scanlon (UK), H. Jesse Smith, Keith T. Smith (UK), Jelena Stajic, Peter Stern (UK), Valerie B. Thompson, Brad Wible **ASSOCIATE EDITORS** Bianca Lopez, Corinne Simonti, Yury V. Suleymanov, Ekeoma Uzogara **LETTERS EDITOR** Jennifer Sills **LEAD CONTENT PRODUCTION EDITORS** Chris Filiatreau, Harry Jach **SR. CONTENT PRODUCTION EDITOR** Amelia Beyna **CONTENT PRODUCTION EDITORS** Julia Haber-Katris, Nida Masiulis, Abigail Shashikanth, Suzanne M. White **SR. EDITORIAL MANAGERS** Carolyn Kyle, Beverly Shields **SR. PROGRAM ASSOCIATE** Maryrose Madrid **EDITORIAL ASSOCIATE** Joi S. Granger **SR. EDITORIAL COORDINATORS** Aneera Dobbins, Jeffrey Hearn, Lisa Johnson, Jerry Richardson, Hilary Stewart (UK), Alice Whaley (UK), Anita Wynn **EDITORIAL COORDINATORS** Maura Byrne, Alexander Kief, Ronmel Navas, Isabel Schnaidt, Qiyam Stewart, Brian White **RESEARCH & DATA ANALYST** Jessica L. Slater **ASI DIRECTOR, OPERATIONS** Janet Clements (UK) **ASI SR. OFFICE ADMINISTRATOR** Jessica Waldock (UK)

News Editor Tim Appenzeller

NEWS MANAGING EDITOR John Travis **INTERNATIONAL EDITOR** Martin Enserink **DEPUTY NEWS EDITORS** Shraddha Chakradhar, Elizabeth Culotta, Lila Guterman, David Grimm, Eric Hand (Europe), David Malakoff **SR. CORRESPONDENTS** Daniel Clery (UK), Jon Cohen, Jeffrey Mervis, Elizabeth Pennisi **ASSOCIATE EDITORS** Jeffrey Brainard, Michael Price, Kelly Servick **NEWS REPORTERS** Adrian Cho, Jennifer Couzin-Frankel, Jocelyn Kaiser, Rodrigo Pérez Ortega (Mexico City), Robert F. Service, Erik Stokstad, Paul Voosen, Meredith Wadman **INTERNS** Zack Savitsky, Viviana Flores, Katherine Irving **CONTRIBUTING CORRESPONDENTS** Warren Cornwall, Andrew Curry (Berlin), Ann Gibbons, Sam Kean, Eli Kintisch, Kai Kupferschmidt (Berlin), Andrew Lawler, Mitch Leslie, Eliot Marshall, Virginia Morell, Dennis Normile (Tokyo), Elisabeth Pain (Careers), Charles Piller, Gabriel Popkin, Michael Price, Joshua Sokol, Richard Stone, Emily Underwood, Gretchen Vogel (Berlin), Lizzie Wade (Mexico City) **CAREERS** Rachel Bernstein (Editor), Katie Langin (Associate Editor) **COPY EDITORS** Julia Cole (Senior Copy Editor), Morgan Everett, Cyra Master (Copy Chief) **ADMINISTRATIVE SUPPORT** Meagan Weiland

Creative Director Beth Rakouskas

DESIGN MANAGING EDITOR Chrystal Smith **GRAPHICS MANAGING EDITOR** Chris Bickel **PHOTOGRAPHY MANAGING EDITOR** Emily Petersen **MULTIMEDIA MANAGING PRODUCER** Kevin McLean **WEB CONTENT STRATEGY MANAGER** Kara Estelle-Powers **DESIGN EDITOR** Marcy Atarod **DESIGNER** Christina Aycock **SENIOR SCIENTIFIC ILLUSTRATOR** Valerie Altounian **SCIENTIFIC ILLUSTRATORS** Austin Fisher, Kellie Holoski, Ashley Mastin **INTERACTIVE GRAPHICS EDITOR** Kelly Franklin **SENIOR GRAPHICS SPECIALISTS** Holly Bishop, Nathalie Cary **SENIOR PHOTO EDITOR** Charles Borst **PHOTO EDITOR** Kaitlyn Dolan **SENIOR PODCAST PRODUCER** Sarah Crespi **VIDEO PRODUCER** Meagan Cantwell **SOCIAL MEDIA STRATEGIST** Jessica Hubbard **SOCIAL MEDIA PRODUCER** Sabrina Jenkins **WEB DESIGNER** Jennie Pajerowski

Chief Executive Officer and Executive Publisher Sudip Parikh

Publisher, Science Family of Journals Bill Moran

DIRECTOR, BUSINESS SYSTEMS AND FINANCIAL ANALYSIS Randy Yi **DIRECTOR, BUSINESS OPERATIONS & ANALYSIS** Eric Knott **DIRECTOR OF ANALYTICS** Enrique Gonzales **MANAGER, BUSINESS OPERATIONS** Jessica Tierney **MANAGER, BUSINESS ANALYSIS** Cory Lipman **BUSINESS ANALYSTS** Kurt Ennis, Maggie Clark **FINANCIAL ANALYST** Isacco Fusi **BUSINESS OPERATIONS ADMINISTRATOR** Taylor Fisher **SENIOR PRODUCTION MANAGER** Jason Hillman **SENIOR MANAGER, PUBLISHING AND CONTENT SYSTEMS** Marcus Spiegler **CONTENT OPERATIONS MANAGER** Rebecca Doshi **SENIOR CONTENT & PUBLISHING SYSTEMS SPECIALIST** Jacob Hedrick **SENIOR PRODUCTION SPECIALIST** Kristin Wowk **PRODUCTION SPECIALISTS** Kelsey Cartelli, Audrey Diggs **DIGITAL PRODUCTION MANAGER** Lisa Stanford **CONTENT SPECIALIST** Kimberley Oster **ADVERTISING PRODUCTION OPERATIONS MANAGER** Deborah Tompkins **DESIGNER, CUSTOM PUBLISHING** Jeremy Huntsinger **SR. TRAFFIC ASSOCIATE** Christine Hall **SPECIAL PROJECTS ASSOCIATE** Sarah Dhere

ASSOCIATE DIRECTOR, BUSINESS DEVELOPMENT Justin Sawyers **GLOBAL MARKETING MANAGER** Allison Pritchard **DIGITAL MARKETING MANAGER** Aimee Aponte **JOURNALS MARKETING MANAGER** Shawana Arnold **MARKETING ASSOCIATES** Aaron Helmbrecht, Ashley Hylton, Mike Romano, Lorena Chirinos Rodriguez, Jenna Voris **SENIOR DESIGNER** Kim Huynh

DIRECTOR AND SENIOR EDITOR, CUSTOM PUBLISHING Sean Sanders **ASSISTANT EDITOR, CUSTOM PUBLISHING** Jackie Oberst **PROJECT MANAGER** Melissa Collins

DIRECTOR, PRODUCT & PUBLISHING DEVELOPMENT Chris Reid **DIRECTOR, BUSINESS STRATEGY AND PORTFOLIO MANAGEMENT** Sarah Whalen **ASSOCIATE DIRECTOR, PRODUCT MANAGMENT** Kris Bishop **PRODUCT DEVELOPMENT MANAGER** Scott Chernoff **PUBLISHING TECHNOLOGY MANAGER** Michael Di Natale **SR. PRODUCT ASSOCIATE** Robert Koepke **PRODUCT ASSOCIATE** Caroline Breul, Anne Mason **SPJ ASSOCIATE MANAGER** Samantha Bruno Fuller **SPJ ASSOCIATE** Casey Buchta

MARKETING MANAGER Kess Knight **BUSINESS DEVELOPMENT MANAGER** Rasmus Andersen **SENIOR INSTITUTIONAL LICENSING MANAGER** Ryan Rexroth **INSTITUTIONAL LICENSING MANAGER** Marco Castellan, Claudia Paulsen-Young **SENIOR MANAGER, INSTITUTIONAL LICENSING OPERATIONS** Judy Lillibridge **SENIOR OPERATIONS ANALYST** Lana Guz **SYSTEMS & OPERATIONS ANALYST** Ben Teincuff **FULFILLMENT ANALYST** Aminta Reyes

DIRECTOR, GLOBAL SALES Tracy Holmes **US EAST COAST AND MID WEST SALES** Stephanie O'Connor **US MID WEST, MID ATLANTIC AND SOUTH EAST SALES** Chris Hoag **US WEST COAST SALES** Lynne Stickrod **ASSOCIATE DIRECTOR, ROW** Roger Goncalves **SALES REP, ROW** Sarah Lelarge **SALES ADMIN ASSISTANT, ROW** Victoria Glasbey **DIRECTOR OF GLOBAL COLLABORATION AND ACADEMIC PUBLISHING RELATIONS, ASIA** Xiaoying Chu **ASSOCIATE DIRECTOR, INTERNATIONAL COLLABORATION** Grace Yao **SALES MANAGER** Danny Zhao **MARKETING MANAGER** Kilo Lan **ASCA CORPORATION, JAPAN** Rie Rambelli (Tokyo), Miyuki Tani (Osaka)

DIRECTOR, COPYRIGHT, LICENSING AND SPECIAL PROJECTS Emilie David **RIGHTS AND PERMISSIONS ASSOCIATE** Elizabeth Sandler **LICENSING ASSOCIATE** Virginia Warren **CONTRACT SUPPORT SPECIALIST** Michael Wheeler

---

MAIN HEADQUARTERS
Science/AAAS
1200 New York Ave. NW
Washington, DC 20005

SCIENCE INTERNATIONAL
Clarendon House
Clarendon Road
Cambridge, CB2 8FH, UK

SCIENCE CHINA
Room 1004, Culture Square
No. 59 Zhongguancun St.
Haidian District, Beijing, 100872

SCIENCE JAPAN
ASCA Corporation
Sibaura TY Bldg. 4F, 1-14-5
Shibaura Minato-ku
Tokyo, 108-0073 Japan

EDITORIAL
science_editors@aaas.org

NEWS
science_news@aaas.org

INFORMATION FOR AUTHORS
science.org/authors/
science-information-authors

REPRINTS AND PERMISSIONS
science.org/help/
reprints-and-permissions

MEDIA CONTACTS
scipak@aaas.org

MULTIMEDIA CONTACTS
SciencePodcast@aaas.org
ScienceVideo@aaas.org

INSTITUTIONAL SALES AND SITE LICENSES
science.org/librarian

PRODUCT ADVERTISING & CUSTOM PUBLISHING
advertising.science.org/
products-services
science_advertising@aaas.org

CLASSIFIED ADVERTISING
advertising.science.org/
science-careers
advertise@sciencecareers.org

JOB POSTING CUSTOMER SERVICE
employers.sciencecareers.org
support@sciencecareers.org

MEMBERSHIP AND INDIVIDUAL SUBSCRIPTIONS
science.org/subscriptions

MEMBER BENEFITS
aaas.org/membership/benefits

AAAS BOARD OF DIRECTORS
CHAIR Susan G. Amara
PRESIDENT Gilda A. Barabino
PRESIDENT-ELECT Keith Yamamoto
TREASURER Carolyn N. Ainslie
CHIEF EXECUTIVE OFFICER
Sudip Parikh
BOARD Cynthia M. Beall
Ann Bostrom
Janine Austin Clayton
Kaye Husbands Fealing
Maria M. Klawe
Jane Maienschein
Robert B. Millard
Babak Parviz
William D. Provine
Juan S. Ramírez Lugo
Susan M. Rosenberg

Science serves as a forum for discussion of important issues related to the advancement of science by publishing material on which a consensus has been reached as well as including the presentation of minority or conflicting points of view. Accordingly, all articles published in *Science*—including editorials, news and comment, and book reviews—are signed and reflect the individual views of the authors and not official points of view adopted by AAAS or the institutions with which the authors are affiliated.

BOARD OF REVIEWING EDITORS (Statistics board members indicated with **$**)

Erin Adams, *U. of Chicago*
Takuzo Aida, *U. of Tokyo*
Leslie Aiello, *Wenner-Gren Fdn.*
Deji Akinwande, *UT Austin*
Judith Allen, *U. of Manchester*
Marcella Alsan, *Harvard U.*
James Analytis, *UC Berkeley*
Paola Arlotta, *Harvard U.*
Delia Baldassarri, *NYU*
Nenad Ban, *ETH Zürich*
Christopher Barratt, *U. of Dundee*
Nandita Basu, *U. of Waterloo*
Franz Bauer, *Pontificia U. Católica de Chile*
Ray H. Baughman, *UT Dallas*
Carlo Beenakker, *Leiden U.*
Yasmine Belkaid, *NIAID, NIH*
Philip Benfey, *Duke U.*
Kiros T. Berhane, *Columbia U.*
Joseph J. Berry, *NREL*
Alessandra Biffi, *Harvard Med.*
Chris Bowler, *École Normale Supérieure*
Ian Boyd, *U. of St. Andrews*
Malcolm Brenner, *Baylor Coll. of Med.*
Emily Brodsky, *UC Santa Cruz*
Ron Brookmeyer, *UCLA* (**$**)
Christian Büchel, *UKE Hamburg*
Dennis Burton, *Scripps Res.*
Carter Tribley Butts, *UC Irvine*
György Buzsáki, *NYU School of Med.*
Mariana Byndloss, *Vanderbilt U. Med. Ctr.*
Annmarie Carlton, *UC Irvine*
Simon Cauchemez, *Inst. Pasteur*
Ling-Ling Chen, *SIBCB, CAS*
Wendy Cho, *UIUC*
Ib Chorkendorff, *Denmark TU*
Karlene Cimprich, *Stanford U.*
James J. Collins, *MIT*
Robert Cook-Deegan, *Arizona State U.*
Virginia Cornish *Columbia U.*
Carolyn Coyne, *Duke U.*
Roberta Croce, *VU Amsterdam*
Christina Curtis, *Stanford U.*
Ismaila Dabo, *Penn State U.*
Jeff L. Dangl, *UNC*
Chiara Daraio, *Caltech*
Nicolas Dauphas, *U. of Chicago*
Frans de Waal, *Emory U.*
Claude Desplan, *NYU*
Sandra Díaz, *U. Nacional de Córdoba*
Samuel Díaz-Muñoz, *UC Davis*
Ulrike Diebold *TU Wien*
Stefanie Dimmeler, *Goethe-U. Frankfurt*
Hong Ding, *Inst. of Physics, CAS*
Dennis Discher, *UPenn*
Jennifer A. Doudna, *UC Berkeley*
Ruth Drdla-Schutting, *Med. U. Vienna*
Raissa M. D'Souza, *UC Davis*
Bruce Dunn, *UCLA*
William Dunphy, *Caltech*
Scott Edwards, *Harvard U.*
Todd Ehlers, *U. of Tübingen*
Nader Engheta, *UPenn*
Karen Ersche, *U. of Cambridge*
Beate Escher, *UFZ & U. of Tübingen*
Barry Everitt, *U. of Cambridge*
Vanessa Ezenwa, *U. of Georgia*
Toren Finkel, *U. of Pitt. Med. Ctr.*
Gwenn Flowers, *Simon Fraser U.*
Natascha Förster Schreiber, *MPI Extraterrestrial Phys.*
Peter Fratzl, *MPI Potsdam*
Elaine Fuchs, *Rockefeller U.*
Jay Gallagher, *U. of Wisconsin*
Daniel Geschwind, *UCLA*
Ramon Gonzalez, *U. of South Florida*
Sandra González-Bailón, *UPenn*
Gillian Griffiths, *U. of Cambridge*
Nicolas Gruber, *ETH Zürich*
Hua Guo, *U. of New Mexico*
Taekjip Ha, *Johns Hopkins U.*
Daniel Haber, *Mass. General Hos.*
Sharon Hammes-Schiffer, *Yale U.*
Wolf-Dietrich Hardt, *ETH Zürich*
Louise Harra, *UCL*
Carl-Philipp Heisenberg, *IST Austria*
Janet G. Hering, *Eawag*
Christoph Hess, *U. of Basel & U. of Cambridge*
Heather Hickman, *NIAID, NIH*
Hans Hilgenkamp, *U. of Twente*
Janneke Hille Ris Lambers, *ETH Zürich*
Kai-Uwe Hinrichs, *U. of Bremen*
Deirdre Hollingsworth, *U. of Oxford*
Randall Hulet, *Rice U.*
Auke Ijspeert, *EPFL*
Gwyneth Ingram, *ENS Lyon*
Darrell Irvine, *MIT*
Akiko Iwasaki, *Yale U.*
Stephen Jackson, *USGS & U. of Arizona*
Erich Jarvis, *Rockefeller U.*
Peter Jonas, *IST Austria*
Johanna Joyce, *U. de Lausanne*
Matt Kaeberlein, *U. of Wash.*
William Kaelin Jr., *Dana-Farber*
Daniel Kammen, *UC Berkeley*
Kisuk Kang, *Seoul Nat. U.*
Sabine Kastner, *Princeton U.*
V. Narry Kim, *Seoul Nat. U.*
Robert Kingston, *Harvard Med.*
Nancy Knowlton, *Smithsonian Institution*
Etienne Koechlin, *École Normale Supérieure*
Alex L. Kolodkin, *Johns Hopkins U.*
LaShanda Korley, *U. of Delaware*
Julija Krupic, *U. of Cambridge*
Paul Kubes, *U. of Calgary*
Chris Kuzawa, *Northwestern U.*
Laura Lackner, *Northwestern U.*
Gabriel Lander, *Scripps Res.* (**$**)
Mitchell A. Lazar, *UPenn*
Hedwig Lee, *Duke U.*
Luis Liz-Marzán, *CIC biomaGUNE*
Omar Lizardo, *UCLA*
Jonathan Losos, *Wash. U. in St. Louis*
Ke Lu, *Inst. of Metal Res., CAS*
Christian Lüscher, *U. of Geneva*
Jean Lynch-Stieglitz, *Georgia Inst. of Tech.*
David Lyons, *U. of Edinburgh*
Fabienne Mackay, *QIMR Berghofer*
Zeynep Madak-Erdogan, *UIUC*
Anne Magurran, *U. of St. Andrews*
Ari Pekka Mähönen, *U. of Helsinki*
Asifa Majid, *U. of Oxford*
Oscar Marín, *King's Coll. London*
Charles Marshall, *UC Berkeley*
Christopher Marx, *U. of Idaho*
David Masopust, *U. of Minnesota*
Geraldine Masson, *CNRS*
C. Robertson McClung, *Dartmouth*
Rodrigo Medellín, *U. Nacional Autónoma de México*
C. Jessica Metcalf, *Princeton U.*
Baoxia Mi, *UC Berkeley*
Tom Misteli, *NCI, NIH*
Alison Motsinger-Reif, *NIEHS, NIH* (**$**)
Danielle Navarro, *U. of New South Wales*
Daniel Nettle, *Newcastle U.*
Daniel Neumark, *UC Berkeley*
Beatriz Noheda, *U. of Groningen*
Helga Nowotny, *Vienna Sci. & Tech. Fund*
Pilar Ossorio, *U. of Wisconsin*
Andrew Oswald, *U. of Warwick*
Isabella Pagano, *Istituto Nazionale di Astrofisica*
Elizabeth Levy Paluck, *Princeton U.*
Jane Parker, *MPI Cologne*
Giovanni Parmigiani, *Dana-Farber* (**$**)
Daniel Pauly, *U. of British Columbia*
Ana Pêgo, *U. do Porto*
Samuel Pfaff, *Salk Inst.*
Julie Pfeiffer, *UT Southwestern Med. Ctr.*
Philip Phillips, *UIUC*
Matthieu Piel, *Inst. Curie*
Kathrin Plath, *UCLA*
Martin Plenio, *Ulm U.*
Katherine Pollard, *UCSF*
Elvira Poloczanska, *Alfred-Wegener-Inst.*
Julia Pongratz, *Ludwig Maximilians U.*
Philippe Poulin, *CNRS*
Lei Stanley Qi, *Stanford U.*
Trevor Robbins, *U. of Cambridge*
Joeri Rogelj, *Imperial Coll. London*
Amy Rosenzweig, *Northwestern U.*
Mike Ryan, *UT Austin*
Miquel Salmeron, *Lawrence Berkeley Nat. Lab*
Nitin Samarth, *Penn State U.*
Erica Ollmann Saphire, *La Jolla Inst.*
Joachim Saur, *U. zu Köln*
Alexander Schier, *Harvard U.*
Wolfram Schlenker, *Columbia U.*
Susannah Scott, *UC Santa Barbara*
Anuj Shah, *U. of Chicago*
Vladimir Shalaev, *Purdue U.*
Jie Shan, *Cornell U.*
Beth Shapiro, *UC Santa Cruz*
Jay Shendure, *U. of Wash.*
Steve Sherwood, *U. of New South Wales*
Brian Shoichet, *UCSF*
Robert Siliciano, *JHU School of Med.*
Lucia Sivilotti, *UCL*
Emma Slack, *ETH Zürich & U. of Oxford*
Richard Smith, *UNC* (**$**)
John Speakman, *U. of Aberdeen*
Tara Spires-Jones, *U. of Edinburgh*
Allan C. Spradling, *Carnegie Institution for Sci.*
V. S. Subrahmanian, *Northwestern U.*
Ira Tabas, *Columbia U.*
Eriko Takano, *U. of Manchester*
A. Alec Talin, *Sandia Natl. Labs*
Patrick Tan, *Duke-NUS Med. School*
Sarah Teichmann, *Wellcome Sanger Inst.*
Rocio Titiunik, *Princeton U.*
Shubha Tole, *Tata Inst. of Fundamental Res.*
Maria-Elena Torres Padilla, *Helmholtz Zentrum München*
Kimani Toussaint, *Brown U.*
Barbara Treutlein, *ETH Zürich*
Jason Tylianakis, *U. of Canterbury*
Wim van der Putten, *Netherlands Inst. of Ecology*
Matthew Vander Heiden, *MIT*
Ivo Vankelecom, *KU Leuven*
Judith Varner, *UC San Diego*
Henrique Veiga-Fernandes, *Champalimaud Fdn.*
Reinhilde Veugelers, *KU Leuven*
Bert Vogelstein, *Johns Hopkins U.*
Julia Von Blume, *Yale School of Med.*
David Wallach, *Weizmann Inst.*
Jane-Ling Wang, *UC Davis* (**$**)
Jessica Ware, *Amer. Mus. of Natural Hist.*
David Waxman, *Fudan U.*
Chris Wikle, *U. of Missouri* (**$**)
Terrie Williams, *UC Santa Cruz*
Ian A. Wilson, *Scripps Res.* (**$**)
Hao Wu, *Harvard U.*
Li Wu, *Tsinghua U.*
Wei Xie, *Tsinghua U.*
Benjamin Youngblood, *St. Jude*
Yu Xie, *Princeton U.*
Jan Zaanen, *Leiden U.*
Kenneth Zaret, *UPenn School of Med.*
Lidong Zhao, *Beihang U.*
Bing Zhu, *Inst. of Biophysics, CAS*
Xiaowei Zhuang, *Harvard U.*
Maria Zuber, *MIT*

EDITORIAL

Science urgencies for Brazil

Last month in Egypt at the United Nations Climate Change Conference, Brazil's president-elect Luiz Inácio Lula da Silva reaffirmed his pledge to make Brazil a global leader in addressing climate change and deforestation. However, when Lula takes the reins on 1 January, he will step into a situation that is quite different from when last he was president (2003–2010). At that time, he prioritized science and education in all government actions and guided Brazil to a prosperous social state and sustainable economy. This time, he will face a much different local and global scenario. The world is still going through an unprecedented health crisis, and like other countries, Brazil needs to establish new ways of tackling the consequential social, educational, environmental, and economic problems. This will be especially challenging given that since 2016, the country has taken the opposite direction of most governments, cutting investments in education at all levels and in science, technology, and innovation (ST&I). The question is how Lula can immediately address the serious poverty and hunger crisis in Brazil while also restoring the environment and a competitive and equitable economy to the country.

> "...Brazil must ... stand behind building a future for today's youth."

In the 21st century, countries are focusing on developing capacities to create scientific knowledge and technologies to improve societal well-being. Science and education thus emerge as priorities. It is therefore urgent for Lula to recompose the budget for the country's education and ST&I sectors. However, the new government will face an unparalleled challenge. Combined with the historic cuts in social and ST&I policies, the budget for 2023 presented by the Bolsonaro administration does not consider basic expenditures that will necessarily have to be resumed. Moreover, Brazil's congress is the most conservative since the country's return to democracy. But investment in science and education is especially important because of Brazil's young population, who need to be adequately educated and be given the kinds of opportunities that innovation can create.

Some indicators of education as well as of ST&I show that as an average, across countries belonging to the Organisation for Economic Cooperation and Development, 47% of adults (25 to 34 years old) have attained tertiary education (a bachelor's degree), compared with those in Brazil (23%). The number of adults in Brazil who do not progress beyond secondary education (precollege) is one of the highest among these nations. Support for aid programs that help students with disadvantaged backgrounds to complete a tertiary education has been deeply cut over the past 4 years. Brazil also has not yet reached full enrollment of children in primary school, one of the benchmark goals for the United Nations Sustainable Development Goals 2030 Agenda.

Brazil's economy ranges from 10th to 12th position (depending on the ranking system) in the world, and this outcome is primarily a direct consequence of the investments made in ST&I in earlier years. For example, Brazil's agricultural success in boosting soybean production is a result of progress attained mainly through research at public universities and institutions. Unfortunately, over the past years, the Bolsonaro government has cut research funding, which will soon affect Brazil's global competitiveness.

Above all, Brazilian science lacks constancy and continuity in ST&I investments. The National Fund for Scientific and Technological Development is now the only source for financing ST&I. The Bolsonaro government claims to have balanced expenditures by restricting use of the fund. The new administration should reinvigorate this resource and embrace ST&I as a priority.

Brazil urgently needs to commit to strategies that achieve leadership in the age of knowledge, such as investing in "big data," artificial intelligence, and communication technologies. These areas will continue to revolutionize the global job market but stand to increase inequalities in Brazil unless special attention is given to proper education. Also, there is a need to cultivate multidisciplinary and transdisciplinary research that consider societal and environmental impacts to ensure that science broadly supports the country's economic and social development.

Twenty years after his first presidency, Lula returns and faces his biggest obstacles yet. The good news is that he still champions science and education. The people of Brazil must come together and stand behind building a future for today's youth.

– Helena B. Nader



PHOTO: CRISTINA LACERDA

Helena B. Nader is president of the Brazilian Academy of Sciences, Rio de Janeiro, Brazil; the honorary president of the Brazilian Society for the Advancement of Science, São Paulo, Brazil; and a professor of molecular biology at the Federal University of São Paulo (UNIFESP), São Paulo, Brazil. hbnader@abc.org.br

10.1126/science.adf9526

NEWS

$$H^2 = \left(\frac{\dot{a}}{a}\right)^2 = \frac{8\pi G}{3}\rho - \frac{kc^2}{a^2}$$

Students at Tsinghua University held up sheets of paper on which they wrote the **Friedmann equation** (left) during protests across China against government repression. The equation, describing the expansion of space, served as a sly reference to "freed man."

IN BRIEF

Edited by **Jeffrey Brainard**



CONSERVATION

Countries vote for sustainable shark fishing

Nearly all shark species hunted for their fins must be caught sustainably, according to new trade rules adopted last week under the Convention on International Trade in Endangered Species of Wild Fauna and Flora. In a move that supporters called historic, 183 countries and the European Union voted to place nearly 100 species of threatened sharks and sharklike rays on the treaty's Appendix II, roughly tripling the number that must be managed to avoid overexploitation. Within 1 year, nations exporting shark fins or meat must certify the animals were caught legally and sustainably. Shark populations have shrunk for 7 decades because of a lack of fishing regulations and enforcement (*Science*, 11 November, p. 617). The trade in fins, which are used for soup, has been particularly devastating, putting 61 species in danger of extinction. Trade in shark products was worth nearly $1 billion in 2015, according to the most recent broad review by the U.N. Food and Agriculture Organization. Also newly listed are animals overexploited for the international pet trade, including more than 160 species of glass frogs and 50 kinds of turtles and tortoises.

Blacktip reef sharks are among dozens of species for which international trade will be regulated.

Monkeypox gets a neutral name

INFECTIOUS DISEASES | The World Health Organization (WHO) announced this week it will start referring to monkeypox disease as "mpox" (pronounced "em-pox") after the current name drew criticism as evoking racist stereotypes and inviting stigmatization. It is also a misnomer: The virus was first identified in laboratory monkeys but is most likely carried by rodents in the wild. During a 1-year transition period, WHO will use both names. Earlier this year, the agency changed the names of the two different clades, or branches, of monkeypox viruses that had been based on the regions where they were first identified. The Congo Basin clade became clade I and the West African clade, clade II. Weekly monkeypox cases have declined globally since August, but hundreds of cases are still reported every week and health authorities continue to call for at-risk people to be vaccinated.

Embryo-editing scientist reboots

GENE THERAPY | He Jiankui, who in 2018 conducted a widely condemned experiment in which his team edited the genes of human embryos and later implanted them into their

PHOTO: KIMBERLY JEFFRIES/WCS

mothers, says he has opened a new lab to develop "affordable" gene therapies. In 2018, Chinese officials detained He, a biophysicist, for using the CRISPR gene editor on the embryos, created through in vitro fertilization. The experiment led to the birth of three babies. A court convicted him of illegal medical practices, and He was released from prison in April. Last week, He described his latest venture on Weibo, a popular social media platform in China: His lab in Beijing will aim to "overcome 3-5 genetic diseases within 2-3 years to benefit families with rare diseases." He cautioned about the recent death of a man with Duchenne muscular dystrophy (DMD) who was in a trial to test a CRISPR-based gene therapy. "History tells us that when any new technology emerges, it is both an angel and a devil," He wrote on Weibo. "Blind pursuit of new technologies and aggressive advancement will definitely be punished by heaven." He told *Science* he has asked Jack Ma, the billionaire head of the Alibaba Group, for $140 million to fund his new lab's efforts against DMD.

NSF rules tighten funding race

INFRASTRUCTURE | Researchers seeking National Science Foundation (NSF) grants for research equipment will likely face longer odds under new rules that don't require institutions to share the cost. This summer, Congress ordered NSF to suspend cost sharing for its $75 million Major Research Instrumentation (MRI) program and foot the entire bill for each successful proposal. In a new solicitation (NSF 23-519), the agency projects the number of awards next year will drop from the current 150 to 100 to accommodate that change, which is intended to diversify the applicant pool and give less wealthy institutions a better shot at winning a grant. The reduction in awards will disappoint some applicants, says comparative biologist Cheryl Hayashi of the American Museum of Natural History, a past recipient of MRI grants. "But I don't see a downside to having a more diverse pool." NSF will allow each institution to submit up to four applications, up from three, provided the fourth proposal is for an environmentally sustainable instrument.

Dam removal to boost salmon OK'd

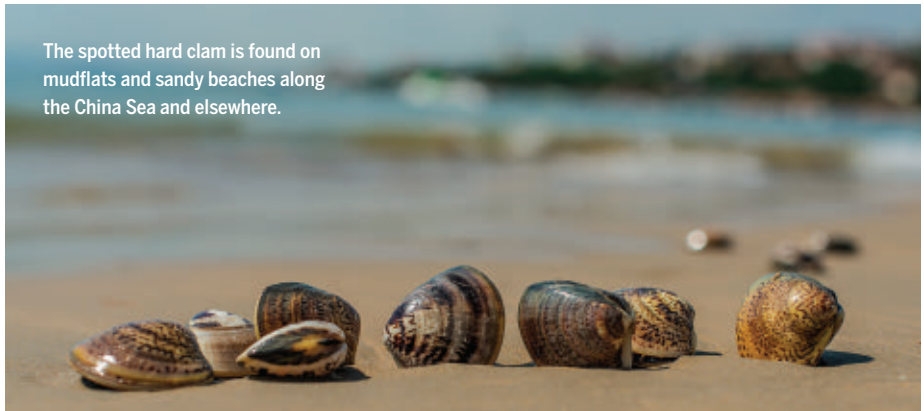
CONSERVATION | The world's largest dam removal project will begin as soon as 2023, after U.S. regulators last month approved tearing down four hydroelectric dams on the Klamath River in Northern California and Oregon. The 17 November unanimous vote by the Federal Energy Regulatory Commission was the last regulatory hurdle. Native American tribes and environmentalists have for years sought removal of the dams, which were built in the early 20th century and block migrating salmon from reaching some 600 kilometers of habitat. Salmon runs on the river have dwindled to less than 5% of historic levels.

Time and other units get tweaks

STANDARDS | The controversial leap second, which time keepers add sporadically to keep atomic clocks aligned with Earth's rotation, will be axed in 2035, the International Bureau of Weights and Measures (BIPM) decided on 18 November. Devised in 1972 and used 27 times since, the leap second wreaks havoc with modern-day telecommunications, banking, and other networks. Its abandonment means that astronomical time, based on Earth's rotation, will slowly diverge from Coordinated Universal Time, based on the vibrations of cesium in atomic clocks. BIPM plans to stop adding leap seconds for 100 years, by which time someone may have figured out a long-term fix for the problem. In addition, BIPM added new prefixes to the International System of Units to define very big and very small measurements. For example, 1 ronnameter (Rm) is 1 billion billion billion meters and 1 quettameter (Qm), 1000 times bigger still; 1 rontometer (rm) is one-billionth of a billionth of a billionth of 1 meter and 1 quectometer (qm), one-thousandth of that.

Cannabis research to open up

BIOMEDICINE | The U.S. Congress has approved its first stand-alone bill enabling marijuana research and sent it to President Joe Biden, who is expected to sign it. The measure directs the Drug Enforcement Administration (DEA) to set up a streamlined system allowing scientists to register to study cannabis for medical purposes. The legislation also orders DEA to speedily register new growers, including universities, to raise and distribute it for research. The bill requires the U.S. attorney general to conduct yearly assessments of whether there is an adequate, uninterrupted supply of cannabis for research. The Senate passed the bill, the Medical Marijuana and Cannabidiol Research Expansion Act, on 16 November, following a lopsided vote of approval by the House of Representatives in July. Separately in October, Biden ordered the U.S. attorney general to consider reclassifying the drug, which would also make it easier to study.



The spotted hard clam is found on mudflats and sandy beaches along the China Sea and elsewhere.

PHOTO: XIN YUE

EVOLUTION

In a first for animals, clam makes its own antibiotic

Natural antibiotics typically come from bacteria or molds. But some clams make their own erythromycin, a study has found—the first animals reported to possess this ability. The spotted hard clam (*Meretrix petechialis*) has a mucus-covered outer lip that contains specialized antibiotic-producing cells, according to an international research team. These may protect the clams, which lack adaptive, lymphocyte-based immune systems, from disease. The scientists found no sign of erythromycin-producing bacteria in the clam's tissues; instead they noticed its DNA contained an erythromycin-making gene that resembled one used by bacteria but differed enough that the invertebrate version might have evolved independently. The researchers found the gene in all the clam's life stages. Its genome also contains other genes needed to produce erythromycin, and a related species of clam possesses these antibiotic genes as well. The findings suggest scientists can engineer cells in other animals to produce their own antibiotic, the authors write this week in the *Proceedings of the National Academy of Sciences*.



IN DEPTH

ANIMAL RESEARCH

Indictment of monkey importers could disrupt U.S. research

Alleged Cambodian smuggling ring poses dangers to wild macaques and the drug studies they're used in

By **David Grimm**

The indictment of several members of an alleged international monkey smuggling ring is sending ripples through the U.S. biomedical community. The U.S. Department of Justice (DOJ) has charged two Cambodian wildlife officials and several members of a Hong Kong–based primate supply company with illegally exporting hundreds—and potentially more than 2000—cynomolgus macaques, an endangered species, to the United States for research. The animals were reportedly captured from the wild in Cambodia and falsely labeled as captive-bred.

The indictment, which carries multiple felony charges, will likely exacerbate the shortage of these monkeys, used in everything from drug safety testing to vaccine research, says Dave O'Connor, a virologist at the University of Wisconsin, Madison, who uses cynomolgus macaques to study infectious disease. Still, he says, the main priority should be stopping this illegal trade, for the sake of research and the animals themselves. "These sorts of unscrupulous actors give a black eye to an already heavily scrutinized industry."

A family of cynomolgus macaques in the wild in Cambodia.

Animal advocacy groups are pushing to ban further monkey imports until more is known about their provenance. And some experts in the biomedical community are suggesting moving the breeding of this species of macaque to the United States and collecting more genetic and pedigree information on the monkeys that come from overseas. They also say labs should find ways to use fewer of these animals.

It's unclear how many of the animals in question have been used in research, but one of two companies that received them is the largest private supplier of monkeys to U.S. research labs, *Science* has learned. The company, Inotiv, tells *Science* that "while we do not yet know if these allegations will be proven true, Inotiv strongly condemns any and all unauthorized trading/importation of endangered species. … To confirm our screening processes are (and were) solid, we have plans in place to conduct the necessary audits to ensure excellence and provide transparency."

Cynomolgus macaques, also known as long-tailed macaques or cynos, are—by far—the monkey species most imported to the United States. Nearly 30,000 entered the country last year, according to data from the U.S. Centers for Disease Control and Prevention (CDC), which regulates the import of nonhuman primates. Most cynos are used by pharmaceutical and biotechnology companies. (Rhesus macaques, another species common in U.S. biomedical research, are mostly used by the academic community, which largely obtains them from national primate research centers.) Cynos are also the main monkey species imported to Europe for research. They are typically bred in large facilities in Asia.

China used to be the main supplier of cynos—exporting approximately 30,000 in 2018—but the country has shut off its supply, which experts have attributed to the trade war with the United States and China's desire to beef up its own biomedical industry. Several countries, mostly in Southeast Asia, stepped in to fill the gap. Cambodia now exports the largest share of cynos—more than 29,000 in 2020, the vast majority of which were shipped to the United States.

Though the actual number of cynos in the wild is unclear, the International Union for Conservation of Nature downgraded the status of the monkeys from vulnerable to endangered this year, citing growing demand from the research industry as a factor that could incentivize illegal trade.

The need for cynos has indeed grown, especially during the pandemic. The species was

PHOTO: GERMAN VOGEL/ALAMY

one of the main animal models employed to test COVID-19 vaccines, and researchers are increasingly using the monkeys to study Alzheimer's, Parkinson's, and other diseases. "There is a sky-high demand for these animals," O'Connor says.

That may be what's fueling the alleged illegal trade in Cambodia. According to the DOJ indictment, two high-ranking employees of Vanny Resources Holdings, a Hong Kong–based company that breeds monkeys for research, paid millions to black market suppliers and Cambodian wildlife officials to capture thousands of cynos from national parks and other protected areas of Cambodia, and to fake their paperwork to indicate the animals had been bred in captivity.

Nearly 1500 of these "laundered" cynos arrived in the United States from 2018 to 2020, according to the indictment, with potentially hundreds more in 2021. They appear to have ended up at facilities in Florida and Texas. The companies running the facilities are not named in the indictment, but in a filing with the U.S. Securities and Exchange Commission, Inotiv disclosed that its principal supplier of nonhuman primates was the target of the DOJ probe, indicating that the company gets most of its monkeys from Vanny.

Last year, Inotiv purchased the major research animal supplier Envigo (under fire recently for a series of animal welfare violations at one of its beagle breeding facilities), making it the world's largest supplier of nonhuman primates for research. The company currently houses more than 9000 monkeys—the vast majority cynos—which it sells to private and academic labs.

Cindy Buckmaster, spokesperson for Americans for Medical Progress, which advocates for the use of animals in scientific studies, says there's not much that companies like Inotiv—or the labs they sell to—can do to check the provenance of the animals they receive. "We have to take the documentation at face value," she says.

Still, she calls the alleged illegal import of cynos "horrible" for the animals, and a violation of the trust both the scientific community and the public put in animal research. She says wild-caught monkeys carry viruses that could infect other animals they're housed with, or humans. And they're prone to stress just from being around people for the first time, which could result in "very different data."

The animal rights group People for the Ethical Treatment of Animals has asked CDC to suspend all nonhuman primate exports from Cambodia. It also asked the U.S. National Institutes of Health "to determine the precise origin of every [cyno] imported from Cambodia since 2017 and currently in publicly funded laboratories."

In a statement, Cambodia's ministry of agriculture said it was "surprised and saddened" by the indictment, and is committed to upholding all laws governing the international trade of animals. It also denied that any of its exported monkeys had been captured from the wild.

"If this is the reaction from the supply side, then we think there needs to be much stricter controls on the demand side," says Eric Kleiman, a researcher at the Animal Welfare Institute, an animal advocacy group that has closely followed the issue. "If monkeys are to be used in research in the U.S., there is a responsibility to ensure they are well cared-for … and sourced responsibly."

> **"There is a sky-high demand for these animals."**
> **Dave O'Connor**, University of Wisconsin, Madison

Sarah Kite, co-founder of Action for Primates, a U.K.-based advocacy organization, agrees. She notes the European Union is poised to pass a law that will ban the import of all wild-caught animals and their offspring. "That's the only way to ensure they're not getting wild-caught animals," she says. "The research community needs to be held accountable for what's happening to this species."

O'Connor suggests one solution: ensuring that all captive-bred animals have extensive pedigree records, which could be kept in a global registry. He also suggests genotyping every monkey used in research studies to better trace their origins.

Major pharmaceutical and biotech companies contacted by *Science* either declined to comment on the issue or did not respond.

"I think [the indictment] is going to constrict the pipeline even more," says a U.S. consultant on industry and academic monkey research who has worked in the field for decades but asked not to be named because of concerns of damaging relationships with his clients. The U.S. biomedical community should invest in breeding these animals domestically, he says. "We need to migrate away from shipping an animal from halfway around the world, where we can't control where it came from."

But the community also needs to work to reduce the number of monkeys it uses, he says. That could be accomplished by designing studies to require fewer animals, and working with regulators to require fewer animals for research such as drug safety studies. "That's easier, faster, and less expensive than building up a bigger pipeline." ■

BIOLOGY

CRISPR is so popular even viruses may use it

Thousands of phages appear to have stolen the gene-cutting mechanism

By **Mitch Leslie**

The gene-editing tool CRISPR started out as a bacterial defense against invading viruses. But it turns out the intended targets have stolen CRISPR for their own arsenals. A new study reveals that thousands of the bacteria-attacking viruses known as bacteriophages (phages, for short) contain the CRISPR system's genetic sequences, suggesting they may use them against rival phages. The finding could boost CRISPR's laboratory usefulness.

The discovery "opens doors for possible new applications of CRISPR systems," says genomicist Mazhar Adli of Northwestern University's Feinberg School of Medicine, who wasn't connected to the research.

Like other viruses, phages cannot reproduce on their own. Instead, they hijack bacteria's molecular machinery, often killing their hosts in the process. The CRISPR system enables bacteria to fight back. It includes repetitive stretches of DNA that match sequences of previously encountered phages. If these same phages attack a bacterium again, it uses this repetitive DNA to encode strands of RNA that can steer a partner enzyme, which acts like a pair of genetic scissors, to cut the phage's genome at specific places.

For about the past decade, scientists have been working to turn this microbial immune defense into a gene-editing technique for myriad uses, including improving crop defenses, detecting pathogens, and fighting diseases such as cancer.

Characteristic DNA that encodes components of the CRISPR system had previously turned up in a handful of phages. At first, scientists regarded these finds as mere "curiosities," says structural biologist Jennifer Doudna of the University of California (UC), Berkeley, who shared the 2020 Nobel Prize in Chemistry for showing how to tailor the CRISPR system to target particular se-

quences. "But they got us wondering if these systems were more common."

To find out, Doudna, UC Berkeley geomicrobiologist Jillian Banfield, and their colleagues went looking for additional examples of CRISPR in the phage world. They probed DNA from a variety of environments that are rich in bacterial hosts for the viruses, including soil and the human mouth. This trawl uncovered more than 6000 types of phages that contain CRISPR system DNA, the scientists reported last week in *Cell*. They also examined phage genome sequences that had been posted to online databases and found even more instances of the CRISPR-carrying viruses. Although fewer than 1% of phages sport the sequences, the researchers did not expect "such a broad distribution of an anti-phage system in phages," Doudna says.

Why would phages acquire a system that evolved to thwart them? The most likely reason, Doudna says, is to beat the competition. Multiple viruses can attack a bacterium at the same time, leading to "phage wars" inside an infected cell, she says. Bacteria are also vulnerable to rogue DNA strands known as plasmids that coerce the cells into copying them. By destroying these rivals with the CRISPR system, phages "can have the replication machinery all to themselves," Doudna says.

The phages presumably swiped these CRISPR system sequences from their microbial victims, she says. Since then, the viruses have customized the systems for their own ends. For instance, some phages seem to have lost the capacity to generate certain molecules that can kill bacteria, possibly to preserve their hosts to produce more phages.

The phages' CRISPR tricks may inspire new biotechnology. For instance, most CRISPR-based approaches now rely on the enzyme Cas9 to cut DNA. However, Cas9 is so large it cannot fit into some viruses used to genetically modify cells. A number of phages, however, boast a slimmed-down version known as Cas-lambda that is about 50% smaller, Doudna and Banfield's team found. Adli says this smaller enzyme could allow new gene-editing uses for CRISPR, such as altering plant genomes, though researchers would first need to overcome several bioengineering hurdles.

Microbiologist Joseph Bondy-Denomy of UC San Francisco says Doudna and Banfield displayed a "[John] Lennon-[Paul] McCartney" level of synergy in ferreting out so many CRISPR-bearing phages that had eluded other scientists. Still, he wants to see evidence the viruses actually put their CRISPR systems to use when they invade bacteria. Bondy-Denomy also suspects many more phages that wield CRISPR are waiting to be discovered. "The next step is more," he says. ■

WORKFORCE

Pandemic accelerates 'GRExit'

Nearly all U.S. Ph.D. programs have dropped the standardized GRE exam as an admissions requirement

By **Katie Langin**

The University of Michigan's biomedical Ph.D. program was a lonely outlier in 2017 when it announced it would stop asking applicants to submit scores for the Graduate Record Examination (GRE) General Test. At the time, the standardized exam was a nearly universal requirement for Ph.D. programs at U.S. universities. But the Michigan program now has plenty of company. The vast majority of STEM Ph.D. programs have stopped requiring GRE scores, according to an investigation by *Science*, and the number of tests taken each year has plummeted.

The COVID-19 pandemic, unease about whether the test puts students from less privileged backgrounds at a disadvantage, and doubts about how well GRE scores predict grad school success all helped drive the changes. But whether they will be permanent and how they are affecting the applicant pool or incoming class composition remain to be seen.

To quantify the trend, *Science* examined the application requirements for Ph.D. programs in eight disciplines at 50 top-ranked U.S. universities. Only 3% currently require prospective students to submit GRE General Test scores, compared with 84% 4 years ago. An additional 5% strongly recommend that prospective students submit scores. Others make it optional; one program's website reads, "In certain cases, a strong GRE score submitted with your application can improve your chances." But 36% of the programs explicitly state that GRE scores will not be accepted or reviewed as part of the admissions process.

Early on, the so-called "GRExit" movement was mostly restricted to the life sciences. But the shift away from the GRE now touches every discipline. "It really did spiral" quickly, says Sarah Ledford, an assistant professor in the geosciences at Georgia State University, who maintains a list of earth sciences programs that don't require GRE scores. In 2018, geology was the only discipline in which every single department *Science* examined required the GRE; now none does.

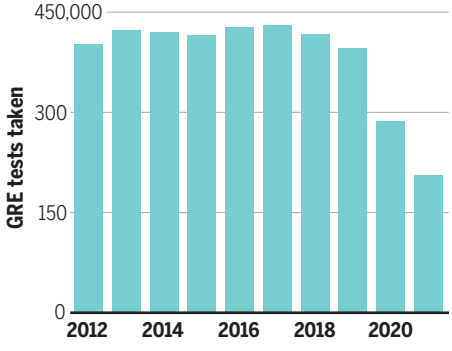
Ledford attributes much of the shift to "a reckoning" around diversity. She and other scientists argue that the cost of the test—$220 per attempt, plus travel expenses and training materials—disadvantages students from lower socioeconomic backgrounds and dissuades them from applying to graduate school. COVID-19 provided another reason to drop the test requirement, as a move to online testing led to concerns about whether some students had access to a suitable testing environment. "This was low-hanging fruit during COVID for places to give it a shot," Ledford says.

Those logistical concerns came on top of research indicating the GRE doesn't predict whether a student will succeed in graduate school. "The data—they have to be relevant. … Otherwise it's just noise," says Jennifer Gomez, an assistant professor of social work at Boston University who has studied the use of GRE scores in psychology admissions. "The GRE … predicts nothing of substance beyond grades." On top of that, the test "unfairly privileges certain groups—white men in particular," she says.

But not everyone is sold on the transition. "I think it's a mistake to remove GRE altogether," says Sang Eun Woo, a professor of psychology at Purdue University. Woo is quick to acknowledge the GRE isn't perfect and doesn't think test scores should be used to rank and disqualify prospective students—an approach many programs have used in the past. But she and some others think the GRE can be a useful element for holistic reviews, considered alongside qualitative elements such as recommendation let-

Fewer tests taken

The number of Graduate Record Examination (GRE) tests administered in the United States has dropped in recent years.



CREDITS: (GRAPHIC) C. BICKEL/*SCIENCE*; (DATA) EDUCATIONAL TESTING SERVICE

ters, personal statements, and CVs. "We're not saying that the test is the only thing that graduate programs should care about," she says. "This is more about, why not keep the information in there because more information is better than less information, right?"

Removing test scores from consideration could also hurt students, argues Alberto Acereda, associate vice president of global higher education at the Educational Testing Service, the company that runs the GRE. "Many students from underprivileged backgrounds so often don't have the advantage of attending prestigious programs or taking on unpaid internships, so using their GRE scores serves [as a] way to supplement their application, making them more competitive compared to their peers."

There's no surefire method for "evaluating people's potential for doing original research," says Danny Caballero, an associate professor of physics education at Michigan State University who has studied graduate admissions in physics. "And that's just because that is a really complicated thing to do." Like Woo, he's advocated for the use of rubrics that ask reviewers to evaluate prospective students holistically, based on the strength of their academic preparation, research track record, initiative and perseverance, and fit with the program. Before the pandemic, his program included GRE scores in its rubric—giving them a weight of 10%—but when the program shifted to making the GRE optional, it eliminated those scores from the rubric. He has no regrets. "The work of science is not taking standardized tests. The work of science is being curious," he says.

At Cornell University, the geological sciences graduate program also made the switch to a rubric-based holistic review shortly before announcing it would no longer accept GRE scores in 2020. Matt Pritchard, the program's graduate director, says the policy switch hasn't been contentious and the program has no plans to reinstate the GRE. "It is a new system to learn, but once you get into the groove of it … it probably takes no more extra time," he says. Pritchard is hopeful the shift will result in a more diverse applicant pool. He says it's too early to tell for sure because there's so much year-to-year variability in applicant demographics. But since the change, "We have more applicants and more diverse applicants and I would say the quality is as strong as ever."

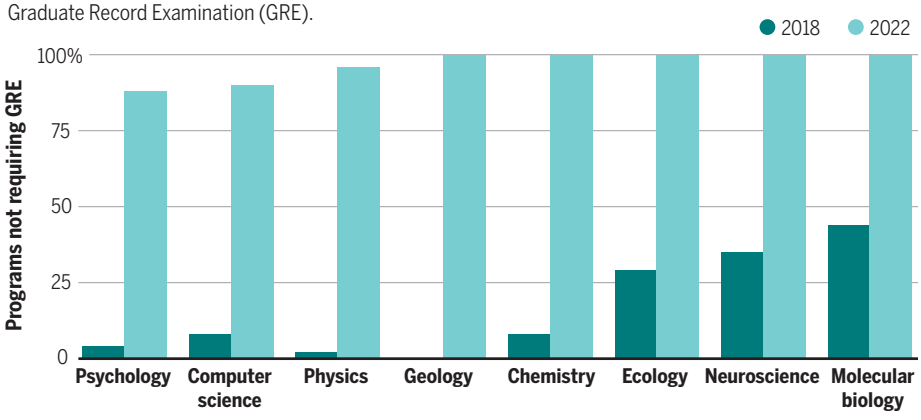
In the long run, many GRExit proponents see the new admission requirements as a policy shift that will be hard to undo. "What I hear from students is this is absolutely something that they look for in considering where to apply," Ledford says. "They don't want to take [the test]."

Joshua Hall, who was an early advocate for dropping the GRE when he worked in graduate admissions for the biological and biomedical science program at the University of North Carolina, Chapel Hill, agrees that in the life sciences a shift back toward the GRE appears unlikely. "Admissions committees seem to have acclimated to the no-GRE format," says Hall, now a senior program officer at the Howard Hughes Medical Institute. "I have heard no rumblings of going back."

But in other disciplines, that may not be the case. Dartmouth College's computer science program has returned to requiring the GRE after waiving the requirement in 2020 and 2021. Carnegie Mellon University's psychology program made a similar change earlier this year. It later backtracked, however, and lifted the requirement again. When asked about the change in policy, the program's graduate director, Vicki Helgeson, wrote in an email to *Science*, "The whole thing is in a state of flux." ■

Giving it a pass

Since 2018, most STEM Ph.D. programs at 50 top U.S. universities have moved away from requiring the Graduate Record Examination (GRE).



GRAPHIC: C. BICKEL/*SCIENCE*

PLANETARY SCIENCE

Europe pledges to launch Mars rover delayed by war

Replacing Russian launcher and lander means probe won't reach Mars until 2030

By **Daniel Clery**

After repeated delays and the loss of its Russian collaborators, Europe's ExoMars rover is go for launch again, in 2028, government ministers agreed last week. The rover was due to set off for the Red Planet in September on a Russian Proton rocket and land with a Russian-built craft, until the European Space Agency (ESA) cut ties with Russia after its invasion of Ukraine. At a budget setting meeting last week, ESA resolved to launch the mission on a yet-to-be-determined U.S. rocket and develop its own lander—with some help from NASA.

"This is fantastic news for science and for the search for signs of life elsewhere," says Andrew Coates of University College London, principal investigator (PI) of a panoramic camera on the rover. "It's something positive: We still have a mission," adds Valérie Ciarletti of the University of Paris-Saclay, PI of the rover's ground-penetrating radar. The golf cart–size rover, dubbed Rosalind Franklin after the British DNA pioneer, carries a sample-collecting drill that can penetrate up to 2 meters underground, where signs of ancient life might be better preserved.

The announcement came at the end of a budget meeting of ESA's 22 member states that occurs every 3 years. Ministers approved €16.9 billion in funding over the next 5 years to cover science, exploration, rockets, Earth observation, and telecommunications. The nearly 17% increase over the previous budget was less than ESA management had asked for, and some programs will feel a squeeze. But the €2.7 billion going to exploration is enough to revive ExoMars, which includes multiple Mars missions.

The project's first phase delivered the Trace Gas Orbiter to Mars in 2016, as well as a landing demonstrator, called Schiapa-

relli, which failed less than a minute before touchdown because of a software error that switched off landing rockets too early. Rosalind Franklin was set to follow in 2018.

Problems mating the rover with the Russian-made lander, called Kazachok, delayed the launch by 2 years. (Mars windows occur roughly every 2 years, when the planets align.) Trouble with the lander's parachutes, solar panels, and wiring forced another delay to this year. Then in March, with Kazachok and Rosalind Franklin ready to go, war intervened.

In building a new, Russia-free landing system, "we are not starting from scratch," says Thierry Blancquaert, ESA's ExoMars team leader. Most components on Schiaparelli worked faultlessly, and ESA provided some systems on Kazachok, including its parachutes, radar, radio, and onboard computer—items engineers will extract from the lander and reuse. But no European manufacturer makes the kind of thrusters needed to set the 310-kilogram Rosalind Franklin gently on the surface. This is where NASA has come in, Blancquaert says. It has offered to source the thrusters from a U.S. manufacturer.

NASA may also provide radioisotope heaters, power packs that use the decay of plutonium-238 to keep the rover from freezing during the frigid martian night. If it does, U.S. regulations require that the probe fly on a U.S. launcher, which would most likely be a SpaceX Falcon-Heavy or a Vulcan from United Launch Alliance. NASA would not confirm any details of its involvement, but Eric Ianson, the agency's Mars Exploration program director, said in a statement: "NASA and ESA are planning key conversations in the coming months on a potential collaboration for ESA's ExoMars Rosalind Franklin rover mission, subject to the availability of U.S. funding."

NASA's Perseverance and China's Tianwen-1 rovers have almost a decade's head start on Mars. But an ESA study found that ExoMars will still provide good science after it lands in 2030—especially investigations using its deep drill. For the scientists involved there is no doubt: "No mission can replace ExoMars," Ciarletti says.

The biggest losers in the new plan are scientists—both Russian and European—who designed instruments to be mounted on Kazachok. Because of the tight timetable for developing the new ESA lander, it will not do any science. "My feeling is of great discouragement due to the current geopolitical situation," says Francesca Esposito of the Astronomical Observatory of Capodimonte, who built a dust sensor for Kazachok. "But I am very happy that this has not stopped this great mission." ■



PHOTO: HOUSSAM SHBARO/ANADOLU AGENCY VIA GETTY IMAGES

GLOBAL HEALTH

Vaccines are in short supply amid global cholera surge

Climate change and pandemic may be fueling outbreaks

By **Kai Kupferschmidt**

On 2 October, Haiti announced cholera had returned to the country for the first time since a decadelong epidemic ended in 2019. The disease killed close to 10,000 Haitians in those years; now, with violent gangs fighting for control over the country and the health system in disarray, things could again get very bad.

A few days later, Lebanon reported its first cholera cases since 1993, in a Syrian refugee and a health care worker in the north of the country. More cases quickly followed, and health organizations fear the Lebanese health system, hard-hit by a yearslong financial crisis, could buckle under the new burden. Two weeks later, Kenya, where millions of people have fled the worst drought in decades, reported its first cholera cases as well.

The outbreaks are part of what the World Health Organization (WHO) calls an "unprecedented" surge in cholera cases, driven in part by climate change and fallout from the COVID-19 pandemic. Thirty countries have reported outbreaks this year, up from fewer than 20 on average the past 5 years. "There is a trend of more countries affected, in more regions, with a longer duration of outbreaks," says Daniela Garone, the international medical coordinator at Doctors Without Borders. A global cholera vaccine stockpile is falling short, forcing health organizations to ration doses—and rethink their control strategy.

Cholera, spread through water or food contaminated with the bacterium *Vibrio cholerae*, can cause severe diarrhea and kills an estimated 20,000 to 140,000 people each year. A lack of clean drinking water, poverty, natural disasters, and armed conflicts—such as the gang violence in Haiti—have traditionally fueled outbreaks.

Just a few years ago, the prospects for reducing the burden seemed to brighten. A new, cheap vaccine, made from inactivated bacteria lacking part of their toxin, was approved in 2015; millions of doses were added to an international stockpile for emergency use. In 2017, WHO launched an ambitious new control strategy that relied on vaccination, improving sanitation, and widening access to clean drinking water and treatment. It was meant to cut cholera deaths by 90% by 2030.

Extreme weather fueled by global warming is part of the reason cases are instead trending up, says Philippe Barboza, who heads WHO's Cholera and Epidemic Diarrheal Diseases section. Droughts in West Africa and the Horn of Africa, massive flooding in Southeast Asia, and cyclones in southern Africa have displaced people and destroyed water and sanitation infrastructure. COVID-19's toll on the health care system made matters worse. The cholera case fatality rate in Africa was almost 3% in 2021, Barboza says, about three times higher than over the previous 5 years. "Every time we have investigated why the [death rate] was so high, the reason was the same: delayed

A man receives an oral cholera vaccine at a barbershop in Akkar, Lebanon, on 12 November.

access to health care," he says.

The 36 million vaccine doses expected to be shipped from the stockpile this year won't be enough. Full protection requires two doses given 2 weeks apart, so the supply covers just 18 million people—"not a lot when you think of [affected] countries like Bangladesh, Pakistan, Ethiopia, Nigeria," Barboza says. Last month, the coordinating group that runs the stockpile announced it would stop administering second doses to stretch supplies. A one-dose strategy has been used successfully before, says Charlie Weller, an immunologist at the Wellcome Trust, but it's unclear how long protection will last. (Even the full two-dose regimen only protects for 3 years.)

David Sack, an infectious disease expert at Johns Hopkins University's Bloomberg School of Public Health, says he is "puzzled" by the decision to abandon the second dose instead of postponing it. A clinical trial in Cameroon that Sack and colleagues published this month suggests giving the second dose after 1 year instead of 2 weeks actually increases the immune response. But unless the outbreaks slow down in the coming months, the vaccine supply won't allow even a delayed second dose, and besides, current WHO guidelines don't allow an interval of more than 6 months.

Meanwhile, Shantha Biotechnics in India, which manufactures 10% of the global cholera vaccine supply, plans to stop production by the end of 2023. WHO Director-General Tedros Adhanom Ghebreyesus has urged Shantha and its parent company, Sanofi, to reconsider its decision, which would leave only one manufacturer, South Korea's EuBiologics. The International Vaccine Institute (IVI), a nonprofit based in South Korea that helped develop the cheap oral vaccine, is working with EuBiologics to increase its production capacity to some 80 million to 90 million doses annually, says Julia Lynch, who directs IVI's cholera program. It's also helping a South African company named Biovac set up a facility to produce the shots, in a project funded by the Wellcome Trust and the Bill & Melinda Gates Foundation. But both efforts will take several years.

Barboza emphasizes that vaccines are only one way to address the crisis. Cholera is easy to treat with oral rehydration solution, as long as it's administered quickly. That makes access to basic health care crucial. "You don't need a respirator, an intensive care unit, and God knows what," Barboza says. Meanwhile, countries should keep working to improve access to clean water and sanitation, he says: "We might have lost a fight, but we have not lost the war." ■

ILLUSTRATION: PHILLIP KRZEMINSKI

EVOLUTION

New look at jaw fossil rewrites centuries-old bird history

Specimen flips evolutionary order of two key groups

By **Gretchen Vogel**

A tiny broken bone, misidentified for decades, has upended scientists' view of bird evolution. For nearly 200 years, zoologists have divided birds into two categories: those with mobile joints in their upper jaw that allow their upper beak to move, and a much smaller group, including ostriches and emus, with a fused upper palate that gives them a less agile upper beak. This fused palate is also found in dinosaurs, including the feathered ones that were ancestors to today's birds, so zoologists thought ostriches and their kin were the evolutionary older group of birds, with mobile upper beaks arriving later in the history of birds.

Now, paleontologists have identified a key skull bone in an ancient bird that lived nearly 67 million years ago—just before the devastating asteroid impact that killed off the dinosaurs. The bone, a piece of the upper jaw, closely resembles its mobile counterpart in today's chickens or ducks, leading the researchers to conclude the ancient bird also had a jointed upper beak. They suspect the jointed beak was present in even older birds, because the rest of the specimen indicates it was a relative of *Ichthyornis*, another ancient bird that lived about 20 million years earlier. Overall, the new analysis suggests a jointed beak was already present in the ancestor of modern birds, and a fused palate re-evolved later in ostriches and their kin.



An artist depiction of *Janavis finalidens*.

"It's changing how we've been looking at the evolution of birds since the time of Linneaus," says Christopher Torres, a paleontologist at Ohio University, Athens, who was not part of the new work. "We thought we had this worked out centuries ago, and now we're finally finding fossils that are showing that we didn't. We got it mixed up."

The fossil, discovered more than 2 decades ago in a Belgian quarry near the Dutch border, was partially described for the first time in 2002, but many of its pieces remained inside a block of sediment. Juan Benito and Daniel Field, paleontologists at the University of Cambridge who study bird evolution, borrowed the fossil in 2018 from the Natural History Museum of Maastricht so they could use computerized tomography to image these remaining bones.

They hoped to find more of the animal's skull, but initial scans only turned up vertebrae and ribs. Disappointed, they put the project aside for more than a year. When Benito returned to the fossil, he was puzzled by a bone the earlier analysis had identified as part of a shoulder but that seemed too small. He realized the piece was a fragment of a bone that had been broken in two.

After identifying the companion piece and putting the two together, Benito, Field, and colleagues concluded the full structure was a particularly delicate part of the upper palate, a bone called the pterygoid that is key to the jointed upper beak. The researchers, who describe the more complete fossil this week in *Nature*, argue the bird is a previously unknown species and name it *Janavis finalidens*, for Janus, the Roman god of beginnings, endings, and transitions. It was a coastal flyer, plying the shallow seas that at the time covered what is now Belgium and the Netherlands, and weighed an estimated 1.5 kilograms—about the size of a gray heron.

University of Texas, Austin, paleontologist Julia Clarke, who studies bird evolution, calls the *Janavis* fossil "an important snapshot that shows the skull in a new way and adds to the evidence for what collection of traits was present in the ancestors of modern birds."

Several skulls of its older *Ichthyornis* relative have been described in recent years with bones that suggested the bird's upper palate might have been jointed, but the evidence was still fuzzy. Now, in the *Janavis* fossil, "the specific skull bone that materialized was the particular one we needed" to show the upper beak was flexible, Field says. Torres agrees. "It's like a puzzle where that one piece was missing, and now we have it," he says. ■



MEETING THE ANCESTORS

DNA from a medieval German cemetery opens a window on the history of today's largest Jewish population

By **Andrew Curry**

On a Sabbath Saturday in March 1349, the Jewish community of Erfurt was wiped out in a pogrom. The archbishop of Mainz, who had granted Jews the right to live and work in the medieval German city, tried the pogrom's ringleaders, local merchants and city council members who owed money to Jewish money lenders. One was executed and the rest exiled. The city's Christian population, meanwhile, was forced to pay restitution.

Five years later, a new Jewish community took root in the narrow, winding streets. Beginning in 1354, the city funded new houses and a synagogue, drawing Jews from across Europe to Erfurt. "That must have convinced them it would never happen again," says Karin Sczech, an archaeologist who works for the city.

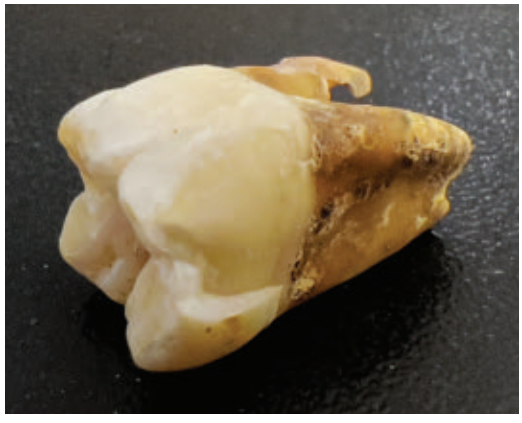
For 100 years, Erfurt's Jews flourished. They bathed in a ritual bath, or mikvah, on the banks of the Gera River and buried their dead in a large cemetery just outside the city walls. Then it all came to an end, again. In 1454, the town council revoked the rights of Erfurt's Jewish population, forcing them to leave town. The city built a granary on top of their cemetery, destroying hundreds of graves and repurposing Jewish tombstones to build its stout stone walls.

On a sunny fall day, Sczech points out a 192-square-meter plot she and a team of other archaeologists excavated on the former cemetery's grounds a decade ago. With a municipal construction project about to start on the site, their goal was to save, study, and rebury any human remains uncovered by the building work. The local Jewish community was closely involved, and "their wish was to do as little excavation as possible," Sczech says.

A meter or two under the ground, in the shadow of the 500-year-old granary, the team found the remains of more than 60 people, almost all of them oriented with their legs pointed east—toward Jerusalem. Their skeletons were well-preserved, along with traces of wooden coffins and nails.

Before the remains were reburied last year at a nearby cemetery, they yielded a gift: DNA that is shedding light on the origins of the Ashkenazim, the major Jewish population that emerged in Germany in the Middle Ages and later expanded into central and Eastern Europe. Together with a smaller scale study published in September that looked at DNA from six individuals from the Middle Ages unearthed in Norwich, England, the Erfurt analysis offers clues to where the Ashkenazim came from centuries earlier, and what happened along the way. The studies also confirm other evidence that today's Ashkenazi Jewish population, which numbers more than 10 million people spread around the world, has roots in a band of no more than a few hundred who survived a population bottleneck in Europe more than 1000 years ago.

The Erfurt study, which appears this week in *Cell*, is the first major study of a medieval Jewish population from a genetic perspective. "We just got a really nice angle from genetic resources that we didn't have before," says Elisheva Baumgarten, a historian at the Hebrew University of Jerusalem who was not involved with the study. "The cumulative evidence can tell us more than history alone—that to me is the really exciting part."



An Orthodox rabbi approved plans to sample loose teeth, but not bones, from Jewish graves.

Perhaps equally important, the archaeological effort was made possible by a rabbinical ruling that may establish a precedent for future studies of ancient Jewish remains that yield precious insights without violating religious sensibilities.

ARCHAEOLOGISTS HAVE UNCOVERED evidence of Jewish communities in Germanic provinces of the Roman Empire as early as the 300s C.E., particularly in what is today the city of Cologne. During the medieval period, a trio of German cities—Worms, Mainz, and Speyer—was known as the cradle of Ashkenazi culture, with records of Jewish life going back to about 900 C.E.

But the period in between largely remains a mystery. Were the Jews of Erfurt and other medieval cities tenacious holdovers from the Roman era, as some have proposed? Or were they the descendants of more recent pioneers who crossed the Alps around 800 C.E. to found tight-knit communities along the Rhine, near modern-day Frankfurt? "Ashkenazi Jews emerge in the Rhineland as migrants," says Leonard Rutgers, a historian at Utrecht University and a coauthor on the *Cell* paper. "But if they came from elsewhere, where did they come from?"

To find out, geneticists have tried to work backward from modern DNA. Today's Ashkenazi populations have high rates of certain genetic diseases because many individuals carry identical mutations, increasing the risks to their offspring. Those mutations, along with other shared DNA sequences, are clues to an early population bottleneck that drastically reduced Jewish genetic diversity. "Whether they're from Israel or New York, the Ashkenazi population today is homogenous genetically," says Hebrew University geneticist Shai Carmi.

Some ultra-Orthodox Ashkenazi communities today regularly administer genetic compatibility tests during matchmaking to limit the risk that children will inherit genetic diseases, and preconception testing is common in other Ashkenazim. But even though modern Ashkenazi genomes have been closely scrutinized, they can't give a clear picture of events 1000 or more years ago. "It helps to have data from the past," Carmi says.

In 2017, Carmi met with Harvard University geneticist David Reich at his lab. Reich—an expert on ancient DNA whose research has been criticized in the past for not engaging meaningfully enough with the concerns of local communities—encouraged him to pursue ancient DNA sampling, if he could find an ethical way to do it. Speaking from his Boston-area home on the morning of Rosh Hashana, the Jewish New Year, Reich said that although he is of Jewish descent, before Carmi reached out he had avoided studying Ashkenazi genetics. "It's hard to study one's own community," he says. "Working on oneself is complicated—you have biases towards what the results would be that are cognitively difficult."

Carmi left that initial meeting feeling pessimistic about studying DNA from ancient Jews. "I thought this would be impossible," he says, "because there would be no permission to sample." Searching for ancient DNA for analysis would mean grinding up tiny bits of bone for sequencing. Destructive sampling would also be needed for radiocarbon dating. "It's a hard rule in Judaism that you don't disturb the dead," says Alexander Nachama, chief rabbi of the Jewish Community of Thuringia and head of the modern-day Jewish community in Erfurt.

Carmi pressed ahead, contacting historians and archaeologists in Europe to see whether suitable samples existed. "The historians thought I was crazy," Carmi says. But

Tombstones from a medieval Jewish ceremony in Erfurt, Germany, are relics of a thriving community.

PHOTOS: KEITH PRUFER; (OPPOSITE PAGE) STEFANIE LOOS

a few got back to him—including Sczech, who had received rabbinical permission to measure bones from the Erfurt cemetery to determine their sex and ages at death, techniques that don't harm the skeletal material.

Carmi also reached out to an Orthodox rabbi in Israel. After studying centuries-old interpretations of Jewish law and listening to Carmi's explanation of the science, the rabbi suggested a workaround: teeth. Because they fall out naturally ("They're deciduous, like the leaves of a tree," Reich says), the rabbi concluded that stray teeth are not part of the body in the same way as a skull or rib. Researchers couldn't go looking for them, but if loose teeth turned up—as part of a rescue excavation, for example—they could be sampled without violating Jewish beliefs.

With a rabbinical ruling in hand, Carmi approached Jewish authorities in Germany, including the chief rabbi of Erfurt at the time. They were hesitant. "They didn't want to be the first to allow an ancient DNA study or go against an established ruling," Carmi says. The Israeli rabbi's reasoning ultimately won over Erfurt's Jewish community, and Carmi was able to sample the loose teeth of 38 individuals from the cemetery before the bodies were reburied in a 2021 ceremony.

For colleagues working on Jewish sites elsewhere in Europe, the ruling represents a religiously acceptable way to apply scientific techniques to date Jewish remains and study their ancestry and diet. Carmi says it might even be applied to DNA analyses of mass graves from World War II. "The use of teeth seems to me to be an excellent compromise," says Pierre Blanchard, an archaeologist working for France's National Institute of Preventive Archaeological Research who was not involved with the study. "I hope that the results of this first study will show what is at stake and what benefits each side—scientists and the Orthodox—can expect."

NO SIMILAR DISCUSSIONS of religious ethics preceded the Norwich study, because it was only after an initial analysis in 2011 that the researchers realized the 17 people whose remains were found during construction work might have been Jews killed in a pogrom. The presence of DNA sequences also found in Ashkenazi Jews today was one clue. "When we first tested the DNA, we got just a few hundred base pairs," says Ian Barnes, an evolutionary geneticist at London's Natural History Museum who worked on the study. "The best I could say was they were compatible with Jewish origin."

The bones were reburied in 2013 in a multidenominational ceremony. Five years later, the local Jewish community asked to move them to a quieter spot. Before they were reburied a second time, the authors secured permission to analyze them again, this time yielding higher-resolution results that definitively linked them to modern Ashkenazi populations. Subsequent radiocarbon dating, meanwhile, showed the bones were about 800 years old, placing them around the same time as an 1190 massacre of the town's Jews, which took place on the eve of the First Crusade. "The minute you get dates, it seems reasonable it could be this one antisemitic event," Barnes says. "Put together, everything helped to build the case."

The DNA results from Norwich and Erfurt both confirm that modern Ashkenazim are descended from a small founding population. Based on modern Jewish DNA, some researchers had speculated this founder group emerged from a population crunch in the 13th and 14th centuries, when the religious fervor of the Crusades and false accusations that Jews spread the Black Death sparked violent pogroms. But the new data point to a different scenario that played out earlier.

"We already see clear evidence for that bottleneck" in the 14th century teeth from Erfurt, Carmi says. Disease mutations and long stretches of identical genetic code in the medieval DNA implied the bottleneck occurred centuries earlier. One type of mitochondrial genetic material—DNA that is passed through the maternal line—was identical in one-third of the people in the excavated plot, evidence that they all descended from a single woman who probably lived 500 to 1000 years earlier.

In the Norwich individuals—which DNA shows included three sisters and a young boy with red hair and blue eyes—geneticists found the same disease markers seen in modern Ashkenazi populations, at about the same frequencies. "That tells you the bottleneck happened prior to these individuals dying in 1190," Barnes says. "This is a clear example of how powerful these data are."

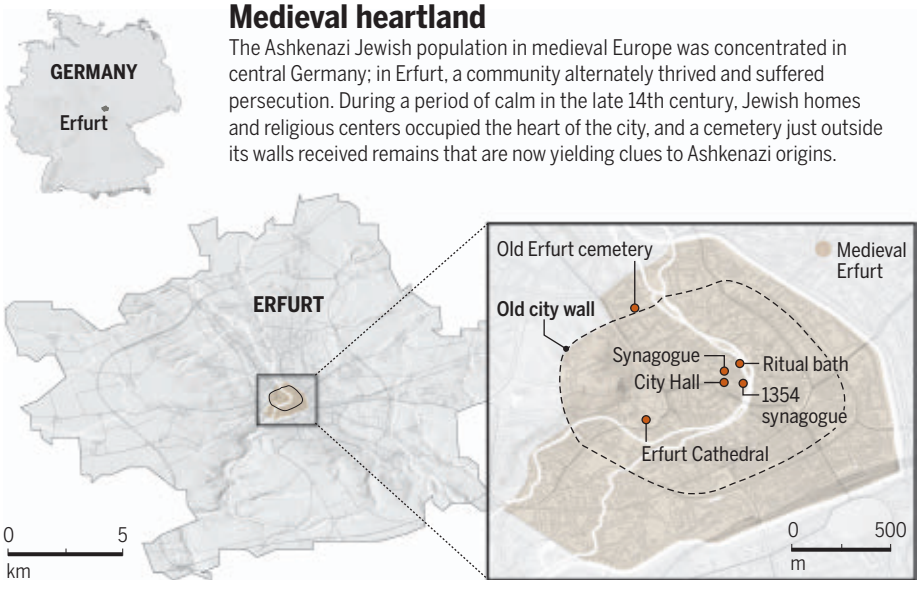
At the same time, small differences among the dozens of Erfurt genomes suggested medieval Ashkenazi communities weren't completely homogeneous, despite the earlier bottleneck. In the city archives, co-author Maike Lämmerhirt of the University of Erfurt found clues to that diversity in tax and property records. Some of the names of 14th century Jewish residents—Salman of Würzburg, Abraham of Rothenburg—suggest family roots in Bavaria, south and west of Erfurt. Other prominent Erfurt Jews, such as Baruch of Pilsen or Jacob of Bohemia, apparently traced their ancestry far to the east, in one case as far away as modern-day Kaliningrad, now in Russia, or beyond.

That mixture of east and west "is exactly what we get from the genetic results," Sczech says: After first branching out from a single, small founding population into small communities across Europe, including medieval Great Britain, the medieval Ashkenazim apparently mixed back together in places like Erfurt generations later.

Isotopic signals in the teeth supported the DNA evidence. Tooth enamel captures the isotopic mixture of the water where a person grew up, and in the Erfurt cemetery the analysis showed parents with distant birthplaces—probably in Eastern Europe—were buried near their children, who grew up locally. "That's a hint that we have the founders," Sczech says. "It's the first time ever

Medieval heartland

The Ashkenazi Jewish population in medieval Europe was concentrated in central Germany; in Erfurt, a community alternately thrived and suffered persecution. During a period of calm in the late 14th century, Jewish homes and religious centers occupied the heart of the city, and a cemetery just outside its walls received remains that are now yielding clues to Ashkenazi origins.



GRAPHIC: K. FRANKLIN/*SCIENCE*



The partial excavation of a cemetery in 2013 to clear the way for a parking garage ramp exposed dozens of graves.

we have all these results coming together."

By comparing the Erfurt genomes with modern and ancient DNA data from many different populations, the researchers were able to peer even further back, to the origins of those scattered European communities. The comparisons suggested the Ashkenazi circa 1350 had a mix of ancestry resembling populations from southern Italy or Sicily today, with components found in modern Eastern Europe and the Middle East mixed in. "That fits the historical data," says Krishna Veeramah, a geneticist at Stony Brook University who was not involved in the work.

One traditional tale about Ashkenazi roots may not be far from the truth: A family or small group of Jews arrived in Germany around 800 C.E., crossing the Alps at the invitation of Charlemagne, the first Holy Roman emperor, and settled in the Rhineland.

BEYOND A LOOK at population dynamics, the Erfurt results offer a window into medieval Jewish culture. Although genetic variations show the postpogrom community drew its members from across Europe, their burials are all similar, reflecting common traditions. "They were all considered Ashkenazi Jews," Carmi says.

The genetic similarity between the Erfurt community and modern Ashkenazim 600 years later was also telling. "These people lived about 25 generations ago, and an intermarriage rate with outsiders of more than one in 500 per generation would have shifted Ashkenazi ancestry by an amount we could detect," Reich says. "But that didn't happen. That's new information."

The Jewish community's central position in medieval European life makes its genetic isolation even more remarkable. The role of Jews as bankers, craftspeople, traders, and money lenders would have put them in constant contact with their Christian neighbors. In Erfurt, as in many medieval cities, synagogues, ritual baths, and Jewish houses were in the heart of town, right next to the city hall and at the intersection of two major roads. Archival records show Jews and Christians went into business together and Christians served as wet-nurses to Jewish children. "Jews and Christians were constantly in each others' lives. But it looks like they didn't have children together," Baumgarten says. "We as modern people don't have the words to describe that complex sense of belonging."

Today Erfurt's Jews are at the center of the city once more, as part of an effort to make its ancient synagogue and mikvah a UNESCO World Heritage Site dedicated to Jewish daily life in the Middle Ages. It's a story Baumgarten says is often overshadowed by the horrors of the Holocaust and the pogroms that punctuated centuries of co-existence. "To make it only into a dark story would be a mistake for European culture at large," she says. "The truth is the Jews of medieval Germany settled there by invitation, were welcomed there when they came and were integrated into medieval German space—and all the while were a religious, and sometimes persecuted, other."

Now their genomes are proving central to the story of all Ashkenazim–including its formative event, the bottleneck that so dramatically marked the DNA of millions of people living today. Though these new studies help pin down its timing, no one knows what caused it. Bottlenecks call to mind catastrophes, such as massacres or discrimination that prevents people from marrying outside their community. "It's fair to say Jewish history is one big sequence of bottlenecks," Rutgers says.

But to Reich, the Erfurt data suggest a brighter possibility: that long before the Erfurt Jews were laid to rest, somewhere in Europe a few dozen people flourished, passing their genes and culture to millions of people living today despite a history of brutal persecution. "Perhaps it's the legacy of a small town that had a tradition of very large families, or maybe a few towns with very strong founder events," Reich says. "Bottlenecks are often thought of as a crisis, but sometimes it's a group that's been incredibly successful." ■

PHOTO: © M. SOWA/THURINGIAN STATE OFFICE FOR HERITAGE MANAGEMENT AND ARCHAEOLOGY



WILDFIRES

What set Siberia ablaze?

Shifting air currents and early snowmelt drove extreme Arctic fires from 2019 to 2021

By **Gabriela Schaepman-Strub**[1] *and* **Jin-Soo Kim**[2]

Extreme wildfires are being reported worldwide, contributing to global warming by emitting substantial amounts of carbon dioxide, destabilizing ecosystems, and causing major socioeconomical damage. Boreal forests and Arctic tundra have experienced devastating fires in recent summers. From 2019 to 2021, more than 90% of these fires occurred in central and eastern Siberia. On page 1005 of this issue, Scholten *et al.* (*1*) report the underlying causes of these events. The main drivers include a northward shift of a major air current (the Arctic front jet stream), early snowmelt, and frequent lightning strikes. These conditions have led to a migration of fires that threaten even the northernmost part of the land, the Arctic coast.

Fires are a naturally occurring ecological disturbance in boreal forests. However, their frequency and the resulting burned areas have almost doubled in the recent decade compared with the previous decade (3.0×10^6 ha) in Siberia (*2*). Wildfires in North America have been connected to spatiotemporal patterns of the polar front jet stream that moves across the continent (*3*). Scholten *et al.* now find similar patterns for the recent extreme fire seasons in Siberia. The polar jet—the strongest wind in the upper atmosphere (troposphere)—blows west to east across Siberia and separates the air masses of the Arctic and the mid-latitudes of the Northern Hemisphere. However, this air stream has migrated northward. This has resulted in slower movement of air masses over Siberia, which stagnate for a long time over the region, a phenomenon known as "blocking." The land surface consequently heats up, accelerating snowmelt. This also intensifies atmospheric convection (the rising of air), which increases lightning activity and the risk of fires.

Anthropogenic greenhouse gas emissions and the consequential warming of Earth and its atmosphere have pushed the Arctic front jet stream northward (*4*). Unless emissions decrease rapidly, lightning activity in the Arctic will occur more frequently (*5*). The impacts of more frequent and intense Siberian boreal fires are wide-ranging, are of large magnitude, and affect all components of Earth's systems—lithosphere (land), hydrosphere (water), atmosphere (air), and biosphere (life). Fires are an ecosystem disturbance. If fire frequency and intensity increase, vegetation might change in structure and composition, for example, from larch forests to deciduous broadleaf or nondeciduous needleleaf forests. Fires also affect local wildlife and livelihoods. Indigenous people in Siberia have reported a northward shift of bears and wolves, driven by fires in the regions south of Siberia, as well as the loss of vast reindeer pastures (*6*). Even faraway ecosystems are affected, because wildfire aerosol deposition may fertilize the Arctic Ocean and increase marine primary productivity (*7*).

Siberian fires also "feed back" to Earth's climate directly through burning highly organic soils and contributing to at least one-third of the total global fire carbon emissions in 2021 (*8*). For example, after the organic soil layer and insulating mosses have burned off, the remaining charcoal that covers the permafrost absorbs most of the incoming solar radiation. The permafrost (ground that has continuously remained below 0°C for at least

[1]Department of Evolutionary Biology and Environmental Studies, University of Zürich, Zürich, Switzerland. [2]Low-Carbon and Climate Impact Research Centre, School of Energy and Environment, City University of Hong Kong, Kowloon, Hong Kong, People's Republic of China. Email: gabriela.schaepman@ieu.uzh.ch

PHOTO: EGOR V. KIRILLIN



Tundra patchwork remains after fire moved through the Indigirka River lowland in Siberia in 2020.

2 years) becomes vulnerable to increased ground heat flux. Yedoma is a distinct type of ancient permafrost found across Siberia that was deposited during the late Pleistocene (between 129,000 and 11,700 years ago). This soil has accumulated carbon over thousands of years, and thawing releases stored carbon into the atmosphere for many years after a fire. Further, when the variability of biomass burning was included in modeling, the effect of fire-producing aerosols on cloud formation led to more warming (*9*). Altogether, extreme fire events might push Arctic permafrost systems to more rapidly reach a climate tipping point that, when crossed, will result in irreversible changes in the Arctic ecosystem and global climate (*10*).

Although climatological conditions are the basic ingredient for fires, they will be influenced by other natural and anthropogenic factors. These include fire-soil and fire-vegetation interactions that can amplify climatic effects on tundra fires. These interactions can also have a dampening effect. For example, burnt areas in Alaska are expected to continue to increase because of climate warming, but areas that once had a fire have run out of fuel for about a decade, limiting fire spread (*11*). Conversely, the development of infrastructure, especially roads, may further increase the likelihood of ignition because of human activities such as campfires, electrical accidents from power lines, and cigarette butts. However, roads can also suppress wildfires by acting as physical barriers and by providing access points for firefighters (*12*). At present, fires in Siberia are only actively suppressed when they threaten villages or infrastructure. But anthropogenic fires could be reduced through policies that strengthen penalties for arsonists, and ecosystem damage could be suppressed by better fire management (*13*). How to manage fires in protected areas remains an area of research across the globe, because more frequent and extreme fires reduce the fuel available for future fires. Hence, if fires are prevented, fire fuel builds up. But a future fire could be much stronger and destroy trees that are normally fire resistant under weaker fire conditions. There is an ongoing debate about whether it is safer to let fires burn if they are not too big to prevent very large fires in the future.

Predicting how the shift in the polar front jet and earlier snowmelt develop under future climate warming, and how this will affect fire occurrence, requires more sophisticated Earth system modeling. Lightning-driven fire ignitions in high latitudes, for example, are not yet adequately represented in such models. Fires might limit Arctic shrub expansion (*14*), but this element is not included in large-scale models that predict future tundra vegetation (*15*). Ground measurements that are important for modeling, but have not yet been made, include determining the depth of soil in Siberia that has been burned; the amount of carbon released to the atmosphere, groundwater, and rivers; vegetation growth after fire; and microclimate effects. Until such measurements are available, scientists can use satellite data to better understand fire events, climatological causes, and their consequences from a distance. ■

REFERENCES AND NOTES

1. R. C. Scholten *et al.*, *Science* **378**, 1005 (2022).
2. V. I. Kharuk *et al.*, *Ambio* **50**, 1953 (2021).
3. P. Jain, M. Flannigan, *J. Clim.* **34**, 6247 (2021).
4. J. A. Francis, S. J. Vavrus, *Geophys. Res. Lett.* **39**, L06801 (2012).
5. Y. Chen *et al.*, *Nat. Clim. Chang.* **11**, 404 (2021).
6. S. Ksenofontov *et al.*, *Polar Geogr.* **42**, 34 (2019).
7. M. Ardyna *et al.*, *Commun. Earth. Environ* **3**, 201 (2022).
8. Reuters Graphics, "Why Arctic fires are releasing more carbon than ever," 8 September 2022; https://graphics.reuters.com/climate-change/wildfire-emissions/zjvqkrwmnvx/index.html.
9. P. DeRepentigny *et al.*, *Sci. Adv.* **8**, eabo2405 (2022).
10. D. I. Armstrong McKay *et al.*, *Science* **377**, eabn7950 (2022).
11. A. Masrur *et al.*, *J. Geophys. Res.* **127**, e2021JG006608 (2022).
12. V. Kuklina *et al.*, *Arct. Sci.* **63**, 41 (2022).
13. J.-S. Kim *et al.*, *Sci. Adv.* **6**, aax3308 (2020).
14. Y. Liu *et al.*, *Nat. Commun.* **13**, 3843 (2022).
15. S. Kruse, U. Herzschuh, *eLife* **11**, e75163 (2022).

ACKNOWLEDGMENTS

J.-S.K. is supported by the Low-Carbon and Climate Impact Research Centre at the School of Energy and Environment, City University of Hong Kong.

10.1126/science.ade8673

GEOLOGY

What lies beneath Yellowstone?

There is more magma than previously recognized, but it may not be eruptible

By **Kari M. Cooper**

What controls how and when a volcano will erupt? Despite some notable successes (*1*, *2*), forecasting volcanic eruptions remains a challenge—not least because there is no way to directly see what is happening beneath volcanoes. Instead, indirect methods are used to glimpse conditions below the surface. An obvious but key requirement for an eruption is the presence of magma (molten rock, consisting of variable proportions of liquid, solid crystals, and volatiles). This magma also needs to be distributed so that it can mobilize and erupt as a coherent body. Therefore, a key issue for eruption hazard assessment is to ascertain how much magma is below the surface and where. On page 1001 of this issue, Maguire *et al.* (*3*) modeled seismic data to image melt (the liquid part of magma) beneath the Yellowstone Caldera. They conclude that more melt is present than had been recognized, and it is located at shallow depths in the crust.

What is known about conditions within a magma reservoir relies on three main approaches: geophysical imaging (such as that presented by Maguire *et al.*), numerical modeling (*4*–*6*), and inferences based on analyses of the erupted products (*7*–*9*). Collectively, this kind of work has led to a revolution in ideas about what magma storage looks like. Early models envisioned a large, mostly liquid magma body that persisted beneath volcanoes for tens or hundreds of thousands of years [the "big tank" model (*10*)]. However, a large body of evidence from more recent studies indicate that magma storage regions are much more complex. At any given time, much of the magma reservoir is likely dominated by solid material rather than liquid [the

Department of Earth and Planetary Sciences, University of California Davis, Davis, CA, USA. Email: kmcooper@ucdavis.edu

mush model (*11*, *12*)] and may be present at relatively cool temperatures for most of the reservoir's history (*8*). Reservoirs also involve storage at multiple depths in the crust ["transcrustal magma reservoirs" (*13*)]. Accumulations of liquid-rich magma in the upper-crustal reservoir are likely short lived, with large eruptions often tapping multiple distinct stored magma bodies (*7*, *14*) that are present simultaneously as separate "pods" of liquid-dominated magma within the larger crystal-dominated mush system.

Thus, ascertaining where the magma is has two parts: the range of depths below the surface where magmas are stored, and how the magma is distributed. Maguire *et al.* found that the largest concentration of melt lies at 3 to 8 km below the surface. Despite the improved spatial resolution of their approach, Maguire *et al.* cannot rule out the presence of liquid-rich magma bodies of a size that could produce lava flows similar to those that erupted since the most recent caldera-forming eruption at Yellowstone. Moreover, "how much" also depends on the distribution of melts; the amount of melt needed to account for the slowest seismic wave speeds in the geophysical data they analyzed ranges from ~10 to 20% depending on whether the melts are concentrated into pods or spread out as thin films between mineral grains.

The eruptive and hazard potential also depend in part on how the melt is distributed. It is easier to mobilize liquid-dominated bodies than to disrupt and mobilize a crystal mush, although both possibilities can occur (*5*, *6*, *15*). The configuration of melts within a mushy magma reservoir undoubtedly encompasses a spectrum ranging between thin films (millimeter scale) to small melt segregations (centimeter to meter scale) and larger melt-rich pods (hundreds of meters to kilometer scale) (see the figure). Determining which distribution exists in which part of the reservoir at any given time requires bringing in information from geochemical and petrological studies. The observation of Maguire *et al.* that the melt is focused within the shallow crust is consistent with depth estimates from studies of past eruptions, and therefore these petrological insights into the past can be used as a window to understand what might be in the reservoir today.

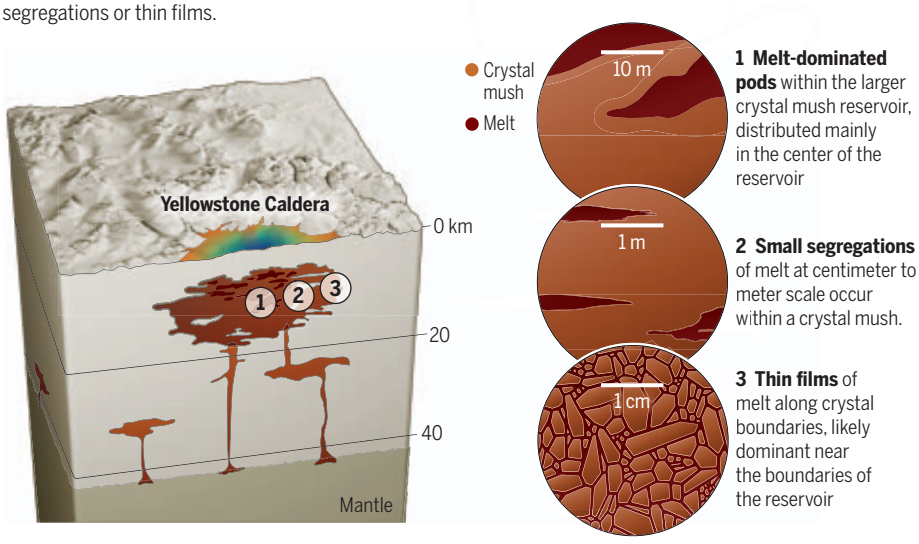
In order to do this, the temptation to overgeneralize from a single sample or from a few analyses should be resisted. Such an approach reflects the "big tank" era, in which magma reservoirs were envisioned as a single body and thus a single sample might be informative. For example, examination of analyses of many mineral grains shows that even individual football-sized samples of eruptions contain minerals that formed from melts with widely varying composition and were stored at differing temperatures at the same time. Such variations are difficult to reconcile with a big tank model, which would predict that minerals would crystallize from a unform magma body and therefore would be compositionally and thermally homogenous at any given time. To move forward, it is necessary to collectively move past the idea that any single component of a magma body is representative of the whole, instead recognizing that each captures distinct information about a different part of the same complex system.

In the future, there is potential to learn about magma reservoirs by using multiple different approaches within the same volcanic system. Geochemical studies can provide insights into melt distribution in the past by understanding how much variability of composition (and therefore how many distinct magma bodies) are sampled by single eruptions. With enough studies that combine the present-day view from seismology with the historical perspective from petrology in enough volcanic systems, a seismic snapshot of a magma reservoir might be captured just before an eruption. This could be compared with the record of past processes contained in deposits from the same eruption and results from numerical models to understand the physical processes that led to an eruption. In turn, this would provide the context needed to interpret seismic snapshots and the signals that precede eruptions in terms of the actual physical and chemical processes occurring in a magma reservoir.

The results of Maguire *et al.* do not indicate that an eruption is more likely than previously thought; the uncertainty about how melts are distributed means that more melt is not necessarily more hazardous, and continuous and careful monitoring of the volcano by the United States Geological Survey (USGS) and partners in the Yellowstone Volcano Observatory has shown no indication of unusual activity. However, with concerted and targeted efforts at understanding processes beneath the surface that lead to eruptions, together with monitoring what volcanoes are doing today, the ambition of understanding what makes volcanoes do what they do is coming closer. ■

Melt distribution within a magma reservoir

Liquid magma (melt) is distributed at different scales in the reservoir beneath the Yellowstone Caldera. Mobilizing melts to produce an eruption is much more difficult if melts are dominantly present as small segregations or thin films.



GRAPHIC: V. ALTOUNIAN/*SCIENCE*

REFERENCES AND NOTES

1. C. G. Newhall, R. S. Punonbayan, Eds., *Fire and Mud: Eruptions and Lahars of Mount Pinatubo, Philippines* (Univ. Washington Press, 1996).
2. P. W. Lipman, D. R. Mullineaux, Eds., "The 1980 eruptions of Mount St. Helens, Washington," *USGS Prof. Paper* 1250 (1981).
3. R. Maguire *et al.*, *Science* **378**, 1001 (2022).
4. C. Annen, *Earth Planet. Sci. Lett.* **284**, 409 (2009).
5. B. Liu, C.-T. Lee, *Earth Planet. Sci. Lett.* **571**, 117113 (2021).
6. G. W. Bergantz, J. M. Schleicher, A. Burgisser, *J. Geophys. Res. Solid Earth* **122**, 6131 (2017).
7. C. J. N. Wilson *et al.*, *Nat. Rev. Earth Environ.* **2**, 610 (2021).
8. K. M. Cooper, A. J. R. Kent, *Nature* **506**, 480 (2014).
9. M. R. Reid, J. A. Vazquez, *Geochem. Geophys. Geosyst.* **18**, 156 (2017).
10. A. F. Glazner, J. M. Bartley, D. S. Coleman, W. Gray, R. Z. Taylor, *GSA Today* **14**, 4 (2004).
11. O. Bachmann, G. W. Bergantz, *J. Petrol.* **49**, 2277 (2008).
12. W. Hildreth, C. J. N. Wilson, *J. Petrol.* **48**, 951 (2007).
13. K. V. Cashman, R. S. J. Sparks, J. D. Blundy, *Science* **355**, eaag3055 (2017).
14. E. J. Swallow, C. J. N. Wilson, B. L. A. Charlier, J. A. Gamble, *J. Petrol.* **60**, 1371 (2019).
15. A. Parmigiani, C. Huber, O. Bachmann, *J. Geophys. Res. Solid Earth* **119**, 6308 (2014).

ACKNOWLEDGMENTS

K.M.C. thanks the National Science Foundation for funding and coauthors and collaborators for contributing to the ideas presented here.

10.1126/science.ade8435

MATERIALS SCIENCE

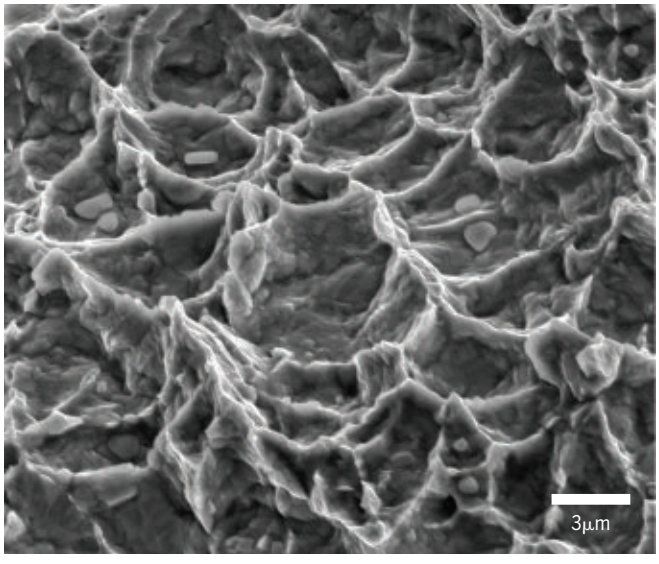
Getting tougher in the ultracold

Certain alloys show exceptional toughness in a liquid helium environment

By **Peng Zhang** *and* **Zhe-Feng Zhang**

The disastrous accident of the *Titanic* in 1912 occurred when the British ocean liner struck an iceberg and sank. Insufficient fracture resistance of the ship's steel at low temperature ensured the ship's demise (*1*). Thereafter, selection of materials with excellent cryogenic toughness became an important prerequisite for low-temperature, load-bearing applications. Despite progress in the understanding of fracture mechanics, most metallic materials show reduced toughness with decreasing temperatures (*2*), especially in the realm of the temperature of liquid helium (−269°C; 4.15 K). Thus, searching for tough alloys in cryogenic temperatures has remained a challenge. On page 978 of this issue, Liu *et al.* (*3*) report that certain alloys containing the metals chromium (Cr), cobalt (Co), and nickel (Ni) show exceptional fracture toughness at 20 K and attribute this property to a sequence of deformation mechanisms. These metal mixtures could potentially be used for applications in especially low temperatures, such as deep-space exploration (*4*).

Medium- and high-entropy alloys are classes of metallic materials that have three or more constituents in equal amounts. Those designed with Cr, Co, and Ni as principal elements display high tolerance to damage, which has triggered a hunt for CrCoNi-based alloys that can withstand extreme environments, such as very low temperatures. But designing alloys with low-temperature toughness stems from understanding the propagation of cracks (fracture properties) and mechanisms that underlie a material's resistance to fracture (*5*)—that is, its toughness. For example, metals with face-centered cubic (fcc) structure usually exhibit excellent toughness at low temperature (*6*). Unfortunately, when the temperature reaches that of the liquid nitrogen environment (reportedly between 63 and 77 K), the resistance to fracturing of most fcc alloys decreases. Clearly, fcc structure alone cannot guarantee low-temperature toughness. Another important property of fcc alloys is the formation of faults in the normal planar stacking of atoms in a crystal. This occurs by decreasing the stacking-fault energy. Such irregularities carry an energy cost because of strain. Stacking-fault energy inversely scales with the amount of mechanical stress needed to deform the crystal lattice (so-called mechanical twinning). Steel comprising iron (Fe), manganese (Mn), and carbon (C), for example, shows increasing toughness at low temperature when the stacking-fault energy decreases (*7*).



Fractography reveals excellent ductile fracture characteristics (dimples) in the high-entropy alloy CrCoNi at ultralow temperature (20 K).

PHOTO: LIU *ET AL.* (*3*)

Liu *et al.* explored the mechanisms underlying the toughness of CrCoNi-based alloys at 20 K (experiments were conducted in a liquid helium environment, but the alloy surface only reached 20 K). The authors measured and observed behaviors such as crack initiation, deformation, and fracture to determine how these metallic materials display increasing resistance to fracture as the temperature decreases, in contrast to most alloys. The authors observed that a low stacking-fault energy promotes changes in deformation mechanisms under high stress that account for fracture toughness. A sequence of such mechanisms simultaneously increases the strength and toughness of CrCoNi-based alloys at cryogenic temperatures (*8*).

The findings of Liu *et al.* support the notion that there are three central principles for optimizing the low-temperature toughness of metallic materials. These principles follow those for improving the strength and plasticity of medium-entropy alloys—that is, optimizing resistance to stress that a material can bear before deforming (strength) and the ability to deform under stress without breaking (plasticity). One of these principles regards achieving a high elastic modulus to inhibit brittle fracture. For brittle materials, such as glass and ceramics, a crack will rupture surfaces with weak atomic binding force and lead to catastrophic fracture (*5*). Conversely, for ductile alloys, a crack will be blunted by emission of dislocations (that is, a crystallographic defect within the structure) and/or increasing mechanical twinning. The latter consumes energy that is dissipated as the microstructure changes—a process known as plastic work. Therefore, the key to improving toughness of materials is to inhibit the occurrence of brittle fracture and improve the plastic work in the vicinity of the crack tip (the point at which a crack propagates).

Among the three principles (*8*), increasing the elastic modulus can increase the load required for fracture. This, in turn, inhibits propagation of a crack, resulting in high fracture toughness. For magnesium, aluminum, copper, and titanium alloys and steels, fracture toughness increases almost synchronously with their elastic modulus (*3*, *9*). The CrCoNi-based medium- and high-entropy alloys examined by Liu *et al.* have a modulus of >200 GPa, similar to that of steel (*10*), which accounts for their high fracture toughness.

Another design principle is reducing the stacking-fault energy to improve the plastic work (*8*). Reducing this energy can simultaneously improve the strength and ductility of copper alloys (*11*), FeMn-based steels (*12*), and various fcc alloys (*13*). Be-

Institute of Metal Research, Chinese Academy of Sciences, Shenyang 110016, China.
Email: pengzhang@imr.ac.cn; zhfzhang@imr.ac.cn

cause plastic work can be estimated as the product of strength and plasticity, reducing the stacking-fault energy can improve the plastic work. Indeed, Liu *et al.* leveraged the stacking-fault energy effect to create a CrCoNi-based high-entropy alloy to achieve excellent low-temperature fracture toughness.

The third design principle relates to fcc structural stability (*8*). A metallic material with this structure may undergo crystal structure transition (phase transformation) during deformation at low temperatures. It is generally believed that this transition will form a brittle structure that is harmful to the toughening of materials. However, not all metals with such transformed structures are brittle (*14*), and the energy generated with the phase transformation can improve toughness. Therefore, the key to controlling fcc stability is ensuring that the plastic work will not decrease as a result of phase transformation but will instead inhibit phase transformation (*8*). This conclusion is also verified by Liu *et al.*

Machine learning, rather than endless experimental searching (*15*), is expected to accelerate the material design process for cryogenic applications. Indeed, elastic modulus, stacking-fault energy, and fcc phase stability could be used in machine learning programs. These three characteristics can be obtained not only through database queries but also through high-throughput experiments and first-principles calculations (*8*). Machine learning combined with better understanding of physical mechanisms should create enormous opportunities for materials discovery. ■

REFERENCES AND NOTES

1. D. Ashkenazi, *Archaeol. Anthropol. Sci.* **12**, 34 (2020).
2. Y. Kimura, T. Inoue, F. Yin, K. Tsuzaki, *Science* **320**, 1057 (2008).
3. D. Liu *et al.*, *Science* **378**, 978 (2022).
4. M. Yang *et al.*, *Scr. Mater.* **172**, 66 (2019).
5. Z. F. Zhang, J. Eckert, *Phys. Rev. Lett.* **94**, 094301 (2005).
6. R. P. Reed, A. F. Clark, *Materials at Low Temperatures* (American Society for Metals, 1983).
7. Y. Wang *et al.*, *Commun. Mater.* **2**, 44 (2021).
8. J. X. Yan *et al.*, *J. Mater. Sci. Technol.* 10.1016/j.jmst.2022.07.031 (2022).
9. M. F. Ashby, *Materials Selection in Mechanical Design* (Butterworth-Heinemann, ed. 4, 2011).
10. A. Haglund *et al.*, *Intermetallics* **58**, 62 (2015).
11. Y. Z. Tian *et al.*, *Acta Mater.* **110**, 61 (2016).
12. R. Q. Bao *et al.*, *Mater. Sci. Technol.* **21**, 451 (2013).
13. X. H. An *et al.*, *Prog. Mater. Sci.* **101**, 1 (2019).
14. S. Zhao *et al.*, *Science* **373**, 1363 (2021).
15. Q.-M. Hu, R. Yang, *Science* **378**, 26 (2022).

ACKNOWLEDGMENTS

The authors acknowledge Z.-J. Zhang and S.-T. Zhao for critical comments as well as support by the National Natural Science Foundation of China under grant no. 52130002 and the K.C. Wong Education Foundation (GJTD-2020-09).

10.1126/science.adf2205

EPIGENETICS

Active DNA demethylation damages DNA

Active DNA demethylation maintains enhancer activity in nonproliferating cells but can damage DNA

By **Isaac F. López-Moyado**[1,2] *and* **Anjana Rao**[1,2]

In mammalian genomes, cytosine residues can be covalently modified by addition of a methyl group. DNA methylation levels at gene regulatory regions change as cells respond to stimuli, but whether this is a cause or consequence of changes in gene expression is unknown. On page 983 of this issue, Wang *et al.* (*1*) show that active DNA demethylation is necessary for enhancer activation and lineage specification in postmitotic neurons and macrophages.

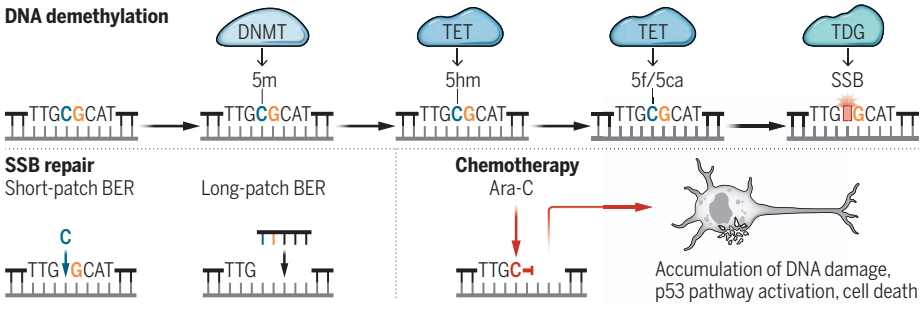
DNA demethylation involves 5-methylcytosine (5mC) oxidation by the ten-eleven translocation (TET) methylcytosine dioxygenases. Most investigations of demethylation have examined proliferating cells, in which the oxidized methylcytosines 5-hydroxymethylcytosine (5hmC), 5-formylcytosine (5fC), and 5-carboxylcytosine (5caC) facilitate "passive," replication-dependent DNA demethylation. The hemi-modified DNA strands containing these bases are poorly recognized by DNA methyltransferase 1 (DNMT1), and therefore methylation is progressively lost. A different process of "active" (replication-independent) DNA demethylation involves thymine DNA glycosylase (TDG), which excises T:G mismatches but also excises the oxidized methylcytosines 5fC and 5caC when normally base-paired to G (see the figure).

In postmitotic cells such as fully differentiated neurons, DNA demethylation is replication independent. Neuronal cells have high levels of 5hmC (*2, 3*), and postmitotic mouse Purkinje neurons require TET proteins and oxidized methylcytosines for DNA demethylation of select gene regulatory regions (*3*). Additionally, in primary neurons and in "iNeurons" derived from human induced pluripotent stem cells (iPSCs), regions that regulate gene expression, such as enhancers, accumulate single-stranded DNA breaks (SSBs) (*4, 5*). These SSBs occurred largely at methylcytosine residues at which TET was active (*4*). Wang *et al.* investigated whether TET-TDG–mediated 5fC and 5caC excision might be the source of these SSBs.

SSBs resulting from 5fC and 5caC excision can be repaired by two distinct processes of base excision repair (BER): short-patch repair by DNA polymerase β (Pol β), which replaces the single missing nucleotide with unmodified C; and long-patch repair, in which Pol ε and Pol δ synthesize 2 to 30 nucleotides using the undamaged strand as a template. Wang *et al.* showed that iNeurons deficient for TDG accumulated far fewer SSBs than iNeurons with active TDG. SSBs

Programmed breaks in active DNA demethylation

CpG dinucleotides are methylated by DNA methyltransferases (DNMTs). During active DNA demethylation, ten-eleven translocation (TET) enzymes oxidize 5-methylcytosine (5mC) to 5-hydroxymethylcytosine (5hmC), 5-formylcytosine (5fC), and 5-carboxylcytosine (5caC). 5fC and 5caC are removed by thymine DNA glycosylase (TDG), which generates a single-stranded DNA break (SSB). This is repaired by short-patch or long-patch base excision repair (BER). Incorporation of chain-terminating cytidine analogs [such as the chemotherapeutic arabinosylcytosine (Ara-C)] blocks BER and results in the accumulation of DNA damage, leading to cell death.



GRAPHIC: A. FISHER/*SCIENCE*

were similarly TDG dependent in mouse "iMacrophages" reprogrammed from precursor B cells (pre-B cells), although different strategies were needed because iNeurons preferentially use long-patch BER, whereas iMacrophages use almost exclusively short-patch BER. This indicates that the SSBs at enhancers are caused by TDG.

Because the highly coordinated activity of the TET-TDG-BER machinery rapidly repairs any SSBs that arise during active DNA demethylation (*6*), Wang *et al.* used a mixture of chain-terminating dideoxynucleosides to optimally detect SSBs associated with active DNA demethylation in iNeurons and iMacrophages. Similar nucleoside analogs, such as arabinosylcytosine (Ara-C, also called cytarabine), are commonly used as anticancer chemotherapeutics to inhibit DNA replication. When used at high doses, these drugs can have neurotoxic side effects (*7*). Wang *et al.* tested the hypothesis that SSBs produced by active DNA demethylation would facilitate the addition of cytidine analogs such as Ara-C, which would be incorporated in place of cytosines during long-patch BER and so would induce DNA damage at enhancers. Indeed, Wang *et al.* found that treatment of iNeurons with Ara-C in culture triggered a robust DNA damage response and resulted in cell death, but notably only when TDG was present in these cells. These results demonstrate that TDG can render cells susceptible to further DNA damage in the presence of nucleoside analogs, and call attention to the potential of TDG inhibitors in preventing the neuronal cell death that is associated with chemotherapy.

Although the study of Wang *et al.* establishes the role of TDG in generating SSBs, the importance of active DNA demethylation in promoting enhancer function is less clear. The transcriptional consequences of TDG deficiency appear to be cell-type and context specific. TDG is essential for reprogramming mouse embryonic fibroblasts to iPSCs (*8*), and germline TDG deficiency results in mouse embryonic lethality (*9, 10*). But TDG deficiency has little effect on demethylation of the paternal genome in mouse zygotes (*11*), and adult mice with conditional deletion of *Tdg* in all tissues show normal T cell differentiation and hematopoiesis (*12*). Wang *et al.* showed that TDG affects only a subset of iMacrophage functions: TDG was not required for pre-B to iMacrophage reprogramming but was necessary for enhancer activity and consequent increased expression of genes involved in iMacrophage function, including CSF1R (macrophage colony-stimulating factor 1 receptor) and the FIRE (fms-intronic regulatory element) super-enhancer, which controls *CSF1R* expression (*13*). Moreover, iMacrophages in which *TDG* was deleted were unable to phagocytose bacteria, suggesting that enhancers required for this process are normally demethylated by TDG. Presumably, enhancers sensitive to TDG depletion contain CpG dinucleotides that if methylated, would interfere with the binding of key transcription factors necessary for enhancer function.

The study of Wang *et al.* reinforces the idea that DNA demethylation stemming from TET-TDG activity can be essential for enhancer function in nonproliferating cells. This may also be the case in other cell types because in every cell type studied, the most active enhancers are also the most highly enriched with 5hmC. Moreover, the study establishes that TDG activity can be a source of programmed breaks (SSBs) in the cell. Although the active DNA demethylation machinery is quite efficient, SSBs can pose a threat for cells when misrepaired—for instance, in the presence of Ara-C. It is also possible that high levels of DNA repair synthesis through long-patch BER make long-lived neurons susceptible to mutagenesis, and this mechanism may explain why mutations in genes encoding SSB repair enzymes are common in several neurodegenerative diseases (*14*). Indeed, recent single-cell sequencing of human neurons revealed an age-dependent increase in mutations enriched at DNA repair hotspots associated with enhancers (*15*), implying that TDG activity might be involved. Future studies should establish how TET-TDG activity, active DNA demethylation, and associated SSBs at enhancers affect neuronal function during development, aging, and the onset of neurological diseases. ■

REFERENCES AND NOTES

1. D. Wang *et al.*, *Science* **378**, 983 (2022).
2. S. Kriaucionis, N. Heintz, *Science* **324**, 929 (2009).
3. E. Stoyanova, M. Riad, A. Rao, N. Heintz, *eLife* **10**, e66973 (2021).
4. W. Wu *et al.*, *Nature* **593**, 440 (2021).
5. D. A. Reid *et al.*, *Science* **372**, 91 (2021).
6. A. R. Weber *et al.*, *Nat. Commun.* **7**, 10806 (2016).
7. J. B. Stone, L. M. DeAngelis, *Nat. Rev. Clin. Oncol.* **13**, 92 (2016).
8. X. Hu *et al.*, *Cell Stem Cell* **14**, 512 (2014).
9. S. Cortellino *et al.*, *Cell* **146**, 67 (2011).
10. D. Cortázar *et al.*, *Nature* **470**, 419 (2011).
11. S. Gkountela, A. T. Clark, *Cell Stem Cell* **15**, 393 (2014).
12. A. Onodera *et al.*, *Genome Biol.* **22**, 186 (2021).
13. R. Rojo *et al.*, *Nat. Commun.* **10**, 3215 (2019).
14. K. W. Caldecott, M. E. Ward, A. Nussenzweig, *Nat. Genet.* **54**, 115 (2022).
15. L. J. Luquette *et al.*, *Nat. Genet.* **54**, 1564 (2022).

ACKNOWLEDGMENTS

A.R. receives support from the National Institutes of Health (grant R35 CA210043).

[1]Division of Signaling and Gene Expression, La Jolla Institute for Immunology, La Jolla, CA, USA. [2]Sanford Consortium for Regenerative Medicine, La Jolla, CA, USA. Email: arao@lji.org

10.1126/science.adf3171

MEDICINE

Triggering rare HIV antibodies by vaccination

Clinical trial shows that an HIV vaccine can elicit rare antibodies, but there is more to do

By **Penny L. Moore**[1,2]

An HIV vaccine is urgent: A recent UNAIDS report entitled "In Danger" showed that in 2021, one adolescent girl or young woman became infected with HIV every 2 min, especially in sub-Saharan Africa (*1*). A vaccine will likely need to elicit broadly neutralizing antibodies (bnAbs), which are able to recognize globally diverse HIV strains and can prevent HIV infection (*2*). However, triggering bnAbs by vaccination has proven impossible so far. A key challenge is that bnAbs rarely develop, even during infection. Furthermore, bnAb precursors (or germlines) are uncommon in human immunological repertoires. Devising vaccines specifically aimed at recruiting these rare precursors, an approach referred to as "germline targeting," has driven major immunological advances with broad applicability for other pathogens. On page 964 of this issue, Leggat *et al.* (*3*) provide clinical proof of concept for the germline-targeting approach for HIV vaccination and detailed immunological insights upon which future vaccine trials can be designed.

HIV bnAbs target multiple epitopes on the envelope protein. One epitope, the CD4 binding site (CD4bs) has been a particular focus for germline targeting because some bnAbs to this site, called VRC01-class bnAbs [named for their prototype, VRC01, a monoclonal antibody isolated from an individual a decade ago (*4*)] have a highly constrained angle of approach to their epitope (*5*). This translates to very limited genetic options with which the otherwise vast immunoglobulin (antibody) repertoire can tackle this epitope (*6*). This focused antibody footprint was highly amenable to the design of the germline-targeting immunogen eOD-GT8, which is

[1]National Institute for Communicable Diseases, Johannesburg, South Africa. [2]Faculty of Health Sciences, University of the Witwatersrand, Johannesburg, South Africa. Email: pennym@nicd.ac.za

a self-assembling nanoparticle that presents 60 copies of an engineered HIV envelope protein bearing mutations designed to enhance its affinity for VRC01-class precursors (*7*–*9*).

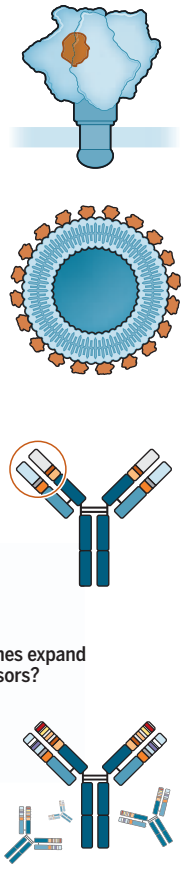
The preclinical evidence supporting eOD-GT8 as a vaccine immunogen was compelling, with preclinical studies confirming that the vaccine bound to rare VRC01-like precursors (*9*, *10*). In mouse models carefully chosen to replicate the scarcity of VRC01-like precursors in humans (many mouse models overexpress antibodies of interest to vaccine designers, giving biased readouts when extrapolated to humans), eOD-GT8 showed good priming or triggering of VRC01-class antibodies (*11*).

The robust preclinical data provided a strong foundation for moving eOD-GT8 into a phase 1 clinical trial of 48 individuals, as reported by Leggat *et al.*, where the safety profile proved favorable. But measuring immune responses to eOD-GT8 was more complicated than in most phase 1 vaccine trials. Vaccine trials generally rely on serological readouts of antibody responses. However, the critical readout for how well eOD-GT8 worked to prime antibodies was a genetic readout. VRC01-class bnAbs have a specific genetic "signature," defined as the use of heavy chain variable gene alleles VH1-2*02 or *04 combined with any light chain complementarity determining region 3 that has a length of five amino acids. This precise genetic signature enables their numbers to be tracked after vaccination. Sampling of blood and tissue from vaccine and placebo recipients and sequencing of immunoglobulin genes showed that eOD-GT8 consistently primed a substantial increase in VRC01-class B cells, which were barely detectable before vaccination (see the figure). However, it is important to note that this reliance on sequencing approaches reflects that these are, at present, low-frequency antibody responses that are not yet detectable by traditional serological methods. Further work remains to be done to amplify these responses to higher concentrations, which are more likely to be associated with protection from infection.

Importantly, the VRC01-class antibodies triggered by eOD-GT8 vaccination also began their journey toward becoming bnAbs. bnAbs undergo a period of maturation where they acquire the ability to bind multiple HIV strains. The germline antibodies must acquire a very specific set of mutations (well defined from studies of CD4bs antibodies in HIV infection) that enables these precursors to become bnAbs. Sequencing of plasma cells and lymph node cells from vaccinated individuals in this trial showed that eOD-GT8–triggered antibodies were accumulating some of the correct mutations and maturing in the direction of bnAbs—but not far enough. Encouraging further mutation through vaccination is the next challenge for HIV vaccine design. Many possibilities are being explored in preclinical and human experimental trials that are aimed at accelerating HIV vaccine discovery. Most are based on the idea of sequential administration of varying vaccines to guide the maturation of breadth (*12*). A key question that needs to be tested experimentally is how large an antigenic leap these primed antibodies can tolerate without immunologically "dropping out" of the vaccination process. Thus, if a booster shot is too different from the previous vaccine, antibodies that have been triggered by the first vaccination may not recognize the booster and will not mature further. However, the incorporation of many different shots into an HIV vaccine regimen is unappealing. Getting the balance right between the need for antibody maturation toward bnAbs and feasibility in the real world will be essential.

Germline targeting

Rare precursors of HIV broadly neutralizing antibodies (bnAbs) were elicited from vaccination with the nanoparticle eOD-GT8. However, for these antibodies to become protective against HIV infection, future vaccines will need to drive further expansion and greater numbers of antibody mutations.



Germline targeting will only work if people have the germline immunoglobulin alleles that are being targeted. For VRC01-like antibodies, most people appear to have the required heavy chain alleles, although Leggat *et al.* identified 1 in 48 donors who did not and thus failed to respond to eOD-GT8 vaccination. A key caveat is that much of what is known about human immunogenetics is limited to Caucasian populations (*13*). There is an urgent need to expand such studies to include people with diverse ancestries, particularly those most burdened by infectious diseases.

The clinical trial reported by Leggat *et al.* provides persuasive human data supporting the concept of germline targeting. However, VRC01-class antibodies can be considered low-hanging fruit for this approach owing to the highly conserved genetics of their precursors. bnAbs to other HIV epitopes are much more promiscuous in their approach to epitope binding (*12*). This has made it harder to engineer vaccines equivalent to eOD-GT8 for other HIV bnAbs, although several candidates are being tested (*12*). Public (shared) antibody responses to other pathogens such as influenza virus and severe acute respiratory syndrome coronavirus 2 (SARS-CoV-2) are being increasingly identified, and germline targeting for these responses will surely gain traction with these clinical data. This trial is an essential step toward the development of a preventative vaccine that is able to trigger VRC01-class CD4bs bnAbs. In parallel, ongoing efforts are being made to trigger bnAbs to other HIV epitopes. An HIV vaccine will need to pull together all these research strands for a multipronged, polyfunctional approach. This will need sustained collaboration and investment in the basic immunological research that resulted in this seminal proof of concept in humans. ■

REFERENCES AND NOTES

1. UNAIDS, "In danger: UNAIDS global AIDS update 2022" (Joint United Nations Programme on HIV/AIDS, 2022); https://bit.ly/3EuL4Ep.
2. L. Corey *et al.*, *N. Engl. J. Med.* **384**, 1003 (2021).
3. D. J. Leggat *et al.*, *Science* **368**, eadd6502 (2022).
4. X. Wu *et al.*, *Science* **329**, 5993 (2010).
5. T. Zhou *et al.*, *Immunity* **39**, 245 (2013).
6. A. P. West Jr., R. Diskin, M. C. Nussenzweig, P. J. Bjorkman, *Proc. Natl. Acad. Sci. U.S.A.* **109**, E2083 (2012).
7. J. Jardine *et al.*, *Science* **340**, 711 (2013).
8. J. G. Jardine *et al.*, *Science* **349**, 156 (2015).
9. J. G. Jardine *et al.*, *Science* **351**, 1458 (2016).
10. C. Havenar-Daughton *et al.*, *Sci. Transl. Med.* **10**, 448 (2018).
11. D. Sok *et al.*, *Science* **353**, 1557 (2016).
12. W. B. Williams, K. Wiehe, K. O. Saunders, B. F. Haynes, *J. Int. AIDS Soc.* **24**, e25831 (2021).
13. A. Auton *et al.*, *Nature* **526**, 68 (2015).

ACKNOWLEDGMENTS

P.L.M. is supported by the South African Research Chairs Initiative of the South African Department of Science and Innovation and the National Research Foundation of South Africa.

10.1126/science.adf3722

GRAPHIC: A. MASTIN/*SCIENCE*

POLICY FORUM

DATA ACCESS

Legal reform to enhance global text and data mining research

Outdated copyright laws around the world hinder research

By **Sean M. Fiil-Flynn[1], Brandon Butler[2], Michael Carroll[1], Or Cohen-Sasson[3], Carys Craig[4], Lucie Guibault[5], Peter Jaszi[1], Bernd Justin Jütte[6], Ariel Katz[7], João Pedro Quintais[8], Thomas Margoni[9], Allan Rocha de Souza[10], Matthew Sag[11], Rachael Samberg[12], Luca Schirru[13], Martin Senftleben[8], Ofer Tur-Sinai[14], Jorge L. Contreras[15,16]**

Researchers engaged in text and data mining (TDM) research collect vast amounts of digitized material and use software to analyze and extract information from it. TDM is a crucial first step to many machine learning, digital humanities, and social science applications, addressing some of the world's greatest scientific and societal challenges, from predicting and tracking COVID-19 to battling hate speech and disinformation (*1*–*3*). Although applications of TDM often occur across borders, with researchers, subjects, and materials in more than one country, a patchwork of copyright laws across jurisdictions limits where and how TDM research can occur. With the World Intellectual Property Organization (WIPO) Standing Committee on Copyright and Related Rights, and legislatures around the world, deliberating the harmonization of copyright exceptions for various research uses, we discuss policy measures that can ensure that TDM research is unambiguously authorized under copyright law.

Most text, images, and other materials that TDM researchers use are subject to copyright law. Copyright law gives the owner of a protected work the legal right to prohibit reproduction, distribution, modification, and other forms of exploitation of that work without the owner's permission. These rights apply even if the material is readily accessible—for example, published on the internet or available in a library.

The justifications for copyright are grounded both in the rights of individual authors in their creations and in instrumentalist incentives for the creation and dissemination of new works. Copyright thus gives the author of a work, or the author's assignee (e.g., a publisher), the exclusive right to reproduce, transmit, and make derivatives of the protected work and to prevent the unauthorized appropriation of these rights (*4*). Although copyright originally subsisted solely in textual works of authorship, today it has expanded to cover graphical and visual works and, in some countries, data and databases [though some countries, including member states of the European Union (EU), have separate statutes protecting databases].

Each stage of a TDM project is potentially constrained by copyright depending on how the scope of protection is interpreted. Copyright prohibitions on unlicensed reproduction may be implicated when sources are digitized, formatted, and compiled into a corpus that can be mined for analysis. Copyright may also limit the application of an algorithm to a TDM corpus, which may make additional temporary copies in computer memory. Copyright restrictions on transmitting and reproducing works may be implicated when researchers collaborate, when examiners validate, and when publishers report results. Thus, without copyright permission, or the application of exceptions under copyright law, much of the world's copyrighted material may be off limits to TDM use.

Some publishers make limited copyright licenses available for TDM uses, often for additional fees charged to libraries or researchers. But paid licensing is not an affordable or viable option for many critical TDM projects. TDM research often requires use of massive datasets with works from many publishers, including copyright owners that cannot be identified or are unwilling to grant licenses. Forcing researchers to use only licensed or public domain content (i.e., content in which there is no enforceable copyright) can restrict topics of study, hamper reproducibility and validation (*5*), bias results (*6*), and dissuade researchers from undertaking projects (*7*). A lack of a license need not, and should not, be an absolute barrier to TDM research.

The rights granted by copyright are not absolute. All international copyright treaties permit, and all countries have, exceptions from copyright protection for various purposes, some of which may authorize TDM research. In the US, for example, a flexible exception exists for "fair use" for purposes such as education and research and has been interpreted by courts to permit at least some TDM uses. Copyright laws in many other countries contain exceptions for research (or "scientific") uses that can be interpreted to apply to TDM uses (*4*). But only about a fifth of these research exceptions are broad enough to permit the full range of TDM research, which requires the ability to copy, share, and analyze whole works in collaboration with others (*8*) (see the figure and table). For example, some countries have research exceptions that permit uses only of excerpts of a work (e.g., Argentina), do not apply to uses of books or other kinds of works (e.g., most post-Soviet countries), or require membership in a specific research institute (e.g., Sweden).

Empirical studies show that copyright exceptions for research matter—with correlations between more permissive research exceptions and higher production of citable works of scholarship (*9*) and increased academic use of TDM methodologies (*10*). But until legal enabling environments for TDM research can be harmonized, the full benefits from this new research frontier will remain inadequately explored.

LEGALLY ENABLING TDM RESEARCH

Ideally for researchers, a minimum standard for global uses of TDM would be implemented everywhere. There are a number of avenues that policy-makers can take to promote more harmonization of copyright exceptions for TDM uses.

[1]Program on Information Justice and Intellectual Property, Project on the Right to Research and International Copyright, American University Washington College of Law, Washington, DC, USA. [2]University of Virginia Library, Charlottesville, VA, USA. [3]Zvi Meitar Center for Advanced Legal Studies, Faculty of Law, Tel Aviv University, Tel Aviv, Israel. [4]Osgoode Hall Law School, York University, Toronto, Canada. [5]Dalhousie University, Schulich School of Law, Law and Technology Institute, Halifax, Canada. [6]Sutherland School of Law, University College Dublin, Belfield, Ireland. [7]Faculty of Law, University of Toronto, Toronto, Canada. [8]University of Amsterdam, Institute for Information Law (IViR), Amsterdam, Netherlands. [9]Centre for IT & IP Law (CiTiP), Faculty of Law, University of Leuven (KUL), Leuven, Belgium. [10]Federal University of Rio de Janeiro (UFRJ), Rio de Janeiro, Brazil. [11]Emory University, School of Law, Atlanta, GA, USA. [12]University of California, Berkeley, Berkeley, CA, USA. [13]Pontifical Catholic University of Rio de Janeiro, Rio de Janeiro, Brazil. [14]Faculty of Law, Ono Academic College, Kiryat Ono, Israel. [15]University of Utah S. J. Quinney College of Law, Salt Lake City, UT, USA. [16]Department of Human Genetics, University of Utah School of Medicine, Salt Lake City, UT, USA. Email: sflynn@wcl.american.edu

International treaties

Nearly all countries provide a high baseline level of copyright protection as the result of several widely adopted multilateral treaties, beginning with the Berne Convention for the Protection of Literary and Artistic Works (Berne, 1886) and continuing through the WIPO "Internet Treaties" (Geneva, 1996). A key feature of these treaties is a requirement that signatory countries impose high standards for protecting copyright but leave exceptions, such as those permitting research, largely to the discretion of national legislatures and courts. The result is the fragmented landscape of exceptions shown in the figure. But the tide is turning. The WIPO's Standing Committee on Copyright and Related Rights is now deliberating over the harmonization of exceptions for uses that include research. Coalitions of researchers and academics are proposing that this forum draft a treaty that would permit cross-border and other uses of research materials to permit TDM everywhere (*11*).

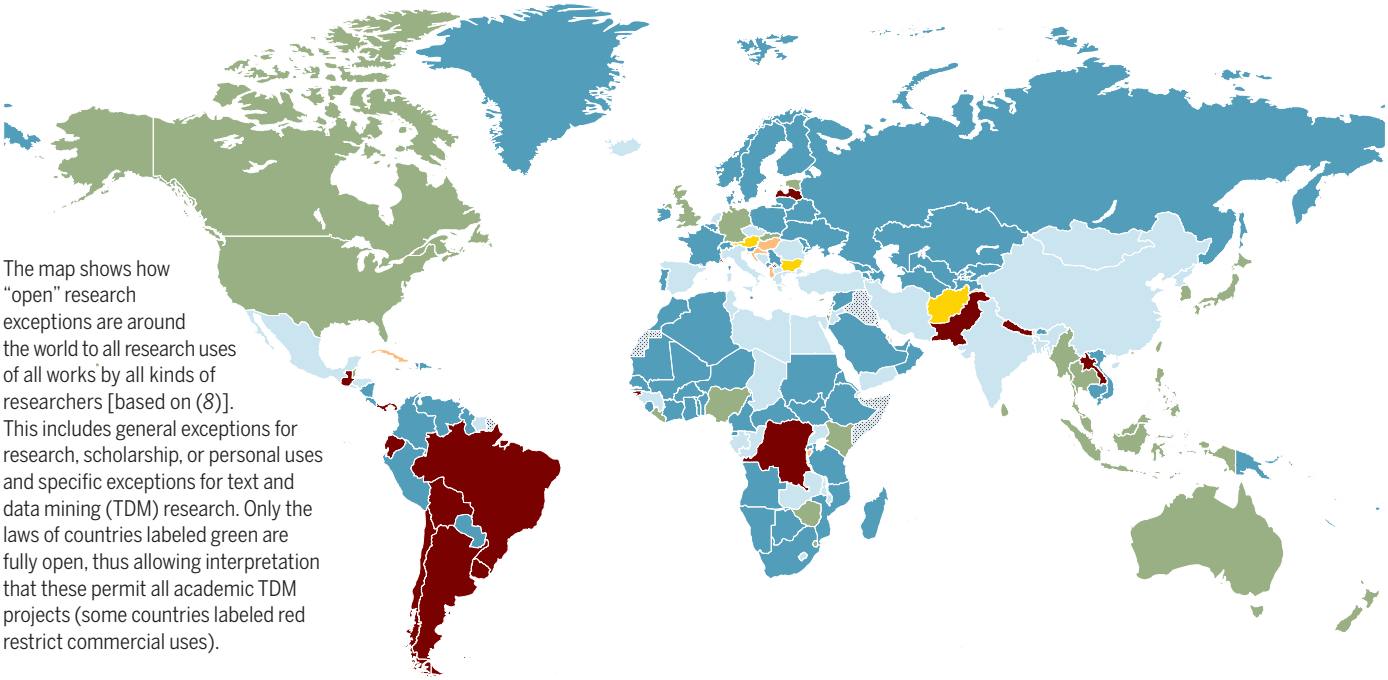
There are important precedents for an international treaty that imposes uniform copyright exceptions around the world. For example, WIPO's last major treaty, the Treaty to Facilitate Access to Published Works for Persons Who Are Blind, Visually Impaired or Otherwise Print Disabled (Marrakesh, 2013), harmonized copyright exceptions for people with visual impairments. In addition, the EU recently enacted an extensive new directive including a requirement that national copyright laws permit at least some TDM research (EU, 2019/790).

Domestic law reform

Domestic legislatures can independently amend their laws to permit TDM and other research uses without any action at the international level. Such legal adjustments are not unprecedented—copyright exceptions to permit TDM have recently appeared in fair use case law in the US (*12*) and in legislative changes in the EU, Singapore, Japan, Switzerland, and the UK (*8*). It is important for a TDM exception to apply to uses of all kinds of works (including audiovisual works used in media monitoring, for example) and enable sharing of materials at least for the purpose of collaboration and validation. Some scholars propose clarifying that all "nonexpressive" (not shared publicly) uses of works in TDM and other research should be deemed to be outside of copyright regulation (*13*). Japan recently implemented this approach into its law, adopting an exception from copyright control "where such exploitation is not for enjoying or causing another person to enjoy the ideas or emotions expressed in such work," such as "in a data analysis" (2018, Article 30-4).

The extension of TDM exceptions to commercial uses may be controversial. On one hand, many commercial users might be capable of paying licensing fees and other transaction costs, and copyright exceptions that simply transfer wealth from copyright owners to commercial TDM users, might seem arbitrary and unjustified. On the other hand, many socially beneficial uses of TDM—including the BlueDot program that originally tracked COVID-19 (*1*) or internet search engines that copy and mine the entire internet (*3*)—would likely not exist if commercial uses were excluded from copyright exceptions. Some countries see commercial TDM as a way to invest in domestic innovation and technology transfer. The EU recently adopted a rule that, although not fully tested, permits copyright holders to opt out of commercial (but not "scientific" or "cultural") TDM uses.

Research exceptions in copyright laws around the world



The map shows how "open" research exceptions are around the world to all research uses of all works by all kinds of researchers [based on (*8*)]. This includes general exceptions for research, scholarship, or personal uses and specific exceptions for text and data mining (TDM) research. Only the laws of countries labeled green are fully open, thus allowing interpretation that these permit all academic TDM projects (some countries labeled red restrict commercial uses).

- **Open research exception:** permits all research uses (including sharing) of all works by all users
- **Restrictions on sharing:** permit reproductions of whole works for research but do not extend to communications with others for purposes such as collaboration or validation
- **Restrictions to private reproduction:** provide a research exception only for use by individuals for a "private" or "personal" use
- **Restrictions to institutional users:** provide a research exception that applies only to institutions, such as nonprofit libraries
- **Restrictions on types of works:** permit research uses of whole works only of certain kinds, often prohibiting uses of whole books and databases
- **TDM restricted:** confine research exceptions to short excerpts, effectively prohibiting TDM uses
- Not mapped

GRAPHIC: ADAPTED BY N. CARY/*SCIENCE*

Another recent TDM exception, enacted by Singapore in 2021, offers a model linking generality and specificity. In addition to a broad fair use exception similar to US law (2021, Part 5, Division 2), Singapore enacted a specific TDM exception for "computational data analysis," including the ability to share reproduced works with others "for the purpose of (i) verifying the results of the computational data analysis" and for "(ii) collaborative research or study relating to the purpose of the computational data analysis" (2021: Part 5, Division 8). Unfortunately, some TDM exceptions in other countries fall short by failing to authorize the sharing of works in collaborative research or otherwise restricting the full scope of TDM methods (see the table).

Policy guidance

Guidance in the interpretation and amendment of copyright law could help policymakers evaluate their options. Even in countries with permissive legislation, there is likely to be value in clarifying the application of national law to TDM research. Such guidance can be provided, for example, through statements of best practices developed by the research community in collaboration with legal experts. Statements of best practices in fair use have been successful in enabling filmmakers, educators, research librarians, and other user-creators to confidently use copyright materials in their work (*14*).

LIBERATE AND REGULATE

The resistance to TDM exceptions in copyright comes primarily from the multinational publishing industry, which is a strong voice in copyright debates and tends to oppose expansions to copyright exceptions. But the success at adopting exceptions for TDM research in the US and EU already—where publishing lobbies are strongest—shows that policy reform in this area is possible. Publishers need not be unduly disadvantaged by TDM exceptions because publishers can still license access to their databases, which researchers must obtain in the first instance, and can offer products that make TDM and other forms of research more efficient and effective.

Policy-makers and the public may fear that expanding TDM rights will empower technology companies and models of surveillance capitalism that are under increasing scrutiny by regulators. But copyright permission does not trump privacy, consumer protection, or other regulation of the activity of technology conglomerates. Countries can liberate TDM research and still regulate these other areas.

Failing to authorize TDM research everywhere aggravates harmful disparities in our global research system. As shown in the figure, the most open regimes for TDM research are concentrated in some of the wealthiest countries and regions, whereas many poorer countries have the most restrictive copyright laws. To ensure that the needs of TDM researchers are heard in the local and national forums where copyright laws can be modified to enable this research, researchers themselves must speak out to voice their concerns and needs. It is time that copyright laws around the world are adapted to enable TDM research. ■

TDM exceptions in copyright laws

The table shows the small number of countries that had enacted specific copyright exceptions for text and data mining (TDM) research as of July 2021 [based on (*8*)]. It applies the same color scheme as that in the figure, thus showing that only a small number of countries with TDM exceptions at the time had legislated to allow all academic TDM research. Some countries (such as the UK, Switzerland, and various EU countries) are different colors in the figure than in this table because the map in the figure identifies the most open research exception, including any general exception for a research use, and this table only analyzes specific TDM exceptions. The UK, Switzerland, and some EU countries have more open general research exceptions than they provide specifically for TDM research (for example, their general research exceptions apply to all uses, not only reproduction). Whether one can apply the more general exception above and beyond the uses allowed by the TDM exception is a local legal question that this study did not attempt to answer. EU DSM Art 3, Article 3 of the EU Directive on Copyright in the Digital Single Market.

COUNTRY	COMMERCIAL	USES PERMITTED	USERS	WORKS	TYPOLOGY
Japan	Yes	Use	All	All	Open to TDM
Singapore	Yes	Reproduction, communication	All	All	Open to TDM
Germany	No	Reproduction, communication, storage	All	All	"Open to TDM (noncommercial)"
Estonia	No	"processing"	All	All	"Open to TDM (noncommercial)"
UK	No	Reproduction	All	All	Reproduction only
Switzerland	Yes	Reproduction	All	All	Reproduction only
EU DSM Art 3	Maybe	Reproduction, storage	Cultural institutions	All	Cultural institutions only
France	No	Reproduction, communication (decree)	All	Scientific writings	Limitation on works
Ecuador	Maybe	Safe harbor for liability of libraries for TDM "acts carried out by their users"	Libraries, archives (safe harbor)	All	Lacks TDM right; safe harbor only

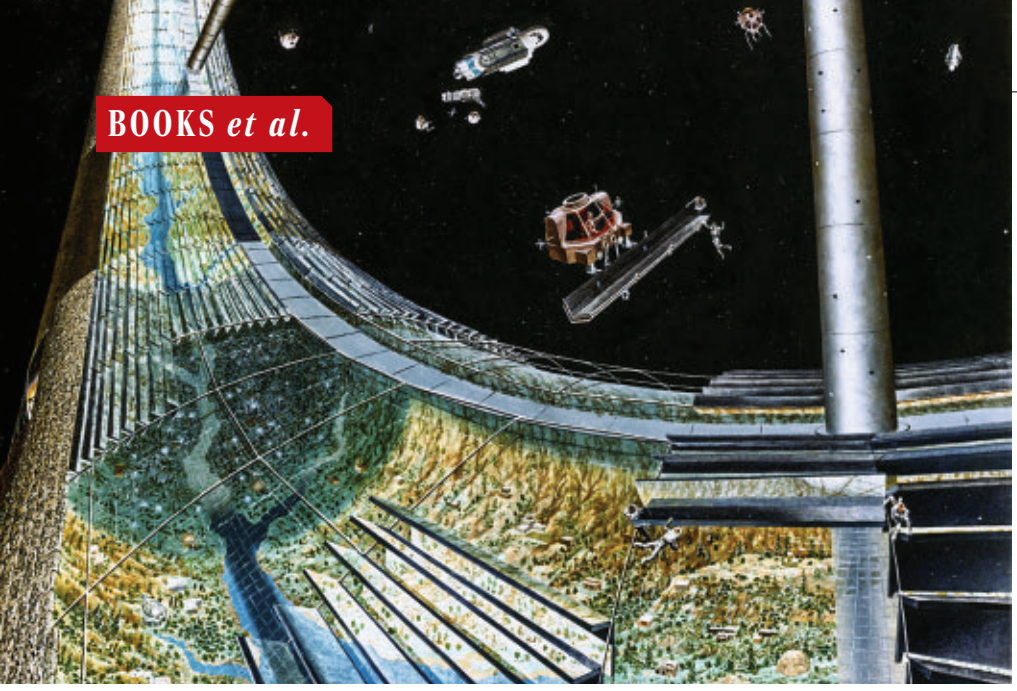
REFERENCES AND NOTES

1. M. Prosser, "How AI Helped Predict the Coronavirus Outbreak Before It Happened," *Singularity Hub* (2020); https://singularityhub.com/2020/02/05/how-ai-helped-predict-the-coronavirus-outbreak-before-it-happened/.
2. W. Knight, "Researchers Will Deploy AI to Better Understand Coronavirus," *WIRED*, 17 March 2020.
3. OpenMinted, TDM Stories, http://openminted.eu/blog/ (2018).
4. P. Goldstein, B. Hugenholtz, *International Copyright: Principles, Law, and Practice* (Oxford Univ. Press, 2019).
5. V. Stodden, "Enabling Reproducibility in Big Data Research: Balancing Confidentiality and Scientific Transparency" in *Privacy, Big Data, and the Public Good: Frameworks for Engagement*, J. Lane, V. Stodden, S. Bender, H. Nissenbaum, Eds. (Cambridge Univ. Press, 2014), chap. 5.
6. A. Levendowski, *Wash. Law Rev.* **93**, 579 (2018).
7. R. G. Samberg, C. Hennesy, "Law and Literacy in Non-Consumptive Text Mining: Guiding Researchers Through the Landscape of Computational Text Analysis" in *Copyright Conversations: Rights Literacy in a Digital World*, S. R. Benson, Ed. (Association of College and Research Libraries, 2019), chap. 17.
8. S. Flynn, L. Schirru, M. Palmedo, A. Izquierdo, "Research Exceptions in Comparative Copyright" (PIJIP/TLS Research Paper Series no.75, 2022); https://digitalcommons.wcl.american.edu/research/75).
9. M. Palmedo, *EFIL J. Econ. Res. J.* **2**, 114 (2019).
10. C. Handke, L. Guibault, J. J. Vallbé, *MDE. Manage. Decis. Econ.* **42**, 1999 (2021).
11. S. Flynn *et al.*, *Eur. Intellect. Prop. Rev.* **42**, 393 (2020).
12. M. W. Carroll, *UC. Davis Law Rev.* **53**, 893 (2019).
13. M. Sag, *Northwest. Law Rev.* **103**, 1607 (2009).
14. M. Jacob, P. Jaszi, P. S. Adler, W. Cross, Facilitators, "Code of Best Practices in Fair Use for OER: A Guide for Authors, Adapters & Adopters of Openly Licensed Teaching and Learning Materials" (American University Washington College of Law, 2021); https://auw.cl/oer.

ACKNOWLEDGMENTS

We acknowledge the contribution of members of the Global Expert Network on Copyright User Rights and the Access to Knowledge Coalition to the research and ideas informing the drafting of this article. Funding was provided by a grant from the Arcadia Fund, a Charitable Fund of Lisbet Rausing and Peter Baldwin, for a project of the Network on the Right to Research in International Copyright. Data used for the figure and table are published in (*8*) and in the GitHub repository at https://github.com/pijip.rtr.

10.1126/science.add6124



A rendering of a proposed space habitat offers an idealized view of space settlement untroubled by problematic aspects of migration and colonization.

PHOTO: DON DAVIS

SPACE EXPLORATION

Religion in space

A sense of divine entitlement pervades private space colonization efforts

By **Roger D. Launius**

Human space exploration has always been about a quest for utopia, laced with a fair measure of religious conceptions. In the early 1970s, Chris Kraft, the godfather of NASA's Mission Control Center and a leader in the Apollo Moon landing program, characterized his support of space exploration in this way: "This step into the universe is a religion and I'm a member of it."

Kraft's statement made clear that those interested in moving beyond Earth, like the migrants to the Americas of the 16th and 17th centuries, endeavored to create a more perfect human experience free from the strictures of known society. Of course, what constitutes "a more perfect human experience" depends very much on individual perspective. Many observers of the space exploration community recognize this reality and have provided stinging critiques about what this might mean for extraplanetary regions explored by humans, who will bring with them all their beliefs and practices, for better and worse.

Mary-Jane Rubenstein, a professor of religion and science in society at Wesleyan University, adds her voice to these critiques with *Astrotopia: The Dangerous Religion of the Corporate Space Race*. She notes how human spaceflight supporters have long insisted that space is the next step in humanity's "natural" and therefore irrepressible need to explore, often framing this inclination as a spiritual quest, a purification of humanity, and a search for absolution and immortality. These deep-seated convictions, she observes, have energized space exploration from the dawn of the space age.



Astrotopia
Mary-Jane Rubenstein
University of Chicago Press, 2022. 224 pp.

Many of Rubenstein's historical examples are well known. Captain Kirk's soliloquy—"Space, the final frontier"—at the beginning of *Star Trek* and John F. Kennedy's 1962 speech about setting sail on "this new sea" invoked journeying to a different land, settling an uncolonized region, and creating a new civilization. Such conceptions conjured images of self-reliant people moving to untouched territories in sweeping waves of discovery, exploration, and settlement. Implied therein were utopian ideals of optimism, individuality, and democracy. But flattening space into a mythological frontier reduced the complexity of events that would transpire during such exploration to a static morality play, avoided matters that challenged or contradicted the myth, framed the settlement experience as inherently good, and ignored the cultural context of migration.

Aspiring space colonizers disappointed with NASA's declension in the 1970s began to imagine an alternative agenda aimed at achieving a bountiful future on a pristine planet, increasingly without government involvement. "New Space" advocates may be thought of as orphans of Apollo who found their way into myriad economic, political, and social camps. They evince distrust of authority, especially governmental authority, and celebrate the entrepreneurial spirit of Elon Musk, Jeff Bezos, and Sir Richard Branson, whom they believe will finally open a boundless space frontier. Such individuals may support NASA's efforts when they converge with their own interests, but they have grown increasingly critical of the space agency and any other large governmental activities.

Along with criticisms of NASA, "New Space" advocates also accept a dystopian future on Earth. They argue that in the 21st century, exponential growth of population and diminishing resources will create cataclysm. The answer, they believe, is to escape. And although humanity does not yet possess the technological capability to send human colonies elsewhere in the Solar System, these obstacles, they maintain, can be overcome.

Such beliefs are why, as Rubenstein makes clear, Musk and Bezos have become messiahs for the "New Space" community. In building the rockets necessary to get off this planet, presumably without government sponsorship, these entrepreneurs are opening the regions beyond Earth to settlement as never before. All will be the better for it, they believe. Notwithstanding the corporate ethos of Musk and Bezos, their supporters view their efforts as immensely more acceptable than the efforts of NASA.

Ultimately, Rubenstein succeeds in highlighting both the debate over whether future space exploration and exploitation should be led by government or entrepreneurial entities and the manner in which neoliberal, private-sector emphases have come to dominate the thinking of a particular segment of the pro-space community. Her criticisms of this phenomenon—part of a growing body of literature in environmental studies, Afrofuturism, and anticolonialism investigations—are on point. ■

The reviewer was associate director for collections and curatorial affairs at the Smithsonian Institution's National Air and Space Museum in Washington, DC, prior to retirement in 2017. He is the author of *Apollo's Legacy: Perspectives on the Moon Landings* (Smithsonian Books, 2019). Email: launiusr@gmail.com

10.1126/science.adf0791

SCIENCE LIVES

Meet the Huxleys

A historian traces the scientific family's complicated lives and influential legacies

The Huxleys: An Intimate History of Evolution
Alison Bashford
University of Chicago Press, 2022. 576 pp.



By **Piers J. Hale**

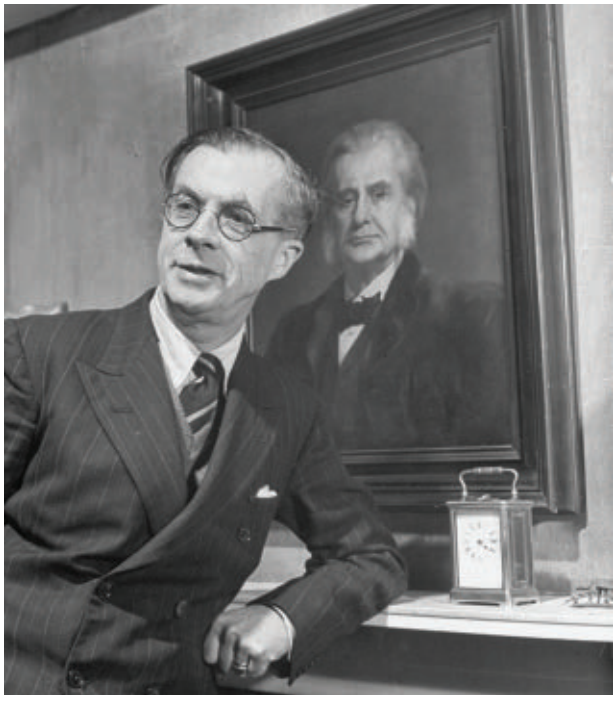
What is our evolutionary inheritance? What has our natural history made us, and how does this affect how we might live? Further, given our understanding of the mechanisms of inheritance, can we and should we direct our own evolution to ensure the betterment of humankind, both in body and in mind? Questions such as these are the intellectual offspring of the evolutionary view of life that Charles Darwin described in 1859. They also motivated the Huxleys, one of science's most famed families and the subject of Alison Bashford's new book, *The Huxleys*.

Bashford's book centers on Thomas Henry Huxley (1825–1895), Darwin's great champion, and his grandson Julian Sorell Huxley (1887–1975), author of, among much else, *Evolution: The Modern Synthesis*, an influential text that popularized evolutionary biology in the mid-20th century (*1*). *The Huxleys* spans the publication and popularization of *On the Origin of Species*, the subsequent eclipse of natural selection as the primary factor in the forging of new species in favor of Mendel's rediscovered mutationist theory of heredity, and the later recognition that selection might be the deciding factor in the sorting out and perpetuation of gene frequency in a population.

For the Huxleys, biology was always political, but it was also full of contradictions. Thomas Henry's hierarchical conceptions of race and sex were still liberal enough and typical enough of his time that he could oppose the more extreme racism of many of his contemporaries in British anthropology and advance sex-segregated science education for women seemingly without internal conflict.

Julian, meanwhile, defended eugenics while declaiming Nazism and fascism; he had sympathy for socialism but rejected Lysenko's opposition to "bourgeois" genetics. In the 1940s, he used his position as director of UNESCO to advance his doctrine of "evolutionary humanism," through which he sought to employ eugenics and population control as a means to human betterment.

In Bashford's account, biology and politics are but the warp and weft of what must be one of the most compelling and tragic multigenerational scientific legacies. For while Thomas Henry, Julian, and their many achievements are in the story's foreground, it is the lives, loves, and losses that wracked this family that underlie Bashford's tale.



Julian Huxley (left) and his grandfather Thomas Henry Huxley (portrait on right) were key voices in early evolutionary thought.

Despite how Thomas Henry embraced and advanced Darwin's views on morality—which shocked critics by discarding the notion of divinely ordained principles of right and wrong—he strove to place himself and his family beyond reproach, adhering to the most conventional moral standards of his day. His son Leonard's children, however, broke rather than pushed societal boundaries.

Julian and his wife experimented with an open relationship; he had a stream of lovers, at least one of whom she shared, and wrote popular articles on birth control, sex, and the future of humanity for *Playboy*. Aldous, for his part, married "a Belgian bisexual beauty," experimented with LSD, and sought to test the nature and limits of the mind. He wrote *Brave New World* in 1932 as Europe tumbled toward authoritarianism, an inclination he recognized in the enthusiasm his brother Julian shared with H. G. Wells for technocratic state solutions to society's problems.

Along with his surname, many of the Huxleys inherited the family patriarch's tendency toward deep depression. Thomas Henry wrestled with this darkness for years, and it almost overthrew him on more than one occasion: once at the loss of his firstborn, Noel, who succumbed to scarlet fever at 4 years old, and again at the death of his daughter Mady, who, struggling with her own mental demons, died suddenly of pneumonia at the age of 27.

Julian, we learn, was in and out of institutions just as his career was taking off. Unable to function, he was forbidden by his doctors even to write, just as he was supposed to be taking up a professorship at Rice University. Noel Trevenen, Julian's younger brother, was similarly troubled. Missing for days on the eve of the Great War, he was later found hanging from a tree in a secluded forest.

Bashford tells the story of these intertwined lives with sympathy and candor but also with dexterity, as she weaves together themes not beholden to a linear chronology. Readers follow the Huxleys as they contemplate nonhuman animals, primates, man, and mind in their intergenerational quest to understand the implications of evolution on what it means, or might mean, to be human. ■

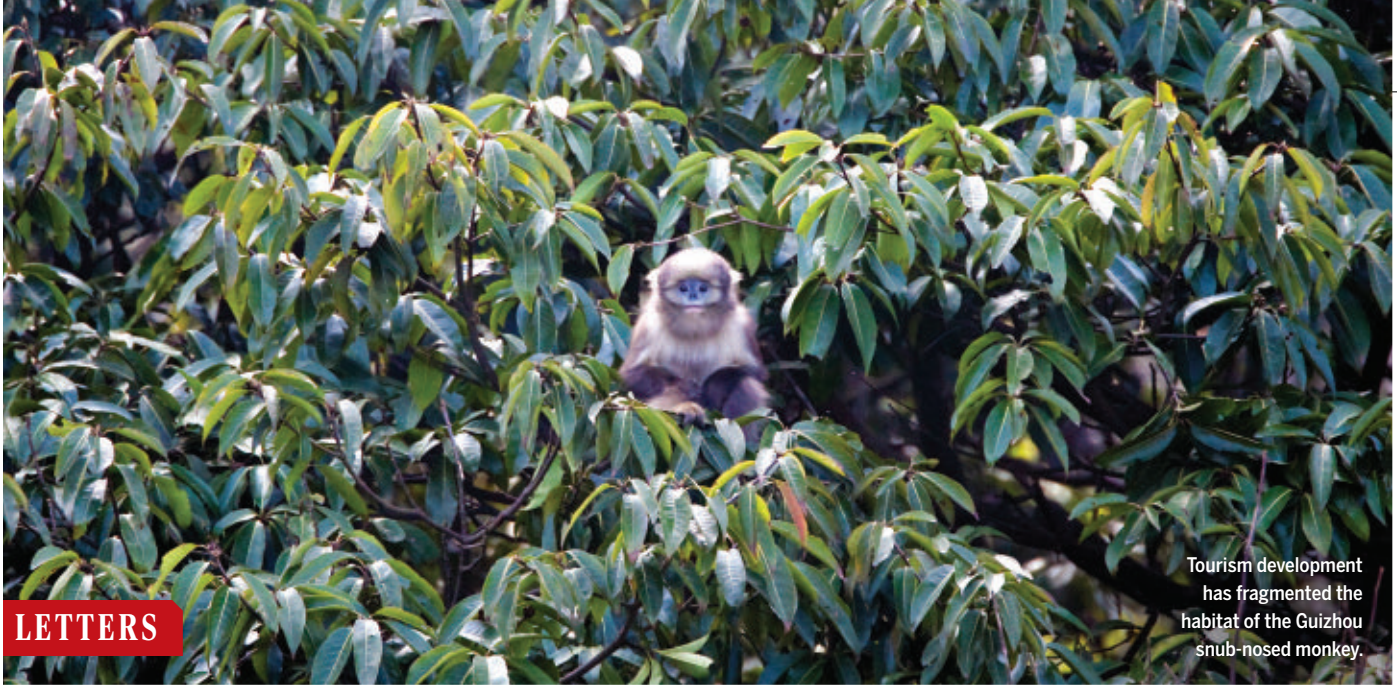
The reviewer is at the Department of the History of Science, Technology, and Medicine, The University of Oklahoma, Norman, OK 73019, USA. Email: phale@ou.edu

REFERENCES AND NOTES

1. J. S. Huxley, *Evolution: The Modern Synthesis* (Allen & Unwin, 1942).

10.1126/science.adf1120

PHOTO: TONY LINCK/THE LIFE PICTURE COLLECTION/SHUTTERSTOCK



Tourism development has fragmented the habitat of the Guizhou snub-nosed monkey.

PHOTO: ZHINONG XI/MINDEN PICTURES

Edited by **Jennifer Sills**

Guizhou snub-nosed monkey in peril

The Guizhou (or gray) snub-nosed monkey (*Rhinopithecus brelichi*), is endemic to Guizhou province in southwestern China. Because of the species' restricted distribution and small population (*1*), the Fanjingshan National Nature Reserve was established to protect it in 1978 (*2*), and it was categorized as China's National Class I key protected wildlife in 1989 (*3*). However, anthropogenic disturbances such as deforestation, farming, livestock grazing, and tourism have continued, degrading the monkey's habitat (*2*, *4*). Without immediate action, the Guizhou snub-nosed monkey could go extinct.

In 2008, there were about 750 Guizhou snub-nosed monkeys surviving in the wild (*2*). In 2009, the construction of an aerial tram divided the monkey's only remaining habitat into two parts, and prevented the population from accessing the southern region. Confined to a small fraction of the Fanjingshan National Nature Reserve, the species' estimated population decreased to between 125 and 336 individuals (*4*, *5*), with low genetic diversity (*6*). In response, the International Union for Conservation of Nature categorized the monkey as Critically Endangered (*5*) and one of the world's most endangered primates (*7*).

To protect the Guizhou snub-nosed monkey from extinction, tourism development in the Fanjingshan reserve should be halted immediately, and tourist numbers should be strictly limited. An ecological corridor should be created by dismantling the aerial tram and replanting evergreen and deciduous broadleaf mixed forest trees between the two habitats. Finally, China's government should attempt to translocate some individuals to other suitable places to establish new populations outside of the present reserve.

Tao Ju[1] and Xianghong Dong[2]*
[1]Guangxi Academy of Sciences, Nanning 530007, China. [2]College of Animal Science, Guizhou University, Guiyang 550025, China.
*Corresponding author. Email: xhdong@gzu.edu.cn

REFERENCES AND NOTES

1. G. Quan, J. Xie, *Acta Theriolog. Sin.* **1**, 113 (1981) [in Chinese].
2. Z. Xiang *et al.*, *Biol. Conserv.* **142**, 469 (2009).
3. "List of national key protected wildlife," *Bulletin of the State Council of PRC* **2**, 46 (1989) [in Chinese].
4. Y. Guo *et al.*, *Glob. Ecol. Conserv.* **24**, e01181 (2020).
5. Y. Long *et al.*, *Rhinopithecus brelichi* (The IUCN Red List of Threatened Species, 2022).
6. X. Zhou *et al.*, *Mol. Biol. Evol.* **33**, 2670 (2016).
7. R. A. Mittermeier *et al.*, "Primates in peril: The world's 25 most endangered primates 2022–2023" (IUCN SSC Primate Specialist Group, International Primatological Society, Washington, DC, 2022).

10.1126/science.adf3707

Combatting national research restrictions

In her *Science* Insider piece "Indonesia bans five foreign scientists, shelves conservation data" (7 October, https://scim.ag/up), D. Rochmyaningsih describes how the Indonesian government is suppressing conservation scientists, research, and data in pursuit of economic development. Other governments have also restricted domestic and international research on politically sensitive topics, sometimes indirectly by controlling data (*1*), restricting funding (*2*), denying access to research sites (*3*) or specimens (*4*, *5*), or labelling researchers as disruptive protesters, foreign spies, or provocateurs (*6*–*8*). To address global environmental challenges, researchers need freedom to collect, analyze, and share data without political constraints. International treaties and organizations could counteract some of these restrictions.

At its 15th Conference of the Parties in December, the Convention on Biological Diversity's (CBD) 196 signatory nations (*9*) will adopt a protocol formalizing its new agreements. To address restrictions imposed on researchers, the CBD could include a requirement for all signatory nations to allow unimpeded access to their territories by biodiversity researchers from all nations, including their own. Countries could enforce compliance through sanctions against exports linked to biodiversity loss, including food, forest, and mineral products. Trade sanctions are limited by the World Trade Organization (WTO), but a CBD research-freedom protocol would comply with WTO related-sector, proportionality, and environmental rules (*10*).

In addition to a CBD protocol, international entities could withhold benefits from countries that deny access to researchers. In the case of Indonesia, the nonprofit Forest Stewardship Council could decertify the country (*11*) from its timber ecolabel, used widely by retailers in the European Union and United Kingdom. Corporations could also penalize countries for restrictions on scientists; airlines that ban the transportation of hunting trophies from threatened species (*12*) could serve as a model. Large importing nations can implement sanctions as well. For example, the United States greatly reduced global harvest of the endangered hawksbill turtle by placing an import embargo on Japanese fish products (*10*).

International cooperation and sanctions

could substantially improve researchers' access to sites and reduce politically charged targeting of scientists. Together, CBD nations and global organizations have the legal and political power to demand reduced impediments to research on biodiversity conservation.

Ralf Buckley[1]* and Aila Keto[2]
[1]Griffith University, Gold Coast, Australia. [2]Australian Rainforest Conservation Society, Brisbane, Australia.
*Corresponding author.
Email: r.buckley@griffith.edu.au

REFERENCES AND NOTES

1. C. Piller, *Science* **369**, 356 (2020).
2. C. Sathya, F. L. Dreier, M. L. Ranney, *Nature* **610**, 30 (2022).
3. S. Devi, *Lancet* **395**, 1331 (2020).
4. S. Mallapat, *Nature* **587**, 341 (2020).
5. A. Oren, M. Göker, R. L. Hahnke, E. R. Moore, I. C. Sutcliffe, *Nat. Microbiol.* **7**, 1711 (2022).
6. N. Gilbert, *Nature* **603**, 372 (2022).
7. J. Mervis, *Science* **377**, 1478 (2022).
8. F. Graham, "Daily briefing: Secretive Iran court sentences cheetah conservationists to prison" (2019); https://www.nature.com/articles/d41586-019-03619-9.
9. Convention on Biological Diversity (2022); https://www.cbd.int.
10. M. Faure, Ed., *Elgar Encyclopedia of Environmental Law, XI, Trade and Environmental Law* (Edward Elgar, Cheltenham, UK, 2021).
11. L. Sutherlin, "FSC media briefer: Forest watchdog says this is a 'make or break' moment for the credibility of the Forest Stewardship Council (FSC)," Rainforest Action Network (2022); https://www.ran.org/press-releases/fsc-media-briefer-forest-watchdog-says-this-is-a-make-or-break-moment-for-the-credibility-of-the-forest-stewardship-council-fsc/.
12. Humane Society International, "45 airlines now have a policy of prohibiting the transportation of hunting trophies" (2020); https://www.hsi.org/news-media/42-airlines-adopt-wildlife-trophy-bans-082715/.

10.1126/science.adf4002

Biological invasions in China's coastal zone

Over the past few decades, China's coastal zone has been subject to extensive land reclamation. As of 2014, approximately 65% of all coastlines in China were affected by the expansion of farmlands, salt pans, aquaculture ponds, roads, and buildings (*1*), resulting in disrupted ecosystem services, ecological security, and sustainability (*2*–*4*). About a decade ago, the Chinese government began addressing the problem (*2*, *5*). On 1 June, a new Wetland Protection Law came into effect, which is expected to build on past success (*6*). However, invasive species now threaten China's coastal wetlands.

Spartina alterniflora, a perennial tallgrass native to North America, was intentionally introduced in China in 1979 for soil amelioration, tidal reclamation, and erosion mitigation (*7*). The species expanded rapidly from 0.001 km^2 in 1981 to about 550 km^2 in 2015 (*7*, *8*). *S. alterniflora* has invaded several protected areas of coastal wetlands, including a world heritage site of migratory bird sanctuaries along the Yellow Sea coast and Bohai Gulf of China (*9*). The *S. alterniflora* saltmarshes prevent shorebirds from finding prey on mudflats and reduce coastal biodiversity (*7*, *8*).

Given the projected global climate change, *S. alterniflora* is likely to continue to spread unabated in China. Warming could enhance its growth and reproduction and facilitate its spread to high latitudes. Sea level rise could increase its competitive advantage over native plants (*7*, *10*).

Although traditional coastal reclamation for development has been controlled, the invasion and expansion of *S. alterniflora* pose a serious threat to the quality and sustainability of China's coastal wetlands. The control of *S. alterniflora* and the restoration of native saltmarshes are desperately needed to maintain the habitat quality and sustainability of China's coastal zone (*11*). Given the high dispersal ability and rapid reinvasion potential of *S. alterniflora*, national coordinated actions and funding mechanisms are urgently needed to effectively control *S. alterniflora* invasions at multiple temporal and spatial scales.

Xinxin Wang[1], Xiangming Xiao[2], Qiang He[1], Xi Zhang[1], Jihua Wu[3], Bo Li[1,4]*
[1]Ministry of Education Key Laboratory for Biodiversity Science and Ecological Engineering, National Observations and Research Station for Wetland Ecosystems of the Yangtze Estuary, Institute of Biodiversity Science and Institute of Eco-Chongming, School of Life Sciences, Fudan University, Shanghai 200438, China. [2]Department of Microbiology and Plant Biology, Center for Earth Observation and Modeling, University of Oklahoma, Norman, OK 73019, USA. [3]State Key Laboratory of Grassland Agro-Ecosystems, and College of Ecology, Lanzhou University, Lanzhou, Gansu 730000, China. [4]Yunnan Key Laboratory of Plant Reproductive Adaptation and Evolutionary Ecology and Centre for Invasion Biology, Institute of Biodiversity, School of Ecology and Environmental Science, Yunnan University, Kunming, Yunnan 650504, China.
*Corresponding author. Email: bool@ynu.edu.cn

REFERENCES AND NOTES

1. X. Hou *et al.*, *Sci. Chin. Earth Sci.* **59**, 1791 (2016).
2. Z. J. Ma *et al.*, *Science* **346**, 912 (2014).
3. X. X. Wang *et al.*, *Remote Sens. Environ.* **238**, 110987 (2020).
4. H. Yang, M. Ma, J. R. Thompson, R. J. Flower, *Proc. Natl. Acad. Sci. U.S.A.* **114**, 5491 (2017).
5. D. Miao, Z. Xue, *Mar. Pol.* **134**, 104782 (2021).
6. D. Mao *et al.*, *Science* **376**, 1061 (2022).
7. B. Li *et al.*, in *Plant Invasion Ecology: The Case of* Spartina alterniflora *in China* (2022), pp. 25–30 [in Chinese].
8. X. Zhang *et al.*, *Remote Sens. Environ.* **247**, 111916 (2020).
9. J. L. Ren *et al.*, *Sci. Adv.* **7**, eabi8943 (2021).
10. D. Zhang, Y. Hu, M. Liu, *Ying Yong Sheng Tai Xue Bao* **30**, 2329 (2019) [in Chinese].
11. X. X. Wang *et al.*, *Nat Sustain.* **4**, 1076 (2021).

10.1126/science.ade9665

NEWS FROM Science
AAAS

Subscribe to **News from Science** for unlimited access to authoritative, up-to-the-minute news on research and science policy.



bit.ly/NewsFromScience

YOUR RESEARCH HAS ITS REWARDS.



Submit an essay by 3/15/23 to enter to win $25K.

The prestigious international *Science* & PINS Prize is awarded annually to outstanding early-career researchers in the emerging field of neuromodulation. Findings already show improved outcomes in several neurological disorders. To enter, just write a 1000-word essay about your research performed in the last three years. The Grand Prize winner will be presented a US$25,000 award, as well as have their essay published in *Science* magazine and on *Science* Online. A runner-up will have their essay published online. For additional inquiries, email SciencePINSPrize@aaas.org.

SCIENCE-PINS PRIZE FOR NEUROMODULATION

SCIENCE-PINS

SCIENCE.ORG/PINS

RESEARCH

IN *SCIENCE* JOURNALS

Edited by **Michael Funk**



Air pollution in Chicago, pictured here, is not evenly distributed and has disproportionate effects on children in poor communities.

AIR POLLUTION

Pollution harms children's development

The harmful effects of neighborhood poverty on children's cognitive development can be partly explained by early exposure to toxic air pollution. Wodtke *et al.* analyzed data from a national sample of American infants matched with information about their exposure to dozens of potentially harmful pollutants. Using causal inference and machine-learning methods, they found that infants who lived in high-poverty neighborhoods were exposed to many different pollutants and that this exposure was linked to impaired cognitive ability when the children were tested at age 4. These findings demonstrate how neighborhood poverty consists not only of economic deprivation but also of environmental health hazards that contribute to the reproduction of poverty across generations. —JEB

Sci. Adv. 10.1126/sciadv.add0285 (2022).

MACHINE LEARNING

Machine learning to play Stratego

Stratego is a popular two-player imperfect information board game. Because of its complexity stemming from its enormous game tree, decision-making under imperfect information, and a piece deployment phase at the start, Stratego poses a challenge for artificial intelligence (AI). Previous computer programs only performed at an amateur level at best. Perolat *et al*. introduce a model-free multiagent reinforcement learning methodology and show that it can achieve human expert–level performance in Stratego. The present work not only adds to the growing list of games that AI systems can play as well or even better than humans but may also facilitate further applications of reinforcement learning methods in real-world, large-scale multiagent problems that are characterized by imperfect information and thus are currently unsolvable. —YS

Science, add4679, this issue p. 990

PLANT SCIENCE

Nitrogen fixation kept in balance

Legumes such as soybeans can assimilate atmospheric nitrogen with the assistance of symbiotic bacteria that reside in root nodules. Nitrogen fixation is energy intensive, and the cellular energy status in the nodule determines the rate of nitrogen fixation. Ke *et al*. investigated that linkage using molecular sensors in the root nodule that respond to AMP concentrations. The sensors regulate access of a nuclear regulatory factor to certain glycolytic genes, thus shifting allocation of phosphoenolpyruvate between competing pathways to drive up nitrogen fixation when the nodule has enough energy. —PJH

Science, abq8591, this issue p. 971

PHOTO: KRISTINE JONES/SHUTTERSTOCK

ULTRACOLD CHEMISTRY

Forming dense, ultracold triatomic gases

After the successful creation of ultracold diatomic molecular gases, the next grand experimental challenge is to prepare and control ultracold gases of triatomic molecules. Because they have more degrees of freedom, these gases offer many exciting research opportunities for molecular precision spectroscopy and quantum simulations. Using adiabatic magneto-association by ramping the magnetic field through a Feshbach resonance between $^{23}Na^{40}K$ and ^{40}K, Yang *et al*. created an ultracold gas of weakly bound $^{23}Na^{40}K_2$ triatomic molecules at about 100 nanokelvin, as confirmed by their direct detection using the radiofrequency dissociation. About 4000 triatomic molecules were created with a high peak density 10 orders of magnitude higher than the best results previously reported, representing an important milestone in ultracold chemistry and physics. —YS

Science, ade6307, this issue p. 1009

MONKEYPOX

Monkeypox antiviral drug

The antiviral drug tecovirimat (TPOXX) was developed to treat smallpox, which is caused by infection with variola virus, an orthopoxvirus closely related to monkeypox virus (MPXV). During the current global MXPV outbreak, TPOXX has been approved for treating infected individuals in Europe and has been used in other countries where available. Warner *et al*. now demonstrate that TPOXX is effective against a 2022 Canadian MPXV isolate both in vitro and in the CAST/EiJ mouse model. This viral isolate is not as lethal in CAST/EiJ mice as previous isolates, despite evidence of respiratory tract replication, and it appears to align with other recent isolates that define a new viral clade. Together, these findings support the therapeutic use of TPOXX against currently circulating MPXV and suggest changes in the virus that alter pathogenicity in mouse models. —CNF

Sci. Transl. Med. **14**, eade7646 (2022).

QUANTUM SIMULATION

Topological quantum photonics

Exploiting the topological properties of materials is expected to provide a route to developing robust platforms for transport and communication systems that are immune to defects. In optics, the demonstration of topological behavior has been confined mainly to classical light. Deng *et al*. introduce a superconducting chip–based platform consisting of a single qubit coupled to a number of resonators. By controlling the photon population in each resonator and the coupling strength, the authors were able to realize several important models in topological physics. The approach bridges the gap between topological states of classical and quantum origin. —ISO

Science, ade6219, this issue p. 966

QUALITY CONTROL

Weeding out faulty membrane proteins

Membrane proteins connect the cell to its environment and are essential for key biological activities and cell survival. To function properly, membrane proteins need to adopt a well-defined three-dimensional structure within the lipid bilayer. Failures in this process give rise to numerous diseases. Zanotti *et al*. found that the human signal peptidase complex, which removes signal peptides from endoplasmic reticulum–targeted secretory and membrane proteins, has an additional quality control function. The complex cleaves faulty membrane proteins, supporting their degradation and helping to maintain a healthy membrane proteome. These findings extend our understanding of molecular quality control in cells and suggest potential targets in protein-folding disorders. —SMH

Science, abo5672, this issue p. 996

IN OTHER JOURNALS

Edited by **Caroline Ash** *and* **Jesse Smith**



DEVELOPMENT

Self-organizing feather patterns

Self-organizing biological systems can produce an array of patterns ranging from meanders and waves to stripes or spots. However, small variations in starting conditions or signaling parameters can produce wildly different patterns. Curantz *et al.* investigated how bird plumage patterns are stabilized in the developing skin. In the developing dermal cells of zebra finch, penguin, and quail, feather follicle patterns emerged early and remained stable, in contrast to emu and ostrich, in which follicle patterns were loosely organized. It appears that a combination of cell shape and skin flexibility influences follicle movement during development and thus how defined or irregular the resulting feather patterns become. —PJH

PLOS Biol. **20**, e3001807 (2022).

MICROBIOTA

Metabolic reconstructionism

A major function of the vertebrate gut microbiota is the fermentation of foodstuffs to extract energy for each partner's benefit. Earlier literature informed Hoces *et al.* that mice lacking a microbiota tended to be less fat than their intact counterparts. The authors built an isolator-housed metabolic cage system to monitor the metabolism of conventional mice, germ-free mice, and mice hosting a model microbiota of 12 bacterial lineages called OligoMM12. All groups extracted about 9 kilocalories per day from their food, but the OligoMM12 mice became fatter. The germ-free mice ate more and excreted more than the other groups, but their feces were less energy dense because they lacked bacterial mass. The OligoMM12 community did not recapitulate the activity of an intact microbiota, but if microbiota species are evolutionarily selected for their contribution to host energy, OligoMM12 could be modified to test this idea. —CA

PLOS Biol. 10.1372/journal.pbio.3001743 (2022).

DEVELOPMENT

Two faces of differentiation

Proper cell differentiation not only requires the correct signals but also needs to avoid confusion with signals from neighboring cells. For instance, anterior intestine cells and liver cells arise from similar nearby progenitor cells, so how do intestinal cell precursors prevent induction by signals from liver cells? Yang *et al.* used a genetic screen in zebrafish to identify a mutation in the Cdx1b homeoprotein that induces intestinal cells to become liver cells. The Cdx1b transcription factor regulates the expression of an inhibitor of Wnt signaling called secreted frizzled related protein 5, which is a cue for liver differentiation. Therefore, intestinal

PHOTO: THEO ALLOFS/MINDEN PICTURES



Australian zebra finches, *Taeniopygia castanotis*, have well-defined plumage patterns because of their relatively inflexible skin.

precursor cells do not rely solely on inductive signals; they are also able to resist neighboring signals to ensure correct differentiation. —LBR

Proc. Natl. Acad. Sci. U.S.A. **119**, e2205110119 (2022).

MICROBIOLOGY

Keeping TB in the lung

Bacterial DNA from *Mycobacterium tuberculosis* has been detected in the skeletons of ancient Egyptian mummies. This means that although tuberculosis (TB) is largely a lung disease, *M. tuberculosis* can sometimes disseminate to bone. Studying a TB outbreak with unusually high levels of skeletal disease, Saelens *et al.* found that the presence of an ancestral version of a specialized bacterial secreted protein called EsxM likely helped to define the clinical course of infection. The authors also found that the ancestral version of EsxM rewired infected host macrophages to become more migratory, which promoted the dissemination of infection. *M. tuberculosis* strains from modern lineages that are broadly distributed geographically contain an inactivating mutation in EsxM, likely limiting the extent of extrapulmonary dissemination and promoting transmission. —SMH

Cell **185**, 1 (2022).



An ancient lineage of the tuberculosis bacterium can still cause the type of skeletal disease seen in this mummy, which dates from 21st dynasty Egypt.

SYNTHETIC CHEMISTRY

User-friendly reaction optimization tool

Recent advances in solving various challenges in synthetic chemistry using data science and machine learning (ML) methods have generated considerable interest in the development of multifunctional ML platforms that could simultaneously optimize complex multiple reaction objectives and remain comprehensible and useful to synthetic chemists with limited programming experience. Garrido Torres *et al.* developed an open-source, multi-objective, active-learning platform based on Bayesian optimization methods. They demonstrated its successful application in a real-world test case: the simultaneous optimization of the reaction yield and enantioselectivity for a nickel/photoredox–catalyzed enantioselective cross-electrophile coupling of styrene oxides with two different aryl iodide substrates. The proposed platform is web accessible and could be expanded to numerous optimization problems in synthetic chemistry. —YS

J. Am. Chem. Soc. **144**, 19999 (2022).

AGRICULTURE

Crop innovation as climate adaptation

Innovations in crop biotechnology focused on environmental adaptation have mitigated an estimated 20% of potential economic damages to US agriculture caused by climate change–induced increases in extreme heat exposure. In addition to the $24 billion in avoided historical damages since 1960, Moscona and Sastry estimate that similar redirection of crop innovation, more specifically by the private sector than the public, could mitigate 13% ($1.05 trillion) of damages projected by 2100. However, they also found that private sector–driven historical innovation has been unresponsive to agricultural conditions beyond the United States, a considerable limitation for addressing threats from climate change in other parts of the world. —BW

Q. J. Econ. 10.1093/qje/qjac039 (2022).

METALLURGY

Getting the carbon out

Recycling iron alloys is important for sustainable development because of the high costs of refining iron ores. However, controlling impurities in the recycling process presents a challenge for producing high-quality alloys. Judge *et al.* used electrorefining to produce ultra-low-carbon steels from recycled metal. The technique avoids using dissolved oxygen, instead relying on a reaction at the slag interface to evolve carbon monoxide. The strategy provides a more direct method for producing high-quality steels for structural applications. —BG

Nat. Mater. **21**, 1130 (2022).

IMAGE: GRAFTON ELLIOT SMITH AND MARC ARMAND RUFFER/WELLCOME IMAGES/CC BY 4.0

ALSO IN *SCIENCE* JOURNALS

Edited by **Michael Funk**

HIV CLINICAL TRIALS

Human vaccination induces bnAb precursors

Each year, more than 1 million new HIV infections occur, highlighting the need for effective HIV vaccines. Vaccine strategies that induce broadly neutralizing antibodies (bnAbs) have promise to combat HIV and other pathogens but have not yet been tested in humans. Leggat *et al*. report the results of a phase 1 clinical trial showing that a germline-targeting priming immunogen was safe and feasible and induced targeted bnAb-precursor responses in 97% of vaccine recipients at substantial frequencies in each individual (see the Perspective by Moore). bnAb-precursor responses made favorable gains in mutation and affinity after a booster vaccination. The results establish proof of principle for this reductionist vaccine approach and encourage the development of additional boosters to induce bnAbs. —PNK

Science, add6502, this issue p. 964; see also adf3722, p. 949

METALLURGY

Too cold to fracture

Finding structural materials that have good fracture properties at very low temperatures is challenging but is important for fields such as space exploration. Liu *et al*. discovered a high-entropy chromium-cobalt-nickel alloy that has an incredibly high fracture toughness at 20 kelvin (see the Perspective by Zhang and Zhang). This behavior is caused by an unexpected phase transformation that, when combined with other microstructures, prevents crack formation and propagation. The fracture toughness of this alloy makes it potentially useful for a range of cryogenic applications. —BG

Science, abp8070, this issue p. 978; see also adf2205, p. 947

BIODIVERSITY

Protecting Madagascar

Madagascar has been isolated from mainland Africa and Asia for more than 80 million years and has developed a distinctive flora and fauna, with more than 90% of its species endemic to the island nation. It is also home to the Malagasy people, with a population of about 30 million, and was first colonized by humans around the first century BCE. The island's biodiverse wildlife is highly threatened, and much of its human population lives below the poverty line. In Reviews, Antonelli *et al*. and Ralimanana *et al*. characterize the biological history and diversity of the island and examine conservation status and actions required to protect biodiversity and improve living standards and well-being for the Malagasy people. —SNV

Science, abf0869, adf1466, this issue p. 962, 963

VOLCANOLOGY

Picturing Yellowstone's plumbing

Yellowstone is an active supervolcano that will cause mass destruction when it next erupts. Maguire *et al*. use full waveform seismic imaging to map the location and amount of melt under the volcano (see the Perspective by Cooper). They find the largest amount of melt is roughly in the depth range where previous eruptions were sourced. However, the amount of melt is much lower than required for a massive eruption anytime in the near future. Continued monitoring of the subsurface should provide a clear picture if the situation begins to dramatically change. —BG

Science, ade0347, this issue p. 1001; see also ade8435, p. 945

MOLECULAR BIOLOGY

Active DNA demethylation in neurons

The DNA of neurons is continually damaged due to lifelong, high-level metabolic and transcriptional activity. Recent studies have also demonstrated extensive "programmed" DNA damage in differentiating postmitotic neurons. Wang *et al*. identified endogenous lesions as single-strand-break intermediates of thymine DNA glycosylase (TDG)–mediated removal of oxidized methylcytosines during active DNA demethylation (see the Perspective by López-Moyado and Rao). Interrupting active DNA demethylation using antineoplastic cytosine analogs triggered TDG-dependent neuronal cell death. This work suggests that the well-known neurotoxic side effects of certain chemotherapies, also called "chemobrain," could be linked to DNA repair processes intrinsic to normal neuronal differentiation. —DJ

Science, add9838, this issue p.983; see also adf3171, p. 948

WILDFIRES

High and dry

High temperatures and dry conditions have produced extreme fire activity in northeastern Siberia recently. Scholten *et al*. report that spring and summer weather conditions from 2019 to 2021, driven by concurrent changes in the frequency of Arctic front jets and seasonally earlier snowmelt, resulted in unusually intense fire activity there and a northward shift of fires (see the Perspective by Schaepman-Strub and Kim). In the future, these trends could accelerate the degradation of carbon-rich permafrost peatlands and contribute even more than they do now to global warming. —HJS

Science, abn4419, this issue p.1005; see also ade8673, p. 944

PHYSIOLOGY

Limiting nutrient loss in the kidney

The kidney filters the blood and retains nutrients through endocytosis and active transport in cells lining the proximal tubule. Rinschen *et al.* investigated how this process is regulated by VPS34, a lipid kinase involved in the vesicular trafficking and endocytic sorting of membrane proteins. VPS34 deficiency in proximal tubule cells in mice decreased the surface levels of nutrient transporters, which enhanced urinary loss of lipids and proteins. VPS34 inhibition could be used to treat diseases in which limiting nutrient loss confers clinical benefit, such as kidney cancer. —WW

Sci. Signal. **15**, eabo7940 (2022).

T CELLS

Activation answers

T cell activation requires changes in metabolism needed for the energy demands of rapid growth and proliferation. Cytokines that engage common gamma chain ($c\gamma$) receptors on T cells are critical to promoting the metabolic changes needed for activation. Villarino *et al.* examined the role of STAT5 engagement, which is a signaling pathway shared by all $c\gamma$ cytokines. STAT5 was defined as a master regulator of amino acid metabolism in $CD4^+$ helper T cells through interactions with enhancers and promoters of genes encoding a wide array of enzymes and transporters. STAT5 controlled transcription of members of the mTOR pathway to license T cells for interleukin-2–mediated mTOR signaling and promoted MYC-driven metabolic changes. Together, these findings provide molecular insights downstream of interleukin-2 engagement that are critical to T cell activation. —CNF

Sci. Immunol. **7**, eabl9467 (2022).

ARCHAEOLOGY

Bronze Age trade networks of tin

Bronze, which is composed of copper and tin, was a key commodity of the ancient world during the second millennium BCE and was used for weapons and everyday tools. The copper sources for bronze have long been known, but those of tin have never been identified with certainty. In a study of 105 tin ingots from the extraordinary shipwreck site of Uluburun off Turkey's southern coast, Powell *et al.* found that one-third of them had their origin in Tajikistan and Uzbekistan, more than 3000 kilometers away. These findings suggest that trade at multiple scales, ranging from households to political elites, contributed to a vast network, challenging previous models of centralized control of commodity trade in this era. —MSA

Sci. Adv. 10.1126/sciadv.abq3766 (2022).

SYNTHETIC BIOLOGY

Tracing a history of cell-cell contact

The ability to monitor the history of cell-cell contact could benefit our understanding of cellular interactions in many biological contexts, from development to various disease states. Zhang ***et al***. modified synthetic receptor systems that could be targeted to cells of interest in mice. Binding of the designed ligand on a sender cell to a compatible receptor on a receiver cell permanently marked the receiver cell through a change in expression of a fluorescent reporter. For example, they could detect endothelial cells that moved during development from the heart to the liver. —LBR

Science, abo5503, this issue p. 965

REVIEW SUMMARY

BIODIVERSITY

Madagascar's extraordinary biodiversity: Evolution, distribution, and use

Alexandre Antonelli* *et al.*

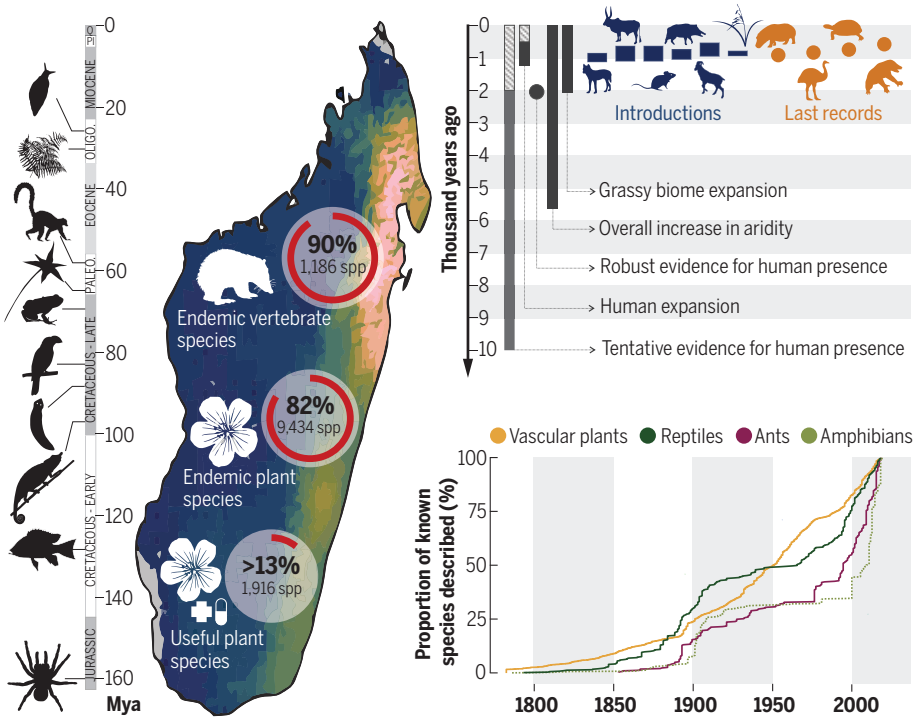
BACKGROUND: The Republic of Madagascar is home to a unique assemblage of taxa and a diverse set of ecosystems. These high levels of diversity have arisen over millions of years through complex processes of speciation and extinction. Understanding this extraordinary diversity is crucial for highlighting its global importance and guiding urgent conservation efforts. However, despite the detailed knowledge that exists on some taxonomic groups, there are large knowledge gaps that remain to be filled.

ADVANCES: Our comprehensive analysis of major taxonomic groups in Madagascar summarizes information on the origin and evolution of terrestrial and freshwater biota, current species richness and endemism, and the utilization of this biodiversity by humans. The depth and breadth of Madagascar's biodiversity—the product of millions of years of evolution in relative isolation —is still being uncovered. We report a recent acceleration in the scientific description of species but many remain relatively unknown, particularly fungi and most invertebrates.

DIGITIZATION: Digitization efforts are already increasing the resolution of species richness patterns and we highlight the crucial role of field- and collections-based research for advancing biodiversity knowledge in Madagascar. Phylogenetic diversity patterns mirror that of species richness and endemism in most of the analyzed groups. Among the new data presented, our update on plant numbers estimates 11,516 described vascular plant species native to Madagascar, of which 82% are endemic, in addition to 1215 bryophyte species, of which 28% are endemic. Humid forests are highlighted as centers of diversity because of their role as refugia and centers of recent and rapid radiations, but the distinct endemism of other areas such as the grassland-woodland mosaic of the Central Highlands and the spiny forest of the southwest is also important despite lower species richness. Endemism in Malagasy fungi remains poorly known given the lack of data on the total diversity and global distribution of species. However, our analysis has shown that ~75% of the fungal species detected by environmental sequencing have not been reported as occurring outside of Madagascar.

Among the 1314 species of native terrestrial and freshwater vertebrates, levels of endemism are extremely high (90% overall)—all native nonflying terrestrial mammals and native amphibians are found nowhere else on Earth; further, 56% of the island's birds, 81% of freshwater fishes, 95% of mammals, and 98% of reptile species are endemic. Little is known about endemism in insects, but data from the few well-studied groups on the island suggest that it is similarly high. The uses of Malagasy species are many, with much potential for the uncovering of useful traits for food, medicine, and climate mitigation.

OUTLOOK: Considerable work remains to be done to fully characterize Madagascar's biodiversity and evolutionary history. The multitudes of known and potential uses of Malagasy species reported here, in conjunction with the inherent value of this unique and biodiverse region, reinforce the importance of conserving this unique biota in the face of major threats such as habitat loss and overexploitation. The gathering and analysis of data on Madagascar's remarkable biota must continue and accelerate if we are to safeguard this unique and highly threatened subset of Earth's biodiversity. ■



Emergence and composition of Madagascar's extraordinary biodiversity. Madagascar's biota is the result of over 160 million years of evolution, mostly in geographic isolation, combined with sporadic long distance immigration events and local extinctions. (Left) We show the age of the oldest endemic Malagasy clade for major groups (from bottom to top): arthropods, bony fishes, reptiles, flatworms, birds, amphibians, flowering plants, mammals, non-flowering vascular plants, and mollusks). Humans arrived recently, some 10,000 to 2000 years (top right) and have directly or indirectly caused multiple extinctions (including hippopotamus, elephant birds, giant tortoises, and giant lemurs) and introduced many new species (such as dogs, zebu, rats, African bushpigs, goats, sheep, rice). Endemism is extremely high and unevenly distributed across the island (the heat map depicts Malagasy palm diversity, a group characteristic of the diverse humid forest). Human use of biodiversity is widespread, including 1916 plant species with reported uses. The scientific description of Malagasy biodiversity has accelerated greatly in recent years (bottom right), yet the diversity and evolution of many groups remain practically unknown, and many discoveries await.

The complete list of authors and their affiliations is available in the full article online.
*Corresponding author. Email: a.antonelli@kew.org (A.A.)
Cite this article as A. Antonelli *et al.*, *Science* 378, eabf0869 (2022). DOI: 10.1126/science.abf0869

READ THE FULL ARTICLE AT
https://doi.org/10.1126/science.abf0869

REVIEW

BIODIVERSITY

Madagascar's extraordinary biodiversity: Evolution, distribution, and use

Alexandre Antonelli[1,2,3,4]*†, Rhian J. Smith[1,3]†, Allison L. Perrigo[2,3]†, Angelica Crottini[5,6,7], Jan Hackel[1], Weston Testo[8,2,3], Harith Farooq[2,3,9], Maria F. Torres Jiménez[10,2,3], Niels Andela[11], Tobias Andermann[12,13,2,3], Andotiana M. Andriamanohera[14], Sylvie Andriambololonera[15], Steven P. Bachman[1], Christine D. Bacon[2,3], William J. Baker[1], Francesco Belluardo[5,6,7], Chris Birkinshaw[15,16], James S. Borrell[1], Stuart Cable[1], Nataly A. Canales[17], Juan D. Carrillo[18,3,13,19], Rosie Clegg[20,1], Colin Clubbe[1], Robert S. C. Cooke[21,2,3], Gabriel Damasco[22,2], Sonia Dhanda[1], Daniel Edler[23,2,3], Søren Faurby[2,3], Paola de Lima Ferreira[24,2,3], Brian L. Fisher[25], Félix Forest[1], Lauren M. Gardiner[26], Steven M. Goodman[8,27], Olwen M. Grace[1], Thaís B. Guedes[28], Marie C. Henniges[1,29], Rowena Hill[1,29], Caroline E. R. Lehmann[30,31], Porter P. Lowry II[16,32], Lovanomenjanahary Marline[14,3,27], Pável Matos-Maraví[24,3], Justin Moat[1], Beatriz Neves[33,3], Matheus G. C. Nogueira[33,3], Renske E. Onstein[34,35], Alexander S. T. Papadopulos[36], Oscar A. Perez-Escobar[1], Leanne N. Phelps[31,30], Peter B. Phillipson[16,32], Samuel Pironon[1,37], Natalia A. S. Przelomska[1,38], Marina Rabarimanarivo[15], David Rabehevitra[14], Jeannie Raharimampionona[15], Mamy Tiana Rajaonah[14], Fano Rajaonary[15], Landy R. Rajaovelona[14], Mijoro Rakotoarinivo[39], Amédée A. Rakotoarisoa[14], Solofo E. Rakotoarisoa[14], Herizo N. Rakotomalala[14], Franck Rakotonasolo[14], Berthe A. Ralaiveloarisoa[14], Myriam Ramirez-Herranz[40, 3, 41], Jean Emmanuel N. Randriamamonjy[14], Tianjanahary Randriamboavonjy[14], Vonona Randrianasolo[14], Andriambolantsoa Rasolohery[42], Anitry N. Ratsifandrihamanana[43], Noro Ravololomanana[15], Velosoa Razafiniary[14], Henintsoa Razanajatovo[14], Estelle Razanatsoa[44], Malin Rivers[45], Ferran Sayol[46,3], Daniele Silvestro[13,19,2,3], Maria S. Vorontsova[1], Kim Walker[1,47], Barnaby E. Walker[1], Paul Wilkin[1], Jenny Williams[1], Thomas Ziegler[48,49], Alexander Zizka[50], Hélène Ralimanana[14]*†.

Madagascar's biota is hyperdiverse and includes exceptional levels of endemicity. We review the current state of knowledge on Madagascar's past and current terrestrial and freshwater biodiversity by compiling and presenting comprehensive data on species diversity, endemism, and rates of species description and human uses, in addition to presenting an updated and simplified map of vegetation types. We report a substantial increase of records and species new to science in recent years; however, the diversity and evolution of many groups remain practically unknown (e.g., fungi and most invertebrates). Digitization efforts are increasing the resolution of species richness patterns and we highlight the crucial role of field- and collections-based research for advancing biodiversity knowledge and identifying gaps in our understanding, particularly as species richness corresponds closely to collection effort. Phylogenetic diversity patterns mirror that of species richness and endemism in most of the analyzed groups. We highlight humid forests as centers of diversity and endemism because of their role as refugia and centers of recent and rapid radiations. However, the distinct endemism of other areas, such as the grassland-woodland mosaic of the Central Highlands and the spiny forest of the southwest, is also biologically important despite lower species richness. The documented uses of Malagasy biodiversity are manifold, with much potential for the uncovering of new useful traits for food, medicine, and climate mitigation. The data presented here showcase Madagascar as a unique "living laboratory" for our understanding of evolution and the complex interactions between people and nature. The gathering and analysis of biodiversity data must continue and accelerate if we are to fully understand and safeguard this unique subset of Earth's biodiversity.

The Republic of Madagascar, an island country off the east coast of Africa, is home to a unique assemblage of taxa and a diverse set of ecosystems. The high levels of terrestrial and freshwater diversity have arisen over millions of years through complex processes of speciation and extinction. Understanding the origins, evolution, current distribution, and uses of this extraordinary diversity is crucial to highlighting its global importance and guiding urgent conservation efforts (*1*, *2*).

Origins of Madagascar's biota

Once part of the Gondwana supercontinent, Madagascar and India split from Africa 150 to 160 million years ago (Ma), with India separating 84 to 91 Ma (*3*). The Malagasy fossil record shows both regional and widespread Gondwanan fauna before continental breakup (Fig. 1A) (*4*) but plant remains are scarce in the record (*5*). The Cretaceous-Paleogene (K-Pg) mass extinction (66 Ma), when Madagascar had already become an island, is believed to have greatly reduced the ancient Malagasy fauna. This species turnover presented new opportunities for the establishment and radiation of colonizers (*6*, *7*). Biotic history during this period is almost entirely inferred from molecular phylogenies as there is a long gap in the fossil record during the Cenozoic (*8*). Molecular clock estimates suggest that few extant groups date back to potential Gondwanan vicariance, including some reptile, fish, and insect lineages (*6*, *9*, *10*) and the plant genus *Takhtajania* (*11*) (Fig. 1A). Most of the current animal, plant, and fungal diversity originated from ancestors with mainly African and Indo-Pacific origin according to phylogenies and biogeographic reconstructions, and reached Madagascar through overseas dispersal (*6*, *10*–*12*) (Fig. 1B). The presence of oceanic surface currents flowing from Africa to Madagascar during the Paleogene, which subsided in the Miocene (*13*), coincided with the arrival of multiple vertebrate lineages that subsequently diversified (*6*, *7*). It has also been proposed that short-lived land bridges in the Mozambique channel during the Neogene may have aided migration (*14*), although the significance of this is debated (*14*, *15*). In addition, stepping-stone islands in the Indian Ocean, now submerged, may have facilitated animal and plant dispersal from the Indo-Pacific region (*16*).

The current peaks and plateaus of Madagascar probably formed in the past 30 to 40 million years (My) through mantle upwelling and volcanism, and the past 10 My have seen accelerated uplift (*17*, *18*). This suggests that rather than evolving on an old stable surface, many of the current patterns of biodiversity were shaped by environmental gradients and dispersal barriers that are relatively young, geologically speaking (*17*).

Regional differences

Madagascar's diverse biota and ecosystems have been categorized using many different systems (e.g., *19*, *20*), but data scarcity means that any inferences on the extent of native vegetation prior to major anthropogenic influences come with a very high level of uncertainty. We summarize the current vegetation types of Madagascar (dry forest, grassland-woodland mosaic, humid forest, mangrove, tapia, spiny forest, and subhumid forest) based on a simplified version of the *Atlas of the Vegetation of Madagascar* (*21*) (Fig. 1 and table S1) (*22*). Although our resulting simplified map is adequate for providing an overview of Madagascar's main vegetation types, a higher resolution map and more detailed classification is needed for in-depth analyses such as systematic conservation planning. We suggest that any

new mapping classification should build on existing mapping [including the updated classification of (*23*)] but follow the suggestions of the IUCN global ecosystem typology (*24*), which is a hierarchical classification system that at its top level defines ecosystems by ecological function and at detailed levels distinguishes ecosystems by species assemblage (*25*).

There is a marked longitudinal rainfall gradient created by the high eastern edge of the mountain range running from north to south, most of which exceeds 800 m above sea level. Humidity brought by easterly trade winds and summer monsoons from the Indian Ocean is captured by the edge and forms a cloud layer at ca. 900 to 1200 m. This rain-producing system sustains the patchy remains of a ca. 100-km–wide band of evergreen humid forest along the east coast, with extensions to certain portions of the north. Rainfall patterns are largely unpredictable throughout the country, and there are frequent but irregular cyclones during the rainy season. This unpredictability is suggested to have led to unique biological adaptations in Malagasy species, including extremes of very fast or slow life histories (*26*, *27*).

The Central Highlands have a subhumid climate, which is cooler and drier during the winter. They are dominated by a grassland-woodland mosaic, where grasslands are mixed with agricultural land, shrubland, and patches of woodland. There are also areas of humid forest and tapia—woodland dominated by the tree species tapia (*Uapaca bojeri*)—from which the vegetation type takes its name. Although grasslands increased as a result of the degradation of woody vegetation types following human settlement, some are derived from the pantropical savanna expansion that started in the late Miocene (*28*). The extent of grasslands at the time of human arrival, especially in the Central Highlands, remains debated (*29*). To the southwest, the highland mosaic transitions into subhumid forests and more extensive tapia.

The highest mountains (>2500 m) are igneous in origin and support sclerophyllous shrublands dominated by species of the plant family Ericaceae in addition to open grasslands around their summits. Humidity and rainfall decrease in the rain shadow to the west of the Central Highlands, with the dominant vegetation type transitioning to dry forest, with some deciduous plant species and succulent elements toward the western coast. Mangroves are mostly found along the Mozambique Channel coast. The southwest region is the driest part of the island, and the rainy season, when present, lasts ≤3 months. This climate supports the spiny forest ecosystem, which in global terms is strictly a thicket but classed as forest within the context of Madagascar (*21*). This ecosystem was previously thought to be Madagascar's oldest and was widespread across the island when it lay at the edge of the tropical belt before the mid-Oligocene. When continental drift moved Madagascar north and directly into the trade wind zone, the spiny forest ecosystem contracted (*3*). However, the humid forest has been found to contain taxa belonging to lineages that date back to the Paleocene, and further evidence from climate reconstructions suggests that Madagascar was moderately humid at the K-Pg boundary (*11*, *30*) (Fig. 1A).

The arrival of humans

Human presence in Madagascar—from both Austronesian and African origins—dates to at least the start of the CE with some evidence pointing to the Early Holocene—8000 BCE onward (*31*, *32*) (Fig. 3). Settlement in the interior and large-scale anthropogenic impacts likely took place after 1000 CE, with subsequent progressive population growth from initially sparse settlements from 1200 CE onward (*33*, *34*). As in other parts of the world once human populations began to expand, their activities had substantial impacts on local biota. This process resulted in landscape transformation from ca. 300 CE onward (*35*, *36*) and subsequent extinction of Madagascar's once rich megafauna (here defined as vertebrates >10 kg) through a combination of hunting and habitat displacement (*34*, *37*–*40*). These extinctions may have accelerated as a result of a shift from hunting and foraging to herding and farming as the predominant methods of obtaining food, which brought land clearance and transformation to agricultural land (*41*). Drought may have further compounded these changes (*42*).

Since settling on the island, humans have introduced crops and livestock for agriculture and husbandry (*43*–*45*) (Fig. 3). Of these, rice and zebu cattle have had the largest impacts on the landscape (*43*, *44*) as a result of their vital role in sustaining human populations. Rice is currently widely cultivated both in the Central Highlands (using paddy production) and in the humid east, where swidden agricultural methods are used (i.e., shifting cultivation involving clearing forest for conversion to cropland, usually by burning). With the latter practice, soils are rapidly depleted and remain fertile for only a short period, meaning that the land is abandoned for long fallow periods with further vegetation being cleared at a new location. The expansion of the Kingdom of Madagascar in the late 1700s, followed by British and French colonialism in the 1800s and 1900s, accelerated trade and landscape transformation, resulting in a substantial loss of native vegetation across the island (*33*). Current patterns of Madagascar's biological diversity are therefore shaped both by ancient evolution and recent anthropogenic activities.

Contemporary patterns of richness, endemism, and use

Madagascar is one of Earth's "hottest" biodiversity hotspots (*46*), with high species richness and exceptional levels of endemism across many taxonomic groups, combined with high rates of habitat degradation and fragmentation

[1]Royal Botanic Gardens, Kew, Richmond, Surrey, UK. [2]Department of Biological and Environmental Sciences, University of Gothenburg, Gothenburg, Sweden. [3]Gothenburg Global Biodiversity Centre, University of Gothenburg, Gothenburg, Sweden. [4]Department of Biology, University of Oxford, Oxford, UK. [5]CIBIO, Centro de Investigação em Biodiversidade e Recursos Genéticos, InBIO Laboratório Associado, Universidade do Porto, Vairão, Portugal. [6]Departamento de Biologia, Faculdade de Ciências, Universidade do Porto, Porto, Portugal [7]BIOPOLIS Program in Genomics, Biodiversity and Land Planning, CIBIO, Campus de Vairão, Vairão, Portugal. [8]Field Museum of Natural History, Chicago, Illinois, USA. [9]Faculty of Natural Sciences, Lúrio University, Pemba, Cabo Delgado Province, Mozambique. [10]Institute of Biosciences, Life Sciences Centre, Vilnius University, Vilnius, Lithuania. [11]School of Earth and Environmental Sciences, Cardiff University, Cardiff, Wales, UK. [12]Department of Organismal Biology, SciLifeLab, Uppsala University, Uppsala, Sweden. [13]Department of Biology, University of Fribourg, Fribourg, Switzerland. [14]Royal Botanic Gardens, Kew, Kew Madagascar Conservation Centre, Antananarivo, Madagascar. [15]Missouri Botanical Garden, Madagascar Program, Antananarivo, Madagascar. [16]Missouri Botanical Garden, St. Louis, Missouri, USA. [17]Natural History Museum of Denmark, University of Copenhagen, Copenhagen, Denmark. [18]CR2P, Muséum National d'Histoire Naturelle, Paris, France. [19]Swiss Institute of Bioinformatics, Fribourg, Switzerland. [20]Department of Geography, University of Exeter, Exeter, Devon, UK. [21]UK Centre for Ecology and Hydrology, Wallingford, UK. [22]Departamento de Botânica e Zoologia, Universidade Federal do Rio Grande do Norte, Natal, Rio Grande do Norte, Brazil. [23]Integrated Science Lab, Department of Physics, Umeå University, Umeå, Sweden. [24]Biology Centre CAS, Institute of Entomology, České Budějovice, Czech Republic. [25]California Academy of Sciences, San Francisco, California, USA. [26]Cambridge University Herbarium, Department of Plant Sciences, University of Cambridge, Cambridge, UK. [27]Association Vahatra, Antananarivo, Madagascar. [28]Instituto de Biologia, Universidade Estadual de Campinas, Unicamp, Campinas, São Paulo, Brazil. [29]School of Biological and Behavioural Sciences, Queen Mary University of London, London, UK. [30]Royal Botanic Garden Edinburgh, Edinburgh, UK. [31]School of GeoSciences, University of Edinburgh, Edinburgh, UK. [32]Institut de Systématique, Évolution, et Biodiversité (ISYEB), Muséum National d'Histoire Naturelle, Paris, France. [33]Museu Nacional, Universidade Federal do Rio de Janeiro, Rio de Janeiro, Brazil. [34]Naturalis Biodiversity Center, Darwinweg 2, 2333CR Leiden, the Netherlands [35]German Centre for Integrative Biodiversity Research (iDiv) Halle-Jena-Leipzig, Leipzig, Germany. [36]School of Natural Sciences, Bangor University, Bangor, Gwynedd, Wales, UK. [37]UN Environment Programme World Conservation Monitoring Centre (UNEP-WCMC), Cambridge, UK. [38]Department of Anthropology, Smithsonian National Museum of Natural History, Washington, DC, USA. [39]Department of Plant Biology and Ecology, University of Antananarivo, Antananarivo, Madagascar. [40]Instituto de Ecología y Biodiversidad, University of La Serena, La Serena, Chile. [41]Programa de Doctorado en Biología y Ecología Aplicada, Universidad Católica del Norte, Universidad de La Serena, La Serena, Chile. [42]Ileiry Geospatial Services, Antananarivo, Madagascar. [43]WWF, Antananarivo, Madagascar. [44]Plant Conservation Unit, Department of Biological Sciences, University of Cape Town, South Africa. [45]Botanic Gardens Conservation International, Kew, Richmond, Surrey, UK. [46]Centre for Biodiversity and Environment Research, Department of Genetics, Evolution and Environment, University College London, London, UK. [47]Royal Holloway, University of London, Egham, Surrey, UK. [48]Cologne Zoo, Cologne, Germany. [49]Institute of Zoology, University of Cologne, Cologne, Germany. [50]Department of Biology, Philipps-University Marburg, Marburg, Germany.

***Corresponding author. Email: h.ralimanana@kew.org (H.Ral.); a.antonelli@kew.org (A.A.)**

†These authors contributed equally to this work.

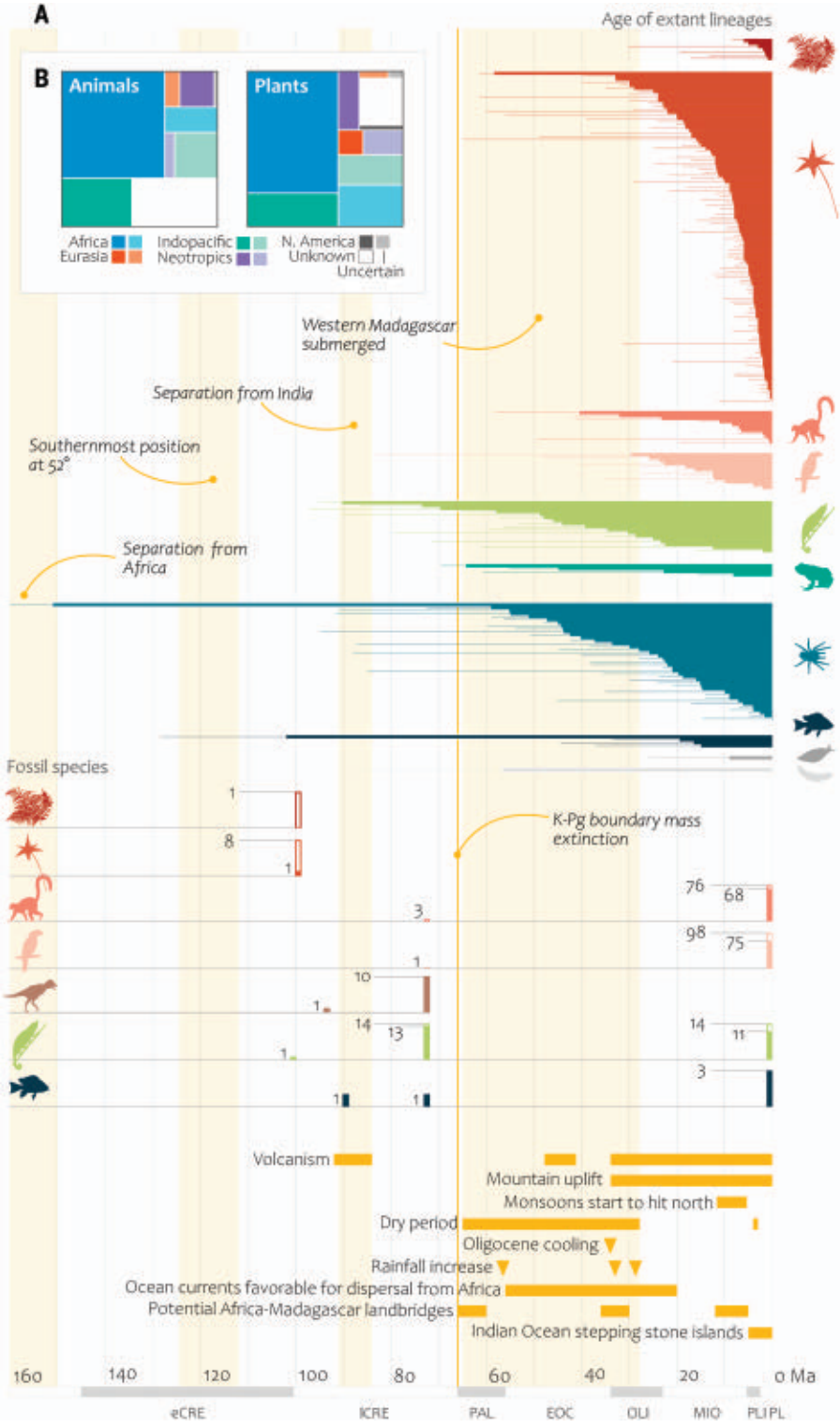


Fig. 1. Timing and origins of Madagascar's biodiversity. (**A**) Geological and environmental events in relation to the age of multiple organismal groups. The dark yellow horizontal bars at the bottom show the timing of landscape and climatic events. Vertical yellow shading along the panel corresponds to longer geographical events. Bars and lines show crown and stem ages of 217 lineages that each produced at least two endemic Malagasy species, estimated from molecular and fossil data. Icons correspond (from top to bottom) to nonflowering vascular plants, flowering plants, mammals, birds, dinosaurs (for fossil data), reptiles (here all Sauropsida, excluding birds), amphibians, arthropods, bony fishes, mollusks, and flatworms. In the fossil data section, the empty bars show the number of unique species in the fossil record through time that were found in Madagascar, with filled bars showing the number of unique species endemic to Madagascar. PL, Pleistocene; PLI, Pliocene; MIO, Miocene; OLI, Oligocene; EOC, Eocene; PAL, Paleogene; lCRE, late Cretaceous; eCRE, early Cretaceous. (**B**) Geographical origins of Madagascar's biodiversity. These treemaps show the proportional origins of the 217 endemic lineages in (A), estimated through biogeographic reconstruction, or if unavailable, the distribution of the sister group. Unsaturated hues represent the proportion of lineages whose origin is ambiguous.

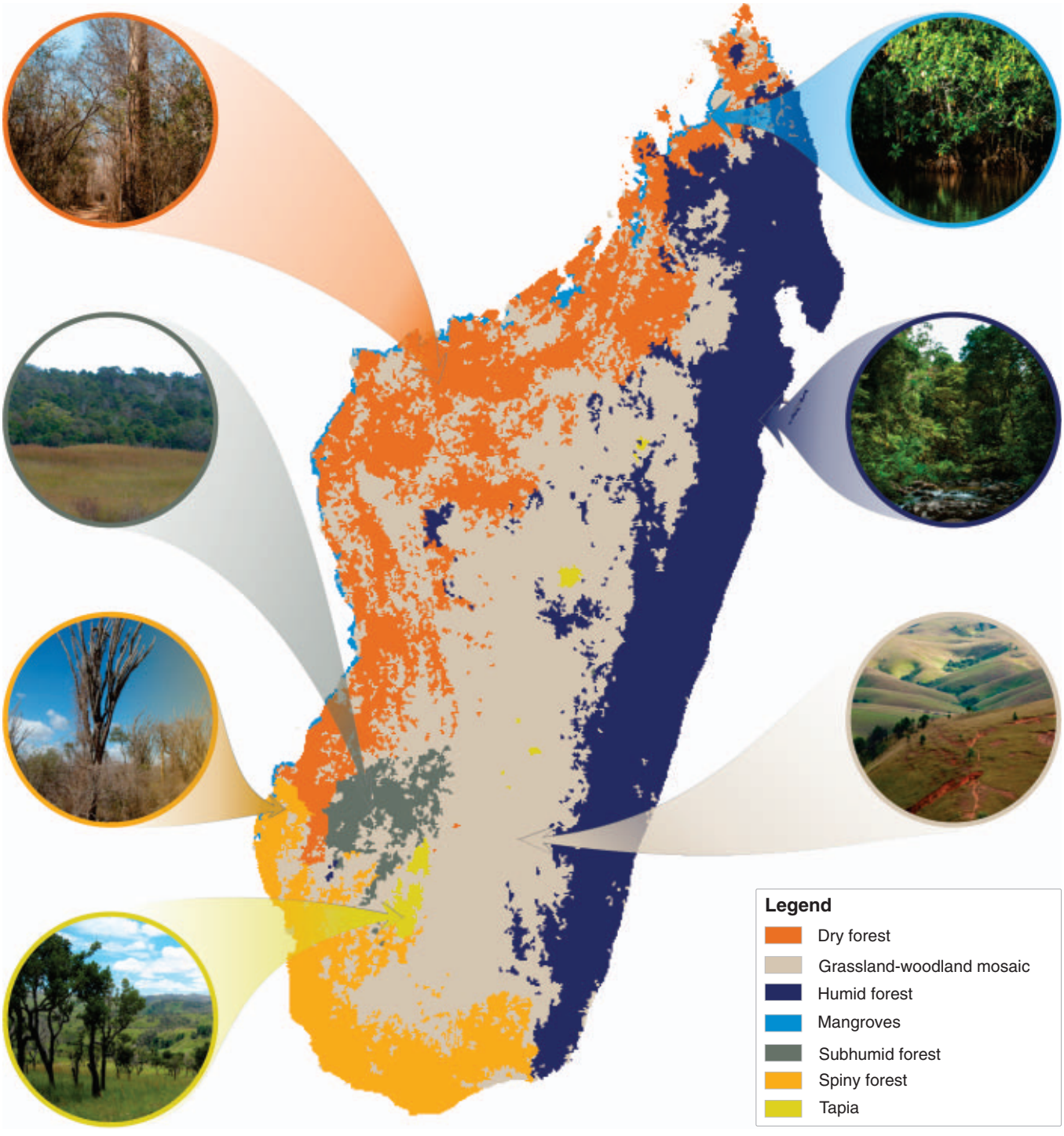


Fig. 2. Map of predominant vegetation types, expanded and simplified from Moat and Smith (*21*).

(Fig. 4) (*46*, *47*). Despite the global significance of Malagasy biodiversity, many taxonomic groups remain poorly known, and Madagascar ranks among the top countries for the predicted percentage of terrestrial vertebrates lacking scientific description (*48*). Most species are represented by only a small number of records in global natural history collections and some groups remain practically unknown, particularly fungi and most invertebrates. Estimates place the global number of fungi at >6.3 million species (*49*), and Madagascar is likely to hold a large proportion of this diversity. However, to date <2000 fungal species and species hypotheses—the latter defined by genetic reference sequences (*50*)—have been reported in public databases (*51*, *52*) and checklists (*53*, *54*).

Concerted efforts, including taxonomic research, improved digital access to natural history collections, and application of molecular techniques for species identification and delimitation, have resulted in a substantial increase in the number of records and species

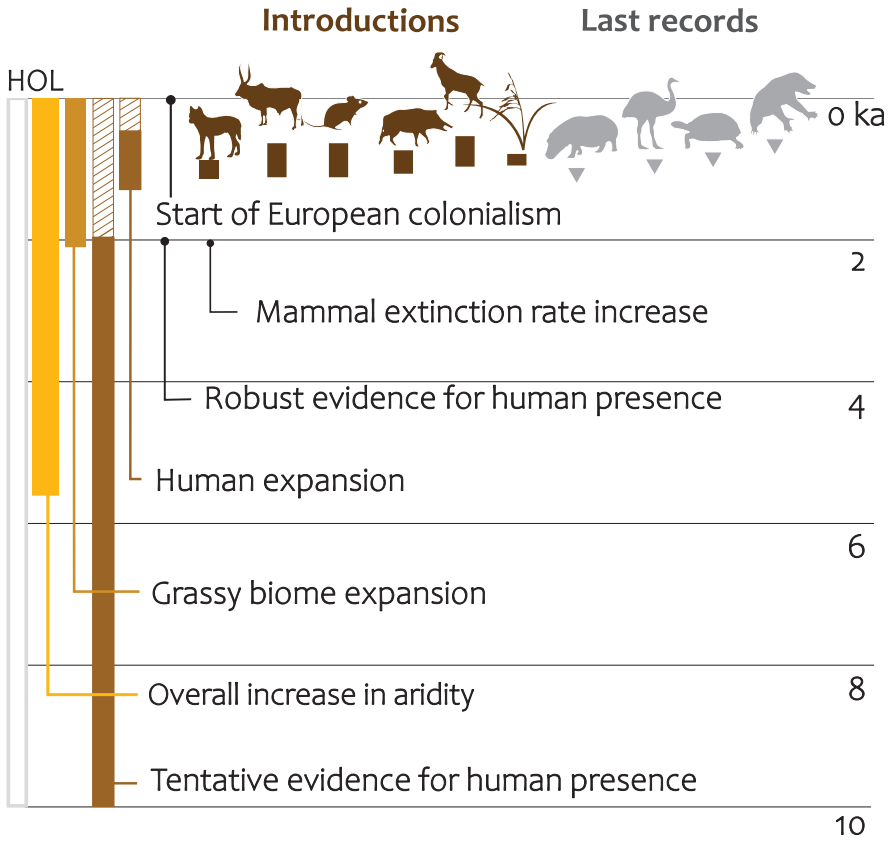


Fig. 3. Human arrival. Holocene events and environmental changes around the time of human arrival. Dates for human introductions of dogs, zebu cattle, rats, bushpigs, goats, and rice are provided as well as last dated records of megafauna (hippopotamus, elephant birds, giant tortoises, and giant lemurs) (*22*).

new to science in recent years, even in relatively conspicuous groups such as reptiles and amphibians (Fig. 5). However, many species remain undescribed across most taxonomic groups (*55*, *56*). For example, as of June 2021, there were 369 described native Malagasy amphibians (*57*) but the true number has been estimated to be well over 500 (*58*). The figures for undescribed species of arthropods could be orders of magnitude higher. Of the estimated 1300 species of ants alone (*59*), only 781 have been formally described (*60*).

For Malagasy grasses, concerted herbarium digitization efforts over just three years resulted in a 43% increase in georeferenced species records. This more than doubled the median number of records per species and improved the resolution of species richness patterns (*28*, *61*). In better-studied groups such as lemurs, continued advancements in our understanding of their distribution, ecology, and genetic diversity allow us to better understand their evolutionary history and inform conservation strategies (*62*). Together, these efforts show the crucial role of field- and collections-based research in advancing biodiversity knowledge and understanding of spatial patterns of richness, endemism, and speciation, while providing opportunities to further investigate the ecological roles of species across Madagascar's ecosystems.

Extensive endemism

Among the 1314 native species of terrestrial and freshwater vertebrates (*4*), levels of endemism are extremely high (90% overall); all native nonflying terrestrial mammals and native amphibians are found nowhere else on Earth, and 56% of birds, 81% of freshwater fishes, 95% of mammals, and 98% of reptile species are endemic (*4*, *63*–*68*) (Fig. 4). Little is known about endemism in insects, but data from the few well-studied groups on the island suggest that it is similarly high (*69*, *70*). Endemism among Madagascar's animals is not limited to lower taxonomic levels: Among birds, the island contains one endemic order (Mesitornithiformes) and three endemic families (Brachypteraciidae, Philepittidae, and Bernieridae) (*71*). Among mammals, higher-level endemism includes the superfamily Lemuroidea, the families Myzopodidae (sucker-footed bats), Eupleridae (native Carnivora), and Tenrecidae (tenrecs), and the subfamily Nesomyinae (nesomyine rodents) (*66*, *68*, *72*, *73*). For amphibians, in the family Mantellidae (mantellid frogs) all but three species (endemic to the Comoro islands) (*74*, *75*) are endemic to Madagascar; there are also three endemic subfamilies: Cophylinae (narrow-mouthed frogs), Dyscophinae (tomato frogs), and Scaphiophryninae (rain frogs) (*63*).

Malagasy flora is also highly diverse and mostly endemic (*76*). It is estimated that over 14,000 vascular plant species occur on the island (*76*), including 11,516 described native species, of which 82% are endemic (*22*, *77*). When the estimated 2550 species that remain to be scientifically described are factored in, the level of endemism could rise to 87% (*76*). Among the island's flowering plants (angiosperms), there are 310 endemic genera, ca. 19% of the generic diversity (*11*); and five endemic families (Asteropeiaceae, Barbeuiaceae, Physenaceae, Sarcolaenaceae, and Sphaerosepalaceae). Five families dominate the flora in terms of species richness: Orchidaceae (orchid family, 922 spp., 84% endemic), Rubiaceae (coffee family, 806 spp., 93% endemic), Fabaceae (pea family, 603 spp., 76% endemic), Poaceae (grass family, 541 spp., 50% endemic, 40% after specialist taxonomic evaluation) (*78*), and Asteraceae (daisy family, 529 spp., 83% endemic) (*5*, *76*, *77*, *79*). These are also the five largest families globally but all five are disproportionately species rich in Madagascar relative to the land area (~0.4% of Earth's total). The Malagasy bryophyte flora is less well studied but is also diverse: of the 1215 described bryophyte species (767 mosses, 443 liverworts, and 5 hornworts), 28% are endemic (*80*).

Endemism in Malagasy fungi is hard to assess given that so little is known about the total diversity of species. However, 14% of the species in the Global Biodiversity Information Facility (GBIF) and almost 75% of the fungal species hypotheses detected by environmental sequencing have not been reported as occurring outside of Madagascar (*22*). A recent molecular assessment of fruiting fungi and root samples from five forest sites in Madagascar based on Internal Transcribed Spacer data (*12*) found similar levels of endemism, with 65% of sequences not known from outside the country and 10% of species potentially new to science, with much of the new diversity extrapolated from ectomycorrhizal samples. This further highlights the possible magnitude of unknown diversity among Malagasy fungi.

Spatial patterns of Malagasy biodiversity

Biodiversity is not evenly distributed across Madagascar, with much of the island's biota occurring in humid forests in the east as well as on the eastern flanks of the Central Highlands and in some northern areas such as the Tsaratanana and Marojejy Massifs (*79*–*82*) (Fig. 4). Overall patterns of species richness correspond closely to collection effort, and the variation in sampling frequency across the country therefore makes it difficult to ascertain true patterns of diversity in many groups

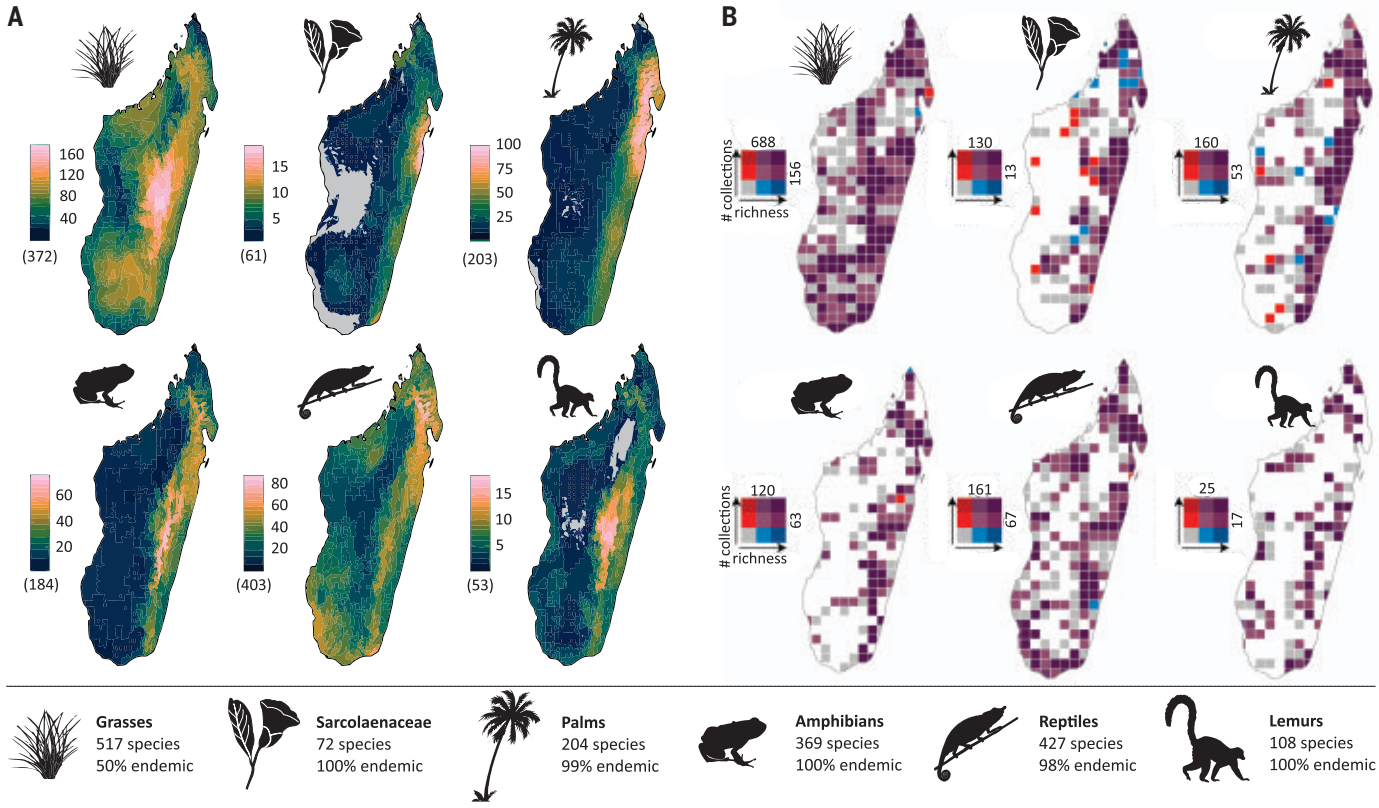


Fig. 4. Diversity patterns. (**A**) Species richness and endemism of six taxonomic groups in Madagascar. Native terrestrial and freshwater species counts and percentages of endemic species are based on estimates using author-curated data compiled from *The New Natural History of Madagascar* (*126*), and the *Catalogue of the Vascular Plants of Madagascar* (*77*). Species richness maps were generated from species distribution models based on specimen occurrence records and bioclimatic data; non-native and marine taxa are not included (*22*). Numbers in parentheses below color ramps are the number of species used to generate the species richness maps. (**B**) Patterns of species richness and collection effort for the same six taxonomic groups. Map grid cells are 25 × 25 km; cell colors correspond to species richness and collection number per cell, based on specimen occurrence records. Gray denotes an absence of records for that cell.

(Fig. 4). Species diversity patterns in amphibians, reptiles, and primates are closely mirrored by corresponding phylogenetic diversity patterns (fig. S3). An exception occurs in water beetles, where phylogenetic diversity is negatively correlated to species richness and endemism, purportedly because narrow endemism in this group is the result of recent radiations (*83*). The few studies investigating the distribution of phylogenetic diversity in plants present varied patterns, some resembling those of vertebrate groups, whereas others differ markedly (*84*, *85*).

The high species richness and endemism of many lineages in the humid forests of eastern and northern Madagascar reflect the role of these ecosystems both as forest refugia during glacial maxima (*82*, *86*, *87*), and centers of recent and rapid evolutionary radiations (*88*–*90*). This scenario is supported by the presence in these areas of high but clustered phylogenetic diversity in reptiles, mammals, and, to a certain extent, amphibians (fig. S3). The grassland-woodland mosaic vegetation of the Central Highlands is marked by its own distinctive endemism despite relatively low species richness (*78*, *91*). Certain groups, including reptiles and some plant families, such as Fabaceae, Euphorbiaceae, and Malvaceae, show additional centers of diversity in spiny forests that dominate the island's southwest region (*77*, *79*, *81*) (Fig. 4).

Species endemism across taxa and regions has arisen through multiple mechanisms, including allopatric speciation across mountain ranges (*92*), between isolated inselbergs (*93*), and in fragments of forests and wetlands created during the wet-dry cycles of the Quaternary (*94*, *95*). Narrow endemism is also linked to adaptive radiation across the island's steep environmental gradients (*81*, *94*, *96*).

Human use of biodiversity

Madagascar's rich biodiversity, particularly its diverse flora, has provided many opportunities for human utilization. Although biodiversity is "useful" in many ways (e.g., ecosystem services or nature's contributions to people, either material or nonmaterial), here we report "utilized species" as those having a documented direct use by humans. Of the 40,283 plant species documented as used by humans worldwide (*97*), 1916 (5%) are found in Madagascar—of these, 1596 are thought to be native and 597 endemic to the island (*98*). Hundreds of utilized species have also been introduced, such as the Mesoamerican vanilla orchid (*Vanilla planifolia*), brought to Madagascar from the island of Réunion by the French in the mid-1800s, following the discovery of a method to speed up hand pollination by Edmond Albius in 1841 (*99*). Vanilla is the second most expensive spice in the world, and Madagascar has become the largest producer globally (*100*). Vanilla agroforestry is currently expanding, especially in northeastern (Sava region) and eastern (Analanjirofo and Atsinanana regions) Madagascar, which can pose additional threats to biodiversity in some cases. However, it can also generate opportunities for conservation and restoration when undertaken in sustainable and safe settings and accounting for local land use history (*100*–*102*). Beyond the widespread cultivation of a few introduced species, the goods and services provided by Madagascar's flora are especially important for subsistence in many rural communities (*103*).

Documented utilized endemic plants include 310 species used for materials (e.g., woods,

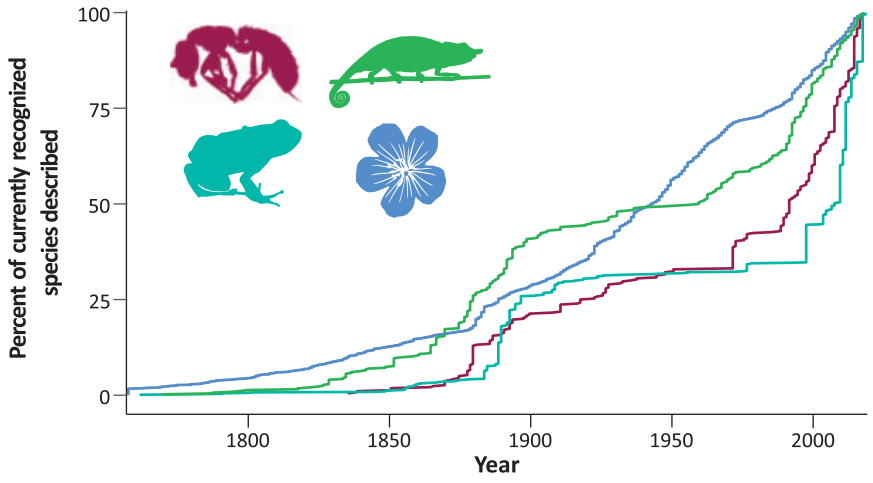


Fig. 5. Rates of scientific documentation. Percentage of described Malagasy ants, amphibians, reptiles, and vascular plants through time, based on year of basionym publication (*22*).

fibers, resins) (*104*), 91 edible species, and an additional 120 crop wild relatives that represent genetic reservoirs for the improvement of food crops. Among the most important edible groups, 38 species of yams (*Dioscorea* spp.) are native to Madagascar, 31 of which are endemic (*105*). Most have edible tubers and are widely consumed throughout the island, especially when primary crops fail (*105*, *106*). Crop wild relatives with potential for commercial benefits include Madagascar's 65 species of coffee, *Coffea* spp. (*107*–*109*), which could be used as gene and trait sources for the improvement of the two non-native but commercially grown coffee species, robusta (*C. canephora*) and Arabica (*C. arabica*), for example to confer greater climate resilience (*110*).

Many of Madagascar's 204 native palm species (99% of which are endemic) are used by people and often for multiple purposes, e.g., construction materials, fibers, medicine, and food (*111*). Structural constraints of palms mean that palm exploitation is often fatal to the trees. Consequently, palm populations are often denuded in otherwise intact habitats as a result of selective extraction, which contributes to palms being among the most threatened of the assessed plant groups in Madagascar, with more than 83% of species evaluated as threatened (*112*).

At least 221 endemic plant species have been documented as having medicinal value (*97*, *113*–*115*). These include several species of *Zanthoxylum*, which have antiplasmodial properties and are used locally to treat malaria (*116*), and the widely cultivated Madagascar periwinkle (*Catharanthus roseus*), which contains diverse and abundant alkaloids used in the treatment of some cancers and other diseases such as diabetes, high blood pressure, and asthma (*117*). Many plant species are used solely in traditional medicine practices in Madagascar. Although scientific knowledge remains incomplete on the topic, medicinal plant species have been documented as being used for a wide range of health conditions across many regions and ecosystems (*103*, *118*–*120*), highlighting the effective and potential value of Malagasy plant diversity for humanity.

The human uses of animals are not as extensive as those of plants, but hunting for meat, especially forest-dwelling species, provides an important source of nutrition and protein for some communities (*121*, *122*) and exerts considerable pressure on wild populations (*123*–*125*). Consumption of insects—particularly orthopterans, lepidopterans, and coleopterans—is also widespread. Beyond what we report, there are certainly additional potential uses of plants that have yet to be published or discovered, and additional uses of currently utilized species that have not been documented by scientists. The data reported here are certainly underestimates.

Madagascar's rich biodiversity has diverse values. Among them, the multitude of known and potential uses reported here reinforce the imperative to conserve the unique Malagasy biota in the face of major threats such as habitat loss and overexploitation (*2*).

Concluding remarks

Our synthesis shows that the depth and breadth of Madagascar's remarkable biodiversity—the product of millions of years of evolution in relative isolation (Figs. 1 and 2)—is still being uncovered. Although the scientific community has accumulated a great amount of information on some taxonomic groups, others remain relatively unknown, particularly fungi and most invertebrates. Fundamental information on biodiversity and its uses is essential for guiding conservation action (*2*). The gathering and analysis of these data must therefore continue and accelerate, through equitable practices, if we are to safeguard the multifaceted aspects of Madagascar's unique biota.

REFERENCES AND NOTES

1. A. D. Barnosky *et al.*, Merging paleobiology with conservation biology to guide the future of terrestrial ecosystems. *Science* **355**, eaah4787 (2017). doi: 10.1126/science.aah4787; pmid: 28183912
2. H. Ralimanana *et al.*, *Science* **378**, adf1466 (2022). doi: 10.1126/science.adf1466
3. N. A. Wells, in *The Natural History of Madagascar*. S. M. Goodman, J. P. Benstead, Eds. (Univ. of Chicago Press, 2003), pp. 16–34.
4. H. Ralimanana *et al.*, Madagascar's extraordinary biodiversity: a data repository, Version 6, Zenodo (2022); https://doi.org/10.5281/zenodo.5017212.
5. L. Gautier, P. P. Lowry II, S. M. Goodman, in *The New Natural History of Madagascar*, S. M. Goodman, Ed. (Princeton Univ. Press, 2022), pp. 452–464.
6. A. Crottini *et al.*, Vertebrate time-tree elucidates the biogeographic pattern of a major biotic change around the K-T boundary in Madagascar. *Proc. Natl. Acad. Sci. U.S.A.* **109**, 5358–5363 (2012). doi: 10.1073/pnas.1112487109; pmid: 22431616
7. K. E. Samonds *et al.*, Imperfect isolation: Factors and filters shaping Madagascar's extant vertebrate fauna. *PLOS ONE* **8**, e62086 (2013). doi: 10.1371/journal.pone.0062086; pmid: 23626770
8. K. E. Samonds, in *The New Natural History of Madagascar*, S. M. Goodman, Ed. (Princeton Univ. Press, 2022), pp. 69–73.
9. E. F. A. Toussaint, M. Fikáček, A. E. Z. Short, India–Madagascar vicariance explains cascade beetle biogeography. *Biol. J. Linn. Soc. Lond.* **118**, 982–991 (2016). doi: 10.1111/bij.12791
10. A. D. Yoder, M. D. Nowak, Has vicariance or dispersal been the predominant biogeographic force in Madagascar? Only time will tell. *Annu. Rev. Ecol. Evol. Syst.* **37**, 405–431 (2006). doi: 10.1146/annurev.ecolsys.37.091305.110239
11. S. Buerki, D. S. Devey, M. W. Callmander, P. B. Phillipson, F. Forest, Spatio-temporal history of the endemic genera of Madagascar. *Bot. J. Linn. Soc.* **171**, 304–329 (2013). doi: 10.1111/boj.12008
12. M. Rivas-Ferreiro, L. M. Suz, S. M. Skarha, F. Rakotonasolo, B. T. M. Dentinger, ITS-based assessment of Madagascar's fungal diversity and arrival of EcM fungi to the island. bioRxiv 2022.2003.2009.483579 [Preprint] (2022); doi: 10.1101/2022.03.09.483579
13. J. R. Ali, M. Huber, Mammalian biodiversity on Madagascar controlled by ocean currents. *Nature* **463**, 653–656 (2010). doi: 10.1038/nature08706; pmid: 20090678
14. J. C. Masters *et al.*, Biogeographic mechanisms involved in the colonization of Madagascar by African vertebrates: Rifting, rafting and runways. *J. Biogeogr.* **48**, 492–510 (2021). doi: 10.1111/jbi.14032
15. J. R. Ali, S. B. Hedges, A review of geological evidence bearing on proposed Cenozoic land connections between Madagascar and Africa and its relevance to biogeography. *Earth Sci. Rev.* **232**, 104103 (2022). doi: 10.1016/j.earscirev.2022.104103
16. B. H. Warren, D. Strasberg, J. H. Bruggemann, R. P. Prys-Jones, C. Thébaud, Why does the biota of the Madagascar region have such a strong Asiatic flavour? *Cladistics* **26**, 526–538 (2010). doi: 10.1111/j.1096-0031.2009.00300.x; pmid: 34875766
17. S. N. Stephenson *et al.*, Cenozoic Dynamic Topography of Madagascar. *Geochem. Geophys.* **22**, e2020GC009624 (2021). doi: 10.1111/j.1096-0031.2009.00300.x; pmid: 34875766
18. G. G. Roberts, J. D. Paul, N. White, J. Winterbourne, Temporal and spatial evolution of dynamic support from river profiles: A framework for Madagascar. *Geochem. Geophys.* **13**, e2020GC009624 (2012). doi: 10.1111/j.1096-0031.2009.00300.x; pmid: 34875766
19. H. Humbert, in *Notice de la carte de Madagascar*, H. Humbert, G. Cours-Darne, Eds. (Travaux de la Section Scientifique et Technique de l'Institut Français de Pondichéry, 1965), vol. hors série, pp. 46–78.
20. P. P. Lowry II, G. E. Schatz, P. B. Phillipson, in *Natural change and human impact in Madagascar*, S. M. Goodman, B. Patterson, Eds. (Smithsonian Institution Press, 1997), pp. 93–123.

21. J. Moat, P. Smith, *Atlas de La Vegetation de Madagascar*. (Royal Botanic Gardens, Kew, 2007).
22. Materials, methods, and supplementary text are available as supplementary materials.
23. L. Gautier, A. J. Tahinarivony, P. Ranirison, S. Wohlhauser, in *The Terrestrial Protected Areas of Madagascar: Their History, Description, and Biota,* S. M. Goodman, M. J. Raherilalao, S. Wohlhauser, Eds. (Association Vahatra, 2018).
24. D. A. Keith *et al*., The IUCN Global Ecosystem Typology v1.01: Descriptive profiles for Biomes and Ecosystem Functional Groups. (IUCN, CEM, 2020).
25. D. Edler, T. Guedes, A. Zizka, M. Rosvall, A. Antonelli, Infomap Bioregions: Interactive Mapping of Biogeographical Regions from Species Distributions. *Syst. Biol.* **66**, 197–204 (2017). doi: 10.1093/sysbio/syw087; pmid: 27694311
26. R. E. Dewar, A. F. Richard, Evolution in the hypervariable environment of Madagascar. *Proc. Natl. Acad. Sci. U.S.A.* **104**, 13723–13727 (2007). doi: 10.1073/pnas.0704346104; pmid: 17698810
27. K. B. Karsten, L. N. Andriamandimbiarisoa, S. F. Fox, C. J. Raxworthy, A unique life history among tetrapods: An annual chameleon living mostly as an egg. *Proc. Natl. Acad. Sci. U.S.A.* **105**, 8980–8984 (2008). doi: 10.1073/pnas.0802468105; pmid: 18591659
28. C. E. R. Lehmann, C. L. Solofondranohatra, J. A. Morton, L. N. Phelps, H. Ralimanana, J. Razanatsoa, V. Rakotoarimanana, M. S. Vorontsova, in *The New Natural History of Madagascar* S. M. Goodman, Ed. (Princeton Univ. Press, 2022), pp. 152–168.
29. B. E. Crowley, L. R. Godfrey, J. P. Hansford, K. E. Samonds, Seeing the forest for the trees-and the grasses: Revisiting the evidence for grazer-maintained grasslands in Madagascar's Central Highlands. *Proc. Biol. Sci.* **288**, 20201785 (2021). pmid: 33978523
30. M. Ohba, K. E. Samonds, M. LaFleur, J. R. Ali, L. R. Godfrey, Madagascar's climate at the K/P boundary and its impact on the island's biotic suite. *Palaeogeogr. Palaeoclimatol. Palaeoecol.* **441**, 688–695 (2016). doi: 10.1016/j.palaeo.2015.10.028
31. K. Douglass *et al*., A critical review of radiocarbon dates clarifies the human settlement of Madagascar. *Quat. Sci. Rev.* **221**, 105878 (2019). doi: 10.1016/j.quascirev.2019.105878
32. J. Hansford *et al*., Early Holocene human presence in Madagascar evidenced by exploitation of avian megafauna. *Sci. Adv.* **4**, eaat6925 (2018). doi: 10.1126/sciadv.aat6925; pmid: 30214938
33. R. E. Dewar, A. F. Richard, Madagascar: A history of arrivals, what happened, and will happen next. *Annu. Rev. Anthropol.* **41**, 495–517 (2012). doi: 10.1146/annurev-anthro-092611-145758
34. D. Pierron *et al*., Genomic landscape of human diversity across Madagascar. *Proc. Natl. Acad. Sci. U.S.A.* **114**, E6498–E6506 (2017). pmid: 28716916
35. D. A. Burney, G. S. Robinson, L. P. Burney, *Sporormiella* and the late Holocene extinctions in Madagascar. *Proc. Natl. Acad. Sci. U.S.A.* **100**, 10800–10805 (2003). doi: 10.1073/pnas.1534700100; pmid: 12960385
36. B. E. Crowley, K. E. Samonds, Stable carbon isotope values confirm a recent increase in grasslands in northwestern Madagascar. *Holocene* **23**, 1066–1073 (2013). doi: 10.1177/0959683613484675
37. B. E. Crowley, A refined chronology of prehistoric Madagascar and the demise of the megafauna. *Quat. Sci. Rev.* **29**, 2591–2603 (2010). doi: 10.1016/j.quascirev.2010.06.030
38. J. P. Hansford, A. M. Lister, E. M. Weston, S. T. Turvey, Simultaneous extinction of Madagascar's megaherbivores correlates with late Holocene human-caused landscape transformation. *Quat. Sci. Rev.* **263**, 106996 (2021). doi: 10.1016/j.quascirev.2021.106996
39. B. E. Crowley *et al*., Island-wide aridity did not trigger recent megafaunal extinctions in Madagascar. *Ecography* **40**, 901–912 (2017). doi: 10.1111/ecog.02376
40. S. W. Hixon *et al*., Late Holocene spread of pastoralism coincides with endemic megafaunal extinction on Madagascar. *Proc. Biol. Sci.* **288**, 20211204 (2021). pmid: 34284627
41. L. R. Godfrey *et al*., A new interpretation of Madagascar's megafaunal decline: The "Subsistence Shift Hypothesis". *J. Hum. Evol.* **130**, 126–140 (2019). doi: 10.1016/j.jhevol.2019.03.002; pmid: 31010539
42. M. Virah-Sawmy, K. J. Willis, L. Gillson, Evidence for drought and forest declines during the recent megafaunal extinctions in Madagascar. *J. Biogeogr.* **37**, 506–519 (2010). doi: 10.1111/j.1365-2699.2009.02203.x
43. A. Crowther *et al*., Ancient crops provide first archaeological signature of the westward Austronesian expansion. *Proc. Natl. Acad. Sci. U.S.A.* **113**, 6635–6640 (2016). doi: 10.1073/pnas.1522714113; pmid: 27247383
44. C. Radimilahy, *L' Ancienne Métallurgie du Fer a Madagascar*. British Archaeological Reports International Series 422 (BAR Publishing, 1988), pp. 246.
45. L. Rakotozafy, S. M. Goodman, Contribution à l'étude zooarchéologique de la région du Sud-ouest et extrême Sud de Madagascar sur la base des collections de l'ICMAA de l'Université d'Antananarivo, (2005).
46. N. Myers, R. A. Mittermeier, C. G. Mittermeier, G. A. B. da Fonseca, J. Kent, Biodiversity hotspots for conservation priorities. *Nature* **403**, 853–858 (2000). doi: 10.1038/35002501; pmid: 10706275
47. S. M. Goodman, J. R. Rakotoson, P. M. Razafimahatratra, M. J. Raherilalao, in *The terrestrial protected areas of Madagascar: Their history, description, and biota,* S. M. Goodman, M. J. Raherilalao, S. Wohlhauser, Eds. (Association Vahatra, 2018), pp. 33–78.
48. M. R. Moura, W. Jetz, Shortfalls and opportunities in terrestrial vertebrate species discovery. *Nat. Ecol. Evol.* **5**, 631–639 (2021). doi: 10.1038/s41559-021-01411-5; pmid: 33753900
49. P. Baldrian, T. Větrovský, C. Lepinay, P. Kohout, High-throughput sequencing view on the magnitude of global fungal diversity. *Fungal Divers.* **114**, 539–547 (2021). doi: 10.1007/S13225-021-00472-Y
50. U. Kõljalg *et al*., Towards a unified paradigm for sequence-based identification of fungi. *Mol. Ecol.* **22**, 5271–5277 (2013). doi: 10.1111/mec.12481; pmid: 24112409
51. Index Fungorum. (Index Fungorum Partnership, 2021); http://www.indexfungorum.org/.
52. Plutof. (Plutof, 2020); https://plutof.ut.ee/.
53. A. Aptroot, Preliminary checklist of the lichens of Madagascar, with two new thelotremoid Graphidaceae and 131 new records. *Willdenowia* **46**, 349–365 (2016). doi: 10.3372/wi.46.46304
54. A. Aptroot, F. Schumm, Lichenized ascomycetes: Lichens, in *The New Natural History of Madagascar,* S. M. Goodman, Ed. (Princeton Univ. Press, 2022), pp. 499–510.
55. Z. T. Nagy, G. Sonet, F. Glaw, M. Vences, First Large-Scale DNA Barcoding Assessment of Reptiles in the Biodiversity Hotspot of Madagascar, Based on Newly Designed COI Primers. *PLOS ONE* **7**, e34506 (2012).
56. D. R. Vieites *et al*., Vast underestimation of Madagascar's biodiversity evidenced by an integrative amphibian inventory. *Proc. Natl. Acad. Sci. U.S.A.* **106**, 8267–8272 (2009). doi: 10.1073/pnas.0810821106; pmid: 19416818
57. Univ. of California, Amphibiaweb. (2021); https://amphibiaweb.org/.
58. R. G. B. Perl *et al*., DNA barcoding Madagascar's amphibian fauna. *Amphib.-Reptil.* **35**, 197–206 (2014). doi: 10.1163/15685381-00002942
59. B. L. Fisher, C. Peeters, *Ants of Madagascar: A Guide to the 62 Genera*. (Association Vahatra, 2019), pp. 260.
60. B. Bolton, An online catalog of the ants of the world. (2022); https://antcat.org.
61. M. S. Vorontsova *et al*., Inequality in plant diversity knowledge and unrecorded plant extinctions: An example from the grasses of Madagascar. *Plants People Planet* **3**, 45–60 (2021). doi: 10.1002/ppp3.10123
62. J. P. Herrera, Prioritizing protected areas in Madagascar for lemur diversity using a multidimensional perspective. *Biol. Conserv.* **207**, 1–8 (2017). doi: 10.1016/j.biocon.2016.12.028
63. F. Glaw, A. Crottini, A. Rakotoarison, M. D. Scherz, M. Vences, in *The New Natural History of Madagascar,* S. M. Goodman, Ed. (Princeton Univ. Press, 2022), pp. 1305–1322.
64. J. S. Sparks, M. L. J. Stiassny, in *The New Natural History of Madagascar,* S. M. Goodman, Ed. (Princeton Univ. Press, 2022), pp. 1245–1260.
65. M. Vences, A. Raselimanana, in *The Terrestrial Protected Areas of Madagascar: Their History, Description, and Biota,* S. M. Goodman, M. J. Raherilalao, S. Wohlhauser, Eds. (Association Vahatra, 2018), pp. 289–327.
66. I. Tattersal, F. Cuozzo, in *The terrestrial protected areas of Madagascar: Their History, Description, and Biota,* S. M. Goodman, M. J. Raherilalao, S. Wohlhauser, Eds. (Association Vahatra, 2018), pp. 403–421.
67. M. V. F. Glaw, C. J. Raxworthy, in *The New Natural History of Madagascar,* S. M. Goodman, Ed. (Princeton Univ. Press, 2022), pp. 1423–1442.
68. S. M. Goodman, V. Soarimalala, in *New Natural History of Madagascar,* S. M. Goodman, Ed. (Princeton Univ. Press, 2022), pp. 1737–1769.
69. B. L. Fisher, in *The New Natural History of Madagascar,* S. M. Goodman, Ed. (Princeton Univ. Press, 2022), pp. 847–853.
70. R. Paulian, P. Viette, in *The Natural History of Madagascar,* S. M. Goodman, J. P. Benstead, Eds. (Chicago Univ. Press, 2003), pp. 503–511.
71. R. J. Safford, S. M. Goodman, M. J. Raherilalao, A. F. A. Hawkins, in *The New Natural History of Madagascar,* S. M. Goodman, Ed. (Princeton Univ. Press, 2022), pp. 1553–1602.
72. D. E. Wilson, D. M. Reeder, Eds., *Mammal Species of the World: A Taxonomic and Geographic Reference (3rd ed)*, (Johns Hopkins Univ. Press, 2005).
73. C. J. Burgin, J. P. Colella, P. L. Kahn, N. S. Upham, How many species of mammals are there? *J. Mammal.* **99**, 1–14 (2018). doi: 10.1093/jmammal/gyx147
74. F. Glaw, O. Hawlitschek, K. Glaw, M. Vences, Integrative evidence confirms new endemic island frogs and transmarine dispersal of amphibians between Madagascar and Mayotte (Comoros archipelago). *Naturwissenschaften* **106**, 19 (2019). doi: 10.1007/s00114-019-1618-9; pmid: 31041592
75. D. R. Vieites, S. Nieto-Román, M. P. Fernández, J. H. Santos-Santos, Hidden in plain sight: A new frog species of the genus *Blommersia* from the oceanic island of Mayotte, Comoros archipelago. *ZooKeys* **994**, 149–166 (2020). doi: 10.3897/zookeys.994.57012; pmid: 33273885
76. P. P. Lowry II, P. B. Phillipson, L. Andrimahefarivo, G. E. Schatz, F. Rajaonary, S. Andriambololonera, in *The terrestrial protected areas of Madagascar: Their History, Description, and Biota*, S. M. Goodman, M. J. Raherilalao, S. Wohlhauser, Eds. (Association Vahatra, 2018), pp. 243–255.
77. Madagascar Catalogue, Catalogue of the Vascular Plants of Madagascar (Missouri Botanical Garden, 2021); http://legacy.tropicos.org/Project/Madagascar. [accessed 12 May 2022].
78. M. S. Vorontsova *et al*., Madagascar's grasses and grasslands: Anthropogenic or natural? *Proc. Biol. Sci.* **283**, 20152262 (2016). pmid: 26791612
79. M. W. Callmander *et al*., The endemic and non-endemic vascular flora of Madagascar updated. *Plant Ecol. Evol.* **144**, 121–125 (2011). doi: 10.5091/plecevo.2011.513
80. L. Marline, C. Ah-Peng, T. A. J. Hedderson, in *The New Natural History of Madagascar,* S. M. Goodman, Ed. (Princeton Univ. Press, 2022), pp. 510–520.
81. J. L. Brown, A. Cameron, A. D. Yoder, M. Vences, A necessarily complex model to explain the biogeography of the amphibians and reptiles of Madagascar. *Nat. Commun.* **5**, 5046 (2014). doi: 10.1038/ncomms6046; pmid: 25297804
82. M. Rakotoarinivo *et al*., Palaeo-precipitation is a major determinant of palm species richness patterns across Madagascar: A tropical biodiversity hotspot. *Proc. Biol. Sci.* **280**, 20123048 (2013). pmid: 23427173
83. B. Isambert *et al*., Endemism and evolutionary history in conflict over Madagascar's freshwater conservation priorities. *Biol. Conserv.* **144**, 1902–1909 (2011). doi: 10.1016/j.biocon.2011.04.016
84. S. Buerki *et al*., Incorporating evolutionary history into conservation planning in biodiversity hotspots. *Philos. Trans. R. Soc. B* **370**, 20140014 (2015). doi: 10.1098/rstb.2014.0014; pmid: 25561675
85. A. Soulebeau, R. Pellens, P. P. Lowry, X. Aubriot, M. E. K. Evans, T. Haevermans, in *Biodiversity Conservation and Phylogenetic Systematics: Preserving our evolutionary heritage in an extinction crisis,* R. Pellens, P. Grandcolas, Eds. (Springer, 2016), pp. 355–374.
86. C. J. Raxworthy, R. A. Nussbaum, Systematics, speciation and biogeography of the dwarf chameleons (*Brookesia*; Reptilia, Squamata, Chamaeleontidae) of northern Madagascar. *J. Zool.* **235**, 525–558 (1995). doi: 10.1111/j.1469-7998.1995.tb01767.x
87. N. Ray, J. M. Adams, A GIS-based Vegetation Map of the World at the Last Glacial Maximum (25,000-15,000 BP). *Internet Archaeol.* **11**, ia.11.2 (2001). doi: 10.11141/ia.11.2
88. H. N. Andriananjamanantsoa, S. Engberg, E. E. Louis Jr., L. Brouillet, Diversification of *Angraecum* (Orchidaceae, Vandeae) in Madagascar: Revised phylogeny reveals species accumulation through time rather than rapid radiation. *PLOS ONE* **11**, e0163194 (2016). doi: 10.1371/journal.pone.0163194; pmid: 27669569
89. F. T. Burbrink *et al*., The origins and diversification of the exceptionally rich gemsnakes (Colubroidea: Lamprophiidae: Pseudoxyrhophiinae) in Madagascar. *Syst. Biol.* **68**, 918–936 (2019). doi: 10.1093/sysbio/syz026; pmid: 31188455

90. C. R. Hutter, S. M. Lambert, Z. F. Andriampenomanana, F. Glaw, M. Vences, Molecular phylogeny and diversification of Malagasy bright-eyed tree frogs (Mantellidae: *Boophis*). *Mol. Phylogenet. Evol.* **127**, 568–578 (2018). doi: 10.1016/j.ympev.2018.05.027; pmid: 29894731
91. M. S. Vorontsova *et al*., in *The New Natural History of Madagascar,* S. M. Goodman, Ed. (Princeton Univ. Press, 2022), pp. 585–598.
92. K. C. Wollenberg *et al*., Patterns of endemism and species richness in Malagasy cophyline frogs support a key role of mountainous areas for speciation. *Evolution* **62**, 1890–1907 (2008). doi: 10.1111/j.1558-5646.2008.00420.x; pmid: 18485110
93. M. N. Rabarimanarivo *et al*., The extraordinary botanical diversity of inselbergs in Madagascar. *Candollea* **74**, 65–84 (2019).
94. M. Vences, K. C. Wollenberg, D. R. Vieites, D. C. Lees, Madagascar as a model region of species diversification. *Trends Ecol. Evol.* **24**, 456–465 (2009). doi: 10.1016/j.tree.2009.03.011; pmid: 19500874
95. L. Wilmé, S. M. Goodman, J. U. Ganzhorn, Biogeographic evolution of Madagascar's microendemic biota. *Science* **312**, 1063–1065 (2006). doi: 10.1126/science.1122806; pmid: 16709785
96. R. G. Pearson, C. J. Raxworthy, The evolution of local endemism in madagascar: Watershed versus climatic gradient hypotheses evaluated by null biogeographic models. *Evolution* **63**, 959–967 (2009). doi: 10.1111/j.1558-5646.2008.00596.x; pmid: 19210532
97. M. Diazgranados *et al*., World Checklist of Useful Plant Species, Version 2.1.1, Knowledge Network for Biocomplexity (2020); doi: 10.5063/F1CV4G34.
98. WCVP, World Checklist of Vascular Plants, version 2.0. (2020); https://wcvp.science.kew.org/.
99. S. Ramachandra Rao, G. A. Ravishankar, Vanilla flavour: Production by conventional and biotechnological routes. *J. Sci. Food Agric.* **80**, 289–304 (2000). doi: 10.1002/1097-0010(200002)80:3<289:AID-JSFA543>3.0.CO;2-2
100. D. S. Correll, Vanilla-its botany, history, cultivation and economic import. *Econ. Bot.* **7**, 291–358 (1953). doi: 10.1007/BF02930810
101. D. Hending, A. Andrianiaina, Z. Rakotomalala, S. Cotton, The use of vanilla plantations by lemurs: Encouraging findings for both lemur conservation and sustainable agroforestry in the Sava Region, Northeast Madagascar. *Int. J. Primatol.* **39**, 141–153 (2018). doi: 10.1007/s10764-018-0022-1
102. D. A. Martin *et al*., Bird diversity and endemism along a land-use gradient in Madagascar: The conservation value of vanilla agroforests. *Biotropica* **53**, 179–190 (2021). doi: 10.1111/btp.12859
103. T. N. Randrianarivony *et al*., The most used medicinal plants by communities in Mahaboboka, Amboronabo, Mikoboka, Southwestern Madagascar. *J. Ethnobiol. Ethnomed.* **13**, 19 (2017). doi: 10.1186/s13002-017-0147-x; pmid: 28279184
104. N. Rakotoarivelo *et al*., Ethnobotanical and economic value of *Ravenala madagascariensis* Sonn. in Eastern Madagascar. *J. Ethnobiol. Ethnomed.* **10**, 57 (2014). doi: 10.1186/1746-4269-10-57; pmid: 25027625
105. P. Wilkin *et al*., in *The New Natural History of Madagascar,* S. M. Goodman, Ed. (Princeton Univ. Press, 2022), pp. 545–551.
106. V. H. Jeannoda *et al*., Les ignames (*Dioscorea* spp.) de Madagascar: Espèces endémiques et formes introduites; diversité, perception, valeur nutritionnelle et systèmes de gestion durable. *Rev. Écol.* **62**, 191–207 (2007).
107. A. P. Davis, R. Govaerts, D. M. Bridson, P. Stoffelen, An annotated taxonomic conspectus of the genus *Coffea* (Rubiaceae). *Bot. J. Linn. Soc.* **152**, 465–512 (2006). doi: 10.1111/j.1095-8339.2006.00584.x
108. A. P. Davis, F. Rakotonasolo, Six new species of coffee (*Coffea*) from northern Madagascar. *Kew Bull.* **76**, 497–511 (2021). doi: 10.1007/s12225-021-09952-5
109. A. P. Davis, F. Rakotonasolo, P. De Block, *Coffeatoshii* sp. nov. (Rubiaceae) from Madagascar. *Nord. J. Bot.* **28**, 134–136 (2010). doi: 10.1111/j.1756-1051.2010.00710.x
110. A. P. Davis *et al*., High extinction risk for wild coffee species and implications for coffee sector sustainability. *Sci. Adv.* **5**, eaav3473 (2019). doi: 10.1126/sciadv.aav3473; pmid: 30746478
111. J. Dransfield, H. Beentje, *The Palms of Madagascar*. (Royal Botanic Gardens and The International Palm Society, 1995).
112. M. Rakotoarinivo, J. Dransfield, S. P. Bachman, J. Moat, W. J. Baker, Comprehensive Red List assessment reveals exceptionally high extinction risk to Madagascar palms. *PLOS ONE* **9**, e103684 (2014). doi: 10.1371/journal.pone.0103684; pmid: 25075612
113. O. M. Grace *et al*., Plant Power: Opportunities and challenges for meeting sustainable energy needs from the plant and fungal kingdoms. *Plants People Planet* **2**, 446–462 (2020). doi: 10.1002/ppp3.10147
114. E. Nic Lughadha *et al*., Extinction risk and threats to plants and fungi. *Plants People Planet* **2**, 389–408 (2020). doi: 10.1002/ppp3.10146
115. T. Ulian *et al*., Unlocking plant resources to support food security and promote sustainable agriculture. *Plants People Planet* **2**, 421–445 (2020). doi: 10.1002/ppp3.10145
116. M. Randrianarivelojosia *et al*., Plants traditionally prescribed to treat *tazo* (malaria) in the eastern region of Madagascar. *Malar. J.* **2**, 25–25 (2003). doi: 10.1186/1475-2875-2-25; pmid: 12921540
117. S. Das, A. B. Sharangi, Madagascar periwinkle (*Catharanthus roseus* L.): Diverse medicinal and therapeutic benefits to humankind. *J. Pharmacogn. Phytochem.* **6**, 1695–1701 (2017).
118. N. H. Rakotoarivelo *et al*., Medicinal plants used to treat the most frequent diseases encountered in Ambalabe rural community, Eastern Madagascar. *J. Ethnobiol. Ethnomed.* **11**, 68 (2015). doi: 10.1186/s13002-015-0050-2; pmid: 26369781
119. A. Miora Henintsoa *et al*., Medicinal plants from the Ankaratra Mountain in Madagascar: Diversity and uses. *Research Square*, (2022).
120. M. Razafindraibe *et al*., Medicinal plants used by women from Agnalazaha littoral forest (Southeastern Madagascar). *J. Ethnobiol. Ethnomed.* **9**, 73 (2013). doi: 10.1186/1746-4269-9-73; pmid: 24188563
121. C. Borgerson *et al*., The use of natural resources to improve household income, health, and nutrition within the forests of Kianjavato, Madagascar. *Madag. Conserv. Dev.* **13**, 45 (2018). doi: 10.4314/mcd.v13i1.6
122. C. D. Golden, L. C. H. Fernald, J. S. Brashares, B. J. R. Rasolofoniaina, C. Kremen, Benefits of wildlife consumption to child nutrition in a biodiversity hotspot. *Proc. Natl. Acad. Sci. U.S.A.* **108**, 19653–19656 (2011). doi: 10.1073/pnas.1112586108; pmid: 22106297
123. C. D. Golden, C. DeSisto, C. Borgerson, H. J. Randriamady, in *The New Natural History of Madagascar,* S. M. Goodman, Ed. (Princeton Univ. Press, 2022), pp. 204–217.
124. Z. J. Farris *et al*., Hunting, exotic carnivores, and habitat loss: Anthropogenic effects on a native carnivore community, Madagascar. *PLOS ONE* **10**, e0136456 (2015). doi: 10.1371/journal.pone.0136456; pmid: 26375991
125. R. K. B. Jenkins *et al*., Analysis of patterns of bushmeat consumption reveals extensive exploitation of protected species in eastern Madagascar. *PLOS ONE* **6**, e27570 (2011). doi: 10.1371/journal.pone.0027570; pmid: 22194787
126. S. M. Goodman, in *The New Natural History of Madagascar* (Princeton University Press, 2022), pp. 2246.

ACKNOWLEDGMENTS

A. Davis (RBG Kew) provided information on Rubiaceae, P. Kirk (RBG Kew) provided data from Index Fungorum, L. M. Suz (RBG Kew) provided information on mycorrhizal fungi, and S. N. Stephenson (University of Oxford) provided feedback on Malagasy geology. We thank J. Aronson (Missouri Botanical Garden), D. Ashley (UK Ambassador to Madagascar and Comoros), J. P. G. Jones (Bangor University), A. Lehavana (Missouri Botanical Garden), J. Ratsimbazafy (Houston Zoo and the Groupe d'Etude et de Recherche sur les Primates de Madagascar), S. Ratsirahonana (Fondation pour les Aires Protégées et la Biodiversité de Madagascar), and G. E. Schatz (Missouri Botanical Garden) for their insightful feedback on the first draft of the manuscript, and three anonymous reviewers for valuable feedback. We stress that all views expressed in this article are only those of the authors. **Funding:** A.A. acknowledges financial support from the Swedish Research Council (2019-05191), the Swedish Foundation for Strategic Research (FFL15-0196) and a grant from the Kew Foundation. T.A. was supported by the SciLifeLab and Wallenberg Data Driven Life Science Program, grant KAW 2020.0239. C.D.B. and M.F.T.J. were supported by a grant from the Swedish Research Council to C.D.B., grant 2017-04980. F.B. was supported by Fundação para a Ciência e a Tecnologia, grant PD/BD/128493/2017. J.B., J.H., S.P., and B.E.W. were supported by a Future Leader Fellowship from RBG Kew. N.A.C. was financed by H2020 MSCA-ITN-ETN Plant.ID, a European Union's Horizon 2020 research and innovation programme under grant agreement 765000. J.D.C. was supported by the Swiss National Science Foundation, grant P400PB_186733 and P4P4PB_199187. A.C. was supported by Portuguese National Funds through the Foundation for Science and Technology, FCT, grant 2020.00823.CEECIND and project PTDC/BIA-EVL/31254/2017. G.D. was supported by Vinnova, grant 2019-02717. D.E. was supported by the Swedish Research Council, grant 2016-00796, and the Swedish Foundation for Strategic Research, grant FFL15-0196. S.F. was supported by the Swedish Research Council, grant 2017-03862. B.L.F. was supported by National Science Foundation, grant DEB-1655076. P.L.F. was supported by the MEMOVA project, EU Operational Programme Research, Development and Education, grant CZ.02.2.69/0.0/0.0/18_053/0016982. T.B.G. is supported by a young researcher grant from São Paulo Research Foundation (FAPESP, #2021/07161-6, #2022/09428-2), Brazil. M.C.H. and R.H. are Natural Environment Research Council funded Ph.D. students with the London NERC DTP (NERC Ref: NE/L002485/1). P.M.M. was funded by the Czech Science Foundation, grant GJ20-18566Y. B.N. was supported by the Coordenação de Aperfeiçoamento de Pessoal de Nível Superior, Brasil (CAPES) – (PDSE 88881.132750/2016-01). R.E.O. acknowledges the support of iDiv funded by the German Research Foundation (DFG–FZT 118, 202548816). A.S.T.P. was supported by the Natural Environment Research Council (NERC), grant NE/R001081/1. L.N.P. was supported by a Swiss National Science Foundation Early Postdoc Mobility Grant, grant P2LAP2_187745. M.R.H. was supported by a beca de doctorado del Instituto de Ecología y Biodiversidad, Chile; Programa de Doctorado en Biología y Ecología Aplicada, Universidad Católica del Norte, Universidad de La Serena, La Serena, Chile Ph.D. and a ANID National Scholarship (grant 21181931); Institute of Ecology and Biodiversity (Project ANID FB210006). E.R. was supported by the NRF / SASSCAL (Southern African Science Service Centre), grant 118589, and the NRF / African Origins Platform, grant 117666. F.S. was supported by European Union's Horizon 2020 research and innovation program under the Marie Skłodowska-Curie grant agreement, grant 838998. D.S. received funding from the Swiss National Science Foundation (PCEFP3_187012) and from the Swedish Research Council (VR: 2019-04739). M.S.V. was supported by a GBIF: Biodiversity Information for Development grant. K.W. was supported by a Techne Arts and Humanities Research Council Doctoral Training Partnership. P.W. was supported by the Darwin Initiative, grants 22-005 and EIDPO049.

Author contributions: The paper was project-led, with overall writing responsibility, by A.A., A.L.P., H.Ral., and R.J.S. The content was divided into two sections, with corresponding working groups, each making full use of the expertise and direct in-country experience of the 25 Malagasy co-authors. The sections were organized, written, and led by A.C., A.L.P., H.Ral., J.H., R.J.S., and W.T. Formal analyses were carried out by D.E., H.F., J.M., M.S.V., O.A.P., R.H., S.P., T.A., and W.T. Visualizations and figures were done by D.E., H.F., M.F.J.T., O.A.P., and W.T. This paper and its sister manuscript on threats and opportunities (*2*) were based on the outputs of a consortium focusing on Madagascar's biodiversity. The data curation, investigation and resources therefore formed the foundation for the project as a whole and we therefore list all co-authors involved in these activities across both papers. Data curation was carried out by A.C., A.M.A., A.Rak., A.Ras., A.Z., B.A.R., B.L.F., B.N., C.D.B., D.E., G.D., D.R., E.R., F.Raj., F.Rak., F.S., H.N.R., H.Ral., H.Raz., J.D.C., J.E.N.R., J.H., J.M., K.W., L.M., L.N.P., L.R.R., M.F.T.J., M.G.C.N., M.Rab., M.R.H., M.Ri., M.S.V., M.T.R., N.A., N.A.C., N.A.S.P., N.R., O.A.P., P.L.F., P.M.M., P.B.P., P.W., R.C., R.E.O., R.H., S.A., S.C., S.D., S.E.R., S.M.G., S.P., T.B.G., T.R., T.Z., V.Ran., V.Raz., and W.T. Investigation was carried out by A.C., A.M.A., A.Rak., A.Ras., A.S.T.P., B.A.R., B.N., F.B., F.Rak., H.N.R., H.Raz., M.G.C.N., O.A.P., O.M.G., P.L.F., P.M.M., P.W., R.A., R.H., R.S.C.C., S.E.R., and T.B.G. Methodology was developed by A.C., A.Z., B.E.W., C.E.R.L., D.S., J.H., J.M., J.S.B., L.N.P., M.S.V., S.P.B., and T.A. Resources were provided by A.C., D.R., E.R., J.R., L.M., M.Rak., M.S.V., M.T.R., N.A.S.P., and T.R. Software was designed by A.Z., B.E.W., D.E., D.S., and H.F. Validations were carried out by A.C., D.E., J.M., and W.J.B. All co-authors were involved in the writing, revision and editing of the text. **Competing interests:** Authors declare no competing interests. **Data and materials availability:** All data is available in the main text or the Supplementary Materials. **License information:** Copyright © 2022 the authors, some rights reserved; exclusive licensee American Association for the Advancement of Science. No claim to original US government works. https://www.sciencemag.org/about/science-licenses-journal-article-reuse

SUPPLEMENTARY MATERIALS

science.org/doi/10.1126/science.abf0869
Materials and Methods
Figs. S1 and S2
Tables S1 and S2
References (*127*–*178*)
MDAR Reproducibility Checklist

Submitted 8 September 2021; accepted 7 November 2022
10.1126/science.abf0869

Validations were carried out by A.C., D.E., J.M., and W.J.B. All co-authors were involved in the writing, revision and editing of the text. **Competing interests:** Authors declare no competing interests. **Data and materials availability:** All data is available in the main text or the Supplementary Materials. **License information:** Copyright © 2022 the authors, some rights reserved; exclusive licensee American Association for the Advancement of Science. No claim to original US government works. https://www.sciencemag.org/about/science-licenses-journal-article-reuse

SUPPLEMENTARY MATERIALS

science.org/doi/10.1126/science.abf0869
Materials and Methods
Figs. S1 and S2
Tables S1 and S2
References (*127*–*178*)
MDAR Reproducibility Checklist

Submitted 8 September 2021; accepted 7 November 2022
10.1126/science.abf0869

REVIEW SUMMARY

BIODIVERSITY

Madagascar's extraordinary biodiversity: Threats and opportunities

Hélène Ralimanana* *et al.*

BACKGROUND: Madagascar is one of the world's foremost biodiversity hotspots. Its unique assemblage of plants, animals, and fungi—the majority of which evolved on the island and occur nowhere else—is both diverse and threatened. After human arrival, the island's entire megafauna became extinct, and large portions of the current flora and fauna may be on track for a similar fate. Conditions for the long-term survival of many Malagasy species are not currently met because of multiple anthropogenic threats.

ADVANCES: We review the extinction risk and threats to biodiversity in Madagascar, using available international assessment data as well as a machine learning analysis to predict the extinction risks and threats to plant species lacking assessments. Our compilation of global International Union for Conservation of Nature (IUCN) Red List assessments shows that overexploitation alongside unsustainable agricultural practices affect 62.1 and 56.8% of vertebrate species, respectively, and each affects nearly 90% of all plant species. Other threats have a relatively minor effect today but are expected to increase in coming decades. Because only one-third (4652) of all Malagasy plant species have been formally assessed, we carried out a neural network analysis to predict the putative status and threats for 5887 unassessed species and to evaluate biases in current assessments. The percentage of plant species currently assessed as under threat is probably representative of actual numbers, except in the case of the ferns and lycophytes, where significantly more species are estimated to be threatened. We find that Madagascar is home to a disproportionately high number of Evolutionarily Distinct and Globally Endangered (EDGE) species. This further highlights the urgency for evidence-based and effective in situ and ex situ conservation.

Despite these alarming statistics and trends, we find that 10.4% of Madagascar's land area is protected and that the network of protected areas (PAs) covers at least part of the range of 97.1% of terrestrial and freshwater vertebrates with known distributions (amphibians, freshwater fishes, reptiles, birds, and mammal species combined) and 67.7% of plant species (for threatened species, the percentages are 97.7% for vertebrates and 79.6% for plants). Complementary to this, ex situ collections hold 18% of vertebrate species and 23% of plant species. Nonetheless, there are still many threatened species that do not occur within PAs and are absent from ex situ collections, including one amphibian, three mammals, and seven reptiles, as well as 559 plants and more yet to be assessed. Based on our updated vegetation map, we find that the current PA network provides good coverage of the major habitats, particularly mangroves, spiny forest, humid forest, and tapia, but subhumid forest and grassland-woodland mosaic have very low areas under protection (5.7 and 1.8% respectively).

OUTLOOK: Madagascar is among the world's poorest countries, and its biodiversity is a key resource for the sustainable future and well-being of its citizens. Current threats to Madagascar's biodiversity are deeply rooted in historical and present social contexts, including widespread inequalities. We therefore propose five opportunities for action to further conservation in a just and equitable way.

First, investment in conservation and restoration must be based on evidence and effectiveness and be tailored to meet future challenges through inclusive solutions. Second, expanded biodiversity monitoring, including increased dataset production and availability, is key. Third, improving the effectiveness of existing PAs—for example through community engagement, training, and income opportunities—is more important than creating new ones. Fourth, conservation and restoration should not focus solely on the PA network but should also include the surrounding landscapes and communities. And finally, conservation actions must address the root causes of biodiversity loss, including poverty and food insecurity.

In the eyes of much of the world, Madagascar's biodiversity is a unique global asset that needs saving; in the daily lives of many of the Malagasy people, it is a rapidly diminishing source of the most basic needs for subsistence. Protecting Madagascar's biodiversity while promoting social development for its people is a matter of the utmost urgency ■

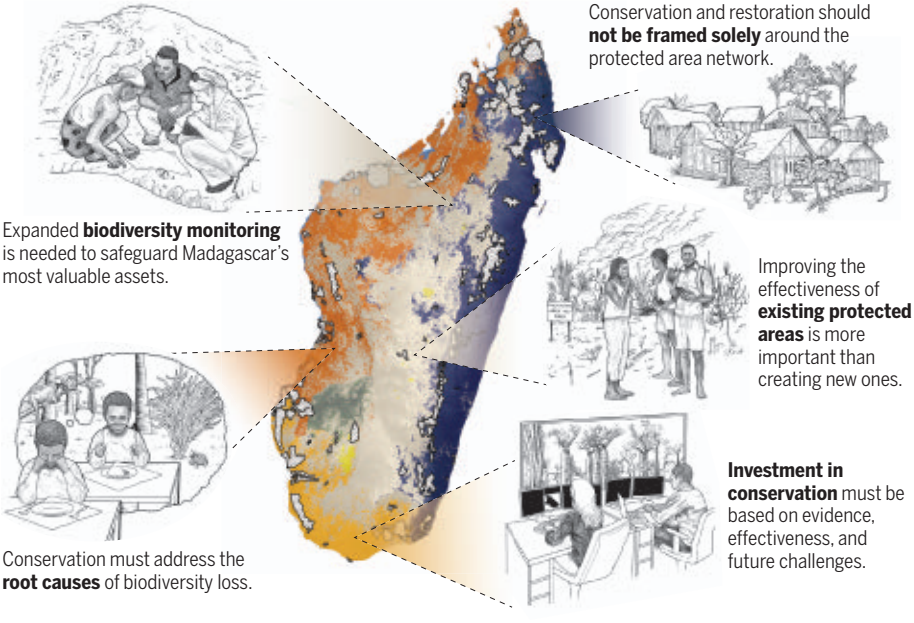


ILLUSTRATION: INESSA VOET

Visual representation of five key opportunities for conserving and restoring Madagascar's rapidly declining biodiversity identified in this Review. The dashed lines point to representative vegetation types where these recommendations could have tangible effects, but the opportunities are applicable across Madagascar.

The complete list of authors and their affiliations is available in the full article online.
*Corresponding authors: Hélène Ralimanana (h.ralimanana@kew.org); Alexandre Antonelli (a.antonelli@kew.org)
Cite this article as H. Ralimanana *et al.*, *Science* **378**, eadf1466 (2022). DOI: 10.1126/science.adf1466

READ THE FULL ARTICLE AT
https://doi.org/10.1126/science.adf1466

REVIEW

BIODIVERSITY

Madagascar's extraordinary biodiversity: Threats and opportunities

Hélène Ralimanana[1]*†, Allison L. Perrigo[2,3]†, Rhian J. Smith[3,4]†, James S. Borrell[4], Søren Faurby[2,3], Mamy Tiana Rajaonah[1], Tianjanahary Randriamboavonjy[1], Maria S. Vorontsova[4], Robert S. C. Cooke[2,3,5], Leanne N. Phelps[6,7], Ferran Sayol[3,8], Niels Andela[9], Tobias Andermann[2,3,10,11], Andotiana M. Andriamanohera[1], Sylvie Andriambololonera[12], Steven P. Bachman[4], Christine D. Bacon[2,3], William J. Baker[4], Francesco Belluardo[13,14,15], Chris Birkinshaw[12,16], Stuart Cable[4], Nataly A. Canales[17], Juan D. Carrillo[3,11,18,19], Rosie Clegg[4,20], Colin Clubbe[4], Angelica Crottini[13,14,15], Gabriel Damasco[2,21], Sonia Dhanda[4], Daniel Edler[2,3,22], Harith Farooq[2,3,23], Paola de Lima Ferreira[2,3,24], Brian L. Fisher[25], Félix Forest[4], Lauren M. Gardiner[26], Steven M. Goodman[27,28], Olwen M. Grace[4], Thaís B. Guedes[29], Jan Hackel[4], Marie C. Henniges[4,30], Rowena Hill[4,30], Caroline E. R. Lehmann[6,7], Porter P. Lowry II[16,31], Lovanomenjanahary Marline[1,3,27], Pável Matos-Maravi[3,24], Justin Moat[4], Beatriz Neves[3,32], Matheus G. C. Nogueira[3,32], Renske E. Onstein[33,34], Alexander S. T. Papadopulos[35], Oscar A. Perez-Escobar[4], Peter B. Phillipson[16,31], Samuel Pironon[4,36], Natalia A. S. Przelomska[4,37], Marina Rabarimanarivo[12], David Rabehevitra[1], Jeannie Raharimampionona[12], Fano Rajaonary[12], Landy R. Rajaovelona[1], Mijoro Rakotoarinivo[38], Amédée A. Rakotoarisoa[1], Solofo E. Rakotoarisoa[1], Herizo N. Rakotomalala[1], Franck Rakotonasolo[1], Berthe A. Ralaiveloarisoa[1], Myriam Ramirez-Herranz[3,39,40], Jean Emmanuel N. Randriamamonjy[1], Vonona Randrianasolo[1], Andriambolantsoa Rasolohery[41], Anitry N. Ratsifandrihamanana[42], Noro Ravololomanana[12], Velosoa Razafiniary[1], Henintsoa Razanajatovo[1], Estelle Razanatsoa[43], Malin Rivers[44], Daniele Silvestro[2,3,11,19], Weston Testo[2,3,28], Maria F. Torres Jiménez[2,3,45], Kim Walker[4,46], Barnaby E. Walker[4], Paul Wilkin[4], Jenny Williams[4], Thomas Ziegler[47,48], Alexander Zizka[49], Alexandre Antonelli[2,3,4,50]*†

Madagascar's unique biota is heavily affected by human activity and is under intense threat. Here, we review the current state of knowledge on the conservation status of Madagascar's terrestrial and freshwater biodiversity by presenting data and analyses on documented and predicted species-level conservation statuses, the most prevalent and relevant threats, ex situ collections and programs, and the coverage and comprehensiveness of protected areas. The existing terrestrial protected area network in Madagascar covers 10.4% of its land area and includes at least part of the range of the majority of described native species of vertebrates with known distributions (97.1% of freshwater fishes, amphibians, reptiles, birds, and mammals combined) and plants (67.7%). The overall figures are higher for threatened species (97.7% of threatened vertebrates and 79.6% of threatened plants occurring within at least one protected area). International Union for Conservation of Nature (IUCN) Red List assessments and Bayesian neural network analyses for plants identify overexploitation of biological resources and unsustainable agriculture as the most prominent threats to biodiversity. We highlight five opportunities for action at multiple levels to ensure that conservation and ecological restoration objectives, programs, and activities take account of complex underlying and interacting factors and produce tangible benefits for the biodiversity and people of Madagascar.

Madagascar's biota, the result of millions of years of evolution in relative isolation, is both unique and under threat. At the same time that the scientific description of new species is accelerating (*1*), so is the overall rate of extinction (*2*), and many species may be disappearing before they are even documented. In this Review, we aim to consolidate information on the conservation status of some of the main elements of Madagascar's biodiversity, evaluate the many and varied threats faced by species assessed under the criteria for the International Union for Conservation of Nature (IUCN) Red List of Threatened Species, and provide some perspectives on future opportunities to ensure the future of this hyperdiverse and unique biota.

Threats to Madagascar's biodiversity

Madagascar's biodiversity is in decline, with some groups more threatened than others (Fig. 1). In our Review of threatened species, we follow the IUCN Red List data (*3*) and threat categories (*4*), unless otherwise specified. Threatened species are those listed as Critically Endangered (CR), Endangered (EN), or Vulnerable (VU). At one extreme, 22% (35 species) of assessed birds are threatened, whereas at the other end of the scale, 73% (66 species) of freshwater fishes and 75% (173 species) of magnoliid plants are threatened. Trees are particularly important in terms of their broad ecological functions and human uses, and 63% of the 3118 assessed tree species in Madagascar are threatened (*5*). Humans have affected the environment since their earliest arrival on Madagascar—not only in recent years. To avoid a shifting baseline effect, it is necessary to view changes in light of human settlement beginning hundreds or even thousands of years ago (*1*). For example, despite the relatively low proportion of bird species currently threatened with extinction, Madagascar has already lost at least 14 species (7% of all species) that were present when humans first settled the island (Fig. 1). The rate of anthropogenic extinction is even higher in mammals, with 23 species (10%) extirpated since the first human settlement. Vertebrate extinctions include the loss of lineages representing millions of years of evolution—e.g., the sloth-, koala-, and monkey-lemurs (families Palaeopropithecidae, Megaladapidae, and Archaeolemuridae) and two species of hippopotamus (family Hippopotamidae). The extinction of four species of elephant birds (order Aepyornithiformes) represents the global loss of a functionally unique clade (*6*, *7*). Extinctions, especially those of megafauna such as these, have broad-scale implications for ecosystem functioning (*6*–*8*).

In total, 13 endemic animal species are listed as Extinct (EX)—defined as extinctions after 1500 AD—and an additional 33 are listed as Extinct Prehistorically (EP)—defined as anthropogenic extinctions before 1500 AD [see (*9*) for a full list of documented anthropogenic extinctions before 1500 AD]. A further nine have been categorized as Critically Endangered (Possibly Extinct) [CR(PE)]. For plants, no species has been assessed as EX, and only one species (*Aloe silicicola*) is categorized as Extinct in the Wild (EW). A further 118 plant species are listed by IUCN as CR(PE) (111 species) or as Critically Endangered (Possibly Extinct in the Wild) [CR(PEW)] (seven species). Of those currently listed as CR(PE), five species are present in ex situ living collections, and their statuses should therefore be updated to CR(PEW) (*3*, *10*).

Malagasy species feature prominently among animal groups that have been considered by the EDGE of Existence program (*11*–*13*), which ranks species according to their evolutionary distinctiveness and the level of threat they face (EDGE = Evolutionarily Distinct and Globally Endangered). Almost one in five species of amphibians (18 species), reptiles (17 species), and mammals (17 species) in the top 100 EDGE species of each group are found in Madagascar (*13*). Yet, only 1 in 20 (four species) of the top 100 EDGE species of birds are found on the island.

Given the narrow geographic range of many Malagasy species [such as (*14*)], numerous undetected anthropogenic extinctions are likely to have taken place (*15*), such as CR *Aloe* species, which may have become extinct in the wild since they were last recorded. This may be especially pronounced in groups with high levels of micro-endemism, for example, freshwater

fishes and amphibians (*16*). Ascertaining extinction events is difficult because of sampling biases, insufficient taxonomic knowledge regarding the morphological features of extant species, and the challenges of comparisons with fossil and subfossil remnants in certain groups, such as frogs (*17*).

Reliability of species conservation assessments

Conservation assessments rely on taxonomic classification, and different opinions on species limits and numbers may influence the proportion of threatened species [such as (*18*)]. This proportion may also be biased by an overassessment of well-known and widespread taxa, or, alternatively, range-restricted species that are more likely to be threatened. To investigate indications of bias, we calculated the fraction of threatened species across different plant groups on the basis of two sets of species: taxa with full threat-status assessments in the Red List compiled by the IUCN and their partners (*19*) and those estimated with a Bayesian neural network approach (Fig. 1) (*9*, *20*), which inferred the threat status for all remaining species. Using this method, we predicted the threat status of 8821 species with an estimated test accuracy of >65%. All taxa with a full threat-status assessment were included, although some assessments may be out of date and could underestimate threat levels.

The neural network approach combined with current IUCN assessments revealed a similar fraction of species inferred to be threatened across most taxonomic groups (Fig. 1). Large deviations from the proportion of threatened species in the current IUCN assessments occur in the ferns and lycophytes and, to a lesser extent, in the magnoliids. The neural network results combined with the known IUCN categories predicted a far higher proportion of threatened ferns and lycophytes {146 of 306 species; 47.7% [95% confidence interval (CI): 38.5 to 56.7%]} than reflected in published IUCN assessments (1 of 33 species; 3.0%), which suggests a bias toward assessing more common species. In the magnoliids, the combined results predict a lower proportion of threatened species [211 of 294 species; 71.8% (95% CI: 68.0 to 75.9%)] compared with published IUCN assessments alone (173 of 225 species; 76.9%), which suggests a bias toward assessing rare species in that group.

Genetic erosion

The reduction of genetic diversity within species resulting from the extirpation of subpopulations is a crucial, yet easily overlooked, facet of biodiversity loss that is often a precursor to extinction. Genetic erosion has negative effects on individual fitness, the health of populations, and a species' ability to adapt to changing environments, reducing their resilience to further change and potentially incurring extinction debt (*21*, *22*). In practice, genetic factors are not directly incorporated into IUCN assessments, which are based on measures of the probability of extinction resulting from population declines, restricted geographic ranges, and small population sizes (*23*).

The reduction in population sizes of wild plants and animals, together with their fragmentation and isolation, is generally expected to increase inbreeding and genetic load, reducing genetic diversity and fitness over time (*22*, *24*). The few studies of intraspecific diversity in Malagasy species to date reveal that some species have maintained high genetic diversity despite habitat fragmentation (*25*, *26*), whereas others have relatively low diversity, possibly as a result of anthropogenic effects (*25*, *27*–*29*). Results differ even within species, such as in the palm *Beccariophoenix madagascariensis*, in which only some populations show strong signals of inbreeding, reflected by an excess of homozygotes (*30*). It is important to note that under some circumstances, population decline may outstrip the speed with which genetic diversity is eroded as a result of inbreeding. Estimates of heterozygosity may therefore not indicate the true genetic health and long-term prospects of populations when considered in isolation (*31*, *32*).

A more powerful although less explored approach is to use coalescence-based demographic modeling, which uses genome-wide data to estimate the longer-term trends in population size, providing more information than metrics of contemporary genetic diversity alone (*25*, *33*). In *Cheirogaleus* dwarf lemurs, genomic analysis suggests that four species have experienced population size declines in the past 50,000 years, with one decline (*Cheirogaleus* cf. *medius*) starting as long as 300,000 years ago—all clearly in prehuman times and resulting in lower genetic diversity (*29*). By contrast, another genomic study shows that 5 out of 10 analyzed plant species with varying extinction risk have experienced substantial population declines since human colonization of Madagascar (*25*). In the golden-crowned sifaka (*Propithecus tattersalli*) (*26*), mouse lemurs (*Microcebus* spp.) (*28*), *Mantella* frogs (*34*), and the Milne-Edwards' sportive lemur (*Lepilemur edwardsi*) (*35*), demographic declines also appear to have taken place after the arrival of humans on the island (although the inherent uncertainties of mutation rates in the microsatellite data used makes the timing of these declines less certain).

The risks of inbreeding and increased genetic load may represent substantial and likely underestimated longer-term threats to the survival of Malagasy species. This is especially relevant considering the high level of fragmentation of native habitats in some vegetation types, such as the humid forests, and is worthy of further investigation.

Predicting future extinction: Direct drivers of loss

Identifying direct threats is part of the IUCN Red List assessment process, and even species

[1]Royal Botanic Gardens, Kew, Kew Madagascar Conservation Centre, Antananarivo, Madagascar. [2]Department of Biological and Environmental Sciences, University of Gothenburg, Gothenburg, Sweden. [3]Gothenburg Global Biodiversity Centre, University of Gothenburg, Gothenburg, Sweden. [4]Royal Botanic Gardens, Kew, Richmond, Surrey, UK. [5]UK Centre for Ecology and Hydrology, Wallingford, UK. [6]School of GeoSciences, University of Edinburgh, Edinburgh, UK. [7]Royal Botanic Garden Edinburgh, Edinburgh, UK. [8]Centre for Biodiversity and Environment Research, Department of Genetics, Evolution and Environment, University College London, London, UK. [9]School of Earth and Environmental Sciences, Cardiff University, Cardiff, Wales, UK. [10]Department of Organismal Biology, SciLifeLab, Uppsala University, Uppsala, Sweden. [11]Department of Biology, University of Fribourg, Fribourg, Switzerland. [12]Missouri Botanical Garden, Madagascar Program, Antananarivo, Madagascar. [13]CIBIO, Centro de Investigação em Biodiversidade e Recursos Genéticos, InBIO Laboratório Associado, Universidade do Porto, Vairão, Portugal. [14]Departamento de Biologia, Faculdade de Ciências, Universidade do Porto, Porto, Portugal. [15]BIOPOLIS Program in Genomics, Biodiversity and Land Planning, CIBIO, Campus de Vairão, Vairão, Portugal. [16]Missouri Botanical Garden, St. Louis, MO, USA. [17]Natural History Museum of Denmark, University of Copenhagen, Copenhagen, Denmark. [18]CR2P, Muséum National d'Histoire Naturelle, Paris, France. [19]Swiss Institute of Bioinformatics, Fribourg, Switzerland. [20]Department of Geography, University of Exeter, Exeter, Devon, UK. [21]Departamento de Botânica e Zoologia, Universidade Federal do Rio Grande do Norte, Natal, Rio Grande do Norte, Brazil. [22]Integrated Science Lab, Department of Physics, Umeå University, Umeå, Sweden. [23]Faculty of Natural Sciences, Lúrio University, Pemba, Cabo Delgado Province, Mozambique. [24]Biology Centre CAS, Institute of Entomology, České Budějovice, Czech Republic. [25]California Academy of Sciences, San Francisco, CA, USA. [26]Cambridge University Herbarium, Department of Plant Sciences, University of Cambridge, Cambridge, UK. [27]Association Vahatra, Antananarivo, Madagascar. [28]Field Museum of Natural History, Chicago, IL, USA. [29]Instituto de Biologia, Universidade Estadual de Campinas, Unicamp, Campinas, São Paulo, Brazil. [30]School of Biological and Behavioural Sciences, Queen Mary University of London, London, UK. [31]Institut de Systématique, Évolution, et Biodiversité (ISYEB), Muséum National d'Histoire Naturelle, Paris, France. [32]Museu Nacional, Universidade Federal do Rio de Janeiro, Rio de Janeiro, Brazil. [33]Naturalis Biodiversity Center, Leiden, Netherlands. [34]German Centre for Integrative Biodiversity Research (iDiv) Halle-Jena-Leipzig, Leipzig, Germany. [35]School of Natural Sciences, Bangor University, Bangor, Gwynedd, Wales, UK. [36]UN Environment Programme World Conservation Monitoring Centre (UNEP-WCMC), Cambridge, UK. [37]Department of Anthropology, Smithsonian National Museum of Natural History, Washington, DC, USA. [38]Department of Plant Biology and Ecology, University of Antananarivo, Antananarivo, Madagascar. [39]Instituto de Ecología y Biodiversidad, University of La Serena, La Serena, Chile. [40]Programa de Doctorado en Biología y Ecología Aplicada, Universidad Católica del Norte, Universidad de La Serena, La Serena, Chile. [41]Ileiry Geospatial Services, Antananarivo, Madagascar. [42]WWF, Antananarivo, Madagascar. [43]Plant Conservation Unit, Department of Biological Sciences, University of Cape Town, South Africa. [44]Botanic Gardens Conservation International, Kew, Richmond, Surrey, UK. [45]Institute of Biosciences, Life Sciences Centre, Vilnius University, Vilnius, Lithuania. [46]Royal Holloway, University of London, Egham, Surrey, UK. [47]Cologne Zoo, Cologne, Germany. [48]Institute of Zoology, University of Cologne, Cologne, Germany. [49]Department of Biology, Philipps-University Marburg, Marburg, Germany. [50]Department of Biology, University of Oxford, Oxford, UK.

***Corresponding author. Email: h.ralimanana@kew.org (H.R.); a.antonelli@kew.org (A.A.)**

†These authors contributed equally to this work.

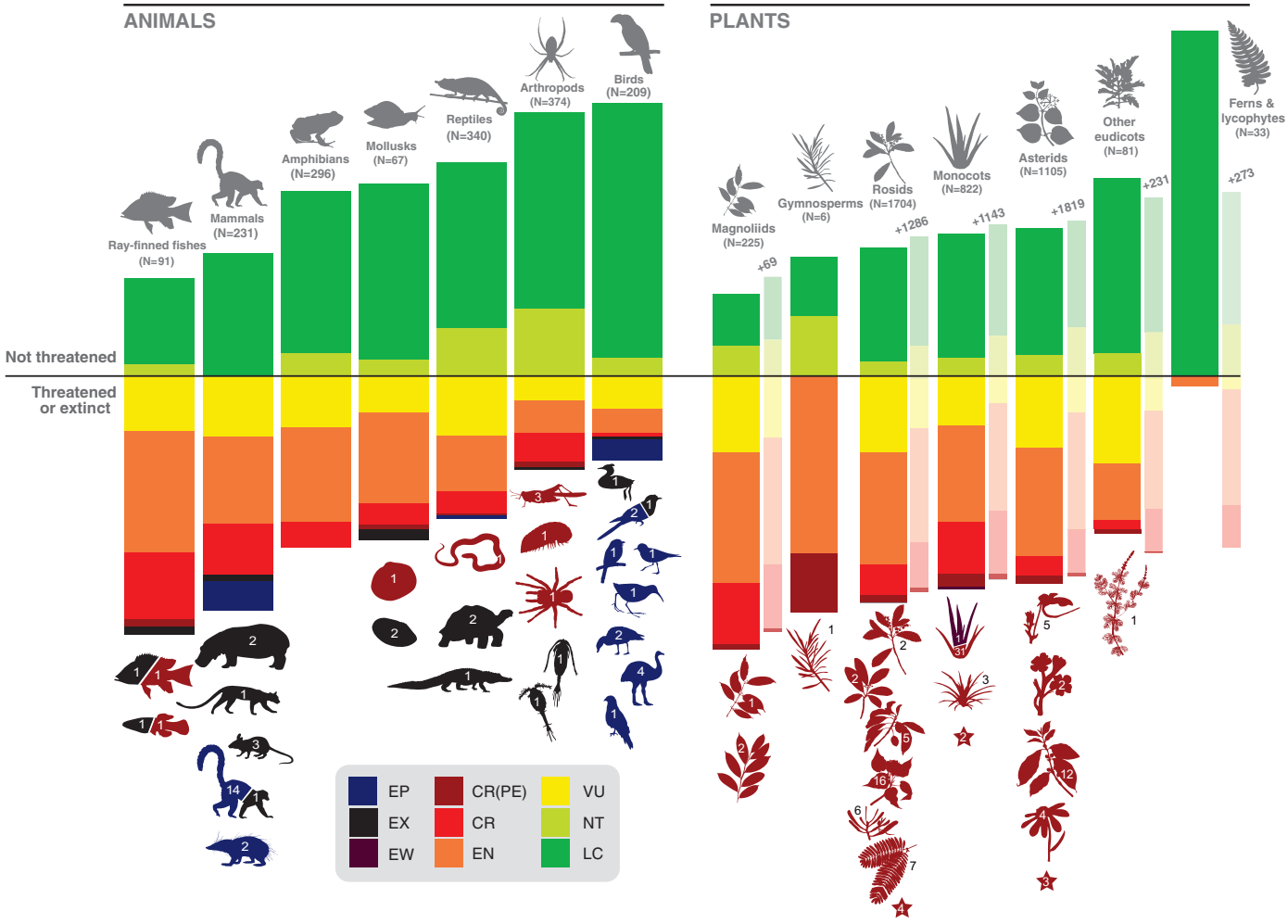


Fig. 1. Madagascar's threatened and lost biodiversity. IUCN Red List assessment categories of major groups of plants and animals from Madagascar. Assessment categories and coloration follow the standards used by the IUCN Red List. Category distributions for animal groups include ray-finned fishes (Actinopterygii, freshwater species only, *N* = 91 species), mammals (Mammalia, *N* = 231), amphibians (Amphibia, *N* = 296), mollusks (Mollusca, *N* = 67), reptiles (Reptilia, *N* = 340), arthropods (Arthropoda, *N* = 374), and birds (Aves, *N* = 209). Category distributions for plants, indicated with saturated, wider bars, include magnoliids (*N* = 225), gymnosperms (*N* = 6), rosids (*N* = 1704), monocots (*N* = 822), asterids (*N* = 1105), other eudicots (*N* = 81), and ferns and lycophytes (*N* = 33). Thinner, unsaturated bars indicate the relative proportion of plant taxa in each threat category for IUCN Red List assessments combined with the taxa where the threat category was predicted in a Bayesian neural network analysis: asterids (*N* = 2924), rosids (*N* = 2990), other eudicots (*N* = 312), magnoliids (*N* = 294), monocots (*N* = 1965), and ferns and lycophytes (*N* = 306). The number indicated above each bar with a plus symbol is the number of taxa for which the threat category was predicted using the neural network analysis. IUCN Red List assessment categories include LC and NT, together making up the not threatened category, whereas VU, EN, CR, CR(PE), EW, EX (i.e., extinct after 1500 CE), and EP (*126*) (i.e., extinct before 1500 CE but with dated records within the past 130,000 years) make up the threatened and extinct category. Silhouettes below the bars depict taxonomic orders with EP, EX, EW, and CR(PE) species, with the number of species in each category per order. For some plant groups, additional orders with single CR(PE) species are indicated with a star. Depicted orders are, from left to right and top to bottom: Perciformes, Cyprinodontiformes, Cetartiodactyla, Carnivora, Rodentia, Primates, Afrosoricida, Venerida, Unionoida, Squamata, Testudines, Crocodilia, Orthoptera, Spirobolida, Araneae, Calanoida, Cyclopoida, Podicipediformes, Cuculiformes, Coraciiformes, Charadriiformes, Gruiformes, Anseriformes, Aepyornithiformes, Accipitriformes, Laurales, Magnoliales, Pinales, Oxalidales, Sapindales, Myrtales, Malvales, Malpighiales, Fabales, Asparagales, Poales, Ericales, Boraginales, Gentianales, Asterales, and Saxifragales.

that are not explicitly threatened [i.e., those that are assessed as Least Concern (LC), Near Threatened (NT), or Data Deficient (DD)] can still have threats listed. Here, we discuss these threats and how they apply to all species. Our analysis of IUCN assessments indicates that overexploitation and agriculture are the most frequently listed threats to Malagasy fauna (excluding invertebrates) and flora (Fig. 2), mirroring global findings (*36*). Overexploitation is unsustainable biological resource use as defined by the IUCN (*37*), including hunting and collecting for subsistence use or national and international trade. Overexploitation is linked in some cases to illegal harvesting—for example, the illegal logging of rosewood for trade (*Dalbergia* spp.)—which has been banned under the Convention on International Trade in Endangered Species of Wild Fauna and Flora since 2013 and under Malagasy law since 2010.

We estimated that 62.1% of vertebrates and 87.1% of plants are threatened by overexploitation and that 56.8% of vertebrates and 87.8% of plants are threatened by agriculture. These two major threats, almost equal in magnitude (Fig. 2), have different modes of impact—overexploitation is more targeted and tends to occur over relatively restricted areas compared with the broad effects of land clearance for agriculture.

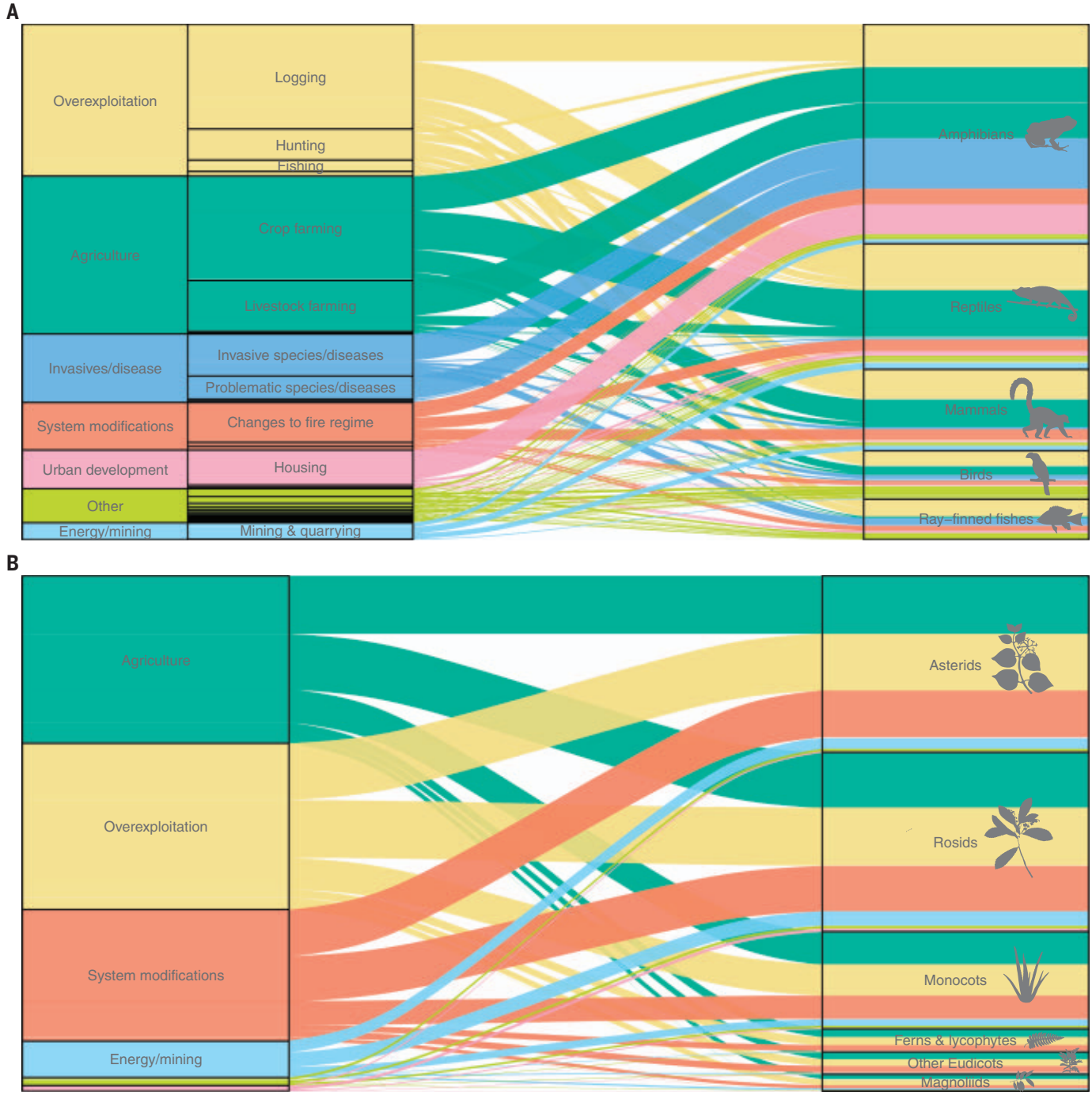


Fig. 2. Threats to Malagasy biodiversity. (**A** and **B**) Alluvial plots showing threats, as defined by the IUCN, and their associations with major groups of terrestrial and freshwater vertebrates (A) (1332 species with IUCN assessments, of which 993 species have at least one listed threat) and plants (B) [9268 species with IUCN assessments or predictions, all of which have at least one listed threat; includes gymnosperms (six species), which could not be visualized]. Widths of the boxes and lines reflect the number of species affected by each threat. Threats for vertebrates are further divided into subthreats, whereas only the highest threat classification was available for assessed plants. The estimates for plants include predictions for unassessed species based on a Bayesian neural network analysis (*9*). The color scheme is consistent across panels. The other threat class includes pollution, climate change, transportation, and human disturbance, plus invasives and diseases for plants. Some threat classes have been renamed for brevity and clarity, including the IUCN category "biological resource use," which is referred to as overexploitation here and in the text for brevity and in line with Intergovernmental Science-Policy Platform on Biodiversity and Ecosystem Services (IPBES) terminology (*36*).

Agriculture, and to a lesser extent overexploitation, are also the primary causes of deforestation in Madagascar. Approximately 44% of the land area covered by native forest in 1953 was deforested by 2014 (*38*). The rate of deforestation has steadily increased, reaching 99.0 kha/year between 2010 and 2014 (*38*) and, according to Global Forest Watch, remains very high at 72.9 kha/year (2014 to 2020) (*39*). Deforestation in Madagascar reflects global patterns (*40*) and is primarily driven by the small-scale but widespread practice of swidden agriculture (also known as shifting cultivation; in Madagascar referred to as *tavy* for rice cultivation in humid and

subhumid areas and *hatsake* for cassava and maize in dry and subarid areas). Additionally, cash crop production, particularly maize and peanut, has become a major driver of deforestation (*41*) alongside the production of products for international markets, such as forest-derived vanilla (*42*). The most frequent threats listed for plants and vertebrates suggest that this trend of increasing deforestation rates will continue, with forest loss and degradation a consequence of the clearance of land for agriculture—potentially associated with small-scale fire activity (*43*)—and overexploitation through selective logging and highly targeted activities, such as the collection of palm hearts. Additionally, natural system modifications (threats from actions that convert or degrade habitat, e.g., anthropogenic fire in forests or changes in water management; Fig. 2) add to deforestation, threaten 23.2% of vertebrates, and are estimated to threaten 68.9% of plants. Some predictions indicate that in the absence of an effective strategy against deforestation, 38 to 93% of forest present in 2000 will be no longer present in 2050 (*41*).

For vertebrates, the greatest threat after overexploitation and agriculture is invasive and problematic species and emerging infectious diseases (referred to as "invasives/diseases" in Fig. 2), which affect 27% of all species (360 species; Fig. 2). This category includes nonnative invasive species as well as problematic native species and diseases of any origin. Changes in habitat because of the spread of non-native plant species can have a large effect, and one study reports that of a total of 546 naturalized non-native plants in Madagascar, 101 have been found to display invasive characteristics (*44*). Many non-native plants, such as the Mexican yellow pine (*Pinus patula*) in terrestrial systems (*45*) and the common water hyacinth (*Pontederia crassipes*) in freshwater systems (*46*), are aggressively invasive and transformative in seminatural habitats and are clearly affecting native fauna and flora. Even within reserves and protected areas (PAs), the issue can be pronounced. For example, three species of invasive or problematic plants—strawberry guava (*Psidium cattleyanum*), Molucca raspberry (*Rubus moluccanus*), and wild cardamom (*Aframomum angustifolium*)—together occupy 17.6% of the Betampona Nature Reserve (*47*) and are also widespread in Ranomafana National Park and other PAs.

Not all impacts are negative, however, and there is some evidence to suggest that, because of their potential for faster growth, some nonnative plants are better able to combat the rapid fragmentation of native vegetation and may be beneficial for endemic vertebrates, providing refuge, food, and vegetation corridors, while also improving human livelihoods (*48*). The potential for such species to become invasive or readily burn must, however, be fully considered before embarking on any planting initiatives (*49*). In addition, effects must be considered at different scales. For example, the presence of strawberry guava has been reported to locally increase species richness in frugivores, but because they are primary dispersers of the seed, this further contributes to the spread of and associated changes in floral and faunal community structure and reduction in taxonomic richness (*50*).

Non-native vertebrates have also had marked and diverse effects, which we illustrate here with some examples. Introduced rats (*Rattus rattus*; present since at least the 14th century) are now ubiquitous, even in remote areas, and there is evidence that their presence is associated with declines in native small mammals (*51*). In freshwater habitats, competition and predation by exotic fish species is considered a major factor in the decline of native freshwater fish (*52*), which have been completely replaced by non-native species across much of the Central Highlands and western areas (*53*). Although not yet listed in current assessments, the recent invasion of the toxic Asian common toad (*Duttaphrynus melanostictus*), along with the predicted vulnerability of most native vertebrates to its toxins (*54*), is expected to represent a new threat to many nocturnal carnivores. The effects of other introduced and naturalized animals on native biodiversity are not well studied; this includes widely occurring species, such as dogs (*Canis familiaris*), cats (*Felis catus*), the common myna (*Acridotheres tristis*), and the marbled crayfish (*Procambarus virginalis*). The threat of emerging infectious diseases is primarily driven by the occurrence of the chytrid fungus *Batrachochytrium dendrobatidis*, widely documented across Madagascar over the past decade and a potential threat to all amphibians, although no mass mortalities associated with chytridiomycosis have been reported in the country (*55*). Species often face multiple threats at the same time, although the effect of each threat can vary between species (Fig. 2).

Among vertebrates, amphibians have the highest number of IUCN-identified threats per species (Fig. 2A), with a mean of 4.8 threats per species, followed by mammals (mean of 2.5 threats per species) and reptiles (mean of 2.2 threats per species). For plants (Fig. 2B), magnoliids have the most threats per species (mean of 2.9 threats per species) followed by rosids (mean of 2.8 threats per species) and other eudicots (mean of 2.8 threats per species). Although there might be some variation in the perception and documentation of threats between the specialists carrying out assessments, all follow the same protocols (*4*).

The number and relative impact of these threats may change in coming decades. The effect of climate change on Malagasy biodiversity remains understudied, and it is not currently indicated in IUCN assessments as a major threat. However, this impact is expected to increase in the future (*56*–*59*) and could potentially result in synergistic negative effects with unsustainable agriculture associated with land clearance, invasive alien species, and inappropriate management of fire regimes that can increase future fire risk (*43*, *56*, *57*, *60*). Extinctions in one group could also have effects on others that depend on them, such as in cases of strong plant-animal mutualisms (*61*, *62*). Although coextinction is hard to quantify, with substantial knowledge and data gaps (*63*), models suggest that the effects of extinction can be amplified as a result of the interactions between species within and between trophic levels, with the potential to lead to secondary and even cascading extinctions (*64*, *65*).

Conservation efforts and effectiveness

Protected areas

PAs are the central political and scientific accomplishment of Madagascar's conservation strategy. The network has been continuously developed since the first PA was established in 1927 (*66*–*70*). Our data compilation shows that the network now encompasses 10.4% of the land area of Madagascar, having grown by more than a third over the past two decades (Fig. 3). This recent and extensive designation of new PAs was carried out through a multistakeholder consultative process, in combination with data and literature analyses, through the Durban Vision initiative conceived in 2003. In addition to preserving diverse ecosystems and landscapes, the focus has been on species groups for which sufficient diversity and distribution data were available, primarily vertebrates (including birds, mammals, amphibians, and reptiles) and some plant groups. Despite the production of considerable data since the Durban Vision began [e.g., many newly described species (*1*)], the network designed during that process remains highly taxonomically comprehensive. From a global perspective, the PA network also excels at capturing the vast majority of Madagascar's many EDGE species: 14 of 18 amphibians, 15 of 17 reptiles, 16 of 17 mammals, and all four birds (*13*).

As of November 2020, there were 110 terrestrial PAs with permanent protected status in Madagascar, covering 61,300 km^2 across the country (Fig. 3) (*69*, *71*, *72*). Eleven of these are orphan PAs—sites abandoned by their former managers, with responsibility reverting to the Ministry of Environment and Sustainable Development (*69*). An additional 89 sites (15,200 km^2), predominantly made up of Key Biodiversity Areas (KBAs), are not under formal protection (*69*, *71*, *73*, *74*).

The long-term security and effective management of Madagascar's PAs is therefore crucial to addressing the country's biodiversity

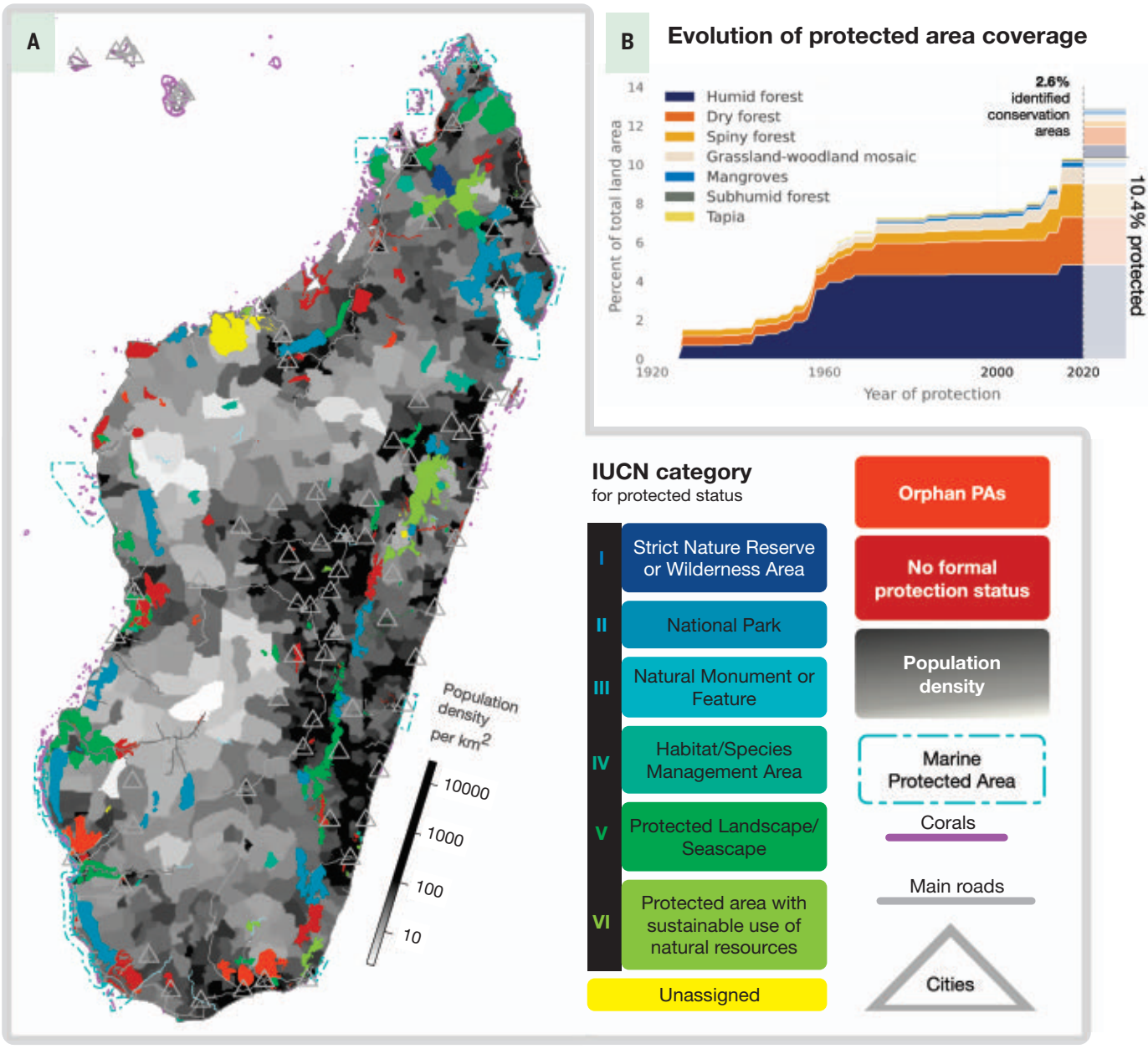


Fig. 3. Madagascar's terrestrial PAs in the context of human population density and changes in coverage of vegetation type over time. (**A**) PAs with IUCN protected status (*127*), orphan status, or no formal protection status (e.g., unprotected KBAs) shown in the context of nearby marine PAs, surrounding bathymetry (*128*), coral reefs (*129*), cities, roads, and population density (*130*). (**B**) The evolution of PA coverage over time, showing the potential increase in area protected that could be gained if the designated areas (those identified as important for biodiversity but not currently under formal protection, mostly KBAs) were protected in the future (*73*, *74*).

challenges. Providing evidence of their effectiveness and cobenefits, such as ecosystem service provision, will be critical to securing ongoing support and management from local communities as well as from local and national governments. However, measuring PA effectiveness is challenging (e.g., its effectiveness at avoiding deforestation or providing alternative livelihoods) while accounting for numerous covariates (*75*), particularly in Madagascar with comparatively little long-term biodiversity monitoring data (*76*). Recent counterfactual analyses (*77*) have sought to address this question by identifying protected and nonprotected sites that are similar across multiple social and environmental variables and then comparing indicators of conservation effectiveness, such as deforestation rate. These analyses indicate that PAs have a small but important role in reducing deforestation (*9*).

We show that since 1990, human impacts have measurably increased across all terrestrial PAs (table S8) (*9*), a trend documented worldwide (*75*). Human activity by local communities inside PAs is not necessarily detrimental to biodiversity, and land use and conservation are therefore not mutually exclusive. Nevertheless, land conversion and unsustainable exploitation remain major drivers of biodiversity loss. This suggests that protecting and realizing the potential of Madagascar's comprehensive PA network will require the application of rigorous monitoring and evaluation strategies matched with extensive community collaboration to understand cobenefits and minimize detrimental human effects.

Scores for deforestation and management effectiveness—for example, from the self-reported Management Effectiveness Tracking Tool (*78*)—have been the main metrics used to monitor effectiveness to date. However, these are not always reliable indicators of management effectiveness (*76*). New and expanded capacity of variables, such as remote-sensed fire and stable night lights, with increased temporal resolution offer promising new monitoring opportunities. How fire is associated with land transformation in Madagascar has been discussed in the literature but has only recently been quantitatively assessed (*43*), demonstrating that tree loss anomalies are highest in environments where landscapes-scale fire (>21 ha) does not occur and where the role of small-scale fires (<21 ha) requires close and urgent investigation. We show that trends in anthropogenic fire are variable, increasing in some areas of forest vegetation in the north, east, and west but decreasing in grassland-woodland mosaic vegetation across central Madagascar (Fig. 4, A and B). Forest loss also reflects this pattern, primarily occurring in the humid forest biome in the east but also in dry forest and spiny forest in the west (Fig. 4, C and D). Deforestation and land use conversion remain key challenges to conservation in Madagascar, and improved remote sensing will accelerate monitoring and developing an understanding of the effectiveness of PAs and other conservation measures.

Ex situ conservation and restoration

Living plant collections in botanic gardens and seed banks represent invaluable sources of taxonomic and genetic diversity for immediate conservation and research and should continue to support restoration efforts. Globally, 29.6% of all known native Malagasy plant species (23.1% of endemic species and 23.1% of native threatened species) are held in botanic gardens, with 15.5% held in Madagascar (*10*), where their cultivation is sometimes linked to educational programs and community engagement essential to raising awareness of biodiversity and conservation issues. The Millennium Seed Bank Partnership in Madagascar, initiated in 1996, hosts collections of an estimated 3500 native Malagasy species, including members of four of the five endemic plant families and all seven of the iconic baobab species (*Adansonia* spp.). The single Malagasy plant species listed as EW, *Aloe silicicola*, now only survives in one living collection outside Madagascar.

For native terrestrial and freshwater vertebrates, 9% of amphibians, 17% of mammals, 20% of reptiles, 21% of freshwater fishes, and 33% of birds are currently held in zoological collections (18% overall) (*9*, *79*). Many are part of active breeding programs, but only 3% of amphibians, 7% of reptiles, 11% of freshwater fishes, 13% of mammals, and 23% of birds were successfully bred during 2020 (*9*). Unsurprisingly, the species held in captive breeding facilities are biased toward the more charismatic, well-known taxa (*80*). For example, among amphibians, 13 of the 34 species in zoos belong to the genus *Mantella*, a group of strikingly colored diurnal frogs, even though

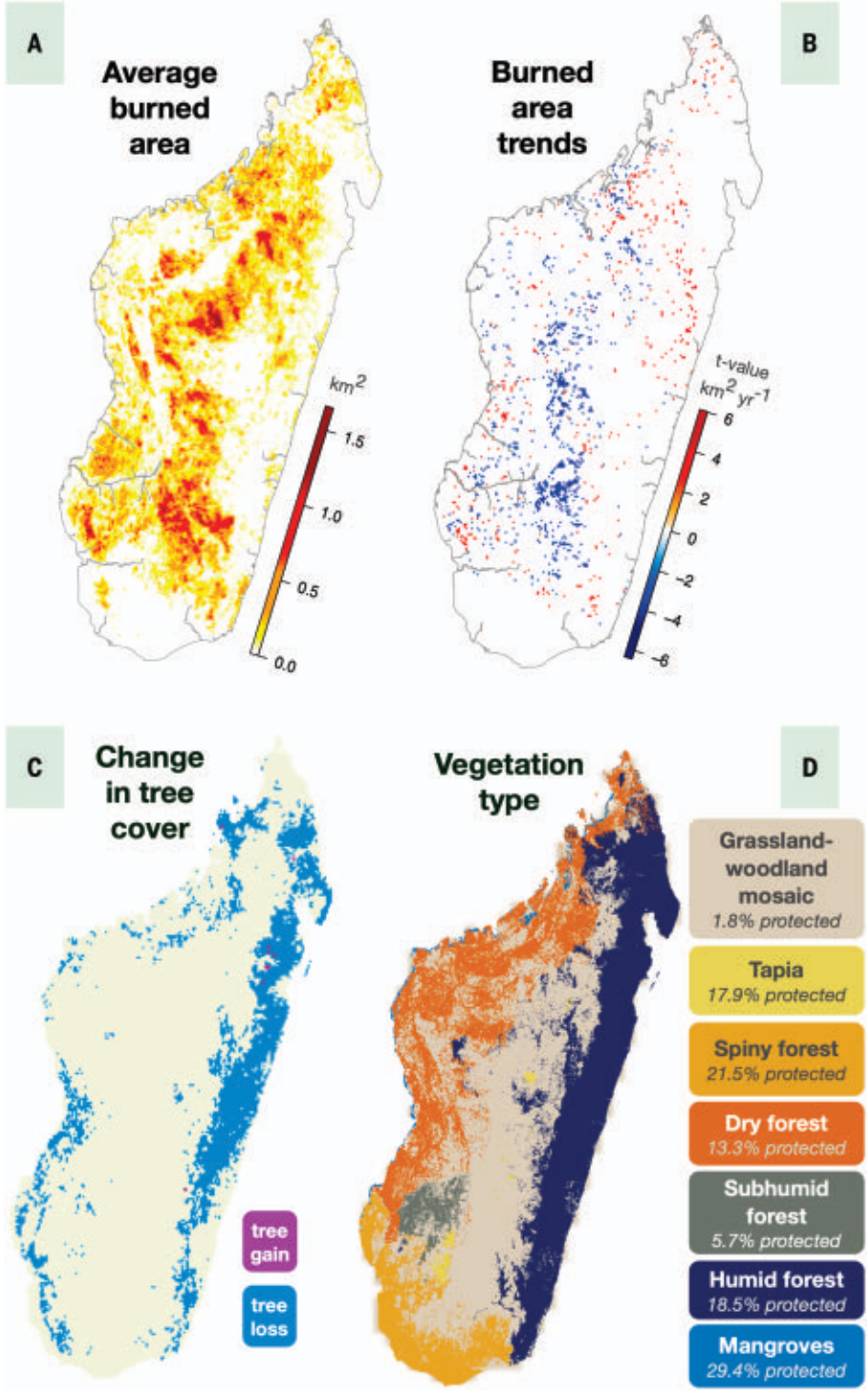


Fig. 4. Recent changes and patterns in burned area and tree cover in Madagascar. (**A**) Average burned area in the period 2003 to 2019. (**B**) Statistically significant trends in burned area (MODIS) (*131*) from 2006 to 2016, not explained by precipitation change (TRMM) (*132*), dates chosen for comparison with Goodman *et al*. (*71*). Red indicates an increasing trend, and blue indicates a decreasing trend. (**C**) Change in tree cover from 2000 to 2012 (*133*). (**D**) Vegetation map, inferred and simplified from Moat and Smith (*134*). The legend indicates the percentage of each vegetation category currently covered by the PA network.

Mantella contains only 4% of Madagascar's amphibian fauna. Freshwater fishes, amphibians, and reptiles are highly suitable for targeted ex situ breeding and reintroduction programs (*81*–*84*). For species in these groups and others with high levels of micro-endemism, such conservation programs continue to represent a major safeguard against extinction (*85*). This complies with the One Plan Approach to species conservation proposed by the IUCN SSC Conservation Planning Specialist Group, which supports the development of conservation and management plans for all populations of a species, even outside of their natural range (*86*). It should be noted that the success of reintroduction relies also on the maintenance of natural habitat and functional diversity at potential reintroduction sites, along with the minimization of risks associated with invasive species and infectious diseases. In addition, particularly for mammals, vulnerability of captive-bred populations to predation can also jeopardize the success of reintroductions (*87*).

Progress toward international conservation commitments

Madagascar continues to make progress toward Convention on Biological Diversity targets but, like most countries, falls short of meeting them in full (*88*). Of particular relevance is that Madagascar did not formally meet Aichi target 11 to protect at least 17% of its total land area (Fig. 3)—as was the case for 48% of the parties reporting their progress (*88*). If areas designated as important for biodiversity but not currently under formal protection were also given protection, the total percentage of PA coverage would rise from the current 10.4 to 13% (Fig. 3B). However, given that even the existing network is widely considered to be chronically under resourced, this action is not a priority for the near future (*89*, *90*).

Target 4 of the Global Strategy for Plant Conservation (GSPC) seeks to protect 15% of each vegetation type. This has been achieved for mangrove (currently at 29.4%), spiny forest (21.5%), humid forest (18.5%), and tapia (17.9%) but not for dry forest (13.3%), subhumid forest (5.7%), and grassland-woodland mosaic (1.8%) (table S6) (*9*). However, expansion of the areas of those vegetation types under protection may not be feasible because of limited financial resources, the large degree of fragmentation and geographical spread of habitats, and the long administrative process involved in extending PAs or designating additional areas, as well as a lack of political will. It also may not be desirable until it can be demonstrated that the existing PAs are well resourced, achieving conservation objectives and providing benefits to communities. Restoration within current PAs may provide a longer-term pathway to meeting this goal, particularly where there are rapidly realizable socioeconomic benefits, such as sustainable silk production from wild native silkworms (*Borocera cajani*) associated with tapia (*Uapaca bojeri*) in the Itremo Massif PA and Ambatofinandrahana KBA. Other targets are more difficult to assess because of a lack of data. For example, there is very little evidence to assess success in the control of invasive alien species, with some exceptions such as the ongoing but promising house crow (*Corvus splendens*) eradication (*91*). Although most of the Aichi and GSPC targets were either not achieved or cannot be assessed, a marked success is that Madagascar has comfortably achieved GSPC target 7 (at least 75% of known threatened plant species conserved in situ), with our analyses indicating that this percentage is currently at 80%.

Realizing the benefits of biodiversity for people

The majority of Madagascar's more than 28 million inhabitants live outside of, but often very close to, PAs (*92*) (Fig. 3A and fig. S1). These communities face challenges connected to widespread poverty, which itself is related to the degradation of natural capital in the landscape, limited access to formal education and health care, crime, corruption, weak governance, and regulatory issues including land tenure (*15*, *93*, *94*). For example, southern Madagascar is severely affected by food and water insecurity, which catalyzes political and social instability, exacerbates economic insecurity, and has led to large-scale migration within the country (*95*). This instability likewise hampers the operations of local, national, and international conservation organizations, which could be compounded further by adverse effects from climate change (*59*). Because the human population in the country is expected to reach 42 to 105 million by the end of this century, of which half will be under 15 years of age and with the majority under the poverty threshold (*96*), the conservation success of PAs will be inextricably linked to the effective provision of livelihoods, food security, and natural capital—a situation echoed across all Malagasy ecosystems and the world over (*97*).

Looking back, moving forward

Despite decades of research and applied conservation programs supported through substantial financial investments (*94*, *98*), Madagascar's remarkable biodiversity continues to face severe challenges (Figs. 1 and 2). It is reasonable to ask whether more of the same tactics—even if better resourced and underpinned with greater scientific understanding and technology—are likely to deliver a tangible reversal in Madagascar's trajectory of biodiversity loss, or whether new approaches are required to bring transformative change (*99*), including greater emphasis on monitoring interventions and addressing underlying drivers through key leverage points. The responsibility for averting humanitarian and biodiversity crises is a shared global challenge (*36*, *100*), with solutions needed at all societal levels—including through local communities, engagement of the private sector, sound leadership and policy from regional and national governments, steady international support for conservation, and increased recognition of how historic and ongoing global and national inequalities have contributed to the current situation. Scientific data and evidence will continue to make a vital contribution, but it is crucial that this is done in an interdisciplinary context, with open communication channels to relevant government departments and third-sector organizations.

Decades of progress in biodiversity science and conservation

We now have a clearer and more detailed understanding than ever before of the past and present diversity and distribution of Madagascar's biodiversity and the threats it faces (*1*) (Fig. 1). The underlying data are the product of decades of research—with an increasing number of Malagasy biologists involved. This body of research and the evidence we have collated and presented here makes a clear case for Madagascar as one of the world's foremost conservation priorities.

Despite multiple competing demands on land, the Malagasy government, in collaboration with a broad group of conservation organizations and donors, has succeeded in designating 10.4% of the country as terrestrial PAs in a network that is largely representative of Madagascar's diverse biomes (Figs. 3 and 4). Most terrestrial and freshwater vertebrate species with known distributions have ranges that overlap with least one PA (94.7% of reptiles, 97.2% of amphibians, 98.1% of mammals, 98.9% of freshwater fishes, 100% of birds, and 97.1% for all groups combined) as do the majority of plants, although to a lesser extent (67.7%) (*9*). For threatened species with known distributions, the percentages are similar for vertebrates (94.3% of reptiles, 99.3% of amphibians, 97.7% of mammals, 100% of freshwater fishes, 100% of birds, and 97.7% for all groups combined) and markedly higher for plants (79.6%). Nonetheless, there are still many threatened species with ranges that do not overlap with the existing PA network, including one amphibian, three mammals, seven reptiles, and 559 plants (*9*) as well as many more that have not yet been assessed but may be threatened. The ranges of all birds overlapped with at least one PA; this was also true when we filtered the analysis to only include resident and breeding areas (*9*).

Since the loss of Madagascar's terrestrial megafauna (here defined as vertebrates larger than 10 kg), there have been few documented modern extinctions, but many species have

perilously reduced population sizes. The continued increase in new species descriptions suggests that there may be undocumented extinctions, especially in poorly studied taxa (*1*). Despite this, with limited resources and/or capacity, Madagascar has made important progress toward achieving international climate, biodiversity, and sustainable development goals, providing a foundation on which to build in the coming decades.

Success stories for individual species highlight how positive collaborative efforts can avert extinction. Examples include work on the Madagascar pochard (*Aythya innotata*) (*101*), which shows a 30% probability that extinction was prevented because of conservation action; the success story of the community-based protection of the tahina palm or dimaka (*Tahina spectabilis*), where local communities were involved in propagation and population reinforcement (*102*); and the work to prevent the extinction of the ploughshare tortoise (*Astrochelys yniphora*) through a captive breeding program (*103*).

Other notable successes have come from Madagascar's biodiversity conservation boom, which started in the 1980s and included a growth in the number of students pursuing university-level education in environmental sciences, biodiversity conservation and management, and related fields at both public and private universities. The result is an increasingly robust national capacity for the conservation and management of biodiversity that extends to international conservation organizations, which have been able to actively recruit Malagasy professionals to the highest administrative and executive positions. Going beyond this, the gap in scientific leadership that underpins conservation evidence is being incrementally filled by Malagasy biodiversity scientists. Researchers from outside Madagascar are increasingly collaborating with Malagasy researchers for mutual benefit. The requirement for international collaborators to provide financial and technical support for Malagasy researchers and their research infrastructure through collaboration protocols—set out in the national strategy for scientific research in Madagascar (*104*)—reinforces the importance of this.

As in many low-income countries, insufficient public funding means that the number of Malagasy professionals is still insufficient to serve the country's needs, there are relatively few PhD positions available to students, and those that are trained at higher levels often move away from academia and into the private sector. Access to up-to-date biodiversity data has also been a limiting factor (*15*). A further challenge is how to successfully engage multiple parts of society in conservation. Efforts that are genuinely socially integrated have been shown to produce more effective and resilient practices, policies, and decision-making, especially in the face of unstable environmental, political, and health situations (*105*). The Madagascar Fauna and Flora Group, the Lemur Conservation Foundation, the Durrell Wildlife Conservation Trust, The Peregrine Fund Madagascar, the Madagascar Biodiversity Center, and Madagasikara Voakajy, as well as the work of the Royal Botanic Gardens, Kew, and the Missouri Botanical Garden, are all examples of successful collaborations involving researchers, conservation partners, and local communities to protect biodiversity and empower local people.

The future of biodiversity in Madagascar

Meeting the Convention on Biological Diversity's Post-2020 Global Biodiversity Framework 2030 targets and milestones and achieving the 2050 goals (*106*) will be challenging—in Madagascar and globally. Evaluating successes and failures over previous decades and learning from these to prioritize effective conservation investment will be particularly important. To embrace diverse views and promote inclusivity in the identification of future directions, we discussed our results and current literature among our coauthors and consulted with Malagasy and external researchers, conservation leaders, and politicians to arrive at five main opportunities for the future, which we present here.

1) Investment in conservation and restoration must be based on evidence, effectiveness, and future challenges. Since the 1980s, billions of US dollars from international donors and conservation organizations, in cooperation with the Malagasy government, have been dedicated to protecting the country's biodiversity and creating today's network of PAs (*98*, *107*). However, the effectiveness of many interventions is poorly understood because impact evaluations are absent or lacking rigor. Evaluating the effectiveness of conservation activities is challenging, but it is the subject of increasingly sophisticated research efforts (*75*, *77*, *108*). Nevertheless, it is imperative that investments reinforce evidence-based and regularly evaluated interventions, requiring greater collaboration and co-design between local communities, regional and national authorities, researchers, the private sector, and other stakeholders. A particular opportunity is to frame these evaluations around community-based conservation interventions that address challenges faced by people and nature in unison. For example, nature-based solutions (*109*) for diversified, locally adapted, and sustainable agriculture can help address livelihood needs, whereas more efficient stoves can substantially decrease the demand on charcoal from native forests for cooking and heating and, further, may reduce the health hazards of smoke inhalation. Such initiatives increase food and energy security (*110*) while providing resilience to climate stochasticity (*111*). Similarly, coordinated, community-based fire management and awareness raising can be used to help mitigate risk to fire-sensitive forests. On-site management is especially important for fire mitigation, as shown by a study conducted during the COVID-19 pandemic (*112*). Fire management also presents the opportunity to mitigate the effect of exotic species by targeting the removal of flammable invasives (e.g., *Pinus*) and guide appropriate tree-planting initiatives to avoid fire-prone plantations near areas of particular biological importance. Such measures can improve the quality of grazing land for livestock while reducing carbon emissions from fire and helping to protect biodiverse habitats.

2) Expanded biodiversity monitoring is key to safeguarding Madagascar's most valuable natural assets. Existing biodiversity data are sufficient to characterize major conservation challenges and robustly support the orientation of conservation efforts in Madagascar. Calling for the collection of additional data risks delivering diminished returns on investment for conservation planning (*113*). Nevertheless, from collating the information for this Review, we acknowledge a clear need to address gaps in understudied ecosystems, taxa, and genetically distinct populations, noting that many newly described species are already threatened (*114*) and in need of immediate protection. Monitoring is also crucial for the detection of new non-native and potentially invasive species as well as for providing important data for the management of those that have already taken hold. Increasing connections with international trading partners without concurrent improvements in capacity for biosecurity increases Madagascar's vulnerability to such species (*115*), and strategies to monitor and mitigate these risks while delivering near-term benefits are needed.

Although there are initiatives that provide broad overviews of conservation effectiveness (*108*), many conservation interventions lack impact evaluations, in part because of a lack of robust, long-term monitoring data for biodiversity and social outcomes. The major gap is a lack of capacity for robust biodiversity monitoring. An example of the increasing value of data and coherency in conservation efforts is the development of the Madagascar Protected Areas website (*116*), which consolidates much of the information about Madagascar's extensive network of PAs. But as with many initiatives, the key is in long-term financing and maintenance of these portals and in ensuring that data flow freely and openly to similar, global initiatives like Protected Planet (*72*).

Biological monitoring needs to be based on consistent, repeatable methodologies with shared data. This information provides the

science-based evidence needed to leverage international funding and government policy support. Monitoring is one area where new technologies will play a key role, such as through the increasing availability of near-real-time satellite images and small and cost-effective unmanned aerial vehicles, which can increase visual access to remote areas (*117*). Similarly, DNA-based biodiversity surveys, including environmental sampling, can greatly improve the speed of site inventories and the identification of unknown and understudied taxa. Advances in monitoring must be delivered with improved and centralized management. This should include open-source and transdisciplinary data on biodiversity, social and conservation governance, and performance. These data should be in formats that are accessible and useful to practitioners, identify relevant baselines, and support evidence-based decisions for conservation and restoration.

3) Improving the effectiveness of existing PAs is more important than creating new ones. Madagascar has an extensive, evidence-based, and highly representative network of terrestrial PAs (Figs. 3 and 4). Madagascar's existing PAs already include at least partial ranges of a substantial proportion of Malagasy taxa, including most Malagasy EDGE species. Focusing on improving their quality and effectiveness will likely lead to positive biodiversity outcomes (*118*), further increasing the already measurable effect that PAs have had on biodiversity. By strengthening PAs, biodiversity can be conserved across ecosystem, species, and genetic levels, all of which are integral in long-term conservation, as discussed above. Investment in restoration of degraded areas within and beyond the existing network (see opportunity 4 below) will provide multiple benefits for biodiversity and people. This could help increase the resilience of habitats to future drivers of biodiversity loss, including climate change, while increasing potential ranges of many species in parallel. Demonstrating the benefits of strengthened PAs to people is a likely prerequisite for societal support to maintain and improve upon the existing network while mitigating the risk of future downgrading, downsizing, or degazettement (legal removal of conservation status) (*119*). Financial benefits that come with strengthened PAs must be distributed appropriately and equitably within the country's political and social contexts, with the full inclusion of local communities at all stages (*118*, *120*).

4) Conservation and restoration should not focus solely on the PA network. Madagascar's PAs are islands of natural capital in a landscape of degraded natural resources (*121*) and therefore provide vital resources for communities living adjacent to them. Traditional fortress conservation—seeking to protect areas by limiting access—is therefore both undesirable and unlikely to be effective. To further reduce the detrimental human impacts that exist in all PAs (*98*) (table S8) (*9*), we argue for strategies to enhance the natural capital of the surrounding landscapes, to reduce pressure on PAs as providers of basic resources, and to increase buffer zones for the species that live in and around them. This could include increasing ecosystem provision, such as productive soils, food, fibers, and other materials and services such as water flow regulation and carbon capture. Such measures would serve to address some of the largest threats to species, including the expansion of agriculture and overexploitation (Fig. 2).

In particular, ecological restoration could benefit people and biodiversity, particularly when targeted to the 89.6% of the country that is not protected. It offers potential to provide new livelihood opportunities that are far from, and independent of, the resources within PAs, further reducing pressure on the system (*122*). Notably, restoration should not only target those ecosystems that traditionally receive the most conservation attention because they hold the greatest biodiversity, for example forests. Other vegetation types, such as grasslands, where most agriculture takes place, are equally vital. Restoration should be carried out following best practice and in places where people will benefit most—not necessarily only adjacent to PAs. Further, restoration should include maximizing biodiversity recovery to meet multiple goals, using resilient species, and working together with local communities (*49*, *123*).

For the species and their inherent genetic diversity not covered by the PA network, particularly those that are challenging to conserve, such as freshwater fishes and palms, ex situ conservation in zoological and botanical gardens is a vital tool to support conservation and restoration. For plants, efforts should especially focus on the 32.3% of plant species that fall outside of the PA network and the species that have cultural or economic value for people (e.g., crop wild relatives). Promoting biobanking for animals and intensifying it for seeds, spores, and fungi will not only support conservation but also contribute material and knowledge to restoration and research (*87*).

5) Conservation actions must address the root causes of biodiversity loss. Our analysis shows that the most frequently listed threats to Madagascar's biodiversity come from overexploitation and agriculture, predominantly a result of forest loss and potentially tied to increases in small-scale anthropogenic fire in forests (Fig. 4, A and B) [see also (*43*)], which significantly affects humid forest areas in the east and dry forest and spiny forest in the west (Fig. 4, C and D). This trend is likely to continue unless the root causes of this forest loss are addressed. Conservationists and their funders must recognize that food, social security, health, and well-being are the utmost priorities for rural communities and that PAs will always be vulnerable when surrounded by impoverished people living in landscapes with eroded natural capital (*124*). Politicians and economists must recognize that sustainable and equitable development in Madagascar is inextricably linked to, and dependent on, the maintenance of ecosystem function and the goods and services they provide. Initiatives that address these issues by working with local communities to identify tailored solutions in health, education, and green entrepreneurship are increasingly successful and should be expanded, but they generally lack data and evidence from monitoring (see opportunity 2). Promising approaches include voluntary savings and loans; inclusive, sustainable agricultural development schemes that promote stable land ownership and build—rather than destroy—natural capital and the ecosystem services it provides; implementation of conservation interventions, including research and monitoring; and PA management that maximizes local employment (*98*, *123*). Such efforts will facilitate improved livelihoods for many while reducing pressure on the PAs themselves, bringing tangible benefits to communities, and contributing to sustainable management (*98*, *125*).

Conclusions

The alarming status of Madagascar's biodiversity is the result of multifaceted, unsustainable practices that include historic and contemporary exploitation. In the eyes of much of the world, Madagascar's biodiversity is a unique global asset that needs saving; in the daily lives of many of the Malagasy people, it is a rapidly diminishing source of the most basic needs for subsistence. Achieving a sustainable future that benefits people and biodiversity is possible by building on and expanding integrated, inclusive conservation efforts. Biodiversity is the greatest opportunity and the most valuable asset for Madagascar's future development.

REFERENCES AND NOTES

1. A. Antonelli *et al*., Madagascar's extraordinary biodiversity: Evolution, distribution, and use. *Science* **378**, eabf0869 (2022). doi: 10.1126/science.abf0869
2. T. Andermann, S. Faurby, S. T. Turvey, A. Antonelli, D. Silvestro, The past and future human impact on mammalian diversity. *Sci. Adv.* **6**, eabb2313 (2020). doi: 10.1126/sciadv.abb2313; pmid: 32917612
3. IUCN, The IUCN Red List of Threatened Species, version 2021-1 (2021); https://www.iucnredlist.org.
4. IUCN, *IUCN Red List Categories and Criteria: Version 3.1, Second Edition* (Gland, 2012).
5. E. Beech *et al*., *The Red List of Trees of Madagascar* (Botanic Gardens Conservation International, 2021).
6. S. M. Goodman, W. L. Jungers, *Les Animaux et Ecosystèmes de l'Holocene Disparus de Madagascar* (Association Vahatra, 2013).
7. F. Sayol, M. J. Steinbauer, T. M. Blackburn, A. Antonelli, S. Faurby, Anthropogenic extinctions conceal widespread

evolution of flightlessness in birds. *Sci. Adv.* **6**, eabb6095 (2020). doi: 10.1126/sciadv.abb6095; pmid: 33268368
8. Y. Malhi *et al*., Megafauna and ecosystem function from the Pleistocene to the Anthropocene. *Proc. Natl. Acad. Sci. U.S.A.* **113**, 838–846 (2016). doi: 10.1073/pnas.1502540113; pmid: 26811442
9. Materials and methods and supplementary text are available as supplementary materials.
10. Botanic Gardens Conservation International, PlantSearch online database (2021); https://tools.bgci.org/plant_search.php.
11. Zoological Society of London, EDGE of Existence; https://www.edgeofexistence.org/.
12. N. J. B. Isaac, S. T. Turvey, B. Collen, C. Waterman, J. E. M. Baillie, Mammals on the EDGE: Conservation priorities based on threat and phylogeny. *PLOS ONE* **2**, e296 (2007). doi: 10.1371/journal.pone.0000296; pmid: 17375184
13. Zoological Society of London, EDGE of Existence: Explore EDGE species by country (2021); https://www.edgeofexistence.org/explore-edge-species-country/.
14. A. Rakotoarison *et al*., Describing the smaller majority: Integrative taxonomy reveals twenty-six new species of tiny microhylid frogs (genus *Stumpffia*) from Madagascar. *Vertebr. Zool.* **67**, 271–398 (2017).
15. M. S. Vorontsova *et al*., Inequality in plant diversity knowledge and unrecorded plant extinctions: An example from the grasses of Madagascar. *Plants People Planet* **3**, 45–60 (2021). doi: 10.1002/ppp3.10123
16. J. P. Benstead *et al*., Conserving Madagascar's Freshwater Biodiversity. *Bioscience* **53**, 1101–1111 (2003). doi: 10.1641/0006-3568(2003)053[1101:CMFB]2.0.CO;2
17. R. D. E. MacPhee, D. A. Burney, N. A. Wells, Early Holocene Chronology and environment of Ampasambazimb, a Malagasy subfossil lemur site. *Int. J. Primatol.* **6**, 463–489 (1985). doi: 10.1007/BF02735571
18. S. Faurby, W. L. Eiserhardt, J.-C. Svenning, Strong effects of variation in taxonomic opinion on diversification analyses. *Methods Ecol. Evol.* **7**, 4–13 (2016). doi: 10.1111/2041-210X.12449
19. IUCN, The IUCN Red List of Threatened Species, version 2020-3 (2020); https://www.iucnredlist.org.
20. A. Zizka, T. Andermann, D. Silvestro, *IUCNN* – Deep learning approaches to approximate species' extinction risk. *Divers. Distrib.* **28**, 227–241 (2021). doi: 10.1111/ddi.13450
21. P. de Villemereuil *et al*., Little adaptive potential in a threatened passerine bird. *Curr. Biol.* **29**, 889–894.e3 (2019). doi: 10.1016/j.cub.2019.01.072; pmid: 30799244
22. R. Lande, Genetics and demography in biological conservation. *Science* **241**, 1455–1460 (1988). doi: 10.1126/science.3420403; pmid: 3420403
23. M. C. Rivers, N. A. Brummitt, E. Nic Lughadha, T. R. Meagher, Do species conservation assessments capture genetic diversity? *Glob. Ecol. Conserv.* **2**, 81–87 (2014). doi: 10.1016/j.gecco.2014.08.005
24. B. Charlesworth, D. Charlesworth, The genetic basis of inbreeding depression. *Genet. Res.* **74**, 329–340 (1999). doi: 10.1017/S0016672399004152; pmid: 10689809
25. A. J. Helmstetter *et al*., The demographic history of Madagascan micro-endemics: Have rare species always been rare? *Proc. R. Soc. B* **288**, 20210957 (2021). doi: 10.1098/rspb.2021.0957; pmid: 34547905
26. E. Quéméré, X. Amelot, J. Pierson, B. Crouau-Roy, L. Chikhi, Genetic data suggest a natural prehuman origin of open habitats in northern Madagascar and question the deforestation narrative in this region. *Proc. Natl. Acad. Sci. U.S.A.* **109**, 13028–13033 (2012). doi: 10.1073/pnas.1200153109; pmid: 22826244
27. L. M. Gardiner, M. Rakotoarinivo, L. R. Rajaovelona, C. Clubbe, Population genetics data help to guide the conservation of palm species with small population sizes and fragmented habitats in Madagascar. *PeerJ* **5**, e3248 (2017). doi: 10.7717/peerj.3248; pmid: 28480141
28. G. L. Olivieri, V. Sousa, L. Chikhi, U. Radespiel, From genetic diversity and structure to conservation: Genetic signature of recent population declines in three mouse lemur species (*Microcebus* spp.). *Biol. Conserv.* **141**, 1257–1271 (2008). doi: 10.1016/j.biocon.2008.02.025
29. R. C. Williams *et al*., Conservation genomic analysis reveals ancient introgression and declining levels of genetic diversity in Madagascar's hibernating dwarf lemurs. *Heredity* **124**, 236–251 (2020). doi: 10.1038/s41437-019-0260-9; pmid: 31435007
30. A. Shapcott *et al*., Can we bring Madagascar's critically endangered palms back from the brink? Genetics, ecology and conservation of the critically endangered palm *Beccariophoenix madagascariensis*. *Bot. J. Linn. Soc.* **154**, 589–608 (2007). doi: 10.1111/j.1095-8339.2007.00676.x
31. P. A. Hagl *et al*., Geographical structure of genetic diversity in *Loudetia simplex* (Poaceae) in Madagascar and South Africa. *Bot. J. Linn. Soc.* **196**, 81–99 (2020). doi: 10.1093/botlinnean/boaa098
32. T. van der Valk, D. Díez-Del-Molino, T. Marques-Bonet, K. Guschanski, L. Dalén, Historical genomes reveal the genomic consequences of recent population decline in eastern gorillas. *Curr. Biol.* **29**, 165–170.e6 (2019). doi: 10.1016/j.cub.2018.11.055; pmid: 30595519
33. C. R. Peart *et al*., Determinants of genetic variation across eco-evolutionary scales in pinnipeds. *Nat. Ecol. Evol.* **4**, 1095–1104 (2020). doi: 10.1038/s41559-020-1215-5; pmid: 32514167
34. A. Crottini, P. Orozco-terWengel, F. C. E. Rabemananjara, J. S. Hauswaldt, M. Vences, Mitochondrial introgression, color pattern variation, and severe demographic bottlenecks in three species of malagasy poison frogs, genus *Mantella*. *Genes* **10**, 317 (2019). doi: 10.3390/genes10040317; pmid: 31018611
35. M. Craul *et al*., Influence of forest fragmentation on an endangered large-bodied lemur in northwestern Madagascar. *Biol. Conserv.* **142**, 2862–2871 (2009). doi: 10.1016/j.biocon.2009.05.026
36. S. Díaz *et al*., "Summary for policymakers of the global assessment report on biodiversity and ecosystem services of the Intergovernmental Science-Policy Platform on Biodiversity and Ecosystem Services" (IPBES, 2019).
37. IUCN, Threats Classification Scheme, version 3.2 (2022); https://www.iucnredlist.org/resources/threat-classification-scheme.
38. G. Vieilledent *et al*., Combining global tree cover loss data with historical national forest cover maps to look at six decades of deforestation and forest fragmentation in Madagascar. *Biol. Conserv.* **222**, 189–197 (2018). doi: 10.1016/j.biocon.2018.04.008
39. GFW, Global Forest Watch - Madagascar (2021); https://gfw.global/3uplmN5.
40. S. L. Maxwell, R. A. Fuller, T. M. Brooks, J. E. M. Watson, Biodiversity: The ravages of guns, nets and bulldozers. *Nature* **536**, 143–145 (2016). doi: 10.1038/536143a; pmid: 27510207
41. G. Vieilledent *et al*., It's not just poverty: Unregulated global market and bad governance explain unceasing deforestation in Western Madagascar. bioRxiv 2020.07.30.229104 [Preprint] (2020). https://doi.org/10.1101/2020.07.30.229104.
42. D. A. Martin *et al*., Land-use trajectories for sustainable land system transformations: Identifying leverage points in a global biodiversity hotspot. *Proc. Natl. Acad. Sci. U.S.A.* **119**, e2107747119 (2022). doi: 10.1073/pnas.2107747119; pmid: 35165148
43. L. N. Phelps *et al*., Madagascar's fire regimes challenge global assumptions about landscape degradation. *Glob. Change Biol.* **28**, 6944–6960 (2022). doi: 10.1111/gcb.16206; pmid: 35582991
44. C. A. Kull *et al*., The introduced flora of Madagascar. *Biol. Invasions* **14**, 875–888 (2012). doi: 10.1007/s10530-011-0124-6
45. R. Baohanta *et al*., Restoring native forest ecosystems after exotic tree plantation in Madagascar: Combination of the local ectotrophic species *Leptolena bojeriana* and *Uapaca bojeri* mitigates the negative influence of the exotic species *Eucalyptus camaldulensis* and *Pinus patula*. *Biol. Invasions* **14**, 2407–2421 (2012). doi: 10.1007/s10530-012-0238-5
46. A. Lehavana, "Distribution, ecological and economic impacts and competition of the invasive alien aquatic weeds (*Pontederia crassipes* Mart., *Pistia stratiotes* L., *Salvinia molesta* D.S. Mitch. and *Azolla filiculoides* Lam.) in Madagascar," thesis, Rhodes University, South Africa (2020).
47. A. Ghulam, I. Porton, K. Freeman, Detecting subcanopy invasive plant species in tropical rainforest by integrating optical and microwave (InSAR/PolInSAR) remote sensing data, and a decision tree algorithm. *ISPRS J. Photogramm. Remote Sens.* **88**, 174–192 (2014). doi: 10.1016/j.isprsjprs.2013.12.007
48. A. Gérard, J. U. Ganzhorn, C. A. Kull, S. M. Carrière, Possible roles of introduced plants for native vertebrate conservation: The case of Madagascar. *Restor. Ecol.* **23**, 768–775 (2015). doi: 10.1111/rec.12246
49. A. Di Sacco *et al*., Ten golden rules for reforestation to optimize carbon sequestration, biodiversity recovery and livelihood benefits. *Glob. Change Biol.* **27**, 1328–1348 (2021). doi: 10.1111/gcb.15498; pmid: 33494123
50. C. M. M. DeSisto *et al*., An invasive species spread by threatened diurnal lemurs impacts rainforest structure in Madagascar. *Biol. Invasions* **22**, 2845–2858 (2020). doi: 10.1007/s10530-020-02293-7
51. S. M. Goodman, V. Soarimalala, in *The New Natural History of Madagascar*, S. M. Goodman, Ed. (Princeton Univ. Press, 2022), pp. 1737–1769.
52. J. P. Benstead, M. L. J. Stiassny, P. N. Loiselle, K. J. Riseng, N. Raminosoa, in *Global Perspectives on River Conservation: Science, Policy, and Practice*, P. J. Boon, B. R. Davies, G. E. Petts, Eds. (Wiley, 2000), pp. 205–231.
53. P. N. Reinthal, M. L. J. Stiassny, The freshwater fishes of Madagascar: A study of an endangered fauna with recommendations for a conservation strategy. *Conserv. Biol.* **5**, 231–243 (1991). doi: 10.1111/j.1523-1739.1991.tb00128.x
54. B. M. Marshall *et al*., Widespread vulnerability of Malagasy predators to the toxins of an introduced toad. *Curr. Biol.* **28**, R654–R655 (2018). doi: 10.1016/j.cub.2018.04.024; pmid: 29870701
55. M. C. Bletz *et al*., Widespread presence of the pathogenic fungus *Batrachochytrium dendrobatidis* in wild amphibian communities in Madagascar. *Sci. Rep.* **5**, 8633 (2015). doi: 10.1038/srep08633; pmid: 25719857
56. J. L. Brown, A. D. Yoder, Shifting ranges and conservation challenges for lemurs in the face of climate change. *Ecol. Evol.* **5**, 1131–1142 (2015). doi: 10.1002/ece3.1418; pmid: 25859320
57. J. C. Ingram, T. P. Dawson, Climate change impacts and vegetation response on the island of Madagascar. *Phil. Trans. R. Soc. A* **363**, 55–59 (2005). doi: 10.1098/rsta.2004.1476; pmid: 15598621
58. J.-N. Wan *et al*., Modeling impacts of climate change on the potential distribution of six endemic baobab species in Madagascar. *Plant Divers.* **43**, 117–124 (2020). doi: 10.1016/j.pld.2020.07.001; pmid: 33997544
59. S. R. Weiskopf, J. A. Cushing, T. L. Morelli, B. J. E. Myers, Climate change risks and adaptation options for Madagascar. *Ecol. Soc.* **26**, 36 (2021). doi: 10.5751/ES-12816-260436
60. J. Busch *et al*., Climate change and the cost of conserving species in Madagascar. *Conserv. Biol.* **26**, 408–419 (2012). doi: 10.1111/j.1523-1739.2012.01838.x; pmid: 22497442
61. G. Chomicki, M. Weber, A. Antonelli, J. Bascompte, E. T. Kiers, The impact of mutualisms on species richness. *Trends Ecol. Evol.* **34**, 698–711 (2019). doi: 10.1016/j.tree.2019.03.003; pmid: 31003875
62. L. P. Koh *et al*., Species coextinctions and the biodiversity crisis. *Science* **305**, 1632–1634 (2004). doi: 10.1126/science.1101101; pmid: 15361627
63. M. L. Moir *et al*., Current constraints and future directions in estimating coextinction. *Conserv. Biol.* **24**, 682–690 (2010). doi: 10.1111/j.1523-1739.2009.01398.x; pmid: 20067486
64. R. K. Colwell, R. R. Dunn, N. C. Harris, Coextinction and persistence of dependent species in a changing world. *Annu. Rev. Ecol. Evol. Syst.* **43**, 183–203 (2012). doi: 10.1146/annurev-ecolsys-110411-160304
65. D. M. Hansen, M. Galetti, Ecology. The forgotten megafauna. *Science* **324**, 42–43 (2009). doi: 10.1126/science.1172393; pmid: 19342573
66. C. A. Kull, in *Conservation and Environmental Management in Madagascar*, I. R. Scales, Ed. (Routledge, 2014), pp. 146–171.
67. C. J. Gardner *et al*., The rapid expansion of Madagascar's protected area system. *Biol. Conserv.* **220**, 29–36 (2018). doi: 10.1016/j.biocon.2018.02.011
68. J. P. G. Jones, O. S. Rakotonarivo, J. H. Razafimanahaka, in *The New Natural History of Madagascar*, S. M. Goodman, Ed. (Princeton Univ. Press, 2022), pp. 2130–2140.
69. S. M. Goodman, H. M. Rakotondratsimba, J. C. Ranivo Rakotoson, in *The New Natural History of Madagascar*, S. M. Goodman, Ed. (Princeton Univ. Press, 2022), pp. 2091–2107.
70. M. Virah-Sawmy, C. J. Gardner, A. N. Ratsifandrihamanana, in *Conservation and Environmental Management in Madagascar*, I. R. Scales, Ed. (Routledge, 2014), pp. 216–252.
71. S. M. Goodman, M. J. Raherilalao, S. Wohlhauser, *The Terrestrial Protected Areas of Madagascar: Their History, Description, and Biota* (Association Vahatra, 2018).
72. Protected Planet, The World Database on Protected Areas (2020); https://www.protectedplanet.net/en/thematic-areas/wdpa?tab=WDPA.
73. Key Biodiversity Areas Partnership, World Database of Key Biodiversity Areas (2021); https://www.keybiodiversityareas.org/kba-data/request.

74. P. Kullberg, E. Di Minin, A. Moilanen, Using key biodiversity areas to guide effective expansion of the global protected area network. *Glob. Ecol. Conserv.* **20**, e00768 (2019). doi: 10.1016/j.gecco.2019.e00768
75. J. Geldmann, A. Manica, N. D. Burgess, L. Coad, A. Balmford, A global-level assessment of the effectiveness of protected areas at resisting anthropogenic pressures. *Proc. Natl. Acad. Sci. U.S.A.* **116**, 23209–23215 (2019). doi: 10.1073/pnas.1908221116; pmid: 31659036
76. J. Eklund, L. Coad, J. Geldmann, M. Cabeza, What constitutes a useful measure of protected area effectiveness? A case study of management inputs and protected area impacts in Madagascar. *Conserv. Sci. Pract.* **1**, e107 (2019). doi: 10.1111/csp2.107
77. J. Eklund *et al*., Contrasting spatial and temporal trends of protected area effectiveness in mitigating deforestation in Madagascar. *Biol. Conserv.* **203**, 290–297 (2016). doi: 10.1016/j.biocon.2016.09.033
78. Protected Planet, Management effectiveness (PAME) (2022); https://www.protectedplanet.net/en/thematic-areas/protected-areas-management-effectiveness-pame?tab=METT.
79. Species 360, Zoological Information Management Software (2021); https://zims.species360.org.
80. A. Miralles, M. Raymond, G. Lecointre, Empathy and compassion toward other species decrease with evolutionary divergence time. *Sci. Rep.* **9**, 19555 (2019). doi: 10.1038/s41598-019-56006-9; pmid: 31862944
81. J. R. Ali, M. Huber, Mammalian biodiversity on Madagascar controlled by ocean currents. *Nature* **463**, 653–656 (2010). doi: 10.1038/nature08706; pmid: 20090678
82. R. A. Griffiths, L. Pavajeau, Captive breeding, reintroduction, and the conservation of amphibians. *Conserv. Biol.* **22**, 852–861 (2008). doi: 10.1111/j.1523-1739.2008.00967.x; pmid: 18616746
83. T. Ziegler *et al*., Keeping and breeding of threatened endemic Malagasy freshwater fishes at Cologne Zoo (Germany): A contribution towards the advancement of a conservation breeding network. *Der Zoologische Garten* **88**, 123–155 (2020).
84. L. Leiss *et al*., Review of threatened Malagasy freshwater fishes in zoos and aquaria: The necessity of an ex situ conservation network—A call for action. *Zoo Biol.* **41**, 244–262 (2022). doi: 10.1002/zoo.21661; pmid: 34870879
85. P. V. Loiselle, in *The Natural History of Madagascar*, S. M. Goodman, J. P. Benstead, Eds. (Univ. Chicago Press, 2003), pp. 1569–1574.
86. K. Traylor-Holzer, K. Leus, O. Byers, in *The Ark and Beyond: The Evolution of Zoo and Aquarium Conservation*, B. A. Minteer, J. Maienschein, J. P. Collins, Eds. (Univ. Chicago Press, 2018), pp. 129–141.
87. A. Britt, B. R. Iambana, C. R. Welch, A. S. Katz, in *The Natural History of Madagascar*, S. M. Goodman, J. Benstead, Eds. (Univ. Chicago Press, 2003), pp. 1547–1552.
88. Secretariat of the Convention on Biological Diversity, Global Biodiversity Outlook 5 (2020); https://www.cbd.int/gbo5.
89. M. D. Barnes, L. Glew, C. Wyborn, I. D. Craigie, Prevent perverse outcomes from global protected area policy. *Nat. Ecol. Evol.* **2**, 759–762 (2018). doi: 10.1038/s41559-018-0501-y; pmid: 29556080
90. R. L. Pressey *et al*., The mismeasure of conservation. *Trends Ecol. Evol.* **36**, 808–821 (2021). doi: 10.1016/j.tree.2021.06.008; pmid: 34303527
91. Critical Ecosystem Partnership Fund, Indian House Crow Eradication and Invasive Species Surveillance in Madagascar (2021); https://www.cepf.net/grants/grantee-projects/indian-house-crow-eradication-and-invasive-species-surveillance-madagascar.
92. INSTAT, instat Madagascar (2022); https://www.instat.mg/.
93. J. P. G. Jones *et al*., Madagascar: Crime threatens biodiversity. *Science* **363**, 825–825 (2019). doi: 10.1126/science.aaw6402; pmid: 30792294
94. J. P. G. Jones *et al*., Last chance for Madagascar's biodiversity. *Nat. Sustain.* **2**, 350–352 (2019). doi: 10.1038/s41893-019-0288-0
95. United Nations World Food Programme, "Southern Madagascar faces drought-driven hunger, threatening millions" (2020); https://www.wfp.org/news/southern-madagascar-faces-drought-driven-hunger-threatening-millions.
96. S. E. Vollset *et al*., Fertility, mortality, migration, and population scenarios for 195 countries and territories from 2017 to 2100: A forecasting analysis for the Global Burden of Disease Study. *Lancet* **396**, 1285–1306 (2020). doi: 10.1016/S0140-6736(20)30677-2; pmid: 32679112
97. T. T. Gatiso *et al*., Effectiveness of protected areas influenced by socio-economic context. *Nat. Sustain.* **5**, 861–868 (2022). doi: 10.1038/s41893-022-00932-6
98. World Bank, "Madagascar—Third Environment Program Support Project. Independent Evaluation Group, Project Performance Assessment Report 158221" (World Bank, 2021).
99. I. R. Scales, The future of conservation and development in Madagascar: Time for a new paradigm? *Madag. Conserv. Dev.* **9**, 5–12 (2014). doi: 10.4314/mcd.v9i1.2
100. S. Díaz *et al*., Pervasive human-driven decline of life on Earth points to the need for transformative change. *Science* **366**, eaax3100 (2019). doi: 10.1126/science.aax3100; pmid: 31831642
101. F. C. Bolam *et al*., How many bird and mammal extinctions has recent conservation action prevented? *Conserv. Lett.* **14**, e12762 (2021). doi: 10.1111/conl.12762
102. L. M. Gardiner, D. Rabehevitra, R. Letsara, A. Shapcott, *Tahina spectabilis*: An exciting new discovery in Madagascar ten years on. *Palms* **61**, 69–82 (2017).
103. Durrell Wildlife Conservation Trust, Durrell Index: Ploughshare Tortoise (2022); https://www.durrell.org/conservation/species/ploughshare-tortoise/.
104. Ministere de l'Enseignement Supérieur et de la Recherche Scientifique, "La Stratégie Nationale de la Recherche Scientifique à Madagascar" (2013); http://www.recherches.gov.mg/IMG/pdf/strategie_nationale_de_la_recherche.pdf.
105. E. Razanatsoa *et al*., Fostering local involvement for biodiversity conservation in tropical regions: Lessons from Madagascar during the COVID-19 pandemic. *Biotropica* **53**, 994–1003 (2021). doi: 10.1111/btp.12967; pmid: 34219750
106. Convention on Biological Diversity, "First draft of the post-2020 global biodiversity framework" (UN Environment Programme, 2020); https://www.cbd.int/doc/c/abb5/591f/2e46096d3f0330b08ce87a45/wg2020-03-03-en.pdf.
107. P. O. Waeber, L. Wilmé, J.-R. Mercier, C. Camara, P. P. Lowry II, How effective have thirty years of internationally driven conservation and development efforts been in Madagascar? *PLOS ONE* **11**, e0161115 (2016). doi: 10.1371/journal.pone.0161115; pmid: 27532499
108. J. Börner, D. Schulz, S. Wunder, A. Pfaff, The effectiveness of forest conservation policies and programs. *Annu. Rev. Resour. Econ.* **12**, 45–64 (2020). doi: 10.1146/annurev-resource-110119-025703
109. N. Seddon *et al*., Getting the message right on nature-based solutions to climate change. *Glob. Change Biol.* **27**, 1518–1546 (2021). doi: 10.1111/gcb.15513; pmid: 33522071
110. O. M. Grace *et al*., Plant Power: Opportunities and challenges for meeting sustainable energy needs from the plant and fungal kingdoms. *Plants People Planet* **2**, 446–462 (2020). doi: 10.1002/ppp3.10147
111. C. Funk *et al*., Warming of the Indian Ocean threatens eastern and southern African food security but could be mitigated by agricultural development. *Proc. Natl. Acad. Sci. U.S.A.* **105**, 11081–11086 (2008). doi: 10.1073/pnas.0708196105; pmid: 18685101
112. J. Eklund *et al*., Elevated fires during COVID-19 lockdown and the vulnerability of protected areas. *Nat. Sustain.* **5**, 603–609 (2022). doi: 10.1038/s41893-022-00884-x
113. H. S. Grantham *et al*., Diminishing return on investment for biodiversity data in conservation planning. *Conserv. Lett.* **1**, 190–198 (2008). doi: 10.1111/j.1755-263X.2008.00029.x
114. J. Liu, F. Slik, S. Zheng, D. B. Lindenmayer, Undescribed species have higher extinction risk than known species. *Conserv. Lett.* **15**, 12876 (2022). doi: 10.1111/conl.12876
115. IUCN, Motion 116 - Building Madagascar's capacity to counter the threat from invasive species (2020); https://www.iucncongress2020.org/motion/116.
116. Madagascar Protected Areas, Protected Areas of Madagascar (2022); https://protectedareas.mg/.
117. L. P. Koh, S. A. Wich, Dawn of drone ecology: Low-cost autonomous aerial vehicles for conservation. *Trop. Conserv. Sci.* **5**, 121–132 (2012). doi: 10.1177/194008291200500202
118. S. L. Maxwell *et al*., Area-based conservation in the twenty-first century. *Nature* **586**, 217–227 (2020). doi: 10.1038/s41586-020-2773-z; pmid: 33028996
119. R. E. Golden Kroner *et al*., The uncertain future of protected lands and waters. *Science* **364**, 881–886 (2019). doi: 10.1126/science.aau5525; pmid: 31147519
120. I. J. Bateman, G. M. Mace, The natural capital framework for sustainably efficient and equitable decision making. *Nat. Sustain.* **3**, 776–783 (2020). doi: 10.1038/s41893-020-0552-3
121. C. Birkinshaw, P. P. Lowry II, J. Raharimampionona, J. Aronson, Supporting Target 4 of the Global Strategy for Plant Conservation by integrating ecological restoration into Missouri Botanical Garden's conservation program in Madagascar. *Ann. Mo. Bot. Gard.* **99**, 139–146 (2013). doi: 10.3417/2012002
122. J. Aronson, A. F. Clewell, J. N. Blignaut, S. J. Milton, Ecological restoration: A new frontier for nature conservation and economics. *J. Nat. Conserv.* **14**, 135–139 (2006). doi: 10.1016/j.jnc.2006.05.005
123. L. Robson, "The history of PHE in Madagascar: Looking back over the last 25 years and forward to the next chapter" (Blue Ventures for the Madagascar PHE Network, 2014); https://phemadagascar.org/wp-content/uploads/2014/10/History-of-PHE-in-Madagascar-Robson-2014.pdf.
124. S. Naeem, R. Chazdon, J. E. Duffy, C. Prager, B. Worm, Biodiversity and human well-being: An essential link for sustainable development. *Proc. R. Soc. B* **283**, 20162091 (2016). doi: 10.1098/rspb.2016.2091; pmid: 27928039
125. M. Poudyal *et al*., Who bears the cost of forest conservation? *PeerJ* **6**, e5106 (2018). doi: 10.7717/peerj.5106; pmid: 30002962
126. S. Faurby *et al*., PHYLACINE 1.2: The Phylogenetic Atlas of Mammal Macroecology. *Ecology* **99**, 2626 (2018). doi: 10.1002/ecy.2443; pmid: 29989146
127. N. Dudley, Ed., "Guidelines for applying protected area management categories including IUCN WCPA best practice guidance on recognising protected areas and assigning management categories and governance types" (IUCN, Gland, 2013).
128. C. Amante, B. W. Eakins, "ETOPO1 1 Arc-minute global relief model: Procedures, data sources and analysis" (National Oceanic and Atmospheric Administration, NOAA Technical Memorandum NESDIS NGDC-24, 2009); https://www.ngdc.noaa.gov/mgg/global/relief/ETOPO1/docs/ETOPO1.pdf.
129. UNEP-WCMC, WorldFish Centre, WRI, TNC, "Global distribution of warm-water coral reefs, compiled from multiple sources including the Millennium Coral Reef Mapping Project," version 4.1 (2021); https://doi.org/10.34892/t2wk-5t34.
130. Center for International Earth Science Information Network (CIESIN), Columbia University, "Gridded Population of the World, Version 4 (GPWv4): Population Density, Revision 11" (NASA Socioeconomic Data and Applications Center, 2018); https://doi.org/10.7927/H49C6VHW.
131. L. Giglio, C. Justice, L. Boschetti, D. Roy, MCD64A1 MODIS/Terra+Aqua Burned Area Monthly L3 Global 500m SIN Grid V006, data set (NASA EOSDIS Land Processes DAAC, 2015); https://doi.org/10.5067/MODIS/MCD64A1.006.
132. G. J. Huffman *et al*., The TRMM Multisatellite Precipitation Analysis (TMPA): Quasi-Global, Multiyear, Combined-Sensor Precipitation Estimates at Fine Scales. *J. Hydrometeorol.* **8**, 38–55 (2007). doi: 10.1175/JHM560.1
133. G. Vieilledent *et al*., Output data from: Combining global tree cover loss data with historical national forest-cover maps to look at six decades of deforestation and forest fragmentation in Madagascar, V2, CIRAD Dataverse (2018); https://doi.org/10.18167/DVN1/AUBRRC.
134. J. Moat, P. Smith, *Atlas of the Vegetation of Madagascar (Atlas de la Végétation de Madagascar)* (Royal Botanic Gardens, Kew, 2007).

ACKNOWLEDGMENTS

C. Cowell (RBG Kew) provided information on Management Effectiveness Tracking Tool assessments and monitoring and K. Freeman (Madagascar Fauna and Flora Group) provided information on invasive vertebrates. A. Rauhaus (Cologne Zoo) as well as J. Kamphausen and L. Leiss (both of the University of Cologne) supported the zoo database analyses. I. Voet illustrated the graphical abstract. J. P. G. Jones (Bangor University) contributed to discussions that shaped and improved the analyses and text. We thank J. Aronson (Missouri Botanical Garden), D. Ashley (UK Ambassador to Madagascar and Comoros), A. Lehavana (Missouri Botanical Garden), J. Ratsimbazafy (Houston Zoo and the Groupe d'Etude et de Recherche sur les Primates de Madagascar), S. Ratsirahonana (Fondation pour les Aires Protégées et la Biodiversité de Madagascar), and G. E. Schatz (Missouri Botanical Garden) for their insightful feedback on the first full draft of the manuscript as well as three anonymous reviewers for valuable feedback. We stress that all views expressed in this article are only those of the authors. **Funding:** A.A. acknowledges financial support from the Swedish Research Council (2019-05191), the Swedish Foundation for Strategic Research (FFL15-0196), and a grant from the Kew Foundation. T.A. was supported by the SciLifeLab & Wallenberg Data Driven Life Science Program, grant no. KAW 2020.0239. C.D.B. and

M.F.T.J. were supported by a grant from the Swedish Research Council to C.D.B., grant no. 2017-04980. F.B. was supported by Fundação para a Ciência e a Tecnologia, grant no. PD/BD/128493/2017. J.B., J.H., S.P., and B.E.W. were supported by a Future Leader Fellowship from RBG Kew. N.A.C. was financed by H2020 MSCA-ITN-ETN Plant.ID, a European Union's Horizon 2020 research and innovation program under grant agreement no. 765000. J.D.C. was supported by the Swiss National Science Foundation, grant nos. P400PB_186733 and P4P4PB_199187. A.C. was supported by Portuguese National Funds through the Foundation for Science and Technology, FCT, grant no. 2020.00823.CEECIND and project PTDC/BIA-EVL/31254/2017. G.D. was supported by Vinnova, grant no. 2019-02717. D.E. was supported by the Swedish Research Council, grant no. 2016-00796, and the Swedish Foundation for Strategic Research, grant no. FFL15-0196. S.F. was supported by the Swedish Research Council, grant no. 2017-03862. B.L.F. was supported by the National Science Foundation, grant no. DEB-1655076. P.d.L.F. was supported by the MEMOVA project, EU Operational Programme Research, Development and Education, grant no. CZ.02.2.69/0.0/0.0/18_053/0016982. T.B.G. is supported by a young researcher grant from São Paulo Research Foundation (FAPESP, #2021/07161-6, #2022/09428-2), Brazil. M.C.H. and R.H. are Natural Environment Research Council–funded Ph.D. students with the London NERC DTP (NERC ref. no. NE/L002485/1). P.M.-M. was funded by the Czech Science Foundation, grant no. GJ20-18566Y. B.N. was supported by the Coordenação de Aperfeiçoamento de Pessoal de Nível Superior, Brasil (CAPES) (PDSE 88881.132750/2016-01). R.E.O. acknowledges the support of iDiv funded by the German Research Foundation (DFG–FZT 118, 202548816). A.S.T.P. was supported by the Natural Environment Research Council (NERC), grant no. NE/R001081/1. L.N.P. was supported by a Swiss National Science Foundation Early Postdoc Mobility Grant, grant no. P2LAP2_187745. M.R.-H. was supported by a beca de doctorado del Instituto de Ecología y Biodiversidad, Chile; Programa de Doctorado en Biología y Ecología Aplicada, Universidad Católica del Norte, Universidad de La Serena, La Serena, Chile and an ANID National Scholarship (grant no. 21181931); and the Institute of Ecology and Biodiversity (project ANID FB210006). E.R. was supported by the NRF/SASSCAL (Southern African Science Service Centre), grant no. 118589, and the NRF/African Origins Platform, grant no. 117666. F.S. was supported by European Union's Horizon 2020 research and innovation program under the Marie Skłodowska-Curie grant agreement, grant no. 838998. D.S. received funding from the Swiss National Science Foundation (PCEFP3_187012) and from the Swedish Research Council (VR: 2019-04739). M.S.V. was supported by a GBIF: Biodiversity Information for Development grant. K.W. was supported by a Techne Arts and Humanities Research Council Doctoral Training Partnership. P.W. was supported by the Darwin Initiative, grant nos. 22-005 and EIDPO049. **Author contributions:** The paper was project-led, with overall writing responsibility, by A.A., A.L.P., H.Ral., and R.J.S. The content was divided into three sections, with corresponding working groups, each making full use of the expertise and direct in-country experience of the 25 Malagasy coauthors. The sections were organized, written, and led by A.L.P., H.Ral., J.S.B., M.S.V., M.T.R., R.J.S., S.F., and T.R. Formal analyses were carried out by A.R., A.Z., D.E., D.S., H.F., J.S.B., L.N.P., M.C.H., M.Ri., M.S.V., R.S.C.C., S.F., T.A., and W.T. Visualizations and figures were done by D.E., F.S., H.F., H.Raz., J.S.B., L.N.P., and R.S.C.C. This paper and its sister manuscript on evolution, distribution, and use (*1*) were based on the outputs of a consortium focusing on Madagascar's biodiversity. The data curation, investigation, and resources therefore formed the foundation for the project as a whole and we therefore list all coauthors involved in these activities across both papers. Data curation was carried out by A.C., A.M.A., A.Rak., A.Ras., A.Z., B.A.R., B.L.F., B.N., C.D.B., D.E., G.D., D.R., E.R., F.Raj., F.Rak., F.S., H.N.R., H.Ral., H.Raz., J.D.C., J.E.N.R., J.H., J.M., K.W., L.M., L.N.P., L.R.R., M.F.T.J., M.G.C.N., M.Rab., M.R.-H., M.Ri., M.S.V., M.T.R., N.A., N.A.C., N.A.S.P., N.R., O.A.P.-E., P.d.L.F., P.M.-M., P.B.P., P.W., R.C., R.E.O., R.H., S.A., S.C., S.D., S.E.R., S.M.G., S.P., T.B.G., T.R., T.Z., V.Ran., V.Raz., and W.T. Investigation was carried out by A.C., A.M.A., A.Rak., A.Ras., A.S.T.P., B.A.R., B.N., F.B., F.Rak., H.N.R., H.Raz., M.G.C.N., O.A.P.-E., O.M.G., P.d.L.F., P.M.-M., P.W., R.A., R.H., R.S.C.C., S.E.R., and T.B.G. Methodology was developed by A.C., A.Z., B.E.W., C.E.R.L., D.S., J.H., J.M., J.S.B., L.N.P., M.S.V., S.P.B., and T.A. Resources were provided by A.C., D.R., E.R., J.R., L.M., M.Rak., M.S.V., M.T.R., N.A.S.P., and T.R. Software was designed by A.Z., B.E.W., D.E., D.S., and H.F. Validations were carried out by A.C., D.E., J.M., and W.J.B. All coauthors were involved in the writing, revision, and editing of the text. **Competing interests:** The authors declare no competing interests. **Data and materials availability:** All data are available in the main text or the supplementary materials. **License information:** Copyright © 2022 the authors, some rights reserved; exclusive licensee American Association for the Advancement of Science. No claim to original US government works. https://www.science.org/about/science-licenses-journal-article-reuse

SUPPLEMENTARY MATERIALS

science.org/doi/10.1126/science.adf1466
Materials and Methods
Fig. S1
Tables S1 to S8
References (*135*–*194*)

Submitted 8 September 2021; accepted 7 November 2022
10.1126/science.adf1466



Pushing the Boundaries of Knowledge

As AAAS's first multidisciplinary, open access journal, *Science Advances* publishes research that reflects the selectivity of high impact, innovative research you expect from the *Science* family of journals, published in an open access format to serve a vast and growing global audience. Check out the latest findings or learn how to submit your research: **ScienceAdvances.org**

Science Advances
AAAS

GOLD OPEN ACCESS, DIGITAL, AND FREE TO ALL READERS

RESEARCH ARTICLE SUMMARY

HIV CLINICAL TRIALS

Vaccination induces HIV broadly neutralizing antibody precursors in humans

David J. Leggat†, Kristen W. Cohen†, Jordan R. Willis†, William J. Fulp†, Allan C. deCamp†, Oleksandr Kalyuzhniy, Christopher A. Cottrell, Sergey Menis, Greg Finak, Lamar Ballweber-Fleming, Abhinaya Srikanth, Jason R. Plyler, Torben Schiffner, Alessia Liguori, Farhad Rahaman, Angela Lombardo, Vincent Philiponis, Rachael E. Whaley, Aaron Seese, Joshua Brand, Alexis M. Ruppel, Wesley Hoyland, Nicole L. Yates, LaTonya D. Williams, Kelli Greene, Hongmei Gao, Celia R. Mahoney, Martin M. Corcoran, Alberto Cagigi, Alison Taylor, David M. Brown, David R. Ambrozak, Troy Sincomb, Xiaozhen Hu, Ryan Tingle, Erik Georgeson, Saman Eskandarzadeh, Nushin Alavi, Danny Lu, Tina-Marie Mullen, Michael Kubitz, Bettina Groschel, Janine Maenza, Orpheus Kolokythas, Nadia Khati, Jeffrey Bethony, Shane Crotty, Mario Roederer, Gunilla B. Karlsson Hedestam, Georgia D. Tomaras, David Montefiori, David Diemert, Richard A. Koup, Dagna S. Laufer, M. Juliana McElrath*, Adrian B. McDermott*, William R. Schief*

INTRODUCTION: Vaccines that induce antibodies with predefined genetic features and binding specificities have promise to combat viruses with high antigenic diversity such as HIV, influenza, hepatitis C virus, and betacoronaviruses. Although these pathogens have eluded the development of vaccines that induce broad immunity covering their antigenic diversity, broadly neutralizing antibodies (bnAbs) have been discovered. Such bnAbs bind to relatively conserved epitopes on membrane glycoproteins of each pathogen, with features of each antibody allowing binding to a particular epitope. If vaccines could be developed to consistently induce similar bnAbs, preferably in conjunction with broad T cell immunity, protection against these pathogens might be achieved.

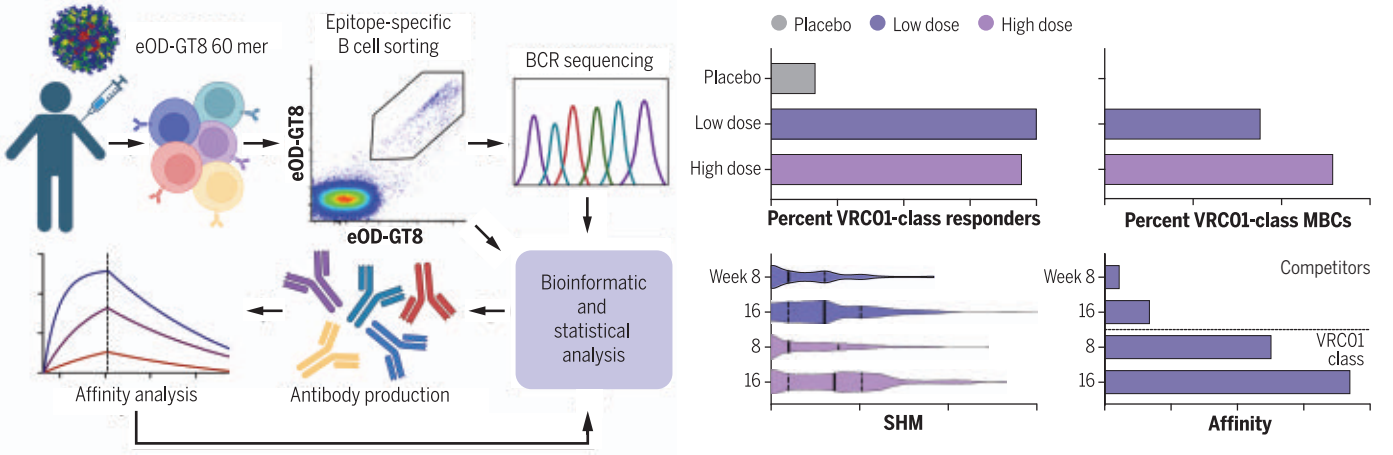
RATIONALE: bnAbs acquire affinity-enhancing mutations when a bnAb-precursor B cell mutates and matures from the original naïve B cell (or "germline") state. Germline-targeting vaccine design aims to induce bnAbs by stimulating rare bnAb-precursor B cells that have antibody genes and other properties needed to develop into bnAbs for a specific epitope. This "priming" step must generate a pool of bnAb-precursor–derived germinal center and/or memory B cells that are susceptible to reactivation by a boost immunogen closer in structure to the native viral glycoprotein. Sequential boosting with immunogens of increasing similarity to the native glycoprotein then aims to guide somatic hypermutation and affinity maturation to produce bnAbs that target the desired epitope.

RESULTS: We conducted a first-in-human test of the germline-targeting strategy by evaluating the safety and immune responses of a germline-targeting priming vaccine candidate, eOD-GT8 60mer nanoparticle adjuvanted with $AS01_B$, in the IAVI G001 phase 1 clinical trial. Each participant received two administrations of placebo, low-dose vaccine, or high-dose vaccine 8 weeks apart. The eOD-GT8 immunogen was designed to activate B cell precursors for HIV VRC01-class bnAbs defined by their usage of heavy chain variable gene alleles VH1-2*02 or *04 and any light chain complementarity determining region 3 with a length of five amino acids. We collected immune cells from the blood and lymph nodes of participants and carried out epitope-specific B cell sorting, B cell receptor (BCR) sequencing, and bioinformatic and statistical analyses. We also produced monoclonal antibodies and measured their binding affinities for the vaccine antigen. The vaccine had a favorable safety profile and induced VRC01-class responses in 97% (35 of 36) of vaccine recipients with median frequencies reaching 0.1% among immunoglobulin G memory B cells in blood. bnAb-precursors shared multiple properties with bnAbs and made substantial gains in somatic hypermutation and affinity with the boost.

CONCLUSION: The results establish clinical proof of concept for the germline-targeting vaccine design priming strategy, support development of boosting regimens to generate VRC01-class bnAb responses against HIV, and encourage application of the germline-targeting strategy to other targets in HIV and other pathogens. ■

The list of author affiliations is available in the full article online.
*Corresponding author. Email: schief@scripps.edu (W.R.S.); adrian.mcdermott@sanofi.com (A.B.M.); jmcelrat@fredhutch.org (M.J.M.)
†These authors contributed equally to this work.
Cite this article as D. J. Leggat *et al.*, *Science* **378**, eadd6502 (2022). DOI: 10.1126/science.add6502

READ THE FULL ARTICLE AT
https://doi.org/10.1126/science.add6502



Test of germline-targeting vaccine priming in healthy humans. Immune cells were isolated from recipients of eOD-GT8 60mer vaccine or placebo, and antibody sequences from vaccine-binding B cells were analyzed to measure the VRC01-class bnAb-precursor response rate among participants and the frequency of VRC01-class bnAb-precursor B cells among memory B cells (MBCs) in each participant. Somatic hypermutation (SHM) and binding affinity were measured.

CREDIT: CHRISTOPHER COTTRELL. CREATED WITH BIORENDER.COM

RESEARCH ARTICLE

HIV CLINICAL TRIALS

Vaccination induces HIV broadly neutralizing antibody precursors in humans

David J. Leggat[1]†‡, Kristen W. Cohen[2]†, Jordan R. Willis[3,4,5]†, William J. Fulp[2]†, Allan C. deCamp[2]†, Oleksandr Kalyuzhniy[3,4,5], Christopher A. Cottrell[3,4,5], Sergey Menis[3,4,5], Greg Finak[2], Lamar Ballweber-Fleming[2], Abhinaya Srikanth[1]§, Jason R. Plyler[1], Torben Schiffner[3,4,5]¶, Alessia Liguori[3,4,5], Farhad Rahaman[6], Angela Lombardo[6], Vincent Philiponis[6], Rachael E. Whaley[2], Aaron Seese[2], Joshua Brand[1]#, Alexis M. Ruppel[1], Wesley Hoyland[1], Nicole L. Yates[7], LaTonya D. Williams[7], Kelli Greene[8], Hongmei Gao[8], Celia R. Mahoney[2], Martin M. Corcoran[9], Alberto Cagigi[1], Alison Taylor[1], David M. Brown[10], David R. Ambrozak[1], Troy Sincomb[3,4,5], Xiaozhen Hu[3,4,5], Ryan Tingle[3,4,5], Erik Georgeson[3,4,5], Saman Eskandarzadeh[3,4,5], Nushin Alavi[3,4,5], Danny Lu[3,4,5], Tina-Marie Mullen[3,4,5], Michael Kubitz[3,4,5], Bettina Groschel[3,4,5], Janine Maenza[2,11], Orpheus Kolokythas[12], Nadia Khati[13], Jeffrey Bethony[14], Shane Crotty[4,15,16], Mario Roederer[1], Gunilla B. Karlsson Hedestam[9], Georgia D. Tomaras[7], David Montefiori[8], David Diemert[14,17], Richard A. Koup[1], Dagna S. Laufer[6], M. Juliana McElrath[2,11]*, Adrian B. McDermott[1]*††, William R. Schief[3,4,5,18]*

Broadly neutralizing antibodies (bnAbs) can protect against HIV infection but have not been induced by human vaccination. A key barrier to bnAb induction is vaccine priming of rare bnAb-precursor B cells. In a randomized, double-blind, placebo-controlled phase 1 clinical trial, the HIV vaccine–priming candidate eOD-GT8 60mer adjuvanted with $AS01_B$ had a favorable safety profile and induced VRC01-class bnAb precursors in 97% of vaccine recipients with median frequencies reaching 0.1% among immunoglobulin G B cells in blood. bnAb precursors shared properties with bnAbs and gained somatic hypermutation and affinity with the boost. The results establish clinical proof of concept for germline-targeting vaccine priming, support development of boosting regimens to induce bnAbs, and encourage application of the germline-targeting strategy to other targets in HIV and other pathogens.

Development of a preventative HIV vaccine is needed to end the HIV/AIDS pandemic (*1*). Broadly neutralizing antibodies (bnAbs), which are Abs that bind the envelope (Env) trimer and neutralize diverse HIV isolates, have been shown to provide sterilizing protection in nonhuman primate (NHP) models (*2*), and infusion of the bnAb VRC01 was shown to protect against neutralization-sensitive HIV isolates in humans (*3*, *4*). It is widely thought that an effective preventative HIV vaccine will need to induce bnAbs.

HIV vaccine design strategies to elicit bnAbs

bnAbs, like all antibodies, are produced by B cells and acquire affinity-enhancing mutations when a B cell matures from the original naïve (or germline) state. The discovery that most HIV Env proteins have no detectable affinity for bnAb germline precursors greatly influenced the development of HIV vaccine strategies, by indicating that special immunogens with affinity for bnAb germline precursors would be needed to prime bnAb responses and that different booster immunogens would be needed to select for antibody maturation to produce bnAbs (*5*–*14*).

The HIV vaccine field is now pursuing at least three strategies to elicit bnAbs, each of which involves sequential vaccination with different antigens to guide the immune response through several stages of maturation. These strategies include (i) B cell lineage vaccine design, in which the series of immunogens derives from the series of Env variants isolated from longitudinal analysis of bnAb development in a person with natural HIV-1 infection, and the first (priming) immunogen is selected to have affinity for the unmutated common ancestor for the bnAb lineage in that case study, and is usually the transmitted-founder Env in that case study (*15*–*20*); (ii) germline-targeting vaccine design, in which the priming immunogen is engineered to bind diverse precursors within a bnAb class (spanning many lineages), and boost immunogens are successively more like native Env trimers (*13*, *14*, *21*–*29*); and (iii) epitope-focused vaccine design, in which the series of immunogens aims to focus responses to one or more particular structural epitopes on the trimer (*30*–*38*). In each strategy, the priming stage is critical, because if appropriate B cell precursors with potential to develop into bnAbs are not stimulated at that stage, then the rest of the sequential vaccine will likely fail. Experimental medicine (phase 1) clinical trials are now underway or planned for each strategy, to test priming immunogens or sequential combinations of immunogens for their abilities to elicit desired Ab responses.

First-in-human test of germline targeting

We conducted a first-in-human test of the germline-targeting strategy by evaluating the safety and immune responses of a germline-targeting priming vaccine candidate, eOD-GT8 60mer adjuvanted with $AS01_B$, in the IAVI G001 phase 1 clinical trial. The vaccine immunogen is a self-assembling nanoparticle presenting 60 copies of an HIV gp120 engineered outer domain, germline-targeting version 8 (eOD-GT8), genetically fused to and arrayed externally on an interior lumazine synthase nanoparticle (*13*, *21*, *39*, *40*). eOD-GT8 was designed to have affinity for inferred-germline precursors to VRC01-class bnAbs (*13*, *21*, *39*). VRC01-class antibodies are minimally defined as those with heavy chain (HC) V gene alleles VH1-2*02 or *04 and any light chain (LC) complementarity determining region 3 (LCDR3) with a length of five amino acids (*13*, *14*, *41*, *42*). These sequence features define a broad class of antibodies with diverse LCs and HCDR3s. In preclinical experiments, eOD-GT8 was shown to bind to

[1]Vaccine Research Center, National Institute of Allergy and Infectious Diseases, National Institutes of Health, Bethesda, MD 20892, USA. [2]Vaccine and Infectious Disease Division, Fred Hutchinson Cancer Center, Seattle, WA 98109, USA. [3]IAVI Neutralizing Antibody Center, The Scripps Research Institute, La Jolla, CA 92037, USA. [4]Center for HIV/AIDS Vaccine Development, The Scripps Research Institute, La Jolla, CA 92037, USA. [5]Department of Immunology and Microbial Science, The Scripps Research Institute, La Jolla, CA 92037, USA. [6]IAVI, New York, NY 10004, USA. [7]Center for Human Systems Immunology, Departments of Surgery, Immunology, Molecular Genetics and Microbiology, Duke University, Durham, NC 27701, USA. [8]Duke University Medical Center, Durham, NC 27701, USA. [9]Department of Microbiology, Tumor and Cell Biology, Karolinska Institutet, SE-171 77 Stockholm, Sweden. [10]The Foundation for the National Institutes of Health, North Bethesda, MD 20852, USA. [11]Department of Medicine, University of Washington, Seattle, WA 98195, USA. [12]Department of Radiology, University of Washington, Seattle, WA 98195, USA. [13]Department of Radiology, School of Medicine and Health Sciences, The George Washington University, Washington, DC 20037, USA. [14]Department of Microbiology, Immunology and Tropical Medicine, School of Medicine and Health Sciences, The George Washington University, Washington, DC 20037, USA. [15]Center for Infectious Disease and Vaccine Research, La Jolla Institute for Immunology, La Jolla, CA 92037, USA. [16]Department of Medicine, Division of Infectious Diseases and Global Public Health, University of California, San Diego, La Jolla, CA 92037, USA. [17]Department of Medicine, School of Medicine and Health Sciences, The George Washington University, Washington, DC 20052, USA. [18]The Ragon Institute of Massachusetts General Hospital, Massachusetts Institute of Technology and Harvard University, Cambridge, MA 02139, USA.

***Corresponding author. Email: schief@scripps.edu (W.R.S.); adrian.mcdermott@sanofi.com (A.B.M.); jmcelrat@fredhutch.org (M.J.M.)**

†These authors contributed equally to this work. ‡Present address: The US Military HIV Research Program, Walter Reed Army Institute of Research, Silver Spring, MD 20910, USA. §Present address: Applied Physics Laboratory, Johns Hopkins University, Laurel, MD 20723, USA. ¶Present address: Leipzig University, Medical Faculty, Institute for Drug Discovery, Liebigstraße 19, 04103 Leipzig, Germany. #Present address: School of Medicine and Public Health, University of Wisconsin–Madison, Madison, WI 53706, USA. ††Present address: Vaccines Research and Development, Sanofi, Swiftwater, PA 18370, USA.

diverse VRC01-class human naïve B cells at an average frequency of ~1 in 300,000 naïve B cells, in 26 of 27 donors tested (96%), and with substantial affinity [geomean dissociation constant (K_D) of 4 μM] (*21*, *43*, *44*). Adjuvanted eOD-GT8 60mer was shown to be capable of priming VRC01-class B cell responses in multiple different engineered mouse models (*27*, *39*, *45*–*49*), including stringent models that mimic two key parameters of human vaccination: precursor frequency and affinity (*27*, *46*, *48*, *49*). Adjuvanted eOD-GT8 60mer was also shown to prime VRC01-class responses that can be boosted toward bnAb development in mouse models (*26*, *27*, *29*). However, adjuvanted eOD-GT8 60mer failed to elicit VRC01-class responses in NHPs despite inducing robust germinal center (GC) B and T cell responses and serum responses (*50*), likely because of the lack of a suitable human VH1-2 analog (*13*, *41*, *51*, *52*) and a lower rate of five–amino acid LCDR3s in NHPs (*50*, *51*). In the IAVI G001 trial, we sought to determine whether human immunization with adjuvanted eOD-GT8 60mer is safe and effective for inducing VRC01-class immunoglobulin G (IgG) B cell responses. Forty-eight participants were immunized with either 20 μg eOD-GT8 60mer and 50 μg $AS01_B$ (N = 18), 100 μg eOD-GT8 60mer and 50 μg $AS01_B$ (N = 18), or the placebo Dulbecco's phosphate-buffered saline (DPBS) sucrose, the buffer diluent used in the vaccine (N = 12) (fig. S1 and table S1). Vaccine or placebo were administered at weeks 0 and 8 intramuscularly in the same deltoid. The full schedule of procedures for safety and immunogenicity evaluation is given in table S2.

Completeness, safety, and reactogenicity

All but one study participant received both vaccinations; one declined the second vaccination because of a medical diagnosis unrelated to the trial. Forty-five of 48 participants completed all study procedures, and only 1.0% of all 768 visits were missed (fig. S1 and table S3). No serious adverse events (AEs) were reported, and no participants acquired HIV-1 infection or developed serum positivity for HIV. Forty-seven of 48 participants (97.9%) reported local and/or systemic AEs (tables S4 to S6), but AEs were generally mild or moderate, resolved in most cases within 1 to 2 days, and were consistent with other vaccines (*53*). Overall, the vaccine had an acceptable safety and tolerability profile.

Serum antibody responses

After the first immunization, all vaccine recipients, but no placebo recipients, produced serum IgG binding antibodies to eOD-GT8 60mer and monomer and to the eOD-GT8 CD4 binding site (CD4bs) epitope, in which CD4bs binding was indicated by stronger binding to eOD-GT8 than to eOD-GT8-KO11, an epitope-knockout mutant that blocks binding by VRC01-class precursor Abs and bnAbs (*43*, *46*–*49*) (figs. S2 and S3 and tables S7 and S8). Vaccine-induced responses to eOD-GT8 60mer and monomer increased after the second vaccination, whereas CD4bs-specific responses remained relatively constant (figs. S2 and S3 and tables S7 and S8). All participants exhibited preimmunization reactivity to the lumazine synthase (LS) base nanoparticle, and LS responses increased with both immunizations in vaccine recipients (figs. S2 and S3 and tables S7 and S8). However, the magnitude of the baseline LS reactivity was not associated with stronger or weaker responses to the eOD-GT8 60mer, eOD-GT8 monomer, or the CD4bs epitope (fig. S4). We detected no serum neutralizing activity to any of several viruses tested (table S9), as expected, because the CD4bs in eOD-GT8 has been substantially modified to enable binding to VRC01-class precursors. Induction of binding antibodies to eOD-GT8 and its CD4bs but not neutralizing antibodies was consistent with preclinical experiments (*27*, *39*, *45*, *46*, *48*–*50*, *54*). We concluded that the vaccine was highly immunogenic and induced class-switched, antigen-specific and CD4bs-specific serum IgG responses.

B cell sorting and receptor sequencing as the critical immunological assay

The major immunological objective of the trial was to determine whether the vaccine could induce VRC01-class IgG B cells, defined as IgG B cells with VRC01-class B cell receptors (BCRs). Toward that end, we developed an analysis workflow to determine and interpret BCR sequences for eOD-GT8 CD4bs-specific IgG B cells using single B cell sorting, reverse transcriptase polymerase chain reaction (RT-PCR), DNA sequencing, and bioinformatic analysis (figs. S5 to S10 and tables S10 to S19). For each trial participant, we attempted to interrogate eight samples with this workflow, including memory B cells and plasmablasts (PBs) from peripheral blood mononuclear cell (PBMC) samples, and GC B cells from lymph node cells obtained by fine-needle aspiration (FNA) (Fig. 1A and tables S10 and S11). Complete data from sorting and sequencing, including quality-filtered sequences for the HC and LC of at least one CD4bs-specific BCR per sample, were obtained for 69.3% (266 of 384) of attempted samples (table S20).

Immunogenicity assessed by antigen- and epitope-specific B cell sorting

In PBMCs, all vaccine recipients produced eOD-GT8– and CD4bs-specific IgG memory B cells after the first immunization, with frequencies significantly higher than in preimmunization or placebo recipient samples, indicating vaccine-induced responses (Fig. 1, B and C; figs. S11 and S12; and tables S21 to S28). Frequencies of eOD-GT8– and CD4bs-specific IgG memory B cells in vaccine-recipient PBMCs increased significantly after the second immunization (Fig. 1, B and C; and tables S29 and S30), although the fraction of eOD-GT8–specific cells that were CD4bs-specific (KO^-) decreased with the boost (Fig. 1D and table S31). CD4bs-specific IgG memory B cell frequencies in PBMC samples peaked 2 weeks after the boost, reaching median frequencies of ~1 in 300 and ~1 in 200 IgG B cells in the low- and high-dose vaccine groups, respectively (Fig. 1C and tables S27 and S30). Thus, the germline-targeting immunogen induced substantial frequencies of CD4bs-specific IgG memory B cells in peripheral blood.

In lymph node and PB samples, eOD-GT8– and CD4bs-specific GC B cell or PB frequencies were significantly higher in vaccine than placebo recipients (Fig. 1, B and C, and tables S23 and S24), indicating vaccine-induced responses. Among vaccine recipients, frequencies of GT8- and CD4bs-specific cells were generally higher among IgG GC B cells or IgD^- PBs than among IgG memory B cells in PBMCs (Fig. 1), reflecting the spatial and/or temporal enrichment of vaccine-specific cells among GC B cells and PBs. Overall, postimmunization class-switched (IgD^-) PBMC memory and lymph node GC B cells specific for eOD-GT8 or CD4bs were predominantly IgG and were enriched for IgG compared with preimmunization memory (fig. S13 and tables S32 to S34), justifying our focus on IgG responses.

Detection and frequency quantification of VRC01-class IgG B cells

A total of 11,372 CD4bs-specific BCR sequences with paired HCs and LCs were available from 266 samples to assess vaccine performance (fig. S14). For each of these samples, we measured the number of VRC01-class IgG B cells and their frequencies among IgG memory B cells, GC B cells, or PBs, and we grouped the results by time point, sample type, and vaccine treatment (Fig. 2, A and B, and tables S35 and S36. We then computed the positivity rate, defined as the percentage of each group with at least one VRC01-class IgG B cell detected, at each time point (Fig. 2C and table S37).

In preimmunization (baseline) samples, we detected one or two VRC01-class IgG memory B cells in 6 of 48 participants (12.5%), with a median frequency over responders of 2.33×10^{-4}% (one VRC01-class B cell in 429,000 IgG memory B cells) (week −4 in Fig. 2, A and B). Thus, preexisting VRC01-class IgG memory was present in at least a minority of participants. In postimmunization PBMC samples (weeks 4, 8, 10, and 16), we detected VRC01-class IgG memory B cells in two placebo recipients (2 of 12, 16.7%), both of whom also showed preimmunization VRC01-class IgG memory (participants 001 and 080 indicated in Fig. 2).

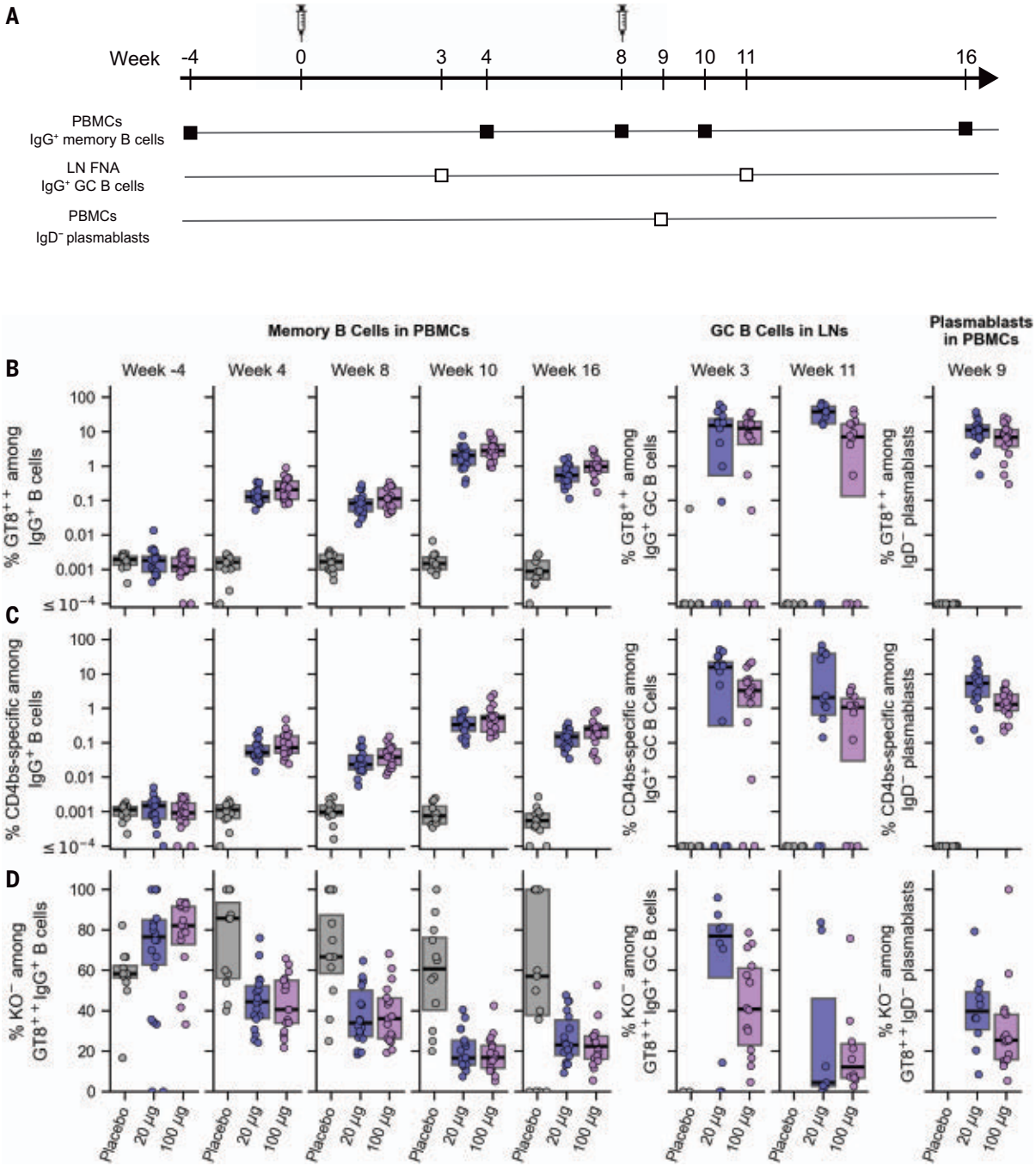


Fig. 1. Frequencies of antigen-specific and epitope-specific B cells. (**A**) Schedule for immunization and B cell sampling. LN, lymph node. (**B**) Frequency of eOD-GT8–specific ($GT8^{++}$) IgG memory B cells (left), IgG GC B cells (middle), and IgD^- PBs (right) shown over time for each participant, grouped by vaccine treatment. $GT8^{++}$ indicates binding to two different eOD-GT8 fluorescent probes. (**C**) Frequency of CD4bs-specific (KO^- $GT8^{++}$) IgG B cells, displayed as in (B). KO^- indicates lack of binding to the eOD-GT8-KO11 probe. (**D**) Percentage of eOD-GT8–specific IgG B cells that are CD4bs-specific (KO^-), displayed as in (B). Each symbol represents the frequency for one participant. Thick lines indicate median values, and boxes indicate 25 and 75% quantiles.

Detection of postplacebo VRC01-class IgG memory B cells in those participants was likely due to preexisting VRC01-class IgG memory.

In postimmunization PBMC samples, we detected VRC01-class IgG memory B cells in significantly higher fractions of vaccine recipients compared with baseline or placebo recipients (Fig. 2C and tables S38 and S39), and frequencies of VRC01-class IgG memory B cells among IgG B cells were significantly higher after vaccination compared with baseline (Fig. 2B and table S40). Our predetermined definition of a vaccine-induced VRC01-class IgG memory B cell response was the detection of one or more VRC01-class IgG memory B cells with a frequency higher than baseline for the same participant. All postvaccination IgG memory samples with VRC01-class B cells detected met that definition (table S36). In week 4 PBMCs, we detected VRC01-class memory B cell responses in 17 of 18 participants in each

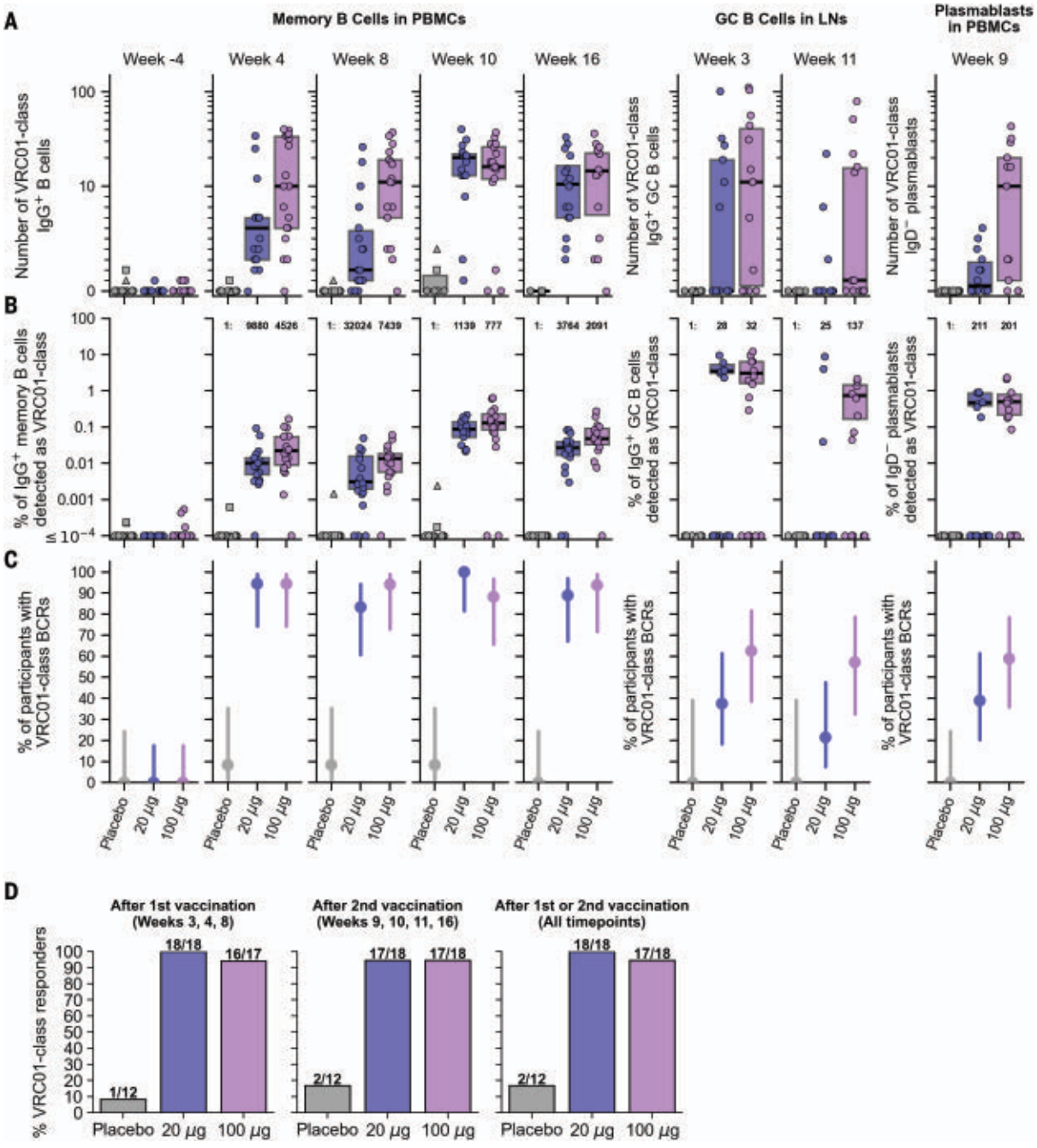


Fig. 2. Detection of VRC01-class IgG B cells in blood and lymph nodes. (**A**) Number of VRC01-class IgG B cells detected over time in each participant. (**B**) Frequency of VRC01-class IgG B cells as a percentage of IgG B cells in each participant. Median postvaccination frequencies are stated as 1:number of IgG B cells. In (A) and (B), symbols represent participants, and the two placebo participants with preexisting (week −4) VRC01-class B cells are indicated as a square and a triangle. Thick lines indicate median values, and boxes indicate 25 and 75% quantiles. Medians and quantiles were computed over nonzero values only because nonresponders are accounted for in (C). (**C**) Positivity of VRC01-class IgG B cell detection, defined as the percentage of participants in each group with at least one VRC01-class B cell detected for each time point and sample type. Circles indicate median values, and lines indicate 95% CIs computed using the Wilson score method. (**D**) Positivity of VRC01-class responses over all time points or only after the first or second vaccination.

vaccine group [94.4%; 95% confidence interval (CI), 74.2 to 99.0%] (Fig. 2C and table S37), with median frequencies of ~1 in 10,000 and ~1 in 4500 IgG B cells among positive responders in the low- and high-dose groups, respectively (Fig. 2B and table S41). These week 4 frequencies of VRC01-class memory B cells in the low- and high-dose groups were higher than the median prevaccination frequency among responders (1 in 429,000) by factors of 43 and 94, respectively, and higher than the previously reported average frequency for naïve VRC01-class precursors [1 in 300,000; (*21*, *43*)] by factors of 30 and 67, respectively. In week 8 PBMCs, VRC01-class positivity remained high, at 83.3% of the low-dose group and 94.4% of the high-dose group (Fig. 2C and table S37). Median VRC01-class IgG

memory frequencies among responders declined modestly from week 4 to week 8 (Fig. 2B and tables S41 and S42), but week 8 median frequencies remained >12-fold above the baseline VRC01-class IgG B cell frequency. We concluded that a single vaccination consistently induced strong VRC01-class IgG memory B cell responses in the peripheral blood.

After the second vaccination, VRC01-class positivity in week 10 and 16 PBMCs remained high (88 to 100%) in both vaccine groups (Fig. 2C and table S37). Median VRC01-class IgG memory frequencies among responders in the low-dose group increased markedly, by a factor of 28, to reach a week 10 peak frequency of 0.088% (1 in 1139) and finally declined, by a factor of 3.3, to a week 16 frequency of 0.027% (1 in 3764) (Fig. 2B and tables S41 and S42). Trends were similar but more favorable in the high-dose group, with frequencies at weeks 10 and 16 of 0.13% (1 in 777) and 0.048% (1 in 2091), respectively (Fig. 2B and table S41). Thus, at the peak response 2 weeks after the second vaccination, median frequencies of VRC01-class IgG memory B cells for >88% of vaccine recipients in the low- and high-dose groups were higher than the median prevaccination frequency by factors of 380 and 550, respectively, and higher than the previously reported average frequency for VRC01-class naïve B cells by factors of 260 and 390, respectively (*21*, *43*). Six weeks after the peak, at week 16, VRC01-class IgG memory B cell frequencies remained significantly higher than on the day of the second immunization (Fig. 2B and table S42). We concluded that the second immunization consistently increased VRC01-class IgG B cell frequencies in the peripheral blood.

In lymph node and PB samples, VRC01-class response rates were generally lower than in PBMC memory B cells (Fig. 2C). However, among positive responders, VRC01-class frequencies among IgG GC B cells and IgD^- PBs were generally higher than among PBMC IgG memory B cells (Fig. 2B), illustrating the strong VRC01-class response in the GC reactions.

Combining all postimmunization data, we detected VRC01-class IgG B cell responses in 100% (18 of 18) of participants in the low-dose group (median of 44 per participant) and 94.4% (17 of 18) of participants in the high-dose group (median of 91 per participant), for an overall response rate of 97% (35 of 36) (Fig. 2D and table S37). After the first vaccination only (weeks 3, 4, and 8), we measured response rates of 94.4% (17 of 18) in both the low- and high-dose groups, giving an overall response rate of 94.4% (34 of 36) (Fig. 2D and table S37). We concluded that the eOD-GT8 60mer vaccine induced VRC01-class IgG B cell responses with high consistency across vaccine recipients and over time after one or two vaccinations, in both dose groups.

VH1-2 genotype analysis

One high-dose vaccine participant contributed samples from all eight visits but had no detectable VRC01-class IgG B cells. Only two of the 540 HC sequences from this individual (PubID 059) were VH1-2, and both used the *06 allele, which suggested that the individual might not possess either of the required *02 or *04 alleles. To evaluate the VH1-2 allele content in that individual and in all other participants, we carried out VH1-2 genotype analysis using IgDiscover for all 48 participants. Across all individuals, we detected five VH1-2 alleles, including *02 and a novel variant of *02 with a noncoding polymorphism, *02_S4953, both of which we will refer to as *02 here. The remaining alleles included *04, *05, and *06. Accounting for hetero- and homozygosity, we identified a total of nine genotypes, among which the most common were *02/*04 (27.1%), *02/*02 (22.9%), *04/*04 (20.8%), and *04/*06 (14.6%) (table S43). Only one of the genotypes, *05/*06, included neither of the required VRC01-class alleles, and that genotype was only carried by the participant who did not produce detectable VRC01-class IgG B cell responses. Thus, we found that vaccine induction of VRC01-class responses by eOD-GT8 60mer is limited by VH1-2 genotype. However, individuals lacking at least one of the required alleles represented only 2% (1 of 48) of this study population, consistent with prior analyses (*13*, *41*, *44*).

Polyclonality of VRC01-class responses

Despite sharing the VH1-2 gene, VRC01-class responses were highly polyclonal, with diverse HCDR3s and LCs (fig. S15). BCR sequence hierarchical clustering showed that all 2865 postvaccination VRC01-class BCRs were represented by 1779 independent clusters (lineages) originating from independent germline recombination events; thus, >60% of VRC01-class responses derived from distinct precursors (Fig. 3, A and B). Very few clusters (0.11%) were shared between participants (Fig. 3C), relatively few clusters (9.7%) were shared over time within individuals (Fig. 3C), and most of the clusters (82.1 and 80.9% in the low- and high-dose groups, respectively) contained a single member (Fig. 3D). The depth of sampling of the CD4bs-specific BCR repertoire was limited by practical constraints, and deeper sampling might have identified additional clusters or members for each cluster. Nevertheless, the number of independent VRC01-class clusters per participant was substantial (medians of 32 and 65 in the low- and high-dose groups, respectively) (Fig. 3E), showing that a large number of distinct precursors were primed in each individual. High VRC01-class polyclonality was observed in memory B cells at all time points after the prime and boost and in PBs, whereas in GCs, we observed reduced levels of polyclonality concomitant with detection of larger clonal families (Fig. 3F). Thus, eOD-GT8 60mer primed responses from a diverse pool of VRC01-class precursors, and the clonal diversity was maintained after the boost.

Competitor responses: Non–VRC01-class CD4bs-specific responses

VRC01-class responses were a minority of CD4bs-specific IgG B cell responses. The VRC01-class fraction of CD4bs-specific IgG BCRs had median per dose group values of 16 to 28% in PBMC memory B cells, and 0 to 36% in lymph node GC B cells and PBMC PBs, across both vaccine groups and over time (Fig. 4A). CD4bs-specific VRC01-class responses were an even smaller fraction of total eOD-GT8–specific IgG B cells, with median per dose group values of 3.5 to 8% in memory B cells (Fig. 4B). These values were substantially higher than results from preclinical experiments with adjuvanted eOD-GT8 60mer in Kymab mice (*46*) and VH1-2 recombining mice (*27*, *54*), in which only 1% and 0.3 to 3.2% of CD4bs-specific IgG BCRs were VRC01-class, respectively, and were similar to results from naïve human B cell sorting with eOD-GT8 tetramers, in which 15 to 20% of CD4bs-specific naïve BCRs were VRC01-class (*21*, *43*, *44*). Here, CD4bs-specific, non–VRC01-class IgG BCRs, defined as any CD4bs-specific BCR not meeting the VRC01-class definition, included non–VH1-2 BCRs as well as VH1-2 BCRs with LCDR3 lengths other than five. However, VRC01-class BCRs made up a dominant 83% of VH1-2/kappa BCRs and 43% of VH1-2/lambda BCRs, owing to strong enrichment for five–amino acid LCDR3s (fig. S16). CD4bs-specific, non–VRC01-class IgG B cells were highly polyclonal (fig. S17), with diverse gene usage and CDR3 lengths (fig. S18), just as VRC01-class were highly polyclonal (Fig. 3). However, non–VRC01-class B cells reached higher frequencies than VRC01-class B cells among all IgG B cells. Median frequencies of CD4bs-specific, non–VRC01-class IgG B cells peaked at week 10 values of 0.27 and 0.39% in the low- and high-dose vaccine groups, respectively (fig. S19 and table S44), compared with VRC01-class frequencies of 0.09 and 0.13%, respectively. Thus, VRC01-class B cells were induced despite a dominant competing CD4bs response by a highly diverse pool of non–VRC01-class B cells.

BCR mutation levels

Changes in vaccine-induced BCR mutation levels over time can provide insight into the immune processes underlying the response. To assess changes in CD4bs-specific BCR mutation levels, we computed the median

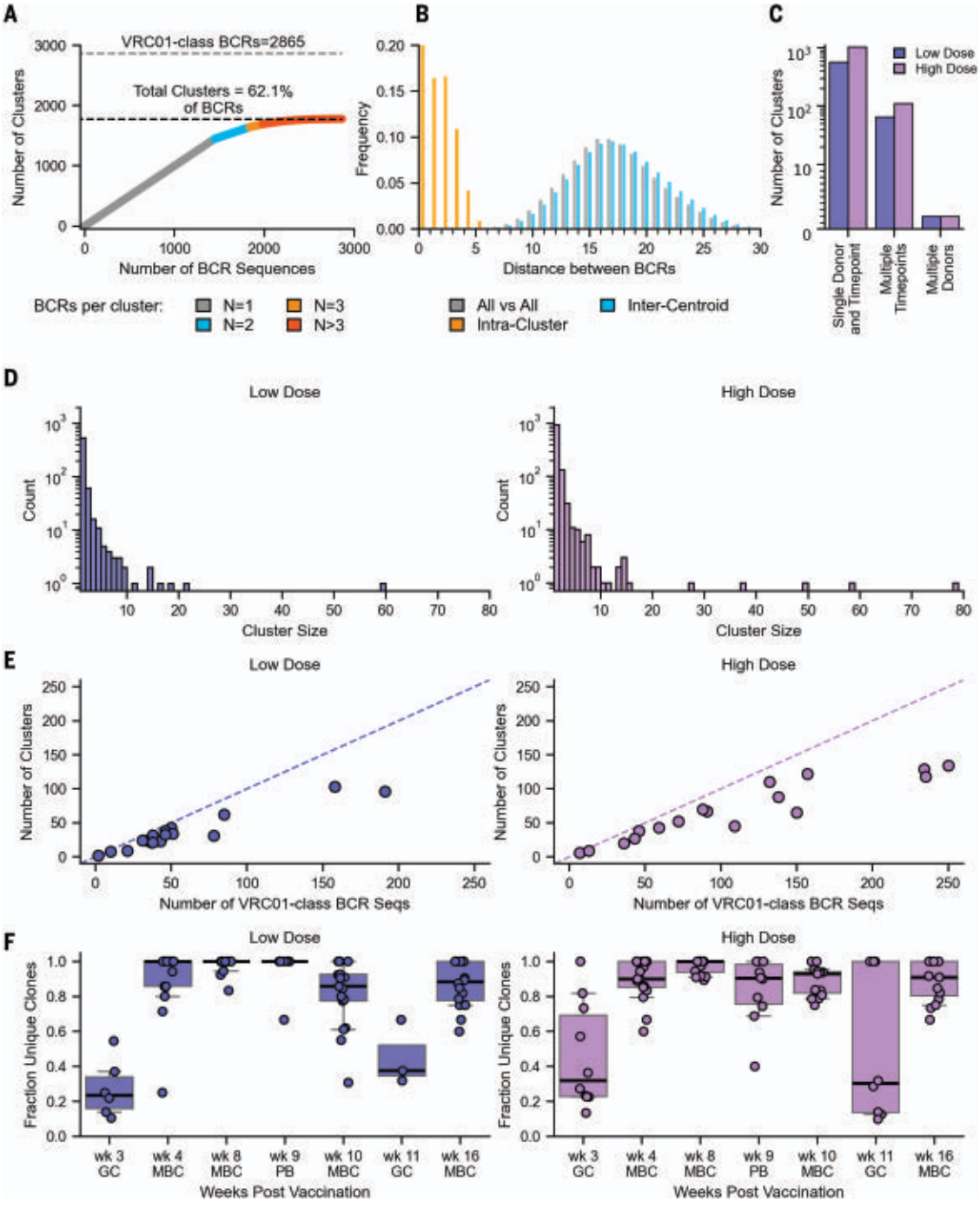


Fig. 3. VRC01-class BCR hierarchical clustering and genetic diversity. (**A**) Number of clusters versus number of BCR sequences, for all postvaccination VRC01-class BCR sequences in both vaccine groups. The number of sequences per cluster is indicated at the bottom. (**B**) Pairwise distance distributions for BCR sequences in (A), including all versus all, intracluster (all versus all within cluster), and intercentroid (between cluster centroids). (**C**) Number of clusters involving single donor and time point, single donor and multiple time points, and multiple donors, separately for the low- and high-dose groups. (**D**) Histogram of cluster size for the low- and high-dose groups. (**E**) Number of clusters versus number of VRC01-class BCR sequences for each participant in the low- and high-dose groups. Dashed lines indicate equality in numbers of clusters and sequences. (**F**) VRC01-class BCR polyclonality over time. Each symbol reports the fraction of BCR sequences that cluster as unique clones within a single donor at a single time point. Thick lines indicate median values, boxes indicate 25 and 75% quantiles, and whiskers approximate 10 and 90% quantiles. MBC, memory B cell.

percent mutation per participant per time point for HC V genes (V_H) and LC kappa and lambda V genes (V_K/V_L), in VRC01-class and non–VRC01-class BCRs for both nucleotide and amino acid mutations (Fig. 5, A and B; fig. S20; and table S45). We made statistical comparisons between time points using paired data in which mutation levels were available from the same individual at two time points (tables S46 to S48). We also monitored the mutation distributions across all antibodies in each group and time point using violin plots (Fig. 5, C and D). In the narrative below, we provide example V_H amino acid mutation values as indicators for change.

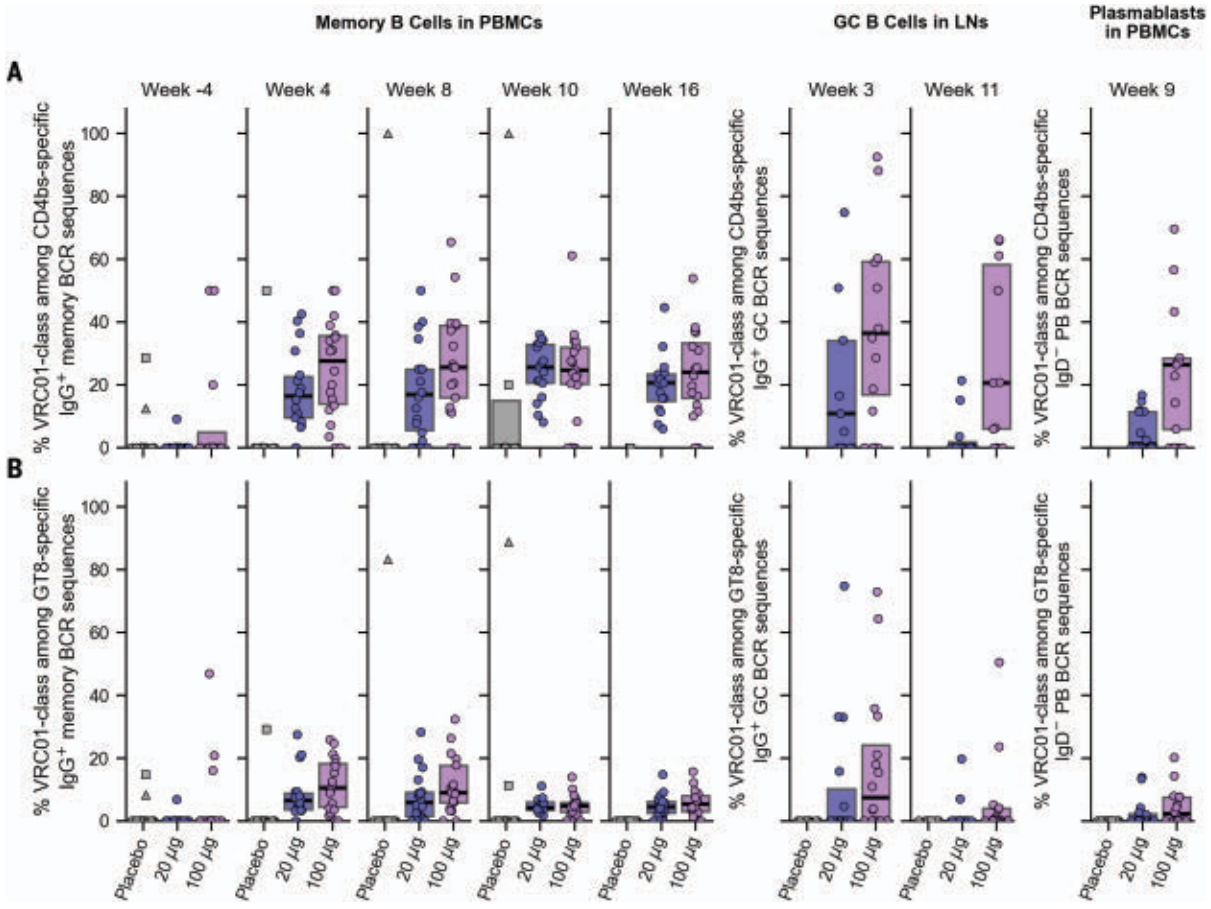


Fig. 4. Frequency of VRC01-class B cells among CD4bs- or eOD-GT8–specific IgG B cells and PBs. (**A**) VRC01-class frequencies among CD4bs-specific B cells. (**B**) VRC01-class frequencies among eOD-GT8–specific B cells. Each symbol represents the frequency for one participant. The two placebo participants with preexisting (week −4) VRC01-class B cells are indicated as a square and a triangle. Thick lines indicate median values, and boxes indicate 25 and 75% quantiles.

After the first immunization, nucleotide and amino acid mutation levels in VRC01-class memory IgG V_H and $V_{K/L}$ genes generally increased significantly from week 4 to week 8 in both vaccine groups, with the only exception being V_H amino acid mutation in the low-dose group, which showed an increase that barely missed significance (Fig. 5, A and C; fig. S20; and tables S46 and S47). Thus, GCs remained active and produced memory B cells with increased somatic hypermutation (SHM) beyond week 4. By week 8, V_H amino acid mutation levels reached median values of 1.5% in both dose groups (table S45).

After the second immunization, nucleotide and amino acid mutation levels in VRC01-class memory BCR V_H genes from both vaccine groups increased significantly from week 8 to week 10 but did not change significantly from week 10 to week 16 (Fig. 5, A and C; fig. S20; and tables S46 and S47). Week 10 V_H amino acid mutation levels in VRC01-class IgG memory BCRs reached median values of 3.0% in both vaccine groups (table S45). Thus, the week 8 boost caused a relatively rapid increase in SHM within the VRC01-class IgG memory pool. Increased mutation levels also appeared in PBs 4 to 8 days after the boost (Fig. 5, A and C; fig. S20; and tables S46 and S47). GCs remained active at week 11, as reflected by the relatively high median V_H amino acid mutation levels of 5.1 and 6.7% in week 11 GC BCRs in the low- and high-dose groups, respectively (table S45). The increased SHM in GCs indicated an ongoing physiological response to the boost in which B cells continued acquiring mutations and a fraction of those cells likely exited to blood. Our finding that an autologous boost immunization increased mutation levels in VRC01-class GC and memory B cells provides support for a key assumption underlying the germline-targeting vaccine design strategy, namely that sequential vaccination can increase the maturation of targeted B cell classes in humans.

Comparing GC BCR mutation levels at weeks 3 and 11 provides insight into mechanism. In GC BCRs, the distributions of V_H and V_K/V_L mutation levels computed over all VRC01-class responders were substantially higher at week 11 than week 3 (Fig. 5, A and C; fig. S20; and table S45). For example, median (interquartile range) V_H amino acid mutation levels were 1.0% (1.0 to 1.8%) and 1.3% (1.0 to 2.0%) at week 3 in the low- and high-dose groups, respectively, compared with 5.1% (4.6 to 5.6%) and 6.7% (5.0 to 7.1%) at week 11 (Fig. 5A; fig. S20; and table S45), and the week 11 violin plot distributions over all BCRs show little similarity to the lower SHM week 3 violin plots (Fig. 5C). With paired data from weeks 3 and 11 available for only a few individuals (N = 1 at low dose and N = 5 at high dose; fig. S21), we could not ascribe significance to the higher mutation levels at week 11 (tables S46 and S47). Nevertheless, the above comparisons between weeks 3 and 11, and the minimal overlap in mutation distributions for four individuals with multiple data points at both weeks 3 and 11 (fig. S21A), suggested that the second immunization did not cause substantial priming of naïve B cells but instead primarily induced additional maturation of VRC01-class GC and/or memory B cells generated by the first immunization.

SHM in non–VRC01-class IgG memory BCRs increased significantly from week 4 to week 8 for the high-dose group only and showed no

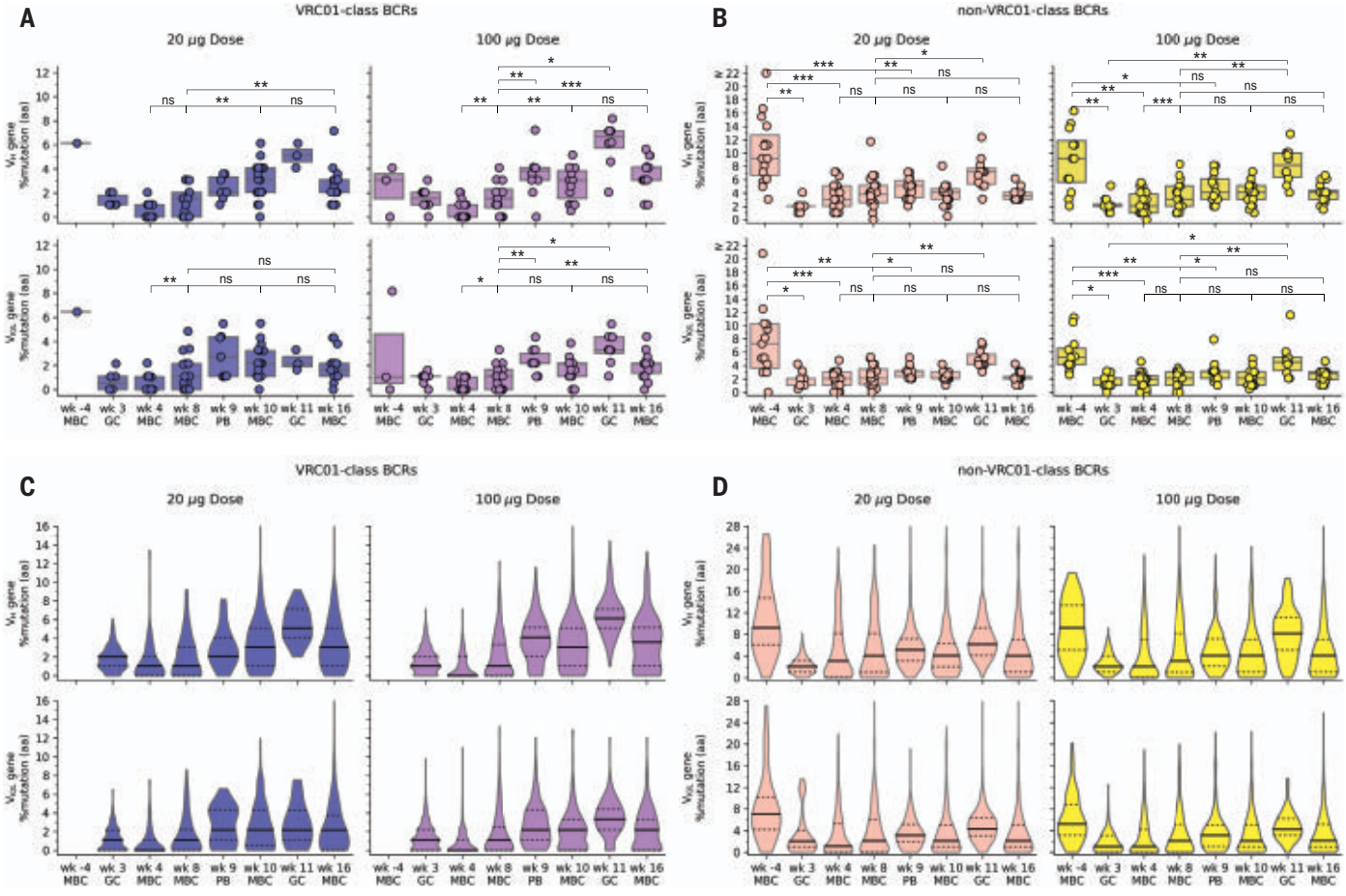


Fig. 5. Amino acid mutation levels in HC and LC V genes over time, for VRC01-class and non–VRC01-class BCRs from vaccine recipients. (**A** and **B**) VRC01-class (A) and non–VRC01-class (B) BCR V_H percentage of amino acid (aa) mutations (top) and $V_{K/L}$ percentage of amino acid mutations (bottom) for the low-dose (left) and high-dose (right) group, with symbols representing the median per participant per time point. (**C** and **D**) VRC01-class (C) and non–VRC01-class (D) BCR V_H percentage of amino acid mutations (top) and $V_{K/L}$ percentage of amino acid mutations (bottom) for the low-dose (left) and high-dose (right) group, with violin plots representing the distribution of all BCRs per group per time point. In (A) and (B), thick lines are medians and box plots show 25 and 75% quantiles for each dose group at each time point. Statistical significance is indicated for all comparisons with pairs of measurements from at least eight participants (tables S46 and S48). Significance testing was done using Wilcoxon signed-rank test for paired data (two-sided, $\alpha = 0.05$); ns, not significant; $^*P < 0.05$; $^{**}P < 0.01$; $^{***}P < 0.001$. In (C) and (D), solid lines indicate medians and dashed lines show 25 and 75% quantiles for each dose group at each time point.

significant increase from week 8 to week 10 or 16 in either group (Fig. 5, B and D; fig. S20; and tables S48 and S49). Thus, the germline-targeting vaccine boost succeeded to increase memory IgG BCR median mutation levels for the targeted class of B cells without causing similar increases in undesired BCRs competing for the same epitope. Non–VRC01-class BCRs did show significant mutational increases between memory B cells at week 8 and either PBs at week 9 or GC BCRs at week 11 (Fig. 5, B and D; fig. S20; and tables S48 and S49). SHM in non–VRC01-class GC BCRs was significantly higher at week 11 than at week 3 for the high-dose group and nearly significantly higher for the low-dose group (Fig. 5, B and D; fig. S21B; and tables S48 and S49), indicating that the second immunization primarily activated previously mutated GC and/or memory B cells instead of naïve B cells, similar to our observation with VRC01-class responses.

Precursor origins

We detected prevaccination VRC01-class IgG memory B cells in only 12.5% (6 of 48) of participants, and 71% (5 of 7) of those BCRs had mutation levels substantially above the levels detected postvaccination at weeks 3 or 4 (tables S45 and S50), indicating that the VRC01-class IgG B cells detected postvaccination predominantly originated from naïve VRC01-class B cells rather than IgG memory B cells. However, clustering analysis indicated that one week −4 VRC01-class IgG memory BCR was potentially clonally related to two postvaccination BCRs in the same individual (fig. S22), providing evidence that at least some VRC01-class IgG BCRs detected postvaccination may have originated from VRC01-class IgG memory B cells.

Non–VRC01-class IgG BCRs had significantly higher mutation levels at week −4 compared with weeks 3 or 4 (Fig. 5, B and D; fig. S20; and tables S45, S48, and S49), indicating that most non–VRC01-class IgG B cells detected postvaccination probably also originated from naïve rather than memory B cells. However, sequence clustering analysis indicated that, among 26 non–VRC01-class memory IgG BCR lineages with members from both pre- and postvaccination time points, evidence allowing for a potential preexisting memory B cell precursor could be found in 11 (42%) of the lineages (fig. S23). Non–VRC01-class BCR mutation levels at weeks 3 to 8 were substantially higher than those for VRC01-class (Fig. 5 and table S45), which might have been due to

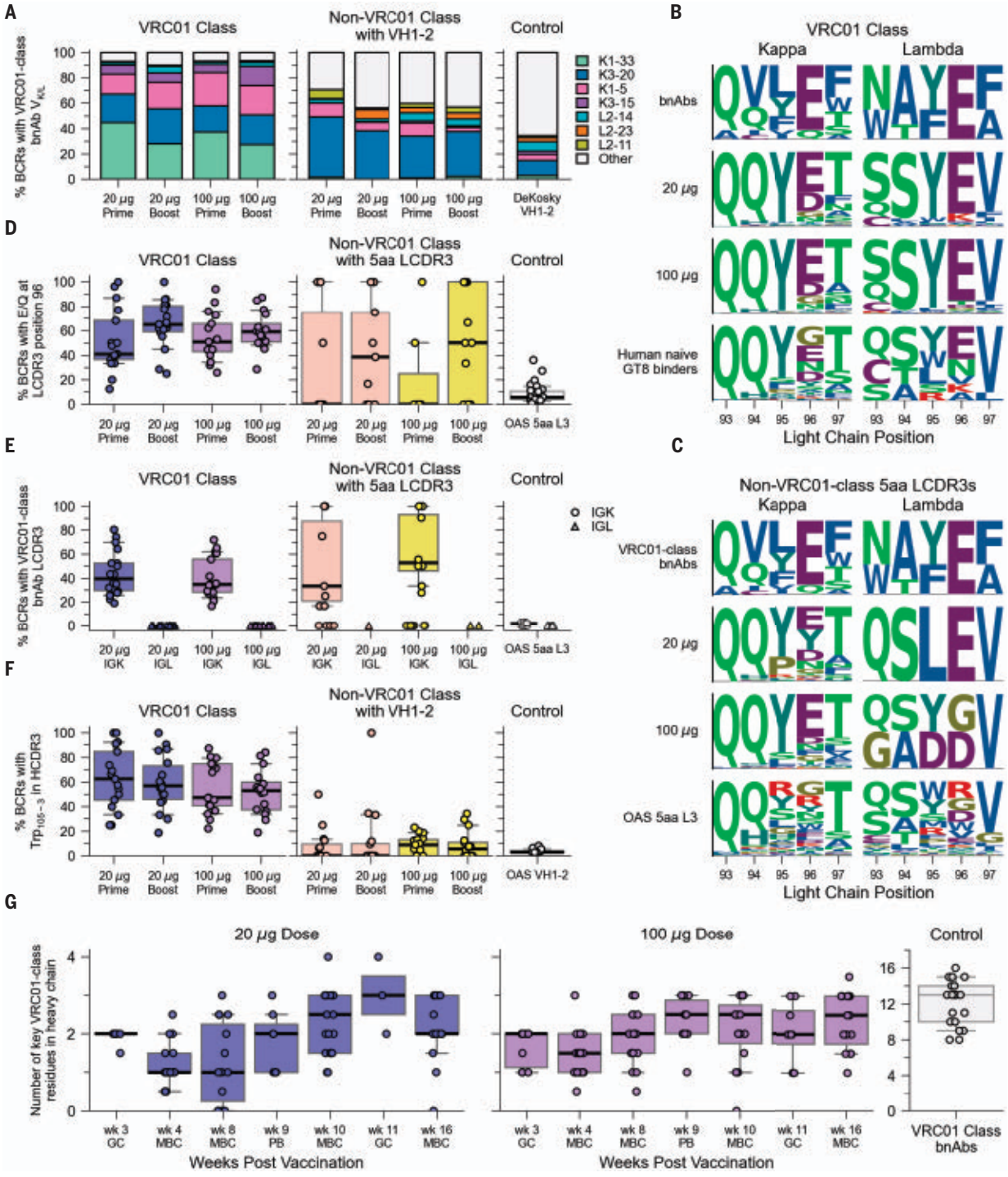


Fig. 6. Properties of postvaccination BCRs shared with VRC01-class bnAbs. (**A**) Percentage of BCRs using VRC01-class bnAb $V_{K/L}$ genes, for VRC01-class and VH1-2-using non–VRC01-class BCRs, and for control VH1-2 BCRs from HIV-unexposed individuals from DeKosky *et al*. (*98*). VRC01-class bnAb $V_{K/L}$ are indicated in the color key. (**B**) Sequence logos for five–amino acid LCDR3s from VRC01-class BCRs for bnAbs (top row), low-dose (second row), high-dose (third row) groups, and human naïve precursors from prior studies (*39*, *43*, *44*) (bottom row), distinguishing kappa (left) and lambda (right) LCs. (**C**) Sequence logos for five–amino acid LCDR3s from non–VRC01-class BCRs from the low-dose (second row) and high-dose (third row) groups, and control data human LCs from HIV-unexposed individuals from the Observed Antibody Space (OAS) (*91*, *92*) (bottom row), with VRC01-class bnAbs (top row) shown for reference, distinguishing kappa (left) and lambda (right) LCs. (**D**) Percentage of BCRs using Glu or Gln at LC position 96, for five–amino acid LCDR3s from VRC01-class BCRs, non–VRC01-class BCRs, and OAS control data LCs (*91*, *92*). (**E**) Percentage of BCRs with LCDR3 matching a VRC01-class bnAb sequence, for five–amino acid LCDR3s from VRC01-class BCRs, non–VRC01-class BCRs, and OAS control data LCs (*91*, *92*), distinguishing IGK and IGL LCs. (**F**) Percentage of BCRs with Trp_{105-3}, for VRC01-class and VH1-2-using non–VRC01-class BCRs and for OAS (*91*, *92*) control data VH1-2 HCs. (**G**) Number of key VRC01-class residues in VRC01-class HCs for all time points in the low-dose (left) and high-dose (middle) groups, with symbols indicating

the 90% quantile per participant per time point, and for VRC01-class bnAbs (right, different *y*-axis scale), with symbols denoting bnAbs. 20 μg, low dose; 100 μg, high dose; prime, data from weeks 3, 4, and 8; boost, data from weeks 9, 10, 11, and 16. In (D) to (G), symbols represent individual participants [except the bnAb controls in (G)]; thick lines indicate median values, boxes show 25 and 75% quantiles, and whiskers approximate 10 and 90% quantiles.

non–VRC01-class responses deriving in part from already mutated memory B cells, but also might have been due to low-affinity, naïve precursor-derived, non–VRC01-class BCRs gaining SHM more rapidly than high-affinity VRC01-class BCRs after the first immunization.

BnAb characteristics shared by vaccine-induced VRC01-class IgG BCRs

Vaccine-induced VRC01-class BCRs shared other characteristic features of VRC01-class bnAbs in addition to the VH1-2 alleles and a five–amino acid LCDR3. VRC01-class bnAbs use a subset of human V_K or V_L genes (data S1), and more than 90% of vaccine-induced VRC01-class IgG BCRs used known bnAb V_K or V_L genes, in both groups after the prime or boost (Fig. 6A and fig. S24A). The LCDR3 is an important site of affinity selection in VRC01-class bnAbs, with all known bnAbs possessing Glu or Gln at position 96, and most bnAbs exhibiting LCDR3 sequence motifs with substantially reduced diversity at several positions compared with naïve VRC01-class precursors (Fig. 6B and data S1) (*21*, *39*, *41*, *43*, *44*, *46*, *55*). LCDR3s from vaccine-induced VRC01-class BCRs showed signs of selection toward bnAb sequences, especially at position 96 (Fig. 6, B to D, and figs. S24B and S25). For VRC01-class BCRs with kappa LCs, the median fraction of LCDR3s perfectly matching a bnAb LCDR3 was 39 or 35% in the low- or high-dose groups, respectively, whereas lambda chain BCRs had no bnAb LCDR3s (Fig. 6E and fig. S24, C and D). Among non–VRC01-class BCRs, a small fraction (1.8%) had five–amino acid LCDR3s, many of which had high similarity to VRC01-class bnAb LCDR3s, whereas control sequences did not (Fig. 6, C to E). This suggested the possibility that eOD-GT8 60mer vaccination might have selected for BCRs using a VRC01-class binding mode with VH genes other than VH1-2, which will be investigated further. Most VRC01-class bnAbs with K3-20 LCs have deletions in LCDR1 important for accommodating the N276 glycan conserved on the HIV spike (*42*, *55*, *56*). We observed K3-20 LCDR1 deletions at rates of 5 to 10% in both VRC01-class and non–VRC01-class BCRs from only a few participants each (fig. S26), indicating that such deletions were not common and were not specifically selected by eOD-GT8, which was not surprising because eOD-GT8 lacks the N276 glycan. VRC01-class bnAbs exhibit a wide range of HCDR3 lengths, from 12 to 18, and nearly all encode a Trp five residues before the end of the HCDR3, a position that we and others have previously inaccurately referred to as "100_B" that we here term "103-5" to count backward from position 103 at the end of the HCDR3 (data S1). $Trp_{103\text{-}5}$ was previously found in ~31% of eOD-GT8–specific human naïve VRC01-class BCRs (*21*, *43*, *44*) (fig. S27). HCDR3 lengths for vaccine-induced VRC01-class BCRs spanned those of VRC01-class bnAbs (fig. S15C), and the percentage of VRC01-class BCR HCDR3s with $Trp_{103\text{-}5}$ had median values over all participants of >47% in both dose groups and after the prime or boost (Fig. 6F and figs. S24E and S27), suggesting enrichment of $Trp_{103\text{-}5}$ due to vaccination. Accounting for combinations of bnAb features, we found that the median fraction of VRC01-class BCRs with four of the above described bnAb features was >25% in both dose groups and after the prime or boost (fig. S28). Finally, we considered the acquisition of key amino acid mutations in the HC, an essential aspect of vaccination to induce bnAbs. From a representative set of 19 potent VRC01-class bnAbs that included all known VRC01-class V_K and V_L genes but also minimized the inclusion of bnAbs with insertions or deletions, we identified a set of 20 positions (19 within VH1-2, plus $Trp_{103\text{-}5}$) at which key VRC01-class residues are observed, four of which are germline-encoded in the VH1-2*02 and *04 alleles compatible with a VRC01-class antibody (data S1). We counted these key VRC01-class residues on a scale ranging from −4 to +16 to allow for all possibilities from losing all germline-encoded key residues to gaining key residues at all 16 positions not containing a germline-encoded key residue. The representative bnAbs had a median of 13 key residues and a range of +8 to +16 (Fig. 6G). We computed 90th percentile values among VRC01-class BCRs in each study participant as representative for the best 20% of BCRs in that individual. The median of 90th percentile values for key HC residues was ≥+2 at nearly all time points at week 8 or later in both the low- and high-dose groups (Fig. 6G). Thus, vaccination selected for the acquisition of important HC residues in VRC01-class BCRs, suggesting that they could be guided toward bnAb activity with further boosting.

BCR affinity dynamics

BCR-antigen affinity influences B cell fate throughout an immune response. To understand how VRC01-class and non–VRC01-class BCR affinities for eOD-GT8 evolved over time, we carried out surface plasmon resonance (SPR) analyses of the interactions between eOD-GT8 monomer and recombinant IgGs corresponding to BCRs from the low-dose vaccine group, including postvaccination BCRs and their inferred-germline (iGL) variants representing naïve precursors (Fig. 7, fig. S29, and data S2).

VRC01-class iGLs had surprisingly high affinities, with a median K_D of 119 nM, ~45-fold higher affinity than the median K_D of 5.3 μM for eOD-GT8–specific human naïve VRC01-class precursors (*21*, *43*) (Fig. 7). The high VRC01-class iGL affinities were not likely due to the presence of affinity-enhancing mutations at CDR3 junctions, because iGL affinities were not higher for parental BCRs with higher SHM levels (fig. S30). Nor were the high VRC01-class iGL affinities due to bias for high affinity in the B cell sorting, because substantially lower-affinity non–VRC01-class BCRs were recovered (Fig. 7). VRC01-class week −4 memory IgG BCRs, which in most cases were not likely to have served as precursors (discussed above), had moderate affinities, with a median K_D of 5.9 μM, in a similar range as naïve VRC01-class BCRs (Fig. 7). Evidently, the vaccine-induced VRC01-class IgG GC and memory B cells that survived GC competition originated predominantly from precursors with the very highest affinities (subset with median K_D of 119 nM) among the naïve VRC01-class precursors.

By contrast, only 43% of non–VRC01-class iGLs had detectable binding (K_D < 100 μM), and the median K_D was the limit of detection of our SPR assay (≥100 μM), ~840-fold lower in affinity than for VRC01-class iGLs (Fig. 7). Non–VRC01-class week −4 memory IgG BCRs also had low affinities, with a median K_D of 16.0 μM, similar in magnitude to the median K_D of 22.8 μM for non–VRC01-class human naïve precursors (Fig. 7). The capacity for low-affinity non–VRC01-class precursors to compete effectively for the CD4bs-specific response against higher-affinity VRC01-class precursors was likely due to the higher non–VRC01-class BCR precursor frequency: Among eOD-GT8 CD4bs-binding naïve BCRs isolated using high-avidity probes to enhance recovery of low-affinity clones, non–VRC01-class are more common than VRC01-class by a factor of ~170 (*44*).

After the first vaccination, VRC01-class affinities increased by an average factor of 4.8 over iGLs, to median K_Ds of 12, 31, and 31 nM in week 3 GC BCRs and week 4 and 8 memory BCRs, respectively (Fig. 7 and fig. S31). Non–VRC01-class median affinities increased by a much larger factor of >833 over iGLs, reaching a median K_D of 120 nM in week 3 GC BCRs, but then declined 40-fold to median K_Ds of 3.7 and 6.0 μM in week 4 and 8 memory BCRs, respectively (Fig. 7 and fig. S31).

After the second vaccination, affinities for VRC01-class memory BCRs increased by a

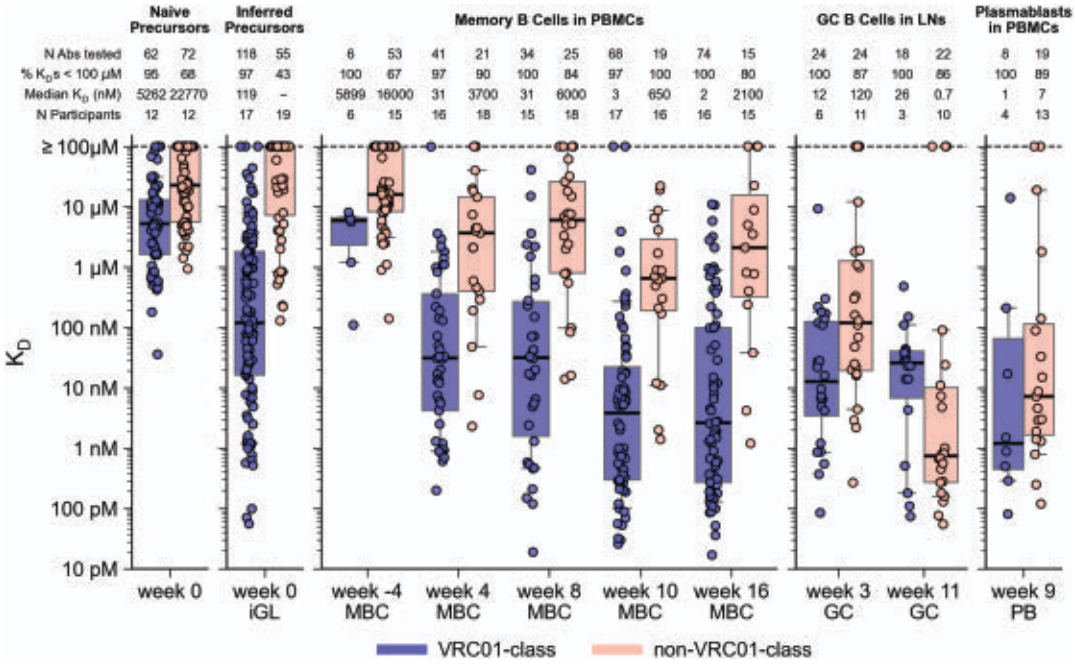


Fig. 7. SPR analysis of BCR affinities for eOD-GT8. Monovalent K_D values for antibody ligands binding to eOD-GT8 monomer analyte for VRC01-class and non–VRC01-class BCRs from the low-dose group postvaccination (weeks 4 to 16) and prevaccination (week −4 and week 0 iGL), and for human naïve BCRs isolated by prior human B cell sorting studies (*21*, *43*) (week 0, far left). Thick lines indicate median values, boxes show 25 and 75% quantiles, and whiskers approximate 10 and 90% quantiles. For median K_D, "–" indicates median ≥100 μM. K_D values were generally representative of multiple measurements. For the 778 K_Ds in this figure, 163 (21%) were measured once, 170 (21.9%) were measured twice, and 445 (57.2%) were measured three or more times.

factor of 12, from a median K_D of 31 nM at week 8 to median K_Ds of 3 and 2 nM at weeks 10 and 16, respectively (Fig. 7). Similarly high affinities were found in PBs at 4 to 8 days after the boost (median K_D of 1 nM). The step-like jump to higher affinities for VRC01-class BCRs in the periphery at weeks 9, 10, and 16 tracked with the step-like increase in mutation levels (Fig. 5, A and C). VRC01-class GC BCRs at week 11 had lower median affinity (K_D of 26 nM), but firm conclusions could not be drawn from that observation because the data were obtained for only three participants (Fig. 7). Non–VRC01-class memory affinities increased by an average factor of 4.4 after the boost, from a median K_D of 6.0 μM at week 8 to median K_Ds of 650 and 2100 nM at weeks 10 and 16, respectively (Fig. 7). Non–VRC01-class PBs (median K_D of 7 nM) and week 11 GC BCRs (median K_D of 0.7 nM) showed substantially higher affinities than memory BCRs at weeks 8, 10, or 16 (e.g., 3000-fold higher at week 11 than week 16), demonstrating that strong and rapid non–VRC01-class affinity maturation occurred in response to the week 8 boost, but the resulting high-affinity BCRs either remained within GCs or populated the plasma compartment rather than the memory compartment. Thus, affinity maturation of the memory pool in response to the boost was more efficient for VRC01-class than non–VRC01-class B cells.

Overall, VRC01-class precursor BCRs started with a massive affinity advantage over CD4bs-specific, non–VRC01-class precursor BCRs (ratio of median K_Ds for iGLs ≥840); this advantage declined but remained high after the first vaccination (ratio of median K_Ds at week 8 equal to 194) and then increased again after the boost (ratio of median K_Ds at week 16 equal to 1050). VRC01-class affinity gains were associated with both increased on rates and decreased off rates, but off-rate reduction was the larger effect (figs. S32 and S33). Thus, although B cell selection in the GC might occur under high avidity conditions (i.e., an array of BCRs on the surface of a B cell interacting with an array of eOD-GT8 60mer antigens on a follicular dendritic cell), the process nevertheless selected BCRs with improvements in monovalent K_D as well as on and off rate, perhaps by follicular dendritic cells regulating antigen availability (*57*). VRC01-class affinities and on rates both increased significantly with SHM, and off rates decreased significantly with SHM, across all postvaccination BCRs (P values for K_D, on-rate (k_{on}), and off-rate (k_{off}), respectively, are <0.001, 0.0003, and <0.0001) and in memory B cells at each time point (figs. S34 to S36), indicating that SHM contributed to maintaining the VRC01-class affinity advantage over time.

Guiding SHM

A key requirement for germline-targeting priming immunogens is the induction of bnAb-precursor-derived GC and/or memory B cells capable of binding antigens that are more similar to the native viral glycoprotein (native-like) than the priming immunogen within the target epitope (*13*, *39*). This is necessary so that a more native-like immunogen can serve as a boost to advance B cell maturation further toward bnAb development. eOD-GT8 was designed to have an "affinity gradient," with stronger binding to bnAbs than to bnAb precursors, based on the hypothesis that if bnAb precursors could be primed, the affinity gradient would guide early SHM toward bnAb development and concomitantly induce bnAb-precursor-derived responses that bind to more native-like antigens (*13*, *21*, *39*). As a result, eOD-GT8 possesses a strong affinity gradient for VRC01-class BCRs, with ~230-fold higher affinity for bnAbs than for naïve precursors (*21*, *43*). To determine if eOD-GT8 60mer immunization selected for VRC01-class BCRs that bind more native-like immunogens, we first tested binding of ≥210 VRC01-class memory BCRs from the low dose group from weeks 4, 8, 10, and 16 to a native-like trimer [BG505 MD39 (*22*)] and a core-gp120 lacking the N276 glycan [core-e-2CC HxB2 N276D (*39*)]. We detected no trimer binding even at the highest trimer analyte concentrations tested (11 μM), even though the trimer analyte allowed for avidity in binding, but ~10% of the antibodies tested from weeks 10 and 16 showed weak binding to core-gp120 (fig. S37). We then tested binding of VRC01-class iGL and postvaccination low-dose–group BCRs to eOD-GT6 (*13*) and four variants of eOD-GT6, each of which had a more native-like CD4bs compared with that of eOD-GT8 (fig. S38). Previous work demonstrated that eOD-GT6 had no detectable affinity for the vast majority of human naïve VRC01-class precursors that bind eOD-GT8, which was explained by the fact that eOD-GT6 lacks several germline-targeting mutations that are present in eOD-GT8 (*21*). Consistent with that prior finding, we found here that eOD-GT6 and its four variants had very limited reactivity to VRC01-class iGL precursors. Whereas

eOD-GT8 bound to 97% of iGLs with a median K_D of 119 nM (Fig. 7), eOD-GT6 and its variants bound to only 2 to 39% of the iGLs and had median K_Ds of ≥100 μM (Fig. 8A). However, postvaccination VRC01-class antibodies showed improved binding for eOD-GT6 and its variants, especially after the boost. For example, eOD-GT6 bound to 78% of BCRs tested at week 16, with an overall median K_D of 6 μM (Fig. 8A), and the four more-native-like variants of eOD-GT6 (GT6v2, GT6v3, GT6v4, and GT6-N276+ with an intact N276 glycosylation site) bound to 75, 29, 24, and 30% of BCRs tested at week 16, respectively, in comparison to binding 39, 17, 2, and 5% of iGLs, respectively (Fig. 8A). Thus, vaccination with eOD-GT8 60mer not only induced VRC01-class responses, but also selected for mutations in VRC01-class BCRs that conferred affinity for antigens with more-native-like CD4bs epitopes. Postvaccination non–VRC01-class antibodies showed substantially weaker binding to eOD-GT6 and variants (fig. S39) compared with VRC01-class antibodies (Fig. 8A), demonstrating that eOD-GT8 60mer vaccination also minimized the induction of competing responses capable of binding more native-like CD4bs epitopes. Finally, VRC01-class affinities for eOD-GT6 and all but one variant increased with affinities to eOD-GT8 (*P* values for eOD-GT6, GT6v2, GT6v3, GT6v4, and GT6-N276+, respectively, are <0.0001, <0.0001, 0.0002, 0.3809, and 0.008; Fig. 8B). Therefore, higher affinity for eOD-GT8 translated into higher affinity for more native-like antigens, providing support for the hypothesis that engineering an affinity gradient into a germline-targeting priming immunogen can help guide SHM selected by that immunogen (*13*). Our data also support the applicability of that hypothesis to boost immunogens, as previously proposed (*26*).

Discussion

Learning how to induce broadly neutralizing antibodies against pathogens with high antigenic diversity, such as HIV, influenza, hepatitis C virus, or the family of betacoronaviruses, represents a grand challenge for rational vaccine design. Germline-targeting vaccine design offers one potential strategy to meet this challenge. The strategy is predicated on the design of priming immunogens that consistently induce responses from rare bnAb-precursor B cells with predefined BCR features, select for at least a modicum of productive BCR maturation, and generate a pool of GC and/or memory B cells likely to be susceptible to boosting by more native-like immunogens. Here, in the first test of this strategy in humans, we found that the eOD-GT8 60mer/AS01$_B$ germline-targeting vaccine prime had an acceptable safety profile and induced the targeted VRC01-class IgG B cells with substantial frequencies in blood and lymph nodes consistently across vaccine recipients. We further demonstrated that the vaccine selected for bnAb-like BCR properties and favorable maturation and consequently generated B cells with capacity to bind less-engineered and more-native-like forms of the CD4bs epitope. These findings establish clinical proof of concept for germline-targeting priming, support developing boost regimens to induce VRC01-class bnAbs, and encourage extending the strategy to other targets in HIV and other pathogens.

Developing germline-targeting priming immunogens for other classes of antibodies will be more challenging owing to the HCDR3 dominance of most antibodies that is not observed for VRC01-class bnAbs, but a generalized method for designing such immunogens has been described (*25*). Deploying the germline-targeting strategy effectively for other antibody classes will require knowledge of population

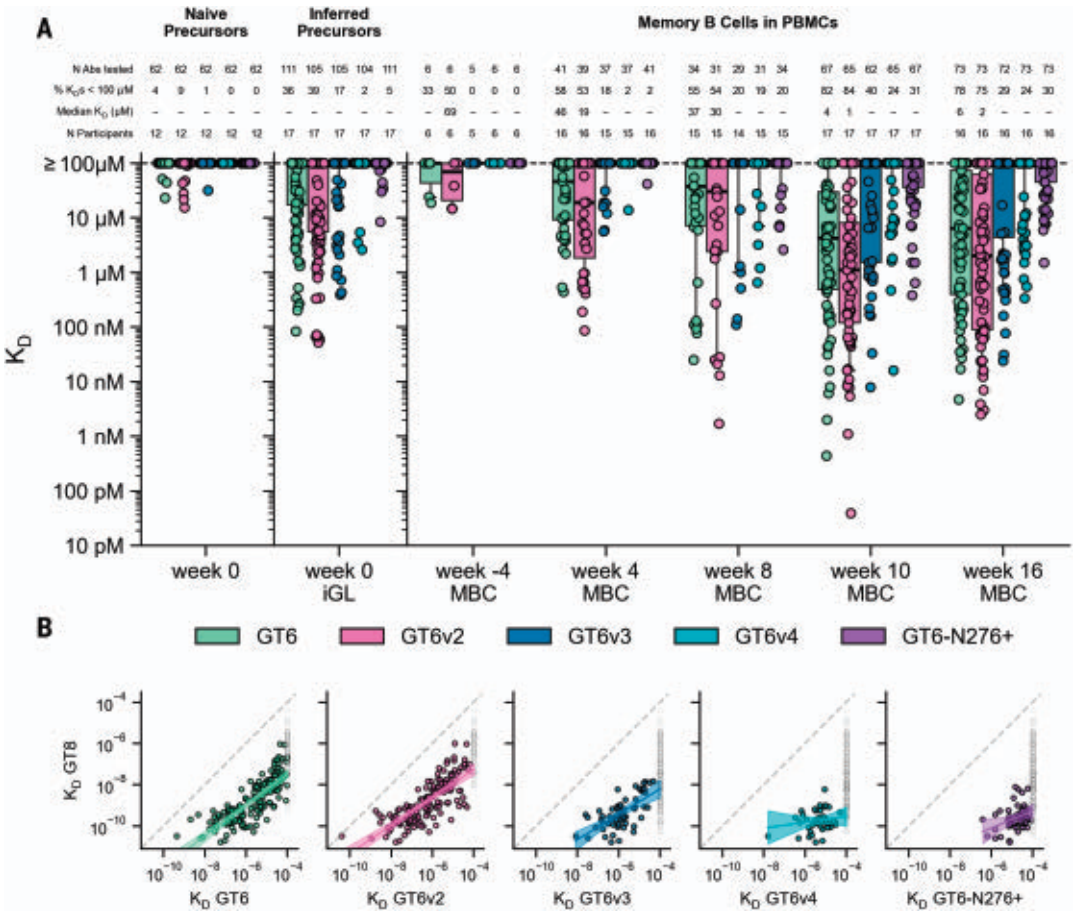


Fig. 8. SPR analysis of VRC01-class BCR affinities for eOD-GT6 and variants. (**A**) Monovalent K_D values for VRC01-class antibody ligands binding to monomeric eOD-GT6 and eOD-GT6 variant analytes (described in fig. S38) for memory BCRs from the low-dose group postvaccination (weeks 4 to 16) and prevaccination (week −4 and week 0 iGL) and for human naïve BCRs isolated by prior human B cell sorting studies (*21*, *43*) (week 0, far left). Thick lines indicate median values, boxes show 25 and 75% quantiles, and whiskers approximate 10 and 90% quantiles. For median K_D, "–" indicates median ≥100 μM. For the 1321 K_Ds in (A), 1171 (88.6%) were measured once, 48 (3.6%) were measured twice, and 102 (8.7%) were measured three times. (**B**) K_D for eOD-GT8 versus K_D for eOD-GT6 and variants, with estimated regression lines shown as solid lines and 95% confidence prediction intervals indicated by shading. Dashed lines indicate equality of K_D values. Regressions were restricted to K_Ds <100 μM. K_Ds ≥100 μM for eOD-GT6 and variants are shown in gray. S, slope of regression line; P, *P* value for slope; ns, not significant (*P* > 0.05).

frequencies of any required gene alleles, analogous to the VH1-2 *02 and *04 alleles here, as well as frequencies of recombination events that produce potential bnAb precursors, analogous to the production of five–amino acid LCDR3s here.

Our BCR sequence hierarchical clustering analysis showed that VRC01-class responses derived from many independent recombination events in each participant. Thus, the ability to prime VRC01-class responses consistently across vaccine recipients was due in part to the immunogen having affinity for diverse VRC01-class precursors. Explicit engineering of priming immunogens with affinity for diverse precursors is one of the hallmarks of germline-targeting vaccine design that distinguishes this approach from others.

The robust serological and B cell immunogenicity observed here, especially the substantial frequencies of eOD-GT8– and CD4bs epitope–specific IgG memory B cells in PBMCs after only one or two vaccinations, was likely due largely to the combination of a high-valency, glycosylated nanoparticle immunogen with a strong adjuvant (*13*, *39*, *47*, *58*). The strong immune responses and acceptable reactogenicity support the use of adjuvanted self-assembling nanoparticle vaccines in humans.

A major challenge for priming and maturation of responses from rare bnAb-precursor B cells is the competition from higher-frequency non-bnAb B cells that can engage the same epitope (*25*–*27*, *39*, *45*–*49*). Here, VRC01-class responses remained in the minority of CD4bs-directed responses at all time points after prime and boost but nevertheless maintained high positivity and exhibited favorable maturation. Our BCR sequence and affinity analyses provide insights into how that was achieved. The affinities required for priming of rare bnAb precursors were relatively high (81% were better than 3 μM and 50% were better than 119 nM) and orders of magnitude higher than for competitors, and the responses were derived predominantly from naïve B cells. Furthermore, the germline-targeting priming immunogen was able to (i) select B cells encoding bnAb-like properties beyond the properties specifically targeted; (ii) stimulate previously matured GC and/or memory B cells by a booster immunization, leading to increased SHM and affinity of bnAb-precursors in the memory pool, with weaker increases for competitors; (iii) maintain a large affinity advantage for bnAb-precursors over competitors; and (iv) guide affinity maturation in bnAb-precursors toward bnAb development, likely by presenting an affinity gradient. Successful priming and boosting of bnAb-precursor B cells with such a multifaceted set of desirable outcomes, even while the targeted cells remained in the minority of epitope-specific B cells, suggests that design of immunogens with appropriate affinities and affinity gradients can circumvent B cell competition as a barrier to steered maturation of bnAb-precursor responses. These findings provide support not only for the concept of germline-targeting priming but also for the broader concept of sequential vaccination to guide evolution of targeted responses.

Our finding that VRC01-class responses derived mostly from precursors with affinities better than 3 μM provides a potential benchmark for other germline-targeting efforts and accords with preclinical mouse model data on eOD-GT8 60mer and analogs (*47*–*49*), supporting the use of such models to predict human responses. Our data on VRC01-class and non-VRC01-class precursor affinities support the hypothesis that relatively high affinities are required for consistent priming of low-frequency precursors, even for highly multivalent nanoparticle immunogens (*13*, *21*, *25*, *39*), and also support the claim that precursor frequency and affinity are interdependent for determining B cell competitive fitness in GCs (*47*–*49*, *59*). Given that interdependence, it will be important to determine whether consistent priming by germline-targeting immunogens for lower-frequency HCDR3-dominant bnAb-precursors (*25*) will require even higher affinities than those observed here.

A germline-targeting vaccine prime should generate as large a pool of bnAb-like memory B cells as possible to facilitate successful boosting by a more native-like immunogen. Prior human naïve B cell sorting revealed that the frequency of VRC01-class B cells that bind eOD-GT8 with affinities better than 3 μM was ~1 in 900,000 among all human naïve B cells (*21*, *43*). Here, we estimated that for the 81% of VRC01-class responses to eOD-GT8 60mer derived from precursors with affinities better than 3 μM, the expansion from naïve B cells to IgG memory B cells was ~37-fold at week 8 (after one vaccination) and 250-fold at week 16 (after two vaccinations), averaging responses from the low- and high-dose groups. These expansion levels provide benchmarks for other germline-targeting priming vaccines. The expansion after one vaccination observed here was substantially stronger than the expansions into memory measured in five different mouse models with human naïve VRC01-class precursors with affinities better than 3 μM and frequencies of either 1 in 1 million [two models, HuGL18 and HuGL17, with 2-fold expansion and >100-fold contraction, respectively (*48*)] or 1 in 10,000 [three models, CLK21, CLK19, and CLK09, with expansions of about 2.5-, 4.0-, and 5.5-fold, respectively (*49*)]. Hence even precisely calibrated mouse models can underestimate the degree to which human germline-targeting vaccines can induce bnAb precursor–derived memory B cell responses, which should be considered when evaluating other priming immunogens in preclinical experiments. A thorough and detailed comparison of the multidimensional human data from this trial (frequencies, SHM, bnAb properties, affinities) with the results of the many mouse models applied to eOD-GT8 60mer vaccination is warranted and may assist the selection and design of models that optimally predict human responses.

A key hypothesis underlying the germline-targeting vaccine design strategy is that sequential vaccination with increasingly more-native-like boost immunogens will be capable of inducing bnAb development by driving bnAb-precursor B cells to undergo repeated rounds of affinity maturation. This could be achieved if each boost stimulated memory B cells to return to GCs and/or supplied new antigen to existing GCs. Raising questions about the practicality of generating sufficient mutation by sequential immunization, results from mouse studies with model antigens indicated that stimulation of previously matured IgG memory B cells generally induces differentiation to antibody-secreting cells rather than GC reentry for further affinity maturation (*60*–*63*) and may suffer from clonality bottlenecks (*60*). Furthermore, repeated immunization with the same antigen was found to increase the number of memory B cells but not significantly increase SHM levels or affinities (*61*). Conversely, sequential immunization with different immunogens can increase SHM of bnAb-precursor memory B cells in knockin mouse models (*23*, *29*), and repeated boosting with HIV trimers in NHPs or with severe acute respiratory syndrome coronavirus 2 (SARS-CoV-2) mRNA vaccines in SARS-CoV-2–naïve humans can increase SHM in antigen-specific memory B cell populations (*64*–*66*). Our human vaccination data showed that for VRC01-class responses, mutation levels and affinities in IgG memory BCRs increased after the boost, and polyclonality remained high after prime and boost. Thus, our data suggest that maturation of human B cells toward bnAb development by sequential vaccination remains plausible, especially considering that heterologous boosting should generate more mutation and diversification than the autologous boost studied here. In the future, it will be important to define the relative contributions of memory B cell reentry to GCs versus antigen refueling of GCs to sequential-vaccination-induced B cell maturation in humans. The degree to which one mechanism or the other dominates could have implications for optimizing design of boosting or shepherding immunogens and regimens and for developing strategies to monitor responses in clinical trials and preclinical models.

With efficient priming of VRC01-class responses established, major challenges remain ahead for sequential vaccination to shepherd these responses to bnAb development. The critical step will be to induce B cells that can

bind fully native trimers with the N276 glycan intact. Succeeding at that step will likely require first taking one or more smaller steps to advance the maturation of VRC01-class bnAb precursor–derived B cells to enable binding to increasingly more-native-like forms of the CD4bs (*26*–*29*, *56*), consistent with our SPR data showing that VRC01-class BCRs induced by eOD-GT8 60mer lack detectable affinity for a native trimer but do show at least low affinity for core-gp120 or eOD-GT6 variants. VRC01-class and non–VRC01-class BCRs induced by eOD-GT8 60mer should be helpful for identifying candidates for the first heterologous boost.

The consistent VRC01-class bnAb precursor priming demonstrated here represents an unprecedented level of vaccine control over the specificity of humoral responses and, as such, may herald a new era of precision vaccine design for HIV and other pathogens. By defining desired B cell responses at the molecular level, the germline-targeting vaccine design approach allows for a highly reductive and iterative design cycle to optimize vaccine discovery and development.

Materials and methods

Study design

IAVI G001, with ClinicalTrials.gov registry number NCT03547245, was a phase 1, randomized, double-blind, placebo-controlled dose escalation study to evaluate the safety and immunogenicity of eOD-GT8 60mer vaccine adjuvanted with $AS01_B$ in HIV-uninfected, healthy adult volunteers. Two doses of 20 μg or 100 μg eOD-GT8 60mer with $AS01_B$ or two doses of placebo were given by deltoid intramuscular injection 8 weeks apart, with both immunizations given to the same arm. Placebo was the buffer used in the vaccine: DPBS containing 10% sucrose at pH 7.5. The consort diagram is shown in fig. S1.

The primary objectives of the study were to evaluate the vaccine for safety and tolerability and the capacity to induce Immunoglobulin G (IgG) B cell responses from rare precursors for VRC01-class bnAbs. The primary end points were the occurrence of adverse events, and the secondary endpoint was induction of eOD-GT8 60mer-specific, eOD-GT8 monomer-specific and CD4-binding-site (CD4bs)-specific serum binding antibody responses. The detection of VRC01-class responses in IgG memory B cells, IgG GC B cells, and plasmablasts were exploratory end points but nevertheless were the critical immunological readouts to judge vaccine efficacy. Additional exploratory immunological analyses included (i) assessing the relative frequencies of the VRC01-class BCRs and competitors; (ii) measuring the changes in somatic hypermutation and eOD-GT8 binding affinities over time for both types of BCRs; (iii) evaluating a wide array of properties of the VRC01-class BCRs, to assess the potential for the BCRs to mature into bnAbs; and (iv) assessing the binding of VRC01-class and competitor BCRs to antigens with CD4bs epitopes closer to native HIV Env compared to the vaccine.

Participants and randomization

Eligible participants were healthy male and female adults aged 18 through 50 years of age who were willing to undergo HIV testing, use an effective method of contraception, understood the study in the opinion of the investigator or designee, and provided written informed consent. Forty-eight participants who met all eligibility criteria were included in the study and were randomly assigned to receive vaccine or placebo within one of two groups. Group 1 included 18 low dose (20 μg) vaccine recipients and 6 placebo recipients, and Group 2 included 18 high dose (100 μg) vaccine recipients and 6 placebo recipients. Twenty-four participants were enrolled at each of two clinical sites: George Washington University (GWU) and Fred Hutchinson Cancer Center (FHCC). There was no attempt to match the participants for any demographic category among the three study groups or between the two clinical sites. Participant demographics are given in table S1. Among enrolled participants, for sex at birth, approximately equal numbers were male (25/48; 52.1%) and female (23/48, 47.9%); the predominant race reported was White (33/48, 68.8%), with Asian and Multiracial (each at 5/48, 10.4%) being the next highest race categories reported. The ethnicity of "Not Hispanic and Not Latino" was reported for the majority of the participants (42/48, 87.5%). The median age and body mass index were 27 years and 25.6 kg/m^2, respectively.

Oversight

The trial was conducted under an Investigational New Drug (IND) application submitted to the US Food and Drug Administration, and was carried out in compliance with the protocol filed within the IND. The trial adhered to IAVI standard operating procedures in accordance with the guidelines formulated by the International Committee on Harmonization for Good Clinical Practice in clinical studies, and complied with applicable local standards and regulatory requirements including review and approval by the institutional review boards at FHCC and GWU. The trial was overseen by a protocol safety review team and independent safety monitoring committee.

Blinding

Study site investigators, staff and volunteers were blinded in terms of vaccine versus placebo. An unblinded study pharmacist at each site was responsible for vaccine preparation and accountability. Staff carrying out immunological assays were blinded. Staff carrying out bioinformatic and statistical analyses were unblinded, which enabled analyses to be carried out during the trial and led to early planning and preparation for follow-on trials (IAVI G002, ClinicalTrials.gov Identifier: NCT05001373; and IAVI G003, NCT05414786).

Safety and tolerability monitoring

Safety and tolerability were monitored during the trial by site investigators, the IAVI medical monitor and the protocol safety review team. The safety and tolerability of the vaccine were evaluated by the safety monitoring committee for, at minimum, the first 14 days after the first vaccination for all participants in the low dose group (group 1) before escalating to the higher dose level (group 2). Participants were followed up to 12 months after the final investigational product administration. Adverse events (AEs) were grouped by Medical Dictionary for Regulatory Activities Terminology (MedDRA) System Organ Class (SOC) and Preferred Term (PT). All AEs were graded for the entire duration of the study, using the National Institutes of Allergy and Infectious Diseases (NIAID) Division of AIDS (DAIDS) Table for Grading the Severity of Adult and Pediatric Adverse Events, Version 2.1, July 2017.

Immunological assays

Serum antibody binding responses were assessed by binding antibody multiplex assay (BAMA), and serum antibody neutralization was assessed using TZM-bl neutralization assays. Frequencies of antigen-specific and CD4bs epitope-specific B cells were assessed by fluorescence-activated cell sorting (FACS). The primary immunological readout, the induction of VRC01-class IgG B cells, was assessed by CD4bs-specific single B cell sorting, B cell receptor (BCR) sequencing, and bioinformatic analysis. Polyclonality and genetic diversity of VRC01-class IgG BCR responses were assessed by bioinformatic analysis including hierarchical sequence clustering.

Definition of CD4bs-specific responses

Assessment of serum or B cell binding to the eOD-GT8 CD4bs epitope was determined by differential binding to eOD-GT8 and eOD-GT8-KO11, a variant of eOD-GT8 with three mutations in the CD4bs (N280R, S365L, and F371R in HxB2 numbering) that essentially abrogates binding by VRC01-class precursor Abs and VRC01-class bnAbs (*43*, *46*–*49*). In SPR experiments, we measured no detectable binding to multiple VRC01-class human naïve precursors and bnAbs at concentrations up to 30 μM of eOD-GT8-KO11 (not shown). eOD-GT8-KO11 was originally referred to as eOD-GT8-KO2 (*43*, *46*, *47*) but has subsequently been referred to as eOD-GT8-KO11 (*48*, *49*). Additional details on how the eOD-GT8 and

eOD-GT8-KO11 antigens were employed for BAMA and B cell sorting are provided below.

Power analysis and rationale for trial size

Group sizes for the study were selected to measure the primary hypothesis that the vaccine will induce VRC01-class IgG B cells with a response rate of at least 50% in at least one of the adjuvanted protein vaccine arms, as well as to satisfy the need to have enough end points for further characterization of that response. We powered the study to have high probability of observing at least five participants with a vaccine-induced VRC01-class IgG B cell response among participants receiving eOD-GT8 60mer in study group 1 or 2 given that the true response rate for this class of B cells was at least 50% or greater among eOD-GT8 60mer recipients in either arm. We assumed a dropout rate of approximately 10%, which translated into an assumption that immunogenicity samples would be obtained from $N = 16$ recipients of eOD-GT8 60mer in each of groups 1 and 2. Under those assumptions, we determined that at least five positive responders for VRC01-class B cells would be required for the 95% confidence interval (CI) about the observed rate to be consistent with a true rate of 50%, because the 95% CI for an observed rate of 5/16 = 31.25% is 14.2 to 55.6%. Furthermore, power was 96.2% to detect five or more positive responders out of 16 when the true rate of response was 50% (fig. S40).

Vaccine and adjuvant

eOD-GT8 60mer was manufactured in accordance with current Good Manufacturing Practice (cGMP) regulations at Paragon BioServices, Inc (Baltimore, MD), as described in detail elsewhere (*40*). In summary, cGMP manufacture was accomplished by a combination of purification techniques following transient expression in suspension-adapted, cGMP-qualified VRC293 human embryonic kidney 293 (HEK293) cells generated at SAFC (Carlsbad, CA) from a Master Cell Bank generously provided by the National Institutes of Health (NIH) Vaccine Research Center (VRC) within the National Institute of Allergy and Infectious Diseases (NIAID). VRC293 cells were grown in serum-free Expi293 medium (Thermo Fischer), transfected with plasmid DNA encoding eOD-GT8 60mer (cGMP manufactured by Aldevron; Fargo, ND) and Polyethylenimide PEIpro-HQ transfection reagent (cGMP manufactured by PolyPlus-Transfection SA; Illkirch, France), and expression was carried out in the presence of 14 μM Kifunensine (cGMP manufactured by GlycoSyn; Graceville, New Zealand). Benzonase endonuclease enzyme (high-purity grade, 250 U/μl, from Millipore; Burlington, MA, USA) was employed to remove residual host cell and plasmid DNA. The eOD-GT8 60mer cGMP clinical material was formulated at 1 mg/ml in 10% sucrose in phosphate-buffered saline (PBS) at pH 7.2, aliquoted at 0.4 ml volume in 2 ml type 1 glass vials with stoppers (13 mm stopper, Rubber with Flurotec, Afton Scientific), sealed with sterile seals from Afton Scientific Corporation (Charlottesville, VA), and stored at −80°C. The material is currently on a stability testing program as per regulatory guidelines (stable for >36 months).

Quality control procedures were performed on the manufactured eOD-GT8 60mer nanoparticle to confirm its identity, determine protein concentration and purity, establish in vitro potency, measure the nanoparticle size, and characterize N-linked glycans. Additionally, the clinical trial lot was tested to quantify host cell residual impurities (host cell proteins and host cell DNA), measure bioburden and bacterial endotoxin, determine subvisible particulate matter, and confirm sterility. Quality control procedures included sandwich ELISA with GL-VRC01 for potency; high pressure liquid chromatography (HPLC) with tandem mass spectrometry (MS/MS) to confirm amino acid sequence; N-terminal Edman sequencing for further sequence confirmation; size exclusion chromatography (SEC) to assess purity; sedimentation velocity analytical ultracentrifugation (AUC-SV) for particle size distribution; dynamic light scattering (DLS) for average particle size; and hydrophobic interaction liquid chromatography coupled to mass spectrometry (HILIC-FLD-MS/MS) for N-linked glycan profiling. eOD-GT8 60mer cGMP material had full glycan occupancy at only 5 of 10 glycosylation sites and had partial occupancy at three sites (*40*). Preclinical material that performed well in mouse models had full glycan occupancy at three sites and partial occupancy at four sites (*43*).

$AS01_B$ adjuvant is an adjuvant system composed of two immunoenhancers combined in a liposomal formulation consisting of dioleoyl phosphatidylcholine (DOPC) and cholesterol in phosphate-buffered saline solution. The immunoenhancers are (i) 3-*O*-desacyl-4′-monophosphoryl lipid A (MPL), a derivative of lipopolysaccharide from the Gram-negative bacterium *Salmonella minnesota*, and (ii) a saponin molecule (QS-21) purified from the bark of the tree *Quillaja saponaria* Molina. $AS01_B$ was manufactured and provided by GlaxoSmithKline Biologicals (Rixensart, Belgium). QS-21 was licensed by GSK from Antigenics LLC, a wholly owned subsidiary of Agenus Inc. (Delaware, USA). The administered dose of $AS01_B$ corresponded to 50 μg each of MPL and QS-21.

DPBS with 10% sucrose was manufactured by SAFC Biosciences.

Study procedures

Vaccine preparation

Vaccine was diluted to the appropriate dose and mixed with adjuvant just prior to administration. For group 1, the low dose (20 μg) group, eOD-GT8 60mer investigational product (IP) was first diluted 1:5 with DPBS Sucrose; then 0.15 ml of this diluted IP was transferred into a vial containing 0.65 ml $AS01_B$; and finally, after gentle inversion to mix, 0.6 mL was withdrawn into a syringe and administered as an injection in the deltoid muscle of the nondominant arm. For group 2, the high dose (100 μg) group, 0.15 ml of eOD-GT8 60mer IP was transferred into a vial containing 0.65 ml $AS01_B$, and after gentle inversion to mix, 0.6 ml was withdrawn into a syringe and administered as an injection in the deltoid muscle of the nondominant arm. For all placebo assignments, 0.6 ml of DPBS sucrose was withdrawn into a syringe and administered as an injection in the deltoid muscle of the nondominant arm. Vaccine or placebo were administered at day 0 and week 8 (day 56 ± 7); for each participant, the first and second injections were administered in the same arm.

Schedule of procedures

The full schedule of procedures is given in table S2.

Safety and tolerability

Weekly follow-up visits were scheduled for study weeks 1 to 4 and 9 to 11, and additional follow-up visits were scheduled for weeks 16, 20, 32, and 56. Participants recorded local and systemic reactogenicity using a memory aid from day 0 through day 7 after vaccination. At each vaccination visit, vital signs were measured by study staff prior to vaccination and at least 30 min postvaccination. Unsolicited adverse events (collected through open-ended questions) were collected from day 0 through 28 days after the second (final) vaccination. Serious adverse events, medically attended adverse events and potential immune-mediated diseases (pIMDs) were collected during the entire study period through 12 months after the second dose administration. Potential immune-mediated diseases were a subset of adverse events that included autoimmune diseases and other inflammatory and/or neurologic disorders of interest which may not have had an autoimmune etiology.

Immunological sample collection and storage

Leukapheresis was performed at two time points, once during screening at week −4 and once at study week 10 (approximately 14 days after the second vaccination). Peripheral blood mononuclear cells (PBMC) were collected at weeks −4, 4, 8, 10, and 16 after the first vaccination by leukapheresis or by venipuncture (whole blood with ACD anticoagulant) and were isolated by density gradient centrifugation and cryopreserved as aliquots of 20×10^6 or 50×10^6 cells. Separately, PBMC aliquots

obtained by a single leukapheresis from an unvaccinated HIV-negative volunteer served as an internal negative control for flow cytometry panel and probe staining for every experiment. Ultrasound-guided fine needle aspirations (FNAs) of axillary lymph node(s) were performed at two time points, approximately 21 days after each vaccination. The procedure was performed by a board-certified radiologist using ultrasound guidance to avoid needle insertion into any adjacent structures. Plasmablast samples (10 ml PBMCs) were collected at week 9 (5 to 8 days after the second vaccination). Lymph node (LN) FNA and plasmablast samples were stored on wet ice but were not frozen before being subjected to cell sorting analyses within 24 hours of collection.

Fine needle aspiration from draining axillary lymph nodes

Aspirates were collected from the draining axillary lymph nodes by fine needle aspiration (FNA) at weeks 3 and 9. Ultrasound was used to visualize the axillary lymph nodes on the same side as the site of the most recent vaccination for lymph node sampling. Following site-specific standard FNA procedures, the overlying skin was swabbed generously with chlorhexidine, betadine, or similar skin disinfectant solution, and 1% lidocaine was injected subcutaneously as local anesthetic. A 22-gauge lumbar puncture needle attached to a 5 ml sterile syringe was then inserted into the largest and most accessible lymph node, and negative pressure was applied by withdrawing the syringe lunger approximately 2 to 3 ml while collecting sample over a 30 s period of "to and fro" needle movement, or until first appearance of blood in syringe. Immediately after withdrawal of each needle from the study participant, syringe and needle contents were expelled into a 50 ml conical tube containing R10 media, flushing out any remaining cells out of the syringe by detaching the lumbar needle from the syringe, withdrawing approximately 2 to 3 ml of fresh R10 media into the syringe barrel, reattaching it to the needle, and expelling the media into the 50 ml conical tube; this flushing procedure was repeated a total of four times for each aspiration. The collection was repeated up to four times for each study participant, using a new sterile needle and syringe for each pass. After collection, the sample was transported to the laboratory on wet ice or cold packs as soon as possible. Lymph node FNA samples ranged in recovery from very few cells up to 4×10^7 cells (median recovery varied between sites from 2.4×10^6 to 4.7×10^6).

Preparation of lymphocytes from fine needle aspirates from axillary lymph nodes

The 50 ml conical FNA sample was spun at $325 \times g$ for 10 min at 4°C (no brake). Supernatant was gently aspirated with a serological pipet down to about 500 μl. If the cell pellet had any redness, cells were resuspended in 5ml of cold 1× red blood cell (RBC) lysis buffer (eBioscience) and incubated for 5 min at ambient temperature while agitating the sample by gently pipetting up and down periodically with a P1000 pipette or using a tube rocker. Cells were washed with 40 ml of cold 10% FBS/1×PBS. Samples were centrifuged at $325 \times g$ for 10 min at 4°C. Supernatant was gently aspirated with serological pipette and the cell pellets were resuspended with 2 ml of cold 10% FBS/1×PBS. Cell numbers and viability of the sample were determined using a hemocytometer, Muse cell analyzer, or Nexcelom Auto 2000.

Production of protein reagents for immunological assays

Reagents for B cell sorting

Avi-tagged and biotinylated versions of eOD-GT8 monomer (*21*, *39*) and eOD-GT8-KO11 monomer (different than the original eOD-GT8-KO) (*43*, *46*) were produced by a cGLP lab under contract at Scripps Research. These proteins were produced as previously described (*13*) in FreeStyle 293F (Invitrogen) suspension cultures by transient transfection using 293Fectin (Invitrogen) of a pHLSec plasmid containing mammalian codon-optimized eOD with a C-terminal His6× affinity tag followed by an Avi tag. Protein was harvested from the supernatant after 5 days and purified by affinity chromatography with a HIS-TRAP column (GE Healthcare) followed by Superdex 75 size exclusion chromatography (GE Healthcare) using an AKTA chromatography system (GE Healthcare). Biotinylation was accomplished using BirA (Avidity), and the level of biotinylation was estimated by PAGE.

Reagents for BAMA

Avi-tagged eOD-GT8 monomer was produced as described above. Non-avi-tagged eOD-GT8-KO11 monomer was produced following similar methods but was produced in the Schief lab at Scripps Research. eOD-GT8 60mer for BAMA assays was also produced in the Schief lab, in FreeStyle 293F (Invitrogen) suspension cultures by transient transfection using 293Fectin (Invitrogen) of a pHLSec plasmid containing mammalian codon-optimized eOD-GT8 60mer. Protein was harvested from the supernatant after 5 days and purified by lectin chromatography followed by size exclusion chromatography with a Superose 6 or Superose 6 Increase column (GE Healthcare). Lumazine synthase nanoparticle was produced by BlueSky Bioservices, in *Escherichia coli*, using heat treatment (75°C for 30 min) of the supernatant from lysed cells followed by centrifugation to again obtain supernatant, and then size exclusion chromatography first with Superdex 75 and finally with Sephacryl 500.

Serum binding analysis by BAMA

Serum IgG responses were measured via a multiplex antigen panel (i.e., eOD-GT8, eOD-GT8-KO11, eOD-GT8 60mer, Lumazine synthase) to determine specificity and magnitude. A binding antibody multiplex assay (BAMA) (*67*–*69*) was modified by lengthening the primary antibody incubation period from 30 to 120 min for enhanced detection sensitivity of early bnAb precursors. The assay was validated for accuracy, specificity, precision, robustness, and limit of detection/quantitation (LLOD/LLOQ). The LLOQ for detection of early bnAb precursors was 0.0041 to 0.0866 μg/ml. Antibodies were measured at day 0 (day of first vaccination), day 14 (2 weeks post-first vaccination), day 28 (4 weeks post-first vaccination, day 56 (day of second vaccination), day 70 (2 weeks post-second vaccination), and day 112 (8 weeks post-second vaccination). Samples were serially diluted (1:50, 1:250, 1:1250, 1:6250, 1:31250, and 1:156250) and incubated for 120 min with a mixture of carboxlyated fluorescent MagPlex microsphere sets (Luminex) that were each covalently coupled to one of the antigens. Antigen-specific IgG was detected using a biotinylated detection antibody to human IgG Fc (Southern Biotech), followed by washing and incubation with Streptavidin PE (BD Pharmingen). Samples were acquired on a Bio-Plex instrument (Bio-Rad), and antibody levels were measured as median fluorescent intensity (MFI) from two wells and then averaged using the mean. The readout was background-subtracted median fluorescent intensity (MFI), where background refers to the antigen-specific plate-level control (i.e., a blank well containing antigen-conjugated beads run on each plate plus detection antibody). Additionally, a blank or reference bead was included to estimate nonspecific antibody binding. Area under the titration curve (AUTC) was used as the magnitude measure of interest. AUTC was calculated using the trapezoid method with truncation in the case of negative background-adjusted MFI minus background-adjusted blank MFI (MFI*) values or MFI* values > 22000. Samples with blank MFI > 5000 were excluded from the analysis. The positive controls were GL-VRC01 (germline VRC01 mAb), VRC01 mAb, anti-6× HIS epitope tag (for His-tagged proteins), CH31 mAb, 2G12 mAb.

The positivity of a response was defined based on background-adjusted MFI values at the screening dilution level (1:50) except lumazine synthase. Lumazine synthase was observed to have high baseline values across participants at the screening dilution, so filtering for high baseline MFI* was not applied and the response call for this antigen was made at the first dilution for which baseline MFI* was

<6500. Antigen-specific positivity thresholds were computed as the maximum of 100 and the 95th percentile of the baseline MFI* by antigen except lumazine synthase, which was set to 100. Samples from postenrollment visits were declared to have a positive binding antibody response by BAMA if they met three criteria:

1. MFI* values were greater than the antigen specific positivity threshold.

2. MFI* values were greater than three times the baseline MFI* values.

3. Background-adjusted MFI values were greater than three times the baseline background-adjusted MFI values.

For differential binding to the CD4 binding site (CD4bs), defined as the difference in AUTC for binding to eOD-GT8 ($AUTC_{Ref}$) and eOD-GT8-KO11 ($AUTC_{KO}$), the positivity of response was defined as a positive response to eOD-GT8 plus an additional criterion:

4. $\Delta AUTC > 0$, where $\Delta AUTC$ was defined as $AUTC_{Ref} - AUTC_{KO}$.

Pseudovirus production and neutralization assays

Neutralizing antibodies against HIV-1 pseudoviruses were measured as a function of reduction in Tat-regulated luciferase (Luc) reporter gene expression in TZM-bl cells (*70*, *71*). Neutralization ID50 titers were measured from specimens obtained at days 0 (visit three, baseline), 14 [visit four, 2 weeks post-first vaccination), and 70 (visit 8, 2 weeks post-second (final) vaccination]. Neutralization titer was defined as the serum dilution at which relative luminescence units (RLUs) were reduced by 50% (ID50) relative to the RLUs in virus control wells (cell + virus only) after subtraction of background RLUs (wells with cells only).

A specialized panel of 426c Env-pseudotyped viruses was used to detect and characterize early intermediates of VRC01-class bnAbs. Some VRC01 early intermediates neutralize 426c in a manner that requires deletion of one or more N-glycans in the vicinity of the CD4bs. Neutralization may be enhanced by Man5-enrichment of remaining N-glycans that otherwise are processed into larger complex-type glycans. Man5-enrichment was achieved by producing Env-pseudotyped viruses in 293S $GnTI^-$ cells. 293T cells were used to produce Env-pseudotyped viruses with fully processed glycans. Mutation D279K was used to confirm CD4bs specificity.

The viruses 426c.N276D/$GnTI^-$ and 426c.N276D.N460D.N463D/$GnTI^-$ can detect germline-reverted forms of VRC01, VRC07, and VRC20 but not germline-reverted forms of other CD4bs bnAbs (*72*).

A specialized panel of CH505 Env-pseudotyped viruses was used to detect and characterize early intermediates of CH235 and CH103 bnAb lineages. Neutralization by CH235 early intermediates is dependent on an N279K.G458Y double mutation and also requires Man5-enrichment of N-glycans that are otherwise processed into larger complex-type glycans. Man5-enrichment was achieved by producing Env-pseudotyped viruses in 293S $GnTI^-$ cells. 293T cells were used to produce Env-pseudotyped viruses with fully processed glycans. Mutation N280D was used to confirm CD4bs specificity. CH505.N279K.G458Y/$GnTI^-$ detects germline reverted and early intermediates of CH235 but not germline-reverted forms of other CD4bs bnAbs (*73*).

Neutralization by early intermediates of CH103 requires deletion of four N-glycans in the vicinity of the CD4bs, combined with Man5-enrichment of remaining N-glycans that otherwise are processed into larger complex-type glycans. Mutation S365P was used to confirm CD4bs specificity. CH505TF.gly4/$GnTI^-$ detects germline-reverted and early intermediates of CH103 (*73*).

Statistical analysis of neutralization assay data

Response to a viral isolate was considered to be positive if the neutralization titer was greater than or equal to 20. Response rates were calculated with 95% Wilson score intervals. Response magnitude analyses included vaccine-recipients only and included responders and nonresponders (with truncated titer measurements). There were no detectable neutralizing antibody responses to the eOD-GT8 vaccine (low-dose or high-dose) that indicated elicitation of early intermediates of VRC01-class, CH235, or CH103 bnAbs. There was one low-level low-dose response (ID50 = 22.47) to CH0505TF.gly4.S365P.2/293S/$GnTI^-$ (CH103 precursor knockout mutant) after the second vaccination, but this was hard to interpret in the absence of a response to CH0505TF.gly4 (CH103 precursor). Negative results do not necessarily indicate a lack of bnAb precursors, since the virus panel only detects a subset of CD4bs bnAb precursors. There were no tier 1A (MW965.26/293T/17 and MN.3/293T/17), placebo, or baseline responses.

Due to overall lack of neutralization response, response rate and magnitude testing were not performed.

Overview of the VRC01-class B cell assay

VRC01-class B cell precursors were identified first based on their ability to bind to the CD4bs of the eOD-GT8 protein, determined using fluorescently-labeled eOD-GT8 proteins and a modified eOD-GT8 protein containing mutations specifically in the CD4bs epitope (eOD-GT8 KO11). Differential staining of B cells to the eOD-GT8 protein but not to the CD4bs mutant (eOD-GT8 KO11) indicated that B cells were specific to the CD4bs. Therefore, fluorescently-labeled eOD-GT8 and eOD-KO11 were combined with a flow cytometry antibody panel to identify and single-cell sort the specific B cell populations of interest: circulating memory B cells, plasmablasts and germinal center (GC) B cells. CD4bs-specific B cells bound two eOD-GT8 tetramers ($GT8^{++}$) but not tetramers of eOD-GT8 KO11 (KO^-). Since the B cell sorting and sequencing needed to be performed on fresh samples for plasmablasts and lymph node (LN) FNAs, the sorting and sequencing was established and performed at two laboratories that were in close proximity to the clinical sites. Procedures and reagents were harmonized (except where noted otherwise) and verified at the two laboratories (figs. S5 to S10 and tables S10 to S19).

PBMC samples from weeks −4, 4, 8, 10, and 16 after the first vaccination were sorted for CD4bs-specific IgG memory B cells; draining axillary lymph node cells, acquired by FNA at weeks 3 and 11, were sorted for CD4bs-specific IgG germinal center (GC) B cells; and PBMC samples at week 9 (5 to 8 days after the second vaccination) were sorted for CD4bs-specific IgD^- plasmablasts (PBs) (Fig. 1A and tables S10 and S11). For each sample, RT-PCR and DNA sequencing were applied to as many CD4bs-specific IgG cells as possible, up to a maximum of two 96-well plates. DNA for HCs and LCs (kappa and lambda) was sequenced by the Sanger method, and selected samples from the low dose vaccine group were resequenced using next-generation sequencing. BCR sequences were subjected to quality filtering and bioinformatic analysis. Additional details of these procedures are described below.

Tetramer probe preparation

Tetramers were prepared at a 4:1 molar ratio of monomeric eOD-GT8 or KO11 proteins to streptavidin. The total volume of protein, 1× PBS, and protease inhibitor (catalog no. 539131-10VL; MilliporeSigma; Burlington, MA, USA) was added to a microcentrifuge tube. Twenty percent of the total streptavidin volume was added and incubated with continuous rotation for 20 min at 4°C in the dark. The incremental addition of streptavidin was repeated four times until the total amount of streptavidin had been added to the protein. Tetramers were made fresh for each experiment (VRC) or stored at 4°C and kept up to 1 month (FHCC).

Monoclonal bead controls

Bead assays were performed on the day of sorting experiments to confirm the functionality of the tetramers by flow cytometry. Anti-mouse Ig kappa beads (BD Bioscience, La Jolla, CA, USA) were washed with 3 ml of R10 in polystyrene FACS tubes and then centrifuged at 650 × *g* for 5 min. Supernatants were discarded and beads were resuspended in 100 μl of R10. Each bead control was given 1 μg of mouse anti-human IgG and incubated for 15 min at room temperature. Beads were washed with 3 ml of R10 and resuspended with either 1 μg

of glVRC01 mAb (to test eOD-GT8 probes) or KG064 mAb (to test eOD-GT8-KO11 probes) in 100 μl. Beads were incubated for 15 min at room temperature, washed with 3 ml of R10, and then resuspended in 100 μl of R10. Both eOD-GT8 probes were added to the glVRC01 positive control beads as well as negative control beads that did not receive glVRC01. The KO11 probe was added to the KG064 mAb-labeled beads as well as a bead-only control that did not receive KG064. Each tube was incubated for a minimum of 25 min at 4°C. Beads were washed with 3 ml of R10, centrifuged, decanted, and resuspended in up to 300 μl R10 for collection.

Enrichment of B cells from cryopreserved PBMC samples

All five cryopreserved PBMC samples from a single participant were sorted in an experimental batch on a given day. Cryopreserved PBMCs were thawed, either by water bath or with use of Thawsome cryovial adapters, into warm benzonase (MilliporeSigma; Burlington, MA, USA) supplemented R10 [RPMI 1640 with 25 mM HEPES buffer and L-glutamine (Thermo Fisher Scientific; Waltham, MA, USA) and 10% fetal bovine serum (FBS; Nucleus Biologics, San Diego, CA, USA)]. Samples were centrifuged at 300 × *g* for 12 min. The supernatant was decanted, and the cells were washed with R10. The cell recovery and viability were optionally determined using the Muse Cell Analyzer (MilliporeSigma; Burlington, MA, USA). B cells were enriched using the EasySep Human Pan-B Cell Enrichment Kit (StemCell Technologies; Vancouver, CA) and the Big Easy magnet (StemCell Technologies; Vancouver, CA) following the manufacturer's instructions summarized here. Samples were resuspended at a concentration of 5×10^7 cells/ml with EasySep buffer. Fifty microliters of Enrichment Cocktail (per ml of sample) were added and mixed. The samples were incubated at room temperature for 10 min. Magnetic particles were vortexed for 30 s, and 75 μl of magnetic particles (per ml of sample) were added and mixed with the samples and incubated at room temperature for 5 min. EasySep Buffer was added to the sample up to 5 ml for samples under 2 ml ($<10^8$ cells) or 10 ml for samples greater than or equal to 2 ml ($>10^8$ cells). The sample was loaded into the EasySep magnet without the lid and incubated at room temperature for 5 min. With the tube on the magnet, the cell suspension was pipetted off and into a new conical. The sample conical was removed from the magnet, and the beads were resuspended with the same amount of EasySep Buffer used previously and then mixed and reincubated on the EasySep magnet (without lid) at room temperature for 5 min. With the tube on the magnet, the cell suspension was pipetted off and combined with the previous matching sample. The cell number and viability of the sample was optionally determined.

Flow cytometry staining procedures

Cells, either fresh PBMCs from the plasmablast time point (week 9), fresh lymph node mononuclear cells (from FNAs at weeks 3 and 11), or enriched B cells from previously cryopreserved samples (at weeks −4, 4, 8, 10, and 16), were resuspended in 100 μl 10% FBS/1× PBS and stained with the fluorescently labeled eOD-GT8 KO11 tetramer for 30 min at 4°C. Cells were washed with 10% FBS/1×PBS and then resuspended in a staining cocktail of antibodies and remaining eOD-GT8 tetramers diluted in Brilliant Buffer (BD Bioscience, La Jolla, CA, USA). The antibody staining panels were tissue dependent and included a panel for PBMC samples (memory B cells and plasmablasts) (table S10) and a separate panel for lymph node FNAs (table S11). After surface staining, the samples were resuspended at about 2×10^6 cells/ml in R10 containing the viability dye (7AAD) and maintained at 4°C until processed by flow cytometry.

Standardized templates for flow cytometry analysis

Standardized templates were designed using BD Diva software for analysis of bead assays, internal controls, and experimental samples for each sample type (fig. S7). These templates were replicated for each flow cytometry experiment to ensure consistent gating and labeling of samples. Templates were tested and compared between both test sites using aliquots of the internal control sample before trial samples were used. Since antigen-specific events were rare in the internal control sample which made setting gates difficult, we developed a standardized gating system that could be implemented at both sites referred to as the M.A.R.I.O gate.

Mathematically articulated and reasoned but independently optimized (M.A.R.I.O.) gating

The analysis of fresh samples for the clinical trial required the use of equipment that was located near the clinical trial sites. The physical differences between flow cytometers, and the subjectivity of gating rare and hard to identify cell populations, can lead to high levels of variability in the sorting of populations like antigen-specific B cells. For this trial, we developed a method of standardizing the gating of antigen-specific B cells by flow cytometry. eOD-GT8 proteins were conjugated to two fluorophores, allowing us to identify fluorescently double-positive events and reduce the fluorophore-specific background that would be selected by using either fluorophore individually. Due to the variability between flow cytometers, developing a method to standardize the gating of antigen-specific events by flow cytometry was important for this trial. Here we utilized FMP (fluorescence minus probe) stained samples (fully stained samples without the addition of fluorescent probes) to determine the background for each channel being used to detect antigen-specific B cells. We then developed a gate based on the ratio of these fluorophores for each flow cytometer which could identify fluorescently well-balanced antigen-specific B cells while also reducing the amount of antigen-non-specific B cells captured by the gate.

FMP samples were used to calculate the coordinates for the 99th percentile of each probe-specific fluorophore using Flowjo software. This serves as the upper threshold of the probe negative gate (fig. S7A; C1). Similarly, twice the 99th percentile of each probe specific fluorophore was determined to serve as the lowest acceptable threshold for probe double positive-specific events (fig. S7A; C2). Axis points for each individual fluorophore were placed at coordinates representing 10 times the 99th percentile for each individual fluorophore (fig. S7A; C4, C5). Additional axis points were added which are based on the proportion of the 99th percentiles for each fluorophore (fig. S7A; C6, C7). These bounds were used to define the area in which acceptable fluorescent probe double positive events were acceptable for sorting by each test facility and account for each facility's individual cytometer characteristics (fig. S7B).

FACS

Individual target cells were index-sorted into empty skirted 96-well plates (Thermo Fisher Scientific; Waltham, MA, USA). Several wells were left empty for subsequent PCR controls. PBMC samples from weeks −4, 4, 8, 10, and 16 after the first vaccination were sorted until either four 96-well plates were filled with eOD-GT8 CD4bs-specific IgG memory B cells ($CD19^+$ $CD20^+$ IgD^- IgG^+ KO^- $GT8^{++}$; fig. S8) or the sample was exhausted; two 96-well plates were subjected to RT-PCR and BCR sequencing, while the other two plates were reserved at −80°C. The number of PBMCs thawed and stained depended on the time point: 200×10^6 (FHCC) or 250×10^6 (VRC) at week −4, 100×10^6 at week 4, 100×10^6 at week 8, 200×10^6 at week 10, and 100×10^6 at week 16.

In planning the trial procedures, we expected that GC B cells from LN FNAs and plasmablasts (PBs) would have lower levels of surface IgG, and hence we were uncertain if sorting of these samples would have sufficient detectable antigen-specific staining by flow cytometry. We therefore decided to sort two plates of phenotype-specific cells without regard to tetramer binding, followed by two plates of phenotype-specific cells that were also CD4bs-specific as determined by differential tetramer

staining. Therefore, up to two plates of total GC B cells ($CD19^+$ IgD^- IgG^+ $CD20^{hi}$ $CD38^{hi}$) were sorted, as well as CD4bs-specific GC B cells ($CD19^+$ IgD^- IgG^+ $CD20^{hi}$ $CD38^{hi}$ KO^- $GT8^{++}$) (fig. S9A). From fresh PBMCs at week 9, two plates of PBs ($CD19^+$ $CD27^+$ IgD^- $CD38^{hi}$) were sorted without regard to tetramer binding followed by the sorting of CD4bs-specific PBs ($CD19^+$ $CD27^{hi}$ $CD38^{hi}$ IgD^- KO^- $GT8^{++}$) (fig. S9B). Note that the PB gating strategy, which included $CD38^{hi}$ and did not gate on CD20, may have included $CD38^{hi}$ $CD20^{hi}$ B cells that have been described as activated B cells as opposed to PBs (*10*). A maximum of four 96-well plates of B cells were sorted for cDNA synthesis per time point. Plates were sealed, centrifuged at 800 × *g* for 1 min and immediately transferred to dry ice. Plates were stored at −80°C for at least overnight before proceeding. A total of 884 (384 at VRC; 500 at FHCC) 96-well plates of sorted cells were produced and stored.

Standardized and direct analysis of sorting flow cytometry data

To allow for direct analysis of the flow cytometry data as it was analyzed during the sorts, the flow cytometry experiments were exported from Diva software as XML files along with the FCS files for the total recorded events and the index files for the sorted cells. These primary data were processed and concatenated at the Vaccine Immunology Statistical Center (VISC), using the Cytoverse suite of R packages. CytoML (*74*) is an R/Bioconductor package that enables cross-platform import, export, and sharing of gated cytometry data. Using CytoML we parsed the XML files created during the Diva experiments, which contained data transformations, compensation matrices, gates and their hierarchical relationships, sample meta-data, and other information required to reproduce the gating analysis. Once the workspaces were imported into R, the analysis was faithfully reproduced for each sample, the gated cytometry data was visualized, and positive proportions for all populations were calculated. As a quality control measure, the calculated percent positive populations were compared to exported tables of populations from the Diva software using Spearman correlations. This data was processed using R (v4.1.1) and Cytoverse packages CytoML (v2.5.4), flowWorkspace (*75*) (v4.5.3), ggcyto (*76*) (v1.20.0), and cytolib (v2.5.3). Frequencies were measured either during the period of sorting (FHCC) or until the samples were exhausted (VRC).

PCR and sequencing positive and negative controls

Early in the trial, the lysates from an immortalized VRC01-class naïve B cell line, referred to as Immo-A1 (*77*), and sorted pooled donor $CD19^+$ B cells were used as PCR controls. These were found to be insufficient as controls, so we developed synthetic positive controls to use for the remainder of the trial. Synthetic positive control DNA sequences compatible with our nested PCR protocol were generated for B cell receptor heavy and both light chains (kappa and lambda). Synthetic sequences were based on natural sequences identified from VRC01-class antibody sequences isolated from human PBMCs. The CDR3 amino acid junctions were altered to distinguish each of the synthetic controls from naturally occurring sequences and from each other by replacing them with amino acid "VRC," "VIP," and "DL" segments separated by chain-specific amino acids. Heavy chain CDR3 sequence tags coded for histidine (H) leading and separating the segments. Similarly, kappa chain CDR3 sequence tags coded for lysine (K) and lambda chain CDR3 sequences coded for leucine (L) leading and separating the segments. The sequence tags are shown below, and the full nucleotide sequences for the synthetic controls are given in table S19.

Sequence tags:

1) 5′ GVRCGVIPGDL 3′ 5′ ggcgtgcgctgcggcgtgattccgggcgatctg 3′

2) 5′ KVRCKVIPKDL 3′ 5′ aaagtgcgctgcaaagtgattccgaaagatctg 3′

3) 5′ LVRCLVIPLDL 3′ 5′ ctggtgcgctgcctggtgattccgctggatctg 3′

To further differentiate the synthetic controls by sequence as well as by physical size using gel electrophoresis for quality control purposes, novel sequences were inserted at both ends of the sequences. Inner and outer primer binding sites were attached to ensure these sequences would amplify with our nested PCR primer sets. Ultimately control sequences were ~50% mutated from natural sequences distributed throughout the sequence to ensure identification even with high mutation and poor sequence quality.

Synthetic controls were tested for primer binding capacity, in frame amino acid translation, Ig chain homology and gene usage, and potential gBlock production issues. All controls were titered and rigorously tested prior to use in the trial.

Single-cell sequencing

In preparation for cDNA synthesis, plates were removed from −80°C storage and again centrifuged at 800 × *g* for 1 min before being placed on wet ice. The cDNA synthesis reaction mix was constructed using the SuperScript III Reverse Transcriptase Kit (Invitrogen). The reaction mix consisted of 1x SuperScript III First Strand Buffer, 4.8 mM DTT and 200 U SuperScript III, as well as 20 U RNaseOUT (Invitrogen), 450 ng Random Hexamers (Gene Link) and 0.77 mM dNTP mix (GeneAmp). The mix was added to every well, including wells 12E through 12H to be used as negative controls. Thermal cycling parameters were 42°C for 10 min, 25°C for 10 min, 50°C for 60 min, and 94°C for 5 min. Once complete, plates were frozen at −20°C. A total of 531 (267 at VRC, 264 at FHCC) unique cDNA plates were generated for subsequent PCR amplification.

Amplification proceeded by three immunoglobulin chain-specific PCRs. The reaction mix generally consisted of 2 U HotStarTaq *Plus* DNA polymerase and 1x HotStar *Plus* PCR Buffer (Qiagen; Hilden, Germany), as well as 0.25 mM dNTP mix and 1.5 mM $MgCl_2$. Each chain was amplified using a chain-specific pool of forward primers (IDT) and isotype-specific reverse primers (IDT) (tables S13, S15, and S17). One reaction mix each was constructed containing 2.1 μM forward and 0.2 μM IgH reverse primers, 0.3 μM forward and 0.625 μM reverse Igκ primers, and 0.8 M forward and 0.625 μM reverse Igλ primers. The template input was 4 μl of cDNA, including carrying forward 4 μl of each negative control from wells 12E through 12H. The cDNA plates were briefly vortexed and centrifuged before template addition. Thermal cycling parameters were 95°C for 5 min and 50 cycles of 95°C for 30 s, either 52°C (IgH) or 58°C (Igκ and Igλ) for 30 s and 72°C for 55 s, followed by a final extension of 72°C for 10 min. Once complete, plates were frozen at −20°C.

An additional nested PCR was performed for all chains to increase specificity. The reaction mix consisted of 1 U Phusion High-Fidelity DNA Polymerase and 1× Phusion High-Fidelity Reaction Buffer (New England Biolabs; Ipswich, MA, USA), as well as 0.2 mM dNTP mix and 1× Q Solution (Qiagen; Hilden, Germany). Each chain was again amplified using a chain-specific pool of forward primers and isotype-specific reverse primers, with one reaction mix each containing 5.5 μM forward and 1.0 μM IgH reverse primers, 4.0 M forward and 5.0 μM reverse Igκ primers, and 3.5 μM forward and 5.0 M reverse Igλ primers (tables S14, S16, and S18). The template input was 4 μl of chain-specific PCR product, again including carrying forward 4 μl of each negative control from wells 12E through 12H. In addition, chain-specific positive PCR controls (synthesized by IDT) were included in wells 12A through 12D. These synthetic constructs were added at 400 copies per well. The PCR plates, including the positive PCR controls, were briefly vortexed and centrifuged before template addition. Thermal cycling parameters were 98°C for 30 s and 35 cycles of 98°C for 30 s, either 58°C (IgH and Igλ) or 52°C (Igκ) for 30 s and 72°C for 55 s, followed by a final extension of 72°C for 10 min. Once complete, the plates were frozen at −20°C and shipped to Genewiz (South Plainfield, NJ) on dry ice. Genewiz conducted an enzymatic clean-up on the PCR products before conducting uni-directional Sanger sequencing using the reverse chain-specific constant region primers (3′Cg CH1, 3′CK 494, and

3′CL shown in tables S14, S16, and S18). Sequencing data were obtained for a total of 3186 PCR plates (six times the total number of cDNA plates), not accounting for repeats.

Quality control measures were taken for all sequence data to determine if sequencing of specific plates needed to be repeated. When PCR controls were not available, we required a minimum of 50% of the sequences on any plate to have identifiable and functional B cell receptor sequences. When PCR controls were available, we required >50% of the positive controls to have identifiable control sequences (two to four) and the negative controls to have <50% of the wells with identifiable sequences (one or zero) (VRC) or we required the negative controls to have <50% of the wells with identifiable sequences (one or zero) (FHCC). Sequences quality was first checked with the Genewiz quality report to determine overall sequencing success for the plate. Sequences were then analyzed by IMGT/V-QUEST for productive B cell receptor sequences or sequences with identifiable B cell receptor gene usage. When synthetic PCR controls were used, all sequences were screened for contamination by the spiking of the controls using the CDR3 amino acid junction sequence tags mentioned previously. All data was transferred to the Vaccine Immunology Statistical Center (VISC) for data repository and analysis. However, sequencing plates that did not pass our criteria were investigated further and either sequenced again directly by Genewiz or PCR amplified from an earlier step with remaining cDNA or PCR material. The new plates were submitted to Genewiz for sequencing, and new sequence data was identified with an increased "Replicate" number.

Additional PCR and NGS BCR sequencing for the low-dose group

To control for potential sequencing errors in the unidirectional/single-read Sanger sequencing data, we resequenced selected samples from the low dose group using next generation sequencing (NGS). To perform NGS on selected cells, cDNA generated for Sanger sequencing was used as the starting point. Plates were removed from −80°C storage and centrifuged at 800 × *g* for 1 min before being placed on wet ice. Selected wells from different plates were collected into a new plate, and PCR was performed using the same nested method used for Sanger sequencing. The nested PCR product from the individual heavy and light chains were pooled in equal volumes of 10 μl from each plate into a single plate. The pooled plate was purified using AmpureXP beads (Beckman coulter Cat: A63881) in the ratio of 0.8× beads to PCR product for a total volume of 24 μl of beads to 30 μl of pooled PCR product. The purified product was eluted into 20 μl of RNase-free water. Each purified plate was quantified using the QuantIT dsDNA high sensitivity kit (Thermofisher Cat: Q33120) and normalized to 0.2ng/μl for optimal NGS library generation using the Illumina Nextera XT kit (Illumina Cat: FC1-31-1096). The normalized plates were processed for NGS library preparation using 1.25 μl of the product with 2.5 μl of Tagmentation buffer and 1.25 μl of the Amplicon Tagmentation mix provided in the Nextera kit. The plates were centrifuged at 800 × *g* for 1 min and placed in the thermocycler at 55°C for 10 min. Following the incubation, 1.25 μl of neutralization buffer was added to the wells and incubated at room temperature for 5 min. The tagmented product was indexed using custom primers generated to multiplex 10 plates together in a single sequencing run. Each plate was indexed with 1.25 μl of a unique 10–base pair Mi7 index at a concentration of 10 μM and each well of the plate was indexed with 1.25 μl of a unique 10 base pair Mi5 index at a concentration of 10 μM, along with 3.75 μl of the NPM reaction mix provided in the Nextera XT kit. The PCR plates were centrifuged at 800 × *g* for 1 min and placed in the thermocycler for indexing. The thermocycler parameters used were 72°C for 3 min, 12 cycles of 95°C for 30 s, 50°C for 30 s, and 72°C for 1 min, followed by a final extension of 72°C for 5 min. The indexed libraries were further PCR purified using the AmpureXP beads at 0.8× concentration and eluted into 10 μl of RNase-free water. The purified product from 10 indexed plates was pooled together for loading onto the Illumina Miseq for sequencing. The final concentration of the pooled library was determined using the Kapa QPCR kit (Roche Cat: KK4835) and diluted to 4 nM for sample denaturating according to the Illumina loading guidelines. The denatured sample was further diluted to 10 pM concentration for loading onto the Miseq V3 600 cycle kit (Illumina cat: MS-102-3003). Demultiplexed fastq files were retrieved from the Miseq and aligned to immunoglobulin genes using BALDR (*78*).

High quality NGS sequences with at least 100 Nextera reads were obtained for a total of 1998 samples and were regarded as perfectly accurate. Comparison of high quality NGS sequences to corresponding Sanger sequences revealed perfect agreement for 82.9% of Sanger reads at the nucleotide level and 85.9% of Sanger reads at the amino acid level. There were differences of 1, 2, 3, 4, or 5 nucleotides for 7.8, 2.3, 1.3, 0.65, or 0.75% of Sanger reads, respectively, and differences of 1, 2, 3, 4, or 5 amino acids for 6.7, 1.8, 1.3, 0.70, or 0.50% of Sanger reads, respectively. Hence, the NGS data confirmed that >94.2% of the Sanger sequencing reads were accurate to within three nucleotides, and >95.6% of the Sanger sequencing reads were accurate to within three amino acids. We concluded that it was not necessary to carry out NGS resequencing on the remaining low dose samples or on any of the high dose samples. Nevertheless, a small fraction (<4.4%) of Sanger reads differed by more than three amino acids from the corresponding high quality NGS sequences. High quality NGS sequences were used in place of the corresponding Sanger sequences for downstream analysis in cases where Sanger and NGS differed by 1 to 19 nucleotides, as described in the NGS module of the BCR bioinformatic analysis pipeline below.

Sample identify confirmation for one case of accidental sample mislabeling

Comparison of serum antibody binding data from BAMA with antigen-specific B cell frequency data from cytometry suggested that samples from visits 8 and 10 (weeks 10 and 16) for placebo-recipient PubID_164 might have been accidentally swapped with samples from the same time points for vaccine-recipient PubID_153 during flow cytometry analysis. Short tandem repeat (STR) analysis along with confirmatory flow cytometry testing was used to confirm the identity of the samples. Duplicate samples were thawed and divided. Small aliquots were lysed and transported to two independent facilities for STR testing to confirm donor sample identity. Remaining samples were processed by trial flow cytometry protocols for comparison of cellular phenotypic data. Both STR testing facilities were in agreement with each other and the confirmatory flow cytometry data to confirm sample identities. This analysis confirmed that a sample labeling error of transposing the participant IDs had occurred during analysis by flow cytometry, effectively swapping the samples for the two participants at the time points listed above. The sample identity confirmation provided justification for the bioinformatic pipeline to correct for the effective "sample swap," as described in the SWAP module below.

Bioinformatic BCR sequence processing

Database

ABI files containing DNA sequence information from Sanger sequencing were organized in a central database at VISC in which each file was regarded as an entry in the database. The files were contained within folders such that each folder represented a 96-well plate. The folder and file naming structure was:

<Date Deposited>/<Plate Tracking Number>/<Participant ID>_<Visit Number>_<Plate Number>_<Round>_<Chain>_<Replicate>_<Well>.abi

Date Deposited was the date the ABI filed was deposited into the database. Plate Tracking Number was the FedEx tracking number associated with shipping the plate to Genewiz. Participant ID was the unique identifier assigned to each participant in the trial. Visit

Number was the visit number as described in fig. S1 and table S2. Plate number was the unique number assigned to each 96-well plate sorted for each participant at each visit. Round was could be either 1 or 2, indicating the first or second of the nested PCR reactions; all samples submitted for sequencing were round 2. Chain was heavy, kappa, or lambda. Replicate was the unique index to indicate which one of several potential attempts at nested PCR and sequencing were made for this plate. Well was the unique number for each well in a 96-well plate. The database contained a total of 158,954 ABI files corresponding to 1724 96-well plates, some of which were only partially filled. The database also contained a sample manifest that linked metadata to each well for which sequencing data was obtained. The data fields in the manifest included several important boolean variables, such as (i) Has_sorted_cell, which was true if the well contained a sorted cell; (ii) Is_negative_control, which was true if the well contained a negative control sample; (iii) Is_positive_control, which was true if the well contained a positive control sample; and (iv) Is_doublet, which was true if the well was known from FACS to contain a doublet (two sorted cells); and many other metadata about the sample (the sample manifest is available in the data repository; see Data and materials availability below). Sequences obtained by NGS for a small subset of samples from the low dose group were also deposited into the central database in a spreadsheet linking each NGS sequence to a unique sequence identifier that could be matched to the Sanger sequence identifiers. NGS sequences were incorporated into the data analysis as described below.

BCR analysis pipeline

Preliminary analyses of BCR sequences were carried out during the trial, as the sequencing data was generated and deposited into the central database. This was necessary to obtain early readouts on the efficacy of the vaccine in order to help guide decision-making about additional preclinical and clinical experiments to build on the findings from this trial. The preliminary analyses also enabled us to select BCR sequences for production as soluble IgGs and subsequent characterization of binding affinities by SPR. Initially, and during most of the trial, the preliminary analysis pipeline employed Abstar [https://github.com/briney/abstar; (*79*)] for BCR gene assignment and annotation, coupled with custom scripts written in various programming languages for analysis. However, toward the end of the trial, and for the final analysis presented in this manuscript, we developed a more streamlined, adaptable, and transparent code base for analysis. The final, improved analysis pipeline used Sequencing Analysis and Data library for Immunoinformatics Exploration (SADIE, https://github.com/jwillis0720/sadie) for BCR gene assignment and annotation, coupled with a series of python modules, and reported BCR sequence characteristics in the standardized Adaptive Immune Receptor Repertoire (AIRR) format (*80*).

The final BCR analysis pipeline (fig. S10), a single installable python package, consisted of 11 independent modules that read as input the dataframe (a data structure that organizes tabular data) from the previous step and produced as output a new dataframe. The modules (FIND, MODEL, SPLIT, CORRECT, ANNOTATE, JOIN, NGS, TAG, SWAP, PAIR, PERSONALIZE, and MUTATION) are described below.

FIND: The FIND module collected information from all ABI files in the central data repository. The filename, file path, nucleotide sequence, and Phred score (*81*, *82*) were stored into a dataframe for subsequent analysis. A total of 158,954 ABI files were found.

MODEL: The MODEL module tokenized the filename and path into expected metadata fields (e.g., verified that participant id was in our list of expected participant ids) and enforced consistent formatting for each field (e.g., rep0, or r0 became REP0 for the replicate field).

SPLIT: The SPLIT module dropped entries that were duplicates or that had incomplete metadata fields assessed in the MODEL module. An entry was determined to be a duplicate if it contained the same metadata fields as well as the same nucleotide sequence and Phred score. Such duplicate entries resulted from duplicate manual uploads to the central data repository. After the SPLIT module, a total of 155,801 entries were available for subsequent analysis.

CORRECT: The CORRECT module applied a curated list of updates to meta data fields and drops of certain sequences or plates that were requested by the FHCC and VRC experimental labs. Updates were generally corrections to manual file-naming errors that violated the predefined naming format (common errors including entering "NA" instead of a valid field entry, or specifying the visit number with an invalid format). Drops were mostly either to eliminate wells for which no cell was known to be sorted, or to eliminate plates that had been named incorrectly and were resubmitted separately with correct naming. A total of 1318 entries were updated, and 701 entries were dropped. A full list of updates and drops was stored in JSON format and can be reviewed in the GitHub repository. The CORRECT module then grouped all entries by participant ID, time point, plate, well, replicate, and chain, to ensure uniqueness. After the CORRECT module, a total of 155,100 entries were available for subsequent analysis.

ANNOTATE: The ANNOTATE module used the Sequencing Analysis and Data library for Immunoinformatics Exploration (SADIE, https://github.com/jwillis0720/sadie) to annotate BCR sequences. The SADIE AIRR module ports IgBLAST (*83*) for analysis of nucleotide sequences and ensures that the data are represented in AIRR recombination schema that defines a data model, field names, data types, and encodings (*80*). In addition, SADIE AIRR provides a versioned and tested python package that includes the IgBLAST executable and allows automatic creation of custom IgBLAST databases, a process that is otherwise difficult. SADIE AIRR provides the user with scriptable, granular control over IgBLAST options via a python API or a command-line interface. SADIE AIRR will try to determine optimized V(D)J alignment penalties to find a productive recombination (adaptable penalty model) and will also correct insertions and deletions that are absent in the germline alignment using current IgBLAST (v 1.17.1). For analysis of the G001 light chain sequences, SADIE AIRR implementation of the adaptable penalty model was helpful for determining likely germline rearrangements for light chains with short LCDR3s with significant VJ gene overlap. In these cases, the use of adaptable penalties facilitated identification of likely boundaries for the V and J genes, which resulted in identification of a slightly increased number of productive recombinations. The adaptable penalty model started with the default value of −1 for both V and J gene penalties, and in that configuration identified 27,913 productive antibody light chain recombinations. Other (V, J) penalty combinations, of (−2, −1), (−1, −3), and (−3, −1), identified 683, 65, and 37 additional light chain recombinations, respectively, increasing the total number of light chain recombinations by 2.8%. The Annotate module joined all AIRR recombination data fields with the previous metadata fields for subsequent analysis. In addition, ANNOTATE calculated a "sliced" Phred score that was the mean Phred score computed over just the V(D)J portion of the sequence. This "sliced" Phred score was used in evaluation of sequence quality in subsequent modules. After the ANNOTATE module, a total of 155,100 entries were available for subsequent analysis.

JOIN: As noted above, a manifest containing additional information about each well in each 96-well plate subjected to DNA sequencing was uploaded to the central data repository. The data fields in the manifest included the tokenized metadata from the FIND module as well as additional information. The JOIN module merged the manifest data with the annotated sequencing data from the ANNOTATE module. There were 22,707 entries with sequence information that could not be found in the manifest, of which only 633 were productive antibody sequences, and JOIN was unable to process those entries. After the JOIN

module, 132,393 entries were available for subsequent analysis.

NGS: The NGS module took the output from the resequencing pipeline, reannotated the sequences using SADIE AIRR, and updated the sequences and annotation fields (substituted the NGS sequences and their associated annotations in place of the corresponding Sanger sequences and annotations) if there were (i) fewer than 20 nucleotide differences as measured by Levenshtein distance (*84*) between the Sanger and NGS; and (ii) more than 100 V(D)J reads were produced by the NGS pipeline. When resequencing was carried out, the original Sanger sequence, the corrected sequence, and the Levenshtein distance were added to the dataframe for the subsequent analysis. Of 1998 high quality NGS sequences, 1656 (82.8%) sequences perfectly matched the corresponding Sanger sequence; 37 (1.9%) differed from the corresponding Sanger sequence by more than 20 nucleotides and were not considered for correcting the Sanger sequence; and 304 (15.2%) differed from the corresponding Sanger sequence by 1 to 19 nucleotides and were used to correct the Sanger sequence.

TAG: The tag module searched the productive sequences and performed a sequence alignment against the positive control sequences used in the PCR reaction, Synth or Immo (described in PCR and sequencing positive and negative controls). A positive match to a Synth or Immo heavy chain required that the HCDR3 nucleotide normalized identity to the true sequence was greater than 0.95 and the normalized V_H gene distance to the true sequence was greater than 0.9. For kappa and lambda matches to Synth, the LCDR3 and V_L gene distances to the true sequence were both required to be greater than 0.9. For kappa and lambda chain matches to Immo, the LCDR3 nucleotide normalized distance to the true sequence was required to be greater than 0.92; and the normalized distance to the true V_K gene sequence was required to be greater than 0.9. In addition, for the kappa chain matches to Immo, an exact match was required to the n-addition nucleotide sequence (*CG*). These parameters were calculated by comparing control sequences from NGS with control sequences from Sanger and adjusting the normalized distances until the controls were all identified by their Sanger sequences.

SWAP: The SWAP module transposed all data in the current dataframe from participant PubID_153 at visits 8 and 10 with participant PubID_164. See Sample identify confirmation for one case of accidental sample mislabeling for additional details.

PAIR: The pair module applied a series of filters to produce a final set of high quality BCR sequences including both heavy and light chains. The first filter eliminated nonfinal sequences, referred to as nonterminal replicates: for plates in which Sanger sequencing was attempted two or three times until the sequencing results passed quality controls ("Single-cell sequencing"), only the sequences from the final, or terminal, run were used. This filter eliminated 8966 nonterminal replicate entries. The second filter eliminated positive control sequences that were either derived from a well labeled as a control in the sample manifest (n = 6898) or were identified from the TAG module (n = 2746). The third filter removed sequences that either had no antibody recombination detected by SADIE AIRR (n = 2536) or corresponded to negative control wells in the manifest (n = 5607). The fourth filter removed 1677 heavy or light chain sequences identified in the manifest as doublets (cases of two cells sorted into a single well). The fifth filter removed 63,036 unproductive or incomplete V(D)J sequences that either contained a stop codon (unproductive; n = 61,374) or contained a recombination that did not start at the first nucleotide of framework 1 and end at the last nucleotide of framework 4 (incomplete V(D)J; n = 1662). Of the incomplete V(D)J sequences, 505 were heavy chains less than 90 amino acids in length, and 836 were light chains less than 80 amino acids in length. The sixth filter removed 1965 entries with mean Phred scores over the V(D)J sequence ("sliced" Phred scores) less than 30. The remaining 41,887 sequences, which included both heavy and light chains, were considered candidates for pairing. Sequences were then grouped by participant id, time point, plate and well. In the seventh and final filter, groups containing more than one heavy or light chain were eliminated (n = 2033), and unpaired heavy or light chains (n = 12,102) were eliminated. The remaining groups were considered proper pairs, because they contained exactly one heavy chain and one light chain. This process yielded 13,876 total BCR sequences with paired heavy and light chains (9862 heavy/kappa; 4014 heavy/lambda). Of those, 11,372 were CD4bs-specific (sorted as $KO^{-}GT8^{++}$) and 2504 were sorted as either GC B cell phenotype (from the first two plates in each FNA sort) or plasmablast phenotype (from the first two plates in each PB sort) without regard to eOD-GT8 tetramer binding (see FACS and fig. S10). Among the 2504 BCRs sorted by phenotype only, 71 (2.8%) were VRC01-class, and 45 of those were produced by a single donor at a single time point (PubID 151 at week 3). We focused our subsequent analyses on the 11,372 BCRs sorted as CD4bs-specific.

PERSONALIZE: The personalize module reannotated all BCR sequences with the personalized IGHV1-2 allele haplotype discovered in the genotype analysis (IGHV1-2 genotype analysis using IgDiscover). SADIE AIRR was run against a personalized reference set curated for each participant using the SADIE reference module. This allowed annotation only against the correct haplotype of IGHV1-2 alleles and thus a more accurate V_H somatic mutation percentage assignment.

MUTATION: The mutation module used SADIE ANARCI to number each VDJ amino acid sequence using the kabat numbering scheme. SADIE ANARCI is a port of the ANARCI program (*85*) that numbers amino acid sequences in a variety of numbering schemes. Both the germline V(D)J and mature V(D)J sequences were numbered in the Kabat scheme. The mutations were recorded and added to the final output dataframe.

Computing VRC01-class frequencies by combining frequencies from FACS and BCR sequencing

Memory B cell data

The frequency of VRC01-class IgG memory B cells was estimated by multiplying two frequencies: (i) the frequency of CD4bs-specific ($KO^{-}GT8^{++}$) IgG memory B cells among all IgG memory B cells sorted by FACS; and (ii) the frequency of VRC01-class BCRs among all CD4bs-specific IgG Memory B cells with sequenced BCRs. If the frequency of CD4bs-specific IgG memory B cells was zero, then the estimate for the VRC01-class frequency was also set to zero. In the case where the frequency of CD4bs-specific IgG memory B cells was positive but no CD4bs-specific IgG memory B cells were successfully sequenced, the estimate for the VRC01-class frequency was set to zero for postvaccination samples or the CD4bs-specific frequency for baseline samples. This approach is conservative or detecting vaccine-induced responses.

Additionally, based on the data for IgG memory B cells from PBMC samples, we estimated the frequencies of VRC01-class B cells among three different populations of B cells in the periphery. First, as an estimate for the frequency of VRC01-class B cells among CD4bs-specific IgG memory B cells, we used the frequency of VRC01-class B cells among BCR-sequenced CD4bs-specific IgG memory B cells. Second, to obtain an estimate for the frequency of VRC01-class B cells among GT8-specific IgG memory B cells, we multiplied the frequency of VRC01-class B cells among CD4bs-specific IgG memory B cells by the ratio of CD4bs-specific IgG memory B cells to GT8-specific IgG memory B cells. Third, to obtain an estimate for the frequency of VRC01-class IgG memory B cells among all B cells, we multiplied the frequency of VRC01-class B cells among CD4bs-specific IgG memory B cells by the ratio of CD4bs-specific IgG memory B cells to all B cells.

GC B cell data

The frequency of VRC01-class IgG GC B cells was estimated similarly as for memory B cells,

by multiplying two frequencies: (i) the frequency of CD4bs-specific IgG GC B cells among all IgG GC B cells sorted by FACS; and (ii) the frequency of VRC01-class BCRs among all CD4bs-specific IgG GC B cells with sequenced BCRs. If the frequency of CD4bs-specific IgG GC B cells was zero, then the estimate for the VRC01-class frequency was also set to zero. If the frequency of CD4bs-specific IgG GC B cells was positive but no CD4bs-specific IgG GC B cells were successfully sequenced, the estimate for the VRC01-class frequency was set to zero.

Analogous to procedures we followed with IgG memory B cells from PBMCs, based on the data for IgG GC B cells from FNA samples, we estimated the frequencies of VRC01-class B cells among three additional populations of B cells from FNA samples. First, as an estimate for the frequency of VRC01-class B cells among CD4bs-specific IgG GC B cells, we used the frequency of VRC01-class B cells among BCR-sequenced CD4bs-specific IgG GC B cells. Second, to obtain an estimate for the frequency of VRC01-class B cells among GT8-specific IgG GC B cells, we multiplied the frequency of VRC01-class B cells among CD4bs-specific IgG GC B cells by the ratio of CD4bs-specific IgG GC B cells to GT8-specific IgG GC B cells. Third, to obtain an estimate for the frequency of VRC01-class IgG GC B cells among all B cells, we multiplied the frequency of VRC01-class B cells among CD4bs-specific IgG GC B cells by the ratio of CD4bs-specific IgG GC B cells to all B cells.

Plasmablast data

The frequency of VRC01-class IgD^- plasmablasts (PBs) was also estimated similarly as for memory B cells, by multiplying two frequencies: (i) the frequency of CD4bs-specific IgD^- PBs among all IgD^- PBs sorted by FACS; and (ii) the frequency of VRC01-class BCRs among all CD4bs-specific IgD^- PBs with sequenced BCRs. If the frequency of CD4bs-specific IgD^- PBs was zero, then the estimate for the VRC01-class frequency was also set to zero. If the frequency of CD4bs-specific IgD^- PBs was positive but no CD4bs-specific IgD^- PBs were successfully sequenced, the estimate for the VRC01-class frequency was set to zero.

Analogous to procedures we followed with memory B cells from PBMCs and GC B cells from FNAs, based on the data for IgD^- PBs from week 9 PBMC samples, we estimated the frequencies of VRC01-class B cells among three additional populations of B cells in the periphery at week 9. First, as an estimate for the frequency of VRC01-class PBs among CD4bs-specific IgD^- PBs, we used the frequency of VRC01-class PBs among BCR-sequenced CD4bs-specific IgD^- PBs. Second, to obtain an estimate for the frequency of VRC01-class PBs among GT8-specific IgD^- PBs, we multiplied the frequency of VRC01-class PBs among CD4bs-specific IgD^- PBs by the ratio of CD4bs-specific IgD^- PBs to GT8-specific IgD^- PBs. Third, to obtain an estimate for the frequency of VRC01-class IgD^- PBs among all B cells, we multiplied the frequency of VRC01-class cells among CD4bs-specific IgD^- PBs by the ratio of CD4bs-specific IgD^- PBs to all B cells.

Key B cell frequencies reported

B cell frequencies and B cell receptor (BCR) signatures were measured by flow cytometry (FACS) and BCR sequencing, respectively. In this section we list the key frequencies reported in the manuscript and/or in the supplementary data files. Additional frequencies not listed here are provided in the supplementary data files. Methods to estimate frequencies based on combined cytometry and BCR sequence analyses are given in the preceding section, Computing VRC01-class frequencies by combining frequencies from FACS and BCR sequencing.

The key frequencies reported for PBMC samples (weeks −4, 4, 8, 10, 16) were as follows.

From cytometry analysis:

- Percent of IgG memory B cells that were $GT8^{++}$ (regardless of KO binding status)
- Percent of $GT8^{++}$ IgG memory B cells that were KO^-
- Percent of IgG memory B cells that were CD4bs-specific

From combined cytometry and BCR sequence analysis:

- Percent of CD4bs-specific IgG memory B cells that were VRC01-class
- Percent of GT8-specific IgG memory B cells detected as VRC01-class
- Percent of IgG memory B cells detected as VRC01-class
- Percent of B cells detected as VRC01-class

The key frequencies reported for FNA samples (weeks 3 and 11) were as follows.

From cytometry analysis:

- Percent of IgG GC B cells that were $GT8^{++}$ (regardless of KO binding status)
- Percent of $GT8^{++}$ IgG GC B cells that were KO^-
- Percent of IgG GC B cells that were CD4bs-specific

From combined cytometry and BCR sequence analysis:

- Percent of CD4bs-specific IgG GC B cells that were VRC01-class
- Percent of GT8-specific IgG GC B cells detected as VRC01-class
- Percent of IgG GC B cells detected as VRC01-class
- Percent of B cells detected as VRC01-class

The key frequencies reported for PB samples (week 9) were as follows.

From cytometry analysis:

- Percent of IgD^- PBs that were $GT8^{++}$ (regardless of KO binding status)
- Percent of $GT8^{++}$ IgD^- PBs that were KO^-
- Percent of IgD^- PBs that were CD4bs-specific

From combined cytometry and BCR sequence analysis:

- Percent of CD4bs-specific IgD^- PBs that were VRC01-class
- Percent of GT8-specific IgD^- PBs detected as VRC01-class
- Percent of IgD^- PBs detected as VRC01-class
- Percent of B cells detected as VRC01-class

VRC01-class response calls

The criteria for determining if detection of one or more VRC01-class B cells in a sample represented a vaccine-induced VRC01-class response were as follows.

Memory B cell data

For each post-baseline visit in which memory B cells from PBMCs were sorted (weeks 4, 8, 10, 16), detection of one or more VRC01-class B cells was labeled a vaccine-induced VRC01-class response if the estimated frequency of VRC01-class IgG memory B cells among all IgG memory B cells was greater than the corresponding baseline frequency. For participants with no sequences of CD4bs-specific memory B cells available at baseline, the baseline frequency was estimated as the frequency of CD4bs-specific (KO^-GT8^{++}) IgG memory B cells, which was a conservative approach.

GC B cell data

For FNA samples (weeks 3 and 11), for which baseline data were not available, detection of one or more VRC01-class B cells was labeled a vaccine-induced VRC01-class response if the estimated frequency of VRC01-class IgG GC B cells among all IgG GC B cells was greater than 0.1% (1 in 1000). This was an arbitrary threshold, but we judged it to be reasonable considering that (i) none of the placebos produced any detectable VRC01-class B cells in FNA samples, and (ii) 0.1% represents a substantial frequency for a single class of B cells (with specific BCR properties) within a polyclonal response.

Plasmablast data

For PB samples (week 9), for which baseline data were also not available, detection of one or more VRC01-class plasmablasts was labeled a vaccine-induced VRC01-class response if the estimated frequency of VRC01-class IgD^- PBs among all IgD^- PB cells was greater than 0.1% (the same numerical threshold used for testing FNA samples). We judged this to be a reasonable threshold, because (i) none of the placebos produced any detectable VRC01-class B cells in PB samples, and (ii) as noted above, 0.1% represents a substantial frequency for

a single class of B cells (with specific BCR properties) within a polyclonal response.

Pretrial evaluation of baseline VRC01-class IgG B cell frequency

During pretrial development of the B cell sorting and BCR sequencing assay, we sought to determine an estimate for the baseline frequency of VRC01-class IgG B cells in humans. We applied the assay to leukapheresis samples from 35 healthy, HIV-unexposed donors, including approximately 12 billion PBMCs and approximately 29.2 million IgG^+ memory B cells. From 142 BCRs with HC and LC sequenced out of 171 CD4bs-specific cells sorted, we detected no VRC01-class B cells, indicating a relatively low baseline frequency of VRC01-class B cells in the human IgG memory B cell repertoire. In contrast, we verified by sorting of human naïve IgM+ B cells that the same assay isolated VRC01-class human naïve precursors at frequencies similar to those reported previously (not shown).

IGHV1-2 genotype analysis using IgDiscover

Genotyping of the G001 participants was performed under an ethics approval from the National Ethical Review Agency of Sweden (decision no. 2021-01850). Total RNA was isolated from frozen PBMC samples prepared from each participant (n = 48) using the Qiagen RNeasy kit and protocol. Two hundred nanograms of total RNA was used for cDNA synthesis with an IgM constant region primer that contained a Unique Molecular Identifier (UMI), according to the procedures described previously (*86*). Two independent 5′ multiplex libraries (L and U) were produced for each case using either a IGHV leader region specific primer set (L) or a primer set that targeted the 5′ UTR (U). The libraries were individually indexed and sequenced on the Illumina MiSeq platform using the V3 2 × 300 cycle kits (Illumina). The Read 1 and Read 2 files for each library were processed using the IgDiscover analysis pipeline as described previously (*86*, *87*). The IgDiscover program (version 0.12.4.dev266+ge9e3119) enabled the analysis of IGHV1-2 allele content in each case, using the two independent libraries for high confidence allele identification.

BCR sequence hierarchical clustering

Average linkage agglomerative clustering (Fig. 3 and figs. S15, S17, S18, S22, and S23) was performed using the SADIE cluster module. The module uses scikit-learn (*88*) to perform clustering specifically on BCR sequences with the AIRR annotation schema. Sequences were split into VRC01-class and non-VRC01-class and then grouped by HCDR3 and LCDR3 length. For each subgroup, the distance between two antibodies was the sum of Levenshtein distances between the corresponding HCDRs and LCDRs (HCDR1 distance + HCDR2 distance + HCDR3 distance + LCDR1 distance + LCDR2 distance + LCDR3 distance). To facilliate clustering of both mutated and unmutated BCRs with a single distance cutoff, the "somatic pad" option was used to subtract all common somatic mutations from the total Levenshtein distance for any pair of BCRs (*89*). With this option, the minimal distance between two BCRs was zero. The sparse upper-triangular distance matrix was then saved into memory. Clustering was then performed using scikit-learn with the precomputed distance matrix using average-linkage clustering and a distance cutoff of 3. The cluster labels were extracted and added to the output dataframe. The centroid of every cluster was computed as the lowest mean distance to every other member in the cluster. The all-vs-all, intracluster, and intercentroid distances were then computed from the saved distance matrix.

Bioinformatic BCR sequence analysis other than VRC01-calls or clustering

BCR V gene assignments and mutation levels were determined using SADIE, which was also used in the ANNOTATION module described above. Mutation analysis for VH1-2 genes was made more accurate by accounting for the personalized IGHV1-2 genotypes as described in the PERSONALIZE module above. Statistical quantile analyses throughout the manuscript were carried out using R and Pandas (https://github.com/pandas-dev/pandas). Confidence intervals for the non-VRC01-class response rate (fig. S19C) were computed using the Wilson score method (*90*). Statistical comparisons for BCR mutation levels at different time points (Fig. 5, fig. S20, and tables S46 to S49), were carried out using a Wilcoxon signed-rank test for paired data using the VISCfunctions R package (https://github.com/FredHutch/VISCfunctions). Analyses of VRC01-class BCR features (Fig. 6 and figs. S16 and S24 to S29) were carried out by custom python functions available as a package in the data repository for G001 (https://github.com/SchiefLab/G001). We detected few recurring VRC01-class clones at different time points, and therefore we did not carry out analyses of intraclonal SHM over time as have been reported elsewhere (*64*). Inferred germline amino acid sequences were computed by reverting templated V, D, and J gene segments to their germline sequences for the alleles predicted on the basis of the antibody nucleotide sequence; in this process, VH1-2 allele predictions were made more accurate by restricting the allowed alleles for each participant to those experimentally determined by VH1-2 genotyping for that participant. When referring to control distributions from OAS (*91*, *92*), we restricted to human, nonvaccinated, no disease state data from OAS. In data we report from OAS, each symbol refers to a separate individual.

Antibody selection and production for SPR

For IgG expression, we selected at least two VRC01-class and one non-VRC01-class BCR from each participant at each postvaccination time point, attempting to represent the genetic diversity and mutation levels of the low dose BCRs. Although some mAbs failed to express, we carried out SPR analyses for 267 VRC01-class and 145 non-VRC01-class BCRs across all participants and postvaccination time points (Fig. 7, fig. S29, and data S2). To assess affinities of potential naïve precursors to the postvaccination BCRs, we evaluated eOD-GT8 binding to inferred-germline antibodies (iGLs) for 118 VRC01-class and 55 non-VRC01-class postvaccination BCRs. For comparison we also measured eOD-GT8 binding to prevaccination IgG memory BCRs (6 of 7 VRC01-class BCRs from both dose groups and 53 of 55 non-VRC01-class BCRs from the low dose group) and human naïve VRC01-class (n = 62) and non-VRC01-class (n = 72) precursors specific for the CD4bs of eOD-GT8 and isolated previously from 12 other HIV-unexposed individuals (*21*, *43*) (Fig. 7 and data S2).

Genes encoding the antibody Fv regions were synthesized by GenScript and cloned into antibody expression vectors pCW-CHIg-hG1, pCW-CLIg-hL2, and pCW-CLIg-hk. Monoclonal antibodies were produced by GenScript using transient transfection in the Expi293F system (ThermoFisher) and were purified using HiTrap MabSelect SuRe columns (Cytiva). Additional antibody production was conducted in house using transient transfection of HEK-293F cells (ThermoFisher) and purification using rProtein A Sepharose Fast Flow resin (Cytiva). We note that the antibodies were produced as IgG1, but our B cell sorting and BCR sequencing workflow did not distinguish between IgG subclasses.

Antigen production for SPR

His-tagged monomeric and trimeric antigens were produced by transient transfection of HEK-293F cells (ThermoFisher) and purified by immobilized metal ion affinity chromatography (IMAC) using HisTrap excel columns (Cytiva) followed be size-exclusion chromatography (SEC) using either Superdex 75 10/300 GL or Superdex 200 Increase 10/300 GL columns (Cytiva).

SPR

We measured the kinetics and affinities of antibody-antigen interactions on a Carterra LSA instrument using HC30M or CMDP sensor chips (Carterra) and 1x HBS-EP+ pH 7.4 running buffer (20× stock from Teknova, cat. no. H8022) supplemented with BSA at 1 mg/ml.

We followed Carterra software instructions to prepare chip surfaces for ligand capture. In a typical experiment, approximately 2500 to 2700 RU of capture antibody (SouthernBiothech catalog no. 2047-01) in 10 mM Sodium Acetate pH 4.5 was amine coupled. The critical detail here was the concentration range of the amine coupling reagents and capture antibody. We used *N*-hydroxysuccinimide (NHS) and 1-ethyl-3-(3-dimethylaminopropyl) carbodiimidehydrochloride (EDC) from Amine Coupling Kit (GE order code BR-1000-50). As per kit instruction 22-0510-62 AG, the NHS and EDC should be reconstituted in 10 ml of water each to give 11.5 mg/ml and 75 mg/ml respectively. However, the highest coupling levels of capture antibody were achieved by using 10 times diluted NHS and EDC during surface preparation runs. Thus, in our runs the concentrations of NHS and EDC were 1.15 mg/ml and 7.5 mg/ml. The concentrated stocks of NHS and EDC could be stored frozen in −20°C for up to 2 months without noticeable loss of activity. The SouthernBiotech capture antibody was buffer exchanged into 10 mM Sodium Acetate pH 4.5 using Zeba spin desalting columns 7K MWCO 0.5ml (catalog no. 89883 from Thermo) and was used at concentration 0.25 mg/ml with 20 min contact time. Phosphoric acid 1.7% was our regeneration solution with 60 s contact time and injected three times per each cycle. Solution concentration of ligands was around 5 ug/ml and contact time was 3 min. Raw sensograms were analyzed using Kinetics software (Carterra), interspot and blank double referencing, Langmuir model. Analyte concentrations were quantified on NanoDrop 2000c Spectrophotometer using absorption signal at 280 nm. A typical SPR run tested six different analyte concentrations using a dilution factor of four. Maximum analyte concentration for eOD-GT8 was generally 10 μM, except for weak binders which were generally rerun at higher maximum analyte concentrations of 50 or 118 μM. For eOD-GT6 and eOD-GT6 variant analytes, maximum analyte concentrations were 9 to 16 μM, but weak or expected weak binders were run at 37 to 63 μM. For MD39 trimer, maximum analyte concentration was 4 or 11 μM, but most interactions were tested at 11 μM. For core-gp120, maximum analyte concentration were 11 or 46 μM. For best results, analyte samples were buffer exchanged into the running buffer using desalting columns or dialysis. We typically covered a broad range of affinities in our runs, and the best referencing practices were different depending on how fast the off-rate was for each particular ligand. For fast off-rates (>9×10^{-3} 1/s 1×10^{-2} 1/s) we used automated batch referencing that included overlay y-align and higher analyte concentrations. For slow off-rates (≤ 9×10^{-3} 1/s), we used manual process referencing that included serial y-align and lower analyte concentrations. After automated data analysis by the Carterra Kinetics software, we also performed additional filtering to remove datasets with highest response signals smaller than signals from negative controls. This additional filtering was performed automatically using an R-script. The script also identified ligands for which capture on the sensor chip was insufficient, and measurements involving those ligands were excluded from subsequent analyses. Many interactions were measured more than once. Whether or not multiple measurements were available, we used the following algorithm to select the representative measurement for any particular interation:

1. If no measurement resulted in a kinetic-fit K_D from the Carterra Kinetics software analysis, the K_D value was set to ≥100 μM.

2. If all available measurements had kinetic-fit K_Ds from the Carterra Kinetics software analysis that were ≥5 times the maximum analyte concentration used in the measurement, the K_D value was set to ≥100 μM. The lowest max analyte concentration for which this was invoked was 37 μM, in which case the kinetic-fit K_D of >185 μM was reported as ≥100 μM.

3. If at least one measurement had a kinetic-fit K_D from the Carterra Kinetics software analysis, and if k_{on} and k_{off} were within range for the instrument ($10\ min^{-1}\ M^{-1} < k_{on} < 1 \times 10^9\ min^{-1}\ M^{-1}$; $1 \times 10^{-5}\ min^{-1} < k_{off} < 5 \times 10^{-1}\ min^{-1}$), the measurement with the lowest chi-squared fit value was chosen as the representative measure.

4. If all available measurements with a kinetic-fit K_D had a k_{off} that was out of range (this only occurred with fast k_{off}), then if the kinetic-fit K_D was within a factor of three to the equilibrium-fit K_D, the ratio of kinetic K_D to equilibrium K_D was calculated, the measurement with ratio closest to one was chosen as the representative, and equilibrium K_D was reported for that measurement. If no kinetic-fit K_D was within a factor of three to the equilibrium-fit K_D, the K_D was reported as ≥100 uM. The reporting of equilibrium-fit K_Ds was not common: in Fig. 7, n = 2 of 267 postvaccination VRC01-class K_D values, and n = 10 of 145 postvaccination non-VRC01-class K_D values, were reported as the equilibrium-fit K_D.

5. We had no cases of k_{on} out of range, thus the algorithm did not have to deal with that case.

SPR reproducibility

The majority of the iGL and postvaccination interactions reported in Fig. 7 were also measured using a different instrument (Biacore 8k) and different analyte preparations and often different ligand preparations. The K_Ds measured by the 8k were highly correlated with those measured by the Carterra LSA, and the conclusions from the two datasets were the same. Also, for the naïve precursor K_Ds measured using the Carterra and reported in Fig. 7, we previously measured and published the same interactions using a different instrument (Proteon XPR) with different analyte and ligand preparations (*21*, *43*); the results of the new and previous analyses were consistent.

Regression analyses involving SPR-measured quantities

Linear mixed effects models (LMEs) were used to analyze the linear dependence of one variable on another, for the following dependencies: (i) dependence of K_D for eOD-GT6 or its variants on K_D for eOD-GT8, for VRC01-class BCRs (Fig. 8B); (ii) dependence of iGL K_D for eOD-GT8 on the number of mutations in the BCRs from which the iGL was inferred, for VRC01-class and non-VRC01-class BCRs (fig. S30B); (iii) dependence of eOD-GT8 K_D on k_{on} and k_{off}, for VRC01-class and non-VRC01-class BCRs (fig. S32C); (iv) dependence of eOD-GT8 K_D, k_{on}, and k_{off}, on the number of BCR V gene mutations (figs. S34 to S36). LMEs were used to estimate the slope of each association [e.g., change in log(K_D) per mutation]. Estimated associations only included antibodies for which the K_D value was measureable (K_D < 100 μM). Each LME had fixed effects for the intercept and slope. Random effects for the intercept and slope were included for each participant, with the exception of estimation for a given week (figs. S34B, S35B, and S36B) or for non-VRC01-class iGL (fig. S30B), where a random effect for only the intercept was included. For non-VRC01-class BCRs at week 16 in figs. S34B, S35B, and S36B, only one antibody per participant was available, so estimates were based on a linear model (K_D, k_{on}, and k_{off}). The estimated regression line and shaded 95% prediction interval were generated using a semiparametric bootstrap method (using 1000 bootstrap datasets). LMEs were fit and P values testing the null hypothesis that the fixed effect for slope is zero were evaluated using Satterthwaite's degrees of freedom method using the lmerTest package in R (*93*). For a $\log_{10}$-transformed y-value depending linearly on x, as in figs. S34 to S36 the effect of x on y is given by $\log(y_2)$-$\log(y_1) = [x_2\text{-}x_1]\cdot s$, where s is the slope. This is equivalent to $y_2/y_1 = 10^{[x2-x1]\cdot s}$. Thus, in figs. S34 to S36 where x represents mutations and y represents log(K_D) or log(k_{on}) or log(k_{off}), an increase of n mutations going from x_1 to x_2 will lead to a change in y as: $y_2/y_1 = 10^{n\cdot s}$. For a $\log_{10}$-transformed y-value depending linearly on a $\log_{10}$-transformed x-value, as in Fig. 8B, the effect of x on y is given by $\log(y_2)$-$\log(y_1) = [\log(x_2)\text{-}\log(x_1)]\cdot s$, where s is the slope. This is equivalent to $y_2/y_1 = (x_2/x_1)^s$. Thus, in Fig. 8B, where x represents the K_D for eOD-GT6 or a GT6 variant, and y represents K_D for eOD-GT8, an increase

in the K_D for eOD-GT6 or a GT6 variant by a factor of α will lead to a change in the K_D for eOD-GT8 according to $y_2/y_1 = \alpha^s$.

Statistical analysis

Placebos in both groups were pooled into a single control group for all statistical analyses. Confidence intervals for frequencies and response rates were based on the Wilson score method (*90*). Spearman correlations were used to evaluate the association between immune responses. To assess if response rates differed by group, Barnard's exact test was used. To assess if response rates differed over time within a group, McNemar's test was used to account for paired data. Response magnitude comparisons between groups were compared using the Wilcoxon rank sum test. Response magnitude comparisons between time points were performed using the Wilcoxon signed-rank test to account for paired data. Comparisons of percent mutation levels over time (Fig. 5, fig. S20, and tables S46 to S49) were performed using the Wilcoxon signed-rank test to account for paired data. Regression analyses were performed as described in Regression analyses involving SPR-measured quantities. Statistical quantile analyses were carried out using R and Pandas (https://github.com/pandas-dev/pandas). The R language and tidyverse R packages were used for graphical and statistical analysis (*94*, *95*).

Figure generation

Most figures were generated with either Matplotlib (*96*) or a custom port of the Seaborn package that incorporates Wilson confidence intervals into the statistical analysis [(*97*); https://github.com/jwillis0720/seaborn-fork], and with Adobe Illustrator for final composition. Figures S4 and S40 were produced using the ggplot package in R. Figure generation can be found in the accompanying data analysis repository (https://github.com/SchiefLab/G001#figures). Figures S5, S6, S8, and S9 were produced using Intaglio (https://intaglio.en.softonic.com/mac). Fig. S10 was produced using BioRender (BioRender.com), and the publishing license can be found in the data repository.

REFERENCES AND NOTES

1. A. S. Fauci, An HIV vaccine is essential for ending the HIV/AIDS pandemic. *JAMA* **318**, 1535–1536 (2017). doi: 10.1001/jama.2017.13505; pmid: 29052689
2. A. Pegu *et al*., A meta-analysis of passive immunization studies shows that serum-neutralizing antibody titer associates with protection against SHIV challenge. *Cell Host Microbe* **26**, 336–346.e3 (2019). doi: 10.1016/j.chom.2019.08.014; pmid: 31513771
3. L. Corey *et al*., Two randomized trials of neutralizing antibodies to prevent HIV-1 acquisition. *N. Engl. J. Med.* **384**, 1003–1014 (2021). doi: 10.1056/NEJMoa2031738; pmid: 33730454
4. P. B. Gilbert *et al*., Neutralization titer biomarker for antibody-mediated prevention of HIV-1 acquisition. *Nat. Med.* **28**, 1924–1932 (2022). doi: 10.1038/s41591-022-01953-6; pmid: 35995954
5. X. Xiao, W. Chen, Y. Feng, D. S. Dimitrov, Maturation pathways of cross-reactive HIV-1 neutralizing antibodies. *Viruses* **1**, 802–817 (2009). doi: 10.3390/v1030802; pmid: 21994570
6. X. Xiao *et al*., Germline-like predecessors of broadly neutralizing antibodies lack measurable binding to HIV-1 envelope glycoproteins: Implications for evasion of immune responses and design of vaccine immunogens. *Biochem. Biophys. Res. Commun.* **390**, 404–409 (2009). doi: 10.1016/j.bbrc.2009.09.029; pmid: 19748484
7. D. S. Dimitrov, Therapeutic antibodies, vaccines and antibodyomes. *MAbs* **2**, 347–356 (2010). doi: 10.4161/mabs.2.3.11779; pmid: 20400863
8. M. Pancera *et al*., Crystal structure of PG16 and chimeric dissection with somatically related PG9: Structure-function analysis of two quaternary-specific antibodies that effectively neutralize HIV-1. *J. Virol.* **84**, 8098–8110 (2010). doi: 10.1128/JVI.00966-10; pmid: 20538861
9. T. Zhou *et al*., Structural basis for broad and potent neutralization of HIV-1 by antibody VRC01. *Science* **329**, 811–817 (2010). doi: 10.1126/science.1192819; pmid: 20616231
10. M. Bonsignori *et al*., Analysis of a clonal lineage of HIV-1 envelope V2/V3 conformational epitope-specific broadly neutralizing antibodies and their inferred unmutated common ancestors. *J. Virol.* **85**, 9998–10009 (2011). doi: 10.1128/JVI.05045-11; pmid: 21795340
11. J. F. Scheid *et al*., Sequence and structural convergence of broad and potent HIV antibodies that mimic CD4 binding. *Science* **333**, 1633–1637 (2011). doi: 10.1126/science.1207227; pmid: 21764753
12. S. Hoot *et al*., Recombinant HIV envelope proteins fail to engage germline versions of anti-CD4bs bNAbs. *PLOS Pathog.* **9**, e1003106 (2013). doi: 10.1371/journal.ppat.1003106; pmid: 23300456
13. J. Jardine *et al*., Rational HIV immunogen design to target specific germline B cell receptors. *Science* **340**, 711–716 (2013). doi: 10.1126/science.1234150; pmid: 23539181
14. A. T. McGuire *et al*., Engineering HIV envelope protein to activate germline B cell receptors of broadly neutralizing anti-CD4 binding site antibodies. *J. Exp. Med.* **210**, 655–663 (2013). doi: 10.1084/jem.20122824; pmid: 23530120
15. B. F. Haynes, G. Kelsoe, S. C. Harrison, T. B. Kepler, B-cell-lineage immunogen design in vaccine development with HIV-1 as a case study. *Nat. Biotechnol.* **30**, 423–433 (2012). doi: 10.1038/nbt.2197; pmid: 22565972
16. H. X. Liao *et al*., Co-evolution of a broadly neutralizing HIV-1 antibody and founder virus. *Nature* **496**, 469–476 (2013). doi: 10.1038/nature12053; pmid: 23552890
17. F. Gao *et al*., Cooperation of B cell lineages in induction of HIV-1-broadly neutralizing antibodies. *Cell* **158**, 481–491 (2014). doi: 10.1016/j.cell.2014.06.022; pmid: 25065977
18. M. Bonsignori *et al*., Maturation pathway from germline to broad HIV-1 neutralizer of a CD4-mimic antibody. *Cell* **165**, 449–463 (2016). doi: 10.1016/j.cell.2016.02.022; pmid: 26949186
19. M. Bonsignori *et al*., Staged induction of HIV-1 glycan-dependent broadly neutralizing antibodies. *Sci. Transl. Med.* **9**, eaai7514 (2017). doi: 10.1126/scitranslmed.aai7514; pmid: 28298420
20. K. O. Saunders *et al*., Targeted selection of HIV-specific antibody mutations by engineering B cell maturation. *Science* **366**, eaay7199 (2019). doi: 10.1126/science.aay7199; pmid: 31806786
21. J. G. Jardine *et al*., HIV-1 broadly neutralizing antibody precursor B cells revealed by germline-targeting immunogen. *Science* **351**, 1458–1463 (2016). doi: 10.1126/science.aad9195; pmid: 27013733
22. J. M. Steichen *et al*., HIV vaccine design to target germline precursors of glycan-dependent broadly neutralizing antibodies. *Immunity* **45**, 483–496 (2016). doi: 10.1016/j.immuni.2016.08.016; pmid: 27617678
23. A. Escolano *et al*., Sequential immunization elicits broadly neutralizing anti-HIV-1 antibodies in Ig knockin mice. *Cell* **166**, 1445–1458.e12 (2016). doi: 10.1016/j.cell.2016.07.030; pmid: 27610569
24. M. Medina-Ramírez *et al*., Design and crystal structure of a native-like HIV-1 envelope trimer that engages multiple broadly neutralizing antibody precursors in vivo. *J. Exp. Med.* **214**, 2573–2590 (2017). doi: 10.1084/jem.20161160; pmid: 28847869
25. J. M. Steichen *et al*., A generalized HIV vaccine design strategy for priming of broadly neutralizing antibody responses. *Science* **366**, eaax4380 (2019). doi: 10.1126/science.aax4380; pmid: 31672916
26. B. Briney *et al*., Tailored immunogens direct affinity maturation toward HIV neutralizing antibodies. *Cell* **166**, 1459–1470.e11 (2016). doi: 10.1016/j.cell.2016.08.005; pmid: 27610570
27. M. Tian *et al*., Induction of HIV neutralizing antibody lineages in mice with diverse precursor repertoires. *Cell* **166**, 1471–1484.e18 (2016). doi: 10.1016/j.cell.2016.07.029; pmid: 27610571
28. K. R. Parks *et al*., Overcoming steric restrictions of VRC01 HIV-1 neutralizing antibodies through immunization. *Cell Rep.* **29**, 3060–3072.e7 (2019). doi: 10.1016/j.celrep.2019.10.071; pmid: 31801073
29. X. Chen *et al*., Vaccination induces maturation in a mouse model of diverse unmutated VRC01-class precursors to HIV-neutralizing antibodies with >50% breadth. *Immunity* **54**, 324–339.e8 (2021). doi: 10.1016/j.immuni.2020.12.014; pmid: 33453152
30. L. Verkoczy *et al*., Induction of HIV-1 broad neutralizing antibodies in 2F5 knock-in mice: Selection against membrane proximal external region-associated autoreactivity limits T-dependent responses. *J. Immunol.* **191**, 2538–2550 (2013). doi: 10.4049/jimmunol.1300971; pmid: 23918977
31. T. Bradley *et al*., HIV-1 envelope mimicry of host enzyme kynureninase does not disrupt tryptophan metabolism. *J. Immunol.* **197**, 4663–4673 (2016). doi: 10.4049/jimmunol.1601484; pmid: 27849170
32. R. Zhang *et al*., Initiation of immune tolerance-controlled HIV gp41 neutralizing B cell lineages. *Sci. Transl. Med.* **8**, 336ra62 (2016). doi: 10.1126/scitranslmed.aaf0618; pmid: 27122615
33. S. M. Alam *et al*., Mimicry of an HIV broadly neutralizing antibody epitope with a synthetic glycopeptide. *Sci. Transl. Med.* **9**, eaai7521 (2017). doi: 10.1126/scitranslmed.aai7521; pmid: 28298421
34. T. Zhou *et al*., Quantification of the impact of the HIV-1-glycan shield on antibody elicitation. *Cell Rep.* **19**, 719–732 (2017). doi: 10.1016/j.celrep.2017.04.013; pmid: 28445724
35. V. Dubrovskaya *et al*., Targeted N-glycan deletion at the receptor-binding site retains HIV Env NFL trimer integrity and accelerates the elicited antibody response. *PLOS Pathog.* **13**, e1006614 (2017). doi: 10.1371/journal.ppat.1006614; pmid: 28902916
36. K. Xu *et al*., Epitope-based vaccine design yields fusion peptide-directed antibodies that neutralize diverse strains of HIV-1. *Nat. Med.* **24**, 857–867 (2018). doi: 10.1038/s41591-018-0042-6; pmid: 29867235
37. D. Fera *et al*., HIV envelope V3 region mimic embodies key features of a broadly neutralizing antibody lineage epitope. *Nat. Commun.* **9**, 1111 (2018). doi: 10.1038/s41467-018-03565-6; pmid: 29549260
38. R. Kong *et al*., Antibody lineages with vaccine-induced antigen-binding hotspots develop broad HIV neutralization. *Cell* **178**, 567–584.e19 (2019). doi: 10.1016/j.cell.2019.06.030; pmid: 31348886
39. J. G. Jardine *et al*., Priming a broadly neutralizing antibody response to HIV-1 using a germline-targeting immunogen. *Science* **349**, 156–161 (2015). doi: 10.1126/science.aac5894; pmid: 26089355
40. V. K. Sharma *et al*., Use of transient transfection for cGMP manufacturing of eOD-GT8 60mer, a self-assembling nanoparticle germline-targeting HIV-1 vaccine candidate. bioRxiv 2022.09.30.510310 [Preprint] (2022); https://doi.org/10.1101/2022.09.30.510310.
41. A. P. West Jr., R. Diskin, M. C. Nussenzweig, P. J. Bjorkman, Structural basis for germ-line gene usage of a potent class of antibodies targeting the CD4-binding site of HIV-1 gp120. *Proc. Natl. Acad. Sci. U.S.A.* **109**, E2083–E2090 (2012). doi: 10.1073/pnas.1208984109; pmid: 22745174
42. T. Zhou *et al*., Multidonor analysis reveals structural elements, genetic determinants, and maturation pathway for HIV-1 neutralization by VRC01-class antibodies. *Immunity* **39**, 245–258 (2013). doi: 10.1016/j.immuni.2013.04.012; pmid: 23911655
43. C. Havenar-Daughton *et al*., The human naive B cell repertoire contains distinct subclasses for a germline-targeting HIV-1 vaccine immunogen. *Sci. Transl. Med.* **10**, eaat0381 (2018). doi: 10.1126/scitranslmed.aat0381; pmid: 29973404
44. J. H. Lee *et al*., Vaccine genetics of IGHV1-2 VRC01-class broadly neutralizing antibody precursor naïve human B cells. *NPJ Vaccines* **6**, 113 (2021). doi: 10.1038/s41541-021-00376-7; pmid: 34489473
45. P. Dosenovic *et al*., Immunization for HIV-1 broadly neutralizing antibodies in human Ig knockin mice. *Cell* **161**, 1505–1515 (2015). doi: 10.1016/j.cell.2015.06.003; pmid: 26091035
46. D. Sok *et al*., Priming HIV-1 broadly neutralizing antibody precursors in human Ig loci transgenic mice. *Science* **353**, 1557–1560 (2016). doi: 10.1126/science.aah3945; pmid: 27608668

47. R. K. Abbott *et al*., Precursor frequency and affinity determine B cell competitive fitness in germinal centers, tested with germline-targeting HIV vaccine immunogens. *Immunity* **48**, 133–146.e6 (2018). doi: 10.1016/j.immuni.2017.11.023; pmid: 29287996
48. D. Huang *et al*., B cells expressing authentic naive human VRC01-class BCRs can be recruited to germinal centers and affinity mature in multiple independent mouse models. *Proc. Natl. Acad. Sci. U.S.A.* **117**, 22920–22931 (2020). doi: 10.1073/pnas.2004489117; pmid: 32873644
49. X. Wang *et al*., Multiplexed CRISPR/CAS9-mediated engineering of pre-clinical mouse models bearing native human B cell receptors. *EMBO J.* **40**, e105926 (2021). doi: 10.15252/embj.2020105926; pmid: 33258500
50. C. Havenar-Daughton *et al*., Rapid germinal center and antibody responses in non-human primates after a single nanoparticle vaccine immunization. *Cell Rep.* **29**, 1756–1766.e8 (2019). doi: 10.1016/j.celrep.2019.10.008; pmid: 31722194
51. V. Vigdorovich *et al*., Repertoire comparison of the B-cell receptor-encoding loci in humans and rhesus macaques by next-generation sequencing. *Clin. Transl. Immunology* **5**, e93 (2016). doi: 10.1038/cti.2016.42; pmid: 27525066
52. N. Vázquez Bernat *et al*., Rhesus and cynomolgus macaque immunoglobulin heavy-chain genotyping yields comprehensive databases of germline VDJ alleles. *Immunity* **54**, 355–366.e4 (2021). doi: 10.1016/j.immuni.2020.12.018; pmid: 33484642
53. C. Hervé, B. Laupèze, G. Del Giudice, A. M. Didierlaurent, F. Tavares Da Silva, The how's and what's of vaccine reactogenicity. *NPJ Vaccines* **4**, 39 (2019). doi: 10.1038/s41541-019-0132-6; pmid: 31583123
54. H. Duan *et al*., Glycan masking focuses immune responses to the HIV-1 CD4-binding site and enhances elicitation of VRC01-class precursor antibodies. *Immunity* **49**, 301–311.e5 (2018). doi: 10.1016/j.immuni.2018.07.005; pmid: 30076101
55. J. Umotoy *et al*., Rapid and focused maturation of a VRC01-class HIV broadly neutralizing antibody lineage involves both binding and accommodation of the N276-glycan. *Immunity* **51**, 141–154.e6 (2019). doi: 10.1016/j.immuni.2019.06.004; pmid: 31315032
56. J. G. Jardine *et al*., Minimally mutated HIV-1 broadly neutralizing antibodies to guide reductionist vaccine design. *PLOS Pathog.* **12**, e1005815 (2016). doi: 10.1371/journal.ppat.1005815; pmid: 27560183
57. B. A. Heesters, C. E. van der Poel, A. Das, M. C. Carroll, Antigen presentation to B cells. *Trends Immunol.* **37**, 844–854 (2016). doi: 10.1016/j.it.2016.10.003; pmid: 27793570
58. Y. Kato *et al*., Multifaceted effects of antigen valency on B cell response composition and differentiation in vivo. *Immunity* **53**, 548–563.e8 (2020). doi: 10.1016/j.immuni.2020.08.001; pmid: 32857950
59. P. Dosenovic *et al*., Anti-HIV-1 B cell responses are dependent on B cell precursor frequency and antigen-binding affinity. *Proc. Natl. Acad. Sci. U.S.A.* **115**, 4743–4748 (2018). doi: 10.1073/pnas.1803457115; pmid: 29666227
60. L. Mesin *et al*., Restricted clonality and limited germinal center reentry characterize memory B cell reactivation by boosting. *Cell* **180**, 92–106.e11 (2020). doi: 10.1016/j.cell.2019.11.032; pmid: 31866068
61. C. Viant *et al*., Antibody affinity shapes the choice between memory and germinal center B cell fates. *Cell* **183**, 1298–1311.e11 (2020). doi: 10.1016/j.cell.2020.09.063; pmid: 33125897
62. K. A. Pape, J. J. Taylor, R. W. Maul, P. J. Gearhart, M. K. Jenkins, Different B cell populations mediate early and late memory during an endogenous immune response. *Science* **331**, 1203–1207 (2011). doi: 10.1126/science.1201730; pmid: 21310965
63. G. V. Zuccarino-Catania *et al*., CD80 and PD-L2 define functionally distinct memory B cell subsets that are independent of antibody isotype. *Nat. Immunol.* **15**, 631–637 (2014). doi: 10.1038/ni.2914; pmid: 24880458
64. G. E. Phad *et al*., Extensive dissemination and intraclonal maturation of HIV Env vaccine-induced B cell responses. *J. Exp. Med.* **217**, e20191155 (2020). doi: 10.1084/jem.20191155; pmid: 31704807
65. A. Cho *et al*., Anti-SARS-CoV-2 receptor-binding domain antibody evolution after mRNA vaccination. *Nature* **600**, 517–522 (2021). doi: 10.1038/s41586-021-04060-7; pmid: 34619745
66. F. Muecksch *et al*., Increased memory B cell potency and breadth after a SARS-CoV-2 mRNA boost. *Nature* **607**, 128–134 (2022). doi: 10.1038/s41586-022-04778-y; pmid: 35447027
67. G. D. Tomaras *et al*., Initial B-cell responses to transmitted human immunodeficiency virus type 1: Virion-binding immunoglobulin M (IgM) and IgG antibodies followed by plasma anti-gp41 antibodies with ineffective control of initial viremia. *J. Virol.* **82**, 12449–12463 (2008). doi: 10.1128/JVI.01708-08; pmid: 18842730
68. N. L. Yates *et al*., Vaccine-induced Env V1-V2 IgG3 correlates with lower HIV-1 infection risk and declines soon after vaccination. *Sci. Transl. Med.* **6**, 228ra39 (2014). doi: 10.1126/scitranslmed.3007730; pmid: 24648342
69. N. L. Yates *et al*., HIV-1 envelope glycoproteins from diverse clades differentiate antibody responses and durability among vaccinees. *J. Virol.* **92**, e01843-17 (2018). doi: 10.1128/JVI.01843-17; pmid: 29386288
70. D. C. Montefiori, Measuring HIV neutralization in a luciferase reporter gene assay. *Methods Mol. Biol.* **485**, 395–405 (2009). doi: 10.1007/978-1-59745-170-3_26; pmid: 19020839
71. M. Sarzotti-Kelsoe *et al*., Optimization and validation of the TZM-bl assay for standardized assessments of neutralizing antibodies against HIV-1. *J. Immunol. Methods* **409**, 131–146 (2014). doi: 10.1016/j.jim.2013.11.022; pmid: 24291345
72. C. C. LaBranche *et al*., HIV-1 envelope glycan modifications that permit neutralization by germline-reverted VRC01-class broadly neutralizing antibodies. *PLOS Pathog.* **14**, e1007431 (2018). doi: 10.1371/journal.ppat.1007431; pmid: 30395637
73. C. C. LaBranche *et al*., Neutralization-guided design of HIV-1 envelope trimers with high affinity for the unmutated common ancestor of CH235 lineage CD4bs broadly neutralizing antibodies. *PLOS Pathog.* **15**, e1008026 (2019). doi: 10.1371/journal.ppat.1008026; pmid: 31527908
74. G. Finak, W. Jiang, R. Gottardo, CytoML for cross-platform cytometry data sharing. *Cytometry A* **93**, 1189–1196 (2018). doi: 10.1002/cyto.a.23663; pmid: 30551257
75. G. Finak, M. Jiang, flowWorkspace: Infrastructure for representing and interacting with gated and ungated cytometry data sets. R package version 4.5.3. 2011.
76. P. Van, W. Jiang, R. Gottardo, G. Finak, ggCyto: Next generation open-source visualization software for cytometry. *Bioinformatics* **34**, 3951–3953 (2018). doi: 10.1093/bioinformatics/bty441; pmid: 29868771
77. K. L. Boswell *et al*., Application of B cell immortalization for the isolation of antibodies and B cell clones from vaccine and infection settings. bioRxiv 2022.2003.2029.485179 [Preprint] (2022); https://doi.org/10.1101/2022.03.29.485179.
78. A. A. Upadhyay *et al*., BALDR: A computational pipeline for paired heavy and light chain immunoglobulin reconstruction in single-cell RNA-seq data. *Genome Med.* **10**, 20 (2018). doi: 10.1186/s13073-018-0528-3; pmid: 29558968
79. B. Briney, D. R. Burton, Massively scalable genetic analysis of antibody repertoires. bioRxiv 447813 [Preprint] (2018); https://doi.org/10.1101/447813.
80. F. Breden *et al*., Reproducibility and reuse of adaptive immune receptor repertoire data. *Front. Immunol.* **8**, 1418 (2017). doi: 10.3389/fimmu.2017.01418; pmid: 29163494
81. B. Ewing, L. Hillier, M. C. Wendl, P. Green, Base-calling of automated sequencer traces using phred. I. Accuracy assessment. *Genome Res.* **8**, 175–185 (1998). doi: 10.1101/gr.8.3.175; pmid: 9521921
82. B. Ewing, P. Green, Base-calling of automated sequencer traces using phred. II. Error probabilities. *Genome Res.* **8**, 186–194 (1998). doi: 10.1101/gr.8.3.186; pmid: 9521922
83. J. Ye, N. Ma, T. L. Madden, J. M. Ostell, IgBLAST: An immunoglobulin variable domain sequence analysis tool. *Nucleic Acids Res.* **41**, W34–W40 (2013). doi: 10.1093/nar/gkt382; pmid: 23671333
84. G. Navarro, A guided tour to approximate string matching. *ACM Comput. Surv.* **33**, 31–88 (2001). doi: 10.1145/375360.375365
85. J. Dunbar, C. M. Deane, ANARCI: Antigen receptor numbering and receptor classification. *Bioinformatics* **32**, 298–300 (2016). pmid: 26424857
86. N. Vázquez Bernat *et al*., High-quality library preparation for NGS-based immunoglobulin germline gene inference and repertoire expression analysis. *Front. Immunol.* **10**, 660 (2019). doi: 10.3389/fimmu.2019.00660; pmid: 31024532
87. M. M. Corcoran *et al*., Production of individualized V gene databases reveals high levels of immunoglobulin genetic diversity. *Nat. Commun.* **7**, 13642 (2016). doi: 10.1038/ncomms13642; pmid: 27995928
88. F. Pedregosa *et al*., Scikit-learn: Machine learning in Python. *J. Mach. Learn. Res.* **12**, 2825–2830 (2011).
89. B. Briney, K. Le, J. Zhu, D. R. Burton, Clonify: Unseeded antibody lineage assignment from next-generation sequencing data. *Sci. Rep.* **6**, 23901 (2016). doi: 10.1038/srep23901; pmid: 27102563
90. A. Agresti, B. A. Coull, Approximate is better than "exact" for interval estimation of binomial proportions. *Am. Stat.* **52**, 119–126 (1998).
91. A. Kovaltsuk *et al*., Observed Antibody Space: A resource for data mining next-generation sequencing of antibody repertoires. *J. Immunol.* **201**, 2502–2509 (2018). doi: 10.4049/jimmunol.1800708; pmid: 30217829
92. T. H. Olsen, F. Boyles, C. M. Deane, Observed Antibody Space: A diverse database of cleaned, annotated, and translated unpaired and paired antibody sequences. *Protein Sci.* **31**, 141–146 (2022). doi: 10.1002/pro.4205; pmid: 34655133
93. A. Kuznetsova, P. B. Brockhoff, R. H. B. Christensen, lmerTest package: Tests in linear mixed effects models. *J. Stat. Softw.* **82**, 1–26 (2017). doi: 10.18637/jss.v082.i13
94. H. Wickham *et al*., Welcome to the tidyverse. *J. Open Source Softw.* **4**, 1686 (2019). doi: 10.21105/joss.01686
95. R Core Team, R: A Language and Environment for Statistical Computing (2019); https://www.R-project.org/.
96. J. D. Hunter, Matplotlib: A 2D graphics environment. *Comput. Sci. Eng.* **9**, 90–95 (2007). doi: 10.1109/MCSE.2007.55
97. M. L. Waskom, seaborn: Statistical data visualization. *J. Open Source Softw.* **6**, 3021 (2021). doi: 10.21105/joss.03021
98. B. J. DeKosky *et al*., In-depth determination and analysis of the human paired heavy- and light-chain antibody repertoire. *Nat. Med.* **21**, 86–91 (2015). doi: 10.1038/nm.3743; pmid: 25501908
99. J. Willis, SchiefLab/G001:First release, Zenodo (2022); https://doi.org/10.5281/zenodo.7334877.

ACKNOWLEDGMENTS

We thank P. Anklesaria, N. Russell, and E. Emini for discussions and trial planning; and L. Stamatatos, B. Correia, M. Azoitei, J. Bohl, S. Deeks, and P. Fast for comments on the manuscript. At IAVI, we thank H. Park, L. Sunner, I. Ayanru, H. Bester, P. Neuenschwander, D. Todd, K. Rutkowski, R. Edelstein, and K. Crisafi for clinical management; J. Ackland for overseeing the toxicology study; S. Hingorani, A. Elnatan, and D. Zachariah for regulatory filings; and V. Tsvetnitsky, E. Sayeed, V. Sharma, J. Ackland, K. Syvertsen, S. Pallerla, S. Avula, P. Kishineskaya, R. Platt, N. Williams, R. Colacot, and T. Hassell for manufacturing oversight and quality assurance. We thank O. Fagbayi and A. Mosley for project management at the IAVI Neutralizing Antibody Center (NAC) at Scripps. At Fred Hutchinson Cancer Center (FHCC), we thank D. Berger, G. Braun, and K. Louis for clinical operations; A. Varni, T. Haight, C. Marty, and S. Ameny for sample and assay management; A. Heit for FNA method development; and M. Shen and J. Hural for laboratory operations. At George Washington University (GWU), we thank E. Malkin, S. Henn, A. Desrosiers, and S. Walker for clinical operations; and L. Scholte, L. Schellhaas, and L. Hoeweler for sample and assay management. Related to BAMA assays at Duke, we thank T. McNair, J. Choi, and M. Archibald for technical expertise; S. Sawant for data analysis; M. Sampson and A. Sharak for data management; J. Lucas for the Good Clinical Laboratory Practice (GCLP)–compliant laboratory environment; and M. Sarzotti-Kelsoe for quality assurance oversight. For neutralization assays at Duke, we thank E. Domin, C. West, and J. Chen. At the National Institutes of Health (NIH) Vaccine Research Center (VRC), we thank J. M. Brenchley for flow cytometry support, and M. Prabhakaran and B. Flach for technical advice. At IAVI and Scripps, we thank D. Sok, B. Briney, P. Skog, D. Nemazee, and D. Burton for a preclinical in vivo test of vaccine and adjuvant. At GlaxoSmithKline Biologicals (GSK), we thank M. Koutsoukos, F. Roman, O. van der Meeren, C. Lorin, and C. Laugier for providing $AS01_B$ and for carrying out preclinical compatibility and toxicity studies. We also thank C. Havenar-Daughton and B. Shakoor for sequences of CLK antibodies, J. H. Lee for providing human naïve BCR sequences from (*44*), X. Wang, and F. Batista for providing data from (*49*). **Funding:** This work was supported by the Bill and Melinda Gates Foundation Collaboration for AIDS Vaccine Discovery (CAVIMC INV-007368 to D.M. and G.D.T.; CCVIMC INV-007371 to R.A.K., A.B.M., and M.J.M.; VISC INV-008017 and INV-032929 to A.C.d.; VxPDC INV-008352 and INV-007375 to IAVI; and NAC INV-007522 and INV-008813 to W.R.S.); IAVI (including IAVI 167627819 to M.J.M., IAVI A08031 research collaboration agreement with Karolinska Intitutet to G.B.K.H., and other support to W.R.S.); the IAVI Neutralizing Antibody Center (NAC) to W.R.S.; National Institute of Allergy and Infectious Diseases (NIAID) P01 AI094419 (HIVRAD Optimizing HIV immunogen-BCR interactions for vaccine development") (to W.R.S.); UM1 AI100663 (Scripps Center for HIV/AIDS Vaccine Immunology and Immunogen Discovery) and UM1 AI144462 (Scripps Consortium for HIV/AIDS Vaccine Development) (to W.R.S. and M.J.M.); and UM1AI069481 (Seattle-Lausanne CTU), U19AI128914 (HIPC), and UM1AI068618 (HVTN LC) to M.J.M. This work was also supported by the Swedish Research Council (grant 2017-00968 to G.B.K.H.) and by the Ragon Institute of MGH, MIT, and Harvard (to W.R.S.). **Author contributions:** K.W.C., A.C.d., S.M., D.S.L., J.R.W., W.J.F., M.J.M., A.B.M., and W.R.S.

designed the study. D.J.L., K.W.C., M.J.M., R.A.K., and A.B.M. supervised B cell sorting, PCR, and sequencing. J.R.W., W.J.F., A.C.d., S.M., G.F., and W.R.S. carried out data organization and BCR sequence analysis. L.B.-F., A.Sr., J.R.P., R.E.W., A.Se., J.Br., A.M.R., W.H., and D.R.A. carried out or assisted B cell sorting and/or PCR. S.M., F.R., A.Lo., and D.S.L. provided trial planning. V.P. and D.S.L. monitored safety and adherence to protocol. N.L.Y., L.D.W., and G.D.T. supervised BAMA studies. K.G., H.G., and D.M. supervised neutralization assays. M.M.C. and G.B.K.H. provided VH1-2 genotype analysis. K.W.C., L.B.-F., A.C., and A.B.M. developed the B cell assay pre-trial. A.T. and D.M.B. assisted data organization. M.R. contributed gating design. S.C. provided guidance on FNAs and FACS. J.M., O.Ko., N.K., J.Be., D.D., and M.J.M. supervised all clinical activities. O.Ka. and A.Li. performed SPR analysis. C.A.C., T.Sc., X.H., and W.R.S. planned SPR studies and analyzed results. R.T., E.G., S.E., N.A., D.L., T.-M.M., M.K., and B.G. produced proteins and antibodies for SPR. W.J.F., C.R.M., and A.C.d. performed statistical analyses. W.R.S. wrote the main text; D.J.L., K.W.C., J.R.W., C.A.C., O.Ka., and W.R.S. wrote the supplementary materials; and all authors commented. J.R.W., W.J.F., A.C.d., T.Si., K.W.C., D.J.L., and W.R.S. created figures and tables. **Competing interests:** W.R.S. and S.M. are inventors on patents filed by Scripps and IAVI on the eOD-GT8 monomer and 60mer immunogens. **Data and materials availability:** All BCR sequences and FACS analysis files produced in this study are available in the public data repository https://github.com/SchiefLab/G001 (*99*). The repository contains four separate modules: (i) FACS analysis, (ii) BCR sequence analysis, (iii) combined B cell frequency and BCR sequencing analysis, and (iv) figure and table generation. Instructions for running each module of the repository are provided in the README file. Sequences for antibody expression vectors were deposited in GenBank under accession numbers ON512569, ON5125670, and ON5125671. All other data are available in the main text or supplementary materials. **License information:** Copyright © 2022 the authors, some rights reserved; exclusive licensee American Association for the Advancement of Science. No claim to original US government works. https://www.science.org/about/science-licenses-journal-article-reuse

SUPPLEMENTARY MATERIALS

science.org/doi/10.1126/science.add6502
Supplementary Text
Figs. S1 to S41
Tables S1 to S50
References (*100*–*114*)
MDAR Reproducibility Checklist
Data S1 and S2

Submitted 24 June 2022; resubmitted 28 September 2022
Accepted 27 October 2022
10.1126/science.add6502

RESEARCH ARTICLE SUMMARY

SYNTHETIC BIOLOGY

Monitoring of cell-cell communication and contact history in mammals

Shaohua Zhang†, Huan Zhao†, Zixin Liu, Kuo Liu, Huan Zhu, Wenjuan Pu, Lingjuan He, Rong A. Wang, Bin Zhou*

INTRODUCTION: Cell-cell communication through direct contact is pervasive in multicellular organisms and is essential in many fundamental biological processes. The ability to experimentally track such cell-cell communication signaling could substantially advance our understanding of diverse biological processes from embryogenesis to tumorigenesis. The existing technologies are not suitable to monitor and trace cell-cell contact for long-term in vivo studies, because many biological processes such as embryogenesis, tumorigenesis, and tissue regeneration develop over time after the initial cell-cell contact.

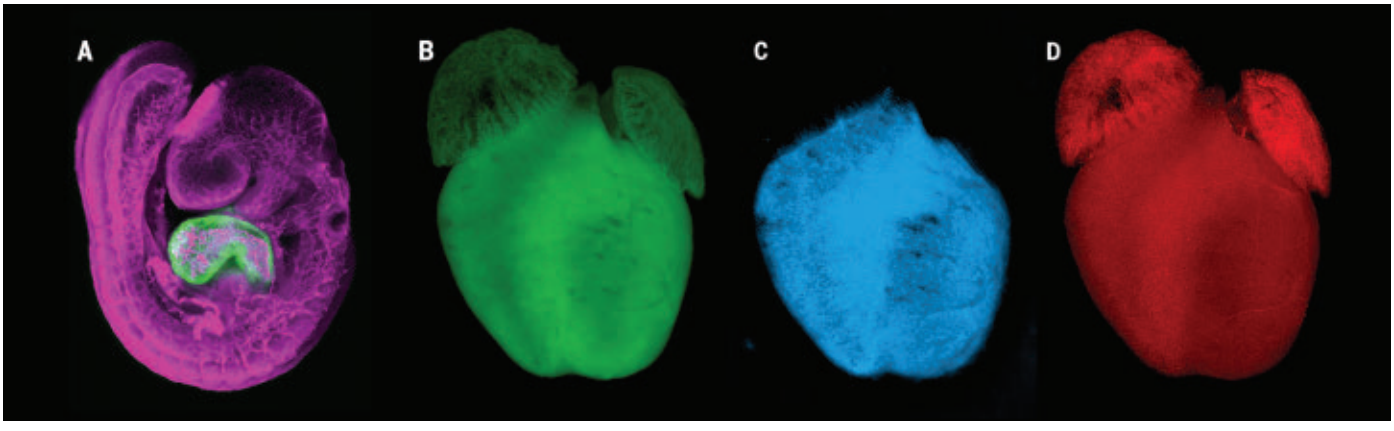
RATIONALE: The Notch pathway transmits signaling through direct cell-cell contact in many cellular processes during development and homeostasis. In the canonical Notch pathway, upon cell contact, the Notch ligand on one cell binds to the Notch receptor on another cell to trigger a signaling pathway that leads to transcription activation of particular genes. To understand the dynamic in vivo cell-cell communications over time, we developed an intercellular genetic approach using the synthetic Notch pathway (synNotch) that converts a cellular contact event into a controllable transcriptional program. We engineered in mice an artificial Notch ligand, a membrane-tethered green fluorescent protein (GFP), into one cell type (the sender cell) and an artificial receptor in which the extracellular and intracellular domains of Notch were replaced with an anti-GFP nanobody and the tetracycline transactivator, respectively, into another cell type (the receiver cell). Contact between the sender and receiver cells triggered synNotch signaling that activated the downstream transcriptional programs in the receiver cell in vivo. To reveal the ongoing cell-cell contact, as reflected by synNotch activation in a receiver cell after direct contact with a sender cell, we used a tet-off system to express detectable reporters. To trace cell contact history, we used the Cre-loxP system to genetically fate map receiver cells, along with their progenies, permanently after cell contact.

RESULTS: In the intercellular genetic system, we demonstrated that endothelial cells (receiver cells) in the developing heart were genetically labeled after contact with neighboring cardiomyocytes (sender cells). The endothelial cells that had contact with cardiomyocytes in early embryogenesis were permanently tagged with the genetic reporter. Their progenies migrated into liver and subsequently formed a substantial portion of the vasculature there, suggesting that part of the liver vasculature originates from the developing heart during embryogenesis. Application of these synNotch mice in tumorigenesis revealed the contact history between tumor cells (sender cells) and endothelial cells (receiver cells) during tumor growth and revealed that tumor vessels not only expanded within the tumor but also outgrew into the periphery of the tumor and had strong angiogenic properties. Upon contacting tumor cells, these endothelial cells gained properties in angiogenic, migratory, and inflammatory responses. Additionally, we generated mice for Cre-induced synNotch ligand or receptor expression, enabling broadly applicable approaches for genetic labeling of cell-cell contact and study of cell contact signaling in vivo. Engineering both the synNotch ligand and receptor, as well as different genetic readouts, in one mouse, we demonstrated simultaneous yet distinct recording of not only ongoing cell-cell contact but also historical cell-cell contact.

CONCLUSION: Our work provides a genetic system for recording cell-cell contact and cell contact history in vivo. The implications of our findings are that endothelial cells in the developing heart migrate and contribute to the liver vasculature, whereas endothelial cells in tumors not only expand within the tumor but also grow outward into the boundary-adjacent normal tissue with robust angiogenesis. The suite of new synNotch mouse lines provides a toolbox for genetic labeling and tracing of contacts between any cell type, offering a useful approach for studying dynamic in vivo cell-cell communications and the resulting cell fate plasticity in diverse life science fields. ■

The list of author affiliations is available in the full article online.
*Corresponding author. Email: zhoubin@sibs.ac.cn
†These authors contributed equally to this work.
Cite this article as S. Zhang *et al.*, *Science* **378**, eabo5503 (2022). DOI: 10.1126/science.abo5503

READ THE FULL ARTICLE AT
https://doi.org/10.1126/science.abo5503



Monitoring of cell-cell contact in the heart. (**A**) Whole-mount fluorescence image of a mouse embryo showing that cardiomyocytes and endothelial cells express the synNotch ligand (green) and the synNotch receptor (purple). (**B** to **D**) Whole-mount images of synNotch neonatal hearts shown in green (B), blue (C), and red (D) fluorescence channels. Present and past cell contact signaling are displayed by blue and red fluorescence, respectively.

RESEARCH ARTICLE

SYNTHETIC BIOLOGY

Monitoring of cell-cell communication and contact history in mammals

Shaohua Zhang[1]†, Huan Zhao[1]†, Zixin Liu[1], Kuo Liu[2], Huan Zhu[1], Wenjuan Pu[1], Lingjuan He[3], Rong A. Wang[4], Bin Zhou[1,2,5]*

Monitoring of cell-cell communication in multicellular organisms is fundamental to understanding diverse biological processes such as embryogenesis and tumorigenesis. To track cell-cell contacts in vivo, we developed an intercellular genetic technology to monitor cell-cell contact and to trace cell contact histories by permanently marking contacts between cells. In mice, we engineered an artificial Notch ligand into one cell (the sender cell) and an artificial receptor into another cell (the receiver cell). Contact between the sender and receiver cells triggered a synthetic Notch signaling that activated downstream transcriptional programs in the receiver cell, thereby transiently or permanently labeling it. In vivo cell-cell contact was observed during development, tissue homeostasis, and tumor growth. This technology may be useful for studying dynamic in vivo cell-cell contacts and cell fate plasticity.

Cell-cell communication is ubiquitous in multicellular organisms and is essential in fundamental biological processes, including embryogenesis, immune responses, stem cell fate decisions, and tumorigenesis (*1*–*4*). Technologies that enable monitoring and recording of cell-cell communication have driven advances in our basic understanding of many biological processes (*5*–*12*). For example, intercellular enzymatic proximity labeling has been used to monitor cell-cell communication in vivo and in vitro (*8*, *11*), providing information on immune cell function, and the generation of a cell-penetrating fluorescent protein secreted from tumor cells can be used to label cells in tumor metastatic niches (*13*). However, for long-term tracing of cell contact, existing methods such as tagging of surface proteins or secretion of fluorescent proteins are unsuitable because many cell-cell interactions are dynamic and transient. Existing technologies also cannot monitor and permanently trace dynamic interactions between T cell progenitors and thymus cells before mature T cells migrate to lymphoid organs (*14*), nor can they track transient interactions between tumor cells and their niche cells during dissemination and metastasis (*13*, *15*). Indeed, many biological processes occur weeks or months after (transient) cell-cell contact, such as tumor immune responses and tissue regeneration (*16*–*18*). To understand the dynamics of complex in vivo cell-cell communication over time, we developed a genetic system that converts a cellular contact event into a controllable genetic program, enabling subsequent monitoring of ongoing cell-cell contacts or tracing of cell contact history in vivo (fig. S1). For broader application, we also generated a Cre recombinase–induced genetic tool box that can be used for identifying and manipulating cell lineages directly influenced by cell-cell contact in vivo.

[1]State Key Laboratory of Cell Biology, CAS Center for Excellence in Molecular Cell Science, Shanghai Institute of Biochemistry and Cell Biology, Chinese Academy of Sciences, University of Chinese Academy of Sciences, Shanghai 200031, China. [2]Key Laboratory of Systems Health Science of Zhejiang Province, School of Life Science, Hangzhou Institute for Advanced Study, University of Chinese Academy of Sciences, Hangzhou 310024, China. [3]School of Life Sciences, Westlake University, Hangzhou, Zhejiang 310030, China. [4]Laboratory for Accelerated Vascular Research, Department of Surgery, Division of Vascular Surgery, University of California, San Francisco, CA 94143, USA. [5]School of Life Science and Technology, ShanghaiTech University, Shanghai 201210, China.
*Corresponding author. Email: zhoubin@sibs.ac.cn
†These authors contributed equally to this work.

Results

Generation of the gLCCC system for monitoring ongoing cell-cell contacts

The Notch signaling pathway mediates communication between neighboring cells in many cellular processes during development and homeostasis (*19*, *20*). In the canonical Notch signaling pathway (*21*), binding of the Notch ligand to the Notch receptor triggers γ-secretase–mediated cleavage within the Notch transmembrane region, and the cleaved Notch intracellular domain then translocates into the nucleus and activates the transcription of target genes (Fig. 1A). Like endogenous delta (ligand)–Notch (receptor) communication, activation of a synthetic Notch (synNotch) pathway depends on direct cell-cell contact, which has been used to program contact-dependent transcriptional regulation (*5*–*7*, *10*, *22*, *23*). Given the contact-dependent feature of synNotch activation, we explored its application for in vivo genetic monitoring and tracing of cell-cell contacts. We engineered two separate mouse alleles through gene targeting: One allele encoded a synNotch ligand and the other a synNotch receptor (Fig. 1B). The synNotch ligand is a membrane-tethered green fluorescent protein (mGFP) that serves as an artificial Notch ligand. The synthetic receptor for Notch is a modified Notch protein in which the extracellular and intracellular domains are replaced with a Myc-tagged anti-GFP nanobody (αGFP) and the tetracycline (tet) transactivator (tTA), respectively, which is abbreviated as αGFP-N-tTA (Fig. 1B). To mitigate the potential influence of artificial ligand–receptor binding on dynamic cell-cell interactions such as postcontact dissociation, we used a low-affinity αGFP nanobody (LaG17) that has an affinity for GFP that is 1/70th of that of another αGFP nanobody (LaG16) (*5*, *24*). To target the synNotch ligand to sender cells [e.g., cardiomyocytes (CMs)], mGFP was driven under a CM-specific promoter. To target the synNotch receptor to receiver cells [e.g., endothelial cells (ECs)], αGFP-N-tTA was driven under an EC-specific promoter. In mice carrying both sender and receiver alleles, as well as a reporter allele such as *tetO-LacZ* that encodes the β-galactosidase enzyme for X-galactosidase (X-gal) staining detection (*25*, *26*), if a sender cell contacts a receiver cell, then the binding between GFP and αGFP-N-tTA triggers cleavage of the Notch transmembrane domain, thereby releasing tTA (Fig. 1, C and D). Cleaved tTA then translocates into the nucleus to activate the *tetO-LacZ* reporter system (Fig. 1D). We refer to mice carrying these three genetic elements (synNotch ligand, receptor, and reporter) as gLCCC mice for "genetic labeling of cell-cell contact."

We used CMs as sender cells and ECs as receiver cells (Fig. 1, E and F) and generated cardiac troponin T2 (*Tnnt2*)-*mGFP* knock-in mice to express mGFP specifically in TNNT2$^+$ CMs (Fig. 1E and fig. S2) and cadherin 5 (*Cdh5*)-*αGFP-N-tTA* knock-in mice to express αGFP-N-tTA in CDH5$^+$ ECs (Fig. 1F and fig. S3). Immunostaining and confocal examination of *Tnnt2-mGFP;Cdh5-αGFP-N-tTA* embryos documented the close physical proximity of GFP$^+$ CMs and αGFP$^+$ ECs in the heart (Fig. 1G). We generated *Tnnt2-mGFP;Cdh5-αGFP-N-tTA;tetO-LacZ* (or heart-gLCCC) mice and tested whether contact between sender and receiver cells triggered LacZ expression specifically in cardiac ECs (Fig. 1D). X-gal staining of mouse tissues was used to detect LacZ expression in ECs (*25*, *26*). Although no LacZ-expressing cells were observed in littermate controls with other genotypes, we did observe LacZ expression in the hearts from embryonic day 9.5 (E9.5) heart-gLCCC embryos (Fig. 1H). Immunostaining of sections prepared from these embryos revealed specific LacZ expression in the endocardial ECs located adjacent to GFP$^+$ CMs (Fig. 1, I and J). To confirm that LacZ expression was specifically triggered by the synNotch pathway, we showed that heart-gLCCC embryos exposed to the γ-secretase

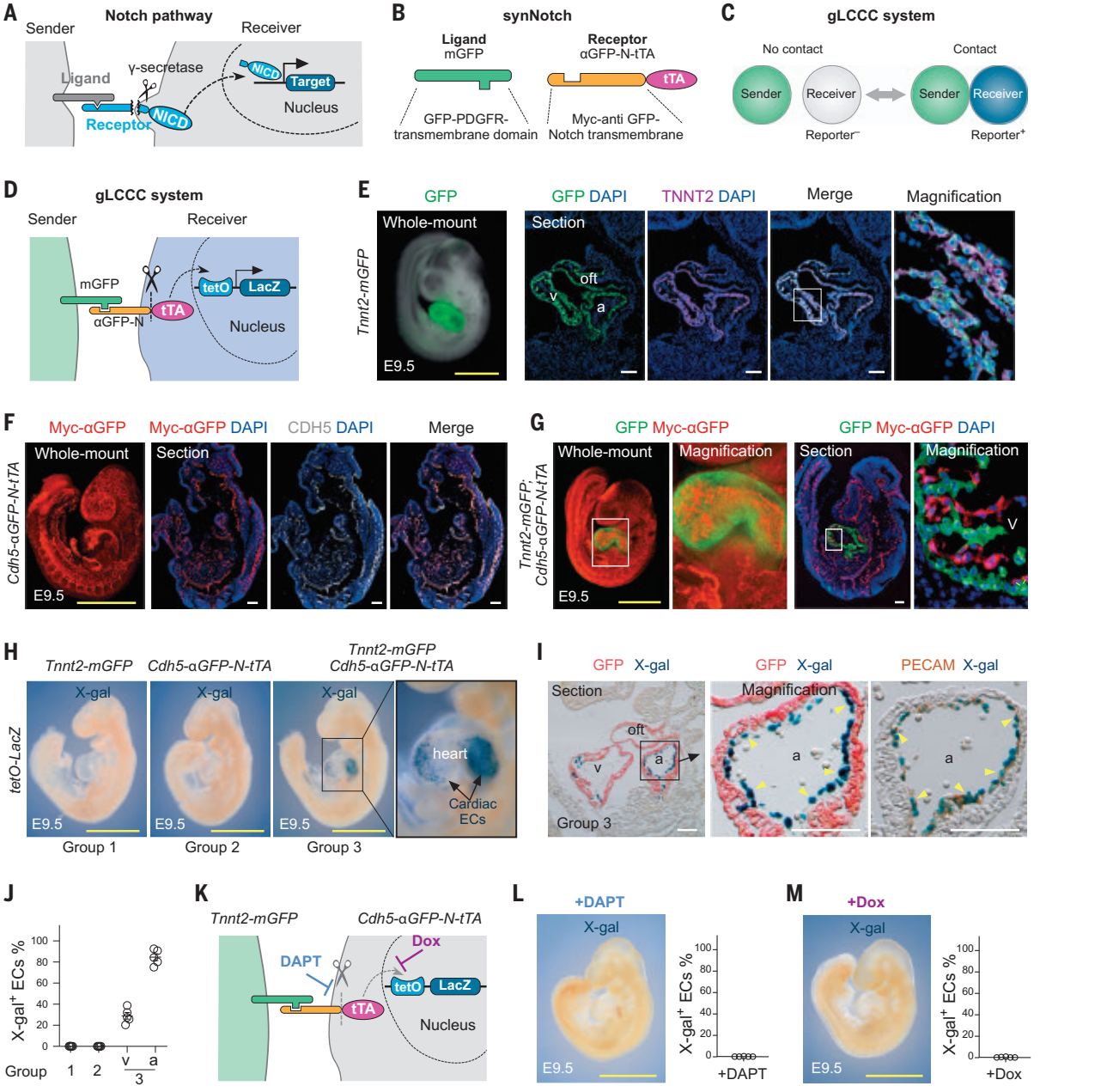


Fig. 1. Genetic labeling of in vivo cell-cell contact. (**A**) Schematic figure showing the canonical Notch signaling pathway. NICD, Notch intracellular domain. (**B**) Schematic showing components of the synNotch pathway: mGFP as ligand and αGFP-N-tTA as receptor. αGFP is myc-tagged. (**C**) Illustration showing the gLCCC system for genetic labeling of cell-cell contact. (**D**) Schematic showing the overall design of the gLCCC system. Binding of GFP to the αGFP nanobody leads to cleavage of the transmembrane domain of the synNotch receptor by γ-secretase. This subsequently releases tTA, which then translocates into the nucleus and activates LacZ expression. (**E** to **G**) Whole-mount and sectional immunostaining images of E9.5 *Tnnt2-mGFP* (E), *Cdh5-αGFP-N-tTA* (F), and *Tnnt2-mGFP;Cdh5-αGFP-N-tTA* (G) embryos. (**H**) Whole-mount X-gal staining for the detection of the β-galactosidase enzyme encoded by the LacZ gene on E9.5 *Tnnt2-mGFP;tetO-LacZ* (group 1), *Cdh5-αGFP-N-tTA;tetO-LacZ* (group 2), and *Tnnt2-mGFP;Cdh5-αGFP-N-tTA;tetO-LacZ* (group 3) embryos. Arrows indicate LacZ$^+$ cardiac ECs. (**I**) X-gal staining with immunostaining of *Tnnt2-mGFP;Cdh5-αGFP-N-tTA;tetO-LacZ* embryonic sections for GFP or PECAM. Arrowheads indicate LacZ$^+$ cardiac ECs. (**J**) Quantification of the percentage of LacZ$^+$ ECs in embryos of different genotypes. Data are shown as the mean ± SEM; n = 5. v, ventricle; a, atrium. (**K**) Schematic showing inhibition of γ-secretase activity by DAPT or inhibition of tTA binding to tetO by Dox. (**L** and **M**) Whole-mount X-gal staining on *Tnnt2-mGFP;Cdh5-αGFP-N-tTA;tetO-LacZ* embryos after DAPT (L) or Dox (M) treatment. Right panel shows the quantification of the percentage of LacZ$^+$ ECs. Data are shown as the mean ± SEM; n = 5. Scale bars: yellow, 1 mm; white, 100 μm. Each image is representative of five individual biological samples.

inhibitor *N*-[*N*-(3,5-difluorophenacetyl)-l-alanyl]-S-phenylglycine t-butyl ester (DAPT) (*27*) had no LacZ$^+$ cells (Fig. 1, K and L). To validate Tet-responsive expression, we showed that heart-gLCCC embryos exposed to doxycycline (Dox), which inactivates tTA (*28*), had no LacZ$^+$ cells (Fig. 1, K to M). We also used *Tnnt2-mGFP;Cdh5-αGFP-N-tTA;tetO-tdT* (where tdT is tdTomato) mice to further validate the dynamic contacts between ECs and CMs in postnatal hearts (fig. S4). Thus, this gLCCC system offers cell contact–specific labeling of ECs in contact with CMs.

To determine how long cell-cell contact is needed to activate the gLCCC system, we cultured sender and receiver cells in vitro and found by fluorescence microscopy that tdT$^+$ cells started to appear after 4 hours of contact (fig. S5, A to D). Alternatively, we used DAPT to inhibit the gLCCC system at different time points and assessed tdT expression after 36 hours of co-culture. Within 2 hours of cell-cell contact, we detected receiver cells expressing tdT (fig. S5, E to H). Free mGFP protein did not lead to tdT expression in receiver cells (fig. S6). Half of cardiac ECs lost tdT 2 days after inhibition of contact-activated gLCCC (fig. S7).

To test whether cardiac ECs continue to interact with surrounding CMs in the adult heart, we collected hearts from 12-week-old *Tnnt2-mGFP;Cdh5-αGFP-N-tTA;tetO-tdT* mice (fig. S8, A and B). Immunostaining of heart sections for GFP, tdT, and CDH5 showed that a proportion of coronary capillary ECs expressed tdT (fig. S8, C and D), suggesting that they were in contact with CMs. Transmission electron microscopy of adult wild-type hearts provided morphological evidence showing the close proximity between the plasma membranes of CMs and ECs (fig. S8, E and F). One advantage of the tdT reporter is that it enables the isolation of cells by flow cytometry for further characterization of ECs that had contact with CMs. Isolated tdT$^+$ ECs showed increased expression of genes for cellular respiration, intrinsic apoptotic signaling, and cellular responses to stress (fig. S8, G to K). In addition to heart-gLCCC, we also generated liver-gLCCC with hepatocyte-specific promoter albumin-driven mGFP (*Alb-mGFP*) mice and *Cdh5-αGFP-N-tTA;tetO-tdT* mice and found that EC-hepatocyte contact activated tdT expression in postnatal day 0 (P0) livers (fig. S9) but not in adult livers (fig. S10). This suggested that gLCCC could be used to study dynamic cell-cell contacts in multiple cell types.

Generation of a gTCCC system for genetic tracing of cell-cell contact history

To enable tracking of receiver cells that had any history of contact with sender cells, we incorporated the Cre-loxP system downstream of the synNotch pathway (Fig. 2A). The tTA reporter was replaced by *tetO-Cre* and a Rosa26 (R26)-floxed-Stop-reporter, which is located in the ubiquitously active gene locus Rosa26 (*29*). Sender-receiver cell contact triggered activation of the synNotch pathway and translocation of tTA into the nucleus, turning on the expression of Cre recombinase in the receiver. Cre then mediated irreversible Cre-loxP recombination, leading to constitutive expression of tdT in the receiver and all of its descendants, thus permanently tagging them (Fig. 2A), even if the receiver no longer had contact with the sender or its descendants had never contacted any sender. Therefore, any contact event would genetically tag the receiver cell, allowing genetic tracing of such receiver cells and their progenies even after they migrated away from the sender cells or differentiated or transformed into other cell lineages. We call mice carrying synNotch and Cre-loxP systems gTCCC mice for "genetic tracing of cell-cell contact."

We studied migration and fate transitions of endocardial ECs in the developing mouse heart. Cardiac ECs contact CMs during early embryonic heart development (*30*). In cardiac valve formation, these endocardial ECs then shift to a mesenchymal fate and migrate into the cardiac cushion through the endothelial-to-mesenchymal transition (EMT) program (*30*) (Fig. 2B). In mice, this dissociation of endocardial ECs away from CMs is already completed before P0, when the cardiac cushion has been remodeled into cardiac valves and mesenchymal cells in the valve no longer express any EC markers (Fig. 2B). We generated *Tnnt2-mGFP;Cdh5-αGFP-N-tTA;tetO-Cre;R26-tdT* or heart-gTCCC mice (Fig. 2A). The tdT signals that we observed in heart-gTCCC mice at E9.0 indicated that the cardiac ECs were successfully genetically labeled, and their mesenchymal descendants maintained tdT expression at E10.0 (Fig. 2, C and D). These data demonstrated that the genetic tracer tdT was permanently maintained in the receiver cells and all of their descendants, even when their descendants changed cell fate, e.g., due to EMT during cardiac valve development.

Whole-mount fluorescence images of organs, immunostaining of tissue sections, and flow cytometric analysis revealed that most of the cardiac ECs retained tdT expression in the heart-gTCCC mice at P0, whereas no tdT expression was observed in their littermate controls of other genotypes (Fig. 2, E to H). We rarely detected tdT$^+$ ECs in other heart-gTCCC mouse organs examined, with the exception of the liver (see below) (fig. S11). Dox administration abolished tdT labeling of cardiac ECs in heart-gTCCC mice, demonstrating controllable genetic regulation by the Tet system (Fig. 2, E to H). At P0, even though the descendants of ECs that became mesenchymal cells in the valve were nowhere near CMs, they maintained tdT expression (Fig. 2I), which verified their EMT fate transition. These tdT$^+$ valve interstitial cells expressed mesenchymal cell marker platelet–derived growth factor receptor α (PDGFRα) (Fig. 2I), but they no longer expressed the EC marker platelet EC adhesion molecule (PECAM) (Fig. 2I). Thus, we could trace ECs even after they switched fate to mesenchymal cells.

Endocardial ECs migrate at E8.5 to the nearby liver bud, where they contribute to the liver vasculature (*31*) (Fig. 2J). We found that a subset of ECs in postnatal liver had contact with CMs at an early embryonic stage. About 20% of ECs in livers collected from P0 heart-gTCCC mice showed tdT fluorescence (Fig. 2, K and L, and fig. S11B). We did not detect any tdT$^+$ ECs in the livers collected from P0 *Cdh5-αGFP-N-tTA;tetO-Cre;R26-tdT* littermate controls (Fig. 2K). Considering that no liver cells expressed mGFP synNotch ligand in the heart-gTCCC mice (fig. S11B), the tdT$^+$ ECs in the liver at P0 likely originated from the heart (*31*), and these ECs probably contacted mGFP$^+$ CMs before their migration into the liver bud (Fig. 2J). Furthermore, these tdT$^+$ ECs were maintained in the adult liver, where they may contribute to the adult liver vasculature (fig. S12, A to D). We therefore were able to detect cell-cell communication temporally and spatially isolated during organogenesis and homeostasis (fig. S12, E and F).

Genetic tracing of cell-cell contact history reveals outgrowth of tumor angiogenesis

To further demonstrate the utility of gTCCC for tracing cell contact histories, we studied vascular ECs in tumor angiogenesis, during which blood vessels are recruited from peripheral tissues into hypoxic tumors (*32*–*34*). In this pathological condition, ECs migrate into tumors, and their contact history with tumor cells may confer them with particular capabilities of tumor blood vessels (*34*). We traced ECs that had contact with tumor cells and followed EC fate during tumor growth in vivo. The mouse lung tumor cell line TC-1 was engineered to constitutively express mGFP (TC-1-mGFP) as sender cells, and these cells were in direct contact with infiltrating ECs from host mice (fig. S13). To genetically trace tumor-infiltrating ECs, we implanted TC-1-mGFP tumor cells into *Cdh5-αGFP-N-tTA;tetO-Cre;R26-tdT* receiver mice (Fig. 3A) and collected tissues for analysis 7 and 14 days after implantation (Fig. 3B). ECs showed tdT fluorescence in TC-1-mGFP tumors at day 7 (Fig. 3, C and D), but not in TC-1 control tumors (Fig. 3, C and D) or other organs at any stage analyzed in *Cdh5-αGFP-N-tTA;tetO-Cre;R26-tdT* mice (fig. S14). *Bandeiraea simplicifolia* lectin injection showed that these tdT$^+$ ECs were functionally connected to circulation (Fig. 3E). These tdT$^+$ ECs were mainly found in tumors, not in the thin layer of peripheral capsule tissue, at day 7 (Fig. 3, F and G).

At day 14, however, we observed tdT$^+$ ECs outside of the tumor, in the peripheral capsule tissues that were free of any mGFP$^+$ tumor cells (Fig. 3, H and I). The thick layer of capsule detected at day 14 was enriched in fibroblasts and macrophages (Fig. 3J), which may produce angiogenesis factors to recruit ECs from within tumors. Indeed, we detected enriched vascular endothelial growth factor A (VEGFA) expression in the thick peripheral capsule at day 14 (Fig. 3J), which may partly explain the strong recruitment of blood vessels by the tumor. We used Dox treatment to inhibit the gTCCC system at different times after

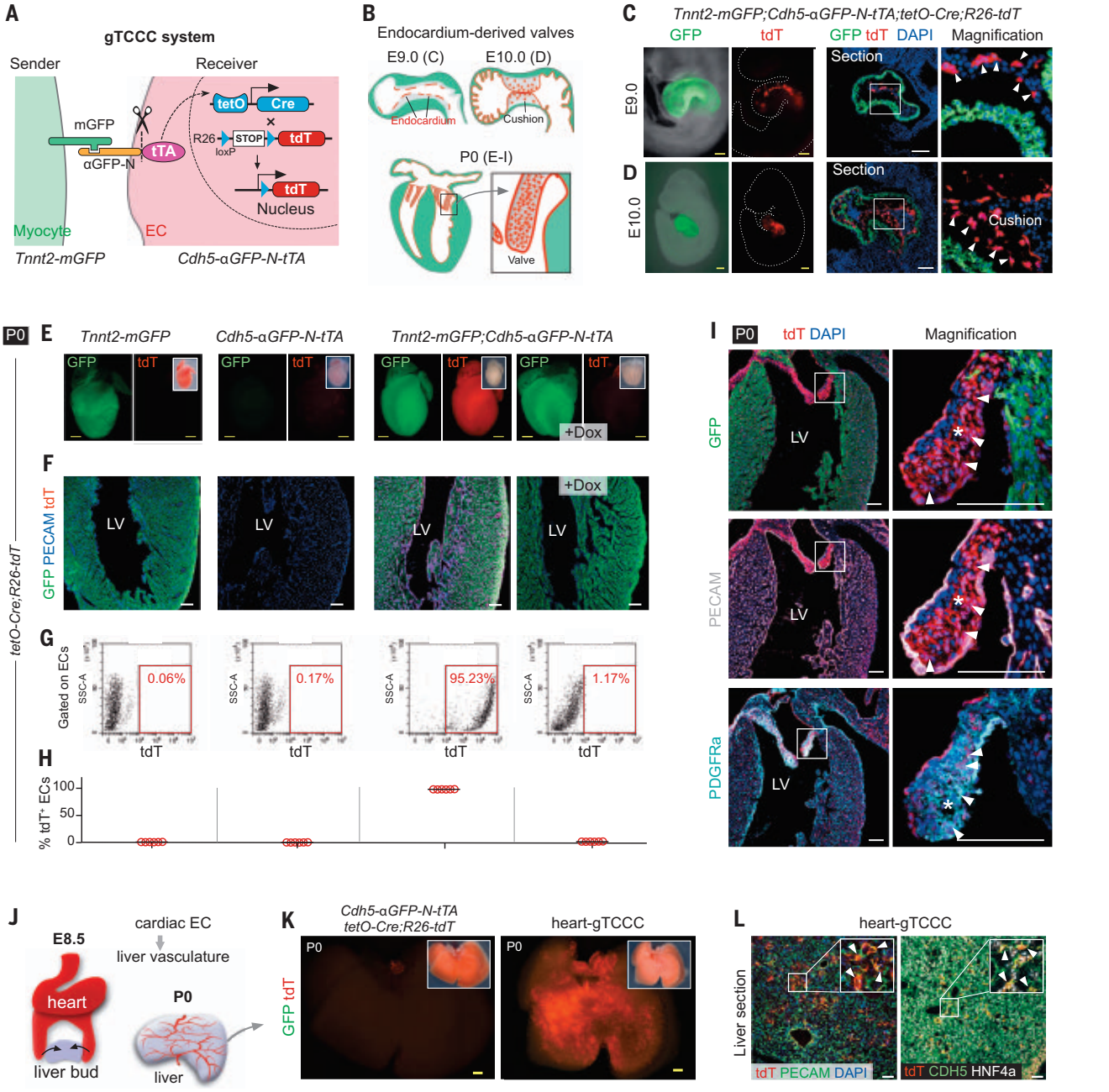


Fig. 2. Genetic tracing of ECs that have had contact with CMs. (**A**) Schematic showing the gTCCC strategy for permanent genetic tracing of cardiac ECs that have had contact with CMs. (**B**) Illustration of the development of the endocardial cushion and cardiac valves (red). Green indicates CMs. (**C** and **D**) Whole-mount fluorescence images of E9.0 (C) and E10.0 (D) *Tnnt2-mGFP;Cdh5-αGFP-N-tTA;tetO-Cre;R26-tdT* (heart-gTCCC) embryos and immunostaining for tdT and GFP. (**E**) Whole-mount fluorescence images of P0 hearts collected from mice of different genotypes as indicated. Inserts are bright-field images. Dox was added to inhibit the Tet system. (**F**) Immunostaining of heart sections for GFP, tdT, and PECAM. (**G**) Fluorescence-activated cell sorting (FACS) analysis of tdT$^+$ cardiac ECs from hearts. (**H**) Quantification of the percentage of ECs expressing tdT. Data are shown as the mean ± SEM; $n = 6$. (**I**) Immunostaining of heart sections for tdT and GFP, PECAM, or PDGFRα. Arrowheads indicate tdT$^+$ mesenchymal cells in valves (asterisks). (**J**) Illustration showing that ECs from the developing heart migrate to the liver bud at E8.5 and subsequently contribute to the liver vasculature. (**K**) Whole-mount fluorescence images of P0 livers. (**L**) Immunostaining of P0 liver sections for tdT and PECAM or tdT, CDH5, and HNF4a. Arrowheads indicate tdT$^+$ ECs. Scale bars: yellow, 400 μm; white, 100 μm. Each image is representative of six individual biological samples. Data are shown as mean ± SEM.

tumor implantation and found that tumor-infiltrating ECs at early stages (i.e., the first 5 days) were genetically labeled and subsequently moved to the tumor capsule (fig. S15). Thus, the ability of our gTCCC system to trace the postcontact history of cells throughout their lifetimes enabled us to show that some vascular ECs, after dissociating from cancer cells, extended into the peripheral tissues with no tumor cells (Fig. 3K).

We sorted three types of ECs from implanted tumors: tdT$^+$ tumor ECs (tdT$^+$ tECs), tdT$^+$ capsule ECs (tdT$^+$ cECs), and cECs lacking tdT fluorescence (tdT$^-$ cECs) (Fig. 3L). Principal component analysis revealed three

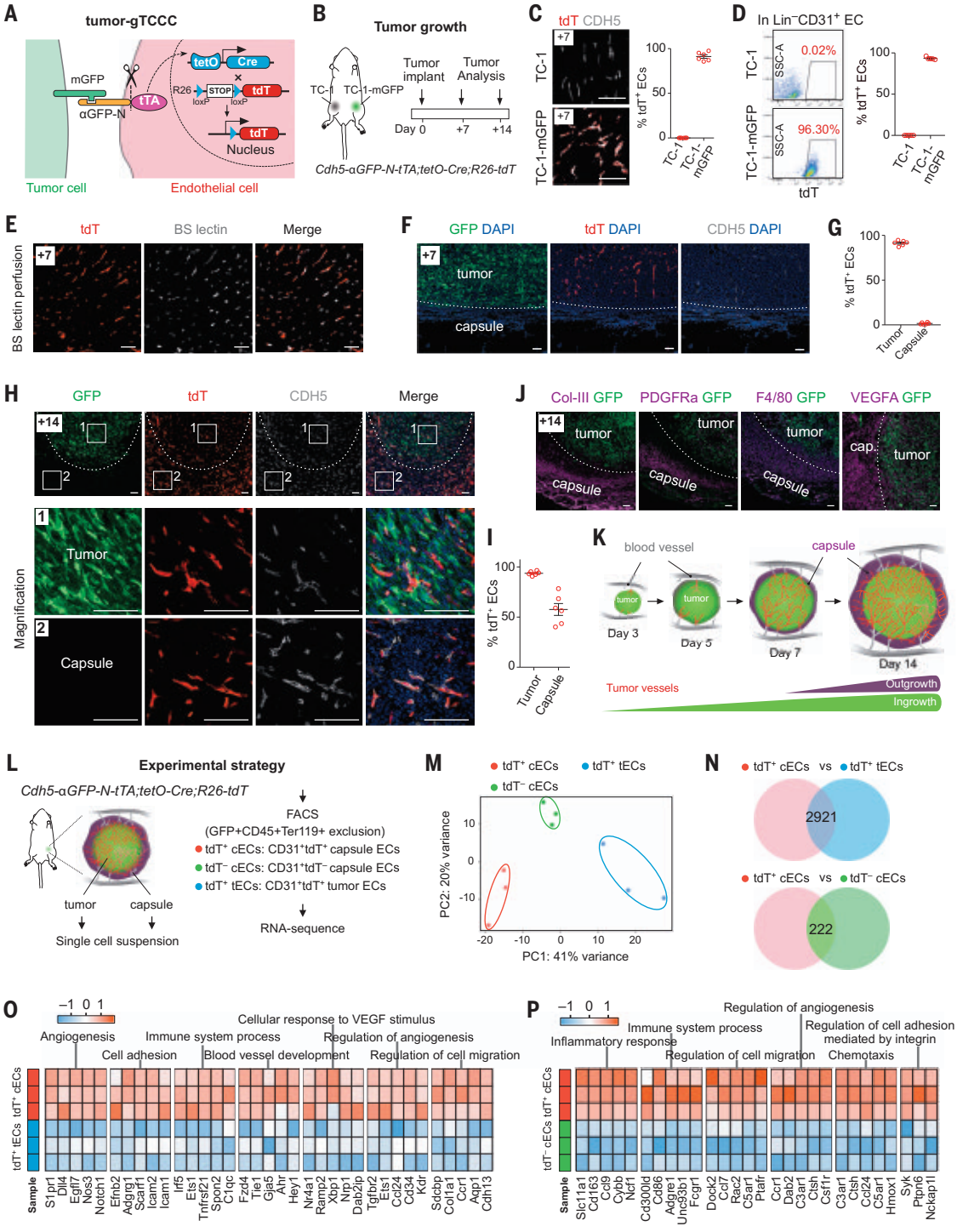


Fig. 3. Genetic tracing of the tumor cell–EC interaction during tumor growth. (**A** and **B**) Schematic showing the tumor-gTCCC strategy to trace tumor cell–EC contact history (A) and experimental design (B). (**C**) Immunostaining of tumor sections 7 days after tumor implantation (+7 day). Right panel shows quantification data for the percentage of ECs expressing tdT. (**D**) FACS analysis of the percentage of $CD31^+$ ECs expressing tdT in +7 day tumors. (**E**) Detection of perfused *Bandeiraea simplicifolia* lectin in tumor tdT^+ ECs showing functional blood vessels in tumors. (**F** and **H**) Immunostaining of tumor sections of +7 day (F) and +14 day (H) tumors for GFP, tdT, and CDH5. (**G** and **I**) Quantification of the percentage of ECs expressing tdT in the tumor or capsule at +7 (G) and +14 (I) days. (**J**) Immunostaining of +14 day tumor sections for fibroblast and macrophage markers. (**K**) Illustration showing that vessels expand from the periphery into the tumor (ingrowth) and tdT^+ vessels expand out of the tumor into the peripheral capsule (outgrowth) during tumor growth and formation of the capsule. (**L**) Schematic diagrams illustrating the experimental strategy for RNA-sequencing experiments. (**M**) Principal component analysis of $GFP^-CD45^-Ter119^-CD31^+$ cell signatures from tECs and cECs. $n = 3$. (**N**) Venn diagram of differentially expressed gene numbers in the tdT^+ cEC versus tdT^+ tEC group and in the tdT^+ cEC versus tdT^- cEC group. (**O** and **P**) Heatmap generated from the top differentially expressed genes in the enriched pathways. Scale bars, 100 μm. Data are shown as mean ± SEM. Each staining is representative of six individual biological samples.

different groups of ECs with distinct transcriptional profiles (Fig. 3M). Comparisons of gene expression between tdT$^+$ cECs and tdT$^+$ tECs highlighted enriched pathways for angiogenesis, cell adhesion, the immune system process, blood vessel development, cellular response to VEGF stimulus, and regulation of cell migration in tdT$^+$ cECs compared with those from tdT$^+$ tECs (Fig. 3, N and O, and fig. S16A). Comparison of gene expression between tdT$^+$ cECs and tdT$^-$ cECs showed increased expression of genes associated with inflammatory responses, immune system processes, positive regulation of cell migration and angiogenesis, chemotaxis, and regulation of cell adhesion in tdT$^+$ cECs versus tdT$^-$ cECs. This suggested that an interaction between ECs and tumor cells may endow these ECs with particular properties in angiogenesis, migration, and the inflammatory response (Fig. 3P and fig. S16B). It appears possible that blood vessels, when recruited into tumors, can grow out of tumors into peripheral capsules.

Cre-induced R26-mGFP mouse line for broad spectrum of cell types as sender cells

To broaden the application of the gLCCC and gTCCC systems to all cell types that contact a particular receiver cell type, we generated a knock-in mouse line, *R26-mGFP*, for Cre-dependent expression of mGFP ligand in sender cells (Fig. 4A). We inserted an mGFP transgene expression cassette into the ubiquitous *Rosa26* locus, with the mGFP coding sequences following a loxP-flanked 3x polyA Stop cassette to render mGFP expression inducible upon Cre recombinase administration (Fig. 4A). Whole-mount fluorescence or sectional staining of E15.5 *R26-mGFP* embryos showed no GFP expression (Fig. 4B), indicating no leakiness of GFP expression without Cre recombinase. By contrast, *ACTB-Cre;R26-mGFP* embryos, which had Cre-loxP–mediated excision in all cells, yielded GFP expression throughout (Fig. 4C), demonstrating that mGFP synNotch ligand expression in targeted cells was Cre dependent.

To use *R26-mGFP* mice to study any other Cre$^+$ cell–EC contacts, we crossed them with *Nestin-CreER*, an inducible Cre driver in Nestin$^+$ cells that include neurons, epididymis vascular smooth mucle cells, and myoblasts. We generated *Nestin-CreER;R26-mGFP* senders and *Cdh5-αGFP-N-tTA;tetO-tdT* receiver or Nestin-gLCCC mice (Fig. 4D). We treated the Nestin-gLCCC mice with tamoxifen (Tam) at E12.5 to induce Cre activation and found, at E15.5, that some GFP$^+$ cells expressed the neuronal nuclear protein (NeuN), and they were in proximity with cadherin 5–positive (CDH5$^+$) ECs (Fig. 4, E to F). Fluorescence imaging of sagittal sections of E15.5 embryos showed that tdT signals mirrored the GFP expression pattern, except in the brain, where there was no detectable tdT expression (Fig. 4G). The tdT$^+$ ECs were located in the trigeminal ganglion, dorsal root ganglion, and intercostal neurovascular bundle, but there were no tdT$^+$ ECs detected in the brain (Fig. 4H and fig. S17). In mice of the same genotype treated with corn oil (designated the "no Tam" group), neurons did not express GFP and ECs remained tdT$^-$ in the trigeminal ganglion (Fig. 4I). We confirmed that tdT expression in ECs was controlled by the tet-regulated genetic system, because Dox administration repressed tdT expression in ECs of Tam-treated Nestin-gLCCC mice (Fig. 4J). Therefore, *R26-mGFP* is applicable for generating sender cells from any Cre-expressing cell type (Fig. 4K).

Cre-induced H11-αGFP-N-tTA mouse line enabling any cell type to be receiver cells

To find all of the cell types that interact with a particular sender cell, we generated a knock-in mouse line, *H11-αGFP-N-tTA*, for Cre-dependent expression of the αGFP-N-tTA receptor in receiver cells (Fig. 5A). We then inserted an αGFP-N-tTA expression cassette into another ubiquitous gene locus, *Hipp11* (*35*), with the αGFP-N-tTA coding sequences following a loxP-flanked 3x polyA stop cassette to render receptor expression inducible upon Cre recombinase administration (Fig. 5A). Sectional staining of E15.5 *H11-αGFP-N-tTA* embryos showed no Myc-αGFP (annotation of αGFP-N-tTA) expression (Fig. 5B), indicating no receptor expression without Cre recombinase. By contrast, *Tie2-Cre;H11-αGFP-N-tTA* embryos, with Cre-loxP–mediated excision in all endothelial lineages, yielded receptor expression throughout (Fig. 5, C and D), demonstrating that αGFP-N-tTA synNotch receptor expression in targeted cells was Cre dependent.

To functionally characterize *H11-αGFP-N-tTA* mice in studying cell-cell interactions, we crossed *Tnnt2-mGFP* mice with *Tie2-Cre;H11-αGFP-N-tTA* mice and used *tetO-tdT* as the readout of their contacts (Fig. 5E). In *Tnnt2-mGFP;H11-αGFP-N-tTA;tetO-tdT* mice, we could not detect tdT expression in the heart unless the mice were crossed with the *Tie2-Cre* mouse line (Fig. 5F). Immunostaining of heart sections of *Tnnt2-mGFP;Tie2-Cre;H11-αGFP-N-tTA;tetO-tdT* mice for GFP and tdT showed tdT expression in a vascular pattern (Fig. 5G). Most of the ECs in the atrium and ventricle were tdT$^+$, except for endocardial ECs on the valves, where they were anatomically separated from CMs (Fig. 5H). No tdT$^+$ ECs were detected in other organs or tissues (Fig. 5I), indicating that the genetic activity of receptor-expressing cells also depends on ligand from sender cells, e.g., mGFP$^+$ CMs. Therefore, *H11-αGFP-N-tTA* is applicable for generating receiver cells from any Cre-expressing cell type (Fig. 5J).

One Tigre-synNotch mouse allele to unravel any cells that contact Cre$^+$ cells

To facilitate the broad application of an intercellular genetic approach, we generated a Cre-induced synNotch allele on the tightly regulated (Tigre) genomic locus (*36*), resulting in a *Tigre-synNotch* mouse that could simultaneously express synthetic ligand in Cre$^+$ cell lineages and receptor in Cre$^-$ cells. In this *Tigre-synNotch* design, tetO-rox-Stop-rox-tdT-insulator-CAG-loxP-αGFP-N-tTA-pA-loxP-mGFP was knocked into the *Tigre* gene locus by CRISPR-Cas9 such that the receptor, ligand, and tTA readouts were all combined in one mouse allele (Fig. 6A). By crossing this *Tigre-synNotch* mouse with any Cre mouse, Cre-loxP recombination would remove the loxP-flanked αGFP-N-tTA cassette, leading to mGFP ligand expression in Cre$^+$ sender cells, whereas Cre$^-$ cells continued to express αGFP-N-tTA receptor as receivers (Fig. 6B). *CAG-Dre* was used to remove rox-Stop-rox in *Tigre-synNotch* allele (Fig. 6B). If any Cre$^-$ cells were in contact with Cre$^+$ cells, then tTA would activate tdT in these αGFP-N-tTA$^+$ receiver cells (Fig. 6B). The generation of *Tigre-synNotch* facilitated the genetic detection of in vivo cell-cell contacts using a single Cre-responsive mouse allele.

To test this *Tigre-synNotch* allele, we crossed it with the TEK receptor tyrosine kinase (*Tie2*)–*Cre* line (*37*) and collected *Tie2-Cre;CAG-Dre;Tigre-synNotch* mouse tissues for analysis. Compared with littermate control *CAG-Dre;Tigre-synNotch*, we could detect patterning of tdT robustly in *Tie2-Cre;CAG-Dre;Tigre-synNotch* mice (Fig. 6C). Immunostaining of *Tie2-Cre;CAG-Dre;Tigre-synNotch* mouse tissues such as heart and lung for GFP and PECAM revealed GFP expression in PECAM$^+$ ECs (Fig. 6D). Immunostaining of tissue sections for GFP and tdT showed a particular patterning of tdT that lined along GFP$^+$ cells throughout different organs or tissues (Fig. 6E). For example, these GFP$^+$ ECs contacted PDGFRβ$^+$ pericytes in the brain, TNNT2$^+$ CMs in the heart, PDGFRα$^+$ fibroblasts in the lung, and hepatocytes in the liver, marking these diverse types of cells as tdT$^+$ (Fig. 6F). By contrast, we detected very few tdT$^+$ cells in *CAG-Dre;Tigre-synNotch* mouse tissues (Fig. 6G). Additionally, we used inducible Cre lines to label their neighboring cells as tdT$^+$. For instance, after induction with a low dose of Tam, *Nestin-CreER*– or *CAG-CreER*–labeled sparse mGFP$^+$ cells activated tdT expression only in their neighboring cells (Fig. 6H and fig. S18). These results demonstrated that *Tigre-synNotch* enables the detection of in vivo cell-cell contacts broadly in any given cell type in a Cre mouse line (Fig. 6I).

Simultaneous application of gLCCC and gTCCC in one mouse

To enable the simultaneous detection of ongoing cell-cell contact and contact history in

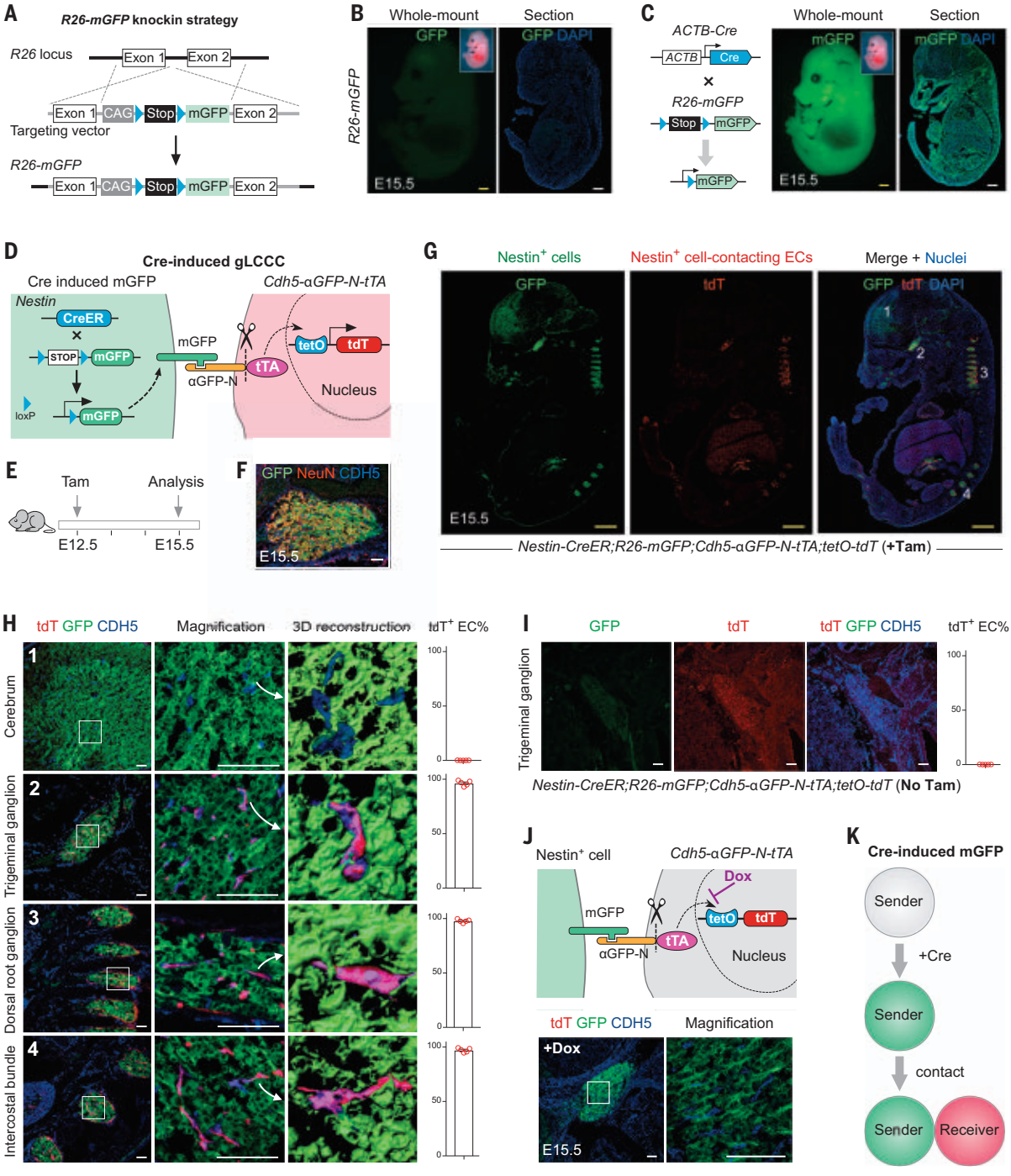


Fig. 4. Generation of the *R26-mGFP* mouse line for Cre-induced mGFP in sender cells. (**A**) Schematic showing the generation of the *R26-mGFP* allele by homologous recombination using CRISPR-Cas9. (**B**) Whole-mount or sectional fluorescence images of E15.5 *R26-mGFP* embryos. Insert, bright-field whole-mount image. (**C**) Whole-mount or sectional fluorescence images of E15.5 *ACTB-Cre;R26-mGFP* embryos. Insert, bright-field whole-mount image. (**D**) Schematic showing the design of the Cre-induced gLCCC system for study of the interaction between Cre$^+$ cells and receiver cells, e.g., the Nestin$^+$ cell–EC interaction. (**E**) Schematic showing the experimental design by Tam induction of Cre (*Nestin-CreER*). (**F**) Immunostaining of an E15.5 tissue section for GFP, NeuN, and CDH5 showing that GFP is specifically expressed in neurons. (**G**) Immunostaining of E15.5 whole embryonic sections for GFP and tdT. Regions 1 to 4 are magnified in (H). (**H**) Immunostaining of E15.5 tissue sections for GFP, tdT, and CDH5. Three-dimensionally reconstructed images show neurons (GFP) and their interacting ECs (tdT). The percentage of ECs expressing tdT in each region is quantified on the right panels. Data are shown as the mean ± SEM; $n = 5$. (**I**) Immunostaining of E15.5 embryonic sections from mice that received no Tam for GFP, tdT, and CDH5. Quantification data are shown in the right panel. Data are shown as the mean ± SEM; $n = 5$. (**J**) Dox treatment inhibits tTA binding to tetO, preventing tdT gene activation. Shown is immunostaining of E15.5 tissue sections from the trigeminal ganglion for tdT, GFP, and CDH5 in *Nestin-CreER;R26-mGFP;Cdh5-αGFP-N-tTA;tetO-tdT* mice treated with Dox and Tam. (**K**) Illustration showing Cre-induced mGFP expression in sender cells. Scale bars: yellow, 1 mm; white, 100 μm. Each image is representative of five individual biological samples.

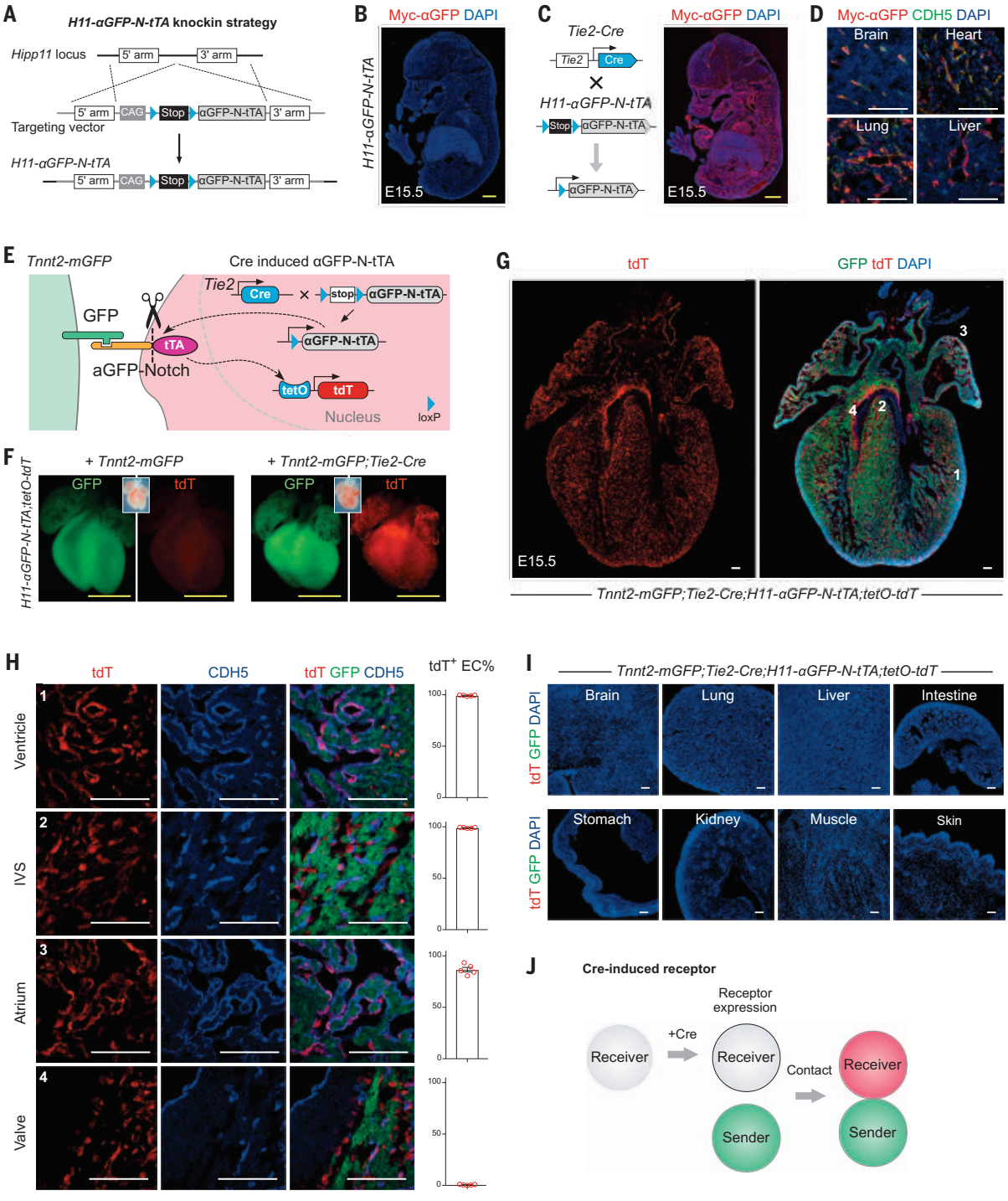


Fig. 5. Generation of the *H11-αGFP-N-tTA* mouse line for Cre-induced αGFP-N-tTA in receiver cells. (**A**) Schematic showing the generation of the *H11-αGFP-N-tTA* allele by homologous recombination using CRISPR-Cas9. (**B**) Immunostaining of *H11-αGFP-N-tTA* embryonic sections for the Myc tag. (**C**) Schematic showing *Tie2-Cre*–induced αGFP-N-tTA expression (left). Shown is immunostaining of *Tie2-Cre;H11-αGFP-N-tTA* sections (right) for the Myc tag. (**D**) Immunostaining of brain, heart, lung, and liver sections from E15.5 *Tie2-Cre; H11-αGFP-N-tTA* embryos for the Myc tag and CDH5. (**E**) Schematic showing the design of the Cre-induced gLCCC system for study of the interaction between sender and Cre$^+$ receiver, e.g., the CM-EC interaction. (**F**) Whole-mount fluorescence images of hearts from E15.5 embryos. Insert, bright-field whole-mount images. (**G** and **H**) Immunostaining of E15.5 heart sections for GFP and tdT (G). Regions 1 to 4 are magnified in (H). The percentage of ECs expressing tdT in each region is quantified on the right panels. Data are shown as the mean ± SEM; n = 5. (**I**) Immunostaining of other tissues of E15.5 embryos for GFP and tdT. (**J**) Illustration showing Cre-induced αGFP-N-tTA expression in receiver cells. Scale bar: yellow, 1 mm; white, 100 μm. Each image is representative of five individual biological samples.

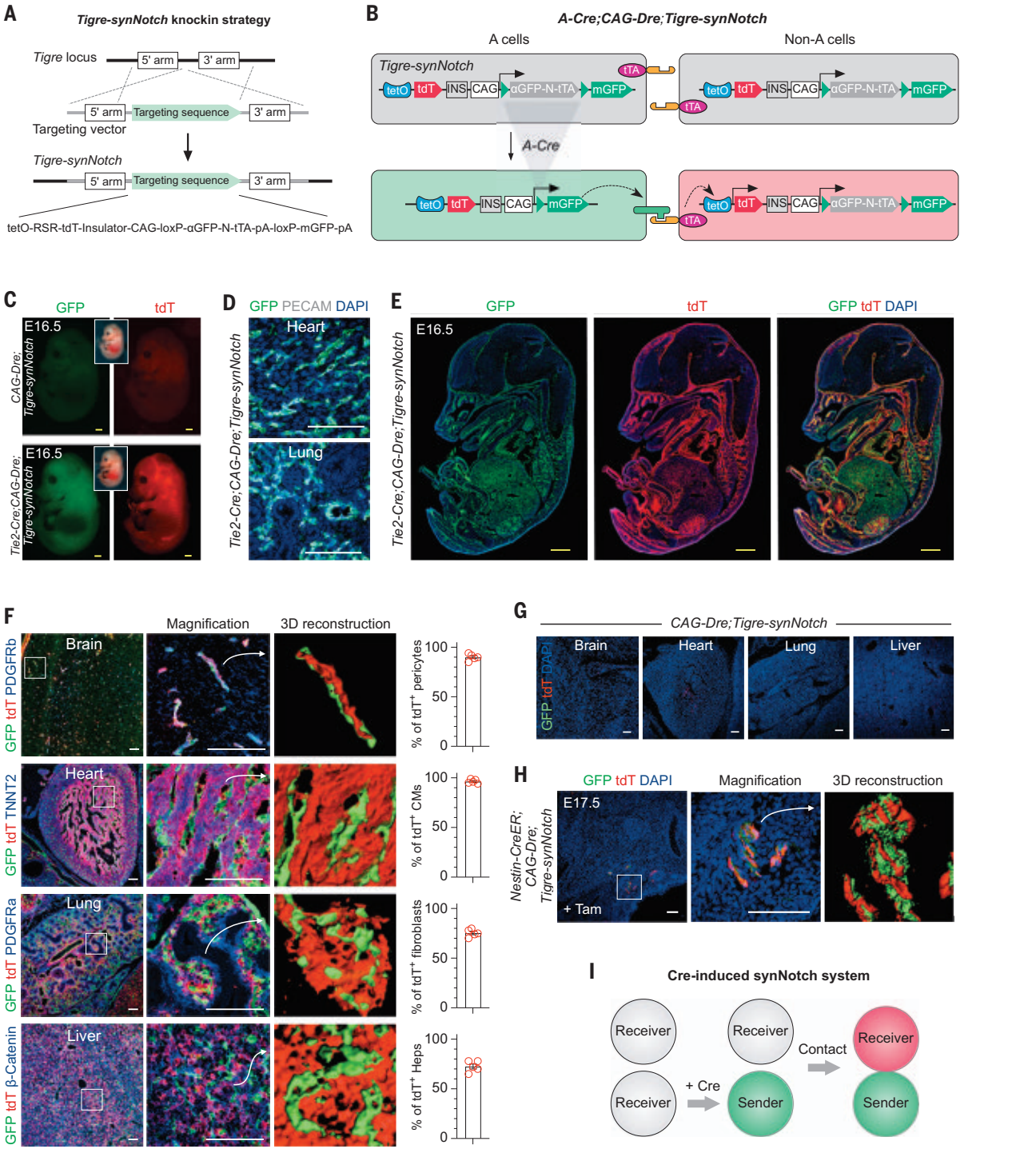


Fig. 6. Generation of the *Tigre-synNotch* mouse line for labeling of cells that contact with any Cre$^+$ cells. (**A**) Schematic showing the generation of the *Tigre-synNotch* allele by homologous recombination using CRISPR-Cas9. (**B**) Schematic showing the design for labeling of cells that contact with any Cre$^+$ cell lineages. (**C**) Whole-mount fluorescence images of E16.5 *CAG-Dre; Tigre-synNotch* and *Tie2-Cre;CAG-Dre;Tigre-synNotch* embryos. Insert, bright-field whole-mount image. (**D**) Immunostaining of E16.5 sections from *Tie2-Cre;CAG-Dre; Tigre-synNotch* embryos for GFP and PECAM. (**E**) Immunostaining of E16.5 whole embryonic sections from *Tie2-Cre;CAG-Dre;Tigre-synNotch* for GFP and tdT. (**F**) Immunostaining of E16.5 tissue sections for GFP, tdT, and PDGFRb, TNNT2, PDGFRα, or β-catenin. Three-dimensionally reconstructed images show GFP$^+$ cells and their interacting tdT$^+$ cells. The percentage of pericytes, CMs, fibroblasts, and hepatocytes expressing tdT in each region is quantified in the right panels. Data are shown as the mean ± SEM; $n = 5$. (**G**) Immunostaining of E16.5 sections from *CAG-Dre;Tigre-synNotch* embryos for GFP and tdT. (**H**) Immunostaining of E17.5 embryonic sections from *Nestin-CreER;CAG-Dre;Tigre-synNotch* for GFP and tdT after a low dose of Tam at E12.5. (**I**) Illustration showing the process of the Cre-induced synNotch system for labeling cells that contact with any Cre$^+$ cell lineage. Scale bars: yellow, 1 mm; white, 100 μm. Each image is representative of five individual biological samples. Data are shown as mean ± SEM.

one mouse, we generated a *tetO-Dre-BFP* reporter line [where Dre is another site-specific recombinase targeting specific 32bp DNA site rox (*38*), and BFP is blue fluorescent protein], by which an insulator-flanked tetO-Dre-IRES-BFP-polyA cassette was knocked into the Rosa26 locus using CRISPR-Cas9 (fig. S19A). In this design, when a mGFP$^+$ receiver cell and an αGFP-N-tTA$^+$ sender cell come into contact, tTA activates Dre-BFP expression, marking receiver cells as BFP$^+$ (gLCCC; fig. S19B). Using *R26-rox-tdT* (Rosa26-rox-Stop-rox-tdTomato), Dre-rox recombination results in permanent genetic tracing of receiver cells by tdT (gTCCC; fig. S19B). We used cardiac EC-CM contact to test this simultaneous gLCCC and gTCCC system using *Tnnt2-mGFP;Cdh5-αGFP-N-tTA;tetO-Dre-BFP;R26-rox-tdT* mice. Using whole-mount fluorescence and sectional immunostaining, we found that BFP and tdT were both expressed in CDH5$^+$ ECs in the heart (fig. S19, C and D). In mice lacking either synthetic ligand or receptor, we did not detect any BFP or tdT in cardiac ECs (fig. S19, C and D), suggesting that simultaneous gLCCC and gTCCC activation requires contact with both the synNotch ligand and the synNotch receptor.

We next used BFP (for gLCCC) and tdT (for gTCCC) to distinguish ongoing cell-cell contact and contact history in one mouse. Considering the established models of endocardial EMT in valve formation (*30*) and endocardial contribution to the liver vasculature (*31*), we examined BFP and tdT reporter in valve mesenchymal cells and ECs in the liver. Immunostaining of heart and liver sections showed that tdT was still expressed in valve mesenchymal cells and liver ECs when they were no longer in contact with GFP$^+$ CMs, but they did not express any BFP (fig. S19, E and F). Coronary ECs that were in contact with CMs expressed both BFP and tdT (fig. S19, E and F). These data demonstrate that ECs that are in contact with CMs remain tdT$^+$BFP$^+$, whereas ECs that dissociate with CMs remain tdT$^+$BFP$^-$ when they have undergone EMT or migrate to the liver (fig. S19G). Thus, *tetO-Dre-BFP* enabled us to reveal ongoing cell-cell contacts and their contact history with distinct reporters simultaneously in one mouse (fig. S19H).

Discussion

We used synNotch modules (*5*, *6*, *10*) to develop an in vivo strategy for monitoring dynamic cell-cell contacts and for tracing cell contact history in mice (table S1 and S2). These two systems can also be applied simultaneously in one mouse if different reporters are selected for separate genetic readouts, enabling both monitoring of ongoing cell-cell contacts and tracing of contact history in diverse biological contexts. One question is whether the affinity of synNotch ligand-receptor binding could influence cell-cell dissociation. Previous studies with the synNotch strategy (*5*, *6*, *10*) may alleviate this concern. We also chose a low-affinity version of the αGFP nanobody LaG17 (*24*) to further mitigate this concern. We studied cardiac tissues because the developing heart offers clear spatial segregation and cell fate transitions to test the performance of our system with a natural readout in a physiological context (Fig. 2B). A second example of endocardial ECs' migration away from the heart to the liver bud and subsequent contribution to the liver vasculature supports the observation of a natural development program (*31*) by our gTCCC system (Fig. 2J). Direct cell-cell contact is needed to activate synNotch, because both the sender lysate and purified mGFP failed to activate the synNotch system in receiver cells (fig. S6), consistent with previous studies showing that the mechanical force exerted by sender cells through contact is required for Notch activation in receiver cells (*5*, *39*). It should also be noted that some cellular contact may not necessarily induce physiological cell-cell communications or regulation of cell fate plasticity. The biological significance of the migration of endocardial cells to the liver and the outgrowth of tumor blood vessels merits further investigation, but these results are a good demonstration of what the technology described here can do.

The dynamic monitoring capacity of our gLCCC system uncovered dynamic interactions of ECs with other cell lineages in development, tissue homeostasis, and pathological conditions. The tracing ability of the gTCCC system detected the contribution of endocardial cells to liver vasculature and tumor vessel outgrowth. The reporter readouts of gLCCC and gTCCC differ in sensitivity, because the reporter in gLCCC reflects the strength of tTA-mediated gene activation, whereas the reporter in gTCCC is a binary readout after permanent recombination and is ubiquitously active due to the Rosa26-CAG promoter (table S1 and S2). In this study, we also generated three special mouse lines for Cre-induced expression of synNotch ligand or receptor. Although the *R26-mGFP* and *H11-αGFP-N-tTA* mouse lines enable synNotch ligand and receptor expression, respectively, in any type of cell with a Cre driver, Tigre-synNotch further made possible ligand and receptor expression in Cre$^+$ cells and all other Cre$^-$ cells in one mouse line, allowing us to explore the cell-cell contact map broadly without predefined cell types in advance (table S1). Contact-dependent labeling could also be useful for studying stem cell–niche cell interactions and their functions in normal and disease contexts. In addition to unraveling cell-cell communication, the contact-dependent cell tracing demonstrated here also offers a potential new method for cell fate mapping in vivo, providing positional information on cells that migrate away from their origins and/or adopt a new fate during development, homeostasis, regeneration, and disease.

REFERENCES AND NOTES

1. R. Daneman, L. Zhou, A. A. Kebede, B. A. Barres, Pericytes are required for blood-brain barrier integrity during embryogenesis. *Nature* **468**, 562–566 (2010). doi: 10.1038/nature09513; pmid: 20944625
2. D. P. Hoytema van Konijnenburg *et al*., Intestinal epithelial and intraepithelial T cell crosstalk mediates a dynamic response to infection. *Cell* **171**, 783–794.e13 (2017). doi: 10.1016/j.cell.2017.08.046; pmid: 28942917
3. E. C. Butcher, L. J. Picker, Lymphocyte homing and homeostasis. *Science* **272**, 60–66 (1996). doi: 10.1126/science.272.5258.60; pmid: 8600538
4. F. R. Balkwill, M. Capasso, T. Hagemann, The tumor microenvironment at a glance. *J. Cell Sci.* **125**, 5591–5596 (2012). doi: 10.1242/jcs.116392; pmid: 23420197
5. L. Morsut *et al*., Engineering customized cell sensing and response behaviors using synthetic Notch receptors. *Cell* **164**, 780–791 (2016). doi: 10.1016/j.cell.2016.01.012; pmid: 26830878
6. K. T. Roybal *et al*., Engineering T cells with customized therapeutic response programs using synthetic Notch receptors. *Cell* **167**, 419–432.e16 (2016). doi: 10.1016/j.cell.2016.09.011; pmid: 27693353
7. L. He, J. Huang, N. Perrimon, Development of an optimized synthetic Notch receptor as an in vivo cell-cell contact sensor. *Proc. Natl. Acad. Sci. U.S.A.* **114**, 5467–5472 (2017). doi: 10.1073/pnas.1703205114; pmid: 28490499
8. G. Pasqual *et al*., Monitoring T cell-dendritic cell interactions in vivo by intercellular enzymatic labelling. *Nature* **553**, 496–500 (2018). doi: 10.1038/nature25442; pmid: 29342141
9. T. C. Branon *et al*., Efficient proximity labeling in living cells and organisms with TurboID. *Nat. Biotechnol.* **36**, 880–887 (2018). doi: 10.1038/nbt.4201; pmid: 30125270
10. S. Toda, L. R. Blauch, S. K. Y. Tang, L. Morsut, W. A. Lim, Programming self-organizing multicellular structures with synthetic cell-cell signaling. *Science* **361**, 156–162 (2018). doi: 10.1126/science.aat0271; pmid: 29853554
11. Y. Ge *et al*., Enzyme-mediated intercellular proximity labeling for detecting cell–cell interactions. *J. Am. Chem. Soc.* **141**, 1833–1837 (2019). doi: 10.1021/jacs.8b10286; pmid: 30676735
12. J. Wang *et al*., Time-resolved protein activation by proximal decaging in living systems. *Nature* **569**, 509–513 (2019). doi: 10.1038/s41586-019-1188-1; pmid: 31068699
13. L. Ombrato *et al*., Metastatic-niche labelling reveals parenchymal cells with stem features. *Nature* **572**, 603–608 (2019). doi: 10.1038/s41586-019-1487-6; pmid: 31462798
14. R. N. Germain, T-cell development and the CD4-CD8 lineage decision. *Nat. Rev. Immunol.* **2**, 309–322 (2002). doi: 10.1038/nri798; pmid: 12033737
15. C. K. Lee *et al*., Tumor metastasis to lymph nodes requires YAP-dependent metabolic adaptation. *Science* **363**, 644–649 (2019). doi: 10.1126/science.aav0173; pmid: 30733421
16. I. Mellman, G. Coukos, G. Dranoff, Cancer immunotherapy comes of age. *Nature* **480**, 480–489 (2011). doi: 10.1038/nature10673; pmid: 22193102
17. E. Tran *et al*., Cancer immunotherapy based on mutation-specific CD4+ T cells in a patient with epithelial cancer. *Science* **344**, 641–645 (2014). doi: 10.1126/science.1251102; pmid: 24812403
18. A. Pardo-Saganta *et al*., Parent stem cells can serve as niches for their daughter cells. *Nature* **523**, 597–601 (2015). doi: 10.1038/nature14553; pmid: 26147083
19. T. Kadesch, Notch signaling: The demise of elegant simplicity. *Curr. Opin. Genet. Dev.* **14**, 506–512 (2004). doi: 10.1016/j.gde.2004.07.007; pmid: 15380241
20. R. Kopan, M. X. Ilagan, The canonical Notch signaling pathway: Unfolding the activation mechanism. *Cell* **137**, 216–233 (2009). doi: 10.1016/j.cell.2009.03.045; pmid: 19379690
21. D. Sprinzak *et al*., Cis-interactions between Notch and Delta generate mutually exclusive signalling states. *Nature* **465**, 86–90 (2010). doi: 10.1038/nature08959; pmid: 20418862
22. K. T. Roybal *et al*., Precision tumor recognition by T cells with combinatorial antigen-sensing circuits. *Cell* **164**, 770–779 (2016). doi: 10.1016/j.cell.2016.01.011; pmid: 26830879
23. S. Srivastava *et al*., Logic-gated ROR1 chimeric antigen receptor expression rescues T cell-mediated toxicity to normal

tissues and enables selective tumor targeting. *Cancer Cell* **35**, 489–503.e8 (2019). doi: 10.1016/j.ccell.2019.02.003; pmid: 30889382
24. P. C. Fridy *et al*., A robust pipeline for rapid production of versatile nanobody repertoires. *Nat. Methods* **11**, 1253–1260 (2014). doi: 10.1038/nmeth.3170; pmid: 25362362
25. P. A. Furth *et al*., Temporal control of gene expression in transgenic mice by a tetracycline-responsive promoter. *Proc. Natl. Acad. Sci. U.S.A.* **91**, 9302–9306 (1994). doi: 10.1073/pnas.91.20.9302; pmid: 7937760
26. X. Tian *et al*., Subepicardial endothelial cells invade the embryonic ventricle wall to form coronary arteries. *Cell Res.* **23**, 1075–1090 (2013). doi: 10.1038/cr.2013.83; pmid: 23797856
27. M. Vooijs *et al*., Mapping the consequence of Notch1 proteolysis in vivo with NIP-CRE. *Development* **134**, 535–544 (2007). doi: 10.1242/dev.02733; pmid: 17215306
28. Z. Zhu, T. Zheng, C. G. Lee, R. J. Homer, J. A. Elias, Tetracycline-controlled transcriptional regulation systems: Advances and application in transgenic animal modeling. *Semin. Cell Dev. Biol.* **13**, 121–128 (2002). doi: 10.1016/S1084-9521(02)00018-6; pmid: 12127145
29. G. Friedrich, P. Soriano, Promoter traps in embryonic stem cells: A genetic screen to identify and mutate developmental genes in mice. *Genes Dev.* **5**, 1513–1523 (1991). doi: 10.1101/gad.5.9.1513; pmid: 1653172
30. J. L. de la Pompa, J. A. Epstein, Coordinating tissue interactions: Notch signaling in cardiac development and disease. *Dev. Cell* **22**, 244–254 (2012). doi: 10.1016/j.devcel.2012.01.014; pmid: 22340493
31. H. Zhang *et al*., Genetic lineage tracing identifies endocardial origin of liver vasculature. *Nat. Genet.* **48**, 537–543 (2016). doi: 10.1038/ng.3536; pmid: 27019112
32. P. Carmeliet, R. K. Jain, Molecular mechanisms and clinical applications of angiogenesis. *Nature* **473**, 298–307 (2011). doi: 10.1038/nature10144; pmid: 21593862
33. M. Potente, T. Mäkinen, Vascular heterogeneity and specialization in development and disease. *Nat. Rev. Mol. Cell Biol.* **18**, 477–494 (2017). doi: 10.1038/nrm.2017.36; pmid: 28537573
34. M. Potente, H. Gerhardt, P. Carmeliet, Basic and therapeutic aspects of angiogenesis. *Cell* **146**, 873–887 (2011). doi: 10.1016/j.cell.2011.08.039; pmid: 21925313
35. B. Tasic *et al*., Site-specific integrase-mediated transgenesis in mice via pronuclear injection. *Proc. Natl. Acad. Sci. U.S.A.* **108**, 7902–7907 (2011). doi: 10.1073/pnas.1019507108; pmid: 21464299
36. H. Zeng *et al*., An inducible and reversible mouse genetic rescue system. *PLOS Genet.* **4**, e1000069 (2008). doi: 10.1371/journal.pgen.1000069; pmid: 18464897
37. Y. Y. Kisanuki *et al*., Tie2-Cre transgenic mice: A new model for endothelial cell-lineage analysis in vivo. *Dev. Biol.* **230**, 230–242 (2001). doi: 10.1006/dbio.2000.0106; pmid: 11161575
38. B. Sauer, J. McDermott, DNA recombination with a heterospecific Cre homolog identified from comparison of the pac-c1 regions of P1-related phages. *Nucleic Acids Res.* **32**, 6086–6095 (2004). doi: 10.1093/nar/gkh941; pmid: 15550568
39. W. R. Gordon *et al*., Mechanical allostery: Evidence for a force requirement in the proteolytic activation of Notch. *Dev. Cell* **33**, 729–736 (2015). doi: 10.1016/j.devcel.2015.05.004; pmid: 26051539

ACKNOWLEDGMENTS

We thank Shanghai Biomodel Organism Co., Ltd. for mice generation, our institutional animal facilities for mice husbandry, J. H. Snyder for editing the manuscript, and H. Zeng for providing reporter mice. **Funding:** This work was supported by the Strategic Priority Research Program of the Chinese Academy of Sciences (CAS grant XDA16010507); the CAS Project for Young Scientists in Basic Research (grant YSBR-012); the Shanghai Pilot Program for Basic Research – CAS, Shanghai Branch (grant JCYJ-SHFY-2021-0); the National Science Foundation of China (grants 32050087, 82088101, 91849202, 31730112, 31922032, 81872241, 91639302, and 31701292); the National Key Research & Development Program of China (grants 2019YFA0110403, 2019YFA0802000, 2018YFA0107900, 2018YFA0108100, 2019YFA0802803,and 2020YFA0803202); the Shanghai Science and Technology Commission (grants 19JC1415700, 19ZR1479800, 20QC1401000, and 20200CXJQ01); funds from the Mildred V. Strouss Trust and the Tobacco-Related Disease Research Program (28IR-0067) to R.A.W.; and an XPLORER PRIZE from the Tencent Foundation. **Author contributions:** S.Z. designed the study, performed the experiments, and analyzed the data. H.Zha., Z.L., K.L., H.Zhu, W.P., and L.H. bred the mice, performed the experiments, and discussed the work. R.A.W. provided intellectual input and revised and edited the manuscript. B.Z. conceived and supervised the study and wrote the manuscript. **Competing interests:** The authors declare no competing interests. **Data and materials availability:** The RNA-sequencing data generated in his study have been deposited in the NCBI Sequence Read Archive under BioProject ID PRJNA866292. Transgenic mice generated in this study are available from B.Z. under a material transfer agreement with the CAS Center for Excellence in Molecular Cell Science. **License information:** Copyright © 2022 the authors, some rights reserved; exclusive licensee American Association for the Advancement of Science. No claim to original US government works. https://www.science.org/about/science-licenses-journal-article-reuse

SUPPLEMENTARY MATERIALS

science.org/doi/10.1126/science.abo5503
Materials and Methods
Figs. S1 to S19
Tables S1 and S2
References (*40*–*53*)
MDAR Reproducibility Checklist

Submitted 12 February 2022; accepted 26 October 2022
10.1126/science.abo5503

Your Legacy to Science

AN ESTATE GIFT TO THE
AMERICAN ASSOCIATION FOR THE ADVANCEMENT OF SCIENCE





Since 1848, our founding year, the American Association for the Advancement of Science (AAAS) has been deeply committed to advancing science, engineering and innovation around the world for the benefit of all people.

By making AAAS a beneficiary of your will, trust, retirement plan or life insurance policy, you become a member of our 1848 Society, joining Thomas Edison, Alexander Graham Bell and the many distinguished individuals whose vision led to the creation of AAAS and our world-renowned journal, *Science*, so many years ago.

Unlike many of its peers, *Science* is not for-profit. Your estate gift would provide long-term financial stability and durable annual income that will support operations and competitive innovation for years to come. **This support is vital.**

"As a teacher and instructor, I bear responsibility for the younger generations. If you have extra resources, concentrate them on organizations, like AAAS, that are doing work for all."

—Prof. Elisabeth Ervin-Blankenheim, 1848 Society member

If you intend to include AAAS in your estate plans, provide this information to your lawyer or financial adviser:

Legal Name: American Association for the Advancement of Science
Federal Tax ID Number: 53-0196568
Address: 1200 New York Avenue, NW, Washington, DC 20005

If you would like more information on making an estate gift to AAAS, cut out and return the form below or send an email to philanthropy@aaas.org. Additional details are also available online at **www.aaas.org/1848Society**.

1848 SOCIETY
AAAS

cut here

Yes, I would like more information about joining the AAAS 1848 Society.

PLEASE CONTACT ME AT:

Name: _____

Address: _____

City: _____ State: _____ Zip code: _____ Country: _____

Email: _____ Phone: _____

RETURN THIS FORM TO:
AAAS Office of Philanthropy and Strategic Partnerships • 1200 New York Avenue, NW • Washington, DC 20005 USA

RESEARCH ARTICLES

QUANTUM SIMULATION

Observing the quantum topology of light

Jinfeng Deng[1]†, Hang Dong[1]†, Chuanyu Zhang[1], Yaozu Wu[1], Jiale Yuan[1], Xuhao Zhu[1], Feitong Jin[1], Hekang Li[1], Zhen Wang[1,2,3], Han Cai[1], Chao Song[1]*, H. Wang[1,2,3]*, J. Q. You[1], Da-Wei Wang[1,3,4]*

Topological photonics provides a powerful platform to explore topological physics beyond traditional electronic materials and shows promising applications in light transport and lasers. Classical degrees of freedom are routinely used to construct topological light modes in real or synthetic dimensions. Beyond the classical topology, the inherent quantum nature of light provides a wealth of fundamentally distinct topological states. Here we implement experiments on topological states of quantized light in a superconducting circuit, with which one- and two-dimensional Fock-state lattices are constructed. We realize rich topological physics including topological zero-energy states of the Su-Schrieffer-Heeger model, strain-induced pseudo-Landau levels, valley Hall effect, and Haldane chiral edge currents. Our study extends the topological states of light to the quantum regime, bridging topological phases of condensed-matter physics with circuit quantum electrodynamics, and offers a freedom in controlling the quantum states of multiple resonators.

The quantum Hall effect (*1*) reveals new phases of matter that are classified by the topological invariants of energy bands (*2*). For two-dimensional electrons in strong magnetic fields, the chiral edge states between Landau levels contribute to the quantized Hall conductivity, which is immune to local defects. This topological effect can also exist without Landau levels, such as in the Haldane model (*3*), which lays the basis for topological insulators (*4*). The optical simulation of quantum Hall edge states (*5*) opens a new research area, topological photonics (*6*–*8*), which brings a wealth of applications in routing and generating electromagnetic waves, such as backscattering-free waveguides (*9*) and topological insulator lasers (*10*). Classical degrees of freedom such as frequencies and orbital angular momenta have been widely used to synthesize new lattice dimensions to embed the topological modes (*11*–*13*). Such pure classical topology of light is in stark contrast to the topological phases of electrons, where the quantum wave and fermionic statistics play a fundamental role. Intriguingly, new topological states emerging from light quantization and bosonic statistics have been predicted beyond classical interpretation (*14*–*17*). Recent development in circuit quantum electrodynamics (QED) (*18*) makes it possible to realize these intrinsic quantum topological states of light, which provide quantum degrees of freedom in engineering photonic topology (*14*, *19*) and offer topological control knobs in bosonic quantum information processing (*20*–*23*).

Compared with lattices of modes in real or synthetic dimensions in classical topological photonics, the topological states of quantized light are embedded in lattices of Fock states $\Pi_i|n_i\rangle$ with n_i being the photon number in the ith mode. In the Fock-state lattice (FSL), a mode provides a dimension (*14*, *19*, *20*, *24*), in contrast to a site in traditional lattices, including those in synthetic dimensions (*11*–*13*, *25*). The FSLs exploit the infinite quantum Hilbert space of light, enabling the construction of high-dimensional lattices with only a few cavity modes. To sketch such dimensional scalability, we use the Jaynes-Cummings (JC) model (*26*), which describes the interaction between a two-level atom with quantized light. However, here we use multiple quantized light modes to couple the atom. With two light modes, the Fock states form one-dimensional (1D) lattices of the Su-Schrieffer-Heeger (SSH) model (Fig. 1A) (*27*). By adding just one other mode, we obtain two-dimensional (2D) strained honeycomb lattices (Fig. 1B) (*28*). These lattices are featured by site-dependent coupling strengths, which originate from the property of the bosonic annihilation operator a

$$a|n\rangle = \sqrt{n}|n-1\rangle \qquad (1)$$

For the vacuum state, $a|0\rangle = 0$, which leads to natural edges of FSLs when the photon number

[1]Interdisciplinary Center for Quantum Information, State Key Laboratory of Modern Optical Instrumentation, and Zhejiang Province Key Laboratory of Quantum Technology and Device, School of Physics, Zhejiang University, Hangzhou 310027, China. [2]Hangzhou Global Scientific and Technological Innovation Center, Zhejiang University, Hangzhou 311215, China. [3]Hefei National Laboratory, Hefei 230088, China. [4]CAS Center of Excellence in Topological Quantum Computation, Beijing 100190, China.
*Corresponding author. Email: chaosong@zju.edu.cn (C.S.); hhwang@zju.edu.cn (H.W.); dwwang@zju.edu.cn (D.-W.W.)
†These authors contributed equally to this work.

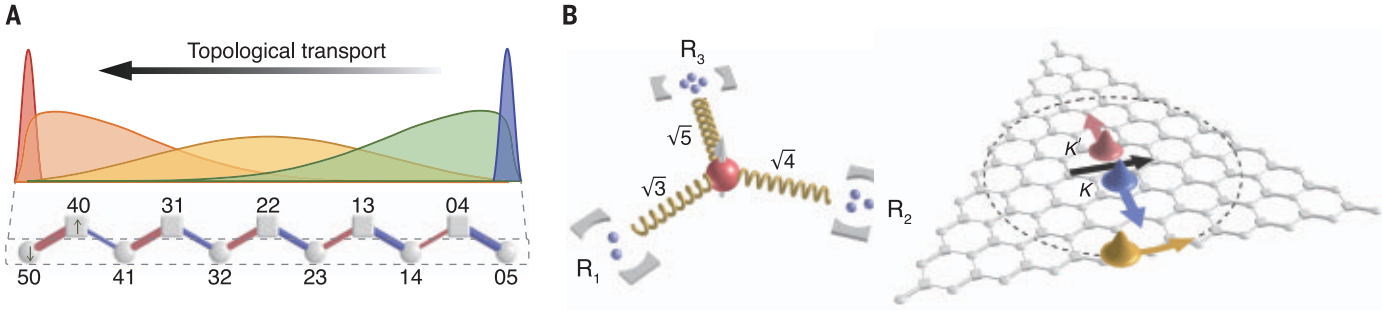


Fig. 1. Fock-state lattices of multimode Jaynes-Cummings models. (**A**) Topological transport of the zero-energy state of the SSH FSL with $N = 5$. The sublattice sites of $s = \uparrow (\downarrow)$ are denoted by squares (circles) and labeled by n_1n_2, the photon numbers in R_1 and R_2. The thicknesses of the lines connecting neighboring sites are proportional to the coupling strengths t_1 (red) and t_2 (blue). The wave function envelopes of four zero-energy states are schematically drawn with different colors. (**B**) The valley Hall response and the Haldane chiral edge state in a 2D FSL with $N = 10$. An excited qubit is coupled to three resonators with different photon numbers n_j (left). The coupling strengths are proportional to $\sqrt{n_j + 1}$, which introduces competition between resonators to obtain a photon from the qubit. All the Fock states with the same N are coupled by the JC Hamiltonian to form a honeycomb lattice (right). The inhomogeneous coupling strengths induce an effective magnetic field in the 2D FSL. The VHE is featured by the wave packets at the two valleys moving in opposite directions perpendicular to an applied force (the black arrow). A Lifshitz topological edge (dashed line) separating the semimetallic and insulator phases locates on the incircle, which can host the Haldane chiral edge states (yellow wave packet with the arrow indicating the moving direction).

in one of the cavities reduces to zero. FSLs also have topological edges that host zero-energy states, resulting from the competition between resonators in exchanging photons with the atom. Such a simple mechanism enables FSLs to realize several important models in topological physics, in particular the seminal SSH and Haldane models, which have been the focus in various quantum platforms (*29*–*36*). Here we demonstrate adiabatic transport of topological zero-energy states in 1D SSH FSLs, where Fock states are topologically transferred from one cavity to another while maintaining the quantumness in superposition states. In 2D FSLs, we observe the valley Hall effect (VHE) (*37*) and the Haldane chiral edge current (*38*), which offer a topological route of engineering quantum states of multiple resonators.

Leveraging the advantageous integrability and tunability of the circuit QED platform (*39*–*42*), we design and fabricate a superconducting circuit to build and engineer the FSLs. The key elements of the circuit are a central gmon qubit (*43*) (Q_0) and three resonators (R_j with j running from 1 to 3), all with tunable frequencies. Each resonator R_j is coupled to Q_0 through an inductive coupler (C_j) (Fig. 2A). The coupling strengths $g_j/2\pi$ can be continuously tuned by changing the magnetic flux in C_j. In addition, each resonator R_j is capacitively coupled to an ancilla qubit Q_j for the preparation and readout of the resonator state. Other characteristics of the resonators and qubits can be found in the supplementary materials.

The Hamiltonian of the coupled system of R_j's and Q_0 can be described by a multimode JC model (*26*) in the rotating-wave approximation

$$H = \frac{\hbar\omega_0}{2}\sigma_z + \sum_{j=1}^{d}\hbar\omega_j a_j^\dagger a_j + \sum_{j=1}^{d}\hbar g_j\left(\sigma^+ a_j + a_j^\dagger\sigma^-\right) \quad (2)$$

where a_j is the annihilation operator of R_j with the transition frequency ω_j, $\sigma^+ \equiv |\uparrow\rangle\langle\downarrow|$ and $\sigma^- \equiv |\downarrow\rangle\langle\uparrow|$ are the raising and lowering operators

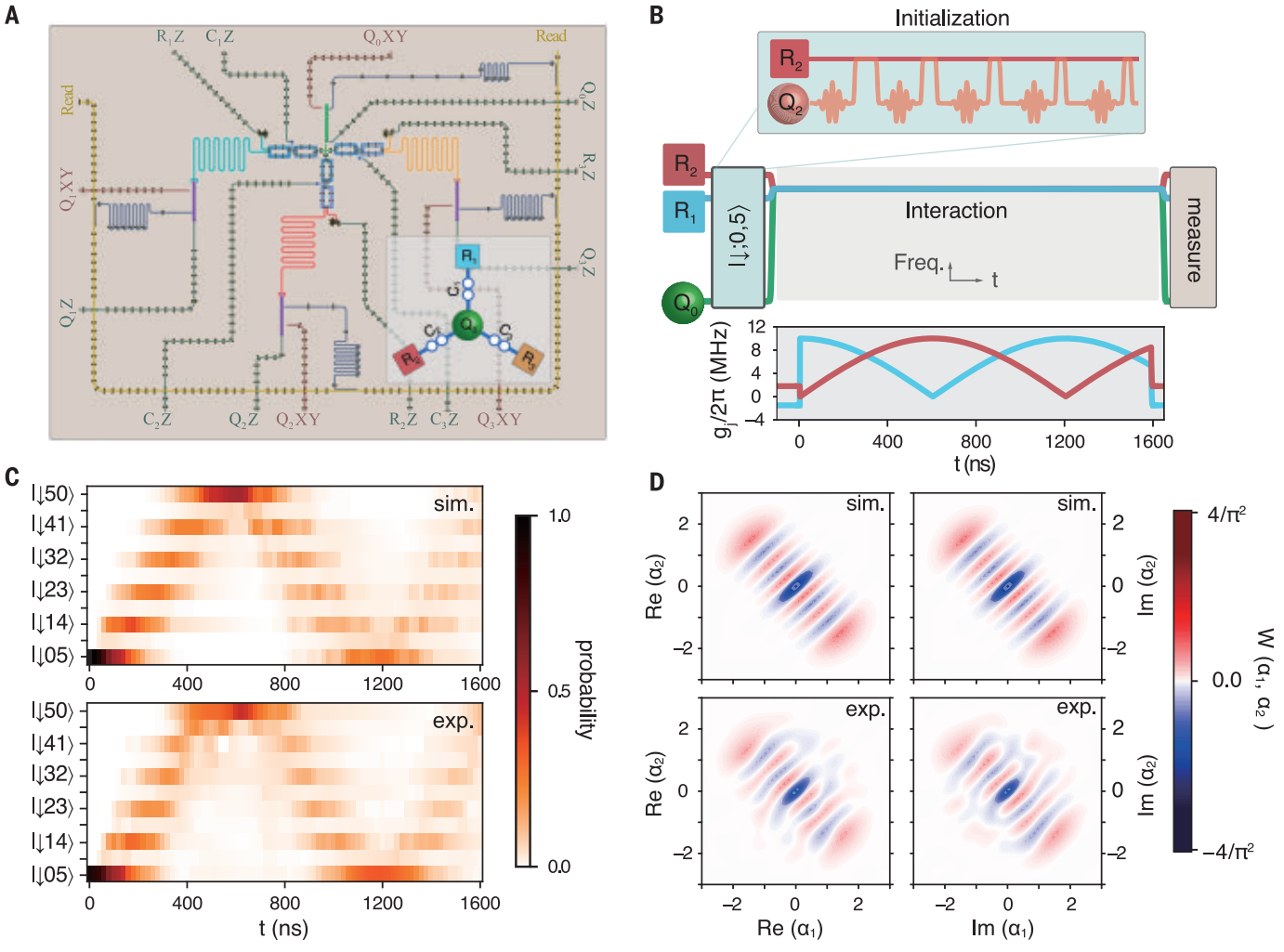


Fig. 2. Adiabatic transport of the topological zero-energy states in the Fock-state Su-Schrieffer-Heeger model. (**A**) False-color circuit image of the device of this experiment. Inset: Symbolized configuration of the key elements, a central gmon qubit Q_0 (green circle) coupled to three resonators (cyan, red and yellow squares for R_1, R_2, and R_3) via tunable couplers (blue twin circles). (**B**) Experimental pulse sequences for the adiabatic transport. We prepare the initial Fock state of R_2 by repeatedly exciting its ancilla qubit Q_2 with a π-pulse and tuning it in resonance with R_2 to swap the photons (upper panel). After the initialization, we tune R_1, R_2, and Q_0 in resonance (middle panel) and modulate C_1, C_2 to tune the coupling strengths g_1 (cyan line) and g_2 (red line) (lower panel). Finally, we measure the joint population of R_1, R_2, and Q_0. (**C**) The observed evolution of the zero-energy state wave packet in the numerical simulation (upper panel) and experiment (lower panel). Obviously $|\Psi_0\rangle$ only occupies the $|\downarrow\rangle$ sublattice. In numerical simulation, we use the parameters of the resonators and qubit listed in the table S1. All data in this paper, except that for quantum state tomography, are averaged over five runs of experiments. (**D**) The two-mode Wigner function of the resonator state at $t = 300$ ns in the plane-cut along axes $\mathrm{Re}(\alpha_1)$-$\mathrm{Re}(\alpha_2)$ and $\mathrm{Im}(\alpha_1)$-$\mathrm{Im}(\alpha_2)$, and the fidelity $F = 0.735$ (see fig. S6 for pulse sequence of tomography and more data at other times).

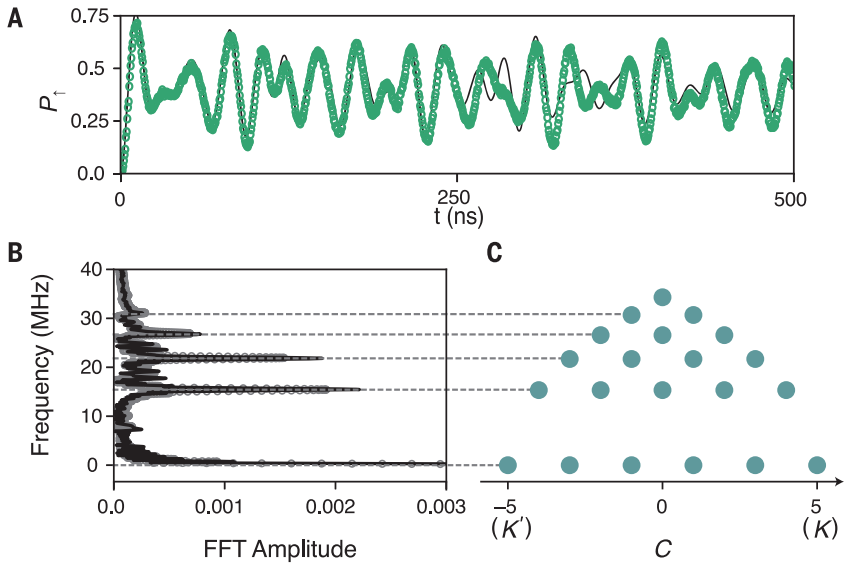


Fig. 3. The pseudo-Landau levels in the 2D Fock-state lattice with $N = 5$. (**A**) The evolution of the excited-state population of the qubit Q_0. (**B**) Fast Fourier transform of the Rabi oscillation. The vertical axis is the frequency component divided by 2. The solid line is the numerical simulation, and the circles are the experimental data. (**C**) The eigenstates in the zeroth and positive pseudo-Landau levels of the 2D FSL, with eigenenergies corresponding to the Fourier peaks. Each point labels an eigenstate characterized by the chirality C. The degeneracy of the nth Landau level is $N - n + 1$.

of Q_0 with the transition frequency ω_0, and d is the number of resonator modes. The Hamiltonian conserves the total excitation number $N = \sum_j n_j + (\sigma_z + 1)/2$, where n_j is the photon number of R_j and $\sigma_z = |\uparrow\rangle\langle\uparrow| - |\downarrow\rangle\langle\downarrow|$.

Topological transport

For $d = 2$ and N excitations, $2N + 1$ states $|s; n_1, n_2\rangle$ are coupled in a bipartite tight-binding lattices with the spin states $s = \uparrow, \downarrow$ labeling the two sublattices (Fig. 1A). When Q_0 is resonant with both resonators, all these $2N + 1$ states have the same energy, which is set as the zero energy. Because the coupling strengths $t_j = g_j\sqrt{n_j}\,(j = 1, 2)$ depend on the photon numbers, $t_1 > t_2$ and $t_1 < t_2$ on the left- and right-hand sides of the FSL, resulting in two different topological phases of the SSH model (*27*). A topological zero-energy state locates around the lattice sites satisfying $t_1 = t_2$, which is the topological edge of the SSH model. We write $g_j = g_0\lambda_j$ where g_0 is a fixed nonzero coupling strength and λ_j's are the tunable parameters satisfying $\lambda_1^2 + \lambda_2^2 = 1$. The topological zero-energy state can be written as a two-mode binomial state (*14*, *44*)

$$|\Psi_0\rangle = \sum_{n=0}^{N} \sqrt{\frac{N!}{n!(N-n)!}} \lambda_2^n (-\lambda_1)^{N-n} \left|\downarrow; n, N-n\right\rangle \tag{3}$$

which only occupies the $|\downarrow\rangle$ sublattice. By adiabatically tuning λ_2 from 0 to 1, we can transport the topological zero-energy state from the right end of the lattice to the left end, or vice versa.

In the experiment we select R_1 and R_2 to construct the SSH FSL, with R_3 being far detuned and effectively decoupled from the system. In the experimental pulse sequences (Fig. 2B), we first prepare the initial state $|\downarrow; 0, 5\rangle$, which is the topological zero-energy state of the SSH FSL with $N = 5$ and $\lambda_1 = 1$, by pumping five photons successively into R_2 via Q_2 (upper panel of Fig. 2B). Then we tune R_1, R_2, and Q_0 in resonance at the frequency $\omega_{\text{int}}/2\pi \approx 4.81$ GHz and sinusoidally modulate the coupling strengths where $g_0/2\pi \approx 9$ MHz, $\lambda_1 = |\cos(2\pi\nu t)|$, and $\lambda_2 = |\sin(2\pi\nu t)|$ with $\nu = 416$ kHz $\ll g_0$ to satisfy the adiabatic condition (lower panel of Fig. 2B). Finally, the wave packet of the zero-energy state in the FSL is measured (see supplementary materials), with the data shown in Fig. 2C. The adiabatic transport of the topological edge state is witnessed by the oscillation of the photons between R_1 and R_2 following Eq. 3 with time-dependent λ_1 and λ_2. The zero-energy state is topologically protected by the energy gap g_0 from other eigenstates of the FSL and maintains coherence during the transport (*45*). To show this, we further measure the density matrix of the two resonators by quantum state tomography (Fig. 2D). The two-mode binomial state remains a Fock state in the combinational dark mode of the two resonators, $\lambda_2 a_1 - \lambda_1 a_2$, and the quantumness of the states is evident from the negative values of the two-mode Wigner functions.

Valley Hall effect

When $d = 3$, the Fock states in the subspace with N excitations form a two-dimensional honeycomb lattice containing $(N + 1)^2$ sites (Fig. 1B). The site-dependent coupling strengths introduce a strain, which has the effect of a magnetic field (*46*–*48*) and results in $\sqrt{n}$-scaling pseudo-Landau levels (*14*) when Q_0 is resonant with all three resonators. We observe the Landau levels by analyzing the spectra of the lattice dynamics (*49*). In the experiment, we prepare the initial state $|\downarrow; 0, 5, 0\rangle$ and resonantly couple R_1, R_2, and R_3 to Q_0 with coupling strengths $g_j/2\pi \approx 9$ MHz. We measure the evolution of the probability of finding Q_0 in the $|\uparrow\rangle$ state and then perform fast Fourier transform. We obtain peaks approximately located at $\sqrt{n}\Omega_0$ with $\Omega_0 = \sqrt{3}g_j$ (Fig. 3C). The degenerate states in the same Landau level are distinguished by their chiralities

$$C = b_+^\dagger b_+ - b_-^\dagger b_- \tag{4}$$

where $b_\pm = \sum_{j=1}^{3} a_j \exp(\mp i 2j\pi/3)/\sqrt{3}$ are the annihilation operators of the two chiral dark modes that are decoupled from the qubit. The chirality C plays the role of the lattice momentum in conventional lattices, and $C = N$ and $C = -N$ correspond to the two corners of the Brillouin zone, denoted as K and K' valleys, respectively (*14*, *50*).

A Lifshitz topological edge (*51*) on the incircle separates the FSL into two phases, a semimetallic phase within the incircle and a band insulator phase outside of it (see the dashed line in Fig. 1B). The states in the zeroth Landau level are confined within the incircle by an outside band gap of the insulator (*14*). In the semimetal, the strain-induced magnetic field has opposite signs at the K and K' valleys (see supplementary materials). By introducing a linear potential to mimic the effect of an electric field to electrons, we can observe the VHE (Fig. 1B); i.e., the Hall response has opposite signs at the two valleys. To experimentally demonstrate this effect, we first prepare an initial state $|\Psi_0\rangle$ with $\lambda_1 = \lambda_2 = 1/\sqrt{2}$ in Eq. 3 following the procedure in Fig. 2B. Such an initial state on the Lifshitz topological edge is a Gaussian wave function in the zeroth Landau level (*14*). Then we bring R_3 in resonance with Q_0 and set $g_j/2\pi \approx 9$ MHz for $j = 1, 2, 3$. The linear potential with horizontal gradient is introduced by slightly shifting the frequencies of R_1 and R_2

$$V = \hbar\delta\left(a_1^\dagger a_1 - a_2^\dagger a_2\right) \tag{5}$$

where the detuning $\delta/2\pi \approx 1.8$ MHz. We then measure populations on each lattice site and obtain the average photon numbers in the three resonators (Fig. 4B). The linear potential drives photons from R_1 and R_2 to R_3 whereas the qubit stays in the ground state. To visualize the evolution of the wave function, we draw the

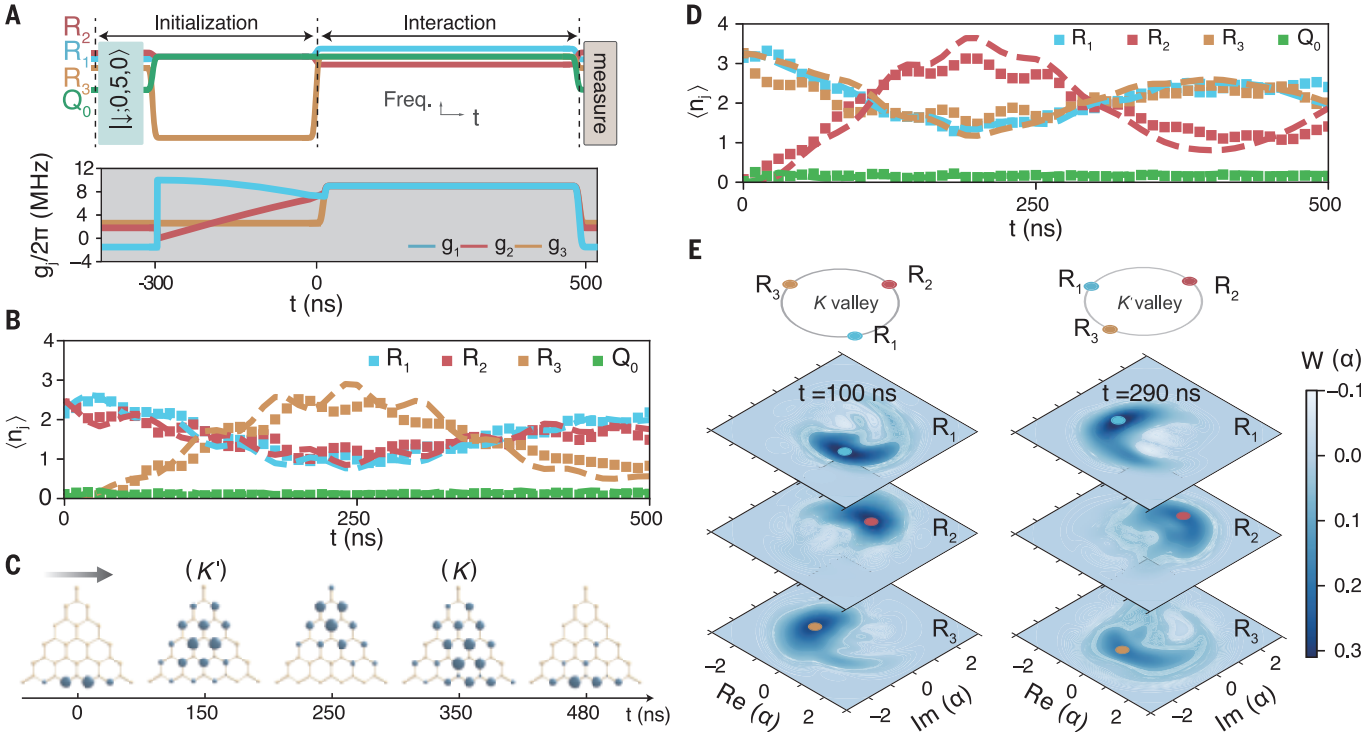


Fig. 4. The valley Hall effect in the 2D Fock-state lattice. (**A**) The pulse sequences for controlling the frequencies (upper panel) and coupling strengths (lower panel). We first prepare the initial state $|\Psi_0\rangle$ through the topological transport in the SSH FSL. Then we tune R_3 and Q_0 in resonance at $\omega_{int}/2\pi \approx 4.81$ GHz while we detune R_1 and R_2 to introduce the linear potential. Meanwhile we set the coupling strengths $g_j/2\pi \approx 9$ MHz for $j = 1, 2, 3$, and finally we measure the joint populations at different times during the evolution. (**B**) The valley Hall evolution of the average photon numbers in the three resonators for an initial two-mode binomial state $|\Psi_0\rangle$ with $N = 5$. The squares are experimental data, and the dashed lines are numerical simulations with the detuning $\delta/2\pi = 1.80$ MHz. (**C**) The populations in the FSL for N = 5 at t = 0, 150, 250, 350, and 480 ns. The left, right, and top vertices correspond to the states with all photons in R_1, R_2 and R_3. The radius of the blue circle on each site is proportional to its population. The trajectory of the wave function is perpendicular to the direction of the effective force (black arrow). (**D**) The evolution of the average photon numbers in the three resonators for the coherent initial state $|\Psi_c\rangle = |\downarrow; \alpha, 0, -\alpha\rangle$ with $\alpha \approx 1.8$. We detune R_1 and R_3 to introduce a linear potential $V = \hbar\delta\left(a_1^\dagger a_1 - a_3^\dagger a_3\right)$. In the numerical simulation (dashed lines), we set $\delta/2\pi = 2.35$ MHz. (**E**) The measured Wigner functions of the three resonator states at time t = 100 and 290 ns (see fig. S3 for the numerical simulation). The phases of the largest amplitudes of the Wigner functions are labeled on the unit circles, which show the chirality of the corresponding states in the two valleys.

population distributions in the FSL at five different times (Fig. 4C). The wave function first moves upward perpendicular to the force direction (black arrow) until being reflected by the Lifshitz topological edge near the top vertex, and then moves downward back to the initial state (up to a phase factor). In particular, when the wave function is at the center of the lattice but in different valleys—e.g., at $t = 150$ and 350 ns—it moves in opposite directions, which is a signature of the VHE (*14*). In contrast to the valley Hall effect in photonic lattices, where edges are routinely needed for the experimental implementation (*52*, *53*), here we coherently transport the quantum states to the two valleys and directly measure the valley Hall drift, thanks to the high tunability, controllability, and readability of the superconducting circuit. It is noteworthy that the qubit remains in the ground state during the evolution, which reflects a fundamental difference between classical and quantum predictions (fig. S5).

Surprisingly, the VHE can also be observed with initial classical states such as $|\Psi_c\rangle = |\downarrow; \alpha, 0, -\alpha\rangle$; i.e., R_1 and R_3 are in the coherent states $|\alpha\rangle$ and $|-\alpha\rangle$ and R_2 is in the vacuum state. This state can be expanded as a superposition of two-mode binomial states with different total excitation numbers N (*14*). Owing to the synchronized dynamics in different subspaces, the fields in the three resonators remain as a direct product of coherent states, and the evolution of the average photon numbers in the three resonators follows curves similar to that for an initial binomial state (Fig. 4D and supplementary materials).

The states in the two valleys are identified by their chiralities. Because the states of the three resonators are separable for coherent initial states, we perform simultaneous quantum state tomography and obtain their Wigner functions (Fig. 4E). As expected, the phases are distributed in a counterclockwise ($C > 0$) and clockwise ($C < 0$) manner at $t = 100$ and 290 ns when the wave function moves to the K and K' valleys, respectively. Therefore, the VHE in FSLs can be used to coherently transport the wave function between two valleys and control the chirality of the quantum states of multiple resonators.

Haldane model

By introducing a Floquet modulation of the coupling strength, $g_j(t) = g_0 + 2g_d\sin[\nu_d t + 2(j-1)\pi/3]$, we synthesize a most important model in topological physics, the Haldane model (*33*, *35*, *36*, *38*). The effective Hamiltonian in the second-order perturbation is (see supplementary materials)

$$H_H = \hbar g_0 \sum_{j=1}^{3}\left(a_j^\dagger \sigma_- + h.c.\right) + \hbar\kappa\sigma_z C \quad (6)$$

where $\kappa = -3g_d^2/\nu_d$. The second term in Eq. 6 introduces the complex next-nearest-neighbor hoppings in the FSL (*14*, *20*) and transforms flat Landau levels to a two-band structure with gapless chiral edge states, which originate from

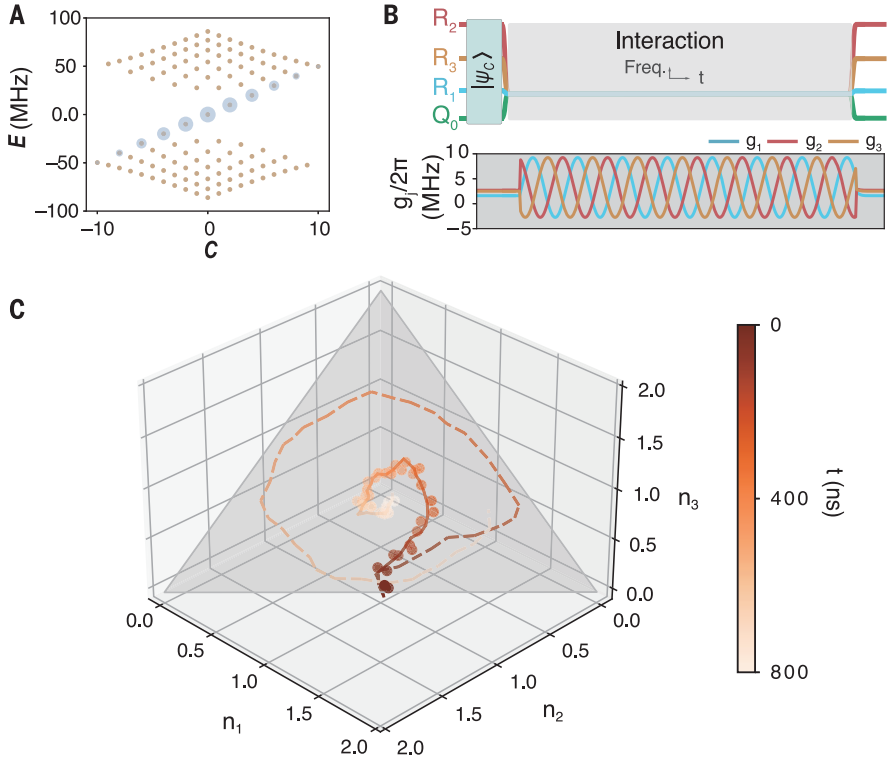


Fig. 5. Chiral edge currents of the Fock-state Haldane model. (**A**) The energy bands of the Hamiltonian H_H in Eq. 6 with total excitation number N = 10. The two energy bands are connected by chiral edge states, with each dot indicating an eigenstate. The populations of a binomial state (with $\lambda_1 = \lambda_2$) on the chiral edge states are proportional to the radii of the shaded circles. (**B**) The control sequence in realizing the Haldane Hamiltonian. We prepare an initial state $|\downarrow;\alpha,-\alpha,0\rangle$ with $\alpha \approx 1$ and tune three resonators and the gmon qubit on resonance at $\omega_{\text{int}}/2\pi \approx 4.82$ GHz, followed by a Floquet modulation of the coupling strengths $g_j(t)$ with static amplitude $g_0/2\pi \approx 2.5$ MHz, dynamic amplitude $g_d/2\pi \approx 3.25$ MHz, and modulation frequency $\nu_d/2\pi = 40$ MHz, such that the effective Haldane coupling strength $\kappa/2\pi = -0.79$ MHz. (**C**) Chiral edge currents shown by the average photon numbers in the three resonators. The total average photon number in the initial state is 2. The gray triangle shows the boundary of the FSL with N = 2, which is the most occupied subspace at the initial time. The circles show the experimental data, and the depths of the colors indicate the evolution time. Dashed lines are numerical simulations in the ideal case, whereas solid lines are those considering relevant parameter imperfections as described in the supplementary materials.

the zeroth Landau level (Fig. 5A). In the experiment, we directly excite R_1 and R_2 to obtain an initial state $|\downarrow;\alpha,-\alpha,0\rangle$ (see Fig. 5A for its distribution in the subspace $N = 10$). Then we periodically modulate the coupling strengths $g_j(t)$ to realize the Haldane Hamiltonian (see the control sequence in Fig. 5B). The average photon numbers are subsequently measured as a function of time (*17*), which shows the chiral motion; i.e., the wave function rotates in a counterclockwise manner in the FSL (Fig. 5C). Ideally the wave function shall be on the incircle, i.e., the Lifshitz topological edge. In the experiment, the chiral rotating wave function moves toward the center of the FSL owing to the decoherence and nonlinearity of the resonators, as well as the imperfect controlling pulses (figs. S8 to S11).

Concluding remarks

In this work, we have demonstrated the coherent control of topological zero-energy states in 1D and 2D FSLs. These states only occupy the sublattice where the qubit is in the $|\downarrow\rangle$ state, and they are protected from other eigenstates by an energy gap of the vacuum Rabi frequency. Perturbations with energy smaller than this gap, such as slow modulation of coupling strengths and small detunings between the resonators, are used to coherently control the zero-energy state to realize topological transport and VHE. Floquet modulations are introduced to realize the Haldane chiral edge currents. The techniques that we have developed in this study can also be applied to control other eigenstates in the FSL, such as the excited states in higher Landau levels. Our methods can be generalized to investigate topological states of more complex qubit-resonator coupled systems, where the number of resonators determines the dimension of the FSLs and each state of the qubits labels a sublattice, with richness beyond known topological phases in condensed-matter physics. Our study paves the way for investigating topological phases in FSLs and developing new control methods for quantum state engineering of bosonic modes.

REFERENCES AND NOTES

1. K. v. Klitzing, G. Dorda, M. Pepper, *Phys. Rev. Lett.* **45**, 494–497 (1980).
2. D. J. Thouless, M. Kohmoto, M. P. Nightingale, M. den Nijs, *Phys. Rev. Lett.* **49**, 405–408 (1982).
3. F. D. M. Haldane, *Phys. Rev. Lett.* **61**, 2015–2018 (1988).
4. C. L. Kane, E. J. Mele, *Phys. Rev. Lett.* **95**, 226801 (2005).
5. F. D. M. Haldane, S. Raghu, *Phys. Rev. Lett.* **100**, 013904 (2008).
6. L. Lu, J. D. Joannopoulos, M. Soljačić, *Nat. Photonics* **8**, 821–829 (2014).
7. A. B. Khanikaev, G. Shvets, *Nat. Photonics* **11**, 763–773 (2017).
8. T. Ozawa *et al.*, *Rev. Mod. Phys.* **91**, 015006 (2019).
9. Z. Wang, Y. Chong, J. D. Joannopoulos, M. Soljacić, *Nature* **461**, 772–775 (2009).
10. M. A. Bandres *et al.*, *Science* **359**, eaar4005 (2018).
11. L. Yuan, Q. Lin, M. Xiao, S. Fan, *Optica* **5**, 1396 (2018).
12. T. Ozawa, H. M. Price, *Nat. Rev. Phys.* **1**, 349–357 (2019).
13. E. Lustig, M. Segev, *Adv. Opt. Photonics* **13**, 426 (2021).
14. H. Cai, D.-W. Wang, *Natl. Sci. Rev.* **8**, nwaa196 (2020).
15. D. Cheng *et al.*, *Phys. Rev. Res.* **3**, 033069 (2021).
16. J. Mumford, Meissner effect in Fock space. arXiv:2208.01539 [quant-ph] (2022).
17. P. Saugmann, J. Larson, A Fock state lattice approach to quantum optics. arXiv:2203.13813 [quant-ph] (2022).
18. I. Carusotto *et al.*, *Nat. Phys.* **16**, 268–279 (2020).
19. J. Yuan *et al.*, *Phys. Rev. B* **104**, 035410 (2021).
20. D.-W. Wang, H. Cai, R.-B. Liu, M. O. Scully, *Phys. Rev. Lett.* **116**, 220502 (2016).
21. Y. Y. Gao *et al.*, *Nature* **566**, 509–512 (2019).
22. L. Hu *et al.*, *Nat. Phys.* **15**, 503–508 (2019).
23. W.-L. Ma *et al.*, *Sci. Bull.* **66**, 1789–1805 (2021).
24. J. Mumford, *Phys. Rev. A* **106**, 033317 (2022).
25. H. M. Price, T. Ozawa, N. Goldman, *Phys. Rev. A* **95**, 023607 (2017).
26. E. Jaynes, F. Cummings, *Proc. IEEE* **51**, 89–109 (1963).
27. W. P. Su, J. R. Schrieffer, A. J. Heeger, *Phys. Rev. Lett.* **42**, 1698–1701 (1979).
28. F. Guinea, M. I. Katsnelson, A. K. Geim, *Nat. Phys.* **6**, 30–33 (2010).
29. E. J. Meier, F. A. An, B. Gadway, *Nat. Commun.* **7**, 13986 (2016).
30. M. Kiczynski *et al.*, *Nature* **606**, 694–699 (2022).
31. O. Gröning *et al.*, *Nature* **560**, 209–213 (2018).
32. S. de Léséleuc *et al.*, *Science* **365**, 775–780 (2019).
33. G. Jotzu *et al.*, *Nature* **515**, 237–240 (2014).
34. P. Roushan *et al.*, *Nature* **515**, 241–244 (2014).
35. J. W. McIver *et al.*, *Nat. Phys.* **16**, 38–41 (2020).
36. W. Zhao *et al.*, Realization of the Haldane Chern insulator in a moiré lattice. arXiv:2207.02312 [cond-mat.mes-hall] (2022).
37. D. Xiao, W. Yao, Q. Niu, *Phys. Rev. Lett.* **99**, 236809 (2007).
38. M. C. Rechtsman *et al.*, *Nature* **496**, 196–200 (2013).
39. F. Arute *et al.*, *Nature* **574**, 505–510 (2019).
40. Y. Wu *et al.*, *Phys. Rev. Lett.* **127**, 180501 (2021).
41. D.-W. Wang *et al.*, *Nat. Phys.* **15**, 382–386 (2019).
42. W. Liu, W. Feng, W. Ren, D.-W. Wang, H. Wang, *Appl. Phys. Lett.* **116**, 114001 (2020).
43. P. Roushan *et al.*, *Nat. Phys.* **13**, 146–151 (2017).
44. H.-C. Fu, R. Sasaki, *J. Math. Phys.* **38**, 3968–3987 (1997).
45. J. Yuan, C. Xu, H. Cai, D.-W. Wang, *APL Photonics* **6**, 030803 (2021).
46. M. C. Rechtsman *et al.*, *Nat. Photonics* **7**, 153–158 (2013).
47. O. Jamadi *et al.*, *Light Sci. Appl.* **9**, 144 (2020).
48. M. Bellec, C. Poli, U. Kuhl, F. Mortessagne, H. Schomerus, *Light Sci. Appl.* **9**, 146 (2020).
49. P. Roushan *et al.*, *Science* **358**, 1175–1179 (2017).
50. A. H. Castro Neto, F. Guinea, N. M. R. Peres, K. S. Novoselov, A. K. Geim, *Rev. Mod. Phys.* **81**, 109–162 (2009).
51. M. O. Goerbig, *Rev. Mod. Phys.* **83**, 1193–1243 (2011).
52. G. Salerno, T. Ozawa, H. M. Price, I. Carusotto, *Phys. Rev. B* **95**, 245418 (2017).
53. F. Gao *et al.*, *Nat. Phys.* **14**, 140–144 (2018).
54. J. Deng, Observing the quantum topology of light [Data set], Zenodo (2022). https://doi.org/10.5281/zenodo.7267558.

ACKNOWLEDGMENTS

We thank K. Wang, W. Ren, J. Chen, and X. Zhang for technical support during the experiment. D.-W.W. is indebted to R. B. Liu

and C. Wu for inspiration, insightful discussion, and encouragement. The device was fabricated at the Micro-Nano Fabrication Center of Zhejiang University. **Funding:** We acknowledge the support of the National Key Research and Development Program of China (grant no. 2019YFA0308100), National Natural Science Foundation of China (grant nos. 11934011, 12174342, 92065204, U20A2076, and 11725419), the Zhejiang Province Key Research and Development Program (grant no. 2020C01019), the Fundamental Research Funds for the Zhejiang Provincial Universities (grant no. 2021XZZX003), and Innovation Program for Quantum Science and Technology (grant no. 2021ZD0303200). **Author contributions:** D.-W.W., C.S., and H. W. designed the experiment; J.D. and H.D. designed the device and carried out the experiments supervised by C.S. and H.W.; H.L. fabricated the device supervised by H.W.; J.D., C.Z., Y.W., and J.Y. performed the numerical simulations supervised by C.S. and D.-W.W.; J.D., C.S., and D.-W.W. wrote the manuscript with comments and inputs from other authors. All authors contributed to the analysis of data and the discussions of the results. **Competing interests:** All authors declare no competing interests. **Data and materials availability:** The data presented in the figures and that support the other findings of this study are available at Zenodo (*54*). **License information:** Copyright © 2022 the authors, some rights reserved; exclusive licensee American Association for the Advancement of Science. No claim to original US government works. https://www.science.org/about/science-licenses-journal-article-reuse

SUPPLEMENTARY MATERIALS

science.org/doi/10.1126/science.ade6219
Supplementary Text
Figs. S1 to S11
Table S1
References (*55*–*61*)

Submitted 28 August 2022; accepted 4 November 2022
10.1126/science.ade6219

PLANT SCIENCE

Phosphoenolpyruvate reallocation links nitrogen fixation rates to root nodule energy state

Xiaolong Ke[1,2,3], Han Xiao[1,2,3], Yaqi Peng[1,2,3], Jing Wang[1], Qi Lv[1,2], Xuelu Wang[1,2,3]*

Legume-rhizobium symbiosis in root nodules fixes nitrogen to satisfy the plant's nitrogen demands. The nodules' demand for energy is thought to determine nitrogen fixation rates. How this energy state is sensed to modulate nitrogen fixation is unknown. Here, we identified two soybean (*Glycine max*) cystathionine β-synthase domain–containing proteins, nodule AMP sensor 1 (GmNAS1) and NAS1-associated protein 1 (GmNAP1). In the high–nodule energy state, GmNAS1 and GmNAP1 form homodimers that interact with the nuclear factor-Y C (NF-YC) subunit (GmNFYC10a) on mitochondria and reduce its nuclear accumulation. Less nuclear GmNFYC10a leads to lower expression of glycolytic genes involved in pyruvate production, which modulates phosphoenolpyruvate allocation to favor nitrogen fixation. Insight into these pathways may help in the design of leguminous crops that have improved carbon use, nitrogen fixation, and growth.

Legumes have evolved specialized nitrogen-fixing organs called root nodules by establishing symbiotic relationships with rhizobia, which require a large amount of extra energy for nitrogen fixation. The symbiotic nodules obtain photoassimilates (mainly sucrose) and metabolize them through glycolysis to produce phosphoenolpyruvate (*1*–*3*). Phosphoenolpyruvate is converted into either malate to fuel atmospheric nitrogen fixation in bacteroids or pyruvate for adenosine triphosphate (ATP) production in mitochondria for nitrogen assimilation and other cellular activities (fig. S1), and its allocation likely regulates nodule nitrogen fixation capacity (*4*–*10*). Soybean (*Glycine max*) nodule nitrogen fixation capacity is low under anaerobic or phosphorus-deficient conditions but increases when the supply of oxygen or phosphorus increases as the nodule energy state changes (*11*, *12*). As the nodule energy state decreases after transfer to darkness or high nitrate supply, leguminous nodule nitrogen fixation capacity also decreases (*13*–*16*). Given the high energy needs of symbiotic nitrogen fixation, it is likely that nodule energy-state changes regulate nodule nitrogen fixation capacity. How nodule energy state is sensed and how the information regulates nodule nitrogen fixation capacity has been unclear.

Cystathionine β-synthase (CBS) domains are conserved protein modules that can bind adenosyl compounds, such as adenosine monophosphate (AMP), adenosine diphosphate (ADP), ATP, and *S*-adenosyl methionine, to regulate biological processes by associating with other functional regions of CBS domain–containing proteins (CDCPs) (*17*–*21*). AMP-activated protein kinases, with α, β, and γ subunits, sense cellular energy status and respond to low-energy stress in mammalian cells (*22*, *23*). The greater AMP concentration associated with low–cellular energy states can enhance AMP binding to the CBS domains of the γ subunit of AMP-activated protein kinases to allosterically activate its catalytic α subunit, thereby initiating downstream signaling to maintain cellular energy homeostasis (*18*, *19*). CBSX proteins contain a pair of CBS domains, bind to AMP, and activate thioredoxins in different organelles to maintain cellular redox homeostasis in *Arabidopsis* (*Arabidopsis thaliana*) (*24*), suggesting a role for CDCPs in plant cellular energy sensing.

GmNAS1 and GmNAP1 sense nodule energy state to regulate nodule nitrogen fixation capacity

To identify CDCPs that might sense nodule energy state in soybean, we examined the expression patterns of 71 soybean *CDCP* genes using Soybean eFP Browser (*25*, *26*). We found that the CDCP gene *GmCBS22* was highly expressed in nodules, flowers, and leaves, whereas its close homolog *GmCBS14* was specifically expressed only in root nodules (fig. S2A). *GmCBS22* and *GmCBS14* are highly expressed in mature nodules, with *GmCBS22* showing a broad expression and *GmCBS14* expressed specifically in the nodule infection zone and vascular bundles (fig. S2, B to N). Knockdown of *GmCBS22* and *GmCBS14* in hairy roots decreased nodule nitrogenase activity by about 50%, whereas nodule number and weight were unaffected (fig. S3, A and B), indicating that *GmCBS22* and *GmCBS14* may regulate nodule nitrogen fixation.

GmCBS22 and *GmCBS14* are predicted to encode proteins with an N-terminal chloroplast transit peptide (cTP), four tandem CBS domains, a Phox and Bem1 (PB1) domain, and a C-terminal transmembrane region (TMR) (Fig. 1A and fig. S4, A and B). We expressed cTP-GFP-GmCBS22 [GmCBS22 fused to green fluorescent protein (GFP) after the cTP] or GmCBS14-GFP-TMR (GmCBS14 fused to GFP before the TMR) in *Nicotiana benthamiana* leaf epidermal cells and soybean nodules and observed localization to mitochondria (Fig. 1B and fig. S4C), which was further confirmed by subcellular fractionation (fig. S4D). When the C-terminal TMR was conformationally obscured by cyan fluorescent protein (CFP) in GmCBS22-CFP and GmCBS14-CFP fusion proteins, CFP fluorescence accumulated in the nucleus and the cytoplasm (fig. S4E), indicating that the C-terminal TMR is required for mitochondrial localization of GmCBS22 and GmCBS14. We noticed occasional ring fluorescence patterns for cTP-GFP-GmCBS22 and GmCBS14-GFP-TMR in *N. benthamiana* leaf epidermal cells, suggesting their localization to the mitochondrial outer membrane (fig. S4F) (*27*).

We then tested the ability of GmCBS22 and GmCBS14 proteins to bind various adenylates and found that one GmCBS22 molecule can bind one AMP with a dissociation constant (K_d) of 3.94 μM and ADP with a K_d of 40.32 μM (Fig. 1, C and D), whereas ATP and cyclic AMP (cAMP) did not bind to GmCBS22 (fig. S5A). By contrast, GmCBS14 did not bind to any of the tested adenylates (fig. S5B). Deletion of any

[1]State Key Laboratory of Crop Stress Adaptation and Improvement, School of Life Sciences, Henan University, Zhengzhou 450046, China. [2]The Academy for Advanced Interdisplinary Studies, Henan University, Zhengzhou 450046, Henan, China. [3]Sanya Institute of Henan University, Sanya 572025, Hainan, China.
*Corresponding author. Email: xueluw@henu.edu.cn

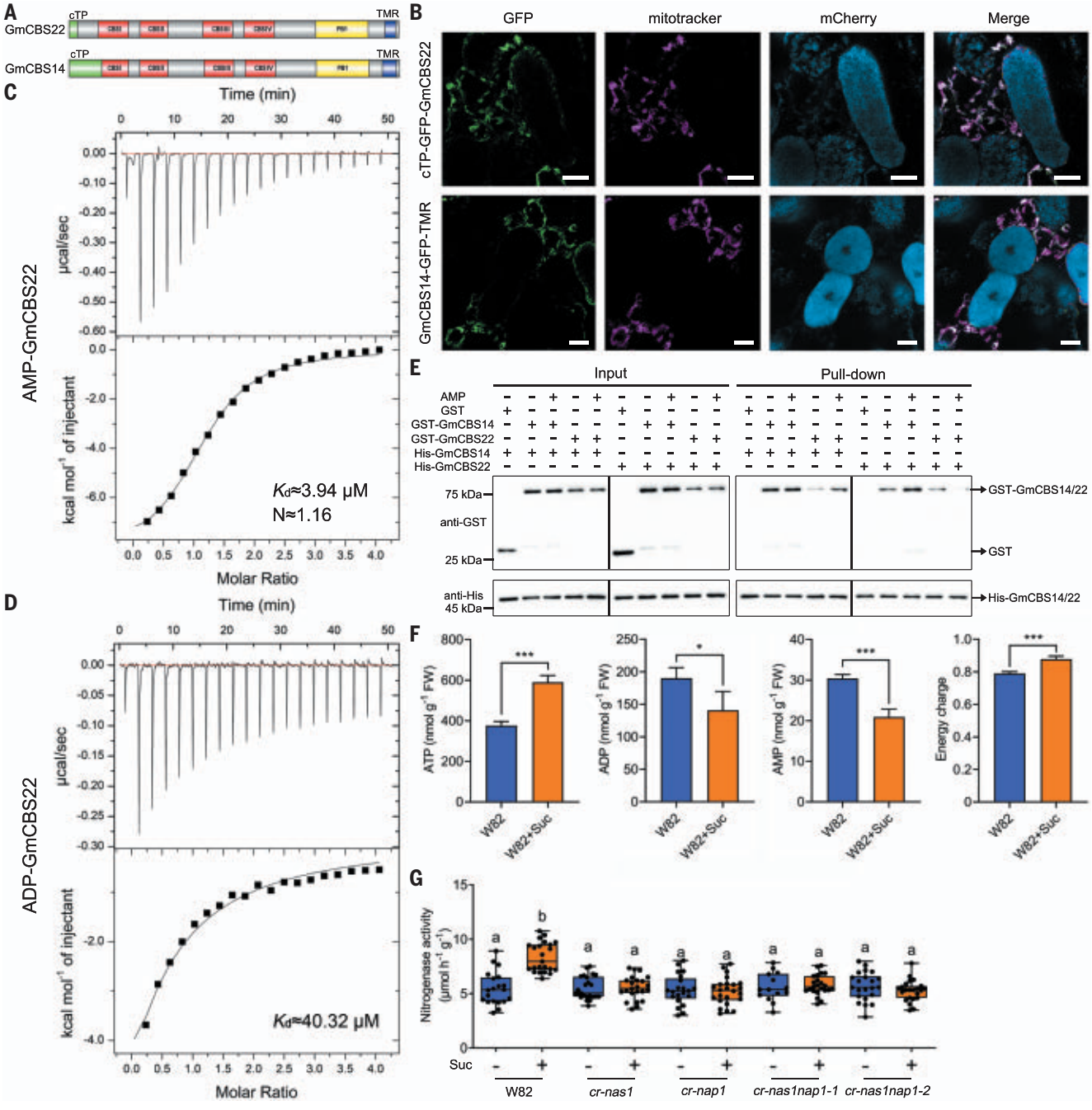


Fig. 1. GmNAS1 and GmNAP1 are nodule energy sensors that regulate the response of nodule nitrogen fixation capacity to nodule energy state. (**A**) Schematic diagram of the GmCBS22 and GmCBS14 proteins. (**B**) GmCBS22 and GmCBS14 localization in nodule cells. Nodules of *pGmCBS22:cTP-GFP-GmCBS22* and *pGmCBS14:GmCBS14-GFP-TMR* transgenic hairy roots were sectioned to observe GFP fluorescence. Mitotracker was used to stain mitochondria; mCherry indicates infected cells containing the strain USDA110-mCherry. Scale bars are 20 µm. (**C** and **D**) Isothermal titration calorimetry analysis of GmCBS22 binding to AMP (C) or ADP (D). The black lines (bottom) are the best fit to the one-site model. (**E**) Pull-down assays of His-GmCBS22, His-GmCBS14, GST-GmCBS22, and GST-GmCBS14. The experiment was performed three times with comparable results. (**F**) Changes in ATP, ADP, and AMP contents and energy charge of W82 nodules after sucrose treatment. Data are means ± SD of four biological replicates. FW, fresh weight. (**G**) Nodule nitrogenase activity of W82 and *GmNAS1* and *GmNAP1* mutants without and with sucrose treatment. Boxes represent the first quartile, median, and third quartile, and whiskers represent minimum and maximum values. Significant differences were determined by Student's *t* test (*$P < 0.05$, and ***$P < 0.001$) in (F) or by one-way analysis of variance (ANOVA) and post hoc Tukey's test, with different lowercase letters indicating significant differences ($P < 0.05$) in (G).

of the four CBS domains in GmCBS22 abolished its AMP binding ability (fig. S6, A to D). The secondary structures of GmCBS22 and GmCBS14 were unaffected by the addition of AMP, ADP, ATP, or cAMP (fig. S7, A and B). Like many other CDCPs (*21*), GmCBS22 and GmCBS14 formed homodimers and heterodimers (Fig. 1E and fig. S8). Recombinant His-GmCBS22 lacking any CBS domain still interacted with GmCBS22 and GmCBS14 tagged with glutathione *S*-transferase (GST) (fig. S9A), whereas deletion of the PB1 domain of GmCBS22

eliminated the homodimerization of GmCBS22 and heterodimerization of GmCBS22 and GmCBS14, and deletion of the PB1 domain of GmCBS14 also eliminated the homodimerization of GmCBS14 and heterodimerization of GmCBS22 and GmCBS14 (fig. S9B). Moreover, the addition of AMP enhanced formation of GmCBS22-GmCBS14 heterodimers but blocked formation of GmCBS22 homodimers (Fig. 1E and fig. S8B). Therefore, GmCBS22 and GmCBS14 may function as energy sensors in soybean nodules by directly binding to AMP and forming dynamic dimers on the mitochondrial membrane. We therefore renamed GmCBS22 as soybean nodule AMP sensor 1 (GmNAS1) and GmCBS14 as NAS1-associated protein 1 (GmNAP1).

Under our growth conditions, sucrose treatment, which significantly increased nodule energy state (Fig. 1F), can enhance nodule nitrogenase activity in soybean "Williams 82" (W82) plants (Fig. 1G). To investigate whether GmNAS1 and GmNAP1 can sense nodule energy state to regulate nodule nitrogen fixation capacity, we created knockout mutants of *GmNAS1* and *GmNAP1*, namely, *cr-nas1*, *cr-nap1*, *cr-nas1nap1-1*, and *cr-nas1nap1-2* (fig. S10, A and B). Under our growth conditions, these mutants showed similar nodule number, weight, and nitrogenase activity relative to the wild type (Fig. 1G and fig. S10C). However, although the nodule energy state of these mutants was similar to that of the wild type (fig. S11, A to D), sucrose treatment failed to enhance nodule nitrogen fixation capacity in all the mutants (Fig. 1G), indicating that *GmNAS1* and *GmNAP1* mediate the linkage between nitrogen fixation capacity and nodule energy state (fig. S11, E to I). Changes in light intensity affected photosynthesis, nodule energy state, and nitrogen fixation capacity (fig. S12, A to F). Knockout of *GmNAS1* and *GmNAP1* also eliminated the increase in nodule nitrogen fixation capacity that follows enhanced light intensity (fig. S12F). Together, these results show that GmNAS1 and GmNAP1 are needed for nodule nitrogen fixation capacity to respond to changes in nodule energy state.

GmNAS1 and GmNAP1 regulate GmNFYC10a nuclear localization

To elucidate how GmNAS1 and GmNAP1 regulate nodule nitrogen fixation capacity in response to nodule energy state, we conducted co-immunoprecipitation (co-IP) assays followed by tandem mass spectrometry (MS/MS). We identified additional GmNAP1 interactors, including a nuclear factor-Y C (NF-YC) subunit, GmNFYC10a (fig. S13, A and B, and data S1). Considering the role of NF-YC subunits in symbiotic nitrogen fixation (*28*, *29*), we tested and confirmed the interaction of GmNAS1 and GmNAP1 with GmNFYC10a (Fig. 2, A and B). The addition of AMP largely blocked the interaction between GmNAS1 and GmNFYC10a but not that between GmNAP1 and GmNFYC10a (Fig. 2B). GmNAS1 lacking any CBS domain still interacted with GmNFYC10a, and the addition of AMP hardly affected their interaction (fig. S14A). Given that AMP impaired GmNAS1 homodimerization (Fig. 1E), we hypothesized that GmNAS1 or GmNAP1 homodimerization is required for their interaction with GmNFYC10a. Indeed, GmNAS1 and GmNAP1 lacking the PB1 domain failed to interact with GmNFYC10a (fig. S14B). Moreover, AMP-promoted GmNAS1-GmNAP1 heterodimerization (Fig. 1E and fig. S8B) also facilitated the dissociation of GmNAP1 homodimers and inhibited its interaction with GmNFYC10a (Fig. 2C). Interaction of GmNAS1 and GmNAP1 with GmNFYC10a was inhibited by AMP (Fig. 2D) but enhanced by sucrose in vivo (fig. S15).

Unlike the fluorescence that was mainly observed on mitochondria during bimolecular fluorescence complementation (BiFC) assays of GmNFYC10a and GmNAS1 and GmNAP1 (Fig. 2A), GmNFYC10a-GFP only localized to the nucleus (Fig. 2E), suggesting that GmNFYC10a is proximal to mitochondria through its interaction with GmNAS1 and GmNAP1. Because higher AMP levels can weaken the interaction of GmNAS1 and GmNAP1 with GmNFYC10a (Fig. 2, B to D), we hypothesized that a low–nodule energy state may enhance GmNFYC10a translocation from mitochondria to nuclei. Indeed, oligomycin, an inhibitor of mitochondrial ATP synthase, or AMP treatment significantly promoted the nuclear accumulation of GmNFYC10a-GFP in nodule cells (Fig. 2F). More GmNFYC10a-GFP localized to the cytoplasm in the *cr-nas1* and *cr-nap1* nodules than in W82 nodules under mock conditions (Fig. 2F and fig. S16, A and B), confirming that GmNAS1 and GmNAP1 maintain GmNFYC10a localization to mitochondria. Oligomycin or AMP treatment promoted GmNFYC10a-GFP nuclear localization in *cr-nap1* but not in *cr-nas1* mutants (fig. S16, A and B), suggesting that GmNAS1 but not GmNAP1 can primarily respond to increased AMP to enhance GmNFYC10a nuclear accumulation. GmNFYC10a-GFP accumulated in the cytoplasm and nucleus in most nodule cells of the *cr-nas1nap1-2* mutant, regardless of whether they were treated with oligomycin or AMP (fig. S16C). Taken together, these results demonstrate that GmNAS1 and GmNAP1 regulate the GmNFYC10a nuclear accumulation in response to changing nodule energy state.

GmNFYC10 regulates glycolysis for pyruvate production

We then created the knockout mutant *cr-nfyc10* through genome editing (fig. S17A) as well as *gGmNFYC10a-Flag* overexpression plants and found that neither showed changes in nodule number, weight, or nitrogenase activity relative to the wild type under normal growth conditions (Fig. 3, A and B, and fig. S17, B to D). However, unlike the wild type, the *cr-nfyc10* and *gGmNFYC10a-Flag* plants did not show the sucrose-enhanced nodule nitrogen fixation capacity (Fig. 3, A and B), indicating that the proper expression level of *GmNFYC10* is required for efficient nitrogen fixation under the high–nodule energy state.

To explore how the GmNAS1-GmNAP1-GmNFYC10 module regulates nodule nitrogen fixation capacity, we conducted RNA sequencing (RNA-seq) analysis of *Ri-GmNAS1-NAP1* (*Ri-GmCBS22-14*) nodules (Fig. 3, C and D). Kyoto Encyclopedia of Genes and Genomes (KEGG) analysis (*30*) of the down-regulated genes showed a variety of biological processes regulated by *GmNAS1* and *GmNAP1* (Fig. 3E). Considering the pivotal role of glycolysis in nodule energy supply (fig. S1) (*1*–*3*), we analyzed 26 down-regulated genes involved in the glycolysis-gluconeogenesis pathway (data S2). Ten glycolytic genes among these genes contain five encoding pyruvate kinases (PKs) (Fig. 3F and fig. S18, A and B). Expression of enolase genes in glycolysis was not down-regulated in *Ri-GmNAS1-NAP1* nodules (fig. S18C). Promoter analysis of 10 down-regulated glycolytic genes revealed a CCAAT element, the binding site of the NF-Y transcriptional complex (fig. S19A) (*31*). Furthermore, we determined that GmNFYC10a binds to the *PK1a*, *GAPC1*, and *PK2a* promoters and activates their expression (Fig. 3, G and H). Expression of most glycolytic genes was down-regulated in *cr-nfyc10* nodules (fig. S19B). Expression of several glycolytic genes was reduced in the *Ri-GmNFYC10* nodules (fig. S19, C and D), whereas expression of most glycolytic genes was higher in the *gGmNFYC10a-Flag* nodules (fig. S19, E and F). Given that half of the regulated glycolytic genes encode PKs (Fig. 3F), we examined pyruvate contents in *Ri-GmNFYC10* and *gGmNFYC10a-Flag* nodules. Compared with wild type nodules, pyruvate contents were about 40% lower in the *Ri-GmNFYC10* nodules and 50% higher in the *gGmNFYC10a-Flag* nodules (fig. S19G). Knockdown of *PK1*, *GAPC1*, or *PK2* decreased nodule nitrogenase activity without affecting nodule number or weight (fig. S20, A and B). Together, these findings indicate that GmNFYC10, regulated by GmNAS1 and GmNAP1, can activate glycolysis for pyruvate production in soybean nodules.

The GmNAS1-GmNAP1-GmNFYC10 module regulates PEP allocation in nodules

Because a reduced nodule energy state can promote GmNFYC10a nuclear accumulation (Fig. 2F), we determined that sucrose treatment leads to diminished nuclear accumulation and enhanced mitochondrial localization of GmNFYC10a (Fig. 4A). Expression levels of the glycolytic genes activated by GmNFYC10

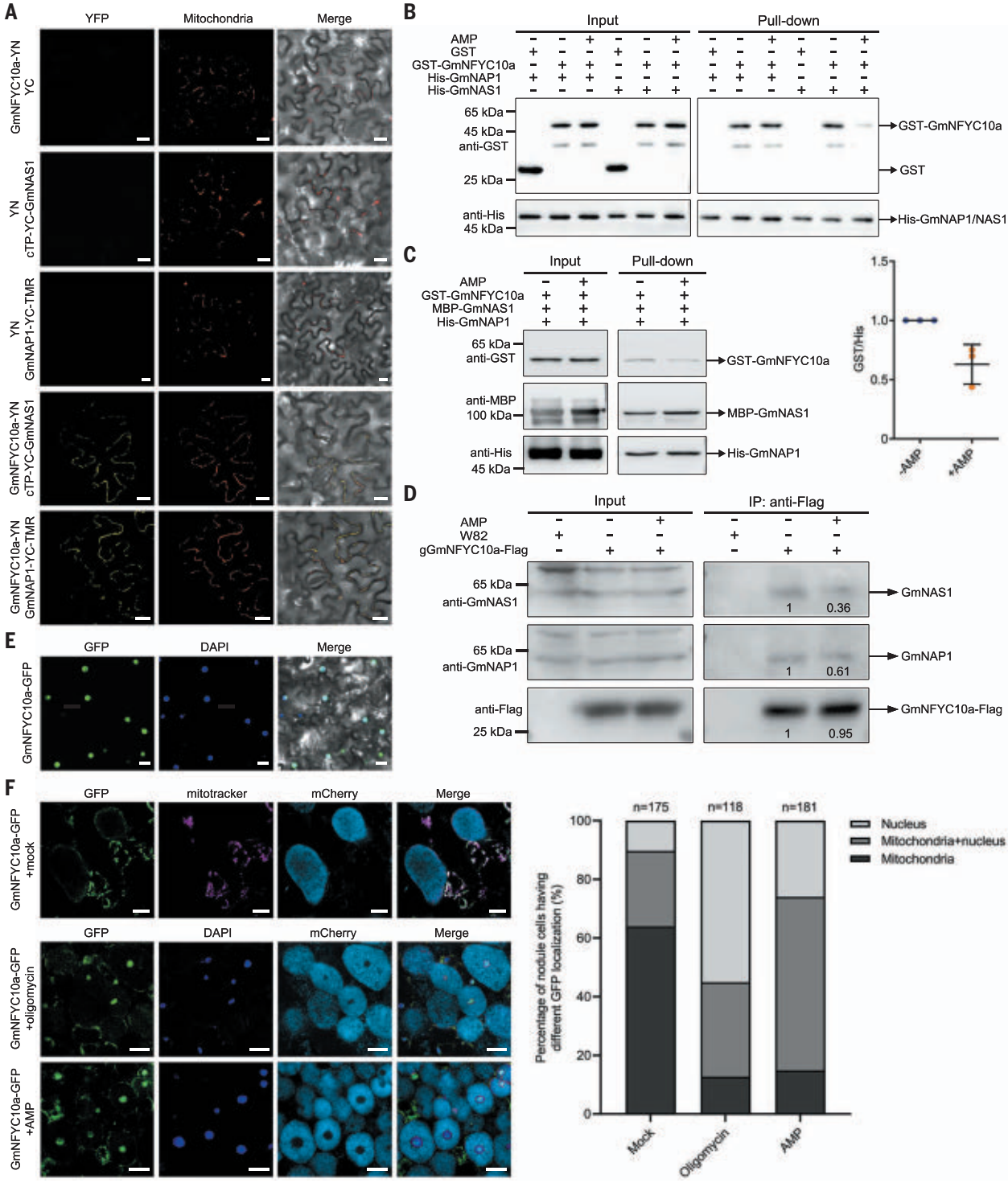


Fig. 2. GmNAS1 and GmNAP1 mediate GmNFYC10a nuclear accumulation in response to nodule energy state. (**A**) BiFC assays of GmNAS1 and GmNAP1 and GmNFYC10a. The mt-rk plasmid was co-infiltrated into *N. benthamiana* leaves to label mitochondria with mCherry fluorescence. YFP, yellow fluorescent protein. (**B**) Pull-down assays of GmNAS1 and GmNAP1 and GmNFYC10a. (**C**) Pull-down assay of GmNAP1 and GmNFYC10a in the presence of GmNAS1. The grayscale ratio of GST-GmNFYC10a to His-GmNAP1 (GST/His) with AMP was normalized to that without AMP; the result of three biological replicates is shown in the scatterplot to the right. (**D**) Co-IP assays of GmNAS1 and GmNAP1 and GmNFYC10a. The numbers under the lanes indicate relative band intensity quantified by ImageJ. (**E**) GmNFYC10a-GFP localization in *N. benthamiana* leaf epidermal cells. (**F**) GmNFYC10a-GFP localization in nodule cells. Nodules of *gGmNFYC10a-GFP* hairy roots were sectioned to observe GFP fluorescence. Mitotracker and 4′,6-diamidino-2-phenylindole (DAPI) were used to label mitochondria and nuclei, respectively; mCherry fluorescence indicates infected cells containing USDA110-mCherry. Nodule slices were treated with oligomycin or AMP to induce energy stress. In (B) to (D), AMP was added to a 0.5 mM final concentration, and the experiments were performed three times with comparable results. In (A), (E), and (F), scale bars are 20 μm.

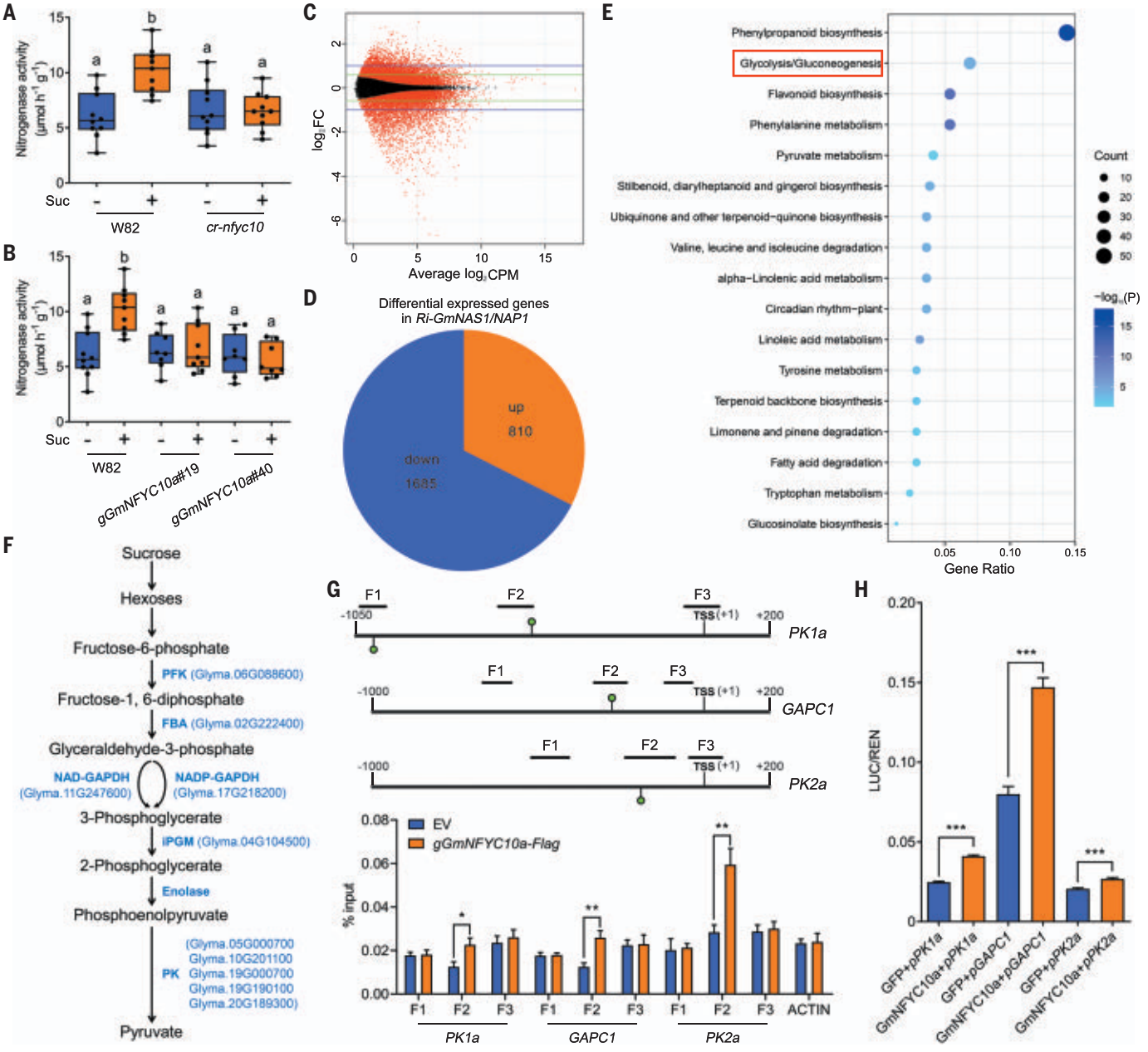


Fig. 3. GmNFYC10 regulates the response of nodule nitrogen fixation capacity to nodule energy state and the expression of glycolytic genes. (**A**) Nodule nitrogenase activity of W82 and *cr-nfyc10* without and with sucrose treatment. (**B**) Nodule nitrogenase activity of W82 and *gGmNFYC10a-Flag* transgenic lines without and with sucrose treatment. (**C**) Volcano plot of differentially expressed genes in empty vector (EV) and *Ri-GmNAS1-NAP1* hairy root nodules. CPM, counts per million; FC, fold change. (**D**) Differentially expressed genes (≥2-fold) in *Ri-GmNAS1-NAP1* nodules. (**E**) KEGG analysis of down-regulated genes (≥2-fold) in *Ri-GmNAS1-NAP1* nodules. The red frame indicates the glycolysis-gluconeogenesis pathway. (**F**) Schematic diagram of the glycolytic pathway. Ten down-regulated glycolytic genes in *Ri-GmNAS1-NAP1* nodules are indicated. FBA, fructose bisphosphate aldolase; GAPDH, glyceraldehyde phosphate dehydrogenase; iPGM, independent phosphoglycerate mutase; NAD, nicotinamide adenine dinucleotide; NADP, nicotinamide adenine dinucleotide phosphate; PFK, phosphofructokinase. (**G**) ChIP-qPCR (chromatin immunoprecipitation–quantitative polymerase chain reaction) analysis of GmNFYC10a binding to the *PK1a*, *GAPC1*, and *PK2a* promoters. NF-Y binding sites and DNA fragments for qPCR analysis are indicated by green circles and short horizontal lines, respectively. Data are means ± SD of three biological replicates. TSS, transcription start site. (**H**) Transcriptional activation of the *PK1a*, *GAPC1*, and *PK2a* promoters by GmNFYC10a. Firefly luciferase (LUC) activity was normalized to *Renilla* luciferase (REN) activity. Data are means ± SD of three biological replicates. Significant differences were determined by one-way ANOVA with post hoc Tukey's test ($P < 0.05$) in (A) and (B) or by Student's *t* test (*$P < 0.05$, **$P < 0.01$, and ***$P < 0.001$) in (G) and (H). In (A) and (B), boxes represent the first quartile, median, and third quartile, and whiskers represent minimum and maximum values.

were also down-regulated after sucrose treatment (Fig. 4B), which did not happen in the *cr-nas1*, *cr-nap1*, *cr-nas1nap1-1*, and *cr-nfyc10* mutants (fig. S21, A to D). In agreement with this result, we observed that the expression levels of these genes are higher in the *cr-nas1*, *cr-nap1*, and *cr-nas1nap1-1* nodules than in wild-type nodules after sucrose treatment (Fig. 4C). Although several glycolytic genes were also down-regulated in sucrose-treated leaves of wild type, the down-regulation was unaffected in sucrose-treated leaves of *cr-nas1*,

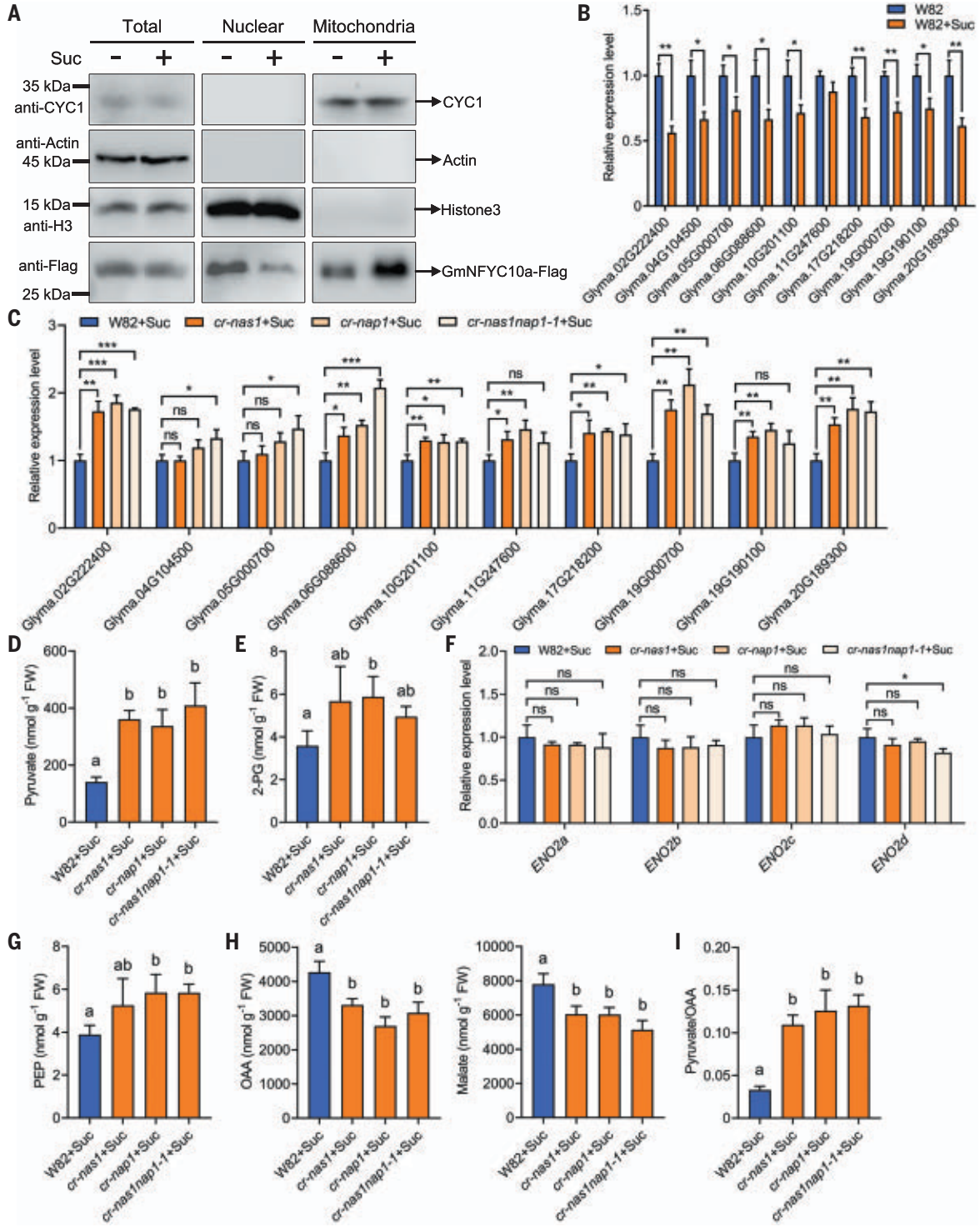


Fig. 4. GmNAS1, GmNAP1 and GmNFYC10 regulate glycolysis to modulate PEP allocation in response to nodule energy state. (**A**) GmNFYC10a-Flag protein abundance in the nucleus and mitochondria of nodule cells. CYC1, actin, and histone H3 were used as mitochondrial, cytoplasmic, and nuclear markers, respectively. The experiment was performed three times with comparable results. (**B**) Relative expression levels of glycolytic genes in W82 nodules without and with sucrose treatment. (**C**) Relative expression levels of glycolytic genes in W82, *cr-nas1*, *cr-nap1*, and *cr-nas1nap1-1* nodules after sucrose treatment. (**D** and **E**) Pyruvate (D) and 2-PG (E) contents in W82, *cr-nas1*, *cr-nap1*, and *cr-nas1nap1-1* nodules after sucrose treatment. (**F**) Relative expression levels of enolase genes *ENO2a*, *ENO2b*, *ENO2c*, and *ENO2d* in W82, *cr-nas1*, *cr-nap1*, and *cr-nas1nap1-1* nodules after sucrose treatment. (**G** to **I**) PEP (G), OAA (H), and malate (H) contents and ratio of pyruvate to OAA (I) in W82, *cr-nas1*, *cr-nap1*, and *cr-nas1nap1-1* nodules after sucrose treatment. Data in (D), (E), and (G) to (I) are means ± SD of at least four biological replicates. Significant differences were determined by Student's *t* test (*$P < 0.05$, **$P < 0.01$, and ***$P < 0.001$) in (B), (C), and (F) or by one-way ANOVA with post hoc Tukey's test ($P < 0.05$) in (D), (E), and (G) to (I); ns is not significant.

cr-nap1, and *cr-nas1nap1-1* (fig. S21E). Sucrose treatment also reduced PK2a protein content and PK activity in W82 nodules, but the decrease was eliminated in the *cr-nas1*, *cr-nap1*, and *cr-nas1nap1-1* nodules (fig. S21, F and G). Therefore, the pyruvate contents in the *cr-nas1*, *cr-nap1*, and *cr-nas1nap1-1* nodules were higher than that in wild-type nodules after sucrose treatment (Fig. 4D). Furthermore, we found that the 2-phosphoglycerate (2-PG) and phosphoenolpyruvate (PEP) contents were far lower than the pyruvate and oxaloacetic acid (OAA) contents in nodules (Fig. 4, D, E, G, and H), and expression of *ENO2a*, *ENO2b*, *ENO2c*, and *ENO2d* in the *GmNAS1* and *GmNAP1* mutants was similar to that in the wild type (Fig. 4F), suggesting that most of the 2-PG and PEP was converted into PEP, and pyruvate and OAA in nodules, respectively, and the total amount of PEP converted into pyruvate and OAA in W82 nodules should be similar to that in the *cr-nas1*, *cr-nap1* and *cr-nas1nap1-1* nodules. OAA and malate contents in these mutant nodules were lower (Fig. 4H), and the ratio of pyruvate to OAA in mutant nodules was increased (Fig. 4I). Moreover, under our growth conditions, the pyruvate, OAA, and malate contents in the *cr-nas1*, *cr-nap1*, and *cr-nas1nap1-1* nodules were similar to those in W82 nodules (fig. S21, H to J), which is in line with the unaffected nodule nitrogen fixation capacity of these mutants under the same growth conditions (Fig. 1H). Therefore, in response to an increased nodule energy state, GmNAS1 and GmNAP1 reduce GmNFYC10 nuclear accumulation, which suppresses glycolysis and pyruvate production, thereby modulating PEP allocation to favor nodule nitrogen fixation.

Discussion

Leguminous plants regulate high-energy-consuming symbiotic nitrogen fixation to optimize carbon utilization for sustaining growth under different environments (*32*). In this study, we identified GmNAS1 and GmNAP1 as nodule-specific energy sensors in soybean. Under our growth conditions, a limited sucrose supply keeps nodule cells in a relatively low-energy state with high AMP levels, which promotes the formation of GmNAS1-GmNAP1 heterodimers and leads to the nuclear accumulation of GmNFYC10, driving glycolysis and pyruvate production (fig. S22, A and B). Upon additional sucrose supply, when nodule energy state rises as AMP levels fall, GmNAS1 and GmNAP1 mainly form homodimers that maintain GmNFYC10 on mitochondria to reduce its nuclear accumulation, leading to lower pyruvate production and more PEP allocated to OAA (fig. S22, C and D). Thus, the ratio of PEP converted into pyruvate and OAA is largely dependent on nodule energy state in the wild type (36/64 at the low–nodule energy state versus 3/97 at the high–nodule energy state) to ensure basic cellular activities at the low–nodule energy state and to power nitrogen fixation at the high–nodule energy state (fig. S22, A and C). In the *cr-nas1nap1* mutant, enhanced allocation of PEP into OAA at the high-energy state was attenuated (pyruvate/OAA = 36/64 at the low–nodule energy state versus 12/88 at the high–nodule energy state) (fig. S22, B and D). Therefore, GmNAS1 and GmNAP1 are activated by the high-energy state under adequate carbohydrate supply to hold GmNFYC10a on the mitochondria, thereby enhancing PEP allocation to OAA and malate for nitrogen fixation, which is different from the canonical energy sensors AMPK, SNF1, and SnRK1 that are activated by the low-energy state in response to lack of nutrients (*22*, *33*, *34*). Although *GmNAS1* and *GmNAP1* knockouts did not affect nodule nitrogen fixation capacity under normal growth conditions (Fig. 1G), *GmNAS1* and *GmNAP1* knockdowns in hairy roots impaired nodule nitrogen fixation capacity (fig. S3). The nodule energy state of hairy roots is lower than that of normal plants (fig. S23A), which could be caused by the retarded plant growth of hairy roots (fig. S23B). The up-regulated genes in hairy root nodules showed that many stress-related pathways are activated (fig. S23, C to E), suggesting that *GmNAS1* and *GmNAP1* may also play a role in maintaining nodule nitrogen fixation capacity under stressful conditions. Phylogenetic analysis showed that GmNAS1 and GmNAP1 and their homologs within the ureide-exporting legumes form an independent cluster (fig. S24A and data S3) and that their homologs in *Phaseolus vulgaris*, but not in *Lotus japonicus* and *Medicago truncatula*, can complement the mutant nodule phenotypes of *cr-nas1* and *cr-nap1* (fig. S24B). Therefore, this set of energy sensors likely emerges in the ureide-exporting legumes to ensure elaborate energy use during nitrogen fixation, which may be necessary because of enhanced de novo purine biosynthesis and one-carbon metabolism in nodules of these legumes (*6*, *9*). Our findings show how legume nodule energy state modulates nodule performance through GmNAS1 and GmNAP1 and reveal targets for designing crops efficient in both carbon utilization, symbiotic nitrogen fixation, and growth under varying environmental conditions.

REFERENCES AND NOTES

1. J. G. Streeter, *Adv. Bot. Res.* **18**, 129–187 (1991).
2. C. Vance, in *Nitrogen-Fixing Leguminous Symbioses* (Springer, 2008), pp. 293–320.
3. M. Udvardi, P. S. Poole, *Annu. Rev. Plant Biol.* **64**, 781–805 (2013).
4. J. B. Peterson, H. J. Evans, *Plant Physiol.* **61**, 909–914 (1978).
5. J. B. Peterson, H. J. Evans, *Biochim. Biophys. Acta* **567**, 445–452 (1979).
6. K. R. Schubert, *Annu. Rev. Plant Physiol.* **37**, 539–574 (1986).
7. A. Millar, D. Day, F. Bergersen, *Plant Cell Environ.* **18**, 715–726 (1995).
8. C. A. Atkins, P. Smith, P. J. Storer, *Plant Physiol.* **113**, 127–135 (1997).
9. P. M. Smith, C. A. Atkins, *Plant Physiol.* **128**, 793–802 (2002).
10. S. Tajima, M. Nomura, H. Kouchi, *Front. Biosci.* **9**, 1374–1381 (2004).
11. T. M. Ching, *Life Sci.* **18**, 1071–1076 (1976).
12. T. M. Sa, D. W. Israel, *Plant Physiol.* **97**, 928–935 (1991).
13. T. M. Ching, S. Hedtke, S. A. Russell, H. J. Evans, *Plant Physiol.* **55**, 796–798 (1975).
14. Y. Kanayama, Y. Yamamoto, *Plant Cell Physiol.* **31**, 893–895 (1990).
15. A. J. Gordon, L. Skøt, C. L. James, F. R. Minchin, *J. Exp. Bot.* **53**, 423–428 (2002).
16. I. Lambert *et al.*, *J. Exp. Bot.* **71**, 5039–5052 (2020).
17. M. Janošík, V. Kery, M. Gaustadnes, K. N. Maclean, J. P. Kraus, *Biochemistry* **40**, 10625–10633 (2001).
18. B. Xiao *et al.*, *Nature* **449**, 496–500 (2007).
19. R. Townley, L. Shapiro, *Science* **315**, 1726–1729 (2007).
20. C. Hackenberg *et al.*, *Proc. Natl. Acad. Sci. U.S.A.* **115**, 7141–7146 (2018).
21. A. A. Baykov, H. K. Tuominen, R. Lahti, *ACS Chem. Biol.* **6**, 1156–1163 (2011).
22. D. G. Hardie, F. A. Ross, S. A. Hawley, *Nat. Rev. Mol. Cell Biol.* **13**, 251–262 (2012).
23. A. González, M. N. Hall, S. C. Lin, D. G. Hardie, *Cell Metab.* **31**, 472–492 (2020).
24. K. S. Yoo *et al.*, *Plant Cell* **23**, 3577–3594 (2011).
25. Q. Hao *et al.*, *Int. J. Mol. Sci.* **17**, 620 (2016).
26. M. Libault *et al.*, *Plant J.* **63**, 86–99 (2010).
27. O. Duncan *et al.*, *Plant Physiol.* **157**, 1093–1113 (2011).
28. M. E. Zanetti, F. A. Blanco, M. P. Beker, M. Battaglia, O. M. Aguilar, *Plant Cell* **22**, 4142–4157 (2010).
29. Q. Zhuang *et al.*, *Plant J.* **108**, 1422–1438 (2021).
30. M. Kanehisa, M. Furumichi, Y. Sato, M. Kawashima, M. Ishiguro-Watanabe, *Nucleic Acids Res.* 10.1093/nar/gkac963 (2022).
31. V. Nardone, A. Chaves-Sanjuan, M. Nardini, *Biochim. Biophys. Acta. Gene Regul. Mech.* **1860**, 571–580 (2017).
32. S. Sulieman, L.-S. P. Tran, *Legume Nitrogen Fixation in a Changing Environment: Achievements and Challenges* (Springer, 2015).
33. P. Crozet *et al.*, *Front. Plant Sci.* **5**, 190 (2014).
34. T. Broeckx, S. Hulsmans, F. Rolland, *J. Exp. Bot.* **67**, 6215–6252 (2016).

ACKNOWLEDGMENTS

We thank J. Zhang, C. Lan, and X. Li (Henan University) for assisting in the determination of pyruvate, OAA, malate, 2-PG, PEP, ATP, ADP, and AMP contents. **Funding:** This research was supported by grants from the National Key Research and Development Program (grant no. 2022YFA0912100 to X.W. and X.K.; grant no. 2018YFE0112100 to X.W.), the National Natural Science Foundation of China (grant no. 31870257 to X.W.), the Zhongyuan Scholar of Henan Province (grant no. 224000510001 to X.W.), the Outstanding Talents Fund of Henan University of China (grant no. CX3050A092004 to X.W.), and the Program for Innovative Research Team in University of Henan Province (grant no. 23IRTSTHN020 to X.W. and X.K.). **Author contributions:** X.K. and X.W. designed the experiments; X.K. performed most of the experiments; H.X. contributed to the vector construction, material collection, and nodulation assays; J.W., X.K., and X.W. analyzed RNA-seq data; Y.P. and Q.L. generated the stable transgenic soybean plants; and X.K. and X.W. wrote the manuscript. **Competing interests:** The authors declare no competing interests. **Data and materials availability:** RNA-seq data can be accessed through the National Center for Biotechnology Information (NCBI) (BioProject ID: PRJNA807470). All other data are available in the main text or supplementary materials. For material requests, please contact the corresponding author. **License information:** Copyright © 2022 the authors, some rights reserved; exclusive licensee American Association for the Advancement of Science. No claim to original US government works. https://www.science.org/about/science-licenses-journal-article-reuse

SUPPLEMENTARY MATERIALS

science.org/doi/10.1126/science.abq8591
Materials and Methods
Figs. S1 to S24
Table S1
References (*35*–*43*)
MDAR Reproducibility Checklist
Data S1 to S3

Submitted 5 May 2022; resubmitted 10 October 2022
Accepted 8 November 2022
10.1126/science.abq8591

METALLURGY

Exceptional fracture toughness of CrCoNi-based medium- and high-entropy alloys at 20 kelvin

Dong Liu[1]†, Qin Yu[2]†, Saurabh Kabra[3], Ming Jiang[1], Paul Forna-Kreutzer[1], Ruopeng Zhang[4,5], Madelyn Payne[4,5], Flynn Walsh[2,4], Bernd Gludovatz[6], Mark Asta[2,4], Andrew M. Minor[4,5], Easo P. George[7,8,9], Robert O. Ritchie[2,4]*

CrCoNi-based medium- and high-entropy alloys display outstanding damage tolerance, especially at cryogenic temperatures. In this study, we examined the fracture toughness values of the equiatomic CrCoNi and CrMnFeCoNi alloys at 20 kelvin (K). We found exceptionally high crack-initiation fracture toughnesses of 262 and 459 megapascal-meters$^{1/2}$ (MPa·m$^{1/2}$) for CrMnFeCoNi and CrCoNi, respectively; CrCoNi displayed a crack-growth toughness exceeding 540 MPa·m$^{1/2}$ after 2.25 millimeters of stable cracking. Crack-tip deformation structures at 20 K are quite distinct from those at higher temperatures. They involve nucleation and restricted growth of stacking faults, fine nanotwins, and transformed epsilon martensite, with coherent interfaces that can promote both arrest and transmission of dislocations to generate strength and ductility. We believe that these alloys develop fracture resistance through a progressive synergy of deformation mechanisms, dislocation glide, stacking-fault formation, nanotwinning, and phase transformation, which act in concert to prolong strain hardening that simultaneously elevates strength and ductility, leading to exceptional toughness.

High-entropy alloys (HEAs) have attracted increasing attention in the metallurgy community as a class of metallic materials that derive their properties from the presence of multiple principal elements, rather than from a single dominant constituent as in most traditional metallic alloys (e.g., Fe in steels). Inspired by two seminal papers (*1*, *2*), the field has grown to encompass equiatomic as well as nonequiatomic alloys, single-phase solid solutions, and multiphase compositionally complex alloys, with the goal of finding combinations of properties that differ from those of conventional alloys (*3*–*7*).

One prominent group of such materials are the single-phase, face-centered cubic (fcc), equiatomic alloys based on the CrCoNi system. Among these, the equiatomic CrMnFeCoNi alloy is the most characterized of all HEAs (*1*, *6*–*11*). It came to prominence because its room-temperature strength and ductility can be substantially enhanced at liquid nitrogen temperature (*8*, *9*) without compromising toughness (*10*). Moreover, its crack-initiation fracture toughness, K_{JIc}, remained at roughly 220 MPa·m$^{1/2}$ over the temperature range 293 to 77 K, with a crack-growth toughness, K_{ss}, of >300 MPa·m$^{1/2}$ (after 2.25 mm of crack extension) (*10*). More recent experiments on this HEA showed a similar increase in strength and toughness (the latter measured in terms of the absorbed deviatoric strain energy) when the strain rate was increased from 10^{-3} s^{-1} (quasistatic compression) up to extremely high rates of 6×10^5 s^{-1} (dynamic shear) (*11*).

There have been several derivatives of the CrMnFeCoNi alloy (*12*–*14*), most notably the single-phase equiatomic CrCoNi medium-entropy alloy (MEA), which displays even better properties. At 77 K, this MEA was found to have a K_{JIc} of 273 MPa·m$^{1/2}$ and a K_{ss} exceeding 400 MPa·m$^{1/2}$ (*15*). Although strength and toughness are often mutually exclusive properties (*16*), the CrCoNi alloy exhibits exceptionally high damage tolerance, with fracture toughness values among the largest ever reported. Such CrCoNi-based multiple principal element alloys are clearly strong candidate materials for potential applications in extreme environments, such as at very high strain rates and cryogenic temperatures.

Results

Given their exceptional damage tolerance, we investigated the mechanical properties of CrCoNi and CrMnFeCoNi alloys at even lower temperatures (~20 K) by performing uniaxial tensile tests and nonlinear elastic *J*-based fracture toughness tests (*17*) in a liquid helium environment (using the testing setup shown in figs. S1 to S3). Impact tests on the CrCoNi alloy have reported high Charpy V-notch energies of close to 400 J at 77 K, which were

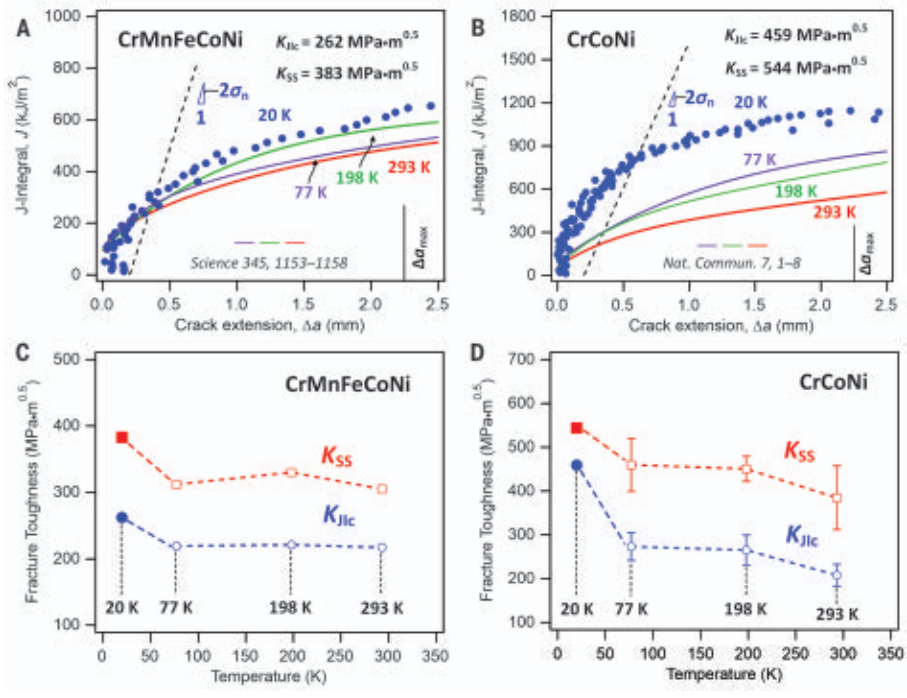


Fig. 1. *J-R* curves and fracture toughness values for the CrCoNi and CrMnFeCoNi alloys as a function of temperature. *J-R* curves showing the variation in the *J*-integral as a function of crack extension Δa for (**A**) the CrMnFeCoNi HEA and (**B**) the CrCoNi MEA, between room temperature (RT, ~293 K) and 20 K. Corresponding *K*-based fracture toughness values back-calculated from the *R*-curves are shown in (**C**) for CrMnFeCoNi and (**D**) for CrCoNi, where K_{JIc} represents the crack-initiation toughness and K_{ss} the crack-growth toughness, defined at the ASTM E1820 maximum limit of valid crack extension where Δa = 2.25 mm. Note how the toughness of both alloys at 20 K is higher than at other temperatures. The toughness values for the CrCoNi alloy are believed to be among the highest toughnesses ever reported.

[1]School of Physics, University of Bristol, Bristol BS8 1TL, UK. [2]Materials Sciences Division, Lawrence Berkeley National Laboratory, Berkeley, CA 94720, USA. [3]ENGIN-X, ISIS Facility, Rutherford Appleton Laboratory, Harwell Campus, Oxon OX11 0QX, UK. [4]Department of Materials Science and Engineering, University of California, Berkeley, CA 94720, USA. [5]National Center for Electron Microscopy, Molecular Foundry, Lawrence Berkeley National Laboratory, Berkeley, CA 94720, USA. [6]School of Mechanical and Manufacturing Engineering, University of New South Wales (UNSW Sydney), Sydney, NSW 2052, Australia. [7]Materials Science and Technology Division, Oak Ridge National Laboratory, Oak Ridge, TN 37831, USA. [8]Materials Science and Engineering Department, University of Tennessee, Knoxville, TN 37996, USA. [9]Institute for Materials, Ruhr University Bochum, 44801 Bochum, Germany.
*Corresponding author. Email: roritchie@lbl.gov
†These authors contributed equally to this work.

reduced by ~10% at 4.2 K (*18*). However, it remains unclear how samples that contain a sharp crack would perform at temperatures below 77 K, where anomalies in the temperature dependence of strength and ductility have been reported (*19*–*22*). Furthermore, full resistance-curve measurements that define both the crack-initiation and crack-growth fracture toughness have not been performed on medium- or high-entropy alloys at low temperatures approaching that of liquid helium. In addition to measurements of the crack-initiation and crack-growth toughnesses (and their corresponding stress intensity–based values), we performed in situ neutron diffraction measurements and extensive postfracture electron backscatter diffraction (EBSD) analysis, fractography, and particularly transmission electron microscopy to examine in detail the salient plastic deformation mechanisms and defect behavior that represent the fundamental basis of their exceptional fracture resistance, which we find progressively increases with decreasing temperature, unlike for most metallic materials.

As described in more detail in the supplementary materials, the CrCoNi and CrMnFeCoNi alloys that we investigated were arc melted, drop cast, and homogenized at 1200°C before being cold worked at room temperature and recrystallized at 800°C to give a single-phase equiaxed grain structure with an average grain size of ~21 μm in CrMnFeCoNi and ~8 μm in CrCoNi. Their uniaxial tensile stress-strain curves and crack-resistance curves (*R*-curves), experimentally measured at 20 K, are shown in fig. S4 and Fig. 1, A and B, respectively. For comparison, Fig. 1, A and B, also shows *R*-curves taken at ambient (293 K), dry ice (198 K), and liquid nitrogen (77 K) temperatures. We back-calculated the corresponding stress intensity–based fracture toughness values from the *J*-values as a function of temperature (20 to 293 K) and plotted K_{JIc} (Fig. 1, C and D), which we determined according to ASTM Standard E1820 (*17*), and K_{ss}, defined at the maximum limit of valid crack extension (*17*), where $\Delta a = 2.25$ mm (near the plateau of the *R*-curve).

Both alloys show markedly rising *R*-curves that progressively increase with decreasing temperature, especially CrCoNi. Exceedingly high fracture toughness values are exhibited at 20 K; the K_{JIc} and K_{ss} values for the CrMnFeCoNi alloy are, respectively, 262 and 383 MPa·m^{½}, whereas the corresponding values for CrCoNi are 459 and 544 MPa·m^{½}. The latter value represents one of the highest toughnesses on record. Fracture surfaces at 20 K showed no sign of brittle fracture features and exhibited 100% ductile failure by microvoid coalescence, in agreement with earlier work at higher temperatures of 77 to 293 K (*10*, *15*), with dimple sizes in the range of several micrometers (Fig. 2, C and D).

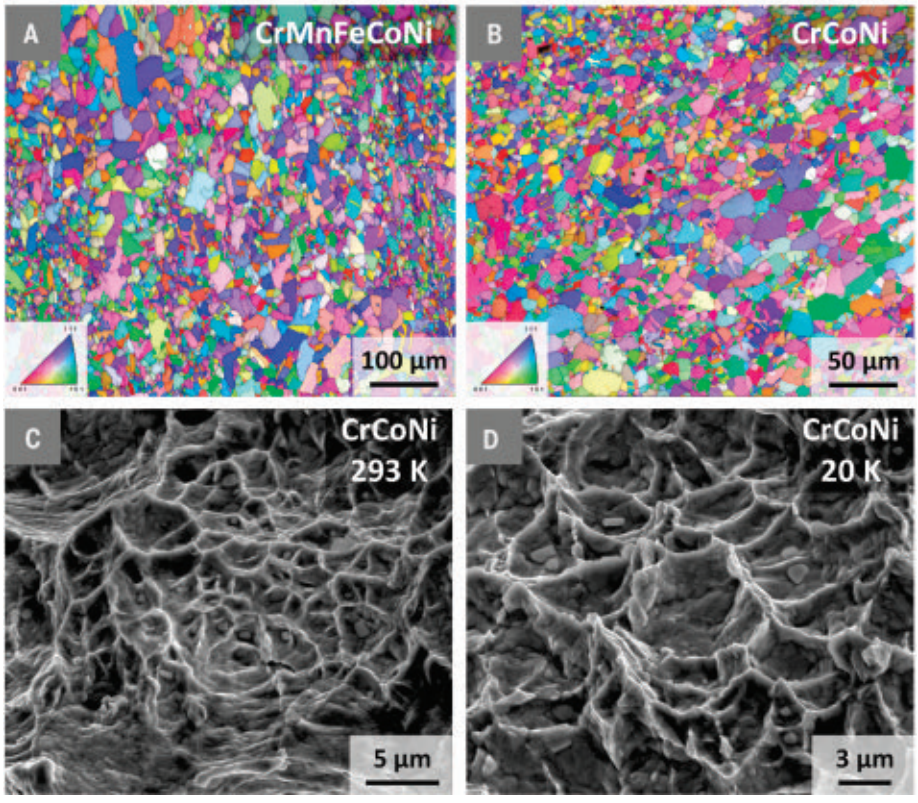


Fig. 2. Microstructure and fractography of the CrCoNi-based alloys. EBSD scans show the equiaxed single-phase microstructures in (**A**) CrMnFeCoNi and (**B**) CrCoNi alloys. The sample direction associated with the IPF coloring is the direction normal to the EBSD scan plane. Fracture in both alloys occurs by microvoid coalescence. Examples of such ductile fractures in CrCoNi are shown at (**C**) 293 K and (**D**) 20 K.

Discussion

Despite their exceptionally high fracture toughness, these alloys do not have complex microstructures, as they are simple single-phase solid solutions (Fig. 2, A and B). Thus, an important question that immediately arises is the origin of this exceptional fracture resistance and why it should be so progressively enhanced at cryogenic temperatures.

To address this, we look to the cooperative defect behavior responsible for plastic deformation in these alloys (*23*–*25*), using mainly the CrCoNi alloy to illustrate the prototypical behavior at 20 K versus room temperature. We used postfracture EBSD analysis and high-resolution transmission electron microscopy (HRTEM) of the heavily deformed regions within the plastic zone, directly adjacent to the crack tip where local strains can readily be on the order of 60 to 100%. Although the microstructure starts off as a rather simple single-phase solid solution, deformation at 20 K transforms the structure into a rich and complex mixture of phases and defect structures.

To investigate the microscopic deformation mechanisms, the compact-tension samples used in the fracture toughness tests were first cut through the midthickness to obtain sections of the fracture path that were predominantly under plane-strain conditions. These were first mechanically and then electrolytically polished for examination with EBSD. EBSD image quality (IQ) and inverse pole figure (IPF) maps (Fig. 3) for the CrCoNi alloy tested at 20 K indicate extensive deformation-induced twinning in the highly deformed grains (under high stress triaxiality) within the plastic zone in the vicinity of the crack tip. Similar deformation mechanisms have been reported for CrCoNi-based alloys at these low temperatures in uniaxial tensile tests where the degree of triaxiality is far lower (*18*–*22*, *25*). We then made sections from these regions into TEM foils using a focused ion beam (FIB) lift-out method, finishing with a 5-kV Ga^+ polish, for HRTEM and four-dimensional scanning transmission electron microscopy (4D-STEM). The CrCoNi samples that were deformed and fractured at both room temperature and at 20 K show a strong propensity for planar deformation features (Fig. 4). We conducted HRTEM imaging to identify the nature of these features. At room temperature, they include both nanotwins and bands of stacking faults, but no well-defined sequence (exceeding three layers) of any hexagonal close-packed (hcp) phases (Fig. 4, A and B). We did identify, however, a

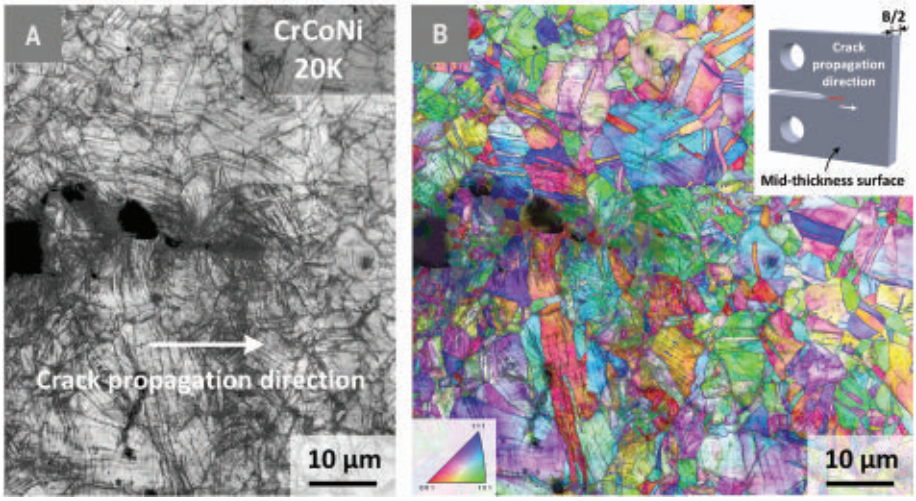


Fig. 3. EBSD maps. (**A**) Image quality (IQ) and (**B**) inverse pole figure (IPF) maps, showing the fracture path and accompanying deformation behavior of the CrCoNi alloy at 20 K. For the fracture propagating from left to right, predominantly plane-strain sections (taken at the midthickness of compact-tension samples) show the microstructure in the heavily deformed region directly ahead of the crack tip (within the plastic zone). The sample direction associated with the IPF coloring is the direction normal to the EBSD scan plane.

considerable number of dislocations in the area between the planar features (shown in detail in fig. S5). In contrast, for samples tested at 20 K, the dominant planar features are deformation bands full of stacking faults (Fig. 4D), with the frequent appearance of "laths" of the hcp phase with a thickness of a few nanometers (Fig. 4H). The latter are notably absent in specimens deformed at room temperature. Additionally, CrCoNi demonstrates a decreased tendency for nanotwinning at 20 K, as well as a smaller size of nanotwins compared with those formed at room temperature.

We conducted successive 4D-STEM experiments to identify the size and distribution of these microstructural features in both CrCoNi (Fig. 4) and CrMnFeCoNi (fig. S6). Both virtual dark-field images and selected-area diffraction patterns were reconstructed to extract the spatially resolved structural information of the planar features in the CrCoNi samples tested at 293 and 20 K. The planar features generated at room temperature are primarily well-defined nanotwins or stacking faults, with the former having sizes in the range of several nanometers (Fig. 4C). In contrast, the planar deformation features identified at 20 K contain a combination of diffuse yet finer nanotwins, stacking faults, and a well-defined hcp phase (Fig. 4, F and I). We believe that this change in deformation modes at 20 K, promoted by low stacking-fault energies, is primarily responsible for the groundbreaking fracture toughness.

Stacking-fault energies for CrMnFeCoNi (*26*) and CrCoNi (*27*) have been experimentally determined as ~30 and 14 $mJ \cdot m^{-2}$, respectively, at room temperature, which are expected to progressively decrease at lower temperatures. Indeed, measurements in $CrFeCoNiMo_{0.2}$ report the stacking-fault energy to decrease from 28 $mJ \cdot m^{-2}$ at 293 K to 11 $mJ \cdot m^{-2}$ at 15 K (*28*). However, microscopy-based measurements obtained from balancing forces on finitely dissociated dislocations in concentrated alloys have drawn criticism for neglecting local variations in the Peierls potential due to chemical fluctuations (*29*) and their associated lattice distortion (*30*), as well as grain-size dependence (*31*). Nevertheless, the trend of reduced stacking-fault energies at lower temperatures in these alloys is inarguable and consistent with theoretical predictions of the increasing energetic stability of the hcp phase relative to the fcc phase with decreasing temperature. In the CrMnFeCoNi samples tested at 20 K, 4D-STEM characterization (fig. S6) revealed the presence of nanotwins similar to those seen in CrCoNi but no evidence of hcp phase formation. This likely explains the former's lower strength (fig. S4) and fracture toughness (Fig. 1, C and D).

Although low stacking-fault energies and the associated phenomena of planar slip, stacking faults, nanotwinning, and hcp phase formation have been individually observed in simpler fcc alloys, the full sequence described above, coupled with strong solid-solution strengthening and prolonged strain hardening, generally has not. Consider, for example, dilute Cu-Al alloys (containing up to 10 atomic % Al) in which the stacking-fault energy can be significantly decreased by the addition of Al (to values even lower than those of CrCoNi and CrMnFeCoNi). Nevertheless, the Cu-Al binaries remain significantly weaker at ~10 K [one-fifth to one-tenth the critical resolved shear stress of CrMnFeCoNi (*26*)]. Similarly, one can contemplate elements that increase solid-solution strengthening (e.g., as a result of large atomic size misfits) but have little to no effect on the stacking-fault energy, and so on for each of the mechanisms discussed above. Because a given element in an alloy will at most influence one or two of the desired mechanisms, multiple alloying elements will likely be needed to simultaneously or sequentially activate all relevant mechanisms. In the long run, this ability to control individual mechanisms, precisely when needed, may well prove to be the single biggest advantage of multiple principal element alloys such as those investigated here (*32*).

The low deformation temperature limits dislocation motion and twin growth by suppressing thermally activated processes. But the increased flow stress increases the formation of twins and hcp phases at 20 K, as compared with room temperature, at which no hcp formation was detected. As twinning in these alloys has been shown to be stress-controlled (*33*, *34*), an fcc→hcp transformation (which involves a similar change in stacking sequence) would be expected to be favored as the flow stress increases with decreasing temperature. A diffuse network of the resulting planar deformation features—nanotwin and phase interfaces—acts to further decrease the mean free path for dislocation motion. Combined with suppressed dynamic recovery at these low temperatures, a synergy of deformation mechanisms—dislocation glide, stacking fault formation, deformation nanotwinning, and deformation-induced phase transformation—is created at increasing strain levels, which presents a highly efficient process for developing and, most importantly, prolonging strain hardening to restrict the localization of deformation in the crack-tip region. In simple terms, the strain hardening naturally increases strength but at the same time delays the onset of necking, which promotes ductility. Micromechanical models for the prediction of the fracture toughness of materials experiencing ductile fracture (*35*, *36*) are based on a critical strain being exceeded over a characteristic microstructural dimension ahead of a crack tip; these models give the J_{Ic} toughness to be directly proportional to the product of the flow strength, strain to failure, and this characteristic dimension (which is related to some multiple of the particle spacing involved in the microvoid coalescence fracture). Accordingly, the corresponding elevations in strength and ductility resulting from the strain hardening, created by the prolonged sequence of multiple deformation mechanisms, act in concert to enhance the toughness. The extent of strain hardening increases as temperature decreases owing to several related factors: (i) the lower

stacking-fault energy, which hinders cross-slip by increasing the spacing between Shockley partials; (ii) the promotion of nanotwinning (also related to lower stacking-fault energy); and (iii) the onset of the deformation-induced transformation to the hcp phase (but only to a limited degree, as too much hcp could embrittle the material).

The role of the fcc→hcp transformation is particularly interesting. The in situ transformation to the hexagonal phase has now been reported in numerous papers (*37*–*39*). It enables further strain hardening at higher strains, but the resulting epsilon martensite is not necessarily beneficial for toughness, as hcp phases are generally not as ductile as fcc phases, which in sufficiently large amounts would likely cause a ductile-brittle transition at 20 K. Indeed, some researchers have reported a decrease in ductility at 4.2 to 20 K, as compared with 77 K, in alloys similar to ours, which they attribute to epsilon martensite formation (*20*, *40*). Intriguingly, 0 K ab initio calculations suggest that, for a given degree of (dis)order, hcp CrCoNi has a lower Gibbs energy than the fcc equivalent; this relationship inverts at higher temperatures owing to the activation of phonon modes (*41*) and likely spin fluctuations as well (*42*). This picture is consistent with the observation of somewhat larger hcp lamellae at 20 K, but it must be asked why, in contrast to similarly metastable Co (*43*) or CoNi alloys (*44*), low-temperature deformation still only minimally induces the martensitic hcp phase, which has been reported in quantities ranging from 0 to a maximum of a few vol % (*18*, *25*, *45*). This observation is also consistent with our in situ neutron diffraction data (fig. S7), where the maximum stacking-fault probability caused by deformation was estimated to be 6.3×10^{-3}. As noted, the theoretical metastability of CrCoNi is of similar magnitude as that of elemental Co (*43*), which demonstrates a clear allotropic phase transition via a martensitic mechanism that is enhanced by mechanical deformation (*43*). Even in more stable fcc CoNi alloys, which far less readily transform spontaneously to hcp, low-temperature deformation has been found to promote sizable hcp regions (*44*). One particularly enticing explanation for the observed behavior is the presence of quenched-in chemical short-range order stabilizing the fcc matrix relative to the formation of less-ordered hcp regions (*46*). This scenario would also address the apparent restriction of existing hcp regions to thin laths within extended planar defect structures (*37*), where local order would be disrupted by the occurrence of earlier slip. Recent simulations (*47*) offer specific insight on the mechanisms by which hcp and twin nuclei freely expand in random, but not in short-range ordered, samples at room temperature. Although the material used in this study was not prepared in a manner intended to promote local ordering (*48*), recent measurements such as those of Oh *et al.* (*49*) have suggested that elusive atomic-scale chemical ordering could be present in even water-quenched samples. In this case, the physics of deformation would be similar to that discussed by Yu *et al.* (*47*), with a greater driving force for hcp formation at lower temperatures. Whatever the reason, because the hcp laths are relatively thin, they can provide a disproportionally large number of barriers to dislocation motion (and, in turn, work hardening), even when the overall volume fraction is small, as in the case of nanotwins (*33*), which contribute little to axial strain (tensile ductility) but significantly to strain hardening. For example, a single hcp lath with finite thickness introduces two new barriers within a grain, thereby splitting the grain into two or three segments (depending on lath thickness). For the sake of simplicity, if the hcp lath is assumed to be very thin and its boundaries are assumed to have the same strength as grain boundaries, the effective grain size is halved when one lath is introduced in each grain, quartered when three laths are introduced per grain, and so on.

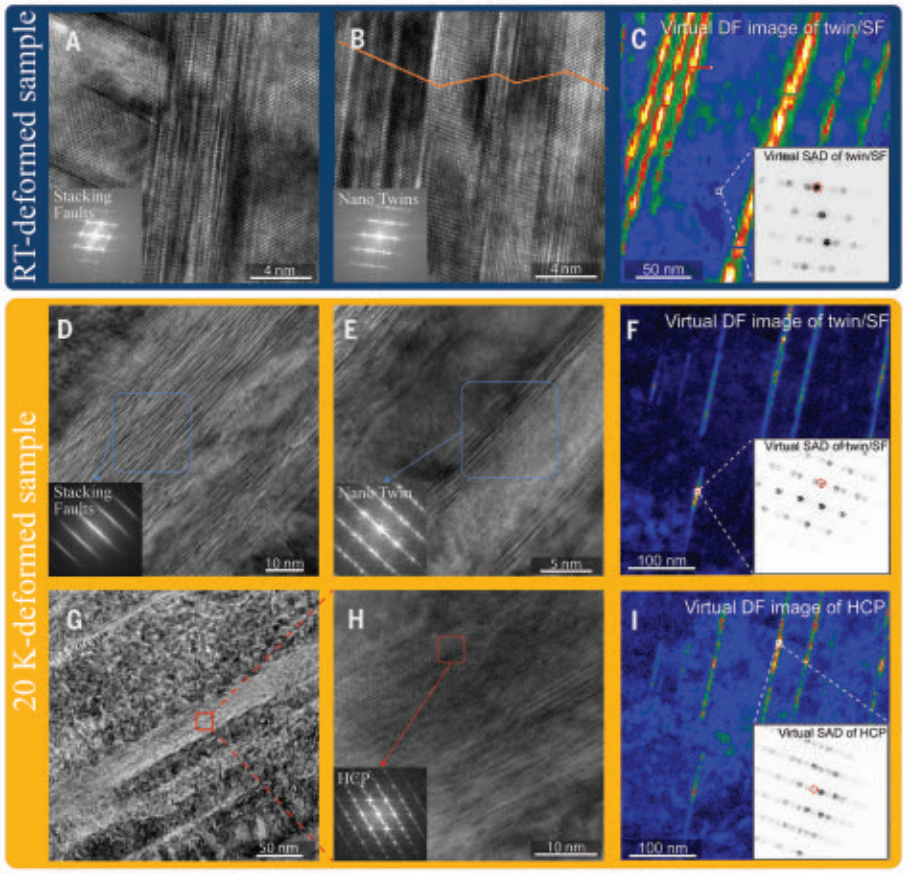


Fig. 4. HRTEM and 4D-STEM characterization of the deformed microstructures in the CrCoNi alloy adjacent to the fracture surfaces at 293 and 20 K. Overview of STEM and bright-field images of samples tested at 293 K [(A) to (C)] and at 20 K [(D) to (I)]. (**A** and **B**) HRTEM images showing representative deformation bands with stacking faults and nanotwins, respectively. (**C**) Virtual dark-field image generated from the 4D-STEM scan (stronger intensity is in warmer color). The position of the virtual aperture is marked by the red circle in the inset. The inset is a virtual selected-area diffraction pattern generated from the region marked in (C), showing the diffraction from the nanotwins. (**D**) HRTEM image showing a representative deformation band in the sample. As shown in the inset, a high density of stacking faults can be identified in the band. (**E**) A nanotwin identified in the 20 K sample. (**F**) Virtual dark-field image generated from the 4D-STEM scan. The virtual aperture is set to pick up the signal from twins and stacking faults, as marked by the red circle in the inset. (**G**) Bright-field image of deformation bands. (**H**) HRTEM image taken from a [110] orientation at 20 K. Multiple nanometer-sized bands with hcp sequence can be identified. The inset shows the fast Fourier transform image from one of the hcp bands, representing a $[11\bar{2}0]$ orientation. (**I**) Virtual dark-field image generated from the 4D-STEM scan. The virtual aperture is set to pick up the signal from the hcp phase, as marked by the red circle in the inset. The insets in (F) and (I) are virtual diffraction patterns from the twin and stacking faults and the hcp phase, respectively.

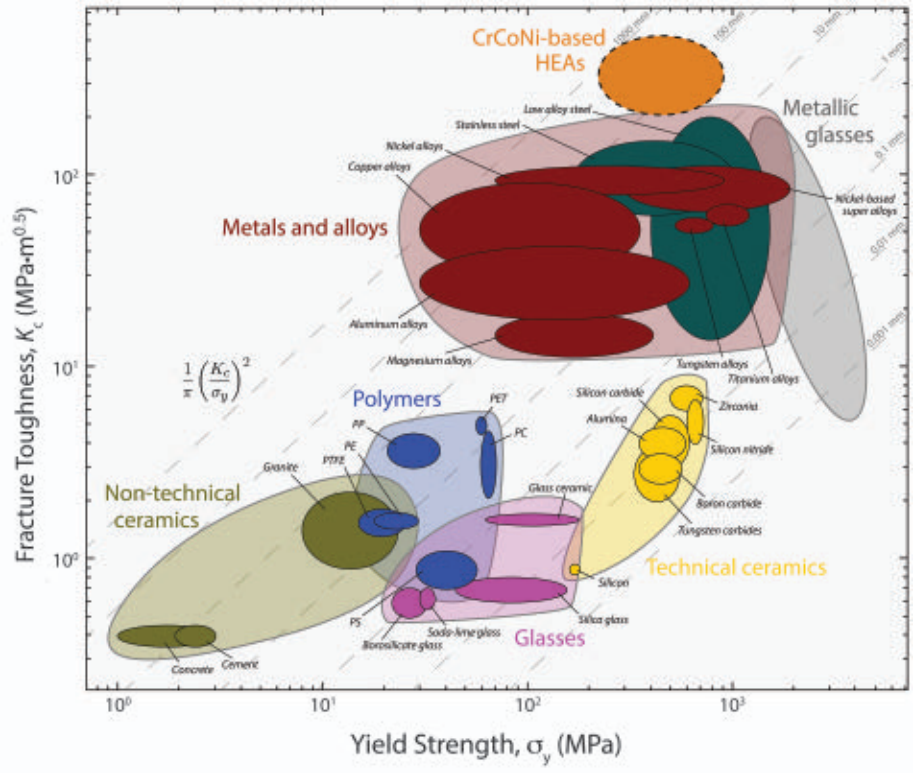


Fig. 5. Ashby map in terms of the fracture toughness, K_c, versus the yield strength, σ_y, for a broad class of materials. Note the exceptional fracture toughness of the CrCoNi-based medium- and high-entropy alloys, which appear to be the highest on record. (The toughness results contained in this figure for materials other than the CrCoNi-based alloys were measured at ambient temperatures.) PC, polycarbonate; PE, polyethylene; PET, polyethylene terephthalate; PP, polypropylene; PS, polystyrene; PTFE, polytetrafluoroethylene.

This would induce substantial strengthening by a dynamic Hall-Petch–type mechanism in the strain-hardening regime because the phase transformation occurs dynamically during straining. As is the case with nanotwins in a polycrystalline HEA (*33*), the main role of the hcp phase is to enhance strain hardening, which leads indirectly to increased ductility by postponing necking instability, rather than directly contributing to the tensile strain. Despite the hcp phase being brittle, this nevertheless serves to enhance the toughness, but with the key constraint that its volume fraction must be small.

The results we present here on the CrCoNi-based MEAs and HEAs show that a monotonic improvement in fracture toughness is possible down to very low temperatures (20 K). This is rarely the case, especially in bcc and hcp alloys that undergo a ductile-brittle transition as the temperature decreases. Even many fcc alloys show a significant drop in toughness below a critical temperature. For example, the Charpy toughness of 304L stainless steel starts dropping around 223 K and by 77 K is ~35 to 67% lower, depending on the heat treatment; 316L stainless steel shows a similar drop in toughness (*50*). Many Al alloys, whose Charpy toughness values are not high to begin with, exhibit a noticeable toughness drop below ~200 K (*51*). The same can be said about Cu-Be alloys, certain bronzes, and hardenable stainless steels. Thus, as cryogenic structural materials, equiatomic, single-phase fcc CrCoNi-based medium- and high-entropy alloys, in particular the CrCoNi alloy, appear to be unique. They possess some of the most impressive mechanical properties of any metallic alloy reported to date. Indeed, their crack-initiation and crack-growth fracture toughness values at 20 K are among the highest ever recorded (Fig. 5), a fact that we ascribe to their effective strain-hardening capacity generated by their synergy of deformation mechanisms created under increasing strains, including dislocation slip, stacking-fault formation, deformation nanotwinning, and limited hcp epsilon martensite formation.

A broader impact of this work is that the sequence of mechanisms outlined here can, in principle, be put to work in other alloy systems, from around room temperature all the way down to 20 K, depending on the temperature regime of interest for a given application. At the low end of temperatures (~20 K), potential applications include the long-distance transportation of liquid hydrogen. With increased emphasis on climate change and the need for clean energy, hydrogen might partially replace fossil fuels, especially if the former can be produced by electrolysis of water using renewable energy. Load-bearing materials that need to operate in the frigid temperatures of distant planets can also make use of the insights gained here. At somewhat higher temperatures (~110 to 115 K), transportation of liquified natural gas across oceans becomes an important potential application because pipelines cannot easily reach everywhere; the present findings can guide the design of damage-tolerant materials for such applications.

Conclusions

The main takeaway here is the realization that multiple strain-hardening mechanisms need to be activated, in exactly the right sequence, for simultaneous increases in strength, ductility, and toughness. This basic insight applies across the entire range of cryogenic temperatures, and HEAs and MEAs are uniquely qualified to make practical use of this because they possess the multiple compositional "dials" needed to tune each individual mechanism separately without adversely affecting the others (*32*)—this can be extremely difficult (if not impossible) in conventional alloys comprising just one or two principal elements.

REFERENCES AND NOTES

1. B. Cantor, I. T. H. Chang, P. Knight, A. J. B. Vincent, *Mater. Sci. Eng. A* **375–377**, 213–218 (2004).
2. J.-W. Yeh *et al.*, *Adv. Eng. Mater.* **6**, 299–303 (2004).
3. E. P. George, W. A. Curtin, C. C. Tasan, *Acta Mater.* **188**, 435–474 (2020).
4. E. J. Pickering, N. G. Jones, *Int. Mater. Rev.* **61**, 183–202 (2016).
5. D. B. Miracle, O. N. Senkov, *Acta Mater.* **122**, 448–511 (2017).
6. Z. Li, S. Zhao, R. O. Ritchie, M. A. Meyers, *Prog. Mater. Sci.* **102**, 296–345 (2019).
7. E. P. George, D. Raabe, R. O. Ritchie, *Nat. Rev. Mater.* **4**, 515–534 (2019).
8. A. Gali, E. P. George, *Intermetallics* **39**, 74–78 (2013).
9. F. Otto *et al.*, *Acta Mater.* **61**, 5743–5755 (2013).
10. B. Gludovatz *et al.*, *Science* **345**, 1153–1158 (2014).
11. S. Zhao *et al.*, *Sci. Adv.* **7**, eabb3108 (2021).
12. Z. Li, K. G. Pradeep, Y. Deng, D. Raabe, C. C. Tasan, *Nature* **534**, 227–230 (2016).
13. F. Da Costa Garcia Filho, R. O. Ritchie, M. A. Meyers, S. Neves Monteiro, *J. Mater. Res. Technol.* **17**, 1868–1895 (2022).
14. Z. Wu, H. Bei, G. M. Pharr, E. P. George, *Acta Mater.* **81**, 428–441 (2014).
15. B. Gludovatz *et al.*, *Nat. Commun.* **7**, 10602 (2016).
16. R. O. Ritchie, *Nat. Mater.* **10**, 817–822 (2011).
17. E08 Committee, ASTM E1820-17a Standard Test Method for Measurement of Fracture Toughness (ASTM International, 2017).
18. M. Yang *et al.*, *Scr. Mater.* **172**, 66–71 (2019).
19. A. S. Tirunilai *et al.*, *J. Mater. Res.* **33**, 3287–3300 (2018).
20. J. Liu *et al.*, *Sci. China Mater.* **62**, 853–863 (2019).
21. A. S. Tirunilai *et al.*, *Acta Mater.* **200**, 980–991 (2020).
22. J. Moon *et al.*, *Mater. Today* **50**, 55–68 (2021).
23. Z. Zhang *et al.*, *Nat. Commun.* **6**, 10143 (2015).
24. Z. Zhang *et al.*, *Nat. Commun.* **8**, 14390 (2017).
25. M. Naeem *et al.*, *Sci. Adv.* **6**, eaax4002 (2020).
26. M. Kawamura *et al.*, *Acta Mater.* **203**, 116454 (2021).
27. L. Li *et al.*, *Int. J. Plast.* **148**, 103144 (2022).
28. L. Tang *et al.*, *Scr. Mater.* **178**, 166–170 (2020).
29. M. Shih, J. Miao, M. Mills, M. Ghazisaeidi, *Nat. Commun.* **12**, 3590 (2021).
30. X. Sun *et al.*, *Mater. Des.* **199**, 109396 (2021).
31. K. V. Werner, F. Niessen, M. Villa, M. A. J. Somers, *Appl. Phys. Lett.* **119**, 141902 (2021).
32. E. P. George, R. O. Ritchie, *MRS Bull.* **47**, 145–150 (2022).
33. G. Laplanche, A. Kostka, O. M. Horst, G. Eggeler, E. P. George, *Acta Mater.* **118**, 152–163 (2016).

34. K. V. S. Thurston *et al*., *Intermetallics* **110**, 106469 (2019).
35. A. C. Mackenzie, J. W. Hancock, D. K. Brown, *Eng. Fract. Mech.* **9**, 167–188 (1977).
36. R. O. Ritchie, A. W. Thompson, *Metall. Mater. Trans. A* **16**, 233–248 (1985).
37. J. Miao *et al*., *Acta Mater.* **132**, 35–48 (2017).
38. B. Schuh *et al*., *Materials* **11**, 662 (2018).
39. S. Chen *et al*., *Nat. Commun.* **11**, 826 (2020).
40. Q. Lin *et al*., *Mater. Res. Lett.* **6**, 236–243 (2018).
41. C. Niu, C. R. LaRosa, J. Miao, M. J. Mills, M. Ghazisaeidi, *Nat. Commun.* **9**, 1363 (2018).
42. Z. Dong, S. Schönecker, W. Li, D. Chen, L. Vitos, *Sci. Rep.* **8**, 12211 (2018).
43. P.-A. Dubos *et al*., *Mater. Lett.* **281**, 128812 (2020).
44. L. Rémy, A.Pineau, *Mater. Sci. Eng.* **26**, 123–132 (1976).
45. H. He *et al*., *Nano Lett.* **21**, 1419–1426 (2021).
46. J. Ding, Q. Yu, M. Asta, R. O. Ritchie, *Proc. Natl. Acad. Sci. U.S.A.* **115**, 8919–8924 (2018).
47. P. Yu, J.-P. Du, S. Shinzato, F.-S. Meng, S. Ogata, *Acta Mater.* **224**, 117504 (2022).
48. R. Zhang *et al*., *Nature* **581**, 283–287 (2020).
49. H. S. Oh *et al*., *Acta Mater.* **216**, 117135 (2021).
50. T. S. Byun, T. G. Lach, "Mechanical Properties of 304L and 316L Austenitic Stainless Steels after Thermal Aging for 1500 Hours," Pacific Northwest National Laboratory Report, US Department of Energy, PNNL-25854, M3LW-16OR040215 (2016).
51. R. M. McClintock, H. P. Gibbons, *Mechanical Properties of Structural Materials: A Compilation from the Literature*, National Bureau of Standards Monograph 13 (US Department of Commerce, National Bureau of Standards, 1960).

ACKNOWLEDGMENTS

We thank M. J. Paul for support in analyzing the tensile stress-strain data. **Funding:** The research was primarily supported by the US Department of Energy, Office of Science, Basic Energy Sciences, Materials Sciences and Engineering Division, through the Damage-Tolerance in Structural Materials program (KC13) at the Lawrence Berkeley National Laboratory (LBNL) under contract DE-AC02-CH11231, and the Multiscale Mechanical Properties and Alloy Design program (ERKCM06) at the Oak Ridge National Laboratory. The authors acknowledge the use of the ENGIN-X, ISIS Facility, at the Rutherford Appleton Laboratory, Chilton, Didcot, Oxon, UK, for the mechanical testing in liquid helium environment, and the microscopy facilities in the National Center for Electron Microscopy, in the Molecular Foundry at LBNL, which is supported by the Office of Science, Office of Basic Energy Sciences of the US Department of Energy under contract DE-AC02-05CH11231. D.L., M.J., and P.F.-K. acknowledge support from the UK Engineering and Physical Sciences Research Council (EP/N004493/2, EP/T000368/1). B.G. acknowledges support from the ARC Future Fellowship (project FT190100484) and the UNSW Scientia Fellowship schemes. **Author contributions:** R.O.R., B.G., and E.P.G. formulated the original idea. E.P.G. supervised the synthesis and processing of alloys. D.L. identified the testing equipment and method, formulated the neutron beamline proposal, and conducted the in situ and ex situ fracture toughness experiments at ENGIN-X with S.K. and P.F.-K. The fracture toughness data were analyzed by Q.Y., B.G., and D.L. under the supervision of R.O.R. The neutron diffraction data were analyzed by M.J. under the supervision of D.L. S.K. performed the uniaxial tensile tests, with guidance from E.P.G. and B.G. The structural characterization was performed by Q.Y., M.J. and D.L (EBSD), and R.Z and M.P. (TEM), the latter under the supervision of A.M.M. Simulation studies were conducted by F.W. under the supervision of M.A. R.O.R. drafted the manuscript, with all authors contributing. R.O.R. supervised the project. **Competing interests:** The authors declare no competing interests, financial or otherwise. **Data and materials availability:** All data that support the findings of this study are reported in the main paper and supplementary materials. **License information:** Copyright © 2022 the authors, some rights reserved; exclusive licensee American Association for the Advancement of Science. No claim to original US government works. https://www.science.org/about/science-licenses-journal-article-reuse

SUPPLEMENTARY MATERIALS

science.org/doi/10.1126/science.abp8070
Materials and Methods
Figs. S1 to S7
References (*52*–*63*)

Submitted 27 February 2022; accepted 7 October 2022
10.1126/science.abp8070

MOLECULAR BIOLOGY

Active DNA demethylation promotes cell fate specification and the DNA damage response

Dongpeng Wang[1]†, Wei Wu[1,2]*†, Elsa Callen[1]†, Raphael Pavani[1], Nicholas Zolnerowich[1], Srikanth Kodali[3,4], Dali Zong[1], Nancy Wong[1], Santiago Noriega[1], William J. Nathan[1], Gabriel Matos-Rodrigues[1], Raj Chari[5], Michael J. Kruhlak[6], Ferenc Livak[1], Michael Ward[7], Keith Caldecott[8], Bruno Di Stefano[3,4], André Nussenzweig[1]*

Neurons harbor high levels of single-strand DNA breaks (SSBs) that are targeted to neuronal enhancers, but the source of this endogenous damage remains unclear. Using two systems of postmitotic lineage specification—induced pluripotent stem cell–derived neurons and transdifferentiated macrophages—we show that thymidine DNA glycosylase (TDG)–driven excision of methylcytosines oxidized with ten-eleven translocation enzymes (TET) is a source of SSBs. Although macrophage differentiation favors short-patch base excision repair to fill in single-nucleotide gaps, neurons also frequently use the long-patch subpathway. Disrupting this gap-filling process using anti-neoplastic cytosine analogs triggers a DNA damage response and neuronal cell death, which is dependent on TDG. Thus, TET-mediated active DNA demethylation promotes endogenous DNA damage, a process that normally safeguards cell identity but can also provoke neurotoxicity after anticancer treatments.

Defects in DNA repair result in cancer predisposition as well as neurological diseases. Although all cell types incur DNA damage and mutations, neurons are exceptionally vulnerable to defects in single-strand break (SSB) repair (*1*). SSBs are detected by XRCC1 and PARP (poly-ADP ribose polymerase), which recruit factors involved in DNA end modification (PNKP, polynucleotide kinase 3′-phosphatase; APTX, aprataxin), DNA gap filling (POLβ, DNA polymerase β family), and ligation (DNA ligase 1 or 3) (*2*). These proteins are essential for most SSB repair events, usually comprising "short-patch" reactions in which only a single missing nucleotide is replaced. More rarely, a long-patch subpathway is employed, which uses extended DNA synthesis before ligation. However, long-patch SSB repair cannot completely compensate for loss of short-patch SSB repair, as evidenced by the association of neurological diseases with mutations in genes required for short-patch repair, like XRCC1, APTX and PNKP (*2*).

[1]Laboratory of Genome Integrity, National Cancer Institute NIH, Bethesda, MD, USA. [2]State Key Laboratory of Molecular Biology, Shanghai Institute of Biochemistry and Cell Biology, Center for Excellence in Molecular Cell Science, Chinese Academy of Sciences, Shanghai, China. [3]Stem Cells and Regenerative Medicine, Center for Cell and Gene Therapy, Department of Molecular and Cellular Biology and Dan L. Duncan Comprehensive Cancer Center, Baylor College of Medicine, Houston, TX, USA. [4]Center for Cancer Epigenetics, The University of Texas MD Anderson Cancer Center, Houston, TX, USA. [5]Genome Modification Core, Frederick National Laboratory for Cancer Research, Frederick, MD, USA. [6]Laboratory of Cancer Biology and Genetics, National Cancer Institute, NIH, Bethesda, MD, USA. [7]National Institute of Neurological Disorders and Stroke, NIH, Bethesda, MD, USA. [8]Genome Damage and Stability Centre, University of Sussex, Falmer Brighton, UK.
***Corresponding author. Email: andre_nussenzweig@nih.gov or wuw@sibcb.ac.cn**
†These authors contributed equally to this work.

Recently, we and others demonstrated that highly active long-patch, synthesis-associated repair (SAR) of SSBs in neurons can be detected by incorporation of 5-ethynyl-2′-deoxyuridine (EdU) (SAR-seq) (*3*, *4*). DNA repair synthesis and SSBs were localized to neuronal enhancers, corresponding to 2% of the genome (*3*, *4*). Why neurons concentrate the repair machinery to these hotspots is an unsolved question; moreover, the source of endogenous SSBs and their physiological relevance remain unclear.

Active DNA demethylation generates SSBs and ADP-ribosylation in neurons

SAR-seq peaks in neurons correlate with oxidized forms of 5-methylcytosine, suggesting the potential involvement of active DNA demethylation via ten-eleven translocation (TET) enzymes (*4*) (fig. S1A). In induced pluripotent stem cell (iPSC)–derived neurons (iNs), all TET family enzymes (TET1, TET2, and TET3) are expressed (fig. S1B). During passive demethylation, TET-mediated oxidized methylcytidines are lost during successive rounds of replication. During active DNA demethylation, the thymidine DNA glycosylase (TDG) excises TET-mediated oxidized methylcytidines 5fC and 5caC to produce SSBs (*5*, *6*). SSBs can be detected by S1-END-seq using chain-terminating dideoxynucleosides (ddN) (Fig. 1A) (*4*). Given the observed accumulation of SSBs near oxidized methylcytosines (*4*), we set out to test whether active DNA demethylation is a source of endogenous DNA damage in postmitotic neurons.

Initially, we used CRISPR interference (CRISPRi) to deplete TDG in human iPSCs (fig. S1C), after which they were differentiated into neurons (iNs) (*7*, *8*). TDG-deficient, but not wild-type (WT) iNs, accumulated high levels of 5fC/caC (fig. S1D). We previously

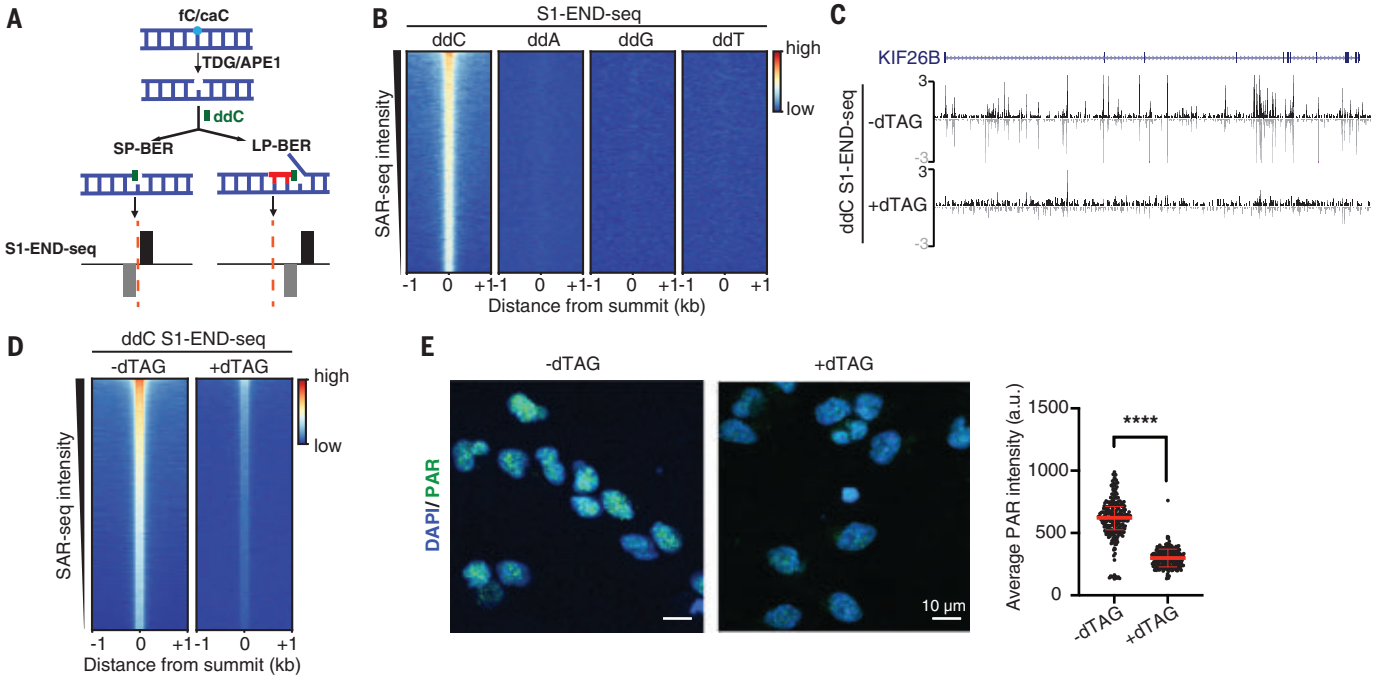


Fig. 1. Single-strand breaks at neuronal enhancers are TDG dependent. (**A**) Schematic overview of SSB generation during SP- and LP-BER and SSB detection by ddC S1-END-seq. (**B**) Heatmaps of S1-END-seq peaks in iN upon overnight treatment with different dideoxynucleoside (ddA, ddC, ddT, or ddG), plotted 1kb on either side of SAR-seq peak summits, ordered by SAR-seq intensity. (**C**) Genome browser screenshot showing single-strand breaks (ddC S1-END-seq) detected in TDG^{degron} iN treated with or without dTAG. (**D**) Heatmaps of ddC S1-END-seq in TDG^{degron} iN treated with or without dTAG. ddC S1-END-seq is ordered by SAR-seq intensity (*4*) and plotted 1 kb on either side of SAR-seq peak summits in iN. (**E**) Representative images (left) and quantification (right) of iN with immunofluorescence staining for DAPI (blue) and PARylation (green) in TDG^{degron} iN treated with or without dTAG. Scale bar, 10 μm. Statistical significance was determined using Mann-Whitney test (****$p < 0.0001$).

found that the mixture of ddNs led to robust accumulation of SSBs detected by S1-END-seq in iNs(*4*). By treating cells with each ddN separately, we found that only ddC, but not ddA, ddT, or ddG, produced single-strand DNA gaps (Fig. 1B). We therefore tested whether the formation of SSBs was dependent on TDG and found that, although SSBs accumulated at enhancers in WT iNs, TDG-depleted iNs harbored far fewer lesions (fig. S1, E and F).

Because TET-mediated active DNA demethylation may be important for transcriptional changes during neuronal differentiation, we inactivated TDG after cells had already differentiated into iNs. To do this, we used the degradation tag (dTAG) system, wherein a FKBP12 tag was knocked into the N terminus of endogenous TDG in iPSCs (fig. S1G). After 6 days of differentiation, TDG was acutely degraded in neurons upon addition of dTAG (fig. S1, H and I). On day 7, we performed ddC S1-END-seq. Consistent with the CRISPRi results, we found that TDG was required for SSB formation (Fig. 1, C and D).

A high level of PARP activity was found in iNs (Fig. 1E) (*4*). To test whether this is related to active DNA demethylation, we measured PARP activity when TDG was acutely degraded with dTAG. Indeed, ADP-ribosylation decreased on average by twofold in neurons lacking TDG (Fig. 1E). Thus, TET-mediated active DNA demethylation is the source of SSBs at neuronal enhancers, although other lesions could also contribute to ADP-ribosylation.

TET2 is required for pre-B to macrophage differentiation

In contrast to neurons, recurrent DNA repair peaks were not observed in other postmitotic cells, including G_0-arrested pre-B cells and iPSC-derived skeletal muscle cells (*4*). To understand whether overall DNA damage and repair is exclusive to neurons, we examined postmitotic macrophages derived by transcription factor–induced transdifferentiation from pre-B cells (Fig. 2A) (*9*). C/EBPα turns on the myeloid program in pre-B cells efficiently (>95%) and rapidly (48 hours) (Fig. 2B) (*9*, *10*). Cell conversion requires up-regulation of the C/EBPα target PU.1, which drives macrophage-specific gene expression and down-regulation of the B cell-specific transcription factor PAX5 to shut down the B cell transcriptional program (*11*). Previous studies demonstrated that TET2 knockdown partially delayed C/EBPα-induced macrophage (iM) differentiation because of impaired up-regulation of myeloid genes (*12*). To confirm the involvement of TET2 in pre-B to macrophage cell differentiation, we knocked out TET2 in pre-B cells by CRISPR-Cas9 targeting (fig. S2A). Consistent with previous findings, the macrophage cell surface marker MAC-1 was induced in more than 95% of control cells 2 days after C/EBPα stimulation, whereas only 4% of *TET2*-deficient cells expressed MAC-1 (fig. S2B). Thus, TET2 is required for pre-B to iM conversion.

Active DNA demethylation triggers SP-BER during macrophage trans-differentiation

To test whether active DNA demethylation operates during macrophage cell conversion, we knocked out TDG in pre-B cells (fig. S2C). In contrast to the severe differentiation block in *TET2*$^{-/-}$ cells (fig. S2B), most *TDG*$^{-/-}$ cells down-regulated B-cell surface marker CD19 and expressed MAC-1 by 2 days post-C/EBPα induction (Fig. 2B). Thus, distinct from TET2, TDG is not required for the generation of macrophage-like cells. Nevertheless, we detected an accumulation of 5fC/caC in *TDG*$^{-/-}$ but not WT iM (fig. S2D). Thus, TDG excises oxidized methylcytosines during the transdifferentiation of pre-B to macrophage cells.

To localize active DNA demethylation and associated repair sites, cells were treated with aphidicolin (APH) for 4 hours after 1 day of C/EBPα induction to inhibit any residual cell division without affecting differentiation (fig. S2E). Cells were then labeled with EdU for 20 hours

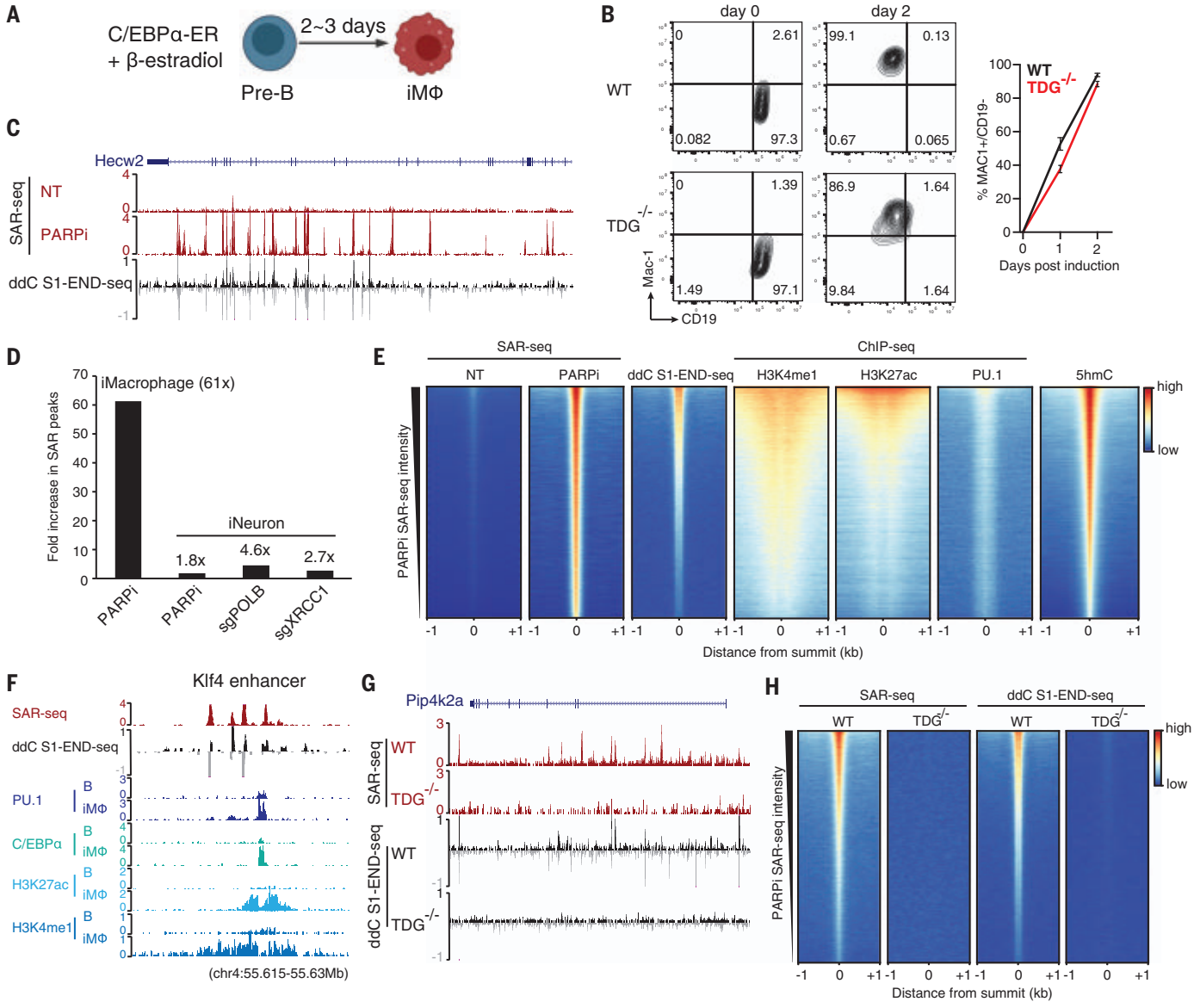


Fig. 2. TDG-dependent SSBs at macrophage enhancers. (**A**) Schematic overview of pre-B to iM transdifferentiation. (**B**) FACS plot (left) and quantification (right) of MAC-1 and CD19 expression in C/EBPα-ER–infected wild type and *TDG*$^{-/-}$ pre–B cells before induction and 2 days after induction with β-estradiol. Statistical significance was determined using unpaired *t* test (mean ± SD). (**C**) Genome browser screenshots illustrating SAR-seq and ddC S1-END-seq in iM. For SAR-seq, cells were either not treated (NT) or treated with PARPi on day 1 and harvested on day 2. (**D**) Bar graph comparing fold increase of SAR-seq peak numbers upon PARPi versus nontreated iM or nontreated iN. Also plotted is the fold-increase in iN expressing POLB-targeted (sgPOLB) or XRCC1-targeted (sgXRCC1) CRISPRi plasmids versus nontargeted control. (**E**) Heatmaps illustrating the correlation in iM between SAR-seq, ddC S1-END-seq, enhancer markers (ChIP-seq for H3K4me1, H3K27ac, and PU.1), and 5hmC (5hmC Seal). (**F**) Genome browser screenshots showing SAR-seq (with PARPi), ddC S1-ENDseq, transcription factor binding (C/EBPα and PU.1), and enhancer markers (ChIP-seq for H3K4me1, H3K27ac) in iM at the Klf4 de novo enhancer. "B" represents pre-B cells and "iMφ" represents induced iM. (**G**) Genome browser screenshot showing SAR-seq (with PARPi) and ddC S1-END-seq in WT and TDG knockout iM. (**H**) Heatmaps showing SAR-seq (with PARPi) and ddC S1-END-seq in WT and TDG-deficient iM.

and processed for SAR-seq (Fig. 2C) (*4*). Distinct from iNs, which exhibited ~55,000 hotspots of DNA repair (*4*), almost no peaks were detectable in iMs (Fig. 2C), reminiscent of our findings in other postmitotic cells (*4*). One potential explanation is that replication-independent active DNA demethylation generates only few SSBs in iMs, making a minor contribution to differentiation, as has been shown in other cell types (*13*). Alternatively, TDG-mediated excision of 5fC/caC might occur at a high frequency, but these bases would be replaced by unmodified cytosine via short patch (SP) base excision repair (BER). SP-BER events triggered by TDG excision of oxidized methylcytosines are undetectable by SAR-seq because this assay measures incorporated EdU, a thymidine analog.

Depletion or inhibition of factors involved in SP-BER, including XRCC1, PARP1, and POLβ, leads to an approximately twofold increase in the number of SAR-seq peaks in iNs (Fig. 2D), suggesting that long patch (LP)–BER is the primary source of the SAR-seq signal in these cells (*4*). Because iMs lack robust SAR-seq signals, we asked whether SP-BER participates in active cytosine demethylation. To investigate

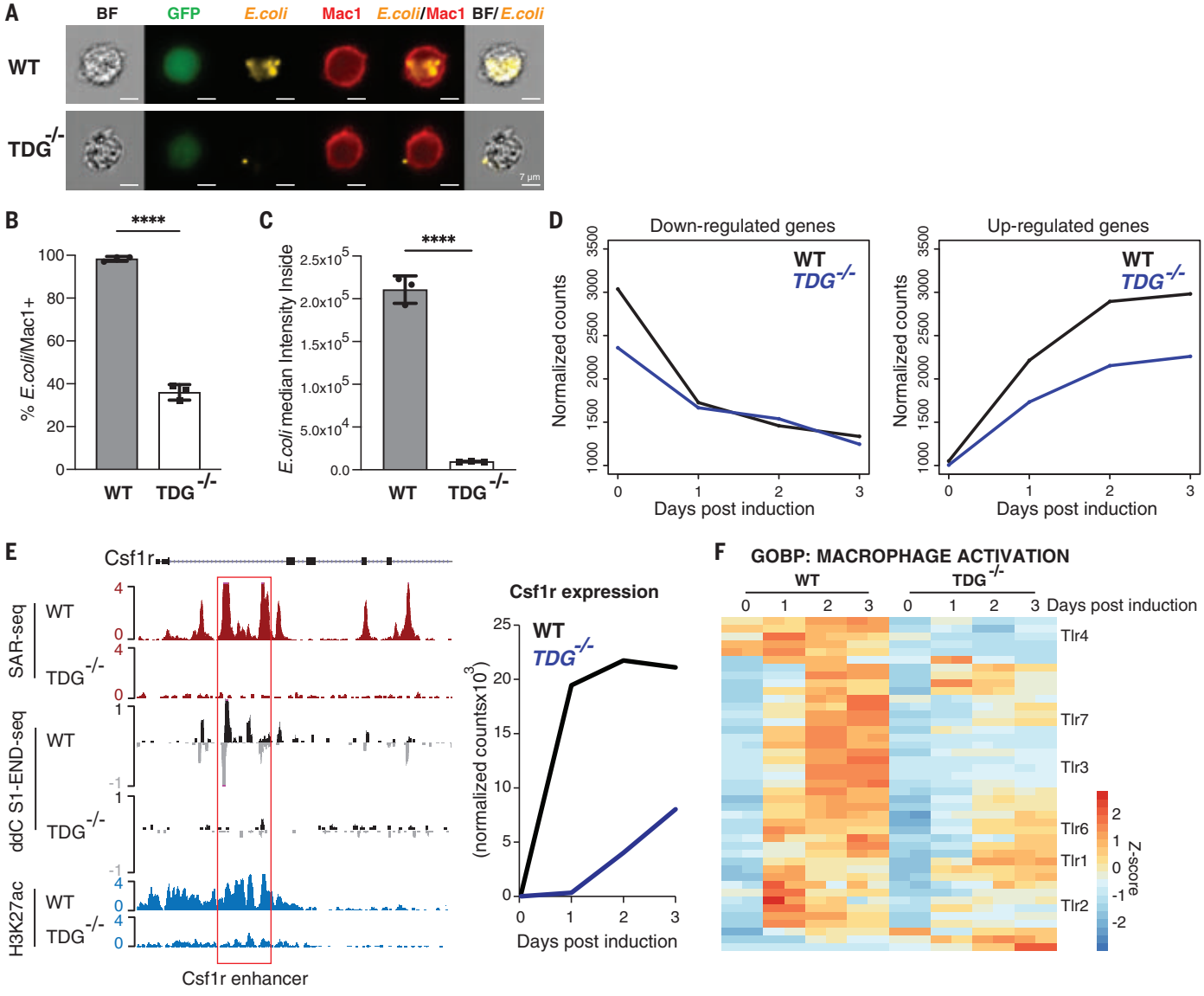


Fig. 3. Active DNA demethylation contributes to iM cell identity. (**A**) Imaging flow cytometric analysis of phagocytosis in iM. Scale bar, 7 μm. BF (bright field), green fluorescent protein (GFP) (C/EBPα expression), MAC-1 (MAC-1 expression, red), *E. coli* (dsRed-*E. coli*, yellow). (**B**) Bar graph of percentages of MAC-1-positive WT and *TDG*$^{-/-}$ iMs that internalized dsRed-*E. coli*. Statistical significance was determined using unpaired *t* test (****$p <$ 0.0001). (**C**) Bar graph and median intensity of internalized dsRed-*E. coli* in MAC-1-positive cells. Statistical significance was determined using unpaired *t* test (****$p < 0.0001$). (**D**) Linear plots showing expression changes of up- or down-regulated genes on average in WT and *TDG*$^{-/-}$ cells. (**E**) Left, genome browser screenshot showing SAR-seq, ddC S1-END-seq, and enhancer activity (H3K27ac ChIP-seq) in WT and *TDG*$^{-/-}$ iM at the Csf1r enhancer. Right, expression of Csf1r in WT and *TDG*$^{-/-}$ iM measured by RNA-seq. (**F**) Heatmap of gene expression associated with macrophage activation in WT and *TDG*$^{-/-}$ cells before and during transdifferentiation. Tlr (toll-like receptor) genes are indicated.

this question, we first inactivated SP-BER via PARP inhibition (PARPi) and found a 60-fold increase in the number of SAR-seq peaks in iMs from 1951 to 119,397 (Fig. 2, C and D). To further evaluate the function of SP-BER in iMs, we treated cells with chain-terminating ddN followed by S1-END-seq. As in iNs, SSBs were detectable only when iMs were treated with ddC alone, but not with ddA, ddT, or ddG (Fig. 2C and fig. S2F). Overall, 24,000 SSB peaks were detectable in iM, which is similar to the number of S1-END-seq peaks found in iN (28,000). Thus, SSBs accumulate in both cell types, but whereas LP-BER contributes to about half of SSB repair in iNs, SP-BER is overwhelmingly dominant in iMs.

SSBs form predominantly at de novo enhancers and are TDG dependent

Like iNs (*3*, *4*), LP-BER sites in iMs, measured after PARPi treatment, colocalized and correlated with enhancers marked with H3K4me1 and H3K27ac (Fig. 2E). Analysis of transcription factor binding motifs revealed an overrepresentation of PU.1 binding sites centered at SAR-seq summits (fig. S2G). ChIP-seq analysis of PU.1 binding confirmed colocalization with sites of SSBs, DNA repair synthesis, and 5hmC (Fig. 2E). Notably, PU.1 and C/EBPα interact with TET2, PU.1- and C/EBPα-targeted enhancers undergo TET2-mediated demethylation, and PU.1 is required for myeloid differentiation (*14*–*16*).

Myeloid enhancers have been described as "preexisting" or "de novo" depending on the order of recruitment of PU.1 and C/EBPα (*16*).

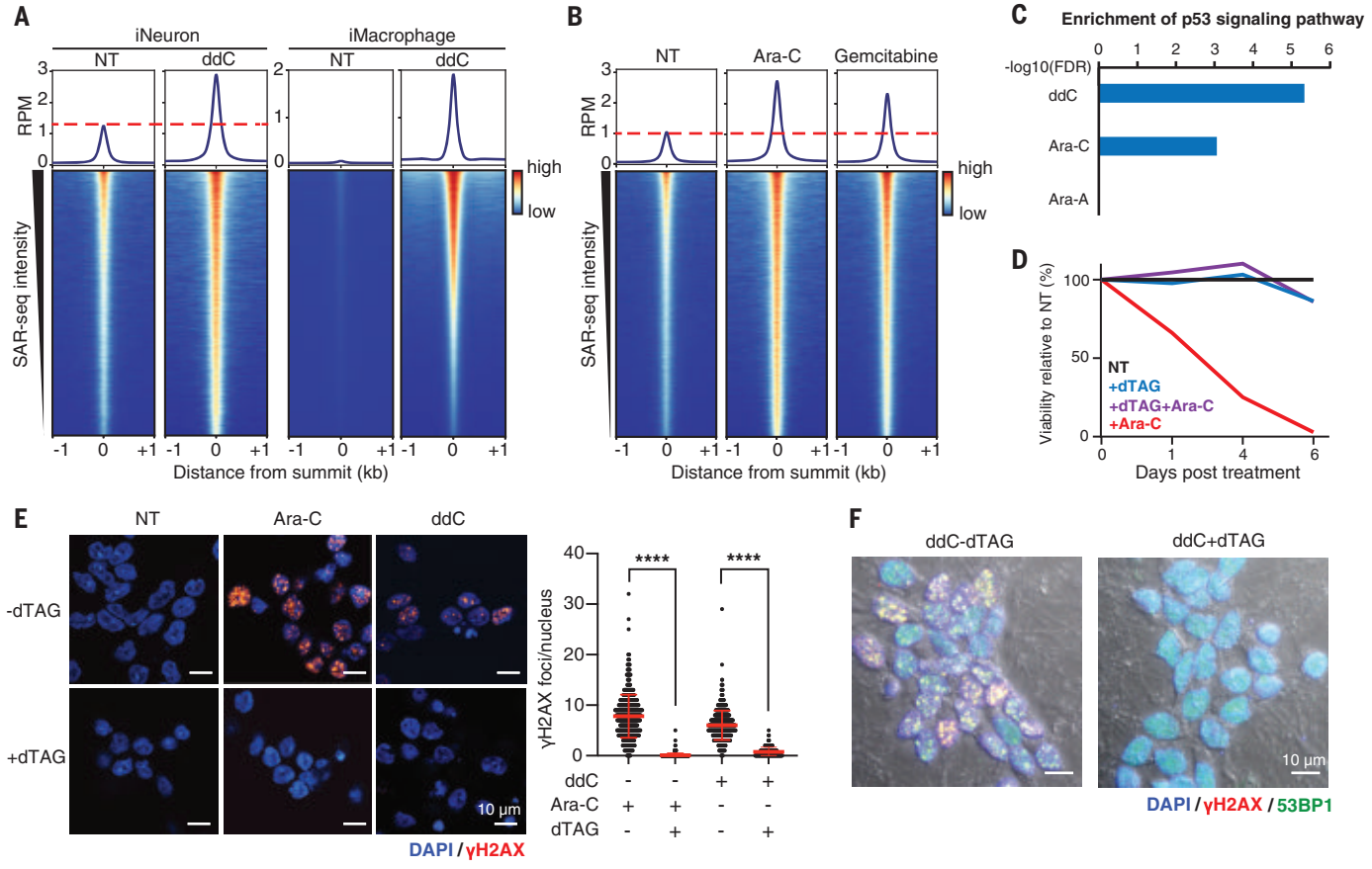


Fig. 4. Anti-C metabolites enhance repair synthesis and trigger the DNA damage response. (**A**) Heatmaps illustrating increased SAR-seq upon ddC treatment in iN and iM. Top, aggregate plots of SAR-seq intensity. (**B**) Heatmaps illustrating increased SAR-seq upon Ara-C and gemcitabine treatment of iN. Top, aggregate plots of SAR-seq intensity. (**C**) Gene Ontology analysis showing the enrichment of p53 target genes differentially expressed (|fold change| > 2) upon ddC, Ara-C, and Ara-A treatment in iN. The *x* axis represents the enrichment value as the logarithm of false discovery rate (FDR). (**D**) Survival of iN treated with Ara-C, dTAG alone, or Ara-C upon TDG depletion (Ara-C+dTAG). Data represent viability relative to nontreated cells. (**E**) Representative images (left) and quantification (right) of γH2AX foci induced upon ddC or Ara-C treatment in TDG^{degron} iNs treated with or without dTAG on day 6. 4′,6-diamidino-2-phenylindole (DAPI) (blue); γH2AX (red). Nontreated (NT). Scale bar, 10 μm. Statistical significance was determined using Mann-Whitney test (****$p < 0.0001$). (**F**) Maximum intensity projection of a confocal z-stack image of γH2AX (red) and 53BP1 (green) foci induced with ddC in TDG^{degron} iNs treated with or without dTAG on day 30. DAPI (blue) shows nuclei and overlaid differential interference contrast image (gray) shows neurites projected from the cell body. Scale bar, 10 μm.

Preexisting enhancers are prebound by PU.1 or C/EBPα and already active in pre-B cells, whereas de novo enhancers are first bound by C/EBPα before PU.1 and gradually become active during macrophage transdifferentiation (*16*). Although SAR-seq and S1-END-seq peaks were found at both types of enhancers, sites of DNA repair were more highly enriched for de novo macrophage enhancers (figs. S2, H to J). Examples of de novo enhancers that become demethylated and activated upon C/EBPα binding include the enhancers of Klf4 and Lefty2 (Fig. 2F and fig. S2K) (*15*). These de novo enhancers harbored peaks of SSBs and DNA repair synthesis that colocalized with C/EBPα and PU.1 (Fig. 2F and fig. S2K). We conclude that PU.1 guides TET2 to de novo macrophage enhancers, which promotes active DNA demethylation, SSB formation, and SP-BER.

To determine whether SSB formation and repair at macrophage enhancers is TDG dependent, we performed ddC S1-END-seq and SAR-seq in WT versus *TDG*$^{-/-}$ cells in the presence of PARPi. These assays revealed that TDG was essential for both SSB formation and DNA synthesis–associated repair in iM (Fig. 2, G and H). Thus, TET-mediated active DNA demethylation is the source of SSBs at both neuronal and macrophage enhancers.

Active DNA demethylation contributes to cell identity

Absence of TDG-mediated excision of 5fC/caC did not prevent the generation of macrophage-like cells (Fig. 2B). Yet, thousands of SSBs were generated (Fig. 2, C and E), and thousands of genes are up- and down-regulated during normal differentiation (*12*). This raises the question of the physiological role of active DNA demethylation. To test the functionality of *TDG*$^{-/-}$ macrophages, we measured the phagocytic activity of C/EBPα-induced cells by incubating cells with prelabeled dsRed fluorescent protein–expressing *Escherichia coli* prior to analysis by image cytometry (Fig. 3A). Whereas 90% of control MAC-1^{+} cells ingested *E. coli* after 48 hours following incubation, the phagocytic capacity of MAC-1^{+}*TDG*$^{-/-}$ cells was reduced to 36% (Fig. 3B). Moreover, there was a 23-fold reduction in the amount of total *E. coli* ingested per mutant cell (Fig. 3C). Thus, TDG loss compromises the ability to phagocytose bacteria in transdifferentiated cells.

To determine the role of active cytosine demethylation on enhancer activity and gene expression, we performed RNA sequencing (RNA-seq) on WT versus *TDG*$^{-/-}$ cells before (0 hours) and during (24, 48, and 72 hours) macrophage differentiation (Fig. 3D). In WT

cells, most down-regulated genes were associated with biological processes involving cell cycle and DNA repair, likely caused by the rapid cell cycle arrest induced by C/EBPα (fig. S3A, left panel) (*10*). Gene Ontology analysis revealed up-regulation of genes relating to macrophage function (fig. S3A, right panel). Although similar gene sets were down-regulated in WT and *TDG*$^{-/-}$ cells, *TDG*$^{-/-}$ cells failed to effectively up-regulate many genes related to macrophage differentiation (Fig. 3D).

We then sorted up-regulated genes into those that were either close to or far from DNA repair (SAR) loci. Because the majority (70%) of up-regulated genes are localized within 100 kb of stable C/EBPα-binding sites (*15*, *16*), we used 100 kb as the cut-off within which genes are considered neighboring enhancers. We observed that *TDG*$^{-/-}$ cells exhibited a defect in the up-regulation of genes that were located close to enhancers active for DNA repair (fig. S3B). Genes that were up-regulated in a TDG-dependent manner included those that are critical for macrophage identity and function (fig. S3C) such as Csf1r, a marker of cells of mononuclear phagocyte lineage. The highly conserved super-enhancer (fms-intronic regulatory element, FIRE) that controls Csf1r expression (*17*) showed robust SAR-seq and ddC S1-END-seq peaks (Fig. 3E). DNA repair, SSB formation, and enhancer activity, as well as Csf1r gene expression, were impaired in the absence of TDG (Fig. 3E).

Because MAC-1^{+}*TDG*$^{-/-}$ cells showed a defect in phagocytosis, we focused on genes known to be critical for macrophage activation (Fig. 3F). Most of these genes were up-regulated in differentiating WT cells but failed to increase in *TDG*$^{-/-}$ cells (Fig. 3F). Notable among them were TLR4 (Fig. 3F) and CD14 (fig S3C), which encode for the innate immune receptor complex that recognizes the lipopolysaccharide (LPS) cell wall component of Gram-negative bacteria including *E. coli*. Thus, active DNA demethylation of lineage-specific enhancers is required for proper up-regulation of genes critical for terminal differentiation and activation of macrophages.

In vivo long-patch tract lengths

TET activity is targeted to methylated CG dinucleotides within enhancers (*5*, *6*). Although ddN (and ddC) S1-END-seq demonstrated the expected prevalence of cytosines at S1-END-seq summits, composite motif analysis failed to reveal CG dinucleotides at ddC S1-END-seq peak summits (*4*). The lack of a CG motif could result from ddC incorporation during LP-BER distal from the initiating methylated CG dinucleotide (Fig. 1A and fig. S4A).

To test this idea, we developed a genome-wide base resolution assay to map 5fC and 5caC residues excised by TDG (fig. S4A). In this method, termed oxEND-seq, 5fC/caC sites are cleaved into double-strand breaks (DSBs) and then detected by END-seq. DNA is first treated with pyridine borane (PB) which converts 5fC and 5caC into dihydrouracil. USER enzyme, a mixture of uracil DNA glycosylase (which excises the uracil base) and endonuclease VIII (which breaks the phosphodiester backbone with lyase activity), generates a single-nucleotide gap. S1 nuclease will then cleave these 5fC:G- or 5caC:G-formed gaps to generate a DSB (fig. S4A). We applied this technique in TDG-knockout iMs, in which 5fC/5caC bases accumulate but SSBs do not form (fig. S2D). OxEND-seq revealed peaks that frequently overlapped with sites of SAR-seq and ddC S1-END-seq (fig. S4B). Motif analysis confirmed the expected pattern of CG dinucleotides at oxEND-seq peak summits (fig. S4C). We then calculated the relative distance of 5fC/caC to the nearest ddC S1-END-seq summit (fig. S4D). We observed a distribution of ddC S1-END-seq summits distal from the initiating CG dinucleotide. Approximately 17% of SSBs were located precisely at the CG dinucleotide, which reflect S1-END-seq detection of SP-BER events (Fig. 1A and fig. S4D). However, 67% were found within 30 residues from the *TDG*$^{-/-}$ oxEND-seq summits, corresponding to long-patch repair (Fig. 1A and fig. S4D). Thus, tract lengths vary considerably in vivo, but most are within 30 base pairs (bp) of the initiating lesion.

Chain termination with cytosine analogs triggers LP-BER and the p53 response

Incorporation of ddC at macrophage and neuronal enhancers results in a single-strand DNA (ssDNA) gap because a phosphodiester bond cannot be formed between the missing 3′ OH group and the next nucleotide. We found that, like PARPi [which triggers LP-BER (*4*)], ddC treatment increased DNA synthesis–associated repair in both iN and iM (Fig. 4A). Moreover, PARPi and ddC SAR-seq peaks overlapped (fig. S5A). This suggests the possibility that chain termination provokes LP-SSB repair (fig. S5B). Consistent with this, we found that other cytosine analogs, such as arabinosylcytosine (Ara-C) and gemcitabine (GEM), similarly increased the intensity of SAR-seq peaks at enhancer sites (Fig. 4B). By contrast, adenine analogs, Ara-A and ddA, did not result in any change in SAR-seq (fig. S5, C and D). We speculate that when antimetabolites (ddC, Ara-C or GEM) are incorporated into DNA during SP-BER, unligated gaps are detected, leading to nucleoside analog excision, and processing by long-patch repair, thereby explaining the observed increase in DNA synthesis–associated repair at enhancers (fig. S5B).

Antimetabolites inhibit replication in mitotic cells and are thereby frequently used to treat cancer. Cancer treatments are also commonly associated with neurotoxicity through unknown mechanisms (*18*). Ara-C–induced cell death is dependent on p53 (*19*, *20*), suggesting that Ara-C may kill neurons by a DNA damage–activated p53-dependent pathway. Consistently, we observed a robust p53 transcriptional response when neurons were treated with ddC and Ara-C, but not when treated with Ara-A (Fig. 4C). Moreover, 6 days after Ara-C treatment, almost all neurons in the culture had died (Fig. 4D). Acute degradation of TDG prevented Ara-C–induced cell death (Fig. 4D). This suggests that antimetabolite-induced neurotoxicity is linked to TET-initiated active DNA demethylation.

Incorporation of nucleoside analogs triggers the DNA damage response

A recent study demonstrated that Ara-C triggers histone H2AX phosphorylation in primary hippocampal neurons (*21*). Terminal deoxynucleotidyl transferase dUTP nick end labeling (TUNEL) did not reveal DSBs in the nuclei of γ-H2AX–positive neurons (*21*). We also observed γ-H2AX and 53BP1 foci formation in almost 100% of iNs after Ara-C or ddC treatment (Fig. 4E and fig. S5E). ddC treatment led to only a small increase in DSBs revealed by END-seq signal, but a marked increase in S1-END-seq (fig. S5F), indicating a greater number of SSBs than DSBs. In line with ssDNA damage, γ-H2AX formation was largely ATR dependent (fig. S5G). Moreover, ddC-induced S1-END-seq and γ-H2AX formation required POLβ (fig S5H), likely because POLβ is highly selective for ddN (*22*). Finally, we observed that γ-H2AX/53BP1 formation was entirely dependent on TDG (Fig. 4E and fig. S5E). The low frequency of DSBs relative to SSBs is consistent with the finding that DSBs rarely arise from symmetrically methylated CGs because of the highly coordinated and sequential action of TET-TDG–mediated base excision repair (*23*).

On average, six and eight γ-H2AX and 53BP1 foci were detectable after overnight treatment with ddC and Ara-C, respectively (Fig. 4E). Foci appeared within 2 hours of ddC and Ara-C treatment and were detectable for at least 16 hours after drug withdrawal (fig. S5I). This suggests that DNA damage either persists or is continually generated. If DNA lesions are continually produced by TET-mediated active DNA demethylation but subsequently repaired, acute degradation of TDG after drug withdrawal would lead to the disappearance of ddC and Ara-C–induced foci. Indeed, DNA damage no longer persisted when TDG was eliminated after the drugs were withdrawn (fig. S5J).

To directly monitor TET activity and DNA repair in living cells, we expressed an mCherry-53BP1 reporter (*24*) in neurons. Upon ddC treatment, we observed that 53BP1 foci appeared, dissolved, and then reappeared throughout the

15-hour time course (movie S1). By tracking individual foci from when they first appeared to when they disappeared, we estimate that most ddC-induced DNA damage events are resolved within 1 to 2 hours (fig. S5K).

Active DNA demethylation in fully differentiated iNs

Induced degradation of TDG on day 7 after iN differentiation led to the disappearance of SSBs, demonstrating the existence of ongoing TET-mediated oxidation. Within 14 to 28 days of maturation, iNs display differentiated neuron markers, action potential firing, and spontaneous synaptic currents, suggesting that they are functional excitatory glutamine-releasing neurons (*8*). Consistent with these findings, the analysis of gene expression profiles during iN differentiation revealed that the transcriptome continued to change beyond day 7, but fewer changes were detected between days 17 and 30 (fig. S6A). Reminiscent of our finding in iMs, genes were similarly down-regulated in WT and *TDG*$^{-/-}$ iN throughout their maturation (fig. S6B). However, TDG knockouts partially impaired the up-regulation of genes that were induced after day 7 (fig. S6B), including those regulating presynaptic signaling (fig. S6 C). Even on day 30, we observed robust generation of ddC-induced γ-H2AX and 53BP1 formation in the vast majority (>95%) of iNs, which was abolished by acute degradation of TDG (Fig. 4F). Thus, TDG-mediated SSBs are generated in both differentiating and fully differentiated iNs.

Discussion

TET is highly active in postmitotic neurons (*25*, *26*) and to a lesser degree in other somatic cell types (*6*). An unsolved question is the extent to which replication-independent demethylation contributes to cell differentiation and function. We have shown that TDG-dependent SSB intermediates accumulate at high levels at lineage-specifying enhancers in iPSC-derived neurons and transdifferentiated macrophages. Moreover, TDG contributes to transcriptome reprogramming in both differentiation systems. There are other examples of DNA demethylation in postmitotic cells in which gene expression is sensitive to loss of TDG. Axonal injury in retinal ganglion neurons (*27*) and dorsal root ganglion neurons (*28*) increases TET- and TDG-dependent active DNA demethylation to induce regeneration-associated gene expression. However, in other cases, TDG does not seem to contribute to transcriptional changes downstream of TET-mediated oxidation. For example, LPS triggers cell cycle exit and 5hmC accumulation in bone-marrow derived macrophages (BMDM) (*13*). The induced transcriptional program is independent of TDG even though 5fC/5caC accumulates at the top latent enhancers (Batf, Mdfic, Il1b and Il6) that acquire H3K27ac after stimulation (*13*). Consistent with this, we observed that LPS induces SSBs at these latent enhancers in BMDM (fig S7). TDG is also dispensable for the active DNA demethylation of 5mC in mouse zygotes (*29*). Removal of oxidized methylcytosines could potentially be mediated by other BER glycosylases. Alternatively, pathways that do not generate DNA breaks might mediate active DNA demethylation, including direct dehydroxymethylation of 5hmC (*30*), decarboxylation of 5caC (*31*), or deformylation of 5fC (*32*). By using high-resolution techniques to trace SSB intermediates and SP- versus LP-BER pathways, it should be possible to clarify the physiological role of active DNA demethylation during cell differentiation, activation, and injury.

Anticancer drugs frequently produce acute and sometimes persistent neurological and neuropsychiatric symptoms referred to as "chemobrain" (*18*). To date, there are no effective treatments or preventive measures for chemobrain, and the underlying mechanisms are poorly understood. We speculate that perturbed gap-filling synthesis at regulatory elements during active DNA demethylation could be one potential mechanism contributing to chemobrain. Notably, Ara-C is the most common chemotherapeutic agent that induces cerebellar dysfunction (*33*), and some patients have permanent impairment due to Purkinje cell loss in the cerebellum (*34*). Moreover, recent studies provide evidence that DNA demethylation is highly active in Purkinje neurons (*26*). Considering our findings, it would be interesting to determine whether inhibitors of TDG, or inhibitors of additional pathway components that trigger the DNA damage response, could be promising candidates to alleviate some of the neurological complications associated with anticancer drug therapies. *Note added in proof*: A recent study demonstrated that SAR sites are enriched for somatic mutations detected by ultradeep genome sequencing of individual neurons from normal individuals, suggesting that active DNA demethylation may contribute to mutation (*35*).

REFERENCES AND NOTES

1. P. J. McKinnon, K. W. Caldecott, *Annu. Rev. Genomics Hum. Genet.* **8**, 37–55 (2007).
2. K. W. Caldecott, *Trends Cell Biol.* **32**, 733–745 (2022).
3. D. A. Reid *et al*., *Science* **372**, 91–94 (2021).
4. W. Wu *et al*., *Nature* **593**, 440–444 (2021).
5. C. J. Lio *et al*., *J. Biosci.* **45**, 21 (2020).
6. X. Wu, Y. Zhang, *Nat. Rev. Genet.* **18**, 517–534 (2017).
7. M. S. Fernandopulle *et al*., *Curr. Protoc. Cell Biol.* **79**, e51 (2018).
8. C. Wang *et al*., *Stem Cell Reports* **9**, 1221–1233 (2017).
9. H. Xie, M. Ye, R. Feng, T. Graf, *Cell* **117**, 663–676 (2004).
10. A. Di Tullio, T. Graf, *Cell Cycle* **11**, 2739–2746 (2012).
11. L. H. Bussmann *et al*., *Cell Stem Cell* **5**, 554–566 (2009).
12. E. M. Kallin *et al*., *Mol. Cell* **48**, 266–276 (2012).
13. A. Onodera *et al*., *Genome Biol.* **22**, 186 (2021).
14. L. de la Rica *et al*., *Genome Biol.* **14**, R99 (2013).
15. J. L. Sardina *et al*., *Cell Stem Cell* **23**, 905–906 (2018).
16. C. van Oevelen *et al*., *Stem Cell Reports* **5**, 232–247 (2015).
17. R. Rojo *et al*., *Nat. Commun.* **10**, 3215 (2019).
18. J. B. Stone, L. M. DeAngelis, *Nat. Rev. Clin. Oncol.* **13**, 92–105 (2016).
19. A. U. Zaidi *et al*., *J. Neurosci.* **21**, 169–175 (2001).
20. C. G. Besirli, T. L. Deckwerth, R. J. Crowder, R. S. Freeman, E. M. Johnson Jr., *Cell Death Differ.* **10**, 1045–1058 (2003).
21. S. Nakayama *et al*., *Neurochem. Int.* **142**, 104933 (2021).
22. J. L. Martin, C. E. Brown, N. Matthews-Davis, J. E. Reardon, *Antimicrob. Agents Chemother.* **38**, 2743–2749 (1994).
23. A. R. Weber *et al*., *Nat. Commun.* **7**, 10806 (2016).
24. N. Dimitrova, Y. C. Chen, D. L. Spector, T. de Lange, *Nature* **456**, 524–528 (2008).
25. S. Kriaucionis, N. Heintz, *Science* **324**, 929–930 (2009).
26. E. Stoyanova, M. Riad, A. Rao, N. Heintz, *eLife* **10**, e66973 (2021).
27. Y. Lu *et al*., *Nature* **588**, 124–129 (2020).
28. Y. L. Weng *et al*., *Neuron* **94**, 337–346.e6 (2017).
29. F. Guo *et al*., *Cell Stem Cell* **15**, 447–459 (2014).
30. C. C. Chen, K. Y. Wang, C. K. Shen, *J. Biol. Chem.* **287**, 33116–33121 (2012).
31. Y. Feng *et al*., *Chem. Sci.* **12**, 11322–11329 (2021).
32. K. Iwan *et al*., *Nat. Chem. Biol.* **14**, 72–78 (2018).
33. W. J. Baker, G. L. Royer Jr., R. B. Weiss, *J. Clin. Oncol.* **9**, 679–693 (1991).
34. L. A. Dworkin, R. D. Goldman, L. S. Zivin, P. C. Fuchs, *J. Clin. Oncol.* **3**, 613–616 (1985).
35. L. J. Luquette *et al*., *Nat. Genet.* **54**, 1564–1571 (2022).

ACKNOWLEDGMENTS

We thank S. Ruiz for discussions and advice; C. Bradfield and I. Fraser for help with bone marrow–derived macrophages; T. Graf for C10 cells; and the NCI/CCR Genomics Core for help with sequencing. This work used the computational resources of the NIH HPC Biowulf cluster. **Funding:** This work is supported by the Intramural Research Program of the NIH funded in part with Federal funds from the NCI under contract HHSN261201500003I; the A.N. lab is also supported by an Ellison Medical Foundation Senior Scholar in Aging Award (AG-SS-2633-11), the Department of Defense Awards (W81XWH-16-1-599 and W81XWH-19-1-0652), the Alex's Lemonade Stand Foundation Award, and an NIH Intramural FLEX Award; W.W. is supported by the NCI Director's Intramural Innovation Award. B.D.S. is a CPRIT Scholar in Cancer Research. B.D.S. is supported by the Cancer Prevention and Research Institute of Texas award RR200079, the NIH R35GM147126 award, and an American Society of Hematology Scholar award. S.K. is supported by the NIH 5T32DK06044519 award. **Author contributions:** D.W., W.W., and E.C. conceived the project; D.W., E.C., R.P., N.Z., S.K., D.Z., N.W., S.N., M.J.K., and F.L., performed experiments; W.W. performed bioinformatic analyses; W.N. helped plan experiments; G.M.R. assisted with USER-END-seq; M.J.K. performed microscopy; F.L. performed image flow cytometry; R.C. generated FKBP12 -tagged TDG; F.L., M.W., K.C., and B.D.S. supervised the project in coordination with A.N. A.N. wrote the paper with help from coauthors. **Competing interests:** The authors declare that they have no competing interests. **Data and materials availability:** The deep sequencing datasets have been deposited in the Gene Expression Omnibus (GEO) database (GSE210317).

License information: Copyright © 2022 the authors, some rights reserved; exclusive licensee American Association for the Advancement of Science. No claim to original US government works. https://www.science.org/about/science-licenses-journal-article-reuse

SUPPLEMENTARY MATERIALS

science.org/doi/10.1126/science.add9838
Materials and Methods
Figs. S1 to S7
References (*36*–*57*)
MDAR Reproducibility Checklist
Movie S1

Submitted 20 July 2022; accepted 8 October 2022
10.1126/science.add9838

MACHINE LEARNING

Mastering the game of Stratego with model-free multiagent reinforcement learning

Julien Perolat*†, Bart De Vylder*†, Daniel Hennes, Eugene Tarassov, Florian Strub, Vincent de Boer‡, Paul Muller, Jerome T. Connor, Neil Burch, Thomas Anthony, Stephen McAleer, Romuald Elie, Sarah H. Cen, Zhe Wang, Audrunas Gruslys, Aleksandra Malysheva, Mina Khan, Sherjil Ozair, Finbarr Timbers, Toby Pohlen, Tom Eccles, Mark Rowland, Marc Lanctot, Jean-Baptiste Lespiau, Bilal Piot, Shayegan Omidshafiei, Edward Lockhart, Laurent Sifre, Nathalie Beauguerlange, Remi Munos, David Silver, Satinder Singh, Demis Hassabis, Karl Tuyls*†

We introduce DeepNash, an autonomous agent that plays the imperfect information game Stratego at a human expert level. Stratego is one of the few iconic board games that artificial intelligence (AI) has not yet mastered. It is a game characterized by a twin challenge: It requires long-term strategic thinking as in chess, but it also requires dealing with imperfect information as in poker. The technique underpinning DeepNash uses a game-theoretic, model-free deep reinforcement learning method, without search, that learns to master Stratego through self-play from scratch. DeepNash beat existing state-of-the-art AI methods in Stratego and achieved a year-to-date (2022) and all-time top-three ranking on the Gravon games platform, competing with human expert players.

Progress in artificial intelligence (AI) has been measured through the mastery of board games since the inception of the field. Board games allow us to gauge and evaluate how humans and machines develop and execute strategies in a controlled environment. The ability to plan ahead has been at the heart of successes in AI for decades in perfect information games such as chess, checkers, shogi, and Go, as well as in imperfect information games such as poker and Scotland Yard (*1*–*6*). For many years, the Stratego (*7*) board game has constituted one of the next frontiers of AI research (for a visualization of the game phases and game mechanics, see Fig. 1). The game poses two key challenges. First, the game tree of Stratego has 10^{535} possible states, which is larger than both no-limit Texas Hold'em poker, a well-researched imperfect information game with 10^{164} states, and the game of Go, which has 10^{360} states. Second, acting in a given situation in Stratego requires reasoning $>10^{66}$ possible pairs of private deployments at the start of the game, whereas in Texas Hold'em poker, players are dealt one of 10^3 different two-card hands for 10^6 possible private configurations with two players. Perfect information games such as Go and chess do not have a private deployment phase, thus avoiding the complexity that this challenge poses in Stratego. Currently, it is not possible to use state-of-the-art model-based perfect information planning techniques nor state-of-the-art imperfect information search techniques that break down the game into independent situations (*5*, *6*).

For these reasons, Stratego is a major challenge for the AI community and provides a hard benchmark for studying strategic interactions at an unparalleled scale. As in most board games, Stratego tests the ability to make relatively slow, deliberative, and logical decisions sequentially. Additionally, in most imperfect information games, other tactics that better reflect decision-making processes in the real world need to be deployed. As von Neumann described it, "real life consists of bluffing, of little tactics of deception, of asking yourself what is the other man going to think I mean to do" (*8*). Most recent successes in large imperfect information games have been achieved in real-time strategy games such as StarCraft, Dota, and Capture the Flag (*9*–*11*) or in racing simulation video games such as Gran Turismo (*12*), in which most decisions must be made quickly and instinctively and are of a continuous-time nature. Stratego is a game for which little progress has been achieved by the AI research community because of the many complex aspects of its structure. Successes in the game have been limited, with artificial agents only able to play at a level comparable to a human amateur [see, e.g., (*13*–*17*)].

This work introduces a novel game-theoretic method that allows an AI for learning to play Stratego in self-play in a model-free manner without human demonstration and from scratch. This new method resulted in a bot called DeepNash that beat previous state-of-the-art AI agents and achieved human expert–level performance in the most complex variant of the game, Stratego Classic. At the core of DeepNash is a principled, novel, model-free reinforcement learning (RL) algorithm called Regularized Nash Dynamics (R-NaD). Our method resulting in DeepNash combines R-NaD with a deep neural network architecture to learn a strategy that plays at a highly competitive level by aiming to find a Nash equilibrium (*18*) (i.e., an unexploitable strategy in zero-sum two-player games). In earlier work, it was formally shown that an R-NaD approach converges to a Nash equilibrium in several classes of matrix games, including two-player zero-sum games (*19*). The present work suggests that R-NaD at scale converges empirically to an approximate Nash equilibrium in Stratego. Figure 2 illustrates a high-level overview of this approach, which underlies DeepNash.

The performance of DeepNash was systematically evaluated against various state-of-the-art Stratego bots and human expert players on the Gravon games platform. DeepNash convincingly won against all current state-of-the-art bots that have been developed to play Stratego, producing a win rate of >97%, and it achieved a highly competitive level of play against human expert Stratego players on Gravon, where it ranked among the top three players, both on the year-to-date 2022 (determined on 22 April 2022) and on all-time

Table 1. Evaluation of DeepNash against existing Stratego bots. The numbers are reported from DeepNash's point of view. More games (800) were played against bots that could be run automatically.

Opponent	No. of games	Wins	Draws	Losses
Probe	30	100.0%	0.0%	0.0%
Master of the Flag	30	100.0%	0.0%	0.0%
Demon of Ignorance	800	97.1%	1.8%	1.1%
Asmodeus	800	99.7%	0.0%	0.3%
Celsius	800	98.2%	0.0%	1.8%
Celsius1.1	800	97.9%	0.0%	2.1%
PeternLewis	800	99.9%	0.0%	0.1%
Vixen	800	100.0%	0.0%	0.0%

DeepMind Technologies Ltd., London, UK.
*Corresponding author. Email: perolat@deepmind.com (J.P.); bartdv@deepmind.com (B.D.V.); karltuyls@deepmind.com (K.T.)
†These authors contributed equally to this work and are co-lead authors.
‡Independent consultant.

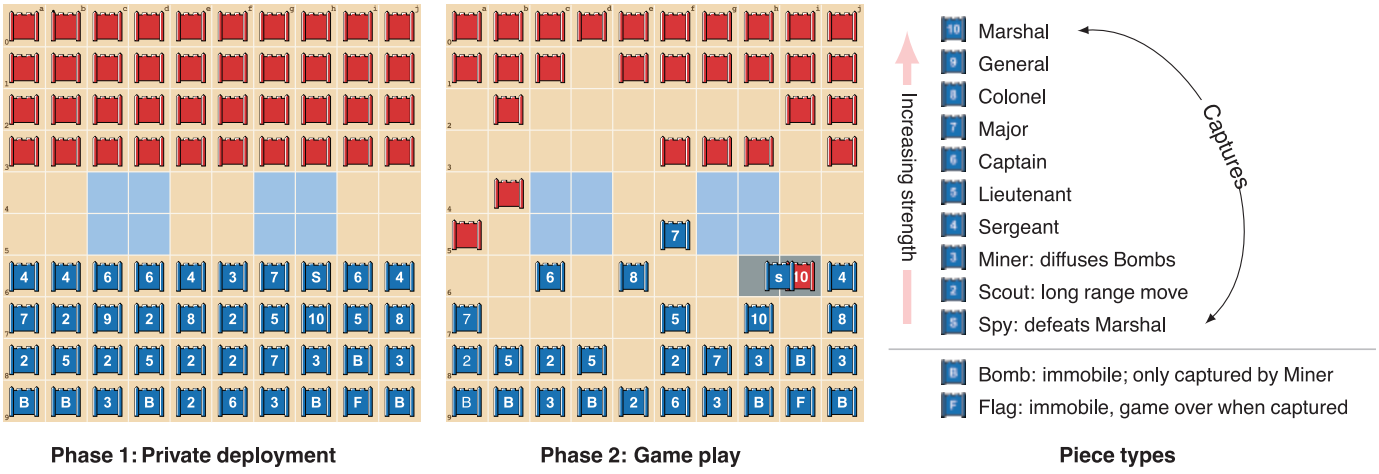


Fig. 1. Stratego is a two-player board game in which players try to capture the opponent's flag. Initially, the players secretly deploy 40 pieces of diverse strengths on the board. Then, they take turns moving pieces, possibly encountering an opponent piece that reveals both piece identities, and then the weaker piece is removed. Two lakes (indicated in blue) cannot be crossed by any piece. The complete rules are defined by the International Stratego Federation.

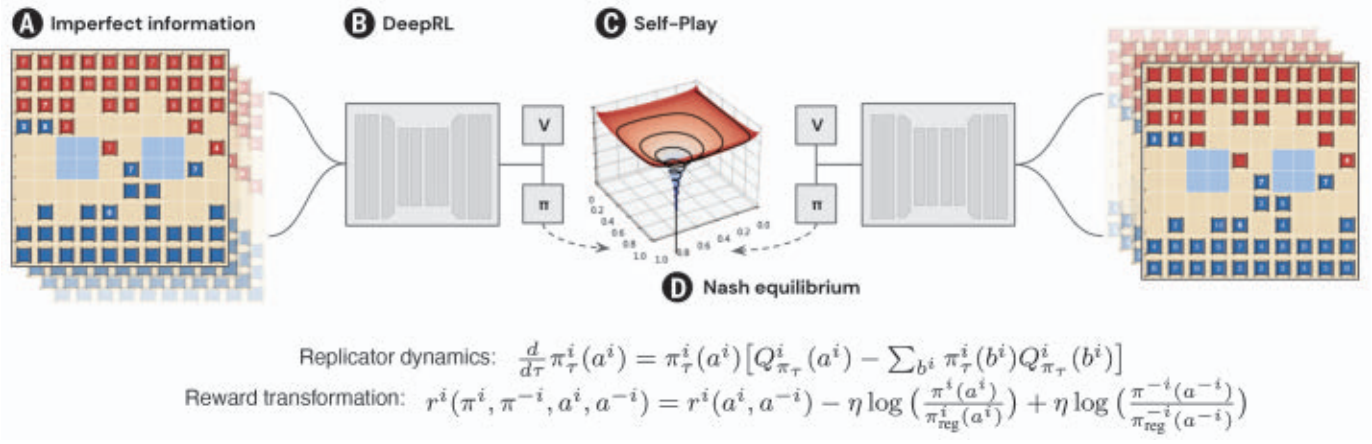


Fig. 2. Overview of R-NaD. (**A**) Overview of the R-NaD approach at scale underlying DeepNash, which allows for learning to play the imperfect information game Stratego. (**B** to **D**) R-NaD learns a policy represented by a deep neural network (B) through self-play from scratch (C) and aims at converging to a Nash equilibrium (D). The approach relies on two core ideas to reach convergence: replicator dynamics and reward transformation. Their equations are shown for illustrative purposes in their simplest form.

leaderboards, with a win rate of 84%. Therefore, to the best of our knowledge, this is the first time an AI algorithm was able to learn to play Stratego at a human expert level. It is worth mentioning that this performance was achieved without deploying any search method, which was a key ingredient of many milestone achievements in AI for board games in the past.

Methods

R-NaD at scale takes an end-to-end learning approach to solving Stratego by incorporating the learning of the deployment phase, i.e., putting the pieces tactically on the board at the start of a game (Fig. 1), into the learning of the game-play phase using an integrated deep RL and game-theoretic approach. As with much work in two-player zero-sum games, the purpose is to learn an approximate Nash equilibrium through self-play. In the context of two-player zero-sum games, a Nash equilibrium guarantees that the agent will perform well, even against a worst-case opponent. Such robustness typically allows an algorithm to perform well against humans [see, e.g., (*3*–*5*)]. In perfect information games, search techniques aided by RL have provided state-of-the-art superhuman bots in Go and chess (*2*, *20*). However, searching for a Nash equilibrium in imperfect information games requires estimating private information of the opponent from public states (*3*, *6*). Given the vast number of such possible private configurations in a public state, Stratego is computationally too challenging for all existing search techniques because the search space becomes intractable. This work therefore chose a different route, without search, and proposed a new method that combines model-free RL in self-play with a game-theoretic algorithmic idea, R-NaD. The model-free part implies that R-NaD does not build an explicit opponent model–tracking belief space (calculating a likelihood of the opponent's state), and the game-theoretic part is based on the idea that by modifying the dynamical system underpinning the reinforcement-learning algorithm, one can steer the learning behavior of the agent in the direction of the Nash equilibrium. The main advantage of this combined approach is that one does not need to explicitly model private states from public ones. A complex challenge, on the other hand, is to scale up this model-free RL approach with

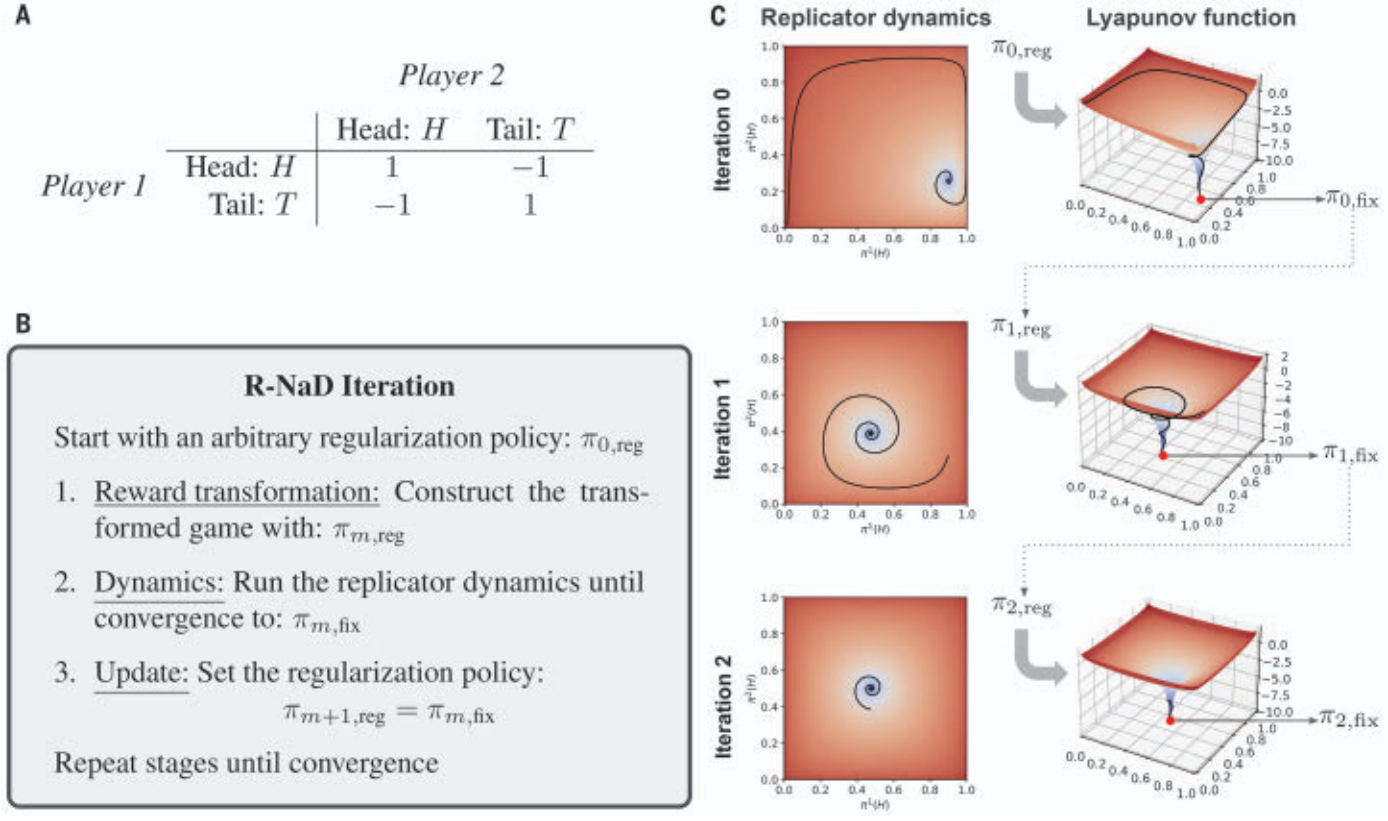


Fig. 3. Illustrating R-NaD using the matching pennies game. (**A**) Payoff table. (**B**) Algorithmic stages. (**C**) Dynamics and Lyapunov function.

R-NaD to make self-play competitive against human expert players in Stratego, which had not been achieved to date. This combined approach is illustrated in Fig. 2.

The following subsections present the learning algorithm behind DeepNash, referring to the supplementary materials for more technical details where relevant.

Learning approach

The approach underpinning DeepNash aims to learn a Nash equilibrium in Stratego through self-play and model-free RL. The idea of combining the two has been tried before, but it has been empirically challenging to stabilize such learning algorithms when scaling up to complex games such as Capture the Flag, Dota, and StarCraft (*9*–*11*). Some empirical work manages to stabilize the learning either by training against past versions of the agent (*9*–*11*) or by adding reward shaping (*10*, *11*) or expert data (*9*) to the training algorithm. Although these approaches help, they lack theoretical foundations, remain difficult to tune, and are rather domain dependent. Furthermore, in a game such as Stratego, it is difficult to define a loss for which minimization would converge to a Nash equilibrium without introducing prohibitive computational obstacles at large scale. For instance, minimizing the exploitability (*21*), a well-known quantity that measures the distance to a Nash equilibrium, requires estimating an agent's best response during training, which is computationally intractable in Stratego. However, it is possible to define a learning update rule that induces a dynamical system for which there exists a so-called Lyapunov function. This function can be shown to decrease during learning and thus guarantees convergence to a fixed point. This is the central idea behind the R-NaD algorithm and is the successful recipe for DeepNash, which scales this approach using a deep neural network.

R-NaD algorithm

The R-NaD learning algorithm used in DeepNash is an actor-critic method based on the idea of regularization for convergence purposes (*19*), which is briefly explained first in the context of zero-sum two-player normal form games (illustrated on the matching pennies game). A normal form game is an abstraction of a decision-making situation involving more than one agent. Each agent (indexed by $i \in \{1,2\}$) needs to simultaneously take an action a^i (in a set of possible actions A^i) according to a policy $\pi^i(.)$ (i.e., a distribution over possible actions A^i), after which it receives a game reward $[r^i(a^1, a^2)]$, and then the game is repeated. For convenience, the opponent of player i is indexed by $-i$. R-NaD relies on three key stages (Fig. 3B), described below.

In the first stage, the reward is transformed based on a regularization policy π_{reg}, which induces a modified game with rewards

$$r^i(\pi^i\pi^{-i}a^ia^{-1}) = r^i(a^ia^{-1}) - \eta\log\left(\frac{\pi^i(a^i)}{\pi^i_{\text{reg}}(a^i)}\right) + \eta\log\left(\frac{\pi^{-i}(a^{-i})}{\pi^{-i}_{\text{reg}}(a^{-i})}\right) \quad (1)$$

where $\eta > 0$ is a regularization parameter and i is the player index ($i \in \{1,2\}$). Note that this transformed reward is policy dependent.

Second, in the dynamics stage, the system evolves according to the replicator dynamics system (*22*, *23*) on this modified game. The basic replicator dynamics equations are a descriptive learning process from evolutionary game theory, equivalent to RL algorithms (*23*), which are also equivalent to an instance of follow-the-regularized-leader (*24*) and are defined as follows:

$$\frac{d}{d\tau}\pi^i_\tau(a^i) = \pi^i_\tau(a^i)\left[Q^i_{\pi_\tau}(a^i) - \sum_{b^i}\pi^i_\tau(b^i)Q^i_{\pi_\tau}(b^i)\right] \quad (2)$$

where $Q^i_{\pi_{fix}}(a^i)$ is the quality or fitness of an action: i.e., $Q^i_{\pi}(a^i) = \mathbb{E}_{a^{-i}\sim\pi^{-i}}\left[r^i(\pi^i, \pi^{-i}, a^i, a^{-i})\right]$. These dynamics reinforce the probability of taking actions with high fitness (relative to other actions). Because of the reward transformation, this system has a unique fixed point, $\pi\,fix$, and convergence to it is guaranteed in zero-sum two-player games [see (*19*)], which can be proven by the Lyapunov function:

$$H_{\pi_{fix}}(\pi) = \sum_{i=1}^{2}\sum_{a^i\in A^i}\pi^i_{fix}(a^i)\log\left(\frac{\pi^i_{fix}(a^i)}{\pi^i(a^i)}\right) \quad (19).$$

However, this fixed point is not yet a Nash equilibrium of the original game.

In the final update stage, the fixed point obtained is used as the regularization policy for the next iteration. These three stages are applied repeatedly, generating a sequence of fixed points that can be proven to converge to a Nash equilibrium of the original (unmodified) game (*19*) in zero-sum two-player games, but not in all general-sum games. Figure 3C illustrates the R-NaD algorithm on the two-player matching pennies game (the payoff table is shown in Fig. 3A). The first iteration starts from $\pi^i_{0,\text{reg}}[H, T] = [0.999, 0.001], (\eta = 0.2)$ and the replicator dynamics converge to $\pi^0_{0,\text{fix}}[H, T] = [0.896, 0.104]$ and $\pi^1_{0,\text{fix}}[H, T] = [0.263, 0.737]$. The right figure shows the evolution of the logarithm of the Lyapunov function and illustrates that it decreases while learning. Three iterations of R-NaD are shown.

R-NaD at scale

Our method consists of three components: (i) a core training component R-NaD, i.e., the model-free RL algorithm presented above, which is implemented using a deep convolutional network; (ii) a component that fine-tunes the learned policy to reduce the residual probabilities of taking highly improbable actions; and (iii) a test-time postprocessing component that uses game-specific knowledge [whereas (i) and (ii) are game agnostic] to filter out low-probability actions and obvious mistakes.

The following section starts by concisely laying out some essential background information on imperfect information games necessary to understand how R-NaD is scaled to a deep learning model. Then, the implementation of the three algorithmic stages of R-NaD are summarized. A detailed description of R-NaD is provided in the supplementary materials.

Imperfect information games

In a two-player zero-sum imperfect information game, two players (player i = 1 or i = 2) sequentially interact in turns. At turn t, the players receive a reward signal $\left(r^1_t r^2_t\right)$, and the current player $i = \Psi_t$ observes the game state through an observation o_t and selects an action a_t according to a parameterized policy function $\pi(.|o_t)$. In model-free RL, the trajectories $\mathrm{T} = \left[\left(o_t, a_t, \left(r^1_t r^2_t\right), \pi(.|o_t)\right), \Psi_t\right]_{0\le t<t_{\max}}$ are the only data the agent will leverage to learn the parameterized policy.

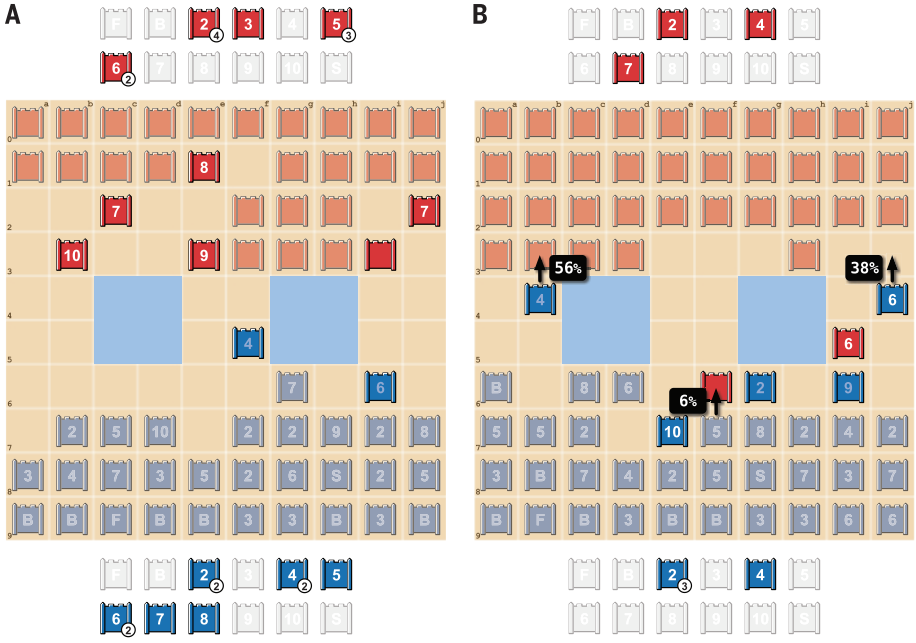


Fig. 4. Illustration of DeepNash's assessment of the relative value of material versus information. Shown is an illustration of DeepNash's assessment of the relative value of material versus information in two human (red) versus DeepNash (blue) matches. (**A**) Although blue is behind a 7 and 8, no pieces are revealed and only two are moved. As a result, DeepNash assesses its chance of winning to still be ~70% (blue indeed won this match). (**B**) Blue to move. DeepNash's policy supports three moves at this state, with the indicated probabilities shown (the move on the right was played in the actual match). Although blue has the opportunity to capture the opponent's 6 with its 9, this move was not considered by DeepNash, likely because the protection of 9's identity was assessed to be more important than the material gain.

Model-free RL with R-NaD

The R-NaD algorithm is scaled by using deep learning architectures. It performs the same three algorithmic stages as before in normal form games: (i) the reward transformation stage, (ii) the dynamics stage that allows for convergence to a fixed point, and (iii) the update stage in which the algorithm updates the policy that defines the regularization function.

The neural architecture consists of the following components: a U-Net torso with residual blocks and skip connections (*25*) and four heads that are smaller replicas of the torso augmented with final layers to generate an output of the appropriate shape. The first DeepNash head outputs the value function as a scalar, and the three remaining heads encode the agent's policy by outputting a probability distribution over its actions at deployment and during game play. The agent architecture is described in detail in the supplementary materials.

The observation is encoded as a spatial tensor consisting of the following components: DeepNash's own pieces, publicly available information about both the opponent's and DeepNash's pieces, and an encoding of the 40 last moves. This public information represents the types each piece can still have given the history of the game. In total, the observation contains 82 stacked frames encoded in a single tensor. The observation's detail is given in the supplementary materials.

Given the regularization policy $\pi_{m,\text{reg}}$ at iteration m and a trajectory, the reward transform used at time step t for player i is $r^i_{t,\pi_{m,\text{reg}}}(a,\pi) = r^i_t - \eta\log\left(\frac{\pi(a|o_t)}{\pi_{m,\text{reg}}(a|o_t)}\right)$ if $i = \Psi_t$ and $r^i_t + \eta\log\left(\frac{\pi(a|o_t)}{\pi_{m,\text{reg}}(a|o_t)}\right)$ if $i \neq \Psi_t$.

The dynamics stage of the method is composed of two parts. The first part estimates the value function, which is done through an adaptation of the v-trace estimator (*26*) to the two-player imperfect information case, resulting in a parameter update direction $Update_{\text{value}}$. The second part learns the policy through the Neural Replicator Dynamics (NeuRD) update (*27*) using a new estimate of the state action value based on the v-trace estimator, resulting in a parameter update direction $Update_{\text{policy}}$. These parts are detailed in the supplementary materials.

After a fixed number of learning steps, an approximate fixed point policy, $\pi_{m,\text{fix}}$, is obtained, which is then used as the next regularization policy, $\pi_{m+1,\text{reg}} = \pi_{m,\text{fix}}$. The three stages are repeated using a smooth transition from the

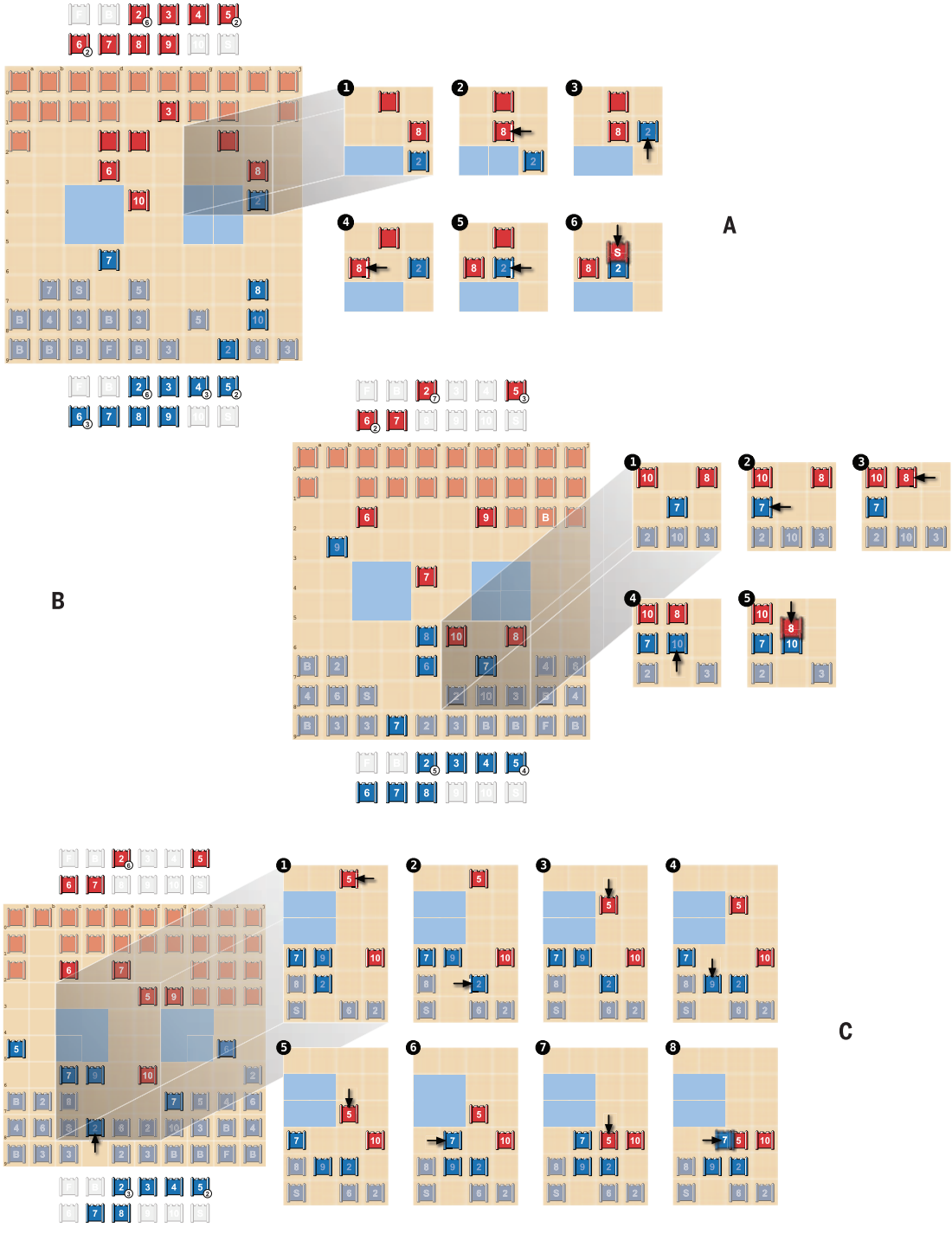


Fig. 5. Illustration of DeepNash bluffing. Shown is an illustration of Deep Nash bluffing in three human (red) versus DeepNash (blue) matches. (**A**) Positive bluffing. (**B**) Negative bluffing. (**C**) DeepNash makes a scout (2) behave like a spy and gains material.

reward transformation of iteration m to the one of step $m + 1$.

Directly learning with the above-described method leads to convergence to an empirically satisfying solution, which, however, is slightly distorted by low-probability mistakes. Those mistakes appear because the *softmax* projection used to compute the policy from the logits assigns a nonzero probability to every action. To alleviate this issue, the policy is fine-tuned during training by performing additional thresholding and discretization to the action probabilities. The supplementary materials provide more details on this aspect and also describe a few additional heuristics applied at test time that remove obvious mistakes from the policy. As opposed to the R-NaD model-free training algorithm, these heuristics are Stratego specific. Qualitatively, they do remove rare mistakes in matches against humans, but they do not give notable quantitative improvements in self-play (see the supplementary materials).

Results

This section presents an overview of the evaluation results of DeepNash against both human expert players and current state-of-the-art Stratego bots. For the former, DeepNash has been evaluated on the Gravon platform, a well-known online games server popular among

Stratego players. For the latter, DeepNash has been tested against eight known AI bots that play Stratego. A detailed analysis is also presented with regard to some of the capabilities of the agent's game play, including deployment, bluffing, and trading off of material versus information.

Evaluation on Gravon

Gravon is an internet platform for human players that offers several online games, including Stratego. It is by far the largest online platform for Stratego, and is where some of the strongest players compete. For more details on the platform and its ranking system, please refer to the supplementary materials.

DeepNash was evaluated against top human players over the course of 2 weeks in the beginning of April 2022, resulting in 50 ranked matches on Gravon. Of these matches, 42 (84%) were won by DeepNash. In the *Classic Stratego Challenge Ranking 2022* at that time, this corresponded to a rating of 1799, which put DeepNash in third place of all ranked Gravon Stratego players (the top two ratings were 1868 and 1831). In the all-time *Classic Stratego Ranking*, this resulted in a rating of 1778, which also put DeepNash in the third place of all ranked Gravon Stratego players (the top two ratings were 1876 and 1823). The rating for this leaderboard considers all ranked games going back to the year 2002.

These results confirm that DeepNash reaches a human expert level in Stratego only through self-play learning and without bootstrapping from existing human data.

Evaluation against state-of-the-art Stratego bots

DeepNash was also evaluated against several existing Stratego computer programs: Probe was a three-time winner of the Computer Stratego World Championship (2007, 2008, and 2010); Master of the Flag won that championship in 2009; Demon of Ignorance is an opensource implementation of Stratego with an accompanying AI bot; and Asmodeus, Celsius, Celsius1.1, PeternLewis, and Vixen are programs that were submitted in an Australian university programming competition in 2012 (see the supplementary materials for more details).

As shown in Table 1, DeepNash won the overwhelming majority of games against all of these bots despite not having been trained against any of them and only being trained using self-play. Therefore, it is not necessarily expected that the residual losses against some of these bots would vanish even if the exact Nash-equilibrium were reached. For example, in most of the few matches that DeepNash has lost against Celsius1.1, the latter played a high-risk strategy of capturing pieces early on with a high-ranking piece and thus was trying to get a significant material advantage. Most often, this strategy does not work, but occasionally it can lead to a win.

Illustration of DeepNash's abilities

The only goal of the algorithm behind DeepNash is to learn a Nash equilibrium policy and, by doing so, to learn qualitative behavior that one could expect a top player to master.

Indeed, the agent is able to generate a wide range of deployments, which makes it difficult for a human player to find patterns to exploit by adapting their own deployment. We describe DeepNash's deployment behavior in more detail in the supplementary materials (see the additional results section). DeepNash was able to make nontrivial trade-offs between information and material, to execute bluffs, and to take gambles when needed. The rest of this section illustrates these behaviors through matches that were played on Gravon.

For convenience, the behavior is described in a way a human observer might naturally interpret it, including terms such as "deception" and "bluffing," which arguably refer to mental states that the program does not have.

Trade-off between information and material

An important tactic in Stratego is to keep as much information as possible hidden from an opponent to gain an advantage. During certain game situations, there will be trade-offs to be considered in which a player needs to balance the value of capturing an opponent's piece (or even moving a piece), and thus revealing information about their own piece, versus not capturing a piece (or not moving) but keeping the identity of a piece hidden. DeepNash was able to make such trade-offs in extraordinary ways.

Figure 4A shows a situation in which DeepNash (in blue) was behind in pieces (it lost a 7 and an 8) but was ahead in information; the opponent in red has its 10, 9, an 8 and two of its 7's revealed. Valuing information and material in Stratego is nontrivial a priori, but the agent has learned a policy through self-play that seems to naturally make this trade-off. In the above example, DeepNash was behind in material but knew the identity of many of the opponent's high-ranked pieces. On the contrary, almost all of DeepNash's remaining pieces had not yet moved and its opponent was left in the dark. The value function ($v = 0.403$) credited this information asymmetry as an advantage for DeepNash (with an expected win rate of ~70%) despite having lesser material on the board. This game was won by DeepNash.

The second example in Fig. 4B shows a situation in which DeepNash had the opportunity of capturing the opponent's 6 with its 9, but this move was not considered, probably because protecting the identity of the 9 was deemed more important than the material gain. The situation also illustrates the stochasticity of DeepNash's policy during game-play.

Deceptive behavior and bluffing

In addition to being able to value asymmetry of information, one can also expect the agent to occasionally bluff to deceive its opponent and potentially gain an advantage. The situations shown in Fig. 5, A to C, illustrate this ability. Figure 5A illustrates positive bluffing, in which a player pretended that a piece had higher value than it actually did. DeepNash (blue) chased the opponent's 8 with an unknown piece, a scout (2), pretending it was the 10. The opponent believed that this piece had a high chance of being the 10 and guided it next to its spy (which could capture the 10). In an attempt to capture this piece, however, the opponent lost its spy to DeepNash's scout.

A second type of bluff, called negative bluffing, is shown in Fig. 5B. In contrast to a positive bluff, this tactic entails pretending a piece is of a lower rank. Here, the movement of the unknown 10 of DeepNash (blue) was interpreted by the opponent as a positive bluff because they tried to capture it with a known 8. DeepNash's move could have been interpreted as moving the spy closer to the opponent's 10, for example. The opponent instead encountered DeepNash's 10 and lost an 8.

A more complex bluff is shown in Fig. 5C, where DeepNash (blue) brought its unrevealed scout (2) close to the opponent's 10, which can be easily interpreted as a spy. This tactic actually allowed blue to capture red's 5 with its 7 a few steps later, thereby gaining material but also preventing the 5 from capturing the scout (2), and revealing that it was actually not the spy.

Conclusion

This work introduces a new game-theoretic method at scale that allows for AI to play the imperfect information game Stratego from scratch in self-play up to a human expert level, as illustrated by our bot DeepNash. This model-free learning method combines a deep residual neural network with the game-theoretical R-NaD multiagent learning algorithm. No form of search or explicit opponent modeling is performed during training, and DeepNash only relies on the use of some game-specific heuristics at test time. As such, the method underlying DeepNash takes a contrasting approach to state-of-the-art search-based learning methods that have been successfully applied to other complex games such as Go and chess and to imperfect information games such as poker and Scotland Yard. However, because of their computational toll and the inherent complexity of the Stratego game itself, those methods are not applicable to such an elaborate game.

The core component behind DeepNash is the at-scale implementation of the R-NaD algorithm. It performs three essential stages in an iteration of the algorithm: reward transformation starting from a random regularized policy to define a modified game, subsequently applying the replicator dynamics on this modified game to converge to a fixed point policy, and finally updating the regularization policy to this new fixed point. Repeatedly applying this three-stage process yields a strategy that is empirically difficult to exploit.

Evaluated against other AI bots, DeepNash achieved a minimum win rate of 97%, and in the evaluation against human expert players on the Gravon platform, DeepNash achieved an overall win rate of 84%, which placed it in the top-three rank of both the year-to-date (2022) and all-time leaderboards. This is an extraordinary result that the Stratego community did not believe would have been possible with current techniques, judging by quotes from Thorsten Jungblut (owner of the Gravon platform) and Vincent de Boer, which can be found in the supplementary materials.

Looking forward, at this stage, there are no indications of how R-NaD fares beyond zero-sum two-player settings. However, it is reasonable to assume that it can unlock further applications of RL methods in real-world multiagent problems with astronomical state spaces characterized by imperfect information, which are currently out of reach for state-of-the-art AI methods to be applied in an end-to-end fashion. For example, state-of-the-art methods on two-player poker (*4*) have successfully transferred to six-player poker (*5*). Many applications can be found in this larger class of games, including crowd and traffic modeling, smart grid, auction design, and market problems.

REFERENCES AND NOTES

1. M. Campbell, A. J. Hoane Jr., F. Hse, *Artif. Intell.* **134**, 57–83 (2002).
2. D. Silver *et al.*, *Science* **362**, 1140–1144 (2018).
3. M. Moravčík *et al.*, *Science* **356**, 508–513 (2017).
4. N. Brown, T. Sandholm, *Science* **359**, 418–424 (2018).
5. N. Brown, T. Sandholm, *Science* **365**, 885–890 (2019).
6. M. Schmid *et al.*, Player of games. arXiv:2112.03178 [cs.AI] (2021).
7. Stratego is a trademark of Jumbo Diset Group and is used in this publication for information purposes only.
8. J. von Neumann, O. Morgenstern, *Theory of Games and Economic Behavior* (Princeton Univ. Press, 1947).
9. O. Vinyals *et al.*, *Nature* **575**, 350–354 (2019).
10. C. Berner *et al.*, Dota 2 with large scale deep reinforcement learning. arXiv:1912.06680 (2019).
11. M. Jaderberg *et al.*, *Science* **364**, 859–865 (2019).
12. P. R. Wurman *et al.*, *Nature* **602**, 223–228 (2022).
13. V. de Boer, L. J. M. Rothkrantz, P. Wiggers, *Int. J. Intell. Games Simul.* **5**, 25 (2008).
14. M. Schadd, M. Winands, in *Proceedings of the Twenty-First Benelux Conference on Artificial Intelligence, Eindhoven, Netherlands, 29 to 30 October 2009* (BNAIC, 2009), pp. 225–232.
15. I. Satz, *J. Int. Comput. Games Assoc.* **34**, 27–29 (2011).
16. S. Redeca, A. Groza, in *2018 IEEE 14th International Conference on Intelligent Computer Communication and Processing (ICCP), Cluj-Napoca, Romania, 6 to 8 September 2018* (IEEE, 2018), pp. 97–104.
17. S. Mcaleer, J. Lanier, R. Fox, P. Baldi, in *Advances in Neural Information Processing Systems 34* (NeurIPS, 2020), vol. 33, pp. 20238–20248.
18. J. Nash, *Ann. Math.* **54**, 286–295 (1951).
19. J. Perolat *et al.*, in *Proceedings of the 38th International Conference on Machine Learning, 18 to 24 July 2021* (ICML, 2021), pp. 8525–8535.
20. D. Silver *et al.*, *Nature* **550**, 354–359 (2017).
21. M. Lanctot *et al.*, OpenSpiel: A framework for reinforcement learning in games. arXiv:1908.09453 [cs.LG] (2019).
22. E. Zeeman, *J. Theor. Biol.* **89**, 249–270 (1981).
23. D. Bloembergen, K. Tuyls, D. Hennes, M. Kaisers, *J. Artif. Intell. Res.* **53**, 659–697 (2015).
24. H. B. McMahan, in *Proceedings of the 14th International Conference on Artificial Intelligence and Statistics, Fort Lauderdale, FL, 11 to 13 September 2011* (AISTATS, 2011), vol. 15, pp. 525–533.
25. K. He, X. Zhang, S. Ren, J. Sun, in *Proceedings of the IEEE Conference on Computer Vision and Pattern Recognition (CVPR), Las Vegas, Nevada, 26 June to 1 July 2016* (CVPR, 2016), pp. 770–778.
26. L. Espeholt *et al.*, in *Proceedings of the 35th International Conference on Machine Learning, Stockholm, Sweden, 10 to 15 July 2018* (ICML, 2018), pp. 1406–1416.
27. D. Hennes *et al.*, in *Proceedings of the 19th International Conference on Autonomous Agents and MultiAgent Systems, Auckland, New Zealand, 9 to 13 May 2020* (AAMAS, 2020), pp. 492–501.
28. J. Perolat *et al.*, Figure data for: Mastering the game of Stratego with model-free multiagent reinforcement learning, Zenodo (2022); https://doi.org/10.5281/zenodo.7118519.

ACKNOWLEDGMENTS

We thank the following DeepMind colleagues for their technical support and feedback during the development of DeepNash: S. Mourad, L. Prince, A. Huang, M. Schmidt, M. Bowling, G. Ostrovski, M. Riedmiller, K. Kavukcuoglu, W. Czarnecki, and S. Singh. We also thank T. Jungblut, the Gravon platform owner, for providing access to Gravon, which allowed us to evaluate DeepNash against human expert players, and for allowing us to use matches played online for illustration purposes in this manuscript, as well as the anonymous reviewers for their comments that improved the quality of this article. **Funding:** This research was funded by DeepMind Technologies Ltd. **Author contributions:** J.P., K.T., and B.D.V. initiated and oversaw the project, developed training infrastructure and algorithms, performed agent analysis, wrote the paper, and provided research direction. D.He., E.T., F.S., N.Bu., M.K., and E.L. developed the training infrastructure and algorithms, performed agent analysis, and wrote the paper. P.M., J.T.C., T.A., S.H.C., Z.W., A.G., A.M., S.Oz., M.L., and J.L. developed the training infrastructure and algorithms and performed agent analysis. D.Ha. and V.d.B. performed the agent analysis and provided research direction. S.M., R.E., F.T., T.P., T.E., S.Om., and R.M. performed the agent analysis. L.S. wrote the paper and provided research direction. M.R. and B.P. wrote the paper. N.Be. initiated and oversaw the project. D.S. and S.S. provided research direction. **Competing interests:** US provisional patent application number 63/356,009 related to this work was filed 27 June 2022: "Model-Free Reinforcement Learning with Regularized Nash Dynamics"; assignee: DeepMind Technologies Ltd. The authors declare no competing interests. **Data and materials availability:** Data for the quantitative figures are available on Zenodo (*28*). All other data needed to evaluate the conclusions in this study are present in the main text or the supplementary materials. **License information:** Copyright © 2022 the authors, some rights reserved; exclusive licensee American Association for the Advancement of Science. No claim to original US government works. https://www.science.org/about/science-licenses-journal-article-reuse

SUPPLEMENTARY MATERIALS

science.org/doi/10.1126/science.add4679
Related Work
Additional Methods
Additional Results
Tables S1 to S3
Figs. S1 to S9
References (*29*–*50*)

Submitted 30 June 2022; accepted 3 November 2022
10.1126/science.add4679

REPORTS

QUALITY CONTROL

The human signal peptidase complex acts as a quality control enzyme for membrane proteins

Andrea Zanotti[1]†, João P. L. Coelho[2]†‡, Dinah Kaylani[2], Gurdeep Singh[3], Marina Tauber[4], Manuel Hitzenberger[2], Dönem Avci[1,4], Martin Zacharias[2], Robert B. Russell[3], Marius K. Lemberg[1,4]*, Matthias J. Feige[2]*

Cells need to detect and degrade faulty membrane proteins to maintain homeostasis. In this study, we identify a previously unknown function of the human signal peptidase complex (SPC)—the enzyme that removes endoplasmic reticulum (ER) signal peptides—as a membrane protein quality control factor. We show that the SPC cleaves membrane proteins that fail to correctly fold or assemble into their native complexes at otherwise hidden cleavage sites, which our study reveals to be abundant in the human membrane proteome. This posttranslocational cleavage synergizes with ER-associated degradation to sustain membrane protein homeostasis and contributes to cellular fitness. Cryptic SPC cleavage sites thus serve as predetermined breaking points that, when exposed, help to target misfolded or surplus proteins for degradation, thereby maintaining a healthy membrane proteome.

Membrane proteins are key to many important biological functions but intrinsically vulnerable to misfolding. This renders molecular quality control indispensable for cellular and organism homeostasis (*1*). For aberrant membrane proteins to be degraded, they must be extracted from the lipid bilayer as it occurs during endoplasmic reticulum (ER)–associated degradation (ERAD) (*2*). Proteolysis can facilitate this energetically unfavorable reaction and synergizes with ERAD. One key

membrane-integral protease of the ER is the signal peptidase complex (SPC), a defining enzyme of the "signal hypothesis" for ER targeting. Its canonical role is to cleave off N-terminal signal peptides (*3*), a process into which a recent cryo–electron microscopy structure has provided molecular insights (*4*). However, the SPC activity can also be hijacked by viruses for maturation of polyproteins (*5*, *6*). This indicates that viruses are capitalizing on a feature inherent to this enzyme and that cleavage by the SPC is not limited to signal peptides.

To address this central open question on the substrate range of the SPC, we analyzed the whole human proteome for N-terminal SPC cleavage sites that are not classical signal peptides (fig. S1A). This approach identified 262 membrane proteins that have a predicted SPC cleavage site following their N-terminal type II–oriented transmembrane (TM) helix (Fig. 1A). Candidates include several connexins, gap junction proteins for which previous in vitro experiments indicated signal peptide–like processing (*7*). Therefore, we first focused on this protein family. Disease-causing mutations distributed over the TM segments of connexin 32 (Cx32) and other connexins gave rise to two species on SDS–polyacrylamide gel electrophoresis (Fig. 1B and fig. S1, B to D). Epitope tagging showed that this was caused by N-terminal cleavage (fig. S1, C and D). Furthermore, mutations of predicted SPC cleavage sites (fig. S1, E and F) and the SPC inhibitor cavinafungin (*8*) blocked Cx32 processing (Fig. 1C), together confirming membrane protein cleavage by the SPC. However, unlike signal peptides, which are cleaved early during biosynthesis (*3*), Cx32 was processed posttranslocationally (Fig. 1D).

If the SPC can cleave after TM regions, its substrate range is vastly underestimated. We thus sought to determine whether the SPC also cleaves after internal type II–oriented TM helices. Indeed, 1297 human membrane proteins contain predicted SPC cleavage sites downstream of our initial N-terminal search window (fig. S2, A and B). Among those, we verified SPC-mediated cleavage for peripheral myelin protein 22 (PMP22) (fig. S2C), a central nervous system protein whose mutations cause human disease, as well as the rhomboid pseudoprotease iRhom2 (fig. S2D), which controls trafficking and activation of the cell-surface sheddase TACE/ADAM17 (tumor necrosis factor–α converting enzyme/A disintegrin and metalloprotease domain–containing protein 17) (*9*, *10*). For iRhom2, cleavage occurred several hundred residues downstream of its N terminus (fig. S2D), whereas PMP22 was cleaved after its third TM helix (fig. S2, E to G).

These findings uncover a much broader SPC client range than previously anticipated. In silico analyses of predicted-to-be-cleaved TM domains revealed clear differences to signal peptides in sequence, hydrophobicity, and length (fig. S3). Together, this raises the

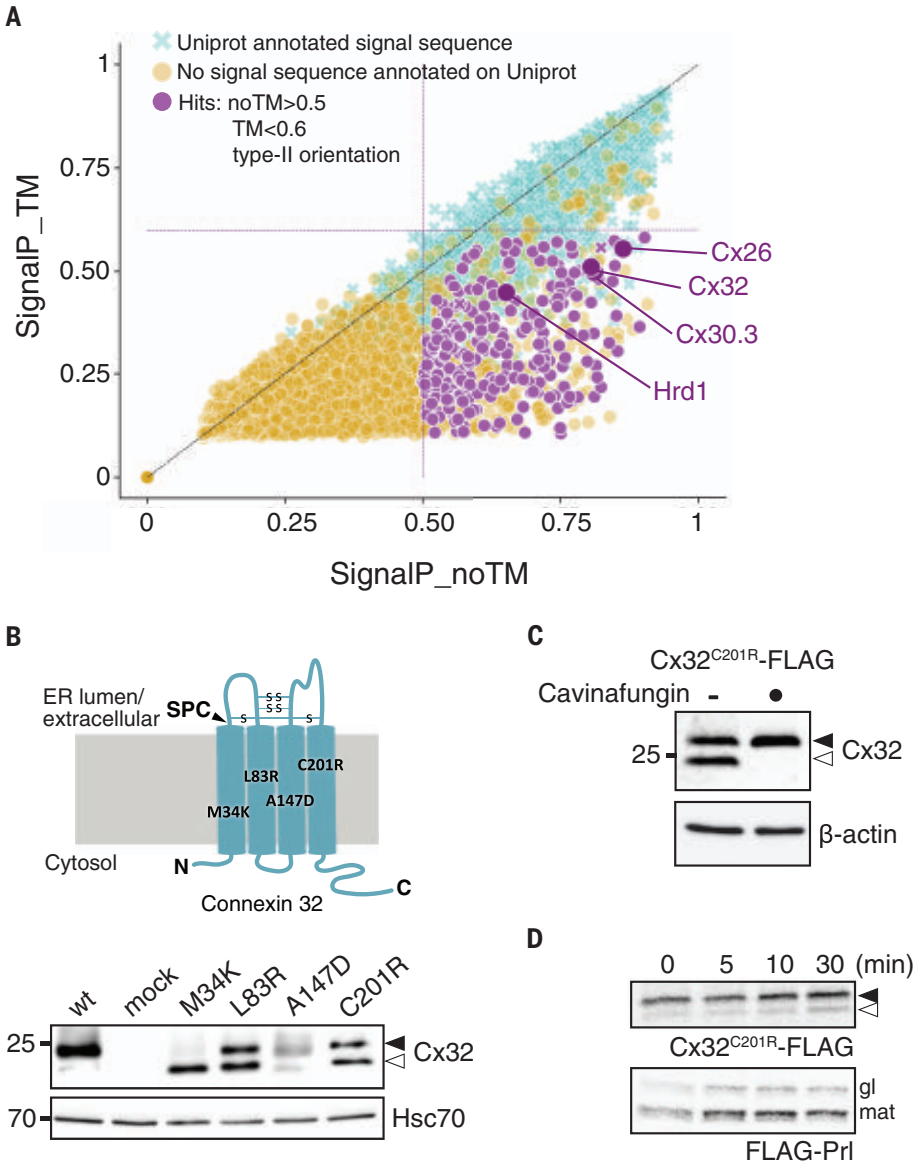


Fig. 1. The SPC posttranslocationally cleaves mutant membrane proteins. (**A**) Analysis of the first 70 amino acids of all human proteins using SignalP4.1, exploiting the two different neural networks [no recognition of TM regions (noTM) or TM region recognition included (TM); see methods for details]. Dark-purple circles indicate hits further analyzed in this study. (**B**) Analysis of Cx32 mutants in human embryonic kidney 293T (HEK293T) cells reveals two species. Hsc70 served as loading control. (**C**) Immunoblot of $Cx32^{C201R}$-FLAG in HEK293T cells treated with the SPC inhibitor cavinafungin (1 μM), where indicated [empty (full) arrowhead: SPC-processed (full-length) $Cx32^{C201R}$]. (**D**) Autoradiograph of immunoprecipitated $Cx32^{C201R}$-FLAG or FLAG-prolactin (Prl), labeled for 2 min and chased for the indicated times (mat: mature Prl; gl: glycosylated mature Prl). Single-letter abbreviations for the amino acid residues are as follows: A, Ala; C, Cys; D, Asp; E, Glu; F, Phe; G, Gly; H, His; I, Ile; K, Lys; L, Leu; M, Met; N, Asn; P, Pro; Q, Gln; R, Arg; S, Ser; T, Thr; V, Val; W, Trp; and Y, Tyr.

[1]Center for Molecular Biology of Heidelberg University (ZMBH), 69120 Heidelberg, Germany. [2]Center for Functional Protein Assemblies (CPA), Department of Bioscience, TUM School of Natural Sciences, Technical University of Munich (TUM), 85748 Garching, Germany. [3]BioQuant and Biochemistry Center (BZH), Heidelberg University, 69120 Heidelberg, Germany. [4]Center for Biochemistry and Cologne Excellence Cluster on Cellular Stress Responses in Aging-Associated Diseases (CECAD), Faculty of Medicine, University of Cologne, 50931 Cologne, Germany.
***Corresponding author. Email: m.lemberg@uni-koeln.de (M.K.L.); matthias.feige@tum.de (M.J.F.)**
†These authors contributed equally to this work.
‡Present address: Department of Cell Biology, Harvard Medical School, Boston, MA 02115, USA.

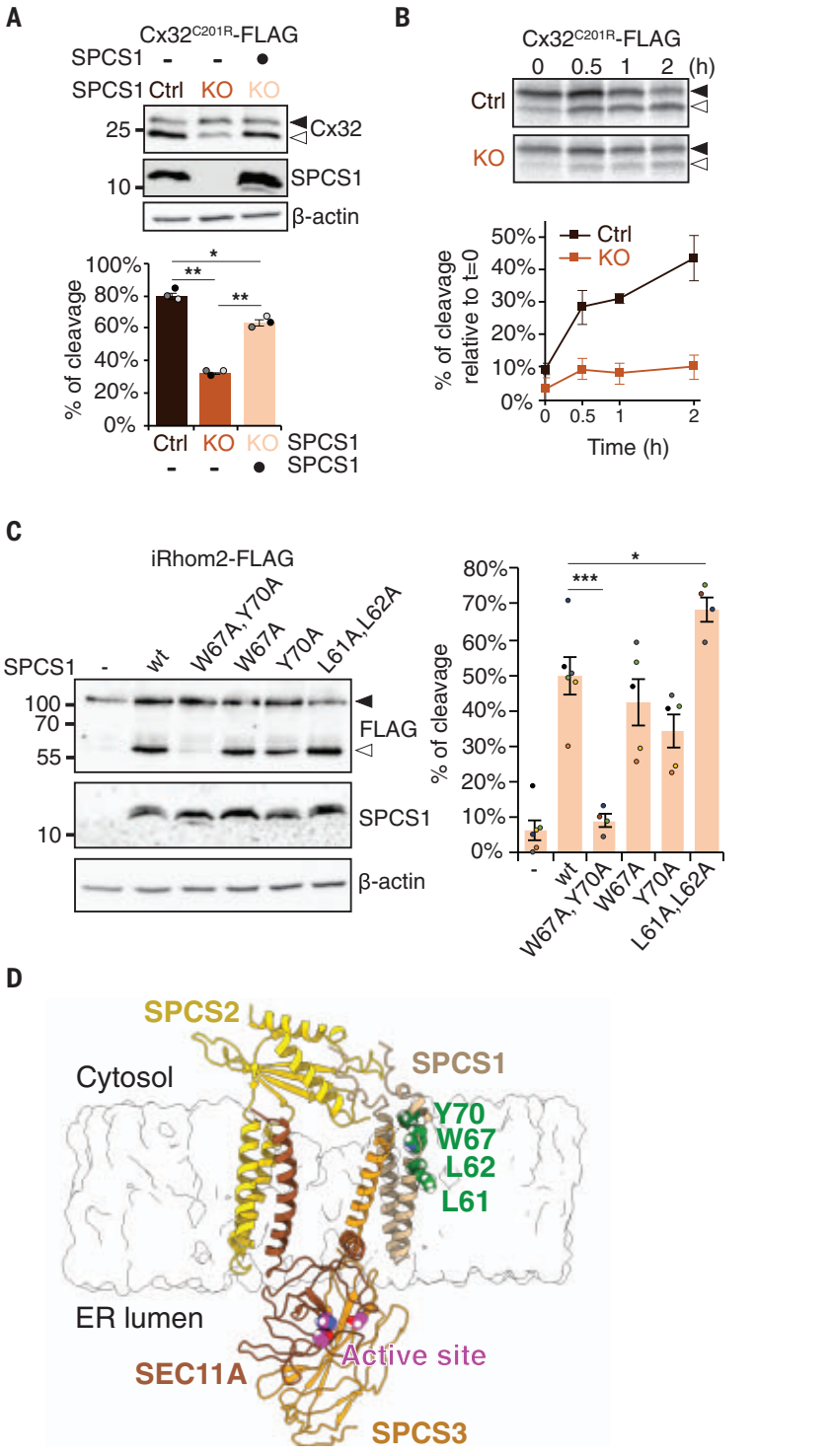


Fig. 2. SPCS1 is critical for membrane protein cleavage. (**A**) (Top) Immunoblot analysis of $Cx32^{C201R}$ cleavage in HEK293T (Ctrl), SPCS1 knockout (KO), or SPCS1 KO cells transiently reexpressing SPCS1. Actin served as loading control. (Bottom) Quantification of cleaved $Cx32^{C201R}$ fraction (mean ± SEM; $n = 3$; $^{*}P < 0.05$; $^{**}P < 0.01$). Empty (full) arrowhead: SPC-processed (full-length) $Cx32^{C201R}$. (**B**) (Top) Autoradiograph of immunoprecipitated $Cx32^{C201R}$-FLAG labeled for 5 min and chased for the indicated times in Ctrl or SPCS1 KO cells. (Bottom) Quantification of cleaved $Cx32^{C201R}$ relative to 0 hours (mean ± SEM). (**C**) (Left) Immunoblot analysis of ectopically coexpressed SPCS1 mutants and iRhom2-FLAG in SPCS1 KO cells [empty (full) arrowhead: SPC-processed (full-length) iRhom2]. (Right) Quantification of iRhom2 cleavage (mean ± SEM; $^{*}P < 0.05$; $^{***}P < 0.001$). (**D**) Structure of the SPC (*4*), highlighting SPCS1 residues that affected iRhom2 cleavage.

question of how cleavage of membrane proteins might be regulated. A previous CRISPR screen revealed the noncatalytic SPC subunit SPCS1 (fig. S4A) to be involved in the maturation of flavivirus polyproteins (*6*), indicating a possible role in the processing of substrates other than signal peptides. Notably, SPCS1 knockout reduced mutant Cx32 cleavage by more than 50%, and complementation with exogenous SPCS1 reestablished it (Fig. 2A). A similar behavior was observed for all other tested substrates (fig. S4, B to E), revealing a key role for SPCS1 in membrane protein cleavage. Knockdown of other SPC subunits affected Cx32 processing to different degrees (fig. S5A), suggesting a complex interplay of the subunits, which goes beyond a general destabilization of the complex when one subunit is missing (fig. S5B). Pulse-chase experiments confirmed the role of SPCS1 in posttranslocational Cx32 cleavage (Fig. 2B). In contrast, SPCS1 ablation did not compromise signal peptide processing (fig. S5, C to E). Instead, it increased secretion of prolactin that contains a classical signal sequence (fig. S5F), arguing that SPCS1-dependent membrane protein cleavage is functionally distinct from its role in signal peptide processing (*11*). Together, these findings led us to query SPCS1 in more detail. Coimmunoprecipitation experiments showed interaction of SPCS1 with iRhom2, but not the iRhom2-binding partner TACE (fig. S6A). Furthermore, mutations of evolutionarily conserved lipid bilayer–exposed residues within SPCS1 (fig. S6B) substantially affected iRhom2 cleavage (Fig. 2, C and D, and fig. S6C), while not disrupting SPC assembly (fig. S6D). Together, these findings support a function of SPCS1 in the recognition and processing of membrane proteins by the SPC.

The fact that disease-linked membrane protein mutants are cleaved by the SPC may indicate a quality control function. We thus hypothesized that incorrectly folded membrane proteins might expose otherwise buried (i.e., cryptic) SPC cleavage sites and become prone to processing. Supporting this idea, every connexin mutant we had found to be cleaved by the SPC was ER-retained and failed to form gap junctions (fig. S7, A and B), indicating misfolding. In contrast, inducing ER retention of correctly folded wild-type Cx32 only had a minor effect on cleavage (fig. S7, C to E). If misfolding indeed caused cleavage, stabilizing the mutation should block proteolytic processing. In agreement with this, cleavage was significantly reduced for a $Cx32^{C201R}$ variant (Cys^{201}→Arg) that contained a computationally designed second mutation to form a stabilizing salt bridge (Fig. 3, A and B). A similar behavior was observed for other Cx32 mutants when secondary mutations stabilizing the first lesion were introduced (fig. S8). Further supporting the idea that misfolding

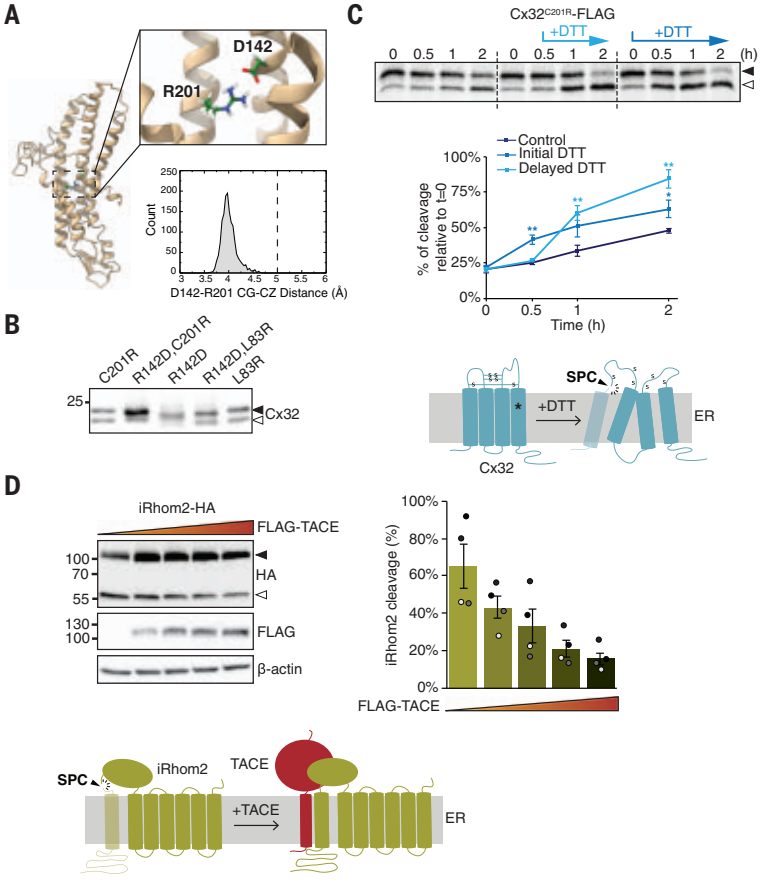


Fig. 3. Misfolding and failed assembly promote SPC cleavage. (**A**) (Top) Cx32^{R142D,C201R} model with inset highlighting D142 and R201. (Bottom) Histogram showing the distance between the terminal side-chain carbon atoms of D142 and R201, as obtained from molecular dynamics simulations (dashed line: 5-Å threshold needed for salt bridge formation). (**B**) Immunoblot of the indicated Cx32 mutants expressed in HEK293T in the presence of CB-5083 to inhibit ERAD. Empty (full) arrowhead: SPC-processed (full-length) Cx32. (**C**) (Top) Autoradiograph of immunoprecipitated Cx32^{C201R}-FLAG labeled for 10 min and chased for the indicated times. (Bottom) Quantification of SPC-mediated processing. Empty (full) arrowhead: SPC-processed (full-length) Cx32^{C201R} (mean ± SEM; n = 3; *P < 0.05; **P < 0.01 relative to control). (**D**) (Left) Immunoblot of hemagglutinin (HA)–tagged iRhom2 with increasing amounts of coexpressed FLAG-tagged TACE. Full (empty) arrowhead: full-length (processed) iRhom2. Actin was used as loading control. (Right) Quantification of the cleaved iRhom2 fractions(mean ± SEM; n = 4).

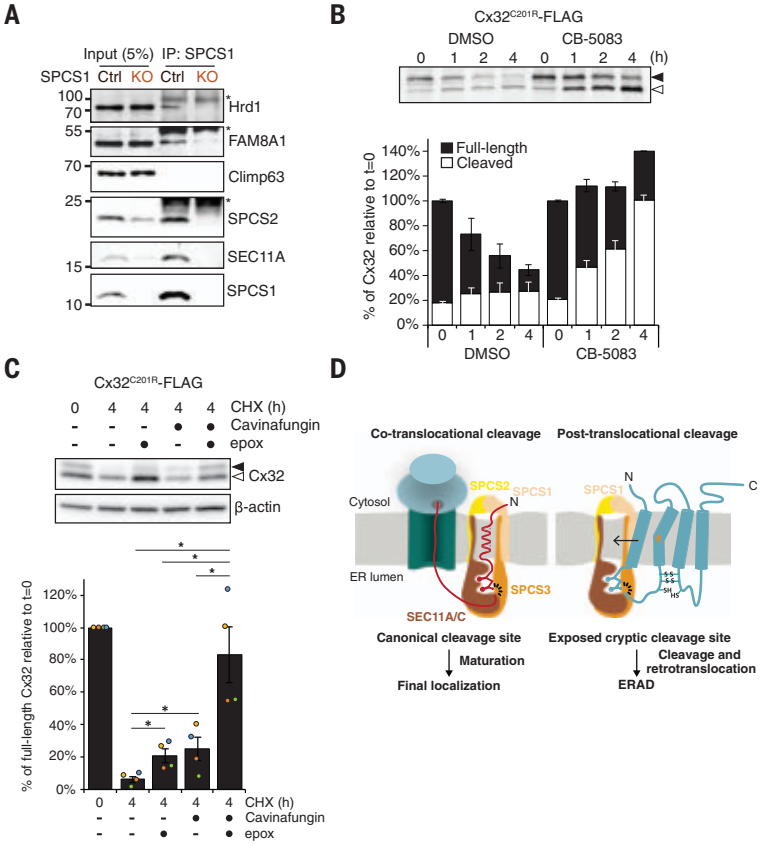


Fig. 4. SPC action synergizes with ERAD. (**A**) Endogenous SPCS1 was immunoprecipitated from HEK293T (Ctrl) and SPCS1 KO cells (nonspecific binding control), and samples were immunoblotted for different subunits of the SPC and Hrd1 complexes. Climp63 served as negative control. Asterisks indicate nonspecific bands. (**B**) (Top) Autoradiograph of HEK293T cells ectopically expressing Cx32^{C201R}-FLAG labeled for 10 min and chased for the indicated times. Where indicated, CB-5083 was added (10 μM) to inhibit p97-mediated dislocation. Full (empty) arrowhead: full-length (processed) Cx32^{C201R}. (Bottom) Quantification of full-length and cleaved Cx32^{C201R} (mean ± SEM; n = 3). (**C**) (Top) Immunoblot of HEK293T cells expressing FLAG-tagged Cx32^{C201R} and treated with CHX, cavinafungin (5 μM), and/or epoxomicin (epox, 5 μM). Actin served as loading control. (Bottom) Quantification of full-length Cx32^{C201R} relative to time t = 0 (mean ± SEM; n = 4; *P < 0.05). (**D**) (Left) Processing of a canonical signal peptide. (Right) Quality control function of the SPC, where noncanonical, cryptic cleavage sites are processed. SPCS1 may bind substrate TM domain followed by transition of the cleavage site into the SEC11 active site. Cleaved fragments are prone to ERAD.

causes SPC-mediated cleavage, disrupting a structural disulfide bridge in Cx32 increased cleavage, whereas other mutations without obvious structural consequences did not (fig. S9A). Pulse-chase experiments revealed that, when disulfide bonds in Cx32 were reduced by dithiothreitol (DTT), cleavage increased at a higher rate when DTT was added with a 0.5-hour delay after protein synthesis than if it was added initially (Fig. 3C and fig. S9B). This increase in $Cx32^{C201R}$ cleavage was independent of ER stress (fig. S9C). Of note, one of the disulfide bonds in Cx32 is close to its SPC cleavage site, so correct oxidative folding may shield this site (fig. S9D). Together, these findings further suggest that SPC cleavage serves as a posttranslational membrane protein quality control step, which may be more efficient when early folding factors have dissociated. In addition to intrinsic misfolding, failed assembly of membrane protein complexes may lead to subunit instability (*12*). To test whether SPC cleavage is also involved in subunit assembly and abundance control, we expressed iRhom2 with its partner TACE. In agreement with SPC cleavage being attributable to imbalanced subunit stoichiometry, TACE coexpression reduced iRhom2 cleavage (Fig. 3D). Likewise, a truncation of the ERAD E3 ubiquitin ligase Hrd1 that is deficient in assembly with ER interaction partners (*13*) was partially cleaved and degraded in an SPCS1-dependent manner (fig. S10).

Our data show that SPC cleavage is caused by defects in membrane protein folding and assembly, which suggests links to ERAD. Previous mass spectrometry analyses indicated an interaction of the SPC with Hrd1 (*14*), which is relevant in the light of the SPC quality control functions. Extending these findings, coimmunoprecipitation experiments revealed interaction of Hrd1 and its cofactor FAM8A1 with the SPC at endogenous levels (Fig. 4A), and the SPC also coimmunoprecipitated with Hrd1 (fig. S11A). In contrast, no pronounced interaction was observed with another major ERAD E3 ubiquitin ligase, gp78 (fig. S11B). Further supporting the functional relevance of this interaction, cycloheximide (CHX) chase showed that Hrd1 plays a role in clearance of SPC-generated $Cx32^{C201R}$ fragments (fig. S11C). Inhibiting p97-mediated retrotranslocation during ERAD caused a strong accumulation of the SPC-cleaved form of $Cx32^{C201R}$, along with a modest effect on the full-length protein (Fig. 4B). This stabilization of the cleavage fragment further indicates that SPC supports degradation of mutant membrane proteins, the generality of which was corroborated by similar results obtained for mutants of PMP22, Hrd1, and other connexins (figs. S2C, S10B, and S11D). In agreement with SPC-catalyzed cleavage promoting ERAD, cavinafungin led to a mild but significant stabilization of full-length $Cx32^{C201R}$ in CHX chase assays (Fig. 4C). This partial stabilization, which showed additive effects with proteasome inhibition, may be due to different ERAD pathways involved in Cx32 degradation (*15*), serving as an example of the general redundancy in ER protein homeostasis (*16*). Together, our data show that noncanonical SPC cleavage contributes to membrane protein quality control, and our computational analyses suggest this to be widespread. SPC-catalyzed cleavage of TM segments may thus be relevant for resilience toward protein folding stress in the ER. Consistent with this, mRNA levels of the SPC subunits were up-regulated upon induction of ER stress (fig. S12A), although ER import generally drops (*17*), and SPCS1 knockout cells performed significantly worse under ER stress conditions (fig. S12B). In conjunction with the absence of observed detrimental effects of SPCS1 ablation on canonical signal peptide processing (fig. S5, C to F), this indicates a role for the SPC in cellular protein homeostasis. This notion was further supported by our findings that SPC played a role in rebalancing Hrd1 levels after ER stress subsided (fig. S12C).

This study reveals that the SPC, discovered in the 1970s to cleave ER signal peptides (*3*), has a previously unanticipated and widespread quality control function for membrane proteins. Cryptic SPC cleavage sites thus might have evolved to serve as predetermined "breaking points" that, when exposed, support targeting misfolded or surplus proteins toward degradation. The quality control activity of the SPC helps to remove faulty membrane proteins from the cellular pool, to control protein assembly, and to mitigate ER stress, together increasing cellular fitness. This second mode of posttranslocational SPC processing (Fig. 4D) shows notable parallels to N-linked glycosylation, which can occur co- and posttranslationally (*18*). The latter depends on recognizing cryptic glycosylation sites within otherwise folded domains as part of a triage-salvage system (*19*). Our data suggest that the noncatalytic SPCS1 subunit, which has recently been shown to be down-regulated in Alzheimer's disease patients' brains (*20*), is critically involved in the SPC quality control functions (Fig. 4D). To protect immature membrane proteins from SPC-mediated cleavage, the large number of membrane-integral and soluble chaperones that are in close proximity to the Sec61 translocon (*21*) may be relevant, whereas folded membrane proteins can be expected to have cryptic cleavage sites no longer accessible to the SPC (fig. S13). In general, the ER translocon appears to provide a protected environment for protein biogenesis. In contrast, at distal sites and/or after a time window that provides an opportunity for folding and further transport, pro-degradation quality control functions are more likely. Extending these concepts, our study now reveals a role of the SPC in ER protein quality control.

REFERENCES AND NOTES

1. J. T. Marinko *et al.*, *Chem. Rev.* **119**, 5537–5606 (2019).
2. M. K. Lemberg, K. Strisovsky, *Mol. Cell* **81**, 2507–2519 (2021).
3. G. Blobel, B. Dobberstein, *J. Cell Biol.* **67**, 835–851 (1975).
4. A. M. Liaci *et al.*, *Mol. Cell* **81**, 3934–3948.e11 (2021).
5. E. L. Snapp *et al.*, *eLife* **6**, e26067 (2017).
6. R. Zhang *et al.*, *Nature* **535**, 164–168 (2016).
7. M. M. Falk, L. K. Buehler, N. M. Kumar, N. B. Gilula, *EMBO J.* **16**, 2703–2716 (1997).
8. D. Estoppey *et al.*, *Cell Rep.* **19**, 451–460 (2017).
9. C. Adrain, M. Zettl, Y. Christova, N. Taylor, M. Freeman, *Science* **335**, 225–228 (2012).
10. D. R. McIlwain *et al.*, *Science* **335**, 229–232 (2012).
11. C. Yim *et al.*, *J. Cell Sci.* **134**, jcs258936 (2021).
12. S. Juszkiewicz, R. S. Hegde, *Mol. Cell* **71**, 443–457 (2018).
13. J. Schulz *et al.*, *J. Cell Sci.* **130**, 3322–3335 (2017).
14. E. J. Fenech *et al.*, *eLife* **9**, e57306 (2020).
15. J. P. L. Coelho *et al.*, *Nat. Commun.* **10**, 672 (2019).
16. J. C. Christianson, P. Carvalho, *EMBO J.* **41**, e109845 (2022).
17. P. Walter, D. Ron, *Science* **334**, 1081–1086 (2011).
18. C. Ruiz-Canada, D. J. Kelleher, R. Gilmore, *Cell* **136**, 272–283 (2009).
19. T. Sato *et al.*, *Mol. Cell* **47**, 99–110 (2012).
20. H. Patel, R. J. B. Dobson, S. J. Newhouse, *J. Alzheimers Dis.* **68**, 1635–1656 (2019).
21. S. O'Keefe, M. R. Pool, S. High, *FEBS J.* **289**, 6835–6862 (2022).
22. G. Singh, russelllab/spc: SPC, version 1.0, Zenodo (2022); https://doi.org/10.5281/zenodo.7299849.

ACKNOWLEDGMENTS

We thank M. Spiess for cavinafungin, M. S. Diamond for SPCS1 knockout cells, I. R. Navi for the FLAG-gp78 plasmid, N. Blömeke for experimental support, and B. Schulman and C. Adrain for critical reading of the manuscript. **Funding:** This work was supported by a PhD fellowship from the German Academic Scholarship Foundation (D.K.) and by the German Research Foundation (DFG) grants LE 2749/2-1 (M.K.L.) and FE1581/1-2 (M.J.F.). M.K.L. and M.J.F. are indebted to the Fritz-Thyssen Foundation for supporting their work on connexins. Funding was also provided by the BMBF-funded de.NBI HD-HuB network, #031A537C (R.B.R. and G.S.). **Author contributions:** A.Z., J.P.L.C., M.K.L., and M.J.F. conceived the study. A.Z. and J.P.L.C. led the experimental work and, together with D.K., M.T., and D.A., performed all experiments. The experimental data were analyzed by A.Z., J.P.L.C., D.K., D.A., M.K.L., and M.J.F. Bioinformatic analyses were performed by G.S. and R.B.R., and molecular dynamics simulations were performed by M.H. and M.Z. The paper was written by A.Z., J.P.L.C., M.K.L., and M.J.F., with contributions from all other authors. **Competing interests:** The authors declare that they have no competing interests. **Data and materials availability:** The code to perform the computational analysis is available at https://github.com/russelllab/spc and has been deposited in Zenodo (*22*). A web application allows for interactive analysis of our predictions (http://spc.russelllab.org). **License information:** Copyright © 2022 the authors, some rights reserved; exclusive licensee American Association for the Advancement of Science. No claim to original US government works. https://www.science.org/about/science-licenses-journal-article-reuse

SUPPLEMENTARY MATERIALS

science.org/doi/10.1126/science.abo5672
Materials and Methods
Figs. S1 to S13
Table S1
References (*23–49*)
MDAR Reproducibility Checklist

Submitted 11 February 2022; resubmitted 7 October 2022
Accepted 7 November 2022
10.1126/science.abo5672

VOLCANOLOGY

Magma accumulation at depths of prior rhyolite storage beneath Yellowstone Caldera

Ross Maguire[1]*, Brandon Schmandt[2], Jiaqi Li[3], Chengxin Jiang[4], Guoliang Li[5], Justin Wilgus[2], Min Chen[6,7]

Seismic tomography has provided key insight into Yellowstone's crustal magmatic system that includes attempts to understand the melt distribution in the subsurface and the current stage of the volcano's life cycle. We present new tomographic images of the shear wave speed of the Yellowstone magmatic system based on full waveform inversion of ambient noise correlations, which illuminates shear wave speed reductions of greater than 30% associated with Yellowstone's silicic magma reservoir. The slowest seismic wave speeds (shear wave speed less than 2.3 kilometers per second) are present at depths between 3 and 8 kilometers, overlapping with petrological estimates of the assembly depth of erupted rhyolite bodies. Assuming that Yellowstone's magmatic system is a crystal mush with broadly distributed melt, we estimate a partial melt fraction of 16 to 20%.

The Yellowstone volcanic system has fueled some of the largest explosive caldera-forming eruptions in the geologic record, including three catastrophic eruptions in the past 2.1 million years (*1*, *2*). Explosive silicic eruptions on this scale can have widespread environmental impacts, including continent-wide ash falls, global climate disruption, and extinction events (*3*, *4*). At Yellowstone, the most recent Lava Creek eruption (0.64 million years ago) emplaced >1000 km^3 of rhyolitic material and blanketed much of the western United States and Great Plains in ash (*1*, *5*). The subsequent collapse of the magma reservoir shaped the current Yellowstone Caldera in northwestern Wyoming, which has since been filled with rhyolite flows as young as 70,000 years old (*1*). Although it is clear from geophysical observations that the modern Yellowstone magmatic system remains active (*6*, *7*), questions persist about the volume and distribution of melt and how it compares with conditions that preceded prior eruptions.

An emerging view of continental magma reservoirs is that a crystal mush zone (a crystal-dominated, partially molten body) can persist in the crust over long time scales (100,000 years or longer) but that eruptible melt-rich zones are likely to be short-lived (<5000 years) (*8*–*10*). From this perspective, layers of eruptible silicic melt rapidly accumulate near the top of the crystal mush zone before eruption. Thus, the presence or absence of a melt-rich zone at or near the top of the silicic magma reservoir could be an important indicator of where Yellowstone currently sits in its eruptive life cycle.

Seismic tomography provides one of the best tools for inferring the presence of melt in crustal magmatic systems, and numerous previous studies have produced images of the subsurface below Yellowstone that reveal a contemporary magma reservoir in the mid- to upper crust (*11*–*15*). The magma reservoir in these studies is typically imaged as a slow shear wave speed (V_S) anomaly of up to 10%, suggesting a relatively melt-poor system (<10% partial melt fraction). However, spatially isolated observations of scattered teleseismic body waves recorded at seismometers in or near Yellowstone Caldera indicate that the degree of partial melt could be much higher (*16*).

Seismic tomography has yielded important clues into Yellowstone's magmatic system, but imaging melt-rich zones remains challenging because small-scale magma bodies with severely reduced seismic wave speed are unlikely to produce substantial travel time delays of first arrivals due to wavefront healing (*17*). Additionally, strong low–wave speed anomalies may be further diminished in seismic images because of assumptions such as locally one-dimensional (1D) or ray-based seismic propagation and inversion regularization (*18*). Advances in tomographic inversions based on 3D numerical modeling of seismic waveforms, sometimes referred to as "full waveform inversion" (FWI), can overcome some limitations of conventional methods that rely on asymptotic ray-based approximations (*19*–*21*). The 3D sensitivity kernels used in FWI are able to account for complex wave propagation effects and thus more accurately map the location and amplitude of seismic wave speed anomalies.

We present new images of the V_S below Yellowstone based on FWI of ambient noise correlations. To take full advantage of the rich and diverse seismic datasets available in the Yellowstone region, our images combine data from numerous broadband deployments over the past 20+ years, including the EarthScope Transportable Array, several dense temporary deployments, and a recently updated seismic network within Yellowstone National Park (Fig. 1). Our tomographic inversion approach uses vertical component noise correlation functions (NCFs) from 4991 interstation pairs and minimizes frequency-dependent travel-time differences between NCFs and 3D synthetic waveforms in six overlapping period bands between 5 and 30 s (*22*). The final model $\mathbf{m}_{10}$ was achieved after 10 adjoint iterations, and it reduces the total misfit by ~50% compared with the starting model $\mathbf{m}_{00}$, which is based on conventional inversion techniques (*22*).

The tomographic images (Fig. 2) illuminate a strong V_S anomaly corresponding to the magma reservoir in the mid- to upper crust centered below the Yellowstone Caldera, with peak V_S reductions of >30%, which is substantially stronger than previously recognized. The slowest seismic wave speeds (V_S < 2.3 km/s) are present at depths between 3 and 8 km, with a minimum of 2.15 km/s at 5 km depth. Previous ray-based seismic tomography studies have imaged a mid- to upper crustal reservoir at ~5 to 15 km depth [for example, (*13*, *14*)]; the peak velocity anomaly typically lies between 7 and 10 km depth, which is deeper than most petrological estimates of the storage depth of previously erupted rhyolitic magmas. For example, a recent petrological study of the Lava Creek Tuff suggested melt storage pressures of 80 to 150 MPa, corresponding to a depth range of ~3 to 6 km (*23*). Similarly, the storage pressure of CO_2-rich magmas from the Central Plateau Member Rhyolites (eruption ages 175,000 to 70,000 years) is estimated to be between 90 and 150 MPa (*24*). Thus, our tomographic images suggest contemporary magma storage in a depth range overlapping with the storage zone of magmas that have supplied both explosive and effusive silicic eruptions at Yellowstone.

In map view, the maximum V_S reduction is offset from the center of the caldera toward the east (Fig. 2A) and overlaps with a cluster of seismicity below Yellowstone Lake. The maximum depth extent of the low V_S region below the caldera is ~30 km, although the anomaly is more subdued below 10 km, which suggests that melt is most concentrated at shallower reservoir depths. In addition to the low-velocity anomaly below Yellowstone Caldera, two other low-V_S regions are notable. First is a region of low V_S in the lower crust (~35 to 40 km depth) that extends to the southwest of Yellowstone along the Snake River Plain and appears to connect to the anomaly below the caldera (Fig. 2B). There, V_S reaches 3.5 to 3.6 km/s (approximately −8 to −9% slower than the regional

[1]Department of Geology, School of Earth, Society, and Environment, University of Illinois, Urbana, IL, USA. [2]Department of Earth and Planetary Sciences, University of New Mexico, Albuquerque, NM, USA. [3]Department of Earth, Planetary, and Space Sciences, University of California, Los Angeles, Los Angeles, CA, USA. [4]Department of Earth Sciences, Australian National University, Canberra, Australia. [5]Southern California Earthquake Center, University of Southern California, Los Angeles CA, USA. [6]Department of Computational Mathematics, Science, and Engineering, Michigan State University, East Lansing, MI, USA. [7]Department of Earth and Environmental Sciences, Michigan State University, East Lansing, MI, USA.
*Corresponding author. Email: rossrm@illinois.edu

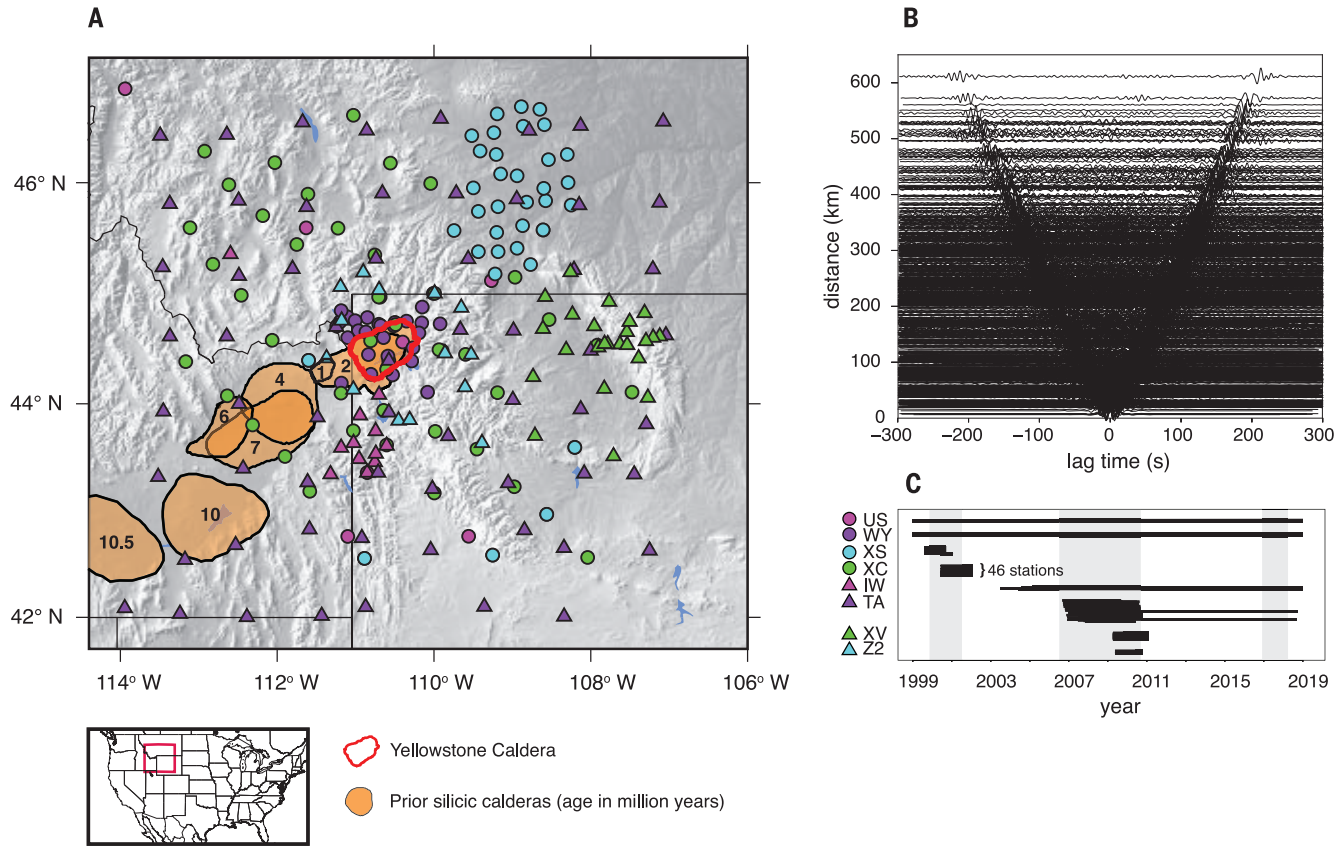


Fig. 1. Broadband seismic data used in this study. (**A**) Map of the station distribution. Symbols depict different seismic networks. (**B**) Record section of vertical component NCFs filtered between 6 and 25 s. Only 10% of the full dataset is plotted. (**C**) Timeline of data availability for each network. The symbols for each network correspond to stations indicated in (A). The gray vertical bars indicate the time periods for which cross correlations were performed.

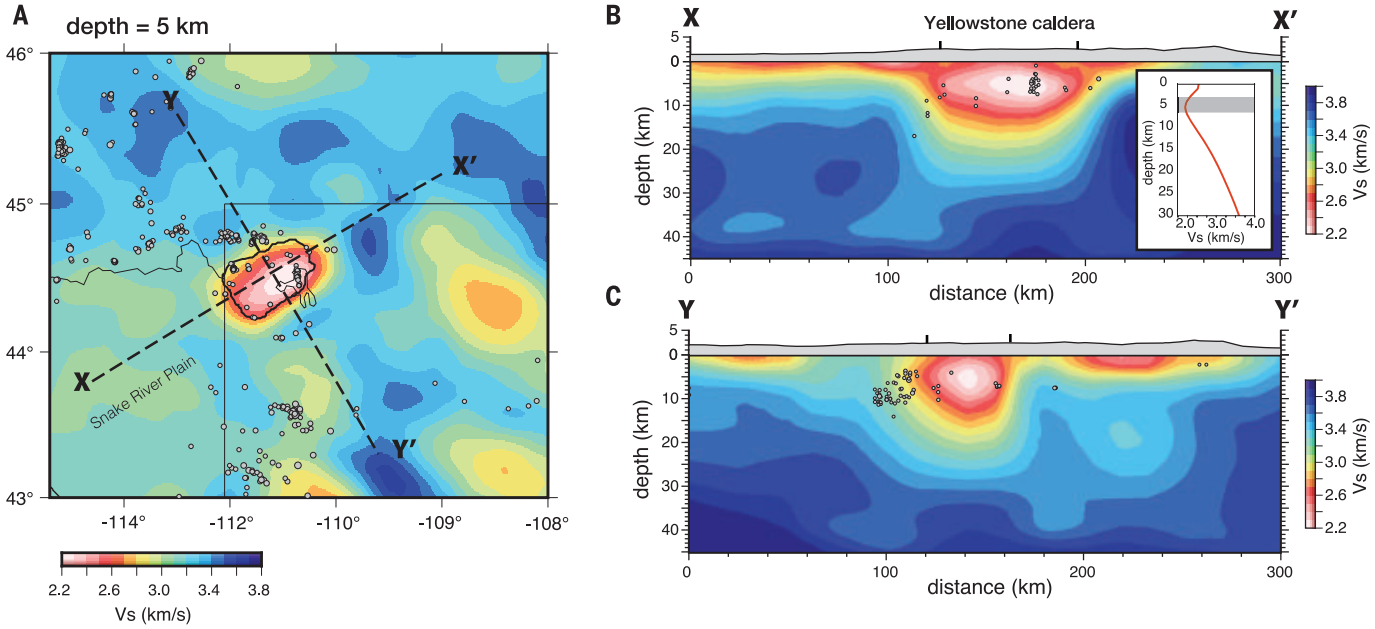


Fig. 2. Yellowstone shear wave speed model. (**A**) Map view of V_S at 5-km depth below the surface. The irregular outline toward the east side of the caldera is Yellowstone Lake. (**B** and **C**) Vertical cross sections along profiles X–X′ and Y–Y′, respectively. Seismic events with M_w > 3.0 that occurred in the past 20 years are plotted as gray circles. In vertical cross sections, seismic events within ±15 km in the lateral direction are projected onto the slice. (Inset) The V_S profile at the center of the caldera. The gray shaded region corresponds to petrologically estimated storage depths of past eruptive reservoirs (*22*, *23*).

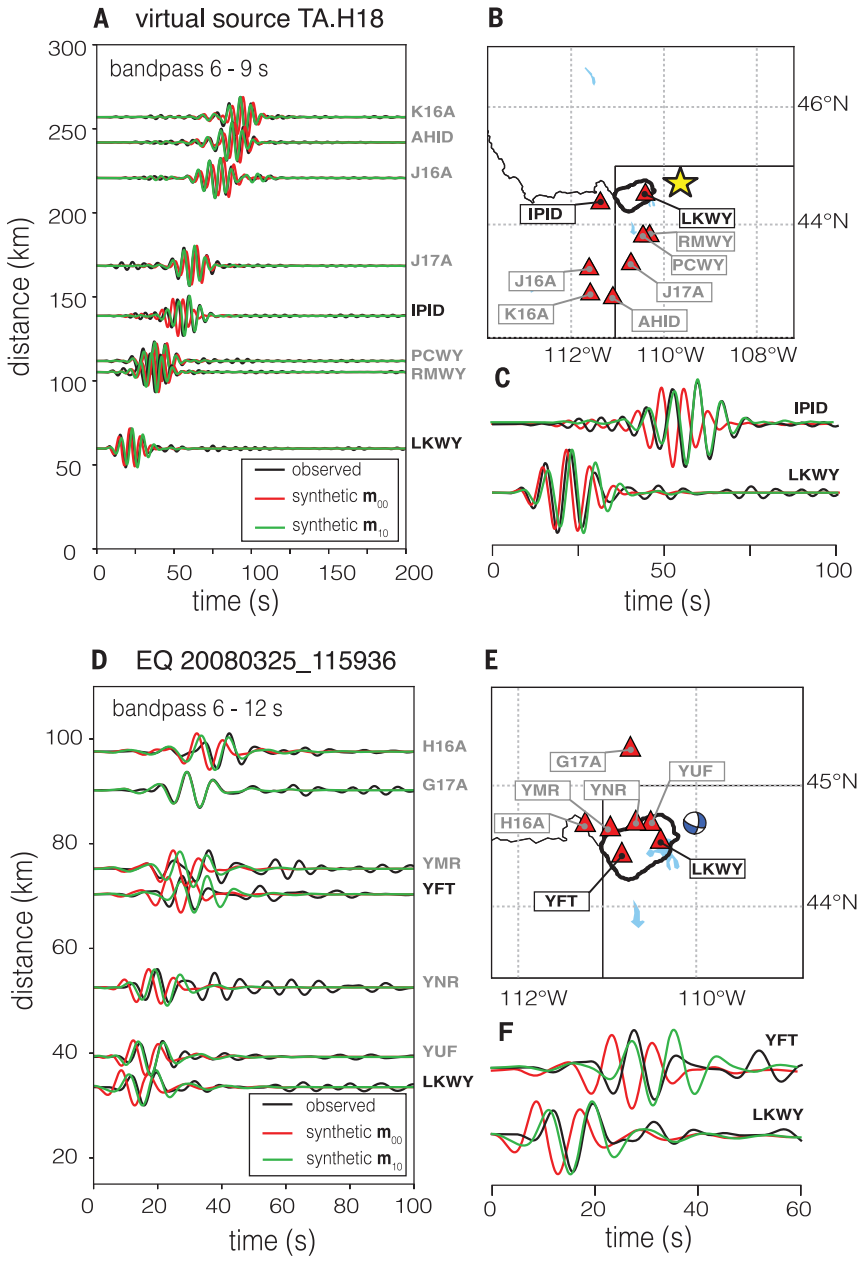


Fig. 3. Waveform fits between observed and synthetic seismic data. (**A** to **C**) Waveforms from virtual source TA.H18 [(B), yellow star], filtered between 6 and 9 s. (**D** to **F**). Waveforms from a M_w 4.2 event located northeast of Yellowstone Caldera, filtered between 6 and 12 s. Observed data are indicated in black, and synthetics from the starting model and final model are indicated in red and green, respectively. Earthquake data were not used in the seismic inversion and are only shown for model validation.

average), which is consistent with previous studies [for example, (*12*)]. This region lies above exceptionally slow mantle (*12*) and could represent a deep crustal reservoir of basaltic melt, although how it connects with the shallow silicic reservoir is unclear. Second, a region of low V_S to the southeast of Yellowstone Caldera is imaged in the mid-crust with a minimum V_S of ~3.4 km/s (Fig. 2C), which is enhanced compared with that in previous studies [for example, (*15*)].

Improved waveform fitting compared with our tomographic starting model demonstrates that the extreme V_S anomaly below the caldera is required by the data (Fig. 3 and figs. S8 to S10). Short-period waveform fits along paths that directly traverse the caldera are most notably improved. Shown in Fig. 3, A to C, is a comparison between observed and synthetic NCFs filtered between 6 and 9 s for a virtual source at station H18A. Although the starting model $\mathbf{m}_{00}$ produces good waveform fits for most of the paths, a large travel-time delay (>5 s) was observed at station IPID, which is located directly opposite from Yellowstone Caldera so that most of the path samples the magma reservoir. The waveform observed along this path is well explained by the final FWI model $\mathbf{m}_{10}$ (Fig. 3C). As further validation, we show waveform fits from a local moment magnitude (M_w) 4.2 earthquake that occurred to the northeast of the caldera on 25 March 2008 (Fig. 3, D to F). Data from this event was not used in the tomographic inversion; however, Rayleigh wave travel-time misfits were noticeably improved with model $\mathbf{m}_{10}$. The improved fit is most appreciable at stations LKWY and YFT, where paths most directly sample the magma reservoir (Fig. 3F).

The presence of partial melt in the crust has the effect of reducing seismic wave speed, although the relationship between the melt fraction and the spatially averaged V_S structure as seen with seismic tomography is difficult to constrain and depends on temperature, composition, and the geometrical organization of melt in the crust. We estimated the melt fraction of Yellowstone's upper crustal reservoir using a theoretical model of a solid-liquid composite with ellipsoidal melt inclusions defined by their aspect ratio (*22*, *25*). We show the modeled relationship between V_S and melt fraction for various aspect ratios, calibrated for a rhyolitic composition at 5 km depth (Fig. 4A). Silicic partial melt in textural equilibrium exhibits a dihedral angle of 20° to 40°, corresponding to an aspect ratio of 0.1 to 0.15 (*26*, *27*), which implies a crystal mush with a melt fraction of 16 to 20% near the top of the upper-crustal reservoir (Fig. 4B). Under these assumptions, we estimated the total volume of silicic melt in the upper-crustal reservoir to be >1600 km^3 (*22*). On the basis of this melt fraction scaling, previous shear wave tomography models of Yellowstone's magmatic system (*12*, *15*) would map to ~10% melt or less. If melt is organized in networks of thin crystal-poor sills (*15*), the aspect ratio could be less than 0.1. However, sills may not contain 100% melt, and silicic partial melt is likely to exist at grain boundaries in crystal-rich portions of the magma reservoir. An aspect ratio of the magmatic system of <0.1 would imply a lower melt fraction but a stronger organization of melt into layered structures, which could decrease the stability of the system because an eruptible body could rapidly assemble from interconnected sills (*28*).

Mobilization and eruption of a crystal mush is possible when the melt fraction exceeds the critical threshold that marks the transition from a crystal-supported framework to a fluid suspension of crystals, which is accompanied by a dramatic viscosity decrease. Estimates of the critical melt fraction range from ~35% (*16*) to ~50% melt (*29*); thus, the melt fraction we

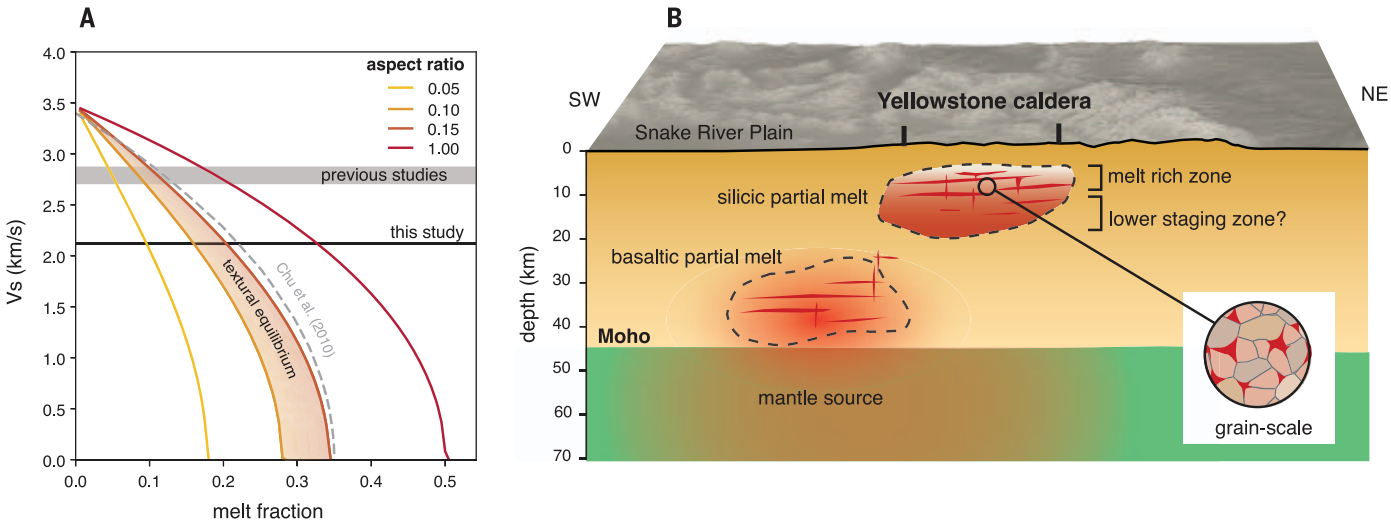


Fig. 4. Conceptual model of Yellowstone's magmatic system. (**A**) Melt fraction modeling. Yellow and red curves indicate the relationship between V_S and melt fraction, assuming different aspect ratios. The black horizontal line indicates the observed V_S in this study at 5-km depth below the center of the caldera, and the gray shaded region indicates results from previous imaging studies. (**B**) Cartoon diagram of Yellowstone's crustal magmatic system from southwest to northeast. Melt in the upper crustal reservoir is likely organized as melt-rich sills surrounded by melt-poor regions where diffuse melt accumulates at crystal grain boundaries. The top of the reservoir is characterized by exceptionally low seismic velocities, indicating the presence of a region with high melt fraction. Low velocities observed in the lower crust below the Snake River Plain may indicate a deeper storage zone of basaltic melt.

estimated is substantially lower than what would be expected if a large fraction of the Yellowstone reservoir were in the eruptible stage of its life cycle. However, the presence of small subset volumes of concentrated silicic melt cannot be ruled out. For example, features smaller than the minimum seismic wavelength (in this case, ~15 km) may not be well resolved, suggesting that high–melt fraction bodies of several hundred cubic kilometers or more could be present in Yellowstone's magma reservoir. Such subset volumes of the magma reservoir would be capable of supplying eruptions comparable in size with those of the 170,000- to 70,000-year-old Central Plateau Member Rhyolites, which included at least 17 flows with volumes of ~5 to 50 km^3 (*1*).

Rapid migration of silicic magma is difficult because of its high viscosity and the low permeability of crystal mushes; however, compaction-driven viscosity reductions from renewed melt injection can facilitate melt extraction on 1000-year time scales (*30*), and viscous "unlocking" of crystal mushes can be triggered by strain events that lubricate grain boundaries (*31*). Although our results indicate that Yellowstone's magma reservoir contains substantial melt at depths that fueled prior eruptions, our study does not confirm the presence of an eruptible body or imply a future eruption. Strain events such as new magma intrusions or tectonic deformation that could begin to mobilize and concentrate magma would likely be accompanied by a host of dynamic processes evident to ongoing geophysical and geochemical monitoring (*1*, *6*).

REFERENCES AND NOTES

1. R. L. Christiansen *et al.*, *Preliminary Assessment of Volcanic and Hydrothermal Hazards in Yellowstone National Park and Vicinity* (US Geological Survey, 2007).
2. C. J. Wilson *et al.*, *Nat. Rev. Earth Environ.* **2**, 610–627 (2021).
3. S. Self, *Philos. Trans. A Math. Phys. Eng. Sci.* **364**, 2073–2097 (2006).
4. M. T. Jones, R. S. J. Sparks, P. J. Valdes, *Clim. Dyn.* **29**, 553–564 (2007).
5. N. E. Matthews, J. A. Vazquez, A. T. Calvert, *Geochem. Geophys. Geosyst.* **16**, 2508–2528 (2015).
6. J. B. Lowenstern, S. Hurwitz, *Elements (Quebec)* **4**, 35–40 (2008).
7. W. L. Chang, R. B. Smith, J. Farrell, C. M. Puskas, *Geophys. Res. Lett.* **37**, n/a (2010).
8. M. E. Stelten *et al.*, *J. Petrol.* **56**, 1607–1642 (2015).
9. J. F. Wotzlaw, I. N. Bindeman, R. A. Stern, F. X. D'Abzac, U. Schaltegger, *Sci. Rep.* **5**, 14026 (2015).
10. A. E. Rubin *et al.*, *Science* **356**, 1154–1156 (2017).
11. S. Husen, R. B. Smith, G. P. Waite, *J. Volcanol. Geotherm. Res.* **131**, 397–410 (2004).
12. J. C. Stachnik, K. Dueker, D. L. Schutt, H. Yuan, *Geochem. Geophys. Geosyst.* **9**, 10.1029/2008GC001992 (2008).
13. J. Farrell, R. B. Smith, S. Husen, T. Diehl, *Geophys. Res. Lett.* **41**, 3068–3073 (2014).
14. H. H. Huang *et al.*, *Science* **348**, 773–776 (2015).
15. C. Jiang, B. Schmandt, J. Farrell, F. C. Lin, K. M. Ward, *Geology* **46**, 727–730 (2018).
16. R. Chu, D. V. Helmberger, D. Sun, J. M. Jackson, L. Zhu, *Geophys. Res. Lett.* **37**, n/a (2010).
17. G. Nolet, F. A. Dahlen, *J. Geophys. Res.* **105** (B8), 19043–19054 (2000).
18. R. Maguire *et al.*, *Geochem. Geophys. Geosyst.* **23**, (2022).
19. C. Tape, Q. Liu, A. Maggi, J. Tromp, *Science* **325**, 988–992 (2009).
20. M. Chen, H. Huang, H. Yao, R. van der Hilst, F. Niu, *Geophys. Res. Lett.* **41**, 334–340 (2014).
21. A. F. Flinders *et al.*, *Geology* **46**, 799–802 (2018).
22. Materials and methods are available as supplementary materials.
23. H. I. Shamloo, C. B. Till, *Contrib. Mineral. Petrol.* **174**, 32 (2019).
24. K. S. Befus, J. E. Gardner, *Contrib. Mineral. Petrol.* **171**, 30 (2016).
25. J. G. Berryman, *J. Acoust. Soc. Am.* **68**, 1820–1831 (1980).
26. M. B. Holness, *J. Petrol.* **47**, 791–800 (2005).
27. Y. Takei, *J. Geophys. Res. Solid Earth* **107**, ECV-6 (2002).
28. K. V. Cashman, G. Giordano, *J. Volcanol. Geotherm. Res.* **288**, 28–45 (2014).
29. L. Caricchi, L. Burlini, P. Ulmer, *J. Volcanol. Geotherm. Res.* **178**, 740–750 (2008).
30. B. Liu, C. T. Lee, *Earth Planet. Sci. Lett.* **571**, 117113 (2021).
31. G. W. Bergantz, J. M. Schleicher, A. Burgisser, *J. Geophys. Res. Solid Earth* **122**, 6131–6159 (2017).

ACKNOWLEDGMENTS

This project benefited greatly from discussions with A. Ficthner, F.-C. Lin, and N. Schmerr as well as the input from three anonymous reviewers. Seismic data were acquired from the IRIS DMC, which is supported by NSF EAR-1851048. We dedicate this work to our coauthor and friend Min Chen, who is dearly missed. **Funding:** R.M. was supported by an NSF postdoctoral Fellowship (EAR-PD 1806412), and B.S. was supported by NSF EAR-1950328. **Author contributions:** Conceptualization: R.M., B.S., and M.C. Methodology and software: R.M., J.L., C.J., J.W., and G.L. Formal analysis: R.M. Writing – original draft: R.M. and B.S. Writing – review and editing: R.M., B.S., J.L., C.J., J.W., and G.L. Supervision: B.S. and M.C. **Competing interests:** The authors have no competing interests to declare. **Data and materials availability:** All data used in this study are available through the IRIS DMC (https://ds.iris.edu/ds/nodes/dmc) by using the metadata in table S1. The codes used for ambient noise signal processing are available at https://gitlab.com/rmaguire/ambient2. **License information:** Copyright © 2022 the authors, some rights reserved; exclusive licensee American Association for the Advancement of Science. No claim to original US government works. https://www.science.org/about/science-licenses-journal-article-reuse

SUPPLEMENTARY MATERIALS

science.org/doi/10.1126/science.ade0347
Materials and Methods
Figs. S1 to S11
Tables S1 and S2
References (*32*–*50*)

Submitted 20 July 2022; accepted 11 October 2022
10.1126/science.ade0347

WILDFIRES

Early snowmelt and polar jet dynamics co-influence recent extreme Siberian fire seasons

Rebecca C. Scholten[1]*, Dim Coumou[1,2], Fei Luo[1,2], Sander Veraverbeke[1]

The summers of 2019, 2020, and 2021 experienced unprecedented fire activity in northeastern Siberia, driven by record high spring and summer temperatures. Many of these fires burned in permafrost peatlands within the Arctic Circle. We show that early snowmelt together with an anomalous Arctic front jet over northeastern Siberia promoted unusually warm and dry surface conditions, followed by anomalously high lightning and fire activity. Since 1966, spring snowmelt has started 1.7 days earlier each decade. Moreover, Arctic front jet occurrences in summer have more than tripled in frequency over the last 40 years. These interconnected climatological drivers promote extreme fire activity in eastern Siberia, including a northward shift of fires, which may accelerate the degradation of carbon-rich permafrost peatlands.

The years 2019, 2020, and 2021 marked the three largest fire years since at least 2001 in eastern Siberia. A considerable portion (38%) of the burned area occurring within the Arctic Circle between 2001 and 2021 occurred in these 3 years only, and almost all (92%) was located in the northern larch forests and tundra of central and eastern Siberia. Larch trees are among the only tree species adapted to poor, shallow permafrost soils (*1*) and they dominate Siberia's northeastern boreal forest. Subsurface, carbon-rich fuels make up about 75% of the carbon emissions from wildfires in this region (*2*). Northern wildfires are a strong accelerator of permafrost thaw (*3*), leading to emissions from both gradual and abrupt thaw processes (*4*). Such emissions are currently not included in the carbon budgets underlying the Paris Climate Agreement (*5*).

The Arctic is warming twice as fast as the global average (*6*, *7*), a phenomenon known as Arctic amplification. Likewise, fire activity in high-latitude regions is intensifying as a result of increases in dry fuels (*8*, *9*) and lightning (*10*, *11*). Fuels are abundant in arctic-boreal ecosystems and fire weather determines fuel flammability, ignition potential, and fire spread behavior. Lightning from convective thunderstorms is responsible for ignition for most arctic-boreal burned areas (*10*). Thus, large fire years in boreal regions usually originate during short periods of extreme weather (*9*). Warm and dry spring and summer conditions also drive circumpolar tundra fires (*12*). In June 2020, a 6-month period of anomalously high temperatures in eastern Siberia culminated in the highest temperature on record (38°C) measured within the Arctic Circle (*13*). Recent studies (*13*, *14*) have linked these extreme temperatures to anthropogenic climate change. Moreover, spring snowmelt occurred exceptionally early over Siberia in 2020, consistent with pronounced downward trends in circumpolar Arctic spring snow cover (*15*). Large fires in southeastern Siberia (*16*) and the western US (*17*) have previously been linked to early snowmelt onsets. Early snowmelt enables a longer period of fuel drying during which ignitions and fire spread can occur (*17*) and influences atmospheric circulation by governing surface heating and evapotranspiration (*18*, *19*).

Over the past decades, notable changes have occurred in hemispheric-scale summer circulation in the mid- to high latitudes of the Northern Hemisphere (*20*–*23*). Although Arctic amplification is generally more prominent during the cold season, it remains pronounced over the warm season as well. In summer, Arctic amplification is characterized by (i) reductions in snow cover over land (*24*), (ii) rapid retreat of sea ice over the Arctic ocean (*25*), (iii) enhanced warming at higher altitudes over the Arctic (*26*), and (iv) associated reductions in the equator-to-pole temperature gradient (*20*). This results in a hemispheric warming pattern that peaks near 65°N and that is likely attributable to anthropogenic carbon emissions (*27*). This warming pattern is likely linked to the observed weakening of the midlatitude westerlies and storm tracks since 1979, something that is also projected by climate models under future emission scenarios (*20*, *21*, *28*). Further, the warming pattern might favor the occurrence of "double jet" states, which are characterized by a narrow subtropical jet and pronounced Arctic front jet (*29*). In fact, recent work has shown that such double jet states have become more frequent and more persistent over the last 40 years, with important implications for weather extremes in the midlatitudes (*21*, *27*, *29*–*31*). Potential effects on the climate-sensitive high latitudes, however, remain poorly understood.

Extreme fire years

We analyzed fire data from the Moderate Resolution Imaging Spectrometer (MODIS) Collection 6 burned area (*32*) and active fire (*33*) products for the years 2001 to 2021 and extracted weeks with extreme fire activity over the study area (Fig. 1), based on deviations from the climatology of the burned area. Between 2001 and 2021 we found a total of 36 weeks during June, July, and August when the burn anomaly in northern (>56°N) larch forests of Siberia exceeded the climatological average by more than one standard deviation

[1]Faculty of Science, Vrije Universiteit Amsterdam, Amsterdam, Netherlands. [2]Royal Netherlands Meteorological Institute (KNMI), De Bilt, Netherlands.
*Corresponding author. Email: r.c.scholten@vu.nl

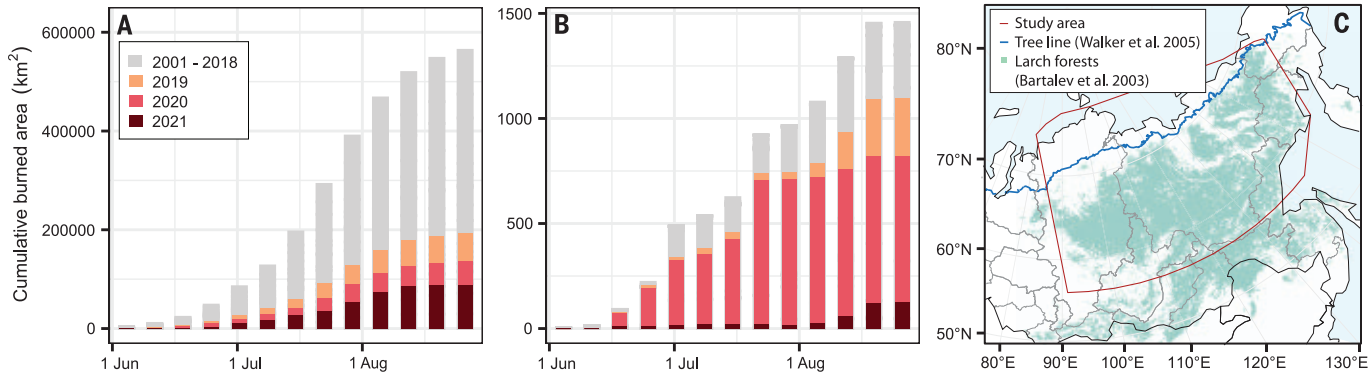


Fig. 1. The years 2019 to 2021 experienced an anomalously high amount of burned areas above 56°N in eastern Siberia. Bars represent cumulative burned areas over the 13 weeks of summer (June, July, August) in (**A**) boreal forest and (**B**) tundra regions. (**C**) Map of the study area.

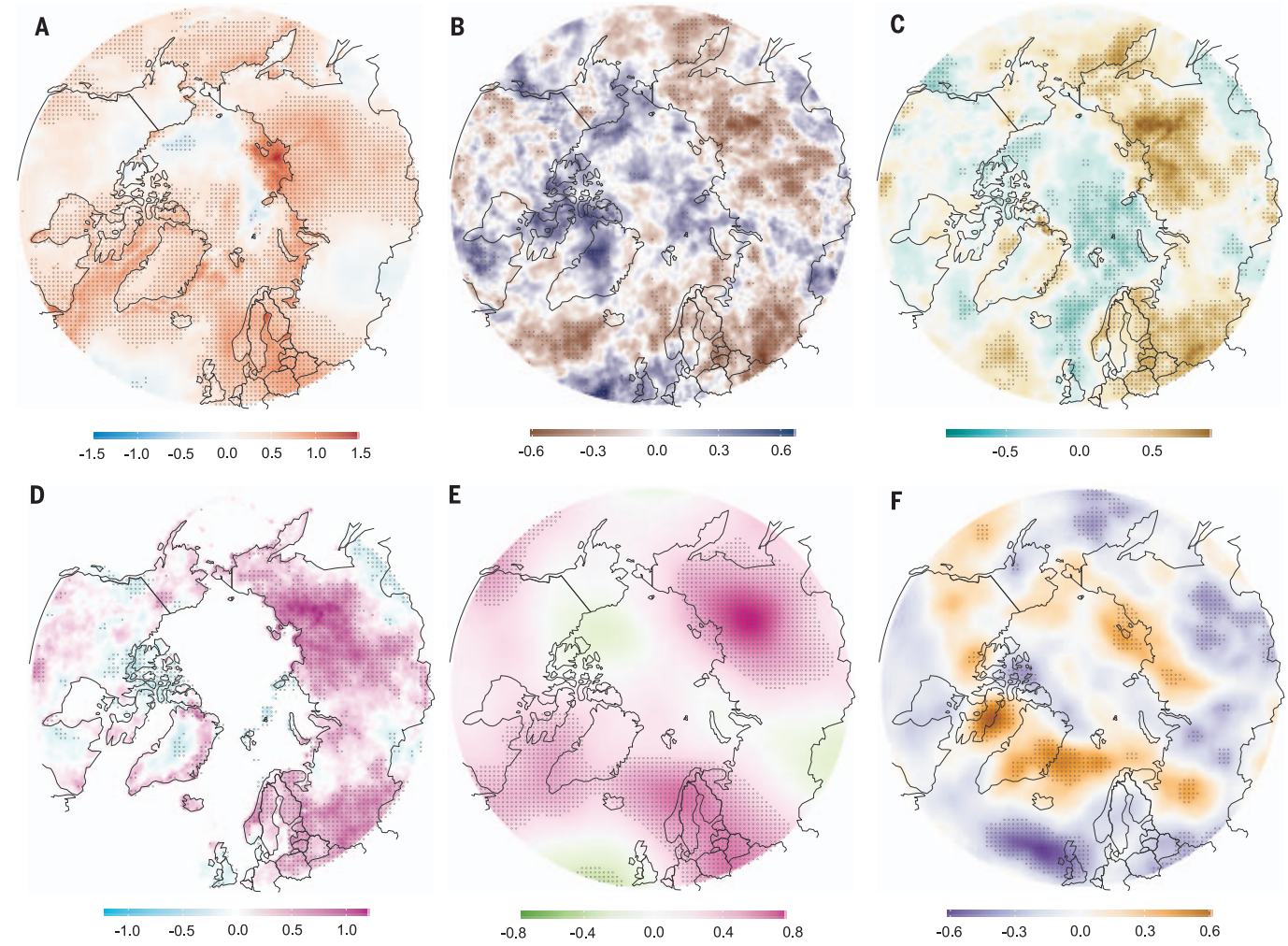


Fig. 2. Composite plots of synoptic and surface weather anomalies during weeks of high fire activity in northeastern Siberia. (**A**) 2-m temperature anomaly, (**B**) total precipitation anomaly, (**C**) 2-m vapor pressure deficit anomaly, (**D**) fire weather index anomaly, (**E**) 500-hPa geopotential anomaly, (**F**) 250-hPa wind anomaly. Weeks of high fire activity were defined as weeks with burned areas exceeding the mean plus one standard deviation of the climatology for June, July, and August in 2001 to 2021 (n = 36). Stippled areas show significant (α = 0.05) differences between the composite and the climatology based on t tests corrected for false discoveries.

(SD), half of which occurred during the summers of 2019 to 2021 (table S1). Burning during these extreme fire weeks accounted for 41% of the total burned area between 2001 and 2021 (Fig. 1A and table S1). The year 2021 was the largest fire year on record, comprising 16% of the burned area in the Siberian larch forests between 2001 and 2021, followed by 2019 and 2020 with 10 and 9%, respectively. In addition, 2019 and 2020 featured extraordinarily large burned areas in northern tundra regions (Fig. 1B). The anomalously large burned area was also associated with elevated fire intensity as measured by satellite-derived fire radiative power (fig. S1).

Compound drivers of extreme fire years

We used meteorological data from the fifth generation ECMWF atmospheric reanalysis, ERA5 (*34*), to assess surface and synoptic weather anomalies during extreme fire weeks. Extreme fire weeks were anomalously warm and dry (Fig. 2, A and B) over northeastern Siberia, as compared to the climatology of 1979 to 2021. These hot and dry conditions are also reflected in higher levels of water vapor pressure deficit and fire weather index (Fig. 2, C and D), which are excellent predictors of fire activity influencing ignition efficiency and fire spread (*35*). Positive geopotential height anomalies over Siberia during extreme fire weeks (Fig. 2E) suggest that blocking events connected to large scale atmospheric circulation are causing these conditions favorable for fire ignition and spread.

Composites of the 250-hPa total wind anomaly reveal an Arctic front jet during the unusually warm and dry extreme fire weeks (Fig. 2F and fig. S2). An Arctic front jet state represents a northward displaced polar jet at around 70°N persisting over a wide range of longitudes. The Arctic front jet pattern is characterized by negative total wind anomalies in the midlatitudes and positive anomalies along the Arctic coastline, particularly in Siberia. We computed the pattern correlation between the circumpolar Arctic front jet pattern during extreme fire weeks (Fig. 2F) and the weekly 250-hPa wind anomaly over the same area to quantify the presence of an Arctic front in any given week (supplementary text). We found strong annual correlations between total summer fire activity and Arctic front jet pattern correlation averaged over all summer weeks (ρ = 0.66, P = 0.001).

In 2020, snowmelt occurred on average 4 days (SD = 9 days) earlier than the 2001 to 2021 climatology in Siberian larch forests and tundra, and 8 days (SD = 7 days) earlier in the Arctic Circle of northeastern Siberia (fig. S3). Snowmelt timing is significantly correlated to summer fire activity (ρ = –0.68, P = 0.001) and is a strong predictor of extreme fire weeks in

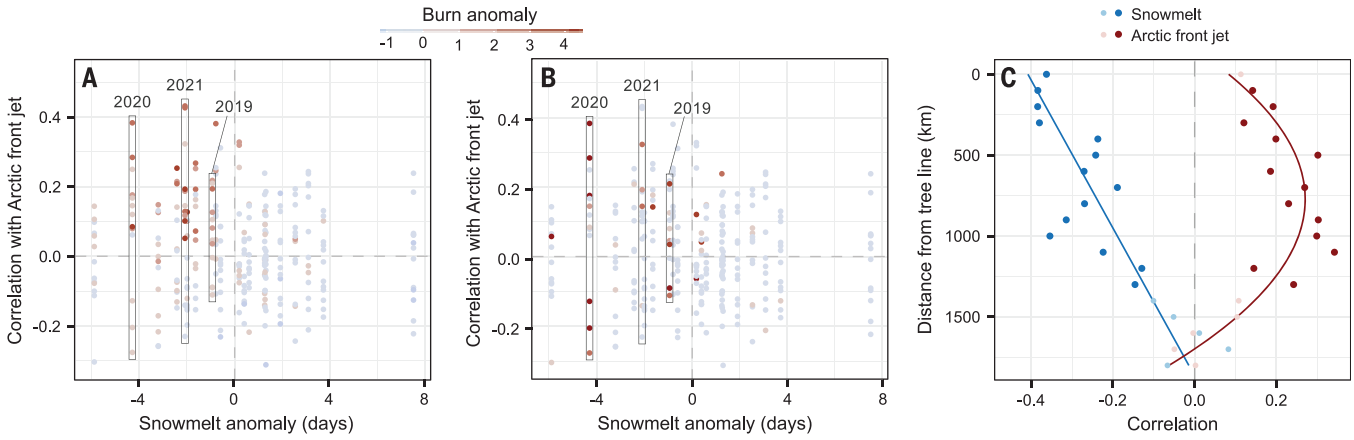


Fig. 3. Compound effect of spring snowmelt and Arctic front jet occurrence on burn anomaly in eastern Siberia between 2001 and 2021. Data points represent weekly averages in (**A**) boreal forest and (**B**) tundra ecosystems. Dashed gray lines denote the zero anomalies in snowmelt and the zero correlation with the Arctic front jet pattern. (**C**) Influence of snowmelt (blue) and Arctic 5 front jet pattern (red) on fire activity in distance from treeline (binned to 100 km, 0 denotes all tundra regions). Darker dots represent significant correlations (α = 0.05), lighter dots insignificant correlations. Lines are fitted using loess regression (span = 5) for Arctic front jet occurrence and linear regression for snowmelt.

Siberia, especially when an Arctic front jet is present. While the probability for an anomalous fire week was 2% in years with late snowmelt (negative snowmelt anomaly), it increased to 25% in years with early snowmelt (positive snowmelt anomaly), and to 44% for weeks with a positive Arctic front jet pattern correlation in addition to an early snowmelt (upper left corner in Fig. 3A). The recent extreme years 2019 to 2021 were all characterized by an earlier-than-usual snowmelt and featured several Arctic front jet occurrences in summer (Fig. 3A). A linear model to estimate the annual burn anomaly from snowmelt and the Arctic front jet pattern correlation yielded an R^2 of 0.77 ($P < 0.001$), with 23.3% of the variation explained by snowmelt timing, 58.3% by the Arctic front jet pattern, and 18.4% by their combined influence. These results were confirmed by a weekly burn anomaly model, which was trained out-of-sample to avoid overfitting (supplementary text). The influences of both drivers were further consistent across different terrain types (fig. S4). The influence of early snowmelt is particularly important in the far north whereas the Arctic front jet is especially important in driving fires south of the northern treeline (Fig. 3C).

Northward shift of lightning and fires

The compound effect of early snowmelt and Arctic front jet occurrences also promoted excessive burning in northern tundra ecosystems (Fig. 3B). Of the total burned area above the northern treeline in northeastern Siberia between 2001 and 2021, 75% occurred between 2019 and 2021. The probability for anomalous fire activity above the northern treeline was 16% for summer weeks during which an Arctic front jet had formed after early snowmelt, compared with only 1% for summer weeks without Arctic front jet and late snowmelt (compare upper left corner and lower right corner in Fig. 3B). Compared with 2019 (272 km^2) and 2020 (694 km^2), 2021 featured less tundra burning (124 km^2) as a result of the more southward position of the Arctic front jet and its associated high-pressure region (fig. S5).

Fires in boreal forest and tundra regions are usually ignited by lightning strikes or human activity. In Yakutia, which comprises 68% of the total burned area within our study area, recent studies estimated that approximately 50% of the burned area has an anthropogenic cause, 31 to 43% stems from lightning strikes, and the remainder results from overwintering fires or has unknown cause (*36*, *37*). However, in sparsely populated northern tundra ecosystems, ignitions are rare and lightning is the source of most burned areas (*10*, *11*). We analyzed Global Lightning Detection (GLD360) lightning data for 2012 to 2021 to assess whether early snowmelt and Arctic front jet formation increased boreal forest and tundra lightning activity. Anomalously high lightning activity (exceeding the 2012 to 2021 climatology by more than one SD) was more than three times as likely during extreme fire weeks (probabilities: 0.38 for boreal forest, 0.33 for tundra) compared with other weeks (probabilities: 0.12 for boreal forest, 0.08 for tundra). More than half (54%) of all lightning strikes above the northern treeline between 2012 and 2021 occurred during these extreme weeks (fig. S6). The blocked anticyclone, associated with an Arctic front jet, creates favorable conditions for the buildup of strong convection needed for the generation of lightning-rich thunderstorms. Anomalous lightning activity was associated with Arctic front jet occurrences in boreal forest (ρ = 0.24, P = 0.005) and tundra ecosystems (ρ = 0.29, P = 0.001, fig. S6C). Likewise, spring snowmelt timing was inversely related to lightning activity in June and July in both boreal forest and tundra regions (fig. S6C), indicating that an early snowmelt incites early summer lightning anomalies.

Climate warming and extreme fires

Regional snowmelt in Siberia's larch forests has started 1.7 days earlier each decade since 1966 (P = 0.001), with even faster acceleration near the treeline (Fig. 4, A and B). To quantify potential trends in the frequency of the Arctic front jet pattern, we performed a sensitivity analysis using various thresholds for the pattern correlation, with the trend of the median threshold shown in Fig. 4C. Our analysis reveals an upward trend in the frequency of the Arctic front jet pattern throughout summer with 0.5 days (SD = 0.2, fig. S7) per decade since 1979. This translates to an increase in the average frequency of Arctic front jet states from 1.0 week (SD = 0.3) per year in 1980 to 3.1 weeks per year (SD = 1.0) in 2020, representing a tripling (average ratio: 3.3, SD = 0.6) in frequency over the last 40 years (fig. S7B). The underlying mechanisms behind these changes in Arctic front jets are not yet fully clear. They might be attributable to changing dynamics driven by a changing pole-to-equator temperature gradient but may also result from thermodynamical changes such as the thermal expansion of the lower troposphere with warming or regional feedbacks driving blockings (*38*). Nevertheless, the upward trends as reported here are consistent with those based on more advanced circulation analyses using self-organizing maps (*29*).

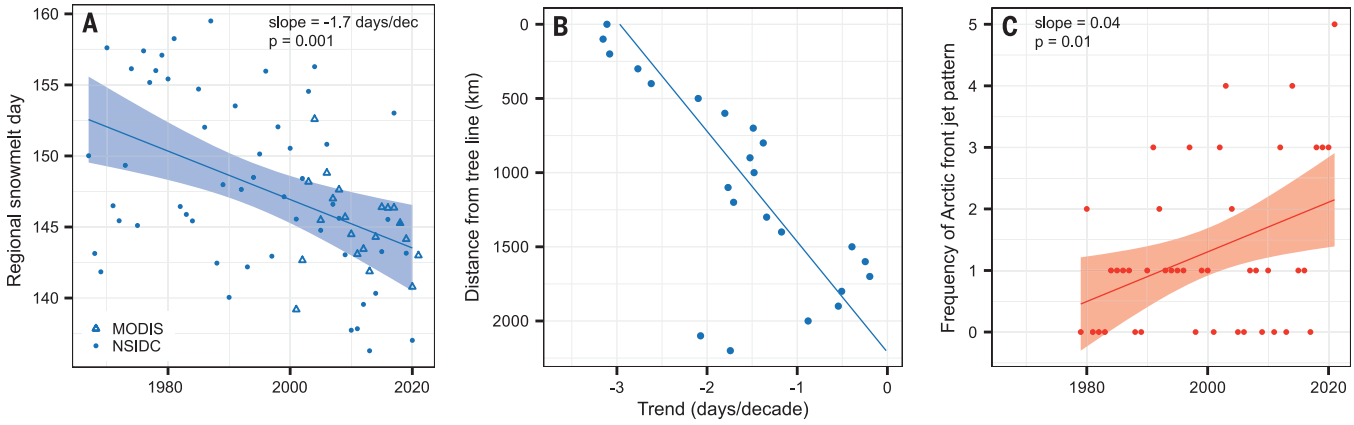


Fig. 4. Trends of the snowmelt timing and frequency of the Arctic front jet pattern. (**A**) Annual snowmelt timing averaged over the study area using the National Oceanic and Atmospheric Administration climate data record weekly snow cover product (NSIDC, filled circles) and the MODIS snow cover product (triangles). The linear trend was based on NSIDC data. (**B**) NSIDC snowmelt trend in relation to distance from treeline (binned to 100 km). All individual trends (dots) are significant (α = 0.05). (**C**) Frequency of the Arctic front jet (in weeks), estimated based on the pattern correlation of weekly 250-hPa wind anomalies with the Arctic front jet pattern (Fig. 2F). An Arctic front jet pattern was assumed for correlations exceeding 0.18 (see fig. S7 and methods for sensitivity analysis of the threshold). Shaded areas show the 95% confidence intervals of the trends.

Snowmelt and atmospheric circulation are strongly interconnected. Atmospheric circulation can accelerate snowmelt by governing the location of high- and low-pressure regions. For example, the early snowmelt in eastern Siberia in 2020 has been attributed to a strong stratospheric polar vortex in the preceding winter and spring that prevented cold Arctic air from penetrating into the midlatitudes (*13*). In addition, we show here that Arctic front jet states are associated with warmer and drier air over northern land areas, which may contribute to accelerating snowmelt in early summer. In return, the timing and magnitude of snowmelt influences atmospheric circulation through its influence on soil moisture and surface albedo. A darker surface and drier and warmer soils induced by early snowmelt inhibit evaporative cooling leading to a warmer atmosphere and positive geopotential height anomalies (*18*, *19*). Furthermore, stark thermal contrasts between the fast-warming land surface and the cooler Arctic ocean facilitate the formation of an Arctic front jet in early summer (*18*, *21*, *29*, *39*). We found that an earlier snowmelt was associated with an earlier formation of Arctic front jets as indicated by a significant negative correlation between snowmelt timing and Arctic front jet development in the first 3 weeks of June (ρ = −0.25, P = 0.02). In our study region, snowmelt usually started in the beginning of May (average day of year when 10% of areas are snow-free, day 128 or 7/8 May), with 50% of areas being snow-free by end of May (average day of year 147 or 26/27 May), and 90% by mid-June (average day of year 166 or 14/15 June). Increases in Arctic front jet states in June may therefore be partly interconnected with accelerating snowmelt. By contrast, we did not find any statistical relationships between snowmelt timing and Arctic front jet occurrence in July and August.

We have shown that Arctic front jets together with early snowmelt favor extreme wildfire conditions and that both drivers have strengthened over the past decades. This strongly contributes to increasing fire activity over northern high latitudes (*8*, *40*). Arctic front jets are often accompanied by a sharp subtropical jet and such double jet states are associated with persistent blocking in the midlatitudes (*29*, *31*, *41*). They can incite persistent weather since they support the formation of waveguides which trap and focus free-traveling Rossby waves, enabling high-amplitude, quasi-stationary waves, for example through resonance processes (*30*). Anticyclonic blocking has long been identified as a driver of large burned areas, as observed in boreal North America (*42*), since it generates tinder-dry fuels and abundant ignitions from thunderstorms. Summer blocking events are widespread in northern Eurasia (*43*) but understanding of the diverse geneses of blocking events remains limited, which hampers accurate modelling of blocking in climate models and medium-range forecasts (*44*–*46*). Eastern Siberia may be particularly susceptible to intensifying fire activity because it experiences faster and more widespread accelerations of snowmelt than other Arctic regions (*15*). Furthermore, previous research suggests that blocked anticyclones over eastern Siberia might be linked to decreases in sea ice and snow cover (*18*), and to the incitement of a wave train pattern in June driven by positive snow water equivalent and soil moisture anomalies in western Siberia (*47*). In addition, intensifying fire seasons can have legacy effects through the occurrence of overwintering fires (*48*). Overwintering fires are increasing in number in eastern Siberia where they accounted for 7.5% of burned areas in 2020 (*37*).

The extension of fire activity into northern tundra regions may incite strong carbon cycle feedbacks. Carbon emissions from large tundra fires considerably surpass decades of carbon accumulation of pan-Arctic tundra ecosystems (*49*). Furthermore, tundra fires may promote thermokarst development (*3*), and catalyze shrub expansion into tundra regions (*50*). We have shown that drivers of recent tundra fire extremes in northeastern Siberia, including snowmelt and atmospheric circulation, are sensitive to climate warming. This may imply that the region will see a rapid intensification of fire activity in the future. Our work therefore calls for integrating changes in atmospheric circulation patterns when projecting future fire regimes in the high latitudes and move beyond simple extrapolations of relationships between regional weather and climate and fire activity. This is needed to fully comprehend the accelerating role of fire on rapidly changing Arctic-boreal ecosystems and their potential carbon losses.

REFERENCES AND NOTES

1. T. Kajimoto, in *Permafrost Ecosystems: Siberian Larch Forests*, A. Osawa, O. A. Zyryanova, Y. Matsuura, R. W. Wein, Eds. (Springer, ed. 209, 2010), pp. 303–330.
2. S. Veraverbeke *et al.*, *Curr. Opin. Environ. Sci. Health* **23**, 100277 (2021).
3. C. M. Gibson *et al.*, *Nat. Commun.* **9**, 3041 (2018).
4. M. R. Turetsky *et al.*, *Nat. Geosci.* **13**, 138–143 (2020).
5. S. M. Natali *et al.*, *Proc. Natl. Acad. Sci. U.S.A.* **118**, e2100163118 (2021).
6. IPCC, in *Climate Change 2021: The Physical Science Basis. Contribution of Working Group I to the Sixth Assessment Report of the Intergovernmental Panel on Climate Change*, V. Masson-Delmotte *et al.*, Eds. (Cambridge Univ. Press, 2021); https://www.ipcc.ch/report/ar6/wg1/.
7. M. Rantanen *et al.*, *Commun. Earth Environ.* **3**, 168 (2022).

8. M. D. Flannigan, K. A. Logan, B. D. Amiro, W. R. Skinner, B. J. Stocks, *Clim. Change* **72**, 1–16 (2005).
9. M. D. Flannigan *et al*., *Clim. Change* **134**, 59–71 (2016).
10. S. Veraverbeke *et al*., *Nat. Clim. Chang.* **7**, 529–534 (2017).
11. Y. Chen *et al*., *Nat. Clim. Chang.* **11**, 404–410 (2021).
12. A. Masrur, A. N. Petrov, J. DeGroote, *Environ. Res. Lett.* **13**, 014019 (2018).
13. J. E. Overland, M. Wang, *Int. J. Climatol.* **41**, E2341–E2346 (2021).
14. A. Ciavarella *et al*., Prolonged Siberian heat of 2020 (World Weather Attribution, 2020).
15. L. R. Mudryk, A. E. Chereque, R. Brown, C. Derksen, K. Luojus, B. Decharme, "Terrestrial Snow Cover" (Report 27902, NOAA, 2020); https://doi.org/10.25923/p6ca-v923.
16. J. S. Kim, J. S. Kug, S. J. Jeong, H. Park, G. Schaepman-Strub, *Sci. Adv.* **6**, eaax3308 (2020).
17. A. L. Westerling, H. G. Hidalgo, D. R. Cayan, T. W. Swetnam, *Science* **313**, 940–943 (2006).
18. Q. Tang, X. Zhang, J. A. Francis, *Nat. Clim. Chang.* **4**, 45–50 (2014).
19. S. I. Seneviratne *et al*., *Earth Sci. Rev.* **99**, 125–161 (2010).
20. D. Coumou, J. Lehmann, J. Beckmann, *Science* **348**, 324–327 (2015).
21. D. Coumou, G. Di Capua, S. Vavrus, L. Wang, S. Wang, *Nat. Commun.* **9**, 2959 (2018).
22. C. G. Gertler, P. A. O'Gorman, *Proc. Natl. Acad. Sci. U.S.A.* **116**, 4105–4110 (2019).
23. E. K. M. Chang, C. G. Ma, C. Zheng, A. M. W. Yau, *Geophys. Res. Lett.* **43**, 2200–2208 (2016).
24. R. Connolly, M. Connolly, W. Soon, D. Legates, R. Cionco, *Geosciences (Basel)* **9**, 135 (2019).
25. J. Stroeve, D. Notz, *Environ. Res. Lett.* **13**, 103001 (2018).
26. S. Y. Philip *et al*., Rapid attribution analysis of the extraordinary heatwave on the Pacific Coast of the US and Canada June 2021. *Earth Syst. Dynam. Discuss*. esd-2021-90 [Preprint] (2021).
27. M. E. Mann *et al*., *Sci. Rep.* **7**, 45242 (2017).
28. B. J. Harvey, P. Cook, L. C. Shaffrey, R. Schiemann, *J. Geophys. Res. Atmos.* **125**, 1–10 (2020).
29. E. Rousi, K. Kornhuber, G. Beobide-Arsuaga, F. Luo, D. Coumou, *Nat. Commun.* **13**, 3851 (2022).
30. K. Kornhuber, V. Petoukhov, S. Petri, S. Rahmstorf, D. Coumou, *Clim. Dyn.* **49**, 1961–1979 (2017).
31. Y. Tachibana, T. Nakamura, H. Komiya, M. Takahashi, *J. Geophys. Res.* **115**, D12125, (2010).
32. L. Giglio, L. Boschetti, D. P. Roy, M. L. Humber, C. O. Justice, *Remote Sens. Environ.* **217**, 72–85 (2018).
33. L. Giglio, W. Schroeder, C. O. Justice, *Remote Sens. Environ.* **178**, 31–41 (2016).
34. Copernicus Climate Change Service, ERA5: Fifth generation of ECMWF atmospheric reanalyses of the global climate. (Copernicus Clim. Chang. Serv. Clim. Data Store, 2017); https://cds.climate.copernicus.eu/cdsapp#!/home.
35. F. Sedano, J. T. Randerson, *Biogeosciences* **11**, 3739–3755 (2014).
36. K. Kirillina, E. G. Shvetsov, V. V. Protopopova, L. Thiesmeyer, W. Yan, *Environ. Res. Lett.* **15**, 035009 (2020).
37. W. Xu, R. C. Scholten, T. D. Hessilt, Y. Liu, S. Veraverbeke, *Environ. Res. Lett.* **17**, 045005 (2022).
38. A. R. Sharma, P. Jain, J. T. Abatzoglou, M. Flannigan, *J. Clim.* **35**, 2867–2884 (2022).
39. S. Matsumura, K. Yamazaki, T. Tokioka, *J. Geophys. Res.* **115**, D20107 (2010).
40. V. I. Kharuk *et al*., *Ambio* **50**, 1953–1974 (2021).
41. D. F. Rex, *Tellus* **2**, 275–301 (1950).
42. W. R. Skinner, B. J. Stocks, D. L. Martell, B. Bonsal, A. Shabbar, *Theor. Appl. Climatol.* **63**, 89–105 (1999).
43. E. Tyrlis, B. J. Hoskins, *J. Atmos. Sci.* **65**, 1638–1652 (2008).
44. M. Matsueda, *Sci. Online Lett. Atmos.* **5**, 113–116 (2009).
45. P. Davini, F. D'Andrea, *J. Clim.* **33**, 10021–10038 (2020).
46. F. Luo *et al*., *Weather Clim. Dyn.* **3**, 905–935 (2022).
47. T. Sato, T. Nakamura, *Sci. Rep.* **9**, 10866 (2019).
48. R. C. Scholten, R. Jandt, E. A. Miller, B. M. Rogers, S. Veraverbeke, *Nature* **593**, 399–404 (2021).
49. M. C. Mack *et al*., *Nature* **475**, 489–492 (2011).
50. Z. A. Mekonnen *et al*., *Environ. Res. Lett.* **16**, 053001 (2021).
51. R. Scholten, screbec/Siberia-fires: Siberian fire analysis, Version v1, Zenodo (2022); https://zenodo.org/record/7198896#.Y1rVtHbMI2w.

ACKNOWLEDGMENTS

R.C.S. wishes to thank D. van Wees for useful technical discussions. We would like to thank the three anonymous reviewers for their thoughtful comments and efforts toward improving our manuscript. **Funding:** This work was funded by the Dutch Research Council (NWO) through a Vidi grant (Fires Pushing Trees North) awarded to S.V. D.C. and F.L. acknowledge support from a NWO Vidi grant (Persistent Summer Extremes "PERSIST"). D.C. acknowledges funding from the European Union's Horizon 2020 research and innovation program under grant agreement 101003469. **Author contributions:** All authors designed the research. R.C.S. performed the analysis and drafted the paper. All authors participated in manuscript editing. **Competing interests:** Authors declare that they have no competing interests. **Data and materials availability:** MODIS burned area (MCD64A1) and active fires data (MCD14ML) are available from University of Maryland (https://modis-fire.umd.edu). The snow cover product (MCD10A1) and derived snow melt dates are available through Google Earth Engine (GEE). ERA5 reanalysis data can be retrieved from the Copernicus Climate Data Store (https://cds.climate.copernicus.eu). Lightning data were retrieved from the global lightning detection network GLD360 developed by Vaisala (www.vaisala.com/en/products/systems/lightning/gld360) for which permissions can be obtained by Vaisala. Code used to analyze the data are available from https://github.com/screbec/Siberia-fires or at Zenodo (*51*).

License information: Copyright © 2022 the authors, some rights reserved; exclusive licensee American Association for the Advancement of Science. No claim to original US government works. https://www.sciencemag.org/about/science-licenses-journal-article-reuse

SUPPLEMENTARY MATERIALS

science.org/doi/10.1126/science.abn4419
Materials and Methods
Figs. S1 to S9
Table S1
References (*52*–*72*)

Submitted 1 December 2021; accepted 14 October 2022
10.1126/science.abn4419

ULTRACOLD CHEMISTRY

Creation of an ultracold gas of triatomic molecules from an atom–diatomic molecule mixture

Huan Yang[1,2]†, Jin Cao[1,2]†, Zhen Su[1,2], Jun Rui[1,2,3], Bo Zhao[1,2,3]*, Jian-Wei Pan[1,2,3]*

In recent years, there has been notable progress in the preparation and control of ultracold gases of diatomic molecules. The next experimental challenge is the production of ultracold polyatomic molecular gases. Here, we report the creation of an ultracold gas of $^{23}Na^{40}K_2$ triatomic molecules from a mixture of ground-state sodium-23–potassium-40 ($^{23}Na^{40}K$) molecules and potassium-40 (^{40}K) atoms. The triatomic molecules were created by adiabatic magneto-association through an atom–diatomic molecule Feshbach resonance. We obtained clear evidence for the creation of triatomic molecules by directly detecting them using radio-frequency dissociation. Approximately 4000 triatomic molecules with a high-peak phase-space density of 0.05 could be created. The ultracold triatomic molecules can serve as a launchpad to probe the three-body potential energy surface and may be used to prepare quantum degenerate triatomic molecular gases.

Ultracold molecules offer an ideal platform to study chemical reactions at the quantum level, quantum simulation of many-body problems in condensed-matter physics, and precision measurement of fundamental constants (*1*, *2*). In recent years, there has been notable success in the preparation and study of ultracold gases of diatomic molecules. These include the production of quantum degenerate diatomic molecular gases (*3*–*5*), the realization of quantum dipolar molecular gases with tunable interactions (*6*, *7*), the observation of atom–diatomic molecule Feshbach resonances (*8*–*10*), and the detection of reaction products and intermediate complexes of ultracold reactions (*11*).

[1]Hefei National Research Center for Physical Sciences at the Microscale and School of Physical Sciences, University of Science and Technology of China, Hefei, Anhui 230026, China. [2]Shanghai Research Center for Quantum Science and CAS Center for Excellence in Quantum Information and Quantum Physics, University of Science and Technology of China, Shanghai 201315, China. [3]Hefei National Laboratory, University of Science and Technology of China, Hefei 230088, China.
***Corresponding author. Email: bozhao@ustc.edu.cn (B.Z.); pan@ustc.edu.cn (J.-W.P.)**
†These authors contributed equally to this work.

After the great success of diatomic molecules, the next experimental challenge is to prepare and control ultracold triatomic molecular gases. Ultracold triatomic molecules will open up many research opportunities. For example, triatomic molecules provide an ideal platform to study the quantum-mechanical three-body problem. The collisions involving triatomic molecules provide a sensitive probe of the four-body, five-body, and six-body potential energy surfaces, which are extremely difficult to calculate with high accuracy for heavy molecules. Triatomic molecules have more freedom to control, thus offering a previously unrealized knob for quantum simulation. Despite these research opportunities, the preparation and control of ultracold triatomic molecular gases are extremely difficult.

Two methods are usually used to prepare ultracold molecules. One method is direct cooling, such as buffer gas cooling, optoelectrical cooling, or laser cooling (*12*–*16*). For polyatomic molecules, it has been reported that the CaOH molecules were laser cooled and trapped in a magneto-optical trap with a temperature of ~100 μK and a peak phase-space density of ~10^{-12} (*17*). Another method is to form molecules from ultracold atomic

gases. In the past two decades, various ultracold diatomic molecules have been created by magneto-association and photoassociation (*18*–*28*). The advantage of ultracold association is that the molecules can inherit the low temperatures and the high density of atomic gases, and thus the molecular gases can have a high phase-space density. With the success of the formation of diatomic molecules, several theoretical groups have started to consider the feasibility of the creation of triatomic molecules from ultracold atom–diatomic molecule mixtures (*29*–*31*). However, the complexity of triatomic molecules makes a quantitative analysis extremely difficult.

The observations of the Efimov resonances between atoms and weakly bound diatomic molecules (*32*), the Feshbach resonances between weakly bound diatomic molecules (*33*), and the Feshbach resonances between atoms and ground-state diatomic molecules (*8*–*10*) open up the possibility of the creation of polyatomic molecules because the polyatomic bound state coincides with the scattering state close to the resonances, and the coupling strength between them is resonantly enhanced. Recently, the association of Efimov trimers has been demonstrated by observing the radio frequency (rf)–induced loss of atoms in an atom-dimer mixture (*34*) or by analyzing the decay dynamics after converting a strongly interacting atomic gas into molecular states (*35*). For the Feshbach resonance between atoms and ground-state diatomic molecules, the association of triatomic molecules has been demonstrated by measuring the loss of diatomic molecules induced by the rf field (*36*). The rf loss spectrum provides indirect evidence for the existence of triatomic molecules and can be used to measure the binding energy. However, the direct detection of triatomic molecules and the preparation of an ultracold gas of triatomic molecules remain elusive.

Here, we report the creation of an ultracold gas of weakly bound $^{23}Na^{40}K_2$ triatomic molecules from a mixture of $^{23}Na^{40}K$ ground-state molecules and ^{40}K atoms. The method of the creation and detection of the triatomic molecules used in our work is illustrated in Fig. 1. The triatomic molecules were created by adiabatic magneto-association by means of ramping the magnetic field through a Feshbach resonance between $^{23}Na^{40}K$ molecules and ^{40}K atoms. We obtained clear evidence for the creation of triatomic molecules by directly detecting them using the rf dissociation. About 4000 triatomic molecules at a temperature of ~100 nK could be created, with a peak density of ~3×10^{11} cm^{-3}. The ultracold triatomic molecular gas had a peak phase-space density of ~0.05, which is ~10 orders of magnitude larger than that of the laser-cooled triatomic molecules. Our work may largely improve the understanding of complicated atom-molecule Feshbach resonance, which is difficult to describe quantitatively because of the high density of states (*9*). Our work may also open up the possibility of the preparation of Bose-Einstein condensates of triatomic molecules and the production of ground-state ultracold triatomic molecules.

Our experiment started with the preparation of a quantum degenerate mixture of $^{23}Na^{40}K$ molecules and ^{40}K atoms. The experimental setup has been introduced in previous works (*5*). The experimental procedures for preparing the ultracold mixture are described in the supplementary materials. In brief, we first prepared a mixture of nearly pure Bose-Einstein condensate of ^{23}Na atoms and deeply degenerate Fermi gas of ^{40}K atoms with $T/T_F \approx 0.2$ (where T is the temperature of the atoms and T_F is the Fermi temperature) at a temperature of ~100 nK. The ground-state $^{23}Na^{40}K$ molecules were created by magneto-association followed by stimulated Raman adiabatic passage at a magnetic field of 77.6 G. The degeneracy of a pure $^{23}Na^{40}K$ molecular gas was $T/T_F \approx 0.4$ to 0.5, which was determined by fitting the two-dimensional (2D) column density distribution to the Fermi-Dirac distribution. After removing ^{23}Na atoms, we obtained an ultracold mixture of $^{23}Na^{40}K$ molecules and ^{40}K atoms.

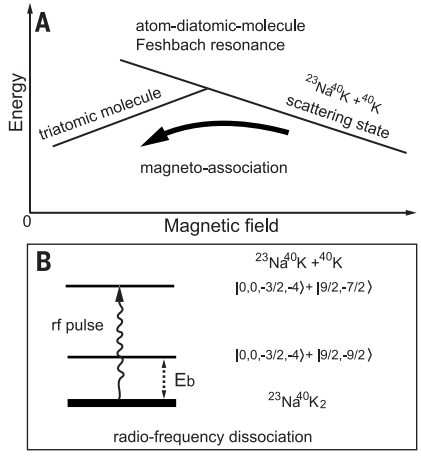


Fig. 1. Illustration of the magneto-association and the rf dissociation of triatomic molecules. (**A**) In the vicinity of the atom–diatomic molecule Feshbach resonance, by adiabatically ramping the magnetic field across the resonance from above the resonance to the triatomic molecular side, pairs of $^{23}Na^{40}K$ molecules and ^{40}K atoms can be coherently converted into $^{23}Na^{40}K_2$ triatomic molecules. (**B**) The $^{23}Na^{40}K_2$ triatomic molecules lie below the $|0, 0, -3/2, -4\rangle, |9/2, -9/2\rangle$ scattering state with the binding energy E_b. By applying an rf pulse driving the atomic transition $|9/2, -9/2\rangle \rightarrow |9/2, -7/2\rangle$, the $^{23}Na^{40}K_2$ triatomic molecules can be dissociated into free $^{23}Na^{40}K$ molecules and ^{40}K atoms when the rf is larger than a threshold equal to the sum of the atomic transition and the binding energy.

The $^{23}Na^{40}K$ molecules were prepared in the maximally polarized state $|\nu, N, m_{Na}, m_K\rangle = |0, 0, -3/2, -4\rangle$, where the first two quantum numbers are the vibrational and rotational quantum numbers, respectively, and m_{Na} and m_K represent the nuclear spin projections of Na and K along the magnetic field. The ^{40}K atoms were prepared in the lowest hyperfine state $|f, m_f\rangle_K = |9/2, -9/2\rangle$, which is also the maximally polarized state (where f is the quantum number of the total angular momentum). For this hyperfine state combination, there is a broad atom-molecule Feshbach resonance at ~48 G (*9*, *37*).

We first characterized the Feshbach resonance by measuring the binding energies of the triatomic molecules through the rf loss spectrum. The experimental details are described in the supplementary materials (section 2). The measured binding energy E_b as a function of the magnetic field B is shown in Fig. 2. The data were fitted to the model $\sqrt{2m_r E_b/\hbar^2} = 1/(a_{bg} - \bar{a}) + \Gamma/\{2\bar{a}[E_b + \delta\mu(B - B_c)]\}$ (*38*), where m_r is the reduced mass, $\hbar$ is the Planck constant, $a_{bg} = -692a_0$ is the background scattering length measured in (*37*), and $\bar{a} = 74a_0$ is the mean scattering length. The fitting parameter $\delta\mu$ is the relative magnetic moment, B_c is the magnetic field at which the bare bound state crosses the scattering threshold, and Γ is the Feshbach coupling strength. The fitting yielded $\delta\mu = 1.5(1)\mu_B$, $B_c = 44.2(1)$ G, and $\Gamma = 1.6(2)$ MHz. We obtained the resonance position $B_0 = 48.2(5)$ G and the resonance width $\Delta = 4.5(5)$ G, which agreed well with the results determined from the measurement of the elastic scattering cross sections (*37*). The strength of the Feshbach resonance is given by $s_{res} = a_{bg}\Delta\delta\mu/\bar{a}E_{vdw} \approx 7$ where $E_{vdw} = 12.5$ MHz is the van der Waals energy (*39*). The strength $s_{res} > 1$ means that this resonance is open channel dominated.

After characterizing the Feshbach resonance, we studied the adiabatic magneto-association

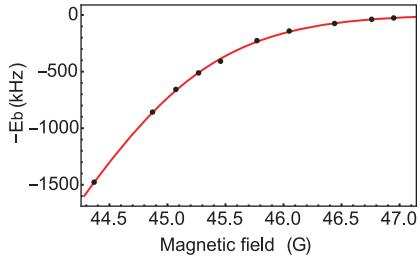


Fig. 2. The binding energy of the triatomic molecules as a function of magnetic fields. The binding energy of the triatomic molecules was measured using the rf loss spectrum. The experimental details are described in the supplementary materials. The data were fitted to the model in (*38*) (see the text for details). Error bars are smaller than the points, so they are not shown.

of triatomic molecules. To perform magneto-association in the vicinity of the atom-molecule Feshbach resonance, we needed to adiabatically ramp the magnetic field from above the resonance to the triatomic molecular side. In this process, the atom–diatomic molecule pairs could be coherently converted into triatomic molecules. Magneto-association has been the primary method to form diatomic molecules from ultracold atomic gases (*39*, *40*). However, it is not clear whether magneto-association will work for triatomic molecules because of some unknown difficulties. The first one is that the conversion efficiency critically depends on the phase-space density of the atom–diatomic molecule mixture. Efficient creation of molecules can only be achieved for a high initial phase-space density. Previously, we tried to use magneto-association to form triatomic molecules in an atom-molecule mixture at ~500 nK with no success (*41*). The second difficulty is that the lifetime of the triatomic molecules is unknown, which is usually believed to be short. If the magnetic-field sweep is too slow, the triatomic molecules will be lost and cannot be detected. However, if the magnetic-field sweep is too fast, the molecules cannot be efficiently formed. In the current work, these two difficulties were mitigated by preparing a quantum degenerate atom-molecule mixture and choosing an open channel–dominated Feshbach resonance to form the triatomic molecules. However, it is not clear whether these advances are sufficient for the magneto-association to work.

We first searched for the possible formation signal by monitoring the loss of $^{23}Na^{40}K$ molecules induced by ramping the magnetic field across the resonance. To this end, after preparing the mixture of $^{23}Na^{40}K$ molecules and ^{40}K atoms at 77.6 G, we quickly changed the magnetic field to 55 G and then ramped the magnetic field downward from 55 to 45 G at a speed of ~5 G/ms. After a variable hold time, we removed the ^{40}K atoms using a 200-μs resonant light pulse. The magnetic field was then ramped to 77.6 G, and the $^{23}Na^{40}K$ molecules were transferred back to the Feshbach state for detection. The magnetic field between 55 and 45 G as a function of time is shown in the inset of Fig. 3. The ramp started at 1 ms. After ramping the magnetic field across the resonance, we observed a sharp decrease in the number of $^{23}Na^{40}K$ molecules. About 73% of the $^{23}Na^{40}K$ molecules were lost (Fig. 3). For such a high ramping speed, the large fractional loss of the $^{23}Na^{40}K$ molecules could not be completely caused by inelastic collisions between the $^{23}Na^{40}K$ molecules and the ^{40}K atoms. To see this clearly, we ramped the magnetic field upward at the same speed. We only observed that ~40% of the $^{23}Na^{40}K$ molecules were lost. From the difference in the fractional loss between the downward and upward ramps,

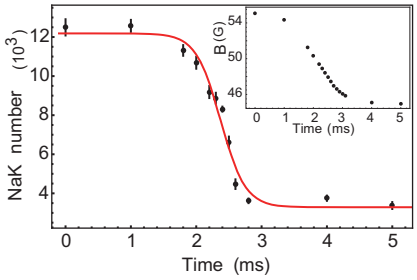


Fig. 3. The loss of $^{23}Na^{40}K$ molecules induced by ramping the magnetic field across the resonance. The magnetic field was swept from 55 to 45 G at a speed of ~5 G/ms. The ramp started at 1 ms. When the magnetic field crossed the atom-molecule Feshbach resonance, the number of $^{23}Na^{40}K$ molecules decreased abruptly. The solid line is the fit of the error function to the data. Each data point represents the average of five measurements, and error bars represent the standard error of the mean. The inset shows the measured magnetic field as a function of time.

we inferred that the extra loss for the downward ramp might be the result of the formation of triatomic molecules. However, we could not exclude the possibility that some unknown mechanism could contribute to these losses.

Unambiguous evidence for the creation of triatomic molecules can be obtained by directly probing the triatomic molecules through dissociating them into free diatomic molecules and atoms. The major challenge for dissociation is the short lifetime of the triatomic molecules, which is limited mainly by three loss mechanisms—i.e., predissociation, inelastic collisions with atoms and diatomic molecules, and photoexcitations by the trap laser (*42*–*44*). The triatomic molecules may decay into free atoms and diatomic molecules if their energies are higher than the lowest atom-molecule scattering threshold. This predissociation mechanism was expected to be suppressed by preparing the ^{40}K atoms in the lowest hyperfine state $|9/2, -9/2\rangle$. For an open channel–dominated Feshbach resonance, the characteristic size of the weakly bound triatomic molecule is the scattering length, which is much larger than the characteristic size of the deeply bound triatomic molecule (*39*). In this case, the loss induced by collisions with the fermionic ^{40}K atoms or $^{23}Na^{40}K$ molecules was expected to be suppressed by the Pauli blocking principle. This is similar to the collision between weakly bound $^{87}Rb^{40}K$ molecules and ^{40}K atoms, where the Fermi suppression of collisional loss has been directly observed (*45*). The effect of photoexcitations by the trap laser was unknown. The observation of photoexcitations of the collision complex in the $^{87}Rb^{40}K + {}^{87}Rb$ collisions (*46*) indicated that the trap laser might also excite the triatomic bound state. However, how strongly it would affect the lifetime of the triatomic bound state was not clear.

In the experiment, we used an rf field to dissociate the triatomic molecules. By applying an rf pulse driving the atomic transition $|9/2, -9/2\rangle \rightarrow |9/2, -7/2\rangle$, the $^{23}Na^{40}K_2$ triatomic molecules could be dissociated into free $^{23}Na^{40}K$ molecules and ^{40}K atoms when the rf is larger than the sum of the atomic transition and the binding energy (Fig. 1B). To suppress the possible photoexcitations by the trap laser, we switched off the optical dipole trap at 2.4 ms, when the magnetic field crossed the resonance. After 0.5 ms, when the magnetic field reached 46.30 G, we applied a 0.2-ms rf pulse to dissociate the triatomic molecules. After that, the optical dipole trap was switched on to recapture $^{23}Na^{40}K$ molecules and ^{40}K atoms. The ^{40}K atoms were then removed by a resonant light pulse, and the number of $^{23}Na^{40}K$ molecules was detected by transferring them back to the Feshbach state at 77.6 G. During the application of the rf dissociation pulse, the magnetic field changed from 46.30 to 45.86 G. In this magnetic field window, the binding energy increased from 95 to 201 kHz, and the atomic transition frequency decreased from 13.230 to 13.115 MHz. These changes partially compensated for each other, and thus we used a single-frequency rf pulse to dissociate the triatomic molecules in this time window. The number of $^{23}Na^{40}K$ molecules as a function of the rf is shown in Fig. 4. We observed a clear asymmetric dissociation spectrum with a threshold behavior. The $^{23}Na^{40}K$ molecules lost in the magnetic-field sweep could be recovered by the rf dissociation pulse. This dissociation occurred only when the rf was larger than a threshold, which in our case was equal to the minimum of the sum of the frequency of the atomic transition and the binding energy in the magnetic-field window. The measured threshold frequency was smaller than the calculated threshold frequency by ~20 kHz. We attributed this small difference to the systematic errors resulting from the different fitting models. The number of $^{23}Na^{40}K$ molecules dissociated from the triatomic molecules could be obtained by subtracting the background signal resulting from the molecules that did not participate in the magneto-association process. A maximum value of ~4000 could be achieved, which means that at least ~30% of the $^{23}Na^{40}K$ molecules could be converted into triatomic molecules by magneto-association. The observation of the dissociation spectrum with a threshold behavior provides clear evidence for the creation of ultracold triatomic molecules. Assuming that the temperature of the triatomic molecular gas was the same as the atom–diatomic molecule mixture and that the polarizability of the triatomic molecule was equal to the sum of the polarizability

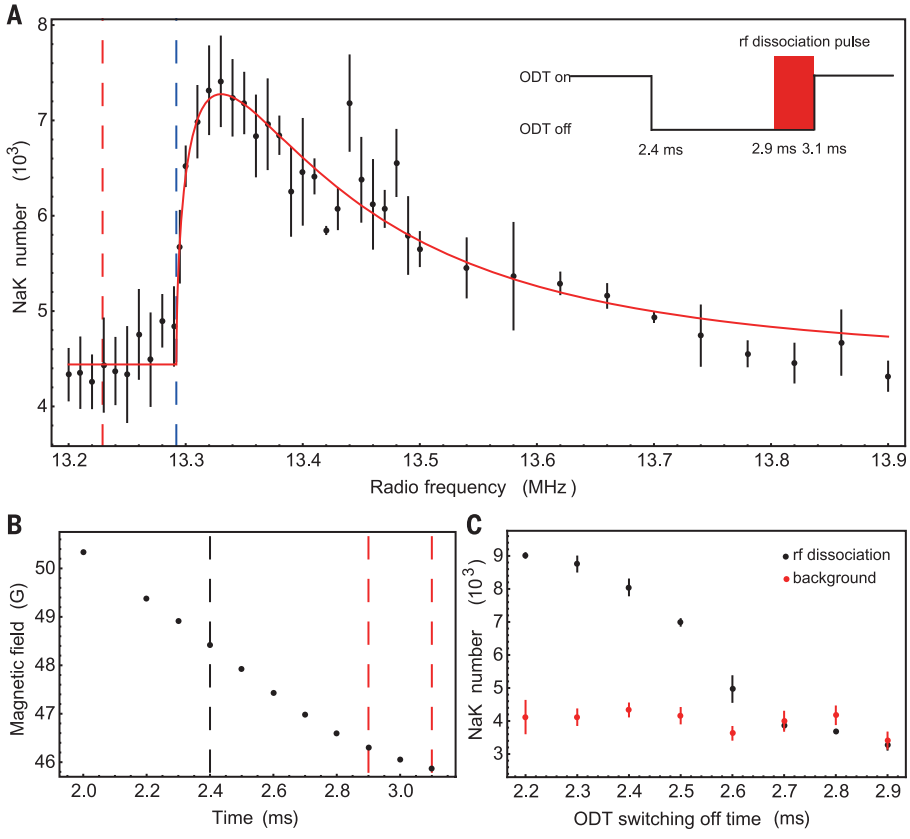


Fig. 4. The rf dissociation spectrum of the triatomic molecules. (**A**) The number of $^{23}Na^{40}K$ molecules as a function of rf. The data were fitted to the dissociation spectrum. The red dashed line represents the frequency of the atomic transition at 46.30 G. The blue dashed line is the fitted threshold dissociation frequency. When the frequency of the rf field is larger than this threshold, the triatomic molecules can be dissociated into $^{23}Na^{40}K$ molecules and ^{40}K atoms. For this measurement, the optical dipole trap (ODT) was switched off at 2.4 ms, and the 0.2-ms rf dissociation pulse was applied at 2.9 ms. Each data point represents the average of three measurements. (**B**) The magnetic field as a function of time. The black dashed line denotes the time at which the optical dipole trap is switched off. The rf pulse was applied in the time window between the two red dashed lines. (**C**) The number of $^{23}Na^{40}K$ molecules as a function of the time at which the optical dipole trap is switched off. The black points represent the data after applying the rf dissociation pulse. The red points represent the background data without applying the rf pulse. The difference between them gave the number of $^{23}Na^{40}K$ molecules dissociated from the triatomic molecules. The optical dipole trap started to affect the formation of triatomic molecules at ~2.3 ms, when the magnetic field reached 48.91 G, slightly above the resonance position. Each data point represents the average of three measurements. Error bars represent the standard error of the mean.

of $^{23}Na^{40}K$ molecules and ^{40}K atoms, we obtained a peak density of ~3×10^{11} cm^{-3}. Therefore, the triatomic molecular gas had a high-peak phase-space density of ~0.05, which is ~10 orders of magnitude higher than the previous results for cold polyatomic molecules (*15*, *17*).

We found that it was critically important to immediately switch off the trap laser when the magnetic field crossed the resonance because the presence of the trap laser could substantially deplete the triatomic molecules. To see this effect clearly, we fixed the dissociation frequency and changed the time at which the optical dipole trap was switched off. The optical dipole trap started to affect the formation of the triatomic molecules when the magnetic field reached ~48.91 G, which is slightly above the resonance position (Fig. 4). The dissociation signals could not be observed when the optical dipole trap was present for a few hundred microseconds, which indicated that the lifetime of the triatomic molecules in the optical dipole trap was short. This was the direct observation that the trap laser could excite the triatomic molecules. Assuming that the triatomic molecules were created when the magnetic field crossed the resonance, the triatomic molecules coexisted with the ^{40}K atoms and $^{23}Na^{40}K$ molecules for a few hundred microseconds before the optical dipole trap was switched on. During this interval, the triatomic molecules may be transferred to a more stable state by lasers.

We have created an ultracold gas of $^{23}Na^{40}K_2$ triatomic molecules from a mixture of $^{23}Na^{40}K$ molecules and ^{40}K atoms by adiabatic magneto-association. The trap laser had strong detrimental effects on the formation of triatomic molecules. We will explore whether the photoexcitation problem can be solved by changing the wavelength of the laser in the future. The photoexcitation problem can also be solved by transferring the triatomic molecules into a magnetic trap because the triatomic molecules were in a weak field–seeking state. The triatomic molecules that could be dissociated by the rf field were weakly bound molecules near the atom-molecule scattering threshold. They could be transferred to closed-channel molecules in a high vibrational state by simply ramping the magnetic field to zero value, where the binding energy was estimated to be on the order of 100 MHz (*9*).

The creation of ultracold triatomic molecular gases opens up many research possibilities. The triatomic molecules are in an excited vibrational state. This state can serve as a launchpad for the full control of the energy and configuration of the triatomic molecules and the probe of the three-body potential energy surface with unprecedented resolution. The triatomic molecules may be transferred to the rovibrational ground state by lasers, similar to diatomic molecules. The phase-space density of the triatomic molecular gas is greatly improved from that in previous works, and further improvement may enable the creation of quantum degenerate gases or Bose-Einstein condensates of triatomic molecules.

REFERENCES AND NOTES

1. L. D. Carr, D. DeMille, R. V. Krems, J. Ye, *New J. Phys.* **11**, 055049 (2009).
2. G. Quéméner, P. S. Julienne, *Chem. Rev.* **112**, 4949–5011 (2012).
3. L. De Marco *et al.*, *Science* **363**, 853–856 (2019).
4. A. Schindewolf *et al.*, *Nature* **607**, 677–681 (2022).
5. J. Cao *et al.*, Preparation of a quantum degenerate mixture of $^{23}Na^{40}K$ molecules and ^{40}K atoms. arXiv:2208.09620 [physics.atom-ph] (2022).
6. G. Valtolina *et al.*, *Nature* **588**, 239–243 (2020).
7. K. Matsuda *et al.*, *Science* **370**, 1324–1327 (2020).
8. H. Yang *et al.*, *Science* **363**, 261–264 (2019).
9. X.-Y. Wang *et al.*, *New J. Phys.* **23**, 115010 (2021).
10. H. Son *et al.*, *Science* **375**, 1006–1010 (2022).
11. M.-G. Hu *et al.*, *Science* **366**, 1111–1115 (2019).
12. E. S. Shuman, J. F. Barry, D. Demille, *Nature* **467**, 820–823 (2010).
13. L. Caldwell *et al.*, *Phys. Rev. Lett.* **123**, 033202 (2019).
14. S. Ding, Y. Wu, I. A. Finneran, J. J. Burau, J. Ye, *Phys. Rev. X* **10**, 021049 (2020).
15. M. Zeppenfeld *et al.*, *Nature* **491**, 570–573 (2012).
16. D. Mitra *et al.*, *Science* **369**, 1366–1369 (2020).
17. N. B. Vilas *et al.*, *Nature* **606**, 70–74 (2022).
18. C. A. Regal, C. Ticknor, J. L. Bohn, D. S. Jin, *Nature* **424**, 47–50 (2003).
19. J. Herbig *et al.*, *Science* **301**, 1510–1513 (2003).
20. K.-K. Ni *et al.*, *Science* **322**, 231–235 (2008).
21. P. K. Molony *et al.*, *Phys. Rev. Lett.* **113**, 255301 (2014).
22. T. Takekoshi *et al.*, *Phys. Rev. Lett.* **113**, 205301 (2014).
23. J. W. Park, S. A. Will, M. W. Zwierlein, *Phys. Rev. Lett.* **114**, 205302 (2015).
24. M. Guo *et al.*, *Phys. Rev. Lett.* **116**, 205303 (2016).
25. T. M. Rvachov *et al.*, *Phys. Rev. Lett.* **119**, 143001 (2017).
26. F. Seeßelberg *et al.*, *Phys. Rev. A* **97**, 013405 (2018).
27. K. K. Voges *et al.*, *Phys. Rev. Lett.* **125**, 083401 (2020).

28. I. Stevenson *et al*., Ultracold gas of dipolar NaCs ground state molecules. arXiv:2206.00652 [cond-mat.quant-gas] (2022).
29. J. Pérez-Ríos, M. Lepers, O. Dulieu, *Phys. Rev. Lett.* **115**, 073201 (2015).
30. J. Schnabel, T. Kampschulte, S. Rupp, J. Hecker Denschlag, A. Köhn, *Phys. Rev. A* **103**, 022820 (2021).
31. R. Hermsmeier, J. Kłos, S. Kotochigova, T. V. Tscherbul, *Phys. Rev. Lett.* **127**, 103402 (2021).
32. T. Kraemer *et al*., *Nature* **440**, 315–318 (2006).
33. C. Chin *et al*., *Phys. Rev. Lett.* **94**, 123201 (2005).
34. T. Lompe *et al*., *Science* **330**, 940–944 (2010).
35. C. E. Klauss *et al*., *Phys. Rev. Lett.* **119**, 143401 (2017).
36. H. Yang *et al*., *Nature* **602**, 229–233 (2022).
37. Z. Su *et al*., *Phys. Rev. Lett.* **129**, 033401 (2022).
38. A. D. Lange *et al*., *Phys. Rev. A* **79**, 013622 (2009).
39. C. Chin, R. Grimm, P. Julienne, E. Tiesinga, *Rev. Mod. Phys.* **82**, 1225–1286 (2010).
40. T. Köhler, K. Góral, P. S. Julienne, *Rev. Mod. Phys.* **78**, 1311–1361 (2006).
41. X.-Y. Wang, "Association of triatomic molecules by ultracold ^{40}K-^{23}Na^{40}K atom-molecule Feshbach resonances," thesis, Institute of Chemistry, Chinese Academy of Sciences (2022).
42. A. Christianen, M. W. Zwierlein, G. C. Groenenboom, T. Karman, *Phys. Rev. Lett.* **123**, 123402 (2019).
43. P. D. Gregory, J. A. Blackmore, S. L. Bromley, S. L. Cornish, *Phys. Rev. Lett.* **124**, 163402 (2020).
44. Y. Liu *et al*., *Nat. Phys.* **16**, 1132–1136 (2020).
45. J. J. Zirbel *et al*., *Phys. Rev. Lett.* **100**, 143201 (2008).
46. M. A. Nichols *et al*., *Phys. Rev. X* **12**, 011049 (2022).
47. H. Yang *et al*., Data of creation of an ultracold gas of triatomic molecules, dataset, Zenodo (2022); https://doi.org/10.5281/zenodo.7247988.

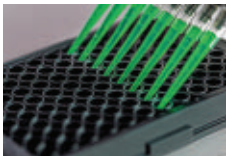
ACKNOWLEDGMENTS

Funding: This work was supported by the National Key R&D Program of China (under grant no. 2018YFA0306502), the National Natural Science Foundation of China (under grant nos. 11904355 and 12274393), the Chinese Academy of Sciences, the Anhui Initiative in Quantum Information Technologies, the Shanghai Municipal Science and Technology Major Project (grant no. 2019SHZDZX01), the Shanghai Rising-Star Program (grant no. 20QA1410000), and the Innovation Program for Quantum Science and Technology (grant no. 2021ZD0302101). **Author contributions:** B.Z. and J.-W.P. conceived the experiment. H.Y., J.C., Z.S., and J.R. carried out the experiment. All authors contributed to the analysis of the data and to the writing of the manuscript. B.Z. and J.-W.P. supervised the project. **Competing interests:** The authors declare no competing interests. **Data and materials availability:** All data needed to evaluate the conclusions in the paper are present in the paper or the supplementary materials. All data presented in this paper are deposited at Zenodo (*47*). **License information:** Copyright © 2022 the authors, some rights reserved; exclusive licensee American Association for the Advancement of Science. No claim to original US government works. https://www.science.org/about/science-licenses-journal-article-reuse

SUPPLEMENTARY MATERIALS

science.org/doi/10.1126/science.ade6307
Materials and Methods
Fig. S1
References (*48*–*50*)

Submitted 29 August 2022; accepted 2 November 2022
10.1126/science.ade6307



Nucleic Acid Extraction Kits for Pathogen Detection

AMS Biotechnology has added several new products to its growing range of magnetic bead–based nucleic acid extraction kits for pathogen detection. The MagSi-NA Pathogens MSP Kit overcomes false negative results by using a nondilutive technique to sequentially capture all viral RNA present in any of up to six samples, all in a single magnetic bead pellet. The automation-ready rQ MagSi-NA Pathogens Kit, consisting of conveniently prefilled deep-well plates, will also help labs increase throughput and allow for the preparation of up to 96 samples in less than 20 min. In addition, the new MagSi-DX Pathogens Kit has been specifically validated for SARS-CoV-2 diagnostic workflow and is ideal for labs requiring CE-in vitro diagnostic (IVD) products for use in human diagnostics. CE-IVD marked versions of MagSi-NA Pathogens MSP and rQ MagSi-NA Pathogens are scheduled for release in the coming months.

AMS Biotechnology
For info: +44-(0)-1235-828200
www.amsbio.com/magsi-na-pathogens-kit

Cas13a Nuclease (Lyophilized)

Cas13a is a class II and type VI CRISPR system effector protein with two higher eukaryotes and prokaryotes nucleotide-binding (HEPN) domains. It is a novel CRISPR protease that can be used for targeted RNA cleavage. While Cas13a recognizes and cleaves target RNA under the guidance of guide RNA, its collateral cleavage activity is activated, which can efficiently cleave nonspecific single-stranded RNA (ssRNA). The lyophilized version of Cas13a can be transported at room temperature, saving the high cost of dry ice transportation.

Beijing SBS Genetech
For info: +86-(0)-10-62969345
www.sbsgenetech.com/store/products/cas13a-nuclease-lyophilized

All-In-One Gene Expression System

Inducible expression vectors are an essential tool in life science research for controlled gene expression. However, transfecting two plasmids and background expression/leakiness in the off state are the primary concerns for such a system. OriGene has created a new and improved All-in-one Tet-On system—an upgraded version of the original system designed to stimulate the expression of the gene of interest. It has a tetracycline (Tet)-on 3G transactivation and a tightly regulated tetracycline-responsive element (TRE) promoter in one vector, making it an ALL-In-One system. Its key features include: (1) the presence of the transactivator and the promoter in the same vector, eliminating the need for another plasmid; (2) a modified 3G transactivator for high doxycycline sensitivity; and (3) a high level of induction with low leakiness. The All-in-One Tet-On system makes your experiments convenient and time-efficient.

OriGene
For info: 1-888-267-4436
www.origene.com

In Situ Hybridization Probes

BioGenex offers a comprehensive range of in situ hybridization (ISH) probes. In situ hybridization technique is used for precise detection and localization of a specific nucleic acid sequence within tissues and cells in molecular diagnostics of genetic variation. The underlying principle of ISH is that the nucleic acids within tissue and cell specimens can be detected by the hybridization of a complementary nucleic acid probe to which a reporter molecule is attached. Common nonradioactive labels for probes are fluorescein and digoxigenin. These probes allow quantitative detection of specific DNA/RNA sequences in their native form within the cells of formalin-fixed paraffin-embedded (FFPE) tissue sections. These probes offer reliable, highly sensitive, and easy-to-perform DNA and RNA ISH assays when used with BioGenex ISH Detection Systems.

BioGenex
For info: 1-800-421-4149
biogenex.com/ish-probes

Real-Time PCR System

Bio-Rad Laboratories announces the launch of the CFX Duet Real-Time PCR System to support researchers in developing singleplex and duplex quantitative PCR (qPCR) assays. The CFX Duet System offers the robust thermal performance and proprietary, accurate optical shuttle system of Bio-Rad's CFX Opus System, with thermal gradient functionality to enable optimization in fewer runs. The CFX Duet is a two-color system that is factory calibrated for common dyes and, without the need for passive reference dyes, allows the precise quantification of up to two targets in genotyping and multiple gene expression analyses. An additional fluorescence resonance energy transfer (FRET) mode supports protein melt analysis for basic protein characterization. The system utilizes CFX Maestro Software to provide easy experimental setup and analysis and to deliver customized reports without exporting data to other programs.

Bio-Rad Laboratories
For info: 1-800-424-6723
bio.rad.com/en-uk/product/cfx-duet-real-time-pcr-system

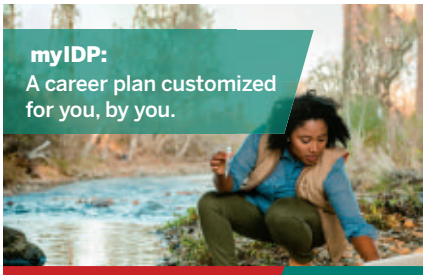
Improved Viral RNA Extraction

The Chromatrap Homogenizer Spin Column from Porvair Sciences maximizes the yield and quality of viral RNA extracted from nasal and throat swab samples. The easy-to-use spin column offers a fast, efficient one-stop alternative to using traditional syringe and needle homogenization techniques. Its novel dual-frit extraction design reduces lysate viscosity and captures insoluble debris by centrifugation; the homogenized lysate sample is then ready for RNA extraction. Employed as a single-use consumable, the column eliminates the possibility of sample cross-contamination. It is fully compatible with all manual RNA extraction kits and provides an ideal sample preparation solution for RNA miniprep and midiprep.

Porvair Sciences
For info: +44-(0)-1978-666222
www.chromatrap.com/homogeniser-spin-column

Electronically submit your new product description or product literature information! Go to www.science.org/about/new-products-section for more information.

Newly offered instrumentation, apparatus, and laboratory materials of interest to researchers in all disciplines in academic, industrial, and governmental organizations are featured in this space. Emphasis is given to purpose, chief characteristics, and availability of products and materials. Endorsement by *Science* or AAAS of any products or materials mentioned is not implied. Additional information may be obtained from the manufacturer or supplier.



There's only one Science

Features in myIDP include:

- Exercises to help you examine your skills, interests, and values.
- A list of 20 scientific career paths with a prediction of which ones best fit your skills and interests.

myIDP Visit the website and start planning today!
myIDP.sciencecareers.org

Science Careers In partnership with:

UCSF University of California San Francisco · UIC · BURROUGHS WELLCOME FUND · UMASS University of Massachusetts Medical School · FASEB Federation of American Societies for Experimental Biology

SAINT LOUIS UNIVERSITY SCHOOL OF MEDICINE

As part of a **four-faculty line expansion**, the Department of Biology at Saint Louis University (**https://www.slu.edu/arts-and-sciences/biology/index.php**) invites applications for **four tenure-track Assistant/Associate Professor positions** in the areas of Microbiology, Biochemistry, Neuroscience and Developmental Biology.

Microbiologist: research should address fundamental questions in areas including, but not limited to bacteriology, virology, mycology, microbial diversity and evolution, microbial ecology, disease ecology, host-pathogen interactions, emerging infectious disease, or antimicrobial resistance.
Biochemist: research should address fundamental questions in areas including, but not limited to, biochemistry, structural biology, enzymology, metabolism, biophysics, and/or biochemical pharmacology.
Developmental Biologist: research should address fundamental questions in areas including, but not limited to: stem cell biology, cell fate specification, aging, growth and regeneration, developmental genomics, evolution and development, and models of developmental disorders.
Neuroscientist: research should address fundamental questions in areas including, but not limited to, developmental neuroscience, neurophysiology, neuroendocrinology, neurochemistry, neuroinflammation, and/or neurodegeneration.

Successful candidates will be expected to: **(a)** establish an externally funded research program, and mentor both undergraduate and graduate (M.S. and Ph.D.) students; **(b)** support the service charge of the university; and, **(c)** contribute to teaching in general biology courses and courses related to their discipline.

Excellent facilities and a competitive start-up package are provided. Many opportunities for collaboration are available on campus, with researchers at SLU School of Medicine, and at world class institutions based in Saint Louis including the Missouri Botanical Gardens, Donald Danforth Plant Science Center, Saint Louis Zoo.

Candidates must have a doctoral degree and postdoctoral experience. Demonstrated experience in diversity, equity, and inclusion is desired.

Please go to this link and search for "biology" **https://slu.wd5.myworkdayjobs.com/Careers**
When prompted to upload your Resume/CV on the "My Experience" page, we ask that applicants submit the following documents:
• Cover letter (should list at least three references with contact information)
• Updated curriculum vitae
• Statement of research accomplishments and future research plans
• Statement of teaching and mentoring philosophy
• Diversity, equity, and inclusion statement

Application review will begin **December 16** and continue until the positions are filled.

Equal opportunity/affirmative action Statement: Saint Louis University is an equal opportunity/affirmative action employer. All qualified candidates will receive consideration for the position applied for without regard to race, color, religion, sex, age, national origin, disability, marital status, sexual orientation, military/veteran status, gender identity, or other non-merit factors. We welcome and encourage applications from minorities, women, protected veterans, and individuals with disabilities (including disabled veterans). If accommodations are needed for completing the application and/or with the interviewing process, please contact Human Resources at 314-977-5847.

UCLA College | Life Sciences Ecology & Evolutionary Biology

TENURE TRACK ASSISTANT PROFESSOR POSITION IN ECOLOGY AND EVOLUTIONARY BIOLOGY

The Department of Ecology and Evolutionary Biology (EEB) at UCLA is searching for a **tenure track Assistant Professor** that complements their research program with an outstanding commitment to equity and inclusion through research, mentorship, teaching, community engagement and/or service. Candidates in any area of ecology or evolutionary biology, broadly defined, will be considered. We particularly encourage applications from women, underrepresented minorities, and individuals with a commitment to mentoring underrepresented groups in the sciences. Necessary qualifications include a PhD degree in a relevant discipline and a strong background in quantitative methods. Evidence of sustained research productivity through journal publications is required. The successful candidate will be expected to develop an externally funded research program, and teach and mentor at both the undergraduate and graduate levels employing inclusive pedagogical approaches. We are especially interested in candidates that can complement existing departmental strengths in inclusive education, and develop courses that satisfy the UCLA undergraduate diversity requirement and/or courses that include topics of diversity, equity and inclusion and how they relate to the fields of ecology and evolutionary biology.

Application packages should be submitted online through **https://recruit.apo.ucla.edu/JPF07968** and include the following individual documents: **1)** curriculum vita; **2)** research statement including future directions (2 pages maximum); **3)** teaching statements that include teaching interests as well as experience employing pedagogies that promote active learning and inclusive teaching practices (1 page maximum); **4)** statement of contributions to equity, diversity, and inclusion that includes previous and planned efforts that advance EDI through formal and/or informal mentoring, research or education activities (no page limit); and **5)** cover letter that includes names of three referees who can be contacted for letters (reference letters will only be requested of select candidates; 1 page maximum). Review of applications will begin on **December 10, 2022** and continue until the position is filled. Inquiries about the position should be sent to search committee chair Professor Karen Sears (**ksears@ucla.edu**).

The University of California is an Equal Opportunity/Affirmative Action Employer. See full recruitment ad on https://recruit.apo.ucla.edu/JPF07968.

Shenzhen Institute of Advanced Technology
Chinese Academy of Sciences



Established in partnership between the Chinese Academy of Sciences and the Shenzhen Municipal Government, the Shenzhen Institute of Advanced Technology (SIAT) is a newly-created university with an objective to become the world's preeminent institute for emerging science and engineering programs. SIAT is equipped with state-of-art teaching and research facilities and is dedicated to cultivating international, visionary, and interdisciplinary talents while delivering research support to pursue innovation-driven development.

SIAT is located in Shenzhen, also known as the "Silicon Valley of China," a modern, clean, and green city, well-known for its stunning architecture, vibrant economy, and its status as a leading global technology hub. SIAT is seeking applications for faculty positions of all ranks in the following academic programs: Computer Science and Engineering, Bioinformatics, Robotics, Life Sciences, Material Science and Engineering, Biomedical Engineering, Pharmaceutical Sciences, Synthetic Biology, Neurosciences, etc. SIAT seeks individuals with a strong record of scholarship who possess the ability to develop and lead high-quality teaching and research programs. SIAT offers a comprehensive benefits package and is committed to faculty success throughout the academic career trajectory, providing support for ambitious and world-class research projects and innovative, interactive teaching methods.

Further information:
https://www.siat-sz.edu.cn/

Who's the top employer for 2022?



Science 2022 TOP EMPLOYER

Science Careers' annual survey reveals the top companies in biotech & pharma voted on by *Science* readers.

Read the article at
sciencecareers.org/topemployers



Science Careers helps you advance your career. Learn how!

- Register for a free online account on **ScienceCareers.org**.
- Search hundreds of job postings and find your perfect job.
- Sign up to receive e-mail alerts about job postings that match your criteria.
- Upload your resume into our database and connect with employers.
- Watch one of our many webinars on different career topics such as job searching, networking, and more.

Visit **ScienceCareers.org** today — all resources are free

ScienceCareers
FROM THE JOURNAL SCIENCE AAAS



SCIENCECAREERS.ORG

CLEMSON UNIVERSITY

ENDOWED CHAIR IN MEDICAL BIOPHYSICS

CLEMSON UNIVERSITY
CLEMSON, SOUTH CAROLINA, USA

Clemson University invites leading scholars to apply to become the founding holder of the **Dr. Waenard L. Miller, Jr. '69 and Sheila M. Miller Endowed Chair in Medical Biophysics.**

The successful candidate will receive a salary commensurate with experience, comprehensive resources and benefits, and faculty appointments to build innovative programs that elevate Clemson University's prominence in medical biophysics. Candidates will possess a vision to tackle major challenges in medical biophysics that will impact our fundamental knowledge of human health.

APPLY
Scan the QR code or
visit **apply.interfolio.com/97767**



By **Alexandra Ridgway**

Writing for the moment

I desperately needed to write. Eighty percent of the way through my Ph.D., with revisions to make and two more chapters to complete, I felt mounting pressure to get words on paper. When I was a child, the words would have come easily. I wrote inspired and quickly, churning out poem after poem for our local newspaper. But the rigid essay structures of high school and university extinguished my love of writing. I would sit at my computer late into the night, forcing the words out at turtle speed. Writing remained slow and laborious during graduate school—until I became a mum to twins.

Before my twins were born, I had envisioned tinkering away at my thesis while the babies slept blissfully in their bassinets. My university offered maternity leave, but I had chosen not to take it. I was nearly done with my doctorate and did not want to wait. I figured things would only get trickier as the twins got older.

But from the day my twins were born, I felt I had no time to do anything besides care for them, let alone write. My vision of bassinet naps was an illusion; the babies slept on my chest, in the pram, or not at all. One morning, I timed how long my son would sleep alone. The result: 6 minutes. How on earth could I complete my Ph.D. in such small snippets of time? With every day that went by without progress, I increasingly felt destined to become ABD: all-but-dissertation.



"As I learned to savor my limited slivers of writing time, my childhood love for it returned."

After my fingers came nowhere close to a keyboard for 6 weeks, I decided enough was enough; I would just have to use the rare minutes I had. I set up my work space, with my thesis cued up and ready to go. As soon as my babies drifted off, I flew to my computer, a sentence already formed in my mind, determined to see whether I could land those words on the page before the babies realized I was gone.

I managed to write a full sentence and a half before I heard whimpers from the other room. Part of me wished I had been able to stay at the computer longer, but I was nonetheless exhilarated by my incremental progress. Maybe this really could be the way forward.

In the weeks that followed, I continued what I dubbed "microwriting." Sometimes a baby would wake even before I made it to the computer. Those days filled me with fears that I would never finish my thesis and that I was fooling myself to think I could both care for my children and pursue my studies. But those moments also hardened my resolve; I had no choice but to try again tomorrow.

Over time, a sentence gradually turned into a paragraph and then a page. Even when I only got one word down, it was still one step forward.

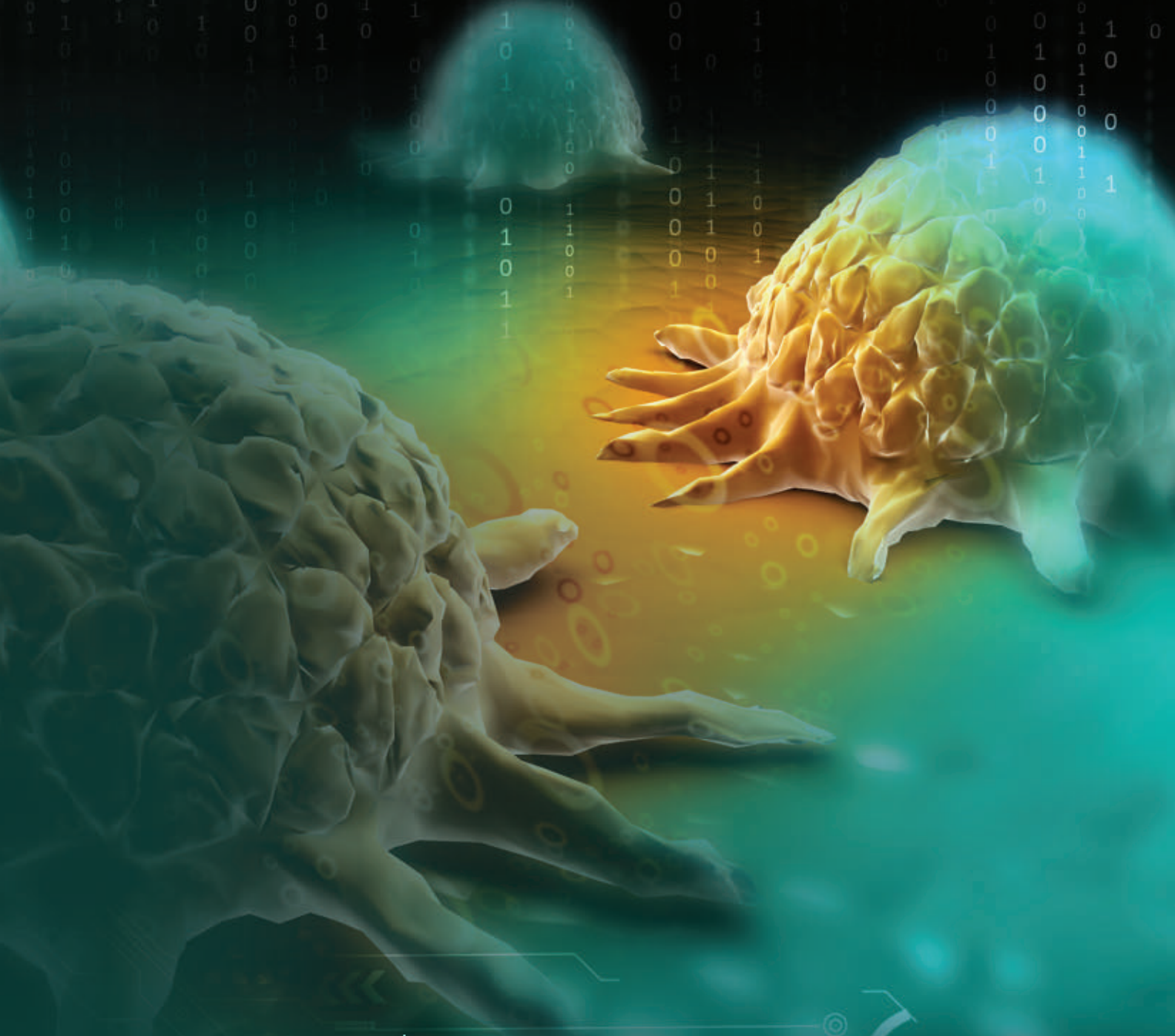
Although it was frustrating to never know whether I would make progress on any given day, I learned to live for the moment. Never had I been more present—with my writing, but also as a mother. Whichever role I was in, I was immersed in it completely. And as I learned to savor my limited slivers of writing time, my childhood love for it returned.

Over time, those slivers grew. My husband was able to reduce his working hours and kind friends walked the babies in the pram while I furiously typed away. When 6 minutes became 60, I was astonished at what I could do. And when I found myself falling back into my old plodding ways, I put the timer on for 6 minutes as a reminder of how valuable this time was. Bit by bit, I typed my way to submitting my thesis when the babies were about 3 months old.

By no means am I recommending that others forgo parental leave or try to race to the finish line as I did. But microwriting, which began as a necessity, has become core to my writing practice. The twins are now 3 years old and although I have more opportunities for extended focus, interruptions are still commonplace. But I've learned there is never a perfect time to write. I have to carve out moments when I can, no matter how small they may be, and cherish each opportunity to get words on paper. The time to write is now. ■

Alexandra Ridgway is a research assistant at the Royal Melbourne Institute of Technology University and a fellow at the University of Hong Kong. Send your career story to SciCareerEditor@aaas.org.

ILLUSTRATION: ROBERT NEUBECKER



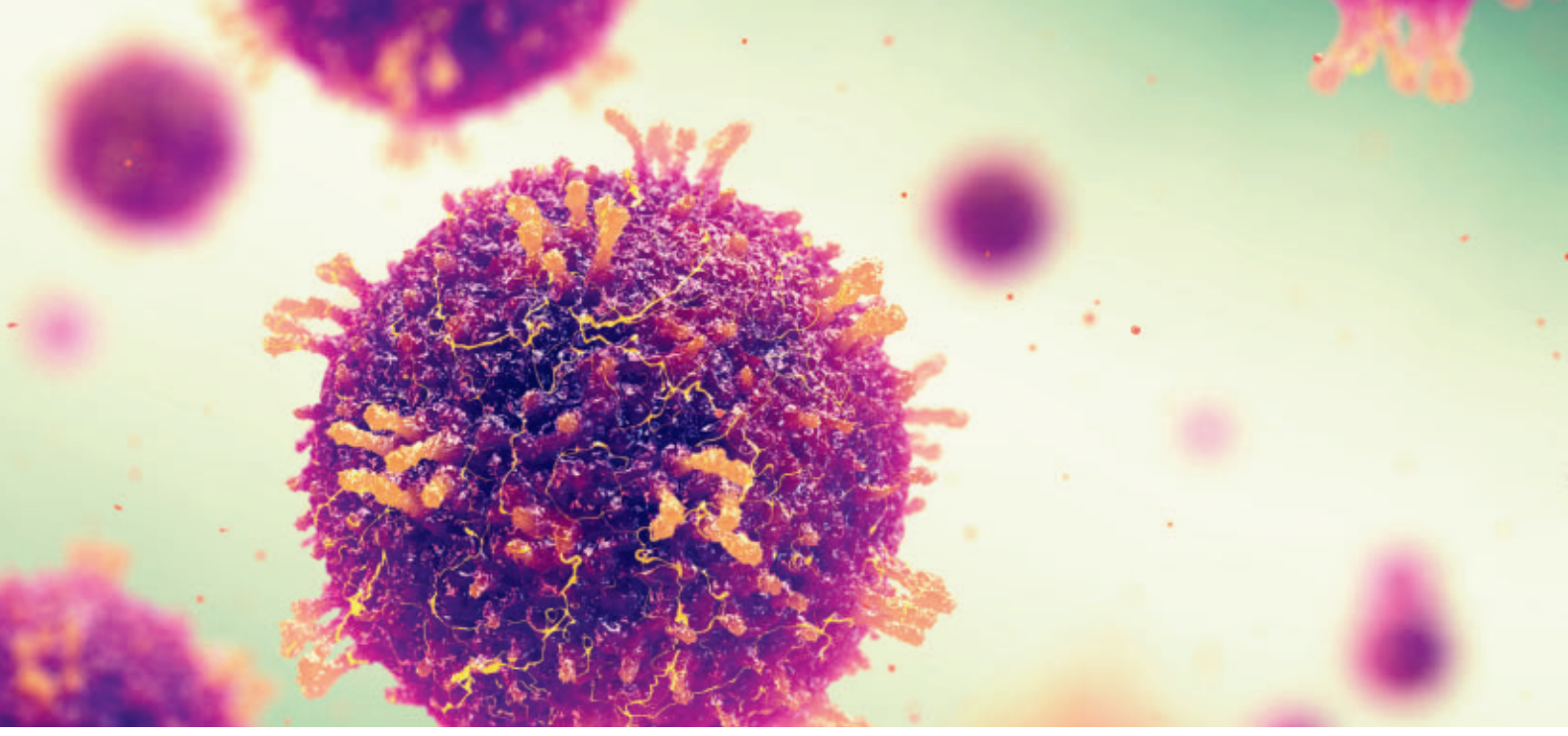
2023

AAAS MARTIN AND ROSE WACHTEL CANCER RESEARCH AWARD

Recognizing the work of an early career scientist who has performed outstanding research in the field of cancer. Award nominees must have received their Ph.D. or M.D. within the last 10 years. The winner will deliver a public lecture on their research, receive a cash award of **$25,000**, and publish a Focus article on their award-winning research in *Science Translational Medicine*.

For more information visit
www.aaas.org/aboutaaas/awards/wachtel
or e-mail wachtelprize@aaas.org.
Deadline for submission: **February 1, 2023**.

AAAS Science Translational Medicine



It's time to think differently.

Find out how NEB can support your infectious disease research and development.

Gaining a better understanding of infectious diseases, including their characterization, evolution and transmission, continues to be a priority, both from an R&D standpoint and as a public health issue. The COVID-19 pandemic has demonstrated the need for a wide range of tools to research infectious diseases, and has highlighted the importance of speed and the ability to pivot as new problems arise. This has emphasized the need for innovation and thinking differently about where to access those critical materials, including genomics reagents.

Many scientists know NEB as a trusted reagent supplier to the life science community, but what you may not know is that we also offer a portfolio of products that can be used in infectious disease research, development of diagnostics and therapies, and in epidemiological studies and disease surveillance. In fact, many of our products have supported the development of COVID-19 diagnostics and vaccines, and can also be utilized with other infectious diseases, such as influenza and malaria.

- Benefit from almost 50 years of experience in molecular biology & enzymology
- Partner with our OEM & Customized Solutions team to find the best solution for your needs
- Take advantage of our expanded manufacturing capabilities
- Access product formats, such as GMP-grade*, lyophilized, lyo-ready and glycerol-free
- Be confident in your product performance with our expanded quality and regulatory systems

Ready to get started? Learn more at
www.neb.com/InfectiousDiseases

"GMP-grade" is a branding term NEB uses to describe reagents manufactured at our Rowley, MA facility, where we utilize procedures and process controls to manufacture reagents in compliance with ISO 9001 and ISO 13485 quality management system standards. NEB does not manufacture or sell products known as Active Pharmaceutical Ingredients (APIs), nor do we manufacture products in compliance with all of the Current Good Manufacturing Practice regulations.

One or more of these products are covered by patents, trademarks and/or copyrights owned or controlled by New England Biolabs, Inc. For more information, please email us at busdev@neb.com. The use of these products may require you to obtain additional third party intellectual property rights for certain applications.

© Copyright 2022, New England Biolabs, Inc.; all rights reserved.

NEW ENGLAND BioLabs® Inc.

be INSPIRED
drive DISCOVERY
stay GENUINE